

NASA  
TT  
F-654  
c.1

G.S.Ivanov-Kholodnyi and G.M.Nikol'skii

# THE SUN AND THE IONOSPHERE

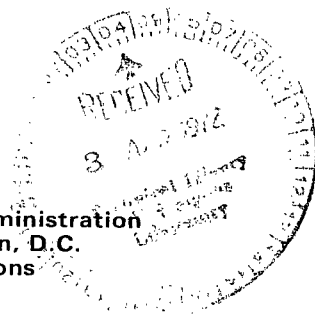
SHORT-WAVE SOLAR RADIATION AND  
ITS EFFECT ON THE IONOSPHERE

LOAN COPY: RETURN  
AFWL (DOUL)  
KIRTLAND AFB, NM



TRANSLATED FROM RUSSIAN

Published for the National Aeronautics and Space Administration  
and the National Science Foundation, Washington, D.C.  
by the Israel Program for Scientific Translations





G. S. Ivanov-Kholodnyi and G. M.

# THE SUN AND THE IONOSPHERE

## SHORT-WAVE SOLAR RADIATION AND ITS EFFECT ON THE IONOSPHERE

(Solntse i ionosfera. Korotkovolnovoe izluchenie solntsa  
i ego vozdeistvie na ionosferu)

Izdatel'stvo "Nauka"  
Moskva 1969

Translated from Russian

Israel Program for Scientific Translations  
Jerusalem 1972

NASA TT F-654  
TT 70-50184

Published pursuant to an agreement with  
THE NATIONAL AERONAUTICS AND SPACE ADMINISTRATION, U. S. A.  
and  
THE NATIONAL SCIENCE FOUNDATION, WASHINGTON, D. C.

Copyright © 1972  
Israel Program for Scientific Translations Ltd.  
IPST Cat. No. 5920  
ISBN 0 7065 1180 8

Translated by IPST Staff

Printed in Jerusalem by Keter Press  
Binding: Wiener Bindary Ltd., Jerusalem

Available from the  
U. S. Department of Commerce  
National Technical Information Service  
Springfield, Va. 22151

## Contents

Foreword . . . . .	vii
Chapter I. RESULTS OF OBSERVATIONS OF THE SHORT-WAVE RADIATION OF THE SUN . . . . .	1
1. Spectrographic observations . . . . .	1
2. Heliograms in the short-wave spectrum . . . . .	21
3. Observations of the X-ray emission of the Sun in wide spectral intervals . . . . .	28
Chapter II. PREDICTION AND IDENTIFICATION OF SHORT-WAVE LINES . . . . .	35
4. The general problem of identification of short-wave lines . . . . .	35
5. Wavelength and intensity prediction for short-wave lines . . . . .	36
6. Identification of short-wave lines . . . . .	45
7. Short-wave radiation energy . . . . .	48
8. Quantitative chemical analysis of the solar atmosphere from the results of short-wave observations . . . . .	52
9. "Unusual" identification in the short-wave spectrum . . . . .	57
Chapter III. THE PHYSICS OF THE SOLAR ATMOSPHERE . . . . .	59
10. Theory of ionization of the solar corona . . . . .	59
11. The temperature of the solar corona . . . . .	69
12. Distribution of temperature and matter in the transitional region between the corona and the chromosphere . . . . .	79
13. Specific features of the transitional region between the chromosphere and the corona . . . . .	92
Chapter IV. BASIC OBSERVATIONAL DATA FOR THE IONOSPHERE . . . . .	100
14. Results of radio sounding from the ground . . . . .	100
15. Rocket measurements of electron and ion concentration at altitudes of 50 — 300 km . . . . .	104
The D region . . . . .	104
The $\bar{n}_e(h)$ profiles . . . . .	105
Measurements of the ion composition . . . . .	113
16. Investigation of the upper ionosphere . . . . .	116
Rocket measurements . . . . .	116
Satellite measurements . . . . .	117



The method of noncoherent backscattering . . . . .	121
Ion and electron temperature . . . . .	124
17. The structure of the upper atmosphere . . . . .	127
Elements of the theory of the vertical structure of the atmosphere . . . . .	127
Temperature . . . . .	129
Density . . . . .	130
Neutral composition of the atmosphere . . . . .	134
Models of the upper atmosphere . . . . .	137
Variation of atmospheric parameters below 90 — 100 km .	139
18. Observations of electron streams in the ionosphere . . . . .	139
Trapped and injected electrons . . . . .	139
Energy flux . . . . .	140
Spectrum . . . . .	141
Indirect data . . . . .	153
Vertical variation . . . . .	154
Photoelectrons and secondary electrons . . . . .	154
Chapter V. PHYSICAL PROCESSES IN THE IONOSPHERE . . . . .	156
19. Ionization by short-wave solar radiation . . . . .	156
Elements of the theory of ion formation . . . . .	157
Ionization cross section in the X-ray spectrum . . . . .	160
Simple layer theory . . . . .	161
Radiation from a wide spectral region . . . . .	163
Ionization by radiation with $\lambda \geq 911 \text{ \AA}$ . . . . .	164
Rate of production of various ions . . . . .	166
Specific rate of ionization . . . . .	168
The energy problem of the ionosphere . . . . .	170
20. Corpuscular radiation . . . . .	172
Computation of the ionization effect . . . . .	172
The range $\rho_I$ . . . . .	174
A power spectrum of electrons . . . . .	175
Estimating $q_{\max}$ . . . . .	177
Examples . . . . .	178
Vertical distribution of ionization sources . . . . .	179
21. Recombination processes . . . . .	180
Dissociative recombination . . . . .	181
Mutual neutralization . . . . .	182
The effective recombination coefficient $\alpha'$ . . . . .	184
Quasi-equilibrium in the ionosphere . . . . .	185
Earlier measurements of $\alpha'$ . . . . .	186
New measurements of $\alpha'$ . . . . .	188
Summary of data on the $\alpha'(h)$ profile . . . . .	191
22. The photochemical theory of the ionosphere . . . . .	193
Elementary chemical processes . . . . .	193
Variations of the ion composition . . . . .	196

23. Ambipolar diffusion . . . . .	199
Definitions . . . . .	199
Chapter VI. THEORY OF FORMATION OF THE IONOSPHERE . . . . .	204
24. Formation of the ionosphere at altitudes $h \leq 100$ km . . . . .	204
Elements of the photochemical theory . . . . .	204
Ionization under quiet conditions . . . . .	206
Ionization during solar flares accompanied by SID . . . . .	209
Estimates of $n_i^-$ and $l^-$ . . . . .	213
25. Formation of the ionosphere at altitudes of 100 — 200 km . . . . .	215
Choosing the absorption (and ionization) cross sections and solar radiation intensities . . . . .	215
Variations of the $q(h)$ profile with time of day and with solar activity . . . . .	220
The rate of variation of $q$ during the day . . . . .	225
The reduced profile $q/n$ . . . . .	227
Relative rates of production of various ions . . . . .	230
Variations of the relative ion concentrations . . . . .	234
Variations of the absolute ion concentrations . . . . .	238
26. Variation of the effective recombination coefficient and formation of the $F_1$ region . . . . .	244
Linear and quadratic recombination . . . . .	244
Variations of the effective recombination coefficient . . . . .	247
Theory of formation of the $F_1$ layer . . . . .	250
27. Ionization of the nocturnal ionosphere at altitudes of 60 — 200 km and the corpuscular hypothesis . . . . .	253
Observation data . . . . .	254
The theory of the nocturnal ionosphere without a source . . . . .	256
Comparison with experiment . . . . .	258
The corpuscular hypothesis of ionization of the nocturnal ionosphere . . . . .	258
The mechanism of formation of the $E_s$ layer . . . . .	261
28. Formation of the $F_2$ region . . . . .	264
Vertical distribution of ions in the upper ionosphere . . . . .	264
The $F_2$ region (statement of the problem) . . . . .	266
Solution for the idealized case . . . . .	268
Exact solution . . . . .	270
Nonstationary solutions . . . . .	279
Summary of the $F$ region theory . . . . .	279
Table I. PREDICTION OF SHORT-WAVE LINES IN THE SOLAR SPECTRUM . . . . .	281
Table II. IDENTIFICATION OF LINES IN THE SHORT-WAVE SOLAR SPECTRUM ( $\lambda \leq 1216 \text{ \AA}$ ) . . . . .	315
BIBLIOGRAPHY . . . . .	342



## FOREWORD

New trends in science that crystallized in the post-war period and have been rapidly developing during the last 20 years include the application of satellites and rockets to outer space research (mainly the Sun) and to the upper atmosphere. The terms "rocket astronomy" and "rocket geophysics" have been coined for these two trends, respectively. The close relationship between solar and geophysical phenomena has become particularly clear through rocket experiments. General problems have emerged whose solution required the concerted efforts of astrophysicists and geophysicists.

The interpretation of the short-wave solar spectrum is among the problems which have come to the foreground following the observations of the short-wave radiation ( $\lambda < 2900 \text{ \AA}$ ) outside the atmosphere and direct sounding of the ionosphere. The solar spectrum at  $\lambda \leq 1500 \text{ \AA}$  was found to consist of numerous emission lines, and the energy at  $\lambda \leq 1000 \text{ \AA}$  was recognized to exceed many orders of magnitudes the photospheric emission in the same wavelength region (see Figure 1). A qualitatively similar picture had been expected long before the launching of space rockets. Once it had been established that the solar corona has a high kinetic temperature of up to a million degrees, Shklovskii showed (in 1945) that the corona would emit lines with wavelengths of a few hundred angstrom.\* Rocket observations, however, also revealed certain new properties of the short-wave spectrum which had not been suspected before. This, in particular, includes the energy distribution in the spectrum and the estimates of the energy, which at  $\lambda \leq 1000 \text{ \AA}$  was found to be 1—2 orders of magnitude higher than previously expected. Emission lines of ions in intermediate ionization stages, i. e., existing in a wide range of temperatures from  $10,000^\circ\text{K}$  (the chromosphere) to  $1,000,000^\circ\text{K}$  (the corona), were discovered for the first time in the solar spectrum. Numerous lines had to be identified, in order to investigate the properties of the transitional region between the chromosphere and the corona and to establish the intensity distribution in the short-wave spectrum and its time-dependent variations (i. e., variation with the phase of the solar cycle). The most remarkable wavelength region is that extending below the bright hydrogen line  $L_\alpha$  ( $1216 \text{ \AA}$ ). The great majority of the lines emitted by the transition region fall in this part of the short-wave spectrum and these wavelengths ionize the atmosphere.

Geophysical rockets have radically changed our concepts of the ionosphere. We are now aware, in particular, that the vertical distribution of the electron density in the daytime ionosphere does not show a distinct layered structure (the  $D$ ,  $E$ , and  $F_1$  "layers"); there actually exist wide regions of increased electron density with smooth transitions between them. Our notions of the ion composition of the ionosphere have also undergone

\* To the best of our knowledge, the suggestion concerning the possible existence of short-wave radiation was first voiced by Kiepenheuer back in 1935.

revolutionary changes: rocket measurements have shown that the ionosphere contains molecular ions in large quantities, which cannot be regarded as products of photoionization by solar radiation but are actually produced by ion-molecular reactions. This meant that the theory of the fundamental elementary processes in the ionosphere had to be reconstructed on entirely new foundations. Rocket data on fast electron fluxes in the lower atmosphere have led to the corpuscular hypothesis of ionization of the ionosphere.

Direct measurements from rockets and satellites have established a number of highly important physical characteristics of the ionosphere which were previously inaccessible to observations from the ground. These parameters include the density, temperature and composition of the neutral atmosphere at various altitudes, the electron and ion temperatures of the ionized component under various conditions, etc. These measurements provided sufficient information for a more consistent theory of the formation of the ionosphere at any altitude and for the prediction of its variations during the day and during a solar activity cycle. As a result, some conventional established ideas about the ionosphere and the mechanisms of its formation had to be revised. This, in particular, related to one of the basic topics, the energetics and the rate constants of ionization and recombination processes in the ionosphere, as well as the basic mechanism of daytime ionization of the upper atmosphere by short-wave solar radiation.

"Pure ionospheric" problems are now known to be inseparably linked with "pure solar" topics, since a physical model of the ionosphere taking full account of ionization by solar radiation cannot be developed unless the origin and the properties of the short-wave solar radiation are known.

Some progress had been made toward the solution of this problem, but further research into solar-geophysical relations is needed. This will assist in tackling such applied problems as the forecasting of solar activity and the state of the ionosphere. No specialized monographs are available in the scientific literature on the subject of the short-wave solar radiation and its interaction with the ionosphere.

Our book naturally does not pretend to provide a full coverage of the problem. One of the reasons for this is purely subjective: each of the authors naturally places the main emphasis on his own research. During the 10 years that the authors have been working on the various problems treated in this book, certain ideas have crystallized which constitute the backbone of the presentation. These ideas are not always shared by other colleagues but, in all fairness, contradictory views are discussed in detail.

In our treatment of the relevant topics, we tried to cover most of the available material, and especially the experimental data which may prove to be of independent interest to the reader.

Chapters I through III (short-wave solar radiation) were written by G. M. Nikol'skii and Chapters IV through VI (the physics of the ionosphere) by G. S. Ivanov-Kholodnyi.

Moscow, February 1969

The authors

## Chapter I

### RESULTS OF OBSERVATIONS OF THE SHORT-WAVE RADIATION OF THE SUN

The review of the observational data presented in the first chapter is by no means complete. To simplify the reading, numerous observational results are presented in conjunction with the theoretical treatment in subsequent chapters, and the preliminary chapter is thus of necessity fairly brief. Experimental data which have no immediate bearing on the main topics of our interest have been omitted. The reader will be able to form a more complete picture by consulting the various review papers (see Bibliography).

#### 1. Spectrographic observations

The spectrum below  $2000 \text{ \AA}$  is generally referred to as the vacuum ultraviolet in spectroscopic laboratory work. In laboratory this spectral region was studied down to  $1200 \text{ \AA}$  by Schumann back in the 19th century. The solar spectrum, on the other hand, was extended beyond  $2900 \text{ \AA}$ , in the direction of shorter wavelengths, only as late as 1946. The development of short-wave spectroscopy in laboratory was characterized by a very fast growth. As early as 1921, Millikan advanced the short-wave limit to  $200 \text{ \AA}$ . In the 1930's, Edlen used a grazing-incidence diffraction-grating spectrograph to obtain the spectrum around  $4 \text{ \AA}$ , i. e., in the region which normally calls for the use of X-ray techniques. In laboratory, the spectroscopist is free to choose a suitable light source emitting a sufficient quantity of energy in the short-wave spectrum. The light beam easily can be transmitted through vacuum to avoid obstructive absorption. The astrophysicist, on the other hand, is handicapped by the necessity of launching his equipment to sufficiently high altitudes where the short-wave radiation can be measured.

After World War II, using captured German V-2 rockets, and subsequently the Aerobee and Viking rockets of their own design, the Americans began studies of the short-wave end of the solar spectrum, which previously had been inaccessible to earthbound observers.\*

The first launching of a rocket-borne spectrograph on 10 October 1946 gave a recording of the spectrum at  $2100-2900 \text{ \AA}$ ; the resolution was

\* Rocket-borne measurements of the solar spectrum had been planned by the German scientists (Kiepenheuer and Wegener), who built suitable equipment back in 1943. The Nazi regime, however, was not interested in "pure science," and the research program did not materialize.

poor, however, not exceeding  $4 \text{ \AA} / 1/$ . In later years, the short-wave edge of the observed spectra remained in the same position, but the resolution was gradually improved. These observations revealed a marked decrease in the spectral intensity at shorter wavelengths: the Planck (color) temperature drops from  $6000^\circ\text{K}$  around  $3000 \text{ \AA}$  to about  $4500^\circ\text{K}$  around  $2000 \text{ \AA}$ . In 1949, the solar spectrum was extended to  $1900 \text{ \AA}$ , although with very low resolution. In parallel with the development of spectrographic techniques, filters defining wide wavebands were being used for observations, in conjunction with phosphors or photon counters as detectors.  $\text{LiF}$  and  $\text{CaF}_2$  isolate the two spectral regions  $1040 - 1340 \text{ \AA}$  and  $1230 - 1340 \text{ \AA}$ , respectively. Similar measurements carried out at the Naval Research Laboratory in the USA established that the solar radiation in these spectral regions cannot be described by a Planckian function. The altitudes in the Earth's atmosphere where the absorption in certain wavebands becomes acceptably low were determined (around  $100 \text{ km}$  for the  $1400 - 1700 \text{ \AA}$  region and over  $20 \text{ km}$  for  $1700 - 2100 \text{ \AA}$ ). Studies of the X-ray spectrum of the Sun began in the same period. Wide-band filters were used, first in conjunction with photographic techniques and subsequently with photon counters. In 1952, a Colorado University group (Rense et al. /2/) obtained the first spectrum showing the  $\text{L}_\alpha$  line of hydrogen ( $1215.7 \text{ \AA}$ ). This is the strongest emission line in the short-wave region of the solar spectrum (below  $2500 \text{ \AA}$ ).

Different research groups photographed the solar spectrum between  $2900 \text{ \AA}$ , the wavelength which suffers from considerable absorption in the lower atmosphere, and  $1500 - 2000 \text{ \AA}$ , where the continuum intensity decreases and a line emission spectrum appears. Besides numerous absorption lines, this part of the spectrum contains the strong emission lines  $\text{Mg II } 2795.5 \text{ \AA}$  and  $2802.7 \text{ \AA}$ . These are reversals in wide absorption lines, analogous to the famous K and H lines of  $\text{Ca II}$ . The total emission energy in the  $\text{Mg II}$  lines reaches  $18 \text{ erg/cm}^2\text{sec}$  /3/. The most detailed identification of lines in this part of the spectrum is given in /4, 5/. However, astrophysicists and geophysicists are mainly interested in the emission spectrum of the Sun between  $2000 \text{ \AA}$  and the X-ray region (Figure 1).

Without going into the remarkable history of the rocket astronomy (see Tousey /6/ on this subject) and without listing all the publications, we will only observe that the principal experimental results for the short-wave radiation of the Sun were obtained in the USA by three groups: Rense et al. (Colorado University, Boulder, Colo.), Friedman and Tousey et al. (Naval Research Laboratory), and Hinteregger et al. (Cambridge Air Force Research Center).

Short-wave spectra have to be taken with diffraction-grating spectrographs, since prisms are inapplicable in the far ultraviolet: no refracting optics is transparent at these wavelengths. Gratings, however, have their characteristic shortcomings: diffraction gratings, which double as camera mirrors, produce strong scattered light, which is a considerable nuisance in rocket spectroscopy. Two different grating systems are used: oblique or grazing incidence gratings and normal incidence gratings. Normal incidence gratings are generally used in conjunction with a pre-dispersion grating which acts as a collector mirror; they are employed for the relatively "long-wave" region of rocket spectra ( $\lambda > 500 \text{ \AA}$ ).

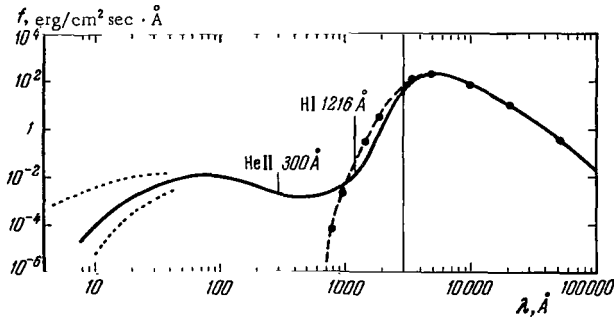


FIGURE 1. The observed energy distribution in the solar spectrum from the X-ray region to the far infrared:

Energy density  $f$  per  $\Delta\lambda = 1 \text{ Å}$  is given at a distance of 1 a.u. from the Sun. The dashed line drawn through the dots plots the blackbody emission at  $T = 6000^\circ\text{K}$ . The dashed lines in the X-ray spectrum indicate possible changes in flux level due to changes in solar activity. The vertical line marks the cutoff in the Earth's atmosphere.

A normal incidence spectrograph is essentially free from aberrations, whereas a grazing incidence spectrograph ensures a substantially higher reflection coefficient and linear dispersion at the shortest wavelengths, while suffering from aberrations and being difficult to adjust. According to Edlen, the same grating used at incidence angles of  $0^\circ$  and  $85^\circ.6$  gave spectra with a short-wave limit at 320 and 53 Å, respectively /7/. Schumann-type gelatine-free emulsions are usually used as photographic material. The spectrum is scanned with a photoelectric detector, whose output signals are telemetered to Earth. Although it has obvious advantages, this method suffers from low resolution and complex equipment.

The determination of the absolute intensities of short-wave lines is a formidable undertaking, especially at wavelengths shorter than 500 Å: virtually no standard radiation sources are available in this spectral region, so that calibration and measurements are conducted under different conditions.

Measurements of short-wave radiation in relatively wide spectral bands or measurements of dominant monochromatic emission (such as the  $L_\alpha$  line) require an entirely different technique. Ionization chambers or photon counters are used as radiation detectors. Counters are more popular, and the filling together with the entrance window act as filters defining the short-wave and the long-wave edges of the counter response curve. This equipment is generally used in recording the emission of weak objects around 1000 Å, in measurements of the solar radiation flux in the  $L_\alpha$  line, and in X-ray observations.

Since unstabilized rockets change their orientation in space, automatic training equipment is used to aim the instruments to the Sun. One of the first systems of this kind was developed at the Colorado University /8/. These tracking systems, however, cannot eliminate the undesirable effect of rotation of the solar image about the rocket—Sun line, which may prove



quite harmful in certain experiments. The training accuracy in individual experiments has already reached 1–2" /9/.

We can now proceed with a description of the rocket spectrograms. The brightest emission line in the solar spectrum below 2000 Å is the resonance emission line of hydrogen  $L_\alpha$  1215.7 Å. The  $L_\alpha$  line is apparently the strongest in the entire short-wave line spectrum of the Sun, since the Mg II emission lines lie in the Fraunhofer spectrum. The  $L_\alpha$  line was first observed by Rense et al. /2/. The intensity of  $L_\alpha$  has been repeatedly measured by various techniques (ionization chambers, counters, photographic spectra). The data obtained for the period 1955–1966 (a total of 23 individual measurements) were analyzed by Weeks /10/, who obtained an  $L_\alpha$  flux of  $6.1 \pm 0.45$  erg/cm<sup>2</sup>sec in epochs of maximum solar activity and  $4.3 \pm 0.35$  erg/cm<sup>2</sup>sec in epochs of minimum. The spectrum in the  $L_\alpha$  region has been studied by various authors /11–15/. The first absolute intensity estimates for individual lines near  $L_\alpha$  were published by Aboud, Behring, and Rense /15/, who determined the intensities of 24 lines in the 1206–1817 Å region from spectrograms taken at altitudes of 95–150 km on 6 August 1957. Numerous spectrograms in this wavelength region were subsequently obtained by other authors.

Spectrograms extending to 84 Å were obtained by Violett and Rense with a Rowland-system grazing-incidence spectrograph launched on 4 June 1958 and 30 March 1959 /16/. A toroidal collector mirror was mounted in front of the slit. A 1×2 cm<sup>2</sup> grating was used for the first launch, but the grating area was subsequently increased to 1.8×3.6 cm<sup>2</sup>. Both gratings were ruled with 600 lines per 1 mm and had a radius of curvature of 50 cm. The dispersion at 1200, 600, and 300 Å was 12.6, 9.3, and 6.6 Å/mm, respectively, and the resolving power reached 0.4 Å in the  $L_\alpha$  region. The Colorado University tracking system was used. A list of some 150 lines, giving wavelengths and visual intensity estimates, was published in /16/. The intensity of  $L_\alpha$  was estimated at 1000 units, and the weakest lines were assigned an intensity of 5 units. The intensities of different lines can be visually compared only if the wavelengths cluster fairly closely, since these intensity estimates ignore the spectral selectivity associated, say, with the wavelength dependence of the reflection coefficients of the optical coatings and absorption in the Earth's atmosphere. About half the lines on the list of Violett and Rense /16/ were identified with the ions of the most abundant elements on the Sun (H, He, C, O, and others) in different ionization stages. These photographs showed for the first time the resonance line He II 303.8 Å, with a halfwidth of less than 0.5 Å (this is an upper-limit figure). Despite the relatively poor quality of the spectrograms in /16/, the authors achieved a significant "leap forward" into the short-wave spectrum and discovered numerous lines, some of which unfortunately proved to be "fakes."

Purcell, Packer, and Tousey at the Naval Research Laboratory, using an Aerobee High rocket, obtained the spectrum in the 500–1800 Å region from an altitude of 198 km on 13 March 1959 /17/. A normal incidence spectrograph was used, with 40 Å/mm dispersion, analogous to the one that had been employed in 1955, but with improved optics which reduced the scattered light. The grating was coated with layers of germanium and aluminum oxide. This combination suppressed the scattered light mainly in the region of its maximum (4000 Å) and gave a reflection coefficient of 15% which remained virtually constant to 600 Å. The diffraction grating

had a reflection maximum around  $1000 \text{ \AA}$ . The collector mirror in front of the grating had been mechanically deformed so as to correct the astigmatism of the grating. The system was thus stigmatic both in the longitudinal and in the transverse direction. However, the tracking system malfunctioned, so the Sun drifted across the slit and no information could be obtained about the variation of line intensities over the solar disk. The maximum exposure plate (30 seconds) showed about 100 lines, including 8 lines of the Lyman series and the continuum  $\lambda < 912 \text{ \AA}$ .

Detwiller, Garrett, Purcell, and Tousey /18/ describe the results obtained from a processing of the 19 April 1960 data /19/. The spectrogram taken with 60-sec exposure at altitudes between 206 and 157 km (Figures 2a, 2b) underwent photometry and was calibrated in energy units.

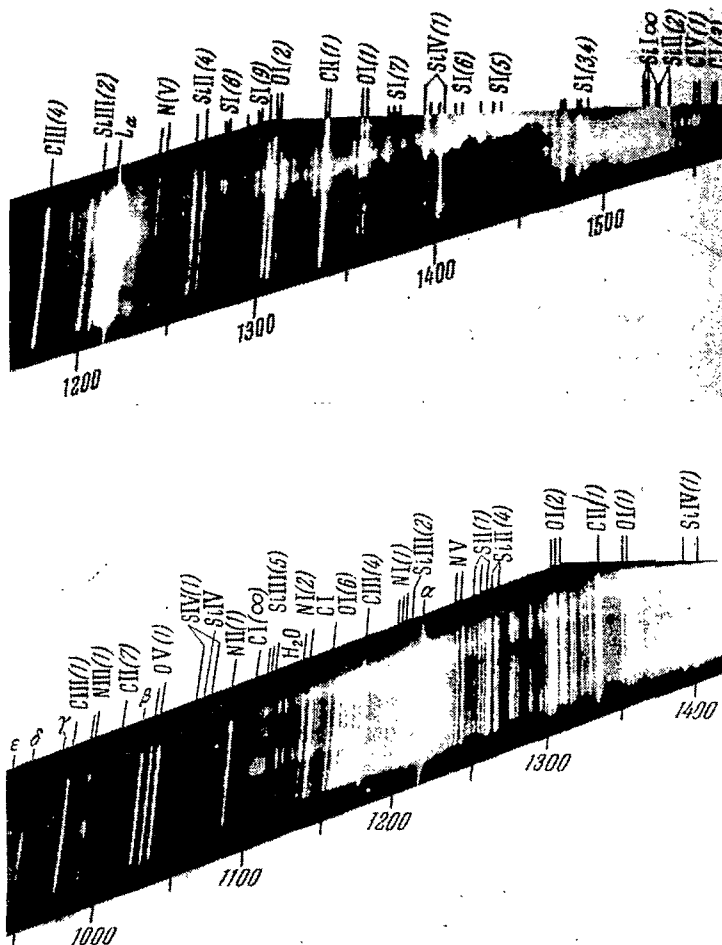
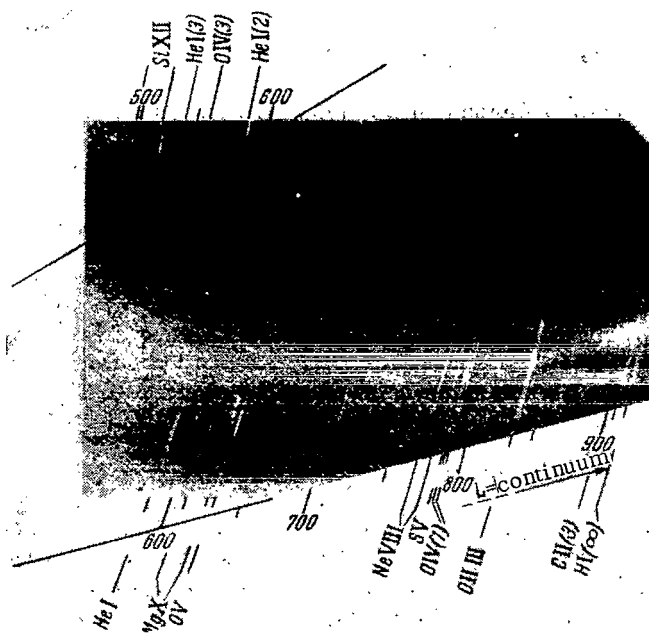


FIGURE 2a. The spectrum of the Sun in the  $1500-1000 \text{ \AA}$  region, obtained by Detwiller, Garrett, Purcell, and Tousey on 19 April 1960.



6

The calibration was conducted by tagging to the  $L_\alpha$  intensity, which had been measured with an ionization chamber mounted on the same rocket. These measurements gave an  $L_\alpha$  flux of  $5.1 \text{ erg/cm}^2 \text{ sec}$ . To obtain the spectral intensities, the authors also had to take into consideration the absorption by molecular nitrogen and oxygen and also the absorption by water vapor lifted by the rocket. Strong  $\text{H}_2\text{O}$  absorption bands are observed at the wavelengths of  $L_\beta$ ,  $1060 \text{ \AA}$ ,  $1110 \text{ \AA}$ ,  $1140 \text{ \AA}$ , and  $L_\alpha$ . The quantity of absorbing  $\text{H}_2\text{O}$  molecules in an elementary column was determined by measuring the depth of these bands. It was found equal to  $4.6 \cdot 10^{16} \text{ cm}^{-2}$ .  $\text{N}_2$  absorption bands crossing the Lyman continuum are also noticeable. The  $L_\gamma$  line  $972.5 \text{ \AA}$  (whose intensity is intermediate to that of  $L_\beta$  and  $L_\delta$ ) does not show on the spectrogram owing to the strong absorption in the  $\text{N}_2$  band which extends from  $972.1 \text{ \AA}$ . The weak line  $972.1 \text{ \AA}$  near  $L_\gamma$  apparently belongs to He II. Spectrograms taken at high altitudes show the  $L_\gamma$  line distinctly, although it is weak. Recombination emission beyond the limit of the Lyman series is very prominent: it extends to  $800 \text{ \AA}$  on the spectrograms. The total intensity in the Lyman continuum is estimated at  $0.24 \text{ erg/cm}^2 \text{ sec}$ , which corresponds to the blackbody emission at  $6600^\circ \text{K}$ . The total radiation flux of the higher members of the Lyman series is  $0.12 \text{ erg/cm}^2 \text{ sec}$ . We recall that all these energy estimates correspond to radiation emitted by the entire solar disk and to a distance of 1 a.u. A list of intensities and identification of the bright lines is reproduced in Table 1.

TABLE 1. The flux  $F$  at a distance of 1 a.u. from the Sun in the bright lines of the short-wave solar spectrum from photographic observations /18/

$\lambda, \text{ \AA}$	Ion	$F, \text{ erg/cm}^2 \text{ sec}$	$\lambda, \text{ \AA}$	Ion	$F, \text{ erg/cm}^2 \text{ sec}$
1892.03	SiIII	0.10	1265.04	SiII	0.020
1817.42	SiII	0.45	1260.66	SiII	0.010
1808.01	SiII	0.15	1242.78	NV	0.003
1670.81	AlII	0.08	1238.80	NV	0.004
1657.00	Cl	0.16	1215.67	HI	5.1
1640.47	HeII	0.07	1206.52	SiIII	0.030
1561.40	Cl	0.09	1175.70	CIII	0.010
1550.77	CIV	0.06	1139.89	Cl	0.003
1548.19	CIV	0.11	1085.70	NII	0.006
1533.44	SiII	0.041	1037.61	OVI	0.025
1526.70	SiII	0.038	1031.91	OVI	0.020
1402.73	SiIV	0.013	1025.72	HI	0.060
1393.73	SiIV	0.030	991.58	NIII	0.010
1335.68	CII	0.050	989.79	NIII	0.006
1334.51	CII	0.050	977.03	CIII	0.050
1306.02	OI	0.025	949.74	HI	0.010
1304.86	OI	0.020	937.80	HI	0.05
1302.17	OI	0.013	835	OII, III	0.010

In subsequent years the Tousey group obtained a number of additional spectrograms /20/ progressively advancing toward shorter wavelengths. The spectral region at  $170 \text{ \AA}$  was attained on 21 June 1961 with a normal incidence spectrograph (600 lines/mm grating, 40 cm radius of curvature). The launchings of 22 August 1962 and 10 May 1963 shifted the short-wave region even further. Better spectra in this region were obtained in 1963 (Figure 2c).

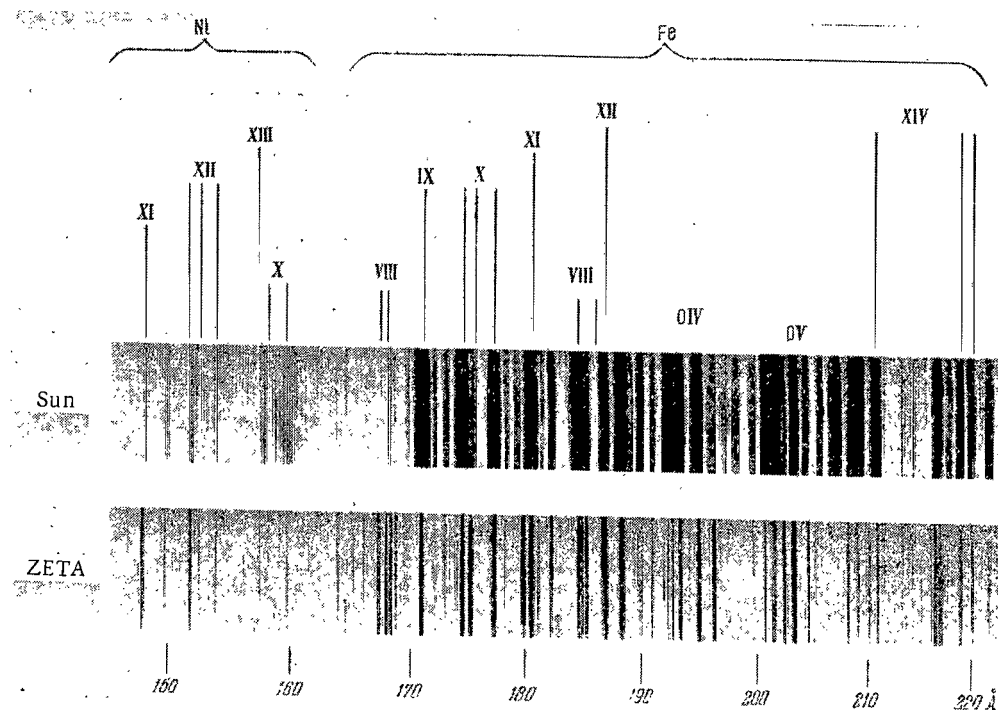


FIGURE 2c. The spectrum of the Sun in the 220–150 Å region, obtained by Austin, Purcell, Tousey, and Widing on 10 May 1963.

The spectrum is compared with the spectrum of a plasma discharge of about  $10^6$ °K produced in laboratory on the British ZETA machine.

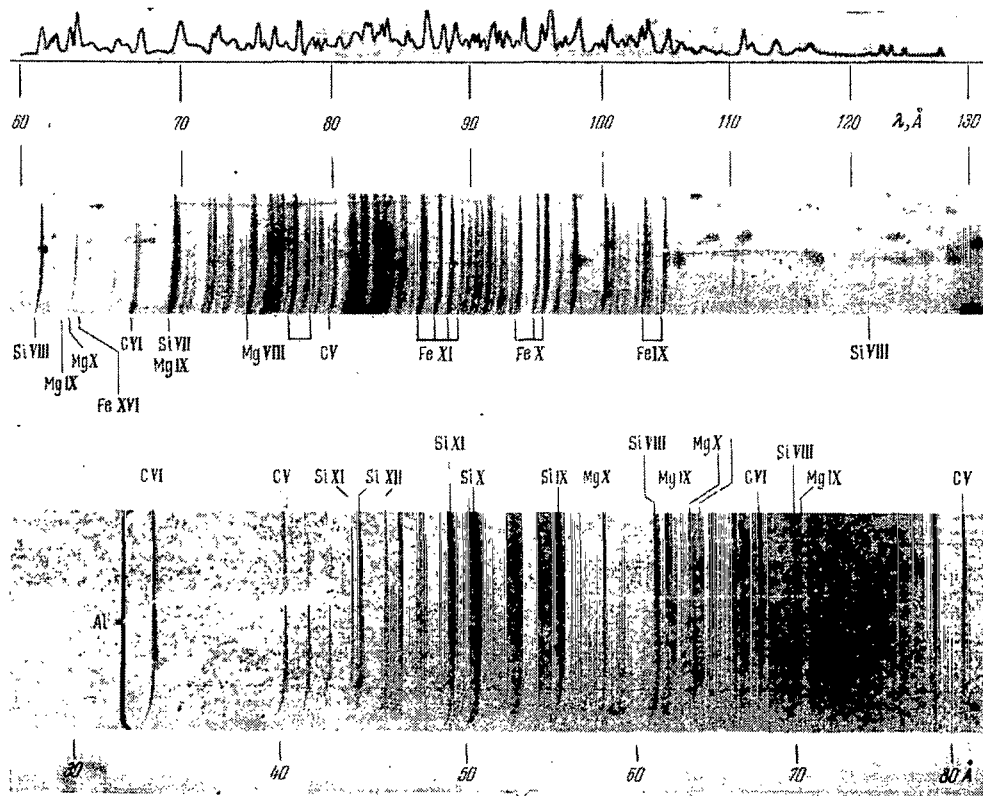


FIGURE 2d. The spectrum of the Sun in the 130–60 Å region (1 February 1966) and in the 80–30 Å region (20 September 1963), obtained by Austin, Purcell, Snyder, Tousey, and Widing.

The spectrophotometer tracing on top of the 130–60 Å spectrum was obtained by Manson (Cambridge, USA) on 3 September 1965 and is reproduced for comparison.

Finally, the spectrum at 33—188 Å was obtained on 20 September 1963 (a 2400 lines/mm grating, Figure 2d). The accuracy of wavelength determination on these spectrograms is between 0.02 and 0.1 Å, and the resolving power is 0.15 Å. The intensity of 30 lines between 33 and 70 Å was estimated by Austin, Purcell, Tousey, and Widing /21/. This is the only spectrogram available for the 33—55 Å region. A survey of the results obtained by the Tousey group will be found in /22/.

Photoelectric measurements of the short-wave spectrum of the Sun were conducted by Hinteregger's group. The first recording was obtained on 12 March 1959. This spectrum (250—1300 Å) was described by Hinteregger, Damon, Heroux, and Hall at the COSPAR symposium /23/. The spectrometer used a grazing-incidence grating at 86° (600 lines/mm, 2 m radius of curvature). The entrance slit was relatively wide, 0.8 mm. The scanning was done by a steel strip with exit slits which moved along the Rowland circle. The radiation passing through an exit slit was recorded with an open-type photomultiplier. The readings were telemetered to Earth. Gratings with 1200 and 2400 lines/mm penetrate as far as 125 and 60 Å. Four lines were recorded with this equipment: 282 Å, 335 Å, 304 Å (He II) and 1216 Å ( $L_{\alpha}$ ). The monochromator had been calibrated in laboratory to permit determining the absolute intensities. However, the emission of the standard laboratory source was so weak, that at wavelength shorter than 500 Å the calibration had to be based on extrapolated instrumental response values. The data of /23/ show that the 304 Å line is mainly absorbed at altitudes below 200 km.

Two subsequent launchings of the monochromator in January 1960 gave a recording of the short-wave spectrum of the Sun at 60—1300 Å. Hinteregger /24/, while computing the degree of ionization of interplanetary gas from his measurements of the solar radiation energy in the short-wave spectrum, gives spectrophotometer tracings obtained on 19 January 1960 (300—1300 Å) and 29 January 1960 (60—300 Å) at altitudes above 200 km. The resolving power varied from 2 Å at 60 Å to 16 Å in  $L_{\alpha}$ . A total of 60 maxima could be counted on the curve, which corresponded to emission lines, including the higher orders of bright lines. The total energy in the 60—1300 Å region in an epoch of high solar activity was 10 erg/cm<sup>2</sup>sec (15 erg/cm<sup>2</sup>sec corrected for atmospheric absorption) /24/.

In summer 1960, Hinteregger applied the same technique to obtain a recording of the 250—1300 Å region with higher resolving power (3—5 Å) /25/, and in 1961, together with Hall and Damon, he improved on these results, attaining resolutions from 1.5 to 3 Å /26/ (Figure 3). The total energy flux outside the Earth's atmosphere in this spectral region is almost a whole order of magnitude less than the previous estimate. This divergence in flux data is attributed by Hinteregger first to the higher quality of the last spectrogram (higher resolution, better suppression of scattered light) and second to an overestimation of atmospheric absorption in his earlier work. The second factor, incidentally, is not particularly significant, since the total fluxes outside the atmosphere and at 210 km altitude in the first experiment differ only by a factor of 1.5. A reduction in the level of solar activity may also have had its effect on the new results (the radio flux at 10.7 cm dropped to 1/2).

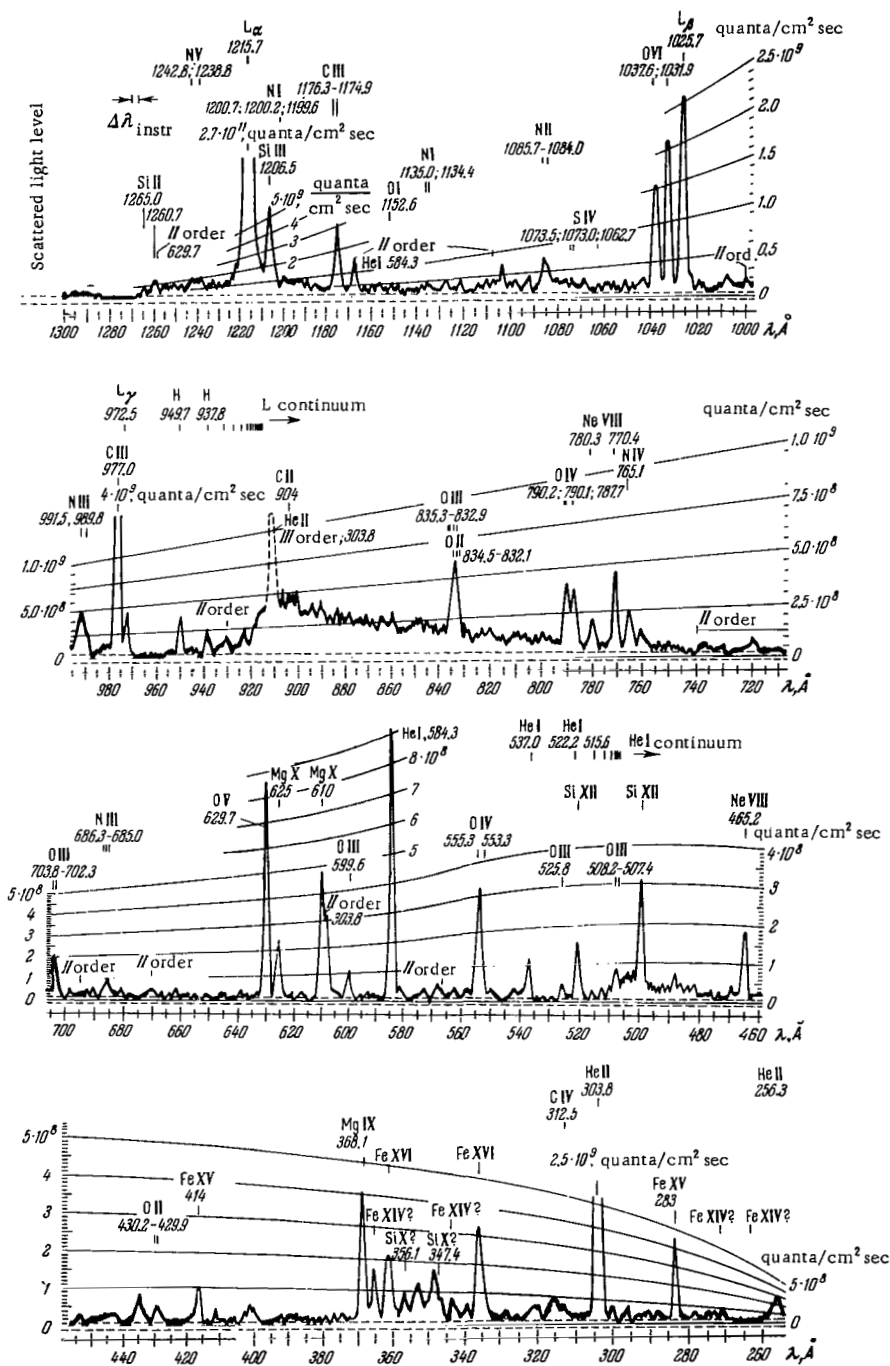


FIGURE 3. Photoelectric recording of the solar spectrum obtained by Hinteregger, Hall, and Damon (Cambridge, USA) on 23 August 1961.



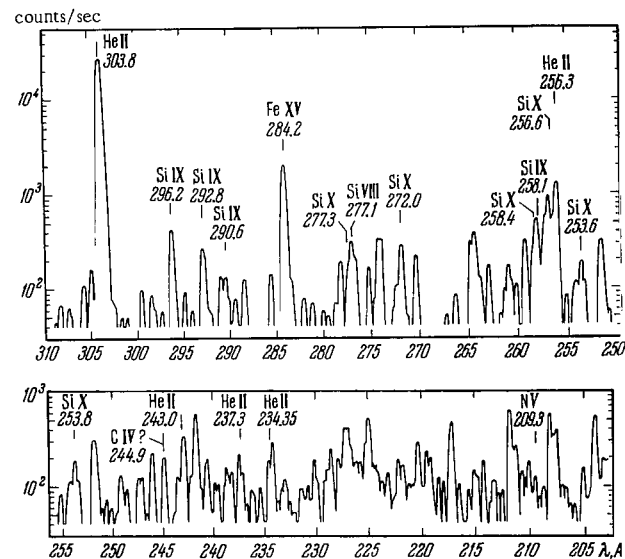
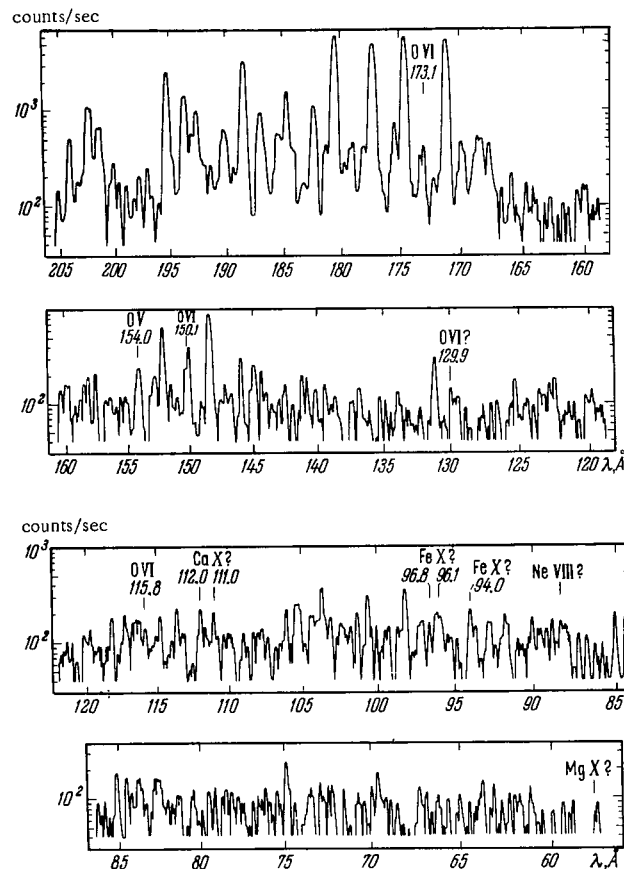


FIGURE 4. Photoelectric recording of the solar spectrum in the 60 — 305 Å region obtained by Hinteregger, Hall and Schweizer on 2 May 1963 (Cambridge, USA).

The last experiments used a grazing-incidence spectrometer with a 2-m Rowland grating (300 lines/mm). The errors in wavelength determination did not exceed 2 Å. According to /26/, energy calibration errors are  $\pm 10\%$  at 540–1216 Å,  $\pm 15\%$  near 400 Å, and  $\pm 25\%$  near 250 Å. The spectrum was recorded at altitudes between 90 and 225 km.

In 1963, Hinteregger's group achieved significant new results: they obtained a photoelectric recording of the spectrum to 55 Å with fair resolution. In particular, Hinteregger, Hall and Schweizer /27/ published a recording (55–310 Å) obtained on 2 May 1963. The spectrometer used a 1200 lines/mm grating with 2 m radius of curvature. The resolution reached about 0.1 Å. This remains the best available recording in this particular region of the spectrum. The curve is reproduced in Figure 4, where the vertical axis gives the logarithm of the counting rate. A conversion factor of  $1.4 \cdot 10^5$  may be used to convert the counting rate into photon flux (quanta/cm<sup>2</sup>sec at a distance of 1 a.u.) to within a factor of 2–3.

Friedman's group achieved excellent results using a new observation technique. A Bragg system spectrometer using an APP crystal (acid potassium phthalate) as the dispersing element was launched on an Aerobee rocket on 25 July 1963. Fourteen lines were registered between 13.7 and 24.8 Å. The wavelengths were accurate to within  $\pm 0.1$  Å. The radiation flux in the lines accounted for 80–90% of the total, and the balance was concentrated in the continuum, which presumably also contained the weaker blending lines. Blake, Chubb, Friedman, and Unzicker /28/ published the list of these lines and their intensities. Identifications with OVII and OVIII ions were carried out using a laboratory spectrum (theta pinch). The identification with Fe XVII and NVII was based on the data of Edlen and Tieren (1938, 1947). The data of Friedman's group provide the only results with absolute calibration for this region of the spectrum.

Highly interesting results were obtained by Mandel'shtam's group (Institute of Physics, USSR Academy of Sciences). Zhitnik et al. /29/ describe spectrograms obtained with geophysical rockets at altitudes of 500 km on 20 September and 1 October 1965. A grazing-incidence diffraction grating spectrograph was used (with 2° "grazing" angle), with a gold-coated grating (radius of curvature 1 m, 600 lines/mm, concentration of light around 60 Å). The slit was wedge-shaped with maximum width of 0.05 mm. The shortest wavelength appearing on the spectrogram taken on 1 October 1965 was the 9.5 Å line identified with Mg XI. A total of 14 lines and blends were recorded in the 9.5–34 Å region. The only new lines were the 10.9–11.9 Å blend, which was observed for the first time and identified in /29/ with Ne IX, Na X, Ne X, and the 28.5 Å line assigned to C VI. The remaining 10 lines had been previously observed by the Friedman group /28/ and two lines (30.0 and 31.8 Å) possibly correspond to the 14.9 and 16.0 Å lines in the second order spectrum. Unfortunately the authors of /29/ give only rough estimates of the radiation fluxes:  $5 \cdot 10^{-3}$  erg/cm<sup>2</sup>sec for the 10.9–11.9 Å blend and  $10^{-2}$  erg/cm<sup>2</sup>sec for the 14.9 Å line (Fe XVII). These fluxes correspond to solar radiation during chromospheric flares. Friedman et al. /28/ estimate the flux of the 14.9 Å line at  $2 \cdot 10^{-4}$  erg/cm<sup>2</sup>sec.

The region 25–33 Å has not been studied with sufficiently high resolution.

TABLE 2. Energy distribution in the short-wave spectrum of the Sun /30/

$\lambda_2 - \lambda_1$ OR $\lambda$ , Å	Identification	$F$ , erg/cm <sup>2</sup> sec
1215.7	HI L $_{\alpha}$	4.4
1206.5	SiIII	0.071
1220 — 1200 (no L $_{\alpha}$ , SiIII)		0.121
1200 — 1180		0.092
1175.7	CIII	0.042
1180 — 1130 (no CIII)		0.100
1130 — 1090		0.079
1085.7	NII	0.009
1090 — 1040 (no NII)		0.078
1037.6	OVI	0.025
1031.9	OVI	0.036
1040 — 1027 (no OVI)		0.013
1215.7 — 1027		5.1
1025.7	HI L $_{\beta}$	0.045
1027 — 990 (no L $_{\beta}$ )		0.056
997.0	CIII	0.081
972.5	HI L $_{\gamma}$	0.011
990 — 950 (no CIII, L $_{\gamma}$ )		0.021
950 — 920		0.031
920 — 911		0.028
1027 — 911		0.28
911 — 890	Lyman continuum	0.089
890 — 860	Lyman continuum	0.096
860 — 840	Lyman continuum	0.047
835 — 832	OII, OIII	0.013
840 — 810 (no OII, OIII)		0.048
810 — 796		0.017
911 — 796		0.31
790.1	OIV	0.003
787.7	OIV	0.008
780.3	NeVIII	0.004
765.1	NIV	0.006
780 — 760 (no NeVIII, NIV)		0.019
760 — 740		0.003
740 — 732		0.005
703.8	OIII	0.007
732 — 700 (no OIII)		0.015
700 — 665		0.020
665 — 630		0.017
796 — 630		0.153
629.7, 625	OV, MgX	0.056
630 — 600 (no OV, MgX)		0.039
584.3	HeI	0.053
600 — 580 (no HeI)		0.013
580 — 540		0.050
540 — 510		0.018
510 — 500		0.041
500 — 480		0.042
480 — 460		0.030
630 — 460		0.34

TABLE 2 (continued)

$\lambda_2 - \lambda_1$ or $\lambda$ , Å	Identification	$F$ , erg/cm <sup>2</sup> sec <sup>-1</sup>
460 — 435		0.022
435 — 400		0.047
400 — 370		0.029
460 — 370		0.098
368.1		
370 — 355 (no MgIX)	MgIX	0.031
355 — 340		0.050
340 — 325		0.044
325 — 310		0.045
303.8		
310 — 280 (no HeII)	HeII	0.047
370 — 280		0.25
		0.113
		0.58
280 — 260		0.062
257.256		
260 — 240 (no SiX, HeII)	SiX, HeII	0.023
240 — 220		0.064
220 — 205		0.081
		0.059
280 — 205		0.29
205 — 190		0.163
190 — 180		0.250
180 — 165		0.371
205 — 165		0.78
165 — 138		0.092
138 — 103		0.099
103 — 83		0.149
83 — 62		0.137
62 — 41		0.135
41 — 31		0.083
31 — 22.8		0.083
22.8 — 15		0.004
15 — 10		0.003
10 — 5		0.001
5 — 3		0.001
3 — 1		10 <sup>-6</sup>
		10 <sup>-7</sup>
165 — 1		0.70
1220 — 1 (no L <sub>a</sub> )		4.2

Table 2 summarizes the experimental data on the distribution of energy in the short-wave spectrum of the Sun. It is based on Hinteregger's review /30/. The accuracy and reliability of these data will be considered later, in Chapter II. The radiation fluxes for the 1216 — 60 Å region in Table 2 are given according to Hinteregger et al. /31/. At shorter wavelengths, Hinteregger obtained upper-bound estimates for an epoch of minimum solar activity on the basis of various sources. On the whole, the energy values in Table 2 correspond to minimum activity.

The determination of line widths in the short-wave spectrum constitutes a difficult problem, since the majority of short-wave lines are narrow: the expected halfwidth of the He II 304 Å line, for example, is approximately 0.04 Å (definitely not more than 0.07 Å /32/), whereas the spectroscopic

equipment used in these measurements has a low resolution (generally lower than  $0.1 \text{ \AA}$ ). The determination of the line widths emitted by ions in various stages of ionization is likely to yield valuable information on the physical conditions in the solar atmosphere and on the exact nature of the short-wave radiation.

So far only the profiles of the strong hydrogen lines ( $L_\alpha$  and  $L_\beta$ ) were determined: these are wide lines with halfwidths of about  $1 \text{ \AA}$ . One of the first photographs of  $L_\alpha$  obtained by Rense et al. /2/ revealed traces of self-reversal at the line center, despite the low resolution (reported at the 10th Congress of the International Astronomical Union in Moscow, 1958). The existence of a narrow dip at the center of  $L_\alpha$  was also predicted theoretically in 1958 /34/. It was suggested /34/ that this dip was produced by neutral hydrogen in interplanetary space.



FIGURE 5a. Spectrum and profile of the  $L_\alpha$  line obtained on 21 July 1959 by Purcell and Tousey (Naval Research Laboratory, USA). Resolving power about  $0.03 \text{ \AA}$ . Note the narrow absorption nucleus associated with the absorption in the geocorona.

Purcell and Tousey obtained a spectrogram of  $L_\alpha$  with  $0.03 \text{ \AA}$  resolution using a double-dispersion diffraction grating spectrograph in the 13th order (21 July 1959, Figure 5a) /35, 36/. Another series of similar spectrograms were taken on 19 April 1960 (Figure 5b). A microphotogram of the line profile is shown in Figure 5a. The most prominent detail is the narrow absorption nucleus at the line center, which is  $0.025 - 0.04 \text{ \AA}$  wide according to /35, 36/. These widths correspond to kinetic temperatures of  $800 - 2000^\circ\text{K}$  in the absorbing

medium. It thus follows that this radiation originates in the upper atmosphere of the Earth, in the so-called geocorona. The temperature of the interplanetary gas cannot be as low as this: the lowest temperatures in interplanetary space are  $10,000^\circ\text{K}$ . Theoretical computations /34/ used exaggerated concentrations of hydrogen in the interplanetary gas and ignored the existence of the geocorona.

The  $L_\alpha$  line also shows a wide reversal, splitting the line into two "peaks" separated approximately by  $0.4 \text{ \AA}$ . This reversal is of solar origin, being a result of the high optical thickness of the chromosphere.

On 22 August 1962, the same group obtained spectrograms of  $L_\alpha$  and  $L_\beta$  /20/ with lower resolution, which was selected so that the geocoronal absorption nucleus disappeared ( $0.07 \text{ \AA}$ ). Figure 5c shows the  $L_\alpha$  profile according to the 1959 and 1962 data for active and unperturbed regions of the solar disc. The wide central reversal varies from one area of the solar disc to another; it also shows variations in time. The profile of the  $L_\beta$  line is similar to that of  $L_\alpha$ , but the reversal is shallower and the separation of the two "peaks" is  $2/3$  of that observed for  $L_\alpha$ . This is not unexpected, since the oscillator strength of  $L_\beta$  is  $1/5$  of the  $L_\alpha$  oscillator strength and the wavelength is shorter. The central depression may be qualitatively accounted for by the theory of noncoherent scattering of resonance radiation in an optically dense medium /37 - 39/. A quantum undergoes multiple emissions and absorptions and eventually escapes from the absorbing region or is converted into heat (true absorption). For variety of reasons, each absorption event takes place at a different frequency, which remains close to the resonance frequency.

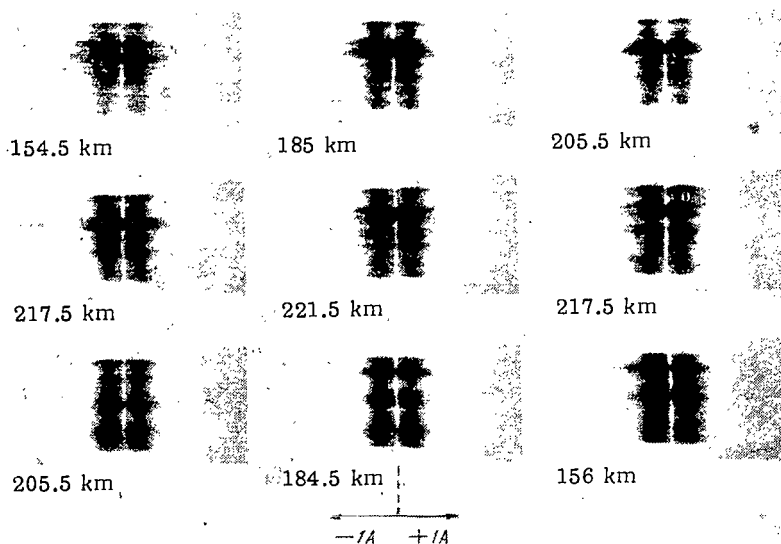


FIGURE 5b. Stigmatic spectrograms of the  $L_\alpha$  line obtained on 19 June 1960 by Purcell and Tousey.

Note the changes in spectrum along the slit, which crosses the solar disc: the line is brighter in active regions, and its wings extend farther. Because of the precession of the rocket, the position of the slit on the solar disc changed from one photograph to the next.

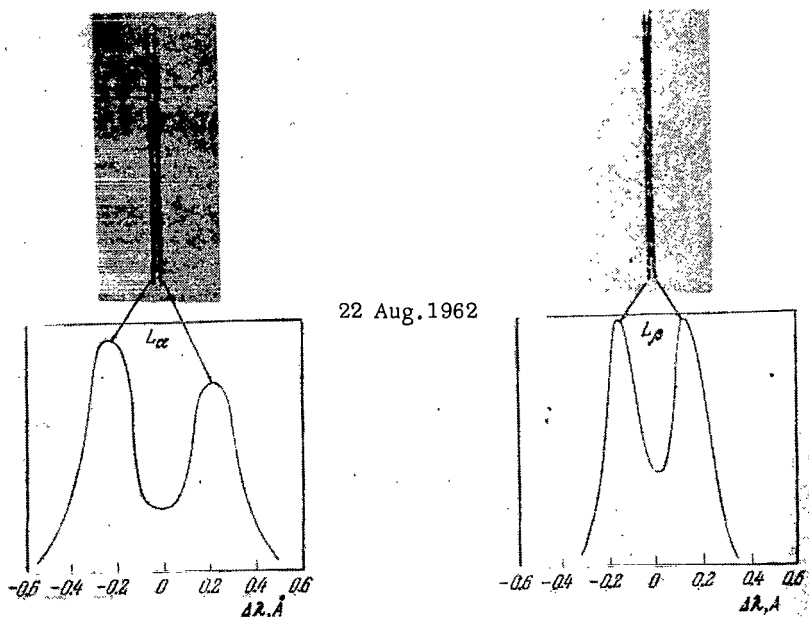
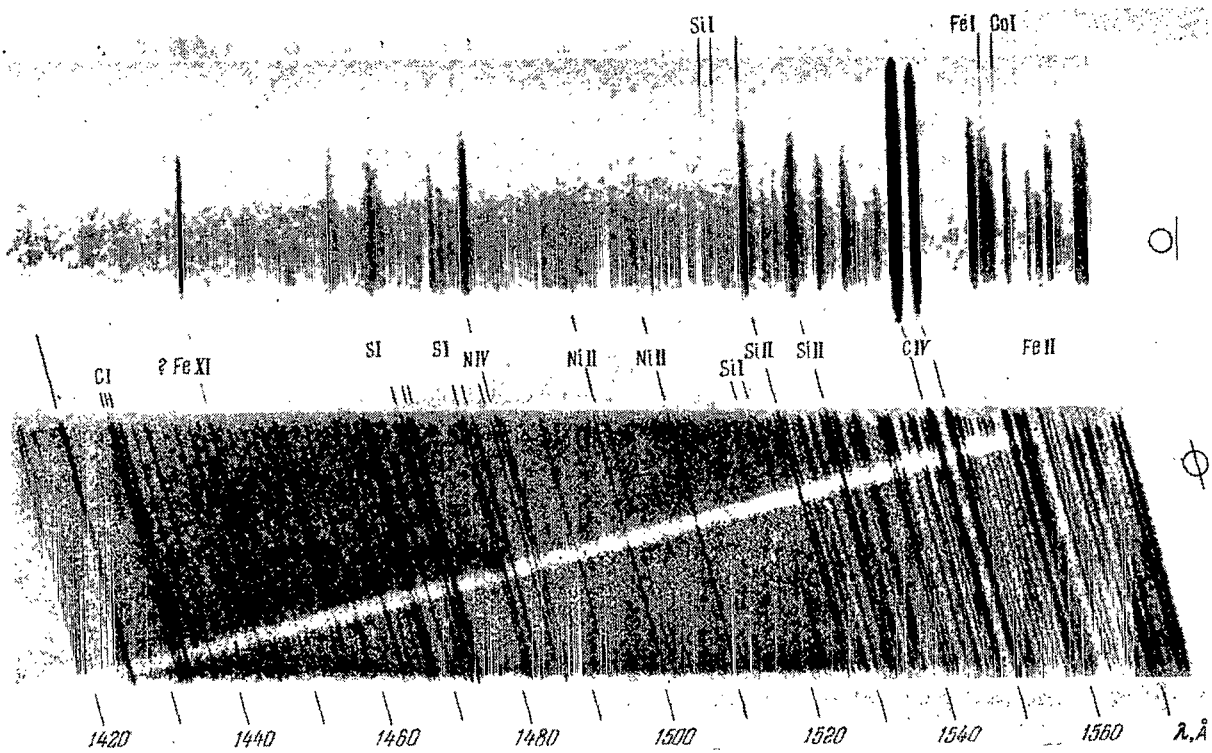


FIGURE 5c. Spectra and profiles of  $L_\alpha$  and  $L_\beta$  lines.

The relatively low resolution ( $0.07 \text{ \AA}$ ) was selected so as to suppress the geocoronal absorption. These photographs were taken by Tousey, Purcell, Austin, Garrett, and Widing in quiet parts of the solar disc.



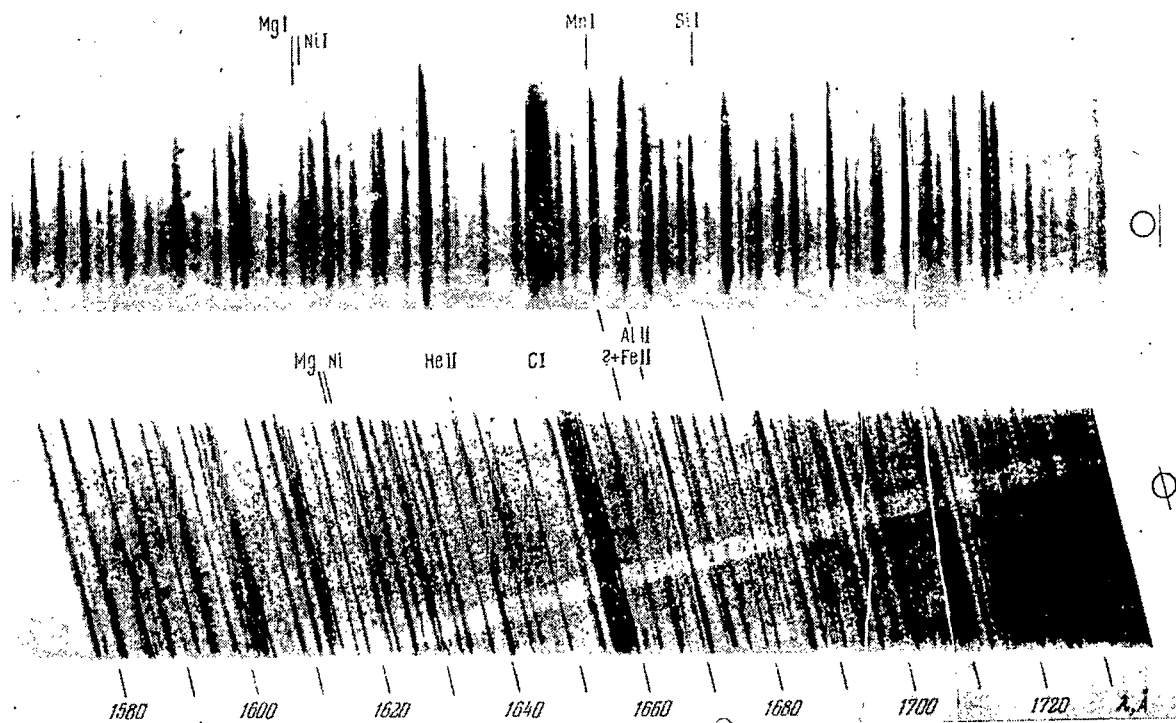


FIGURE 6. The short-wave spectrum of the solar chromosphere obtained by Burton, Ridgeley, and Wilson, 9 April 1965.

The spectrograph slit was aligned tangentially to the Sun's image at a distance of 7000 km from the limb. The stigmatic spectrum of the solar disc obtained at the Naval Research Laboratory is given at the bottom for comparison.



The main reason for the changes in frequency is the Doppler effect due to the movement of the atoms. Since the absorption coefficient diminishes with the distance from the line center, the probability of escape of a quantum increases, but the probability of production of such quanta decreases (the effect of the velocity distribution of the atoms). This mechanism is responsible for the appearance of the characteristic "two-hump" profile.

A theoretical analysis of the observation results for the  $L_\alpha$  line was carried out by Morton and Widing /40/. These authors used the theory of formation of optically thick lines in noncoherent scattering /38/ to determine the temperature of the regions where the wide central reversal originated. The results ranged between 50,000 and 100,000°K. These are inordinately high temperatures, especially if we remember that the major fraction of the  $L_\alpha$  emission originates in regions with temperatures of about 7000°K (the corresponding blackbody temperature). A number of critical comments aimed at Morton and Widing /40/ were made by Obridko /41/, who pointed to the inner inconsistencies in /40/ and estimated the upper-bound temperature for  $L_\alpha$  emission at  $T < (1-2) \cdot 10^4$ °K.

In conclusion of this section, let us consider the interesting results of Burton, Ridgeley, and Wilson /9/, who obtained the spectrum of the chromosphere at 977 — 2803 Å using a Rowland diffraction grating spectrometer with a slit oriented tangentially to the Sun's image at an altitude of 7000 km from the solar limb (9 April 1965). Part of the spectrum is shown in Figure 6. A special guiding system maintained a fixed slit orientation to within  $\pm 1500$  km. The spectrogram showed about 300 lines, and over 90% were identified. The line intensities were determined in absolute units. Unfortunately, no spectrum of the solar disc had been taken simultaneously with the spectrograms, and it was impossible to carry out a precise comparison of the intensities of corresponding lines in the chromosphere and on the disc. The authors therefore had to compare their intensities with the data of the Naval Research Laboratory which referred to the solar disc on 19 April 1960 /18/. The limb-to-disc intensity ratio varies for different ions between 0.01 and 0.1, and a fairly distinct growth of the ratio with the ionization potential of the emitting ion is observed. This dependence is shown in

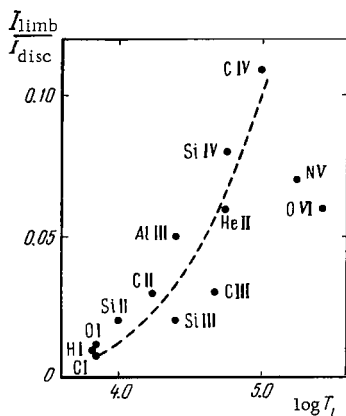


FIGURE 7. Intensity ratio of short-wave lines of various ions in the chromosphere and on the disc from the observations of Figure 6 vs. the ionization temperature of the ions.

Figure 7, where the ionization potentials are replaced with the ionization temperatures based on our data (see Chapter III). The two points NV and O VI, corresponding to the "hottest" ions, are somewhat puzzling. It should be remembered, however, that considerable errors have crept in, as different sets of initial data obtained in different periods were used.

Further development of these observations is of the greatest importance, as they provide new information about physical conditions in the solar atmosphere.

## 2. Heliograms in the short-wave spectrum

Heliograms taken in the light of various lines and in various regions of the spectrum constitute a highly important source of information about the short-wave radiation of the Sun. The distribution of the short-wave radiation brightness over the solar disc can be determined by a number of methods: 1) scanning with the spectrometer slit over the disc; 2) using a pinhole camera; 3) using a grazing-incidence reflector; 4) using slitless diffraction-grating spectrographs.

The first heliograms in soft X-rays were obtained by Chubb et al. in 1960 /42/. Subsequently, heliograms in other emissions (e.g., in He II 304 Å and He I 584 Å lines) were obtained in the USA, USSR, and England.

Heliograms in the X-ray spectrum ( $\lambda < 100$  Å) are particularly difficult to obtain because of unavailability of suitable optics.

The first heliogram and a number of later heliograms in the X-ray spectrum were obtained with a strikingly simple device — a pinpoint camera. In 1960, an assembly comprising eight pinpoint cameras was launched on a rocket. The diameters of the pinpoint apertures were 0.13 mm, and the "focal length" was 160 mm; this gave a picture of the Sun 1.5 mm in diameter with a resolution of 3' (1/10 of the diameter of the Sun's image). The cameras remained aimed at the Sun by a tracking system to within 1'. The tracking system in the first experiment /42/ did not correct for the rotational motion of the rocket about the camera axis, and all the features were "smeared" during the exposure along arcs 160° long on the photograph. These shots were processed by Blake, Chubb, Friedman, and Unzicker /43/. The X-ray emission (20 — 60 Å) was found to be concentrated in active regions coinciding with calcium flocculi and in areas emitting centimeter radio waves /42/. According to /42/, the contrast between the active and the quiet parts of the solar disc ranged between 37 and 108, with an average of about 55.\* The total solar emission at wavelengths shorter than 60 Å on 19 April 1960 (the date of the experiment) was 0.3 erg/cm<sup>2</sup>sec. Table 3 lists some basic data on the distribution of short-wave radiation over the solar disc. Unfortunately, no brightness contrast data between active regions and the quiet "background" are available, except for the first observations of the Sun in the soft X-ray region and some observations in L<sub>1</sub>. And yet calibration of heliograms is not a difficult undertaking. Heliograms can be calibrated, say, by taking a number of small photographs of the Sun with an assembly of equal length pinpoint cameras having entrance apertures of different diameters (an analog of a tube photometer). In certain cases, a rough estimate of contrast can be obtained by indirect methods, proceeding from the data of some publications. The corresponding figures in Table 3 are enclosed in parentheses.

The most promising methods for obtaining high-quality heliograms call for the use of slitless spectrographs and reflection telescopes using grazing incidence /22, 33, 47, 51, 57/ (Figures 8, 9). Although pinpoint cameras are attractively simple, the small area of the entrance aperture results in very low sensitivity. Experiments with reflectors have already led to very considerable advances: given the high resolving power, the exposures for heliograms around 10 Å were stepped up to a few seconds. Figure 10 shows a schematic diagram of a two-element telescope /57/ and Figure 11 is a

\*A high contrast ( $\approx 100$ ) between active and quiet regions in the X-ray spectrum of the sun has been predicted theoretically /90/.

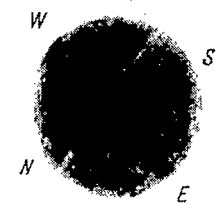
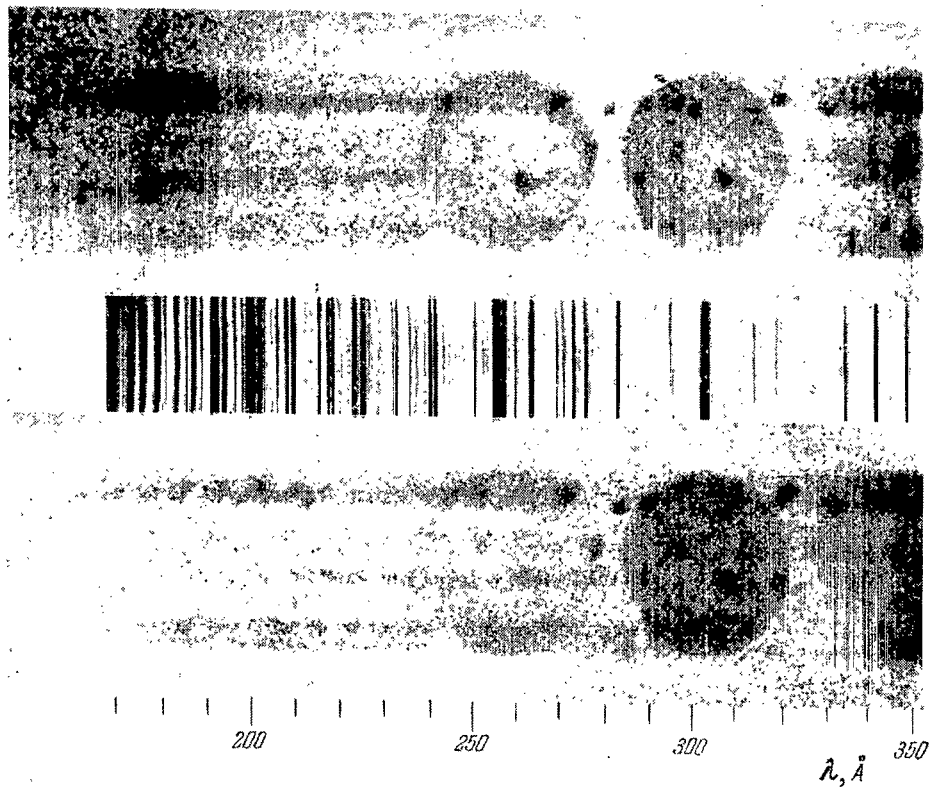
TABLE 3. Summary of observation results of the Sun in the short-wave spectrum (heliograms)

Date	$\lambda_2 - \lambda_1$ or $\lambda$ , Å	Contrast of active and quiet regions	Resolution	Method, comments	Authors, references
8.V.1956	$L_\alpha$ 1216	$> 1$	2'	Slitless spectrograph with an objective and 15° prism. Active region qualitatively coincides with $Ca^+$ flocculi, $d_\odot = 2.8$ mm	Rense, Miller, Mercure, Stuart /44/
13.III.1959	$L_\alpha$ 1216	$\approx 5$	0'.5	Two concave gratings. $L_\alpha$ flocculi coincide with $Ca^+$ , though larger. Prominences on limb.	Purcell, Pecker, Tousey /45/
19.IV.1960	20 — 60 34 — 108 40 — 90	$\approx 55$  High	3'  2'	Pinhole camera, $d_\odot = 1.6$ mm. Image diffuse because of rotation through 160°	Blake, Chubb, Friedman, Unzicker /42/
21.VI.1961	23 — 40 12 — 25	Higher Even higher	3' 6'	Pinhole camera. Image diffuse because of rotation through 180°	
4. IV.1963	8 — 15	( $\approx 200$ )	1'.3	Slit scanning over the disc. Contrast estimates based on size of emitting active region and its contrast relative to the background	Blake, Chubb, Friedman, Unzicker /28/
25. VII.1963	44 — 60 8 — 20 44 — 60	(35)* (90) (30)	0'.5		
*Contrast between weak and strong parts of an active region.					
10. V.1963	$L_\alpha$ 1216 $L_\beta$ 1025 OVI 1032 — 1038 CIII 977	Low	$\sim 1'$	Spectroheliogram of a 7' wide strip of the solar disc. Growth of brightness toward the limb, reaching maximum at 5303 Å (Fe XIV). Strongest in OVI lines	Tousey et al. /22, 46/
10. V.1963 28.VI.1963	FeXV 284 HeII 304 FeXVI 335 361 MgIX 368 HeI 584 OV 630			Slitless spectrograph with a concave grating	Purcell, Garrett, Tousey /47/
6. VI.1963	170 — 400 10 — 110 10 — 90		3'	Pinhole cameras. Image oscillates through $4R_\odot$	Zhitnik, Krutov, Malyavkin, Mandel'shtam /48/
25. VII.1963	44 — 70	High	2'	Pinhole camera used on 19 April 1960 and 21 June 1961	Blake, Chubb, Friedman, Unzicker /28/
20. IX.1963	FeXV 284 HeII 304 FeXVI 335 361 256	High ( $> 2-3$ )  High		Concave-grating slitless spectrograph. Brightness increase toward the limb, particularly at 5303 Å (Fe XIV)	Purcell, Garrett, Tousey /47, 22/
11. VIII.1964	< 25 44 — 70	High		Pinhole camera. Brightness increase toward the limb.	Russell /49/
17. XII.1964	< 60			Active regions coincide with $Ca^+$ flocculi	Blake, Booker, Burton, Jones, Shenton, Wilson /50/

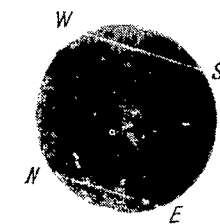
TABLE 3 (Continued)

Date	$\lambda_2 - \lambda_1$ or $\lambda$ , Å	Contrast of active and quiet regions	Resolution	Method, comments	Authors, references
16. II. 1965	$I_\alpha$ 1216	2 — 5	1'	Spectrograph launched on OSO-2 satellite. Quiet Sun	Tousey /33/
4. III. 1965	HeII 304	2 — 3	1'		
17. III. 1965	< 8 < 12 < 44	} Very high	< 1'	Grazing-incidence parabolic reflector. Coronal emission softer than the emission from disc flocculi	Giacconi, Reidy, Zehnpfennig, Lindsay, Muney /51/
9. IV. 1965	60 — 150 FeIX 171 HeII 304				
		} Very high	3' and 10'	Pinhole camera and plane grating. Marked limb brightening at 60 — 150 Å	Burton, Wilson /52/
		Low			
12. IV. 1965	MgII 2803 ± 2	Weak	1'	Cassegrain-Maksutov telescope with Scholtz interference- polarization filter. Low-con- trast absorption details noticeable	Fredga /53/
20. IX. 1965	< 10	Very high	1' and 5'	Pinhole cameras. Oscillation through $1.5 R_\odot$ . Our contrast es- timates from data of /29/	Zhitnik, Krutov, Malyavkin, Mandel'shtam, Cheremukhin /29/
1. X. 1965	< 20	High			
	< 25, 170 — 200	(≥ 20)			
20. X. 1965	$L_\alpha$ 1216	≈ 2	2"	Cassegrain telescope with ioni- zation chamber. Details smaller than 2" observed	Sloan /54/
20. X. 1965	< 24 < 40 < 32, 44 — 48	} Very high	2" 0'.1 2'.4'	Pinhole cameras. Details less than 1'. High-quality image	Russell, Pounds /55/
1. II. 1966	HeII 304 MgIX 368 FeXV 284 FeXVI 335 FeXVI 361	Average  } High		Slitless spectrograph. Quiet Sun. MgIX brighter at the limb. Underexposed in Fe light; only flocculi visible	Tousey /33/
6. IV. 1966	≈ 14 ≈ 24 ≈ 45	} (50 — 50)	2'	Pinhole cameras	Cauchois, Senemand, Bonnell, Montel, Senemand /56/
28. IV. 1966	150 — 700 MgIX 368 NeVII 465 SiXII 499 522 OIV 555 HeI 584 HeII 304 OV 630 FeIX — XVI (150 — 300)		10"	Slitless spectrograph. Numerous overlapping images of different brightness. Active Sun. Spec- troheliogram described in /33/. All images except HeI, HeII, ring-shaped. In HeI, HeII, rings around the limb, vanishing near the poles. Active regions in MgIX show lower contrast and are more diffuse than in FeXIV — FeXVI	Purcell, Snyder, Tousey /38/
20. V. 1966	< 8 8 — 12 12 — 16 16 — 20	} Very high	20"	Grazing-incidence two-element reflector, $d_\odot = 5.8$ mm. Photo- graphs of exceptional quality. Emitting regions extend beyond the solar disc.	Underwood, Muney /57/

Parenthetical figures are our contrast estimates.



Ca-K

 $H\alpha$

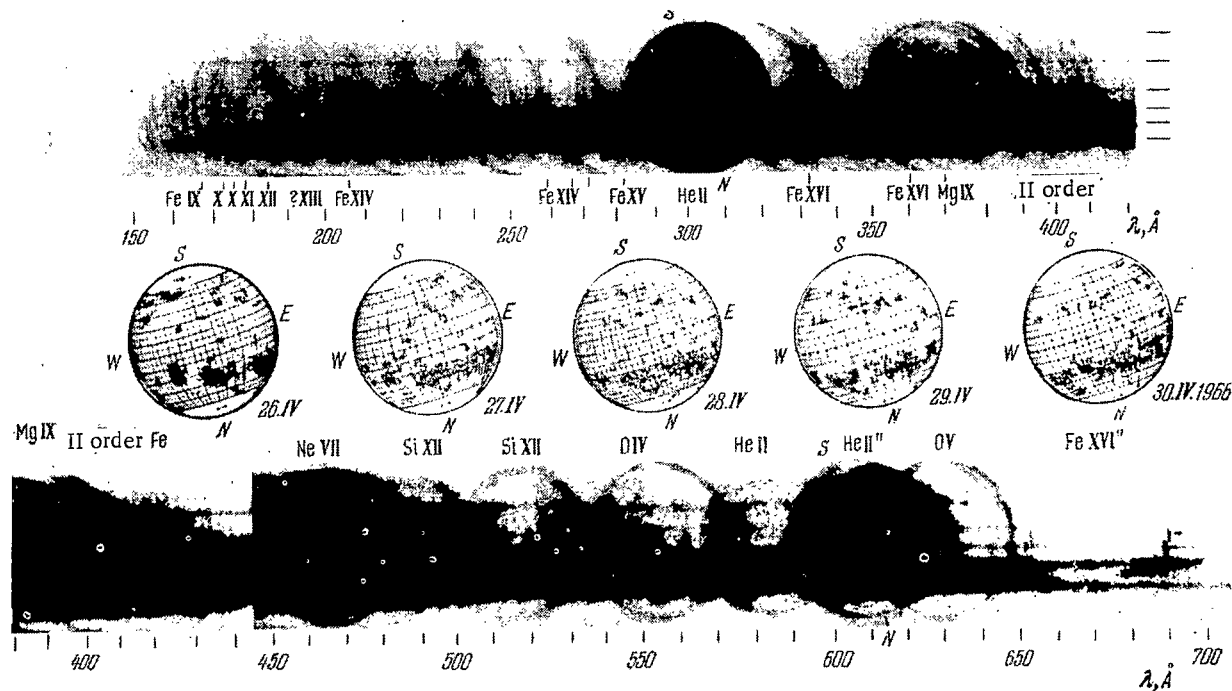


FIGURE 8a. Heliograms in the light of various short-wave lines, taken with a slitless spectrograph (Tousey's group, Naval Research Laboratory, USA).

Top: 10 May 1963. Center, slitless comparison spectrum of the Sun; right, heliograms taken from the ground in K and  $H_\alpha$  lines of Ca II. The slitless spectrograms clearly show three images of the entire disc: 257 Å, a blend of He II, Si X, S X, S XIII, and Si IX lines; 304 Å, He II; 348 Å, a blend of Si X and Si IX lines. The spots represent flocculi (active solar regions) in various lines.

Bottom, 28 April 1966. Resolution 10". At the center, charts of the Sun showing the position of the flocculi.

reproduction of the heliogram taken with this instrument on 20 May 1966. The stainless steel mirror with an entrance aperture of  $1.6 \text{ cm}^2$  effective area increased the reflection coefficient to 70% at about  $5 \text{ \AA}$  ("grazing" angle  $54'$ ).

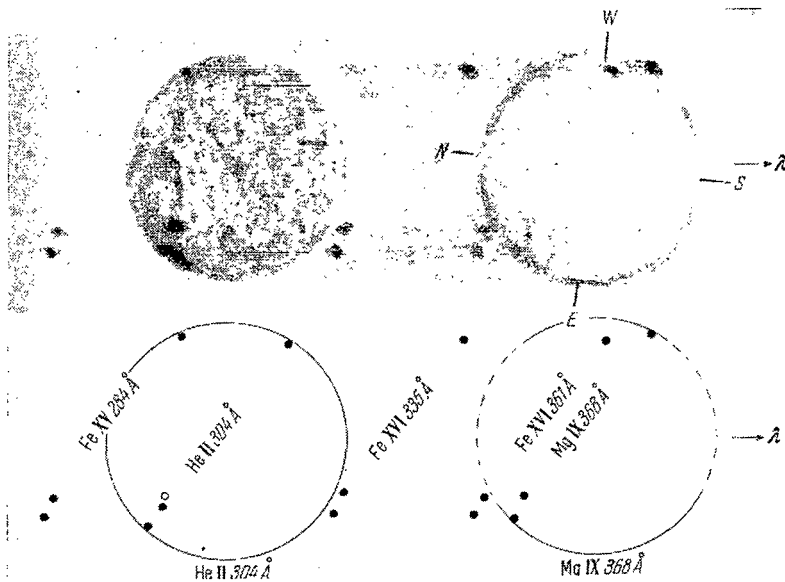


FIGURE 8b. Heliograms in the light of various short-wave lines, taken with a slitless spectrograph on 1 February 1966 (quiet Sun) /33/.

Note the difference in heliograms photographed in coronal lines and in the lines of the transitional region between the corona and the chromosphere. The schematic drawing at the bottom shows the position of the various emissions on the solar disc.

The basic results which emerge from heliograms amount to the following. The contrast between active and quiet parts of the solar disc in the soft X-ray region ( $\lambda < 100 \text{ \AA}$ ) is high and actually increases at shorter wavelengths. The quiet areas on the Sun virtually do not radiate at  $10 - 20 \text{ \AA}$ . In the X-ray spectrum and in the lines of highly ionized atoms (Fe XV, Fe XVI, C VI, and also O VI), the brightness of the limb increases so that the emitting regions actually spread beyond the solar disc to altitudes of about  $5 \cdot 10^4 \text{ km}$  ( $1'$ ) and higher. It is this emission that remains unobscured during the total solar eclipses, ionizing the *E* layers of the ionosphere. The measurements of Friedman's group carried out during the total eclipse of 12 October 1958 showed that the radiation at  $8 - 20 \text{ \AA}$  and  $44 - 60 \text{ \AA}$  reached 10—15% of the radiation of the uneclipsed Sun /58/.

Heliograms taken in the lines of ions of relatively low ionization stages (He II, C III, etc.) clearly show the entire solar disc, with relatively low-contrast active regions standing out prominently against the background. The increase in brightness toward the limb is either absent or very slight in this case. The contrast of the active regions thus increases with the

increase in the ionization potential of the emitting ions. This fundamental conclusion based on analyses of heliograms explained the existence of strong and weak variations of radiation in various short-wave lines. For example, the total emission of the Sun in  $L_\alpha$  (contrast about 5, Figure 12) may change by a factor of 1.5—2 from maximum to minimum, whereas in the X-ray region ( $\lambda < 40 \text{ \AA}$ ), where the contrast is at least 30, the variation amplitude is a factor of 10 or more.

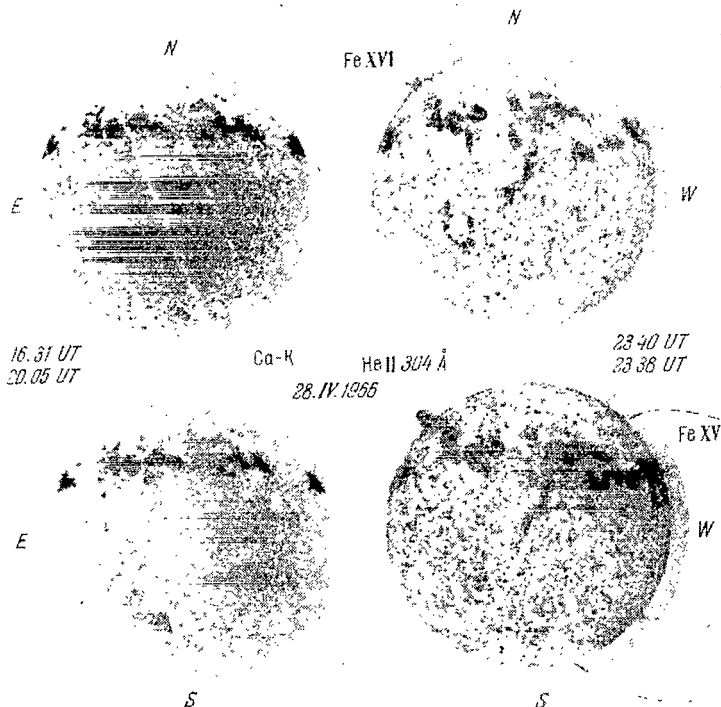


FIGURE 9. Comparison of the heliograms obtained on 28 April 1966 by Tousey /33/ in the  $\text{He II } 304 \text{ \AA}$  line with the heliograms taken in  $\text{Ca II K}$  light (McMath-Hulbert and Mount Wilson observatories).

The overall dimensions of the active regions reveal a tendency to decrease in "higher contrast" radiation. This points to a relative decrease in the volume of the active elements with increasing temperature.

The results of Sun's photographs taken with a reflector on 17 March 1965 were published recently /51/ (see Table 3). Reidy, Vaiana, Zehnpfennig, and Giacconi /722/ gave density contour lines for Sun's photographs around 8 and 44  $\text{\AA}$ . A calibration curve is given for the short wavelengths in /722/, which can be used to show that the brightest part of the active region ( $\lambda \approx 8 \text{ \AA}$ ) measuring 40" across has a contrast of 30 relative to the nearest "background" areas (the outermost density contour line with a diameter of some  $0.5 R_\odot$ ). A detailed chart of density contour lines at 44  $\text{\AA}$  was also published. The coronal emission extends up to altitudes of  $0.2 R_\odot$ .



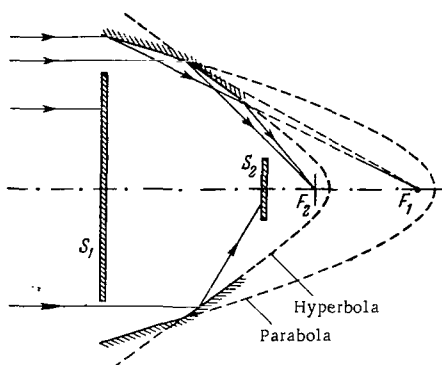


FIGURE 10. Schematic diagram of a grazing-incidence two-element Schwarzschild telescope.

Incidence angle  $89^\circ$ . Underwood and Muney (National Academy of Science and Goddard Space Center, USA) used this telescope to obtain the X-ray heliograms shown in Figure 11.  $S_1, S_2$  are screens which protect the emulsion from exposure to direct light.  $F_1, F_2$  are the foci of the parabolic and the hyperbolic mirror (diagonally hatched surfaces in the figure).

### 3. Observations of the X-ray emission of the Sun in wide spectral intervals

Let us briefly consider the observations of soft X-ray radiation from the Sun. The very hard radiation at wavelengths shorter than  $1 \text{ \AA}$  is generated by certain nonstationary processes on the Sun, which are not considered in this book. Moreover, radiation at these wavelengths does not have a substantial effect on the Earth's ionosphere.

The first measurements of the solar X rays were conducted by Friedman's group, who used photon counters with various gas fillings and entrance windows made of various materials (beryllium and aluminum foil, organic foils) as radiation detectors. This equipment permitted recording radiation in various spectral regions ( $\lambda < 4$ ,  $\lambda \approx 0 - 10$ ,  $44 - 60$ ,  $20 - 100 \text{ \AA}$ ). Thus, the very first measurements in the X-ray spectrum were carried out back in 1949 by photographic methods (using foil filters) /59/ and with phosphors /60/. These methods are hardly used at present because of the difficulties of cassette recovery.

The Friedman group launched several rockets with this equipment during an 11-year cycle of solar activity. The X-ray radiation flux from the quiet Sun varies during the cycle with an amplitude of a factor of 40 between maximum and minimum in the  $8 - 20 \text{ \AA}$  region and even larger in the  $2 - 8 \text{ \AA}$  region /61/. During bright flares, the X-ray flux may increase by more than one order of magnitude (details of the X-ray emission of flares are given in Section 24). Changes in X-ray flux are associated with sudden ionospheric disturbances (SID) which accompany the solar flares.

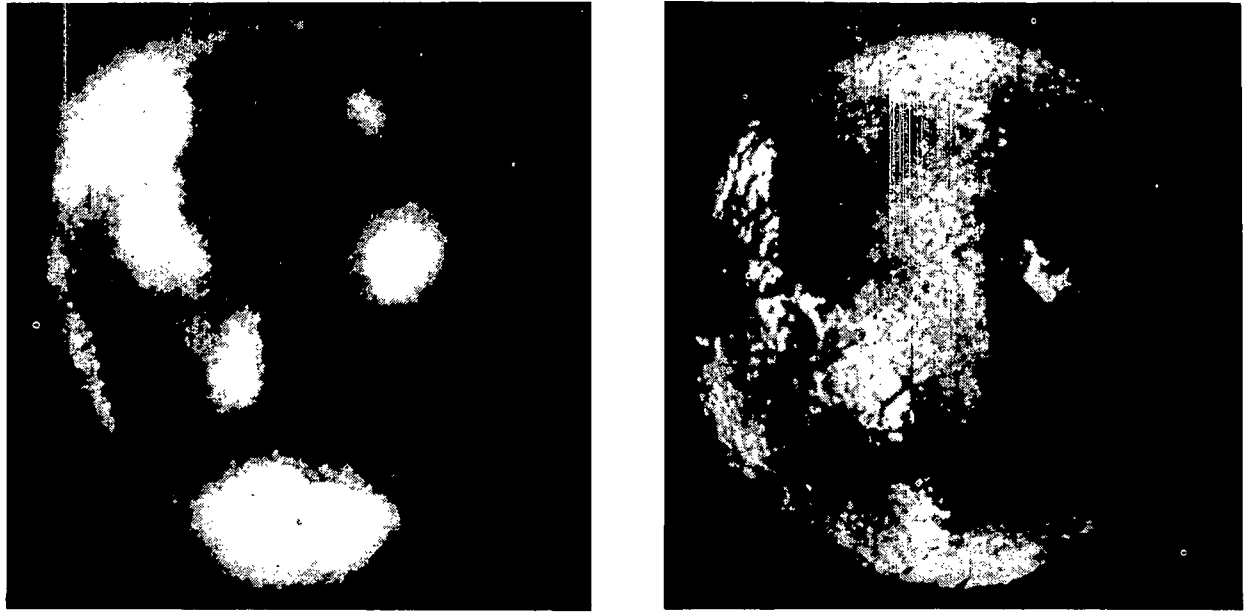


FIGURE 11. X-ray heliogram ( $\lambda \leq 44 \text{ \AA}$ ) taken by Underwood and Muney, 20 May 1966.

Sun's image about 5.8 mm in diameter, resolution about  $20''$ . Right, photograph of the Sun in  $H_{\alpha}$  6563  $\text{\AA}$  light (taken on the same day).

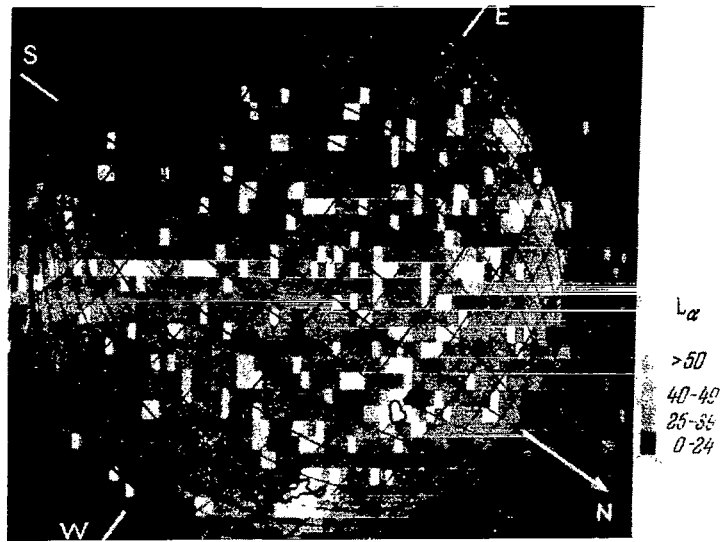
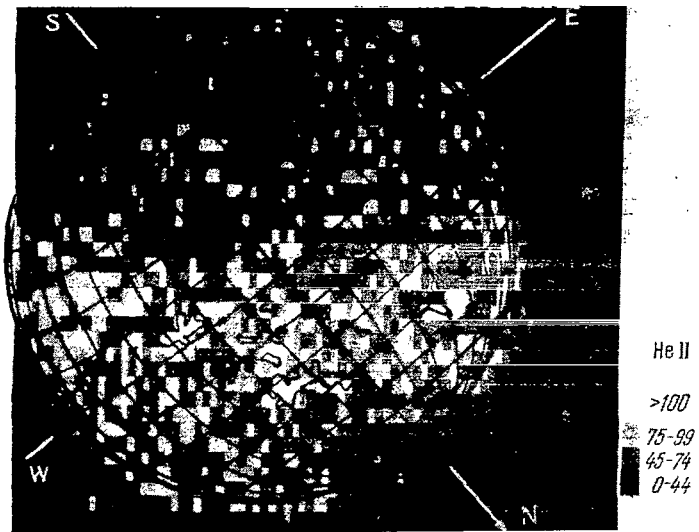


FIGURE 12. Spectroheliograms in resonance lines of hydrogen and ionized helium.

The spectroheliograms are based on telemetered transmissions from OSO-2 NASA satellite on which the Naval Research Laboratory spectrograph was launched. Left, scale showing the brightness gradation in relative units. The contours of the active solar regions (faculae) are marked on the spectroheliograms, from the observations of the Fraunhofer Institute. The  $L_{\alpha}$  heliogram was taken on 16 February 1965; the He II 304 Å heliogram was taken on 4 March 1965.

An interesting procedure was applied by American scientists at the beginning of the International Geophysical Year, before the two-stage guided rockets became available. They used a so-called Rockoon system; a rocket was held by a balloon at an altitude of over 20 km in the air until a launch signal was received from Earth. The system was not quite convenient, since the balloon with the rocket would often drift far from the launch point before the appearance of a flare, thus rendering the radio launch impossible.

In subsequent years, solar X rays were repeatedly measured in the USSR, USA, and England. The measurements were carried out with various radiation detectors: photon counters, electron multipliers, scintillation counters. Calibration was conducted by different methods, and a considerable scatter of data therefore could be expected.

The greatest number of measurements are available in the spectral intervals below 8 Å, below 20 Å, and 44 — 60 Å. Table 4 summarizes the measurement results prior to 1965; the table also gives the radio flux of the Sun  $F_{10.7}$  at 10.7 cm wavelength (from the data of the Ottawa Observatory), which is adopted as a measure of solar activity. Note that the correlation of the X-ray radiation with other activity indices, e.g., Wolf numbers, is much worse /62/. Allen reached a similar conclusion /63/. If we trace the dependence of the X-ray flux on solar activity, we notice a distinct correlation, despite the substantial scatter. The growth of the radiation flux with activity becomes more pronounced for harder radiation. The average amplitude from a minimum ( $F_{10.7} = 60 \cdot 10^{-22}$  watt/m<sup>2</sup>Hz) to a maximum ( $F_{10.7} = 250 \cdot 10^{-22}$  watt/m<sup>2</sup>Hz) is a factor of 100 at wavelengths shorter than 8 Å, a factor of 15 at wavelengths shorter than 20 Å, and a factor of 5 for 40 — 60 Å. The X-ray spectrum or the "color" temperature of X-ray radiation thus changes during a solar activity cycle.

The X-ray flux significantly increases during chromospheric flares: the increase is by two and three orders of magnitude for  $\lambda < 20$  Å and  $\lambda < 8$  Å, respectively /77/. The case of a bright X-ray region independent of active formations on the Sun was described by Mandel'shtam et al. /29/ who observed this phenomenon on 1 October 1965 on a heliogram taken at  $\lambda < 10$  Å.

The nature of the hard X rays in flares is discussed by Korchak /89/.

At wavelengths longer than 8 Å, the X-ray radiation is probably of thermal origin. The changes in energy distribution in its spectrum are probably associated with temperature variation in the corona, and the changes in the absolute X-ray flux result from variations in material density in the emitting regions (more precisely, the square of the density integrated over the emitting region, the so-called measure of emission, see Chapters II and III). The emission at wavelengths longer than 8 — 10 Å is attributed to lines of highly ionized atoms: the contribution from continuous radiation is small. This is evident from the X-ray spectrum recordings obtained by the Friedman group /82/, who established that at 10 — 25 Å the continuous spectrum is 17% of the line emission. Similar results emerge from the spectrograms of Mandel'shtam's group ( $\lambda \geq 9.5$  Å).

It is interesting to establish how far the line spectrum extends in the short-wave direction. According to Friedman /88/, lines of Na XI, Mg XI, Al XII, Si XIII, and Si XIV were identified between 6 and 8 Å in a spectrum taken on 4 October 1966. Continuous emission apparently plays a leading role in this region and at still shorter wavelengths.

TABLE 4. Observations of soft solar X-rays

Date	Radio emission at 10.7 cm in units of $10^{-22}$ watt/m <sup>2</sup> Hz	Flux at a distance of 1 a.u., erg/cm <sup>2</sup> sec			Authors and comments
		$\lambda < 8 \text{ \AA}$	$< 20 \text{ \AA}$	$40 - 60 \text{ \AA}$	
29. IX. 1949	114	$1.5 \cdot 10^{-3}$	—	—	Friedman, Kreplin /64, 65/
1. V. 1952	71	$1.7 \cdot 10^{-3}$	—	—	
5. V. 1952	75	$< 5 \cdot 10^{-4}$	—	—	
15. XII. 1952	88	$< 6 \cdot 10^{-4}$	0.2 (?)	—	
15. XI. 1953	62	$< 10^{-5}$	$< 1.5 \cdot 10^{-3}$	0.06 * (0.03) **	
25. XI. 1953	61	$3 \cdot 10^{-6}$	$< 1.3 \cdot 10^{-3}$	—	* 44 — 100 Å ** Our estimate
1. XII. 1953	60	$< 10^{-6}$	$4 \cdot 10^{-4}$	0.024	
18. X. 1955	85	$< 10^{-6}$	$1.2 \cdot 10^{-3}$	—	
17. XI. 1957	228	—	—	(0.02) **	
21. VII. 1959	189	$2.5 \cdot 10^{-4}$ $1.5 \cdot 10^{-4}$	— —	— —	
24. VII. 1959	181	0.013	$9 \cdot 10^{-3}$	0.15	Friedman, Kreplin /64, 65, 68/
7. VIII. 1959	212	$10^{-3}$	0.023	—	
14. VIII. 1959	189	$10^{-3}$	0.023	0.085	
29. VIII. 1959	308	$3.3 \cdot 10^{-3}$	—	0.17	
17. X. 1959	170	$< 10^{-3}$ $1.5 \cdot 10^{-3}$	0.011 † 0.08	— —	
18 — 23, 26. VII, 16, 19. VIII, 14. IX. 1960	$\leq 160$	$(4 - 8) \cdot 10^{-4}$	—	—	Kreplin, Chubb, Friedman /65, 71/; SR-1 satellite
27. IV. 1962	100	$1.7 \cdot 10^{-4}$	$6 \cdot 10^{-3} \dagger \dagger$	—	
3. V. 1962	94	$1.2 \cdot 10^{-5}$	$3.7 \cdot 10^{-3}$	—	Bowen, Willmore, Pounds, et al. /81/, Ariel satellite †† $\lambda < 15 \text{ \AA}$
18. X. 1962	89	$1.7 \cdot 10^{-4}$	0.014	—	
25. X. 1962 2. V. 1963	80	$1.2 \cdot 10^{-4}$	$2.5 \cdot 10^{-3}$	—	Manson /83/
23. VII. 1963	—	—	—	0.08	
26. I. 1964 22 — 24. II. 1964	60	$< 2 \cdot 10^{-4}$	$< 9 \cdot 10^{-4}$	0.02	Thomas, 21-C satellite Kreplin /84/; SR-4 satellite
14 — 22. II. 1964	70	$\leq 10^{-5}$	$2 \cdot 10^{-3}$	—	
1. VIII. 1964	75	$5 \cdot 10^{-4}$	$10^{-3}$	0.03	Tindo /85/, Elektron-2 satellite
1 — 15. III. 1964 7 — 29. IV. 1964	75	— —	— —	0.025 0.018	
					Thomas et al. /86/, OID-1964 satellite
					Landini et al. /87/, OID-1964 satellite

While working on this book, we were informed of the preliminary results of Neupert, Gates, Schwartz, and Young, who took the solar spectrum at  $1.3 - 20 \text{ \AA}$  with a Bragg spectrometer launched on the American OSO-2 satellite on 7 March 1967. In their paper delivered at the 13-th Congress

of the International Astronomical Union (Prague, September 1967) they reported on their observations of a strength 2 chromospheric flare on 22 March 1967 (Figures 13, 14). The growth of the continuous spectrum in Figure 13 is associated with an instrumental effect, which produced an increase in scattered light intensity. The recording of the spectrum taken before the flare does not show any lines at  $\lambda < 6 \text{ \AA}$ . Very strong lines appeared during the flare, which were identified with the emission of very highly ionized iron (corresponding to  $T \geq 10^7 \text{ K}$ ). The observations are highly valuable for interpreting the physical processes in flares. Of particular interest is the bright line or blend at  $1.83 \text{ \AA}$ , which is identified by the authors with the emission of a "helium-like" ion Fe XXV (see Figure 13). Their results were published in /723/.

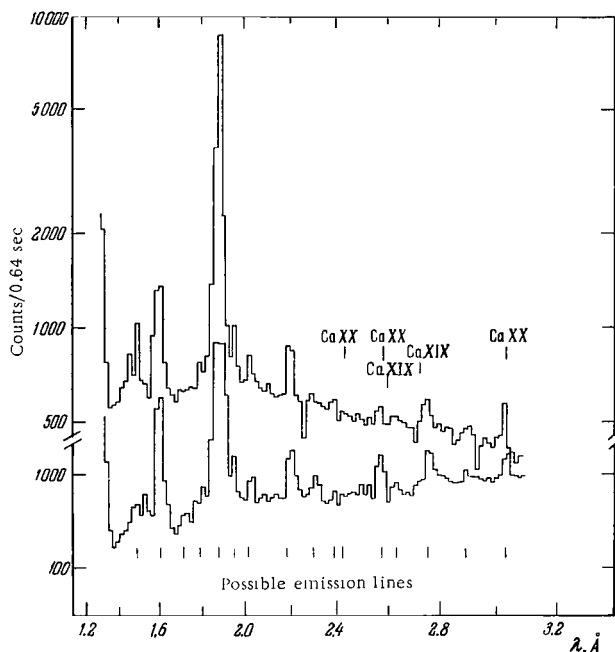


FIGURE 13. X-ray spectrum of the Sun taken on 22 March 1967 by Neupert, Gates, Schwartz, and Young (Goddard Space Center) taken with a 5-min delay during the initial phase of an X-ray flare.

New observations were published while the book was being prepared for press. A highly interesting study was published by a group at the Naval Research Laboratory /726/, who discuss the results obtained with a telemetered solar spectrum at  $1.9 - 25 \text{ \AA}$ , taken with a rocket-borne Bragg spectrometer on 4 October 1966. A total of 63 lines were recorded, of which 55 were identified. Laboratory or theoretical data for 88 lines of various ions are also given for this spectral region in /726/. These results, unfortunately, could not be included in Tables I and II at the end of our book.



## *Chapter II*

### *PREDICTION AND IDENTIFICATION OF SHORT-WAVE LINES*

#### **4. The general problem of identification of short-wave lines**

The most important and in fact unavoidable problem in the investigation of any line spectrum is the identification of the observed radiation with certain spectral transitions of molecules, atoms, or ions. Identification actually determines to what extent all further steps aimed at studying the physical properties of the emitting medium will succeed. This is a difficult task, however, especially if the physical conditions in the emitting medium allow a considerable variety of energy states and atomic species, and consequently lead to very numerous lines. It will become clear from what follows that this is the particular case which applies to the short-wave emission of the solar atmosphere.

Several tens of photographic and photoelectric spectrograms of the Sun are currently available for the wavelengths between 10 and 3000 Å (see Chapter I). Most lines, especially the weak ones, remain unidentified. Intensity estimates are unreliable and contradictory, primarily at wavelengths shorter than 300 Å.

What are the guidelines for the identification of a given line with a particular transition of some atom? The main identification criterion in spectroscopy is the matching of the observed wavelength of the unknown line with the wavelength of some other line which has been measured in laboratory or computed theoretically. A suitable correction for the wavelength shift due to Doppler and other effects should naturally be introduced, whenever they apply. The wavelength matching criterion, however, often proves to be unreliable because of the inexact pinpointing of the line position of the spectrogram (many of the observed lines are blends) and the errors inherent in the theoretical wavelength determination procedure. A better identification procedure calls for a comparison of the relative intensities of a group of lines belonging to one multiplet, i. e., lines associated with transitions between two quantum states, each separated into individual terms. This method is not universally effective either: first, the observed intensities are fairly inaccurate (this applies even to relative intensities) and second, relatively few atoms have strong lines with a "good" multiplet structure. A "direct" method of comparison of the short-wave spectra of the Sun with laboratory spectra of plasma machines assumes simulation of the solar atmospheric conditions in the machine. The reproduction of the natural conditions — temperature, chemical composition, excitation — is relatively crude, however, since the ultimate aim of the identification is to establish these parameters with maximum precision.



The short-wave spectrum contains a dozen or two of reliably identifiable strong lines with accurately measured intensities. These lines generally lie at wavelengths above 700 Å, where the intensity calibration methods reach their maximum accuracy for the short-wave spectrum. Therefore, in view of the above considerations, it is advisable to apply the method of theoretical "forecasting" of the short-wave spectrum based on reliably identified lines and the minimum of assumptions concerning the emission mechanism. Comparison of the actual observed spectrum with the "forecast" spectrum will ensure fairly reliable identification.

The importance of identification for investigating the physical nature of the solar atmosphere is quite clear. The point to consider is its importance for purely geophysical purposes associated with the emission of the Earth's ionosphere. At a first glance it would seem that we need not concern ourselves with the question of the exact atomic or ionic species which emit the short-wave radiation: we would only require the energy distribution in the spectrum in order to allow for the interaction of this radiation with the ionosphere. In fact, however, the situation is radically different: unless we know what exact regions of the solar atmosphere emit the radiation in different spectral regions and what physical conditions (temperature, concentration, excitation mechanism, etc.) prevail in these regions, we cannot intelligently discuss the variation of the short-wave energy and spectrum with the phase of the solar activity or the changes which occur during the shorter time intervals characteristic of such solar-activity features as flares, faculae, and spots. It is therefore clear that no thorough and far-sighted investigation of the interaction of the hard solar radiation with the Earth's atmosphere is possible without accurate identification of the principal (in terms of energy) part of the short-wave lines in various spectral regions. Still another fairly important point should be borne in mind. Since energy calibration of the short-wave spectrum is reliable only for the "long-wave" part of the region, identification and subsequent comparison of the observed line energy fluxes with the theoretical predictions will enable the energy fluxes to be determined in other parts of the short-wave spectrum also.

## 5. Wavelength and intensity prediction for short-wave lines

Lines for which reliable identification is available include those emitted by atoms from different ionization stages, e.g., Mg II, C III, O IV, O VIII, Si XII, Fe XVI, etc. This points to a great diversity of temperature conditions in the emitting regions. Therefore ions which exist in the entire range of solar temperatures — from 6000° to  $(2-3) \cdot 10^6$ °K — should be chosen for the purpose of line prediction. This temperature range covers various ionization states, from neutral atoms in the lower chromosphere to Ca XV type ions in the "hot" regions of the corona. The corresponding range of ionization potentials is approximately 10 — 1000 eV.

Since there is virtually no continuum radiation in the short-wave region of the solar spectrum, line excitation may only be produced by collisions of ions with electrons — the most mobile particles present. The contributing collisions are those which involve an upward change of the quantum state (electron impact excitation) or a downward change in the ionization stage

with the formation of an excited state (photorecombination). Recombination excitation in the solar atmosphere is generally three orders of magnitude less effective than electron impact. The most effective mechanism for downward transitions of excited ions is the spontaneous transition, whose probability (even for "forbidden" radiation) in the solar atmosphere is almost always higher than the probability of the "quenching" process associated with electron impact.

We thus come to the following conclusions: 1) almost all the ions occupy the lowermost (ground) quantum state, 2) lines associated with the ground state, and in particular lines characterized by the lowest excitation potential (resonance lines) show the maximum intensity among the various emission lines of a given ion. These conclusions follow from the stationarity equation which relates the ground level (1) to an excited level (2):

$$n_{i1}n_e W_{12} = n_{i2}A_{21}; \quad (\text{II.1})$$

here  $n_e$  and  $n_i$  are the electron and the ion concentration,  $W_{12}$  is the coefficient of excitation by electron impact,  $A_{21}$  is the Einstein probability of spontaneous transition. The right member of the equation is proportional to the flux of quanta from  $1 \text{ cm}^3$  emitted in the  $2-1$  line by an ion in ionization stage  $i$ . Integrating this flux along the normal to the solar surface (the height  $h$ ) and changing over from the flux of quanta to the radiation flux  $F$  in  $\text{erg/cm}^2 \text{sec}$  at a distance of  $1 \text{ a.u.}$ , we readily find /90/

$$\int n_{i2}A_{21}dh = 2.3 \cdot 10^{11} F \lambda \text{cm}^{-2} \text{sec}^{-1}; \quad (\text{II.2})$$

$\lambda$  is the wavelength of the resonance line, in  $\text{\AA}$ . It is implied that the radiation is emitted by a spherical, and not by a plane, layer. A bright ring is thus formed at the limb whose emission is equal to the emission of the entire solar disc.

Consider the left member of (II.1) which represents the numbers of excitations of a given line in 1 sec in  $1 \text{ cm}^3$ . The coefficient of electron impact excitation may be written in the Born approximation /90, 91/

$$W_{12} = \frac{10f_{12}}{T^{3/2}} \left[ \frac{e^{-x}}{x} - Ei(x) \right] = \frac{f_{12}}{T^{3/2}} W'(x), \quad (\text{II.3})$$

where  $f_{12}$  is the oscillator strength,  $x = \chi_{12}/kT$ ,  $\chi_{12}$  is the excitation potential,  $Ei(x)$  is the integral-power function,  $T$  is the electron temperature. This expression is known to be universally applicable apart from a factor of  $2-3$ . The ion concentration in the ground state is virtually equal to the total concentration, counting all the possible quantum states. If we write  $n_i/\Sigma n_i$  for the fractional content of an ion of a given ionization stage in relation to the total number of different ions of the particular chemical element (the degree of ionization), we find  $n_{i1}n_e \approx n_e^2 \kappa \frac{n_i}{\Sigma n_i}$ , where  $\kappa$  is the abundance of the given element relative to hydrogen (expressed in the number of particles). The sign of approximate equality reflects the fact that hydrogen is not the only source of electrons (in the solar atmosphere  $n_H \approx n_e$  to within better than 20%).

The degree of ionization in the corona and in the topmost layers of the chromosphere is entirely determined by electron collisions. In this case (see next chapter for more details) the degree of ionization only depends



The generalized measure of emission may thus be expressed in terms of parameters and observation data for any of the short-wave solar lines. We have from (II.1), (II.2), and (II.4)

$$\Delta\varphi_i = \frac{4.6 \cdot 10^{12} F \lambda}{\kappa_{f_{12}} W' (T_i, \lambda)} . \quad (\text{II.5})$$

Using (II.5) and adopting the ionization temperature as the parameter, we can compute the generalized measure of emission for the emission lines of ions in the entire temperature range of the solar atmosphere. The function  $\Delta\varphi(T_i)$  is plotted from data for reliably identified and sufficiently strong lines which lie in that region of the short-wave spectrum where the most accurate intensity data are available. The ionization temperature was found by computing the curves of  $n_i/\Sigma n_i$  as a function of  $T$  /90, 91/. The dependence of  $T_i$  on the ionization potential  $\chi_i$  constructed using the data for 50 ions may also be represented by a simple curve (Figure 16). Most of the points cluster around one curve, with the exception of ions with filled outer shells, which fall along another slightly displaced curve. The plot in Figure 16 may be used to interpolate for other ions as well.

To determine  $\Delta\varphi_i$ , we require the relative content or abundance of the chemical elements in the solar atmosphere and the oscillator strengths of "reference" lines. The abundance of the chemical elements is considered in detail in Section 11, which deals with the chemical composition of the solar atmosphere. Anticipating the results of this section, we give here a table which lists the abundances of the common elements whose ions may be used for line prediction (Table 5).

TABLE 5. Content of elements in the solar atmosphere

H 1	Na $2 \cdot 10^{-6}$	Cl $7 \cdot 10^{-8}$	Mn $8 \cdot 10^{-8}$
He 0.1	Mg $4 \cdot 10^{-6}$	Ar $3 \cdot 10^{-6}$	Fe $2 \cdot 10^{-5}$
C $2 \cdot 10^{-4}$	Al $3 \cdot 10^{-6}$	K $5 \cdot 10^{-8}$	Co $6 \cdot 10^{-7}$
N $3 \cdot 10^{-5}$	Si $3 \cdot 10^{-5}$	Ca $4 \cdot 10^{-6}$	Ni $2 \cdot 10^{-6}$
O $6 \cdot 10^{-4}$	P $2 \cdot 10^{-7}$	Ti $5 \cdot 10^{-8}$	
Ne $3 \cdot 10^{-3}$	S $1 \cdot 10^{-5}$	Cr $2 \cdot 10^{-7}$	

The figures for most of these elements are close to conventionally used abundances for the Sun and the solar system /92/.

The data on oscillator strengths are highly inconclusive. Satisfactory estimates of  $f_{12}$  for some ions and isoelectron series (mainly the HI, He I, alkali, and alkaline-earth series) will be found in the handbook by Allen /93/ and in the paper of Veselov /94/.

Table 6 lists some basic data and the values of  $\Delta\varphi_i$  (in CGS units) computed from (II.5) for 15 ions with emission lines between 700 and 800 Å and ionization temperatures between  $1 \cdot 10^4$  and  $6 \cdot 10^5$ °K. Unfortunately, no reliably identified lines of ions with higher ionization temperatures fall at these wavelengths. Therefore other data should be used for  $T > 6 \cdot 10^5$ °K.

The radiation fluxes in the lines of 10 ions in Table 6 are based on the photoelectric observations of Hinterreger et al. /26/ and those for the lines of the other 5 ions are based on the photographic observations of Detwiller

et al. /18/. Hinteregger's observations refer to a solar activity minimum, and they in fact determine the trend of the  $\Delta\varphi(T)$  curve. Detwiller's data correspond to a higher activity level, but they nevertheless adequately follow the general curve. This is probably due to the fact that the relevant lines belong to ions of low ionization stages (which are relatively insensitive to the phases of the activity cycle).

TABLE 6. Generalized measure of emission computed from "reference" short-wave lines

Ion	$\log T_i$	$\lambda, \text{\AA}$	$f_u$	$F_i$ erg/cm <sup>2</sup> sec	$\log \Delta\varphi_i$
MgII	4.05	2796 2803	0.9	18	24.34
CII	4.25	903.6— 904.5	(0.1) •	0.003	22.62
SiIII	4.40	1206.5	1.1	0.085	21.71
SiIV	4.65	1394 1403	0.7	0.070	20.33
CIII	4.67	977.0	1.38	0.082	19.77
SiV	4.67	1062.7 1073.3	0.6	0.007	20.13
CIV	5.00	1548 1551	0.3	0.170	19.00
OIV	5.05	790	0.23	0.015	18.10
NIV	5.08	765	0.8	0.007	18.40
SVI	5.20	933 944	0.6	0.001	18.75
NV	5.28	1238.8 1242.8	0.23	0.005	17.90
OVI	5.40	1032 1038	0.2	0.074	17.70
NeVII	5.60	892	0.1	0.002	17.44
MgVII	5.75	843	(0.1) <sup>1)</sup>	0.002	17.08
NeVIII	5.82	770.4 780.3	0.15	0.015	17.82

\* Approximate figures computed using Allen's rule (see p. 43).

Let us consider some additional data (for  $T > 6 \cdot 10^5 \text{°K}$ ) derived from observations of "forbidden" coronal lines which are accessible to observations from Earth. The excitation mechanism for these lines is the same as for the short-wave lines. Although the continuum emission in the visible spectrum is quite strong, electron impact excitation prevails (see, e.g., /90, 91/).

The intensity of these lines in "quiet circumstances" on the ground can be determined with higher accuracy than the intensity of short-wave lines in rocket experiments. This advantage is partly offset by our inability to conduct observations of the very weak coronal lines directly against the solar disc (they have to be observed beyond the limb). Special techniques have to be used, which will be described below (also see /95/). Table 7 lists the basic data and the results obtained for  $\Delta\varphi_i$  from "forbidden" coronal lines for an epoch of minimum solar activity.

Figure 17 is a plot of  $\Delta\varphi(T_i)$ . Despite the fairly crude analysis of the initial data, the values of  $\Delta\varphi_i$  cluster closely about a common curve. The "coronal" points from Table 7 point to the existence of a maximum in  $\Delta\varphi$  around  $\log T_i = 6.15$ . An additional check on the coronal values of  $\Delta\varphi(T_i)$  is

provided by the computations based on the electron concentration distribution in the corona (Chapter III). For  $T = 1.4 \cdot 10^6 \text{°K}$  and  $\bar{n}_e^2/(\bar{n}_e)^2 \approx 3$  (see also Chapter III), we find  $\Delta\varphi_c \approx 7 \cdot 10^{17}$  in an epoch of minimum and  $\Delta\varphi_c \approx 5 \cdot 10^{18}$  in an epoch of maximum. These figures are consistent with the independent values of  $\Delta\varphi(T_i)$  obtained from coronal lines. The general trend of the  $\Delta\varphi(T_i)$  curve points to a decrease of the generalized measure of emission with the increase in temperature. This curve may be used as a point of departure for the determination of radiation fluxes in short-wave lines.

TABLE 7. Generalized measure of emission computed from "forbidden" coronal lines

Ion	$\log T_i$	$\lambda, \text{Å}$	$F \cdot 10^9$ erg/cm <sup>2</sup> sec	$\log \Delta\varphi_i$
FeX	5.78	6374	10	17.40
FeXI	5.90	7892	10	17.35
FeXIV	6.11	5303	60	17.75
NiXII	6.00	4231	1.8	17.24
NiXIII	6.08	5116	2.3	17.38
NiXV	6.20	6702	3.6	17.54
NiXVI	6.25	3601	1.8	16.90
CaXII	6.28	3328	0.9	16.25
CaXIII	6.42	4086	0.4	15.56
CaXV	6.55	5694	0.6	16.00

The following considerations are highly important for an assessment of the flux predictions. The only starting data needed in order to find  $F$  by the above method are the radiation fluxes in the "reference" lines (Tables 6 and 7). Indeed, there is a single-valued empirical dependence of  $\Delta\varphi_i$  on  $T_i$  for the solar atmosphere with the points spread within  $\pm 0.5$  of an order of magnitude. The existence of this dependence enables us to determine with the same accuracy ( $\pm 0.5$  of an order of magnitude) the radiation flux in any short-wave line assuming known physical conditions in the solar atmosphere.

It follows from (II.5) that /90/

$$\frac{F}{\kappa f_{12}} = 2.2 \cdot 10^{-13} \frac{W'(\lambda, T_i)}{\lambda} \Delta\varphi(T_i). \quad (\text{II.6})$$

The ratio  $F/(\kappa f_{12})$  is thus dependent on two parameters: the relevant line wavelength and the ionization temperature. We clearly may adopt a purely empirical approach to the method for the determination of  $F$ . We may assume that the result hardly depends on whether the excitation cross section  $W_{12}$  corresponds to the actual figure and whether the main assumptions regarding the emission and ionization mechanisms are valid. Indeed, when determining  $F$  for a line of wavelength  $\lambda$ , which corresponds to some ion of ionization temperature  $T_i$ , our procedure is the exact reverse of the procedure for the construction of  $\Delta\varphi(T_i)$ .

The determination of  $F$  for a line  $\lambda$  of ionization potential  $\chi$  thus reduces to the following steps:

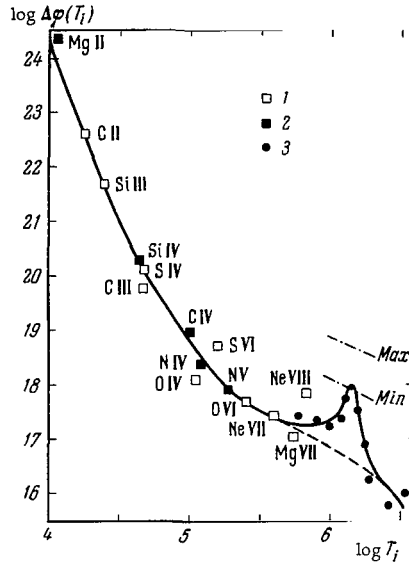


FIGURE 17. The generalized measure of emission of the solar atmosphere for the region of emission of ions of ionization temperature  $T_i$ .

Epoch of minimum solar activity: 1 — from rocket data for  $\lambda > 750 \text{ \AA}$  /26/; 2 — from rocket data for  $\lambda > 750 \text{ \AA}$  /18/; 3 — from coronal lines (Table 7). The dash-dotted lines plot the data based on the coronal distribution of  $n_e$  for minimum and maximum solar activity.

1) using the curves in Figure 16, we find the temperature  $T_i$  from the ionization potential  $\chi_i$ ;

2)  $W'$  is computed from  $\lambda$  and  $T_i$  (using (II.3));

3)  $\Delta\varphi_i$  is determined from  $T_i$  (the curve in Figure 17);

4) the ratio  $F/(\kappa f_{12})$  is computed from (II.6);

5)  $F$  is computed for known  $\kappa$  and  $f_{12}$ .

All the lines listed in Tables 6 and 7 are resonance lines. If several transitions may originate at the excited level 3 ( $3 \rightarrow 2$ ,  $3 \rightarrow 1$ ), the flux in the fundamental series line will be

$$F_{31} \approx F \frac{A_{31}}{\sum A},$$

and in a subordinate series line

$$F_{32} = F \frac{A_{32}}{\sum A} \frac{\lambda_{31}}{\lambda_{32}}, \quad (\text{II.7})$$

where  $F$  corresponds to the line  $\lambda_{31}$ ,  $\sum A$  is the sum of the probabilities of all the possible spontaneous transitions from an excited level.

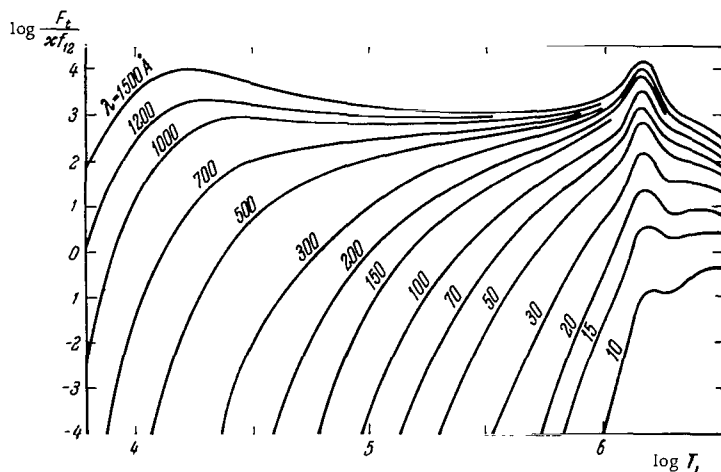


FIGURE 18. A nomogram for computing the radiation fluxes ( $F_l$ ) in short-wave solar lines in an epoch of minimum activity:

$T_i$  is the ionization temperature,  $\lambda$  is the resonance wavelength in  $\text{\AA}$ ,  $x$  is the content of the element in relation to hydrogen,  $f_{12}$  is the oscillator strength.

The computations can be markedly simplified by using nomograms which plot the ratio  $F/(x f_{12})$  vs.  $T_i$  for different values of the parameter  $\lambda$  (Figure 18).

The most tedious stage in the prediction of short-wave lines is the selection and the computation of the wavelengths for various transitions which produce lines of sufficient intensity.

Table I at the end of the book lists the computed results for  $F$  for 700 multiplets belonging to 146 ions of 21 chemical elements. In these computations 26 isoelectronic series from HI to Fe I were used. The line wavelengths lie between 10 and 2800  $\text{\AA}$ . The wavelengths were mainly determined using Moore's tables /96/. A number of terms for some ions, especially the high ionization stages, are missing. In these cases the term energies were obtained by extrapolation along the isoelectronic series. Extrapolation (or interpolation) was based on such combinations of wave number  $\nu$  and ionization stage  $Z$  which do not change much along the isoelectronic series (combinations of the form  $\nu \cdot Z^k$ ).

Mainly "allowed" transitions were considered, i. e., transitions for which Laporte's rule is observed and the selection rules for the orbital ( $\Delta L = 0, \pm 1$ ) and the inner ( $\Delta J = 0, \pm 1$ , except  $0 \rightarrow 0$ ) quantum numbers are satisfied.

As we have seen before, estimates of  $f_{12}$  are available for some transitions. In addition to /93, 94/, there are the data of Varsavsky /97/, who computed the wavelengths and the oscillator strengths for 205 short-wave lines. Good data for  $f_{12}$  of the ions Fe X and Fe XIV will be found in /98/. However, no  $f_{12}$  are available for most lines in Table I. In these cases, a very crude estimate of  $f_{12}$  was obtained using Allen's rule /99/ which states that  $f_{12}$  is determined by the type of the transition:

$\Delta n$	1	1	0	0
$\Delta l$	+1	-1	+1	$s^2 p^k - s p^{k-1}$
$f_{12}$	0.5	0.1	0.2	0.05



Here  $n$  is the principal quantum number;  $\Delta l > 0$  if  $l$  is greater for the top level than for the bottom level.

Intercombination transitions (involving a change in multiplicity) were considered in some cases; for these transitions we took  $f_{12} = 0.01$ . The parenthetical figures for  $f_{12}$  in Table I indicate that no direct data were available and Allen's rule was applied. The ions in Table I are selected according to isoelectronic series, where the leading terms are arranged in the order of atomic numbers. The first symbol under "Transition" corresponds to the lower level, and it is not repeated in the following lines. For each ion, the lines of the principal series are first considered. The wavelengths obtained by term extrapolation are enclosed in parentheses.

Table I contains lines with  $F > 10^{-6}$  erg/cm<sup>2</sup>sec. Lines with lower intensities are not included in the list, although they may be considered if necessary.

The table of predicted lines is substantially more comprehensive than the previous publications [115]. Additional data on wavelengths and oscillator strengths were borrowed from various publications dealing with computations of line parameters or line identification in the short-wave solar spectrum. Data on some lines of Ni X — Ni XIII are contained in [100 — 102], on lines of Fe VIII — Fe XIV in [101 — 104], and on lines of Ne IV in [105]. These publications also give the lines of a number of other elements. Data on lines in the soft X-ray spectrum were borrowed from Landolt-Börnstein [106] and from [28] (which deals with line identification for  $\lambda \geq 13.7$  Å). The new book by Striganov and Sventitskii [107] proved most instrumental in the preparation of the table: this book presents the exact wavelengths of virtually all the transitions for relatively low ionization stages (not higher than VI — VIII) of the most abundant elements.

Additional data have been published recently on oscillator strengths and wavelengths for the lines of some highly ionized ions. The oscillator strengths for the resonance lines of the Ne I — Fe XVII isoelectronic series are published in [108]. The wavelengths for some lines of the ions Ca XII — Ca XIV are published in [20]. Some lines of the Ar I series will be found in [110]. The oscillator strengths for a number of lines of Fe XVII, OVII — OVIII, NVII, and Ne IX were computed by Froese (unpublished data quoted in [111]). Some wavelengths between 57 and 310 Å are cited in [112], which primarily deals with the identification of short-wave solar lines.

We have already discussed the reliability of the predicted intensities of the short-wave lines in Table I. Besides the inherent method errors (which do not exceed 0.5 of an order of magnitude), additional errors may be introduced by the "reference" lines used as the basis of the procedure (see Table 6). A highly ingenious method was proposed by Shklovskii [113] for estimating the flux  $F$  of some short-wave lines; this method was also applied in [95]. Before the beginning of rocket observations of the short-wave spectrum, back in 1945, Shklovskii [113] proposed to identify the coronal lines in the visible spectrum with the emission of highly ionized atoms (see Table 7) and proceeded to establish that these ions should of necessity emit short-wave lines with wavelengths of a few hundreds of angstroms. In [113] Shklovskii estimated the lower bound for the intensity of the Fe XV 424 Å line, which is the product of "cascade" emission following the subordinate "forbidden" line at 7059 Å. Semiquantitative considerations led Shklovskii to an estimate of the total radiation energy in

the short wave spectrum ( $\lambda < 500 \text{ \AA}$ ). Although his result ( $\approx 0.01 \text{ erg/cm}^2\text{sec}$ ) is low in the light of modern data, the basic idea of Shklovskii's work is most promising.

If an ion has three levels such that the transitions  $2 \rightarrow 1$  and  $3 \rightarrow 1$  produce a "visible" and a short-wave line, respectively, the flux ratio in these lines should be equal with fair accuracy to the ratio of the excitation frequencies of the initial levels. This follows from the stationarity equation (II.1). Thus,

$$\frac{F_{31}}{F_{21}} = \frac{\lambda_{12}}{\lambda_{13}} \frac{W_{13}(\lambda_{13}, T_i)}{W_{12}(\lambda_{12}, T_i)}. \quad (\text{II.8})$$

This method is independent of the abundance of the particular element. It was essentially developed by the present authors for the determination of fluxes in the short-wave "coronal" lines of iron, nickel, and calcium ions, since the generalized measure of emission  $\Delta\phi_i$  in the corona was constructed from the data on the visible coronal lines of these particular elements.

## 6. Identification of short-wave lines

Given the table of predicted wavelengths and intensities for short-wave lines (Table I), we can proceed with the identification of the observed lines, which number a few hundreds in the spectral region  $\lambda \leq 1215.7 \text{ \AA}$ . This region, which has a natural upper limit in the form of the bright  $L_\alpha$  line of hydrogen, is of particular interest in astrophysics and geophysical work.

Table II is a list of the predicted lines from Table I, rearranged in the order of increasing wavelengths. The identifying numbers of the lines from Table I are retained. In the principal cases, the wavelengths of the individual components were computed for the multiplets for which Table I only gives the upper and the lower values of  $\lambda$ .

In matching the observed and the predicted lines we utilized both the wavelengths  $\lambda$  and the flux values. In this way, maximum reliability of identification was ensured, and the weakest candidates were dropped from the start. For example, among a group of observed lines with close wavelengths  $\lambda$ , the brightest line was identified with the line of the highest intensity in the corresponding group of predicted lines.

The results of this matching are also given in Table II. In the last column, + corresponds to a reliable identification, — to lack of identification, and +? to a doubtful identification.

In 1962 the authors applied this method /114/ and obtained identifications for 180 lines from among the 225 lines observed by Violett and Rense /16/ and by Hinteregger /23, 24/. In 1964, one of the authors /115/ somewhat extended the list of predicted lines and used the additional observation data of Tousey et al. /20/ and Hinteregger, Damon, and Hall /26/. Of the 297 registered lines, 239 were thus identified /116/.

New observations have been published during the recent years. Our identification is based on the most important results (see Chapter I): 1) the spectral region from 13.7 to 24.8  $\text{\AA}$ , 25 July 1963 /28/; 2) 33 — 80  $\text{\AA}$ , 20 September 1963 /21/ (unfortunately, no new data are available for the 25 — 33  $\text{\AA}$  region); 3) 55 — 310  $\text{\AA}$ , 2 May 1963 /27/ (the counting rate is given

in /27/, and  $F$  was obtained using the conversion coefficient from /117/: number of quanta  $= 1.4 \cdot 10^5 \times$  number of counts; the wavelengths were read directly off the microphotometer tracing to within  $0.5 \text{ \AA}$ ; 4)  $250 - 1216 \text{ \AA}$ , 23 August 1961 /26/ (wavelengths and  $F$  determined from the microphotometer tracing to within  $1 - 2 \text{ \AA}$  in  $\lambda$ ). Data on line wavelengths between  $9.5$  and  $34 \text{ \AA}$  were also used /29/. All the observed  $\lambda$  and  $F$  are listed in Table II (at the end of the book).

In our first identifications we used Violet and Rense's data /16/ on wavelengths and visual estimates of line intensities. These authors obtained two spectrograms on 4 June 1958 and 30 March 1959. The list in /16/ covers 159 lines. Despite the numerous critical comments regarding the low reliability of this list, voiced by a number of observers, the Colorado University group will clearly be remembered for its pioneering work which markedly advanced our knowledge of the short-wave spectrum. Most of the short-wave lines from /16/ (101 lines) were confirmed in later observations. Of the 74 identifications given in /16/, 47 are quite reliable. Using this spectrum, we managed to identify back in 1961 /90/ the lines of S VI ( $945$  and  $934 \text{ \AA}$ ), Si XII ( $499 \text{ \AA}$ ), and Ne VII ( $464 \text{ \AA}$ ).

Let us compare our results with the most extensive lists of identified lines currently available. This category includes the work of Zirin /112/, who identified on Hinteregger spectrograms 88 lines in the  $57.5 - 308.4 \text{ \AA}$  region and 11 lines in the  $313 - 558 \text{ \AA}$  region. Virtually all the identifications are correct. Only 16 lines are definitely known to have been incorrectly identified. Tousey et al. /22/ carried out an identification of their spectrum ( $33 - 500 \text{ \AA}$ ). The list covers 58 lines, with only 4 identified incorrectly. One of the unidentified lines from /22/ was identified by us with C V.

At the shortest wavelengths ( $9.5 - 34 \text{ \AA}$ ), Soviet and American observers have recorded some 20 lines. Of the 14 lines observed and identified by Friedman's group /28/, 10 identifications have been confirmed. Identifications of 15 lines in the  $9.5 - 34 \text{ \AA}$  region were also published by the Physics Institute of the USSR Academy of Science, and of these 12 lines have been confirmed (8 of these lines coincide with the previous identifications published by the Naval Research Laboratory, USA). The wavelength determinations in /29/ were probably less accurate than indicated by the authors ( $< 0.15 \text{ \AA}$ ), since the observed and laboratory wavelengths differ by  $0.3 \text{ \AA}$ .

After the completion of the first version of our identification /114/, we received the proceedings of the Liege Symposium where Allen had reported his identification of short-wave lines /99/. Allen gave the results of intensity computations for 96 multiplets, of which 76 lie in the  $44 - 1216 \text{ \AA}$  region. Allen's computations were based on Oster's model of the solar atmosphere /119/: he computed the measure of emission  $\int n_e^2 dh$  in a number of temperature intervals proceeding from the model values of  $n_e(h)$  and  $T(h)$ . Allen published 31 identifications for  $\lambda < 1216 \text{ \AA}$ , of which 24 were confirmed by our results and only one had not been available before (Si II  $992 \text{ \AA}$ ).

Pecker and Rohrlach /120/ computed four coronal "forbidden" lines,  $1058.7 \text{ \AA}$  (Al XIII),  $1048.9 \text{ \AA}$  (Si VII),  $952.4 \text{ \AA}$  (Si IX), and  $658.7 \text{ \AA}$  (Ar XIII). The first two lines had been observed by Violet and Rense /16/.

TABLE 8. Log ionization temperatures of ions emitting in the solar atmosphere

Elec- trons	Ele- ment	I	II	III	IV	V	VI	VII	VIII	IX	X	XI	XII	XIII	XIV	XV	XVI	XVII
2	He	4.25	4.75															
6	C	3.85	4.25	4.68	5.00	5.1 6.0	6.3											
7	N	3.91	4.40	4.7	5.05	5.25	5.28 6.18	6.4										
8	O	3.85	4.50	4.80	5.05	5.26	5.42	5.58 6.36	6.5									
10	Ne	—	4.6	4.90	5.20	5.37	5.52	5.6	5.82	5.92 6.66	6.7							
11	Na	—	4.00	4.75	5.2	5.43	5.58	5.7	5.86	5.97								
12	Mg	—	4.05	4.70	5.25	5.4	5.63	5.75	5.82	5.90	6.08	6.2 6.9						
13	Al	—	4.10	4.40	4.90	5.51	5.66	5.82	5.92	6.00	6.1	6.2						
14	Si	—	4.0	4.40	4.75	5.55	5.70	5.82	5.96	6.05	6.08	6.14	6.23					
16	S	3.7	4.23	4.48	4.67	5.00	5.18	5.92	6.00	6.1	6.20	6.25	6.3	6.33	6.36			
18	Ar	—	—	4.59	4.88	5.03	5.15	5.35	5.45	6.16	6.25	6.3	6.4					
20	Ca	—	3.85	4.5	4.8	5.08	5.28	5.39	5.47	5.63	5.68	6.25	6.28	6.42	6.48	6.55		
26	Fe	—	4.1	4.5	4.78	5.2	5.25	5.38	5.59	5.73	5.78	5.90	5.95	6.04	6.12	6.18	6.28	6.52 6.96
28	Ni	—	—	4.57	4.8	5.0	5.42	5.45	5.5	5.6	5.75	5.95	6.00	6.1	6.18	6.3	6.35	6.4
Chromosphere																		
Transitional region																		
Corona																		

Zirin, Hall, and Hinteregger /121/ analyzed the photoelectric tracing of the short-wave solar spectrum from /26/ and also identified a number of lines. Some of these identifications had not been covered by Detwiler et al. /19/. In particular, the lines at 270, 344, and 365 Å are identified with Fe XIV. The first two lines had been previously identified by us /114/, whereas the last line is identified with the bright line of Si XI. The lines at 332 and 361 Å, which we identified with Fe XVI, were independently identified by Edlen and Tousey (see /121/). Note that the work of Zirin et al. /121/ provides a qualitative confirmation of the low content of N and Ne in the Sun and the high content of Fe, in compliance with our determinations of the chemical composition of the solar atmosphere (see below).

To test the photoelectric spectrometer intended for the OSO satellite, Behring, Neupert, and Lindsay /122/ took a recording in the 120 — 380 Å region. They published a table listing 42 lines and 24 identifications. Of these, 7 coincide with our results and the rest are incorrect. Thus, the 316 and 333 Å lines should be identified with the strongest emission Si VIII and Al X, and not with Ni XV; the 284 and 274 Å lines belong to Fe XIV and Si VII, and not to Fe XV and Cu XIX; the 263 Å line belongs to Fe XVI and not to Ar XIV; the bright line at 184 Å can hardly be assigned to the low-abundance Cl IX: it is better identified with O VI.

The spectrum published by Hinteregger et al. /27/ for the 55 — 310 Å region gives 77 identifications, of which 44 coincide with our results.

Table 8 is a summary of the ionization temperatures for the various stages of ionization of the 14 chemical elements mainly used in our identification work. When a filled electron shell is broken, two ionization temperatures are given, which determine an anomalously wide range of existence of the particular ion. Table 8 also provides some information

about the identification results: the ionization temperatures of ions whose lines have been reliably identified are given in bold face.

To sum up: about 90% of the 450 lines observed in the 9.5—1216 Å region of the solar spectrum were identified using the predicted intensities for over 1000 lines. Only 40 of these identifications are doubtful.

## 7. Short-wave radiation energy

Line identification permits solving a number of important problems. For each of the identified lines, we have two values of the radiation flux: the observed flux ( $F_o$ ) and the theoretical or predicted flux ( $F_i$ ). These fluxes often differ markedly, but on the average the differences between the two sets of figures fall within  $\pm 0.5$  of an order of magnitude. There are numerous reasons for these discrepancies, but on the whole they may be classified as "accidental" or "random," i. e., which make the ratio  $F_i/F_o$  greater or less than 1 with equal probability for any given line, and "biased," which make the ratio  $F_i/F_o$  deviate consistently in one direction from 1. Using a small set of identified lines, we obviously cannot differentiate between the two "types" of deviations. "Biased" deviations are primarily caused by errors in the energy calibration of the observed spectrum (for all the lines in the particular spectral region) and by inaccurate data on the abundance of various elements in the solar atmosphere (for the lines of the elements involved only).

Figure 19 plots the ratio  $F_i/F_o$  vs.  $\lambda$  from the data for the 350 reliably identified lines in Table II. The scatter of the experimental points around the mean curve is quite substantial but most of the points (some 75%) deviate at most by 0.5 of an order of magnitude. Some points, including fairly bright and firmly identified lines of Fe ions, are very substantially offset from the mean curve (more than by one order of magnitude). There may be different reasons for these large deviations, viz., breakdown of the stationarity equation (II.1) used in deriving the relation between the measure of emission and the line intensity, inaccurate determination of the ionization temperature, and some other factors.

It is highly significant that, despite the substantial scatter of the points, the mean curve can be traced with fair certainty. The errors in  $F$  definitely cannot be classified as biased, since a "unified" theory for the determination of  $F$  has been applied to ions with widely differing spectral characteristics, irrespective of  $\lambda$ . The predicted flux is therefore expected to deviate in either direction from the true flux. The mean curve  $F_i/F_o = f(\lambda)$  is essentially a calibration curve for the reduction of observed radiation fluxes.

According to Figure 19, observations at  $\lambda < 60$  Å give correct fluxes, whereas in the 60—80 Å region the ratio  $F_i/F_o$  drops from 1 to 1/16. At 80—200 Å, the observed fluxes are approximately a factor of 20 higher than the theoretical figures, at 250—400 Å the radiation factors are slightly higher (a factor of 1.6), and at 400—1000 Å they are again correct. Near  $L_z$ , the radiation fluxes are somewhat high (by a factor of 2—3, according to Hinteregger /26/).

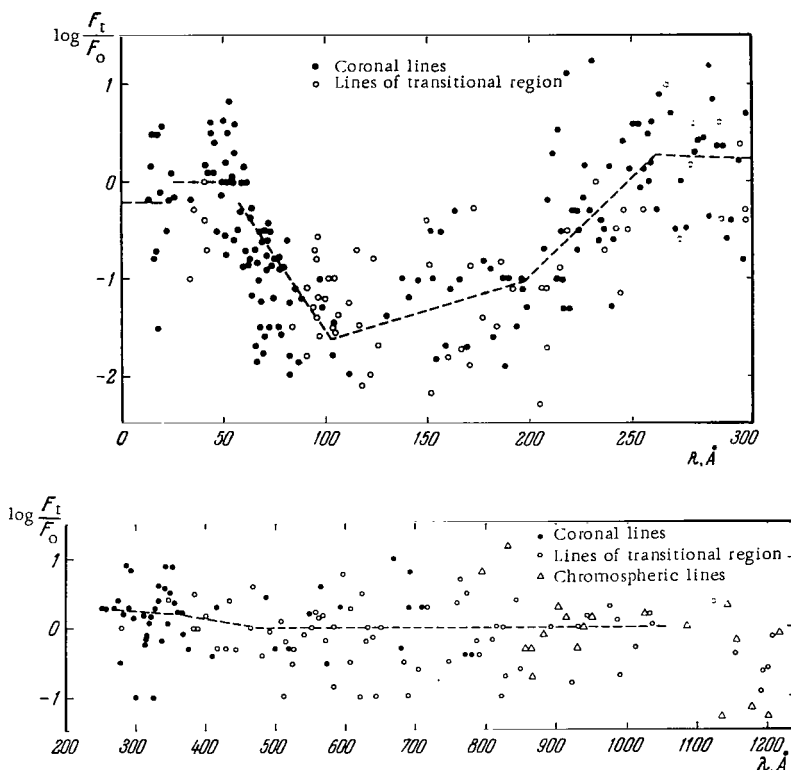


FIGURE 19. Energy calibration of the short-wave spectrum of the Sun in the 0 — 300 Å and 200 — 1200 Å regions using the ratio of predicted ( $F_t$ ) to observed ( $F_o$ ) radiation fluxes in lines from Table II.

Since the theoretical flux estimates may significantly deviate from the true fluxes and they are applicable on the average only, the total radiation energy in the short-wave spectrum ( $E$ ) must not be computed by simple summation of  $F_t$ , as we did before /114/. The energy  $E$  should be obtained from the calibration curve  $F_t/F_o(\lambda)$  reduced using the observed spectrum. This approach, however, implies absence of marked changes in the relative intensities of the observed spectrum, and this assumption is not unlikely for the main absorption mechanism of the Earth's atmosphere (photoionization). Table 9 lists the reduction coefficients as determined from Figure 19, the totals of the observed radiation fluxes in various wavelength intervals of the short-wave spectrum, and the true radiation fluxes. Let us consider this table in more detail. The observed energy distribution in the short-wave spectrum is based on Hinteregger's data /30/. We did not compute the observed energy distribution by summing the line intensities from Table II, because in our identification procedure we naturally ignored the low-intensity lines which merge and produce a significant background. Hinteregger /30/, on the other hand, gives energy values taking into account all the lines. A comparison of some line intensities from /30/ with the intensities obtained from the spectrum tracings reveals small

differences, not exceeding  $\pm 30\%$ . The first column in Table 9 lists the wavelengths, the second column the energy flux in the corresponding wavelength interval according to Hinteregger, the third the reduction coefficient  $F_t/F_o$ , and the fourth the reduced energy flux. The table covers the wavelengths extending below 1027 Å. It is this part of the spectrum that has the maximum effect on the Earth's atmosphere (the oxygen ionization threshold lies near 1027 Å).

TABLE 9. Calibration of the short-wave spectrum of the Sun

$\lambda_1 - \lambda_2, \text{ Å}$	$F_o/30, \text{ erg/cm}^2\text{sec}$	$F_t/F_o$	$F_t, \text{ erg/cm}^2\text{sec}$	$\lambda_1 - \lambda_2, \text{ Å}$	$F_o/30 = F_t, \text{ erg/cm}^2\text{sec}$
1 — 5	$10^{-3}$	?	—	500 — 540	0.059
5 — 15	0.002	?	—	540 — 580	0.050
15 — 31	0.007	0.64	0.004	580 — 630	0.161
31 — 41	0.083	1	0.083	630 — 700	0.037
41 — 62	0.135	1	0.135	700 — 740	0.027
62 — 103	0.286	1/10	0.029	740 — 780	0.049
103 — 165	0.191	1/25	0.008	780 — 810	0.051
165 — 205	0.780	1/16	0.049	810 — 860	0.108
205 — 240	0.140	1/3	0.047	860 — 911	0.185
240 — 280	0.149	1.6	0.238	911 — 920	0.028
280 — 304	0.250	1.6	0.400	920 — 950	0.031
304 — 325*	0.160	1.6	0.256	950 — 990	0.113
325 — 370	0.125	1.6	0.200	990 — 1027	0.101
370 — 460	0.098	1.2	0.120		
460 — 500	0.072	1	0.072		

\* Excluding the He II 304 Å line.

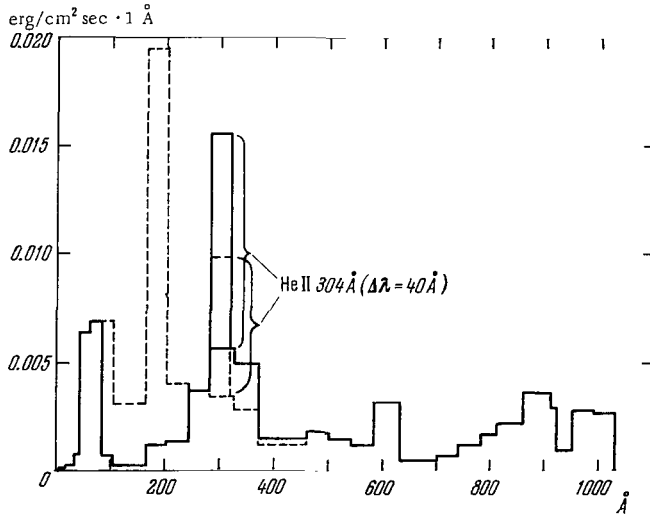


FIGURE 20. Energy distribution in the short-wave spectrum of the Sun in an epoch of minimum activity.

The solid line plots the reduced spectrum. The original observation data /30/ are plotted by a dashed line.

Figure 20 shows the energy distribution in the short-wave spectrum: it plots the spectral energy density in  $\text{erg}/(\text{cm}^2 \text{sec} \cdot 1 \text{ \AA})$  vs. wavelength. The He II 304  $\text{\AA}$  line, because of its exceptional intensity, has been computed for a 40  $\text{\AA}$  waveband. The same figure shows the original spectrum /30/. The most significant consequences of the reduction are the marked decrease of the energy density at 85—180  $\text{\AA}$ : the observation data pointed to a sharp energy maximum at these wavelengths, whereas the reduced spectrum reveals a broad minimum. The existence of this minimum becomes clear after considering the identification table. Turning to Figure 19 and Table II, we see that this spectral region is a characteristic "zone of avoidance" for the coronal lines: more than half of the identified lines are emitted by the ions of the transitional region (with ionization temperatures ranging from  $3 \cdot 10^4$  to  $6 \cdot 10^5^\circ\text{K}$ ), whereas in the nearby spectral region  $\lambda < 100 \text{ \AA}$  virtually the entire emission is due to coronal lines ( $T_i > 6 \cdot 10^5^\circ\text{K}$ ). Even in the long-wave adjoining band (190—300  $\text{\AA}$ ) the coronal lines account for about 75% of the total number. This feature is a result of the specific arrangement of the terms of the ions of the most abundant elements. The radiation in the 100—200  $\text{\AA}$  is thus weaker because of the relatively low efficiency of excitation of lines in a region which is colder than the corona. This fact provides a qualitative confirmation of the validity of our reduction procedure.

Let us consider the energy flux  $E$  emitted in the geoeffective part of the short-wave spectrum ( $\lambda < 1027 \text{ \AA}$ ) and its variations during a solar activity cycle. We recall that the predicted fluxes (Tables I, II) and the reduced spectrum (Table 9) correspond to an epoch of minimum activity, since the fluxes in the "reference" lines used to plot the function  $\Delta\varphi(T_i)$  and hence the nomogram for  $F_i$  are based on the data for 23 August 1961 /26/. The solar activity at that period was low: sunspot area  $48 \cdot 10^{-6}$ , area of  $\text{Ca}^+$  flocculi 0.017, radio-wave flux at 10.7 cm was  $160 \cdot 10^{-22} \text{ watt} \cdot \text{m}^{-2} \cdot \text{Hz}^{-1}$ . The total short-wave radiation flux in Table 9 therefore corresponds to minimum activity:

$$E_{\min}(\lambda < 1027 \text{ \AA}) \approx 2.6 \text{ erg}/\text{cm}^2 \text{ sec}.$$

In order to establish the variation of  $E$  during the activity cycle, we will need the fraction of energy emitted by the regions of the solar atmosphere having different temperatures. To this end, all the identified lines were divided into 4 groups: 1) lines originating in very hot regions ( $T \geq 3 \cdot 10^6^\circ\text{K}$ ), 2) lines of the quiet corona ( $T = 6 \cdot 10^5 - 3 \cdot 10^6^\circ\text{K}$ ), 3) lines of the transitional region ( $T = 3 \cdot 10^4 - 6 \cdot 10^5^\circ\text{K}$ ) and 4) chromospheric lines ( $T < 3 \cdot 10^4^\circ\text{K}$ ). The fluxes of the lines in each of these groups were added up to give the data of Table 10. These are clearly highly tentative figures, since the weak lines were ignored altogether.

Thus in an epoch of minimum activity the corona emits about 1/3 of the total geoeffective flux, the transitional region emits slightly more than 1/3, and the chromosphere accounts for 1/4 of the flux. The amplitude of flux variation during the activity cycle is different for each group; it is furthermore different for each line and primarily depends on the ionization temperature of the emitting ions. The observational material on hand is still very poor: it includes photoelectric recordings obtained at different times /123, 124/, OSO-1 satellite data (March—May 1962) /125, 126/. This material has been analyzed by Ivanov-Kholodnyi. Table 10 gives some



figures which show the extent of variation of the flux in each of the regions having different temperatures (from minimum to maximum activity). Using the data of Table 10, we conclude that the geoeffective flux in an epoch of maximum activity is 3 times higher than the flux in an epoch of minimum activity:

$$E_{\max}(\lambda < 1027 \text{ \AA}) \approx 8 \text{ erg/cm}^2 \text{ sec.}$$

TABLE 10. Contribution from different regions of the solar atmosphere to the geoeffective radiation at  $\lambda < 1027 \text{ \AA}$  in epochs of minimum and maximum solar activity

The region of the solar atmosphere and the corresponding temperature range	Contribution to radiation		Variation amplitude max/min	Contrast of active and quiet regions
	min	max		
Corona $> 3 \cdot 10^6 \text{ }^\circ\text{K}$	5%	15%	10	30
$6 \cdot 10^5 - 3 \cdot 10^6 \text{ }^\circ\text{K}$	30%	50%	5	14
Transitional region $3 \cdot 10^4 - 6 \cdot 10^5 \text{ }^\circ\text{K}$	40%	25%	2	5
Chromosphere $< 3 \cdot 10^4 \text{ }^\circ\text{K}$	25%	10%	1.3	2
The entire solar atmosphere	2.6 erg/cm <sup>2</sup> sec	8 erg/cm <sup>2</sup> sec	3	8

The third column of Table 10 gives the fractions of the total flux emitted by each region in an epoch of maximum activity. Note that the estimate for the radiation in an epoch of maximum is probably close to the upper limit. Indeed, if the relative area of the active region in an epoch of maximum activity is taken to be 0.3, the amplitudes of variation of the hard radiation component should correspond to the following brightness contrast estimates: for hot regions (X rays)  $\approx 30$ , for the corona  $\approx 15$ , for the transitional region  $\approx 5$ , for the chromosphere  $\approx 2$ .

## 8. Quantitative chemical analysis of the solar atmosphere from the results of short-wave observations

The short-wave spectrum, with its abundance of resonance lines of the ions of various elements and with its characteristic optically thin lines, is exceptionally suitable for quantitative chemical analysis. The Fraunhofer spectrum with subordinate lines has a much smaller potential in this respect.

In 1961, when constructing the generalized measure of emission  $\Delta\varphi(T_i)$ , we discovered /90/ that the points corresponding to NV and NIV ions markedly deviated from the mean curve. This pointed to a significantly lower content of nitrogen ( $\kappa \approx 10^{-5}$ ) than what had been previously assumed. A more careful analysis comparing the  $F_i$  and  $F_o$  values of several lines (NII 1085 Å, NIII 764.4 and 990 Å, NIV 765.1 Å, NV 1238.8 Å /114/) gave the final figure  $\kappa_N = 3 \cdot 10^{-5}$ , which is  $1/3 - 1/10$  of the previously accepted values.

The content of a particular element can be found from a comparison of the theoretical and the observed line intensities (see Figure 19) only if the function  $\Delta\varphi(T)$  has been constructed without using the lines of the ions of the sought elements. In any case, the corresponding points must not alter the shape of the curve  $\Delta\varphi(T)$ . In our construction, we used corrected values of the elemental contents to plot the function  $\Delta\varphi(T)$ . In the ideal case,  $\Delta\varphi(T)$  is best constructed using the lines of one element whose content is known from independent data. Attempts of this kind undertaken by Pottasch and other authors are discussed in what follows. Unfortunately, this approach is not quite accurate, since the "reference" lines at  $\lambda > 500 \text{ \AA}$  used for the construction of  $\Delta\varphi(T)$  contain relatively few bright and reliably identified lines, not to mention lines belonging to one element. The initial dependence  $\Delta\varphi(T)$  (see Figure 17) at temperatures  $T < 3 \cdot 10^5 \text{ }^\circ\text{K}$  is adequately determined by the lines of the C and O ions, and at  $T > 6 \cdot 10^5 \text{ }^\circ\text{K}$  it is determined by the Fe/Ni ratio and by the measure of emission of the entire corona, as it emerges from coronal observations in the continuous spectrum. The ratio  $\kappa_{\text{Fe}}/\kappa_{\text{Ni}} = 10$  is obtained with fair accuracy from an analysis of the intensities of the "forbidden" coronal lines which are emitted by ions of one isoelectronic series, e.g., Fe X and Ni XII, Fe XIV and Ni XVI. At the same time, the correct choice of the C and O contents is monitored by comparing the  $F_i/F_o$  ratios corresponding to "cold" ( $T < 3 \cdot 10^5 \text{ }^\circ\text{K}$ ) and "hot" ( $T > 6 \cdot 10^5 \text{ }^\circ\text{K}$ ) ions. The best fit of the points for the ions of C (12 lines), O (39 lines), Fe (60 lines), and Ni (15 lines) in Figure 19 is achieved if we assume abundances of  $2 \cdot 10^{-4}$ ,  $6 \cdot 10^{-4}$ ,  $2 \cdot 10^{-5}$ , and  $2 \cdot 10^{-6}$ , respectively. This abundance was obtained for Fe back in 1962 from an analysis of fewer lines /129/. All these points fix with fair certainty the average dependence of  $F_i/F_o$  on wavelength. Six hydrogen lines can be added to this group.

The abundances of these four elements and hence the average dependence of  $F_i/F_o$  on  $\lambda$  are in fact determined by the dependence of the generalized measure of emission in the corona on temperature (the curve  $\Delta\varphi(T)$  for  $T > 6 \cdot 10^5 \text{ }^\circ\text{K}$  in Figure 17) which is obtained from ground observations of the coronal continuum and the "forbidden" coronal lines in the optical spectrum.

Let us consider some other elements whose lines have been identified in the short-wave spectrum ( $\lambda < 1216 \text{ \AA}$ ).

1. Helium. Six lines identified, good fit for  $\kappa_{\text{He}} = 0.1$ .
2. Nitrogen. Fifteen lines identified; previous value  $\kappa_{\text{N}} = 3 \cdot 10^{-5} / 114/$  confirmed.
3. Neon. The content of neon in the Sun has not been determined, because no neon lines fall in the visible spectrum. The astrophysical data for hot stars, planetary nebulae, and meteorites give an average figure of  $\kappa_{\text{Ne}} = 5 \cdot 10^{-4}$ . The short-wave spectrum of the Sun contains fairly strong neon lines. The 19 identified lines give  $\kappa_{\text{Ne}} = 3 \cdot 10^{-5}$ .\*
4. Sodium. Only one line has been identified, for which the upper limit value of the observed flux is available. The usual abundance figure  $\kappa_{\text{Na}} = 2 \cdot 10^{-6}$  may be slightly exaggerated.
5. Magnesium. Twenty-three lines identified. Relatively small scatter of points,  $\kappa_{\text{Mg}} = 4 \cdot 10^{-5}$ .
6. Aluminum. Seven lines identified,  $\kappa_{\text{Al}} = 3 \cdot 10^{-6}$ .
7. Silicon. Apparently an element with the largest number of (relatively strong) lines in the entire spectrum below  $1216 \text{ \AA}$ . Sixty-five lines identified. Reliable abundance figure  $\kappa_{\text{Si}} = 3 \cdot 10^{-5}$ .

\* Lambert /730/ analyzed the Ne IV — Ne VIII lines and obtained  $\kappa_{\text{Ne}} = 5 \cdot 10^{-5}$ .

8. Sulfur. Twenty-five lines identified. Small scatter of points. Abundance  $\kappa_S = 1 \cdot 10^{-5}$ .

9. Argon. Six lines identified. Best value  $\kappa_{Ar} \approx 3 \cdot 10^{-6}$ .

10. Calcium. Nine lines identified. Uncertain abundance figure  $\kappa_{Ca} \approx 4 \cdot 10^{-6}$ .

In summing, note that the above abundances for the 14 chemical elements (excluding sodium) are on the average accurate to within a factor of about 2. For the remaining 6 elements, the abundances are taken from /92/. The abundances of the elements relative to hydrogen obtained in this way were used for predicting the short-wave line intensities.

The chemical composition data (ours and from /92/) are presented in graphic form in Figure 21, which plots the abundance vs. the atomic number.

Let us consider other determinations of the chemical composition of the solar atmosphere based on analyses of short-wave lines. Since 1963, Pottasch has published a number of papers on this subject /130—133/. Plotting the measure of emission  $M$  vs. temperature from rocket observations of the short-wave spectrum, as suggested by us, Pottasch /117, 130/ found the abundances of the 9 elements whose 28 lines had been used to plot  $M(T)$ . The abundances were determined relative to oxygen by displacing the points along the  $\log M$  axis until the best fit with the average  $\kappa_0 M(T)$  curve was obtained. Points corresponding to the same element were naturally displaced by equal amounts. Equal displacements along the  $\log M$  axis multiply the abundance  $\kappa$  in the expression for  $M$  by the same factor. Note that this method is not particularly accurate, especially when the deviations of the experimental points from the average curve are relatively small: these deviations may be associated with inadequacy of the theory and errors in line intensities, and not only with errors in the abundance of the element.

Pottasch applied a similar method to determine the abundance of various elements relative to oxygen. The abundance of oxygen (relative to hydrogen,  $\kappa_0$ ) was obtained from various observations of the Sun in the radio spectrum (at wavelengths between 1 and 100 cm), i.e., from the curve of the radio temperature  $T_r$  as a function of  $\lambda$ . For various values of  $\kappa_0$  and hence various  $M(T)$  (which is proportional to the abundance of oxygen), Pottasch obtained the function  $T_r(\lambda)$ . Comparison of this curve with the experimental findings gives  $\kappa_0$ . According to /130/, the theory provides the best fit of observations for  $\kappa_0 = 7 \cdot 10^{-4}$ . Later /131/, Pottasch used a slightly different figure,  $\kappa_0 = 4.5 \cdot 10^{-4}$ .

In 1966 Pottasch /132/ analyzed the short-wave lines of the ions Fe VIII — Fe XIV and obtained  $(4-6) \cdot 10^{-5}$  for the iron/hydrogen ratio. In a later work, he examined the line intensities of O VIII/Fe XVII and O VII/Fe XIV from /133/ and determined the abundances  $\kappa_O/\kappa_{Fe}$ , which were found to be 10—20 and 6, respectively (our result is around 30).<sup>\*</sup> Pottasch also obtained  $\kappa_O/\kappa_N = 6.3$  and  $\kappa_O/\kappa_{Ne} = 29$  (our data give 20 for both ratios).

Comparing the results of Pottasch /131/ with our abundances, we conclude that the average abundance of 12 elements according to Pottasch is double our figure. The only exception is oxygen (a factor of 1.2 less).

The conclusion of Pottasch that the content of the heavy elements in the corona is higher than in the photosphere is questionable in our opinion. A significant difference (by a factor of 5—10) is observed only for Fe, but the determination of the content of Fe in the photosphere from subordinate absorption lines is highly inaccurate owing to difficulties in the transition

<sup>\*</sup> Beigman and Vainstein /731/ obtained  $\kappa_O/\kappa_{Fe} = 30$  using O VIII and Fe XVII lines /28/.

to the ground state and primarily lack of data on the degree of ionization of Fe in the photosphere.

Let us briefly review the recent determinations of the photospheric abundance of Fe. Goldberg, Kopp, and Dupree /134/ obtained  $\kappa_{\text{Fe}} = 4.4 \cdot 10^{-6}$  from Fe I lines (in the visible spectrum). Withbroe /135/ obtained from the Fe I lines at 3100 — 3800 Å a figure which was 4 times less and proposed possible explanations for this discrepancy. This result shows to what extent the method of determination of Fe in the photosphere is unreliable.

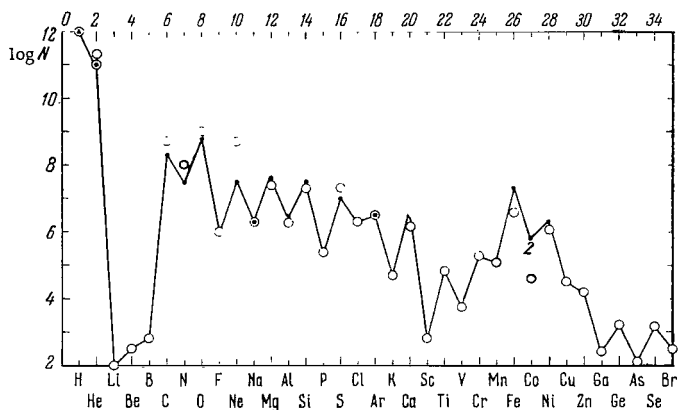


FIGURE 21. Content of elements in the solar atmosphere relative to hydrogen ( $\log N_{\text{H}} = 12$ ).

Dots — our data from short-wave spectrum; circles — standard data for the Sun and outer space /92/.

Pottasch's considerations concerning the possible accretion of meteorite matter by the outer corona and the enrichment of the heavy ions in the inner corona by this mechanism /131, 136/ are hardly acceptable.

Van de Hulst's comment (see discussion in /131/) deserves particular attention: he is of the opinion that the directional flow of matter from the corona (the "solar wind") rules out downward diffusion of meteorite atoms, even assuming that the concentration of meteorite matter near the Sun is a factor of 100 higher than in the interplanetary space (a necessary condition for effective accretion).

Following Pottasch's work, Jordan published a similar analysis of the intensities of 15 short-wave lines of Fe VIII — Fe XV, 8 lines of Ni X — Ni XIII, and 17 lines of Si VI — Si X and determined the abundances of these three elements /137/. The intensity data were borrowed from Hall, Damon, and Hinteregger /26/, and the ionization temperatures were computed with allowance for dielectron recombination.

Jordan's result (Si:Fe:Ni = 8:10:0.8) is little different from our results (15:10:1). The maximum divergence (a factor of 2) is observed for Si, but remember that this is the overall accuracy of the abundances of the chemical elements on the Sun. The conversion to "absolute" abundances, i. e., abundances relative to hydrogen, was carried out in /137/ using Jordan's figure  $\kappa_{\text{Fe}} = 6 \cdot 10^{-5}$ .

In another work /138/, Jordan analyzed the excitation of "forbidden" lines in the visible spectrum and "allowed" short-wave lines of iron ions; the results gave  $\kappa_{\text{Fe}} = 5 \cdot 10^{-5}$ . Jordan's results are consistent with the findings of Pottasch to the extent that there is a 10-fold excess of iron and nickel in the corona compared with the photosphere.

Warner /139/ considered the relative abundance of elements in the corona and the photosphere. A comparison of the coronal and the photospheric abundances of the elements relative to Fe (taken as 100%) indicates that the results for the corona are close to the data of various authors for the photosphere (the only significant divergence is with the results of Goldberg, Müller, and Aller /140/). Warner found the abundance of Fe and Ni relative to hydrogen in the photosphere from the "forbidden" absorption lines [Fe II] and [Ni II]; his results give  $6 \cdot 10^{-5}$  and  $6 \cdot 10^{-6}$ , respectively.\* By comparing the ratio of the coronal to photospheric abundances ( $\kappa_{\text{cor}}/\kappa_{\text{ph}}$ ) with the excitation potential ( $\chi$ ) of the lines used to compute  $\kappa_{\text{ph}}$ , Warner detected a growth of  $\kappa_{\text{cor}}/\kappa_{\text{ph}}$  with decreasing excitation potential: the ratio increased from 1 for  $\chi \approx 10$  eV to 10 for  $\chi \approx 2$  eV. The last two facts, as it was noted in /139/, suggest that the conclusion concerning the coronal excess of Fe and Ni was premature. A critical reassessment of the method for the determination of the abundance of elements in the photosphere is thus needed.

Pottasch's work is closely related to the paper by Dupree and Goldberg /141/ in which the abundances of Si, O, and Fe are determined and the distribution of  $T(h)$  is obtained. Let us analyze the results of this work in some detail. The starting data are the fluxes in the following resonance lines: O II — O VI, Si II — Si IV, Si VI, Si VIII, Si X — Si XII, and Fe XV, Fe XVI (primarily from Hinteregger's observations).

The abundances of Fe and O relative to Si were used according to the data of Goldberg, Müller, and Aller /140/ for the photosphere. The content of Si was found by comparing the computed curve  $(T, \lambda)$  with observations. The results give  $\kappa_{\text{Si}} = 3.2 \cdot 10^{-5}$ , which coincides with our figure. The abundances of O and Fe are  $9.3 \cdot 10^{-4}$  and  $3.8 \cdot 10^{-6}$ , respectively. The last figure is highly questionable, as  $\kappa_{\text{Fe}}$  is fixed quite arbitrarily: two points used in /141/, Fe XV and Fe XVI, may be displaced vertically along the  $M(T)$  curve (see the corresponding graph in /141/) by up to one order of magnitude. The abundance of Fe ( $2 \cdot 10^{-5}$ ) that we obtained from 60 lines of various ions is clearly nearer the true figure.

The method of computation of  $T_r(\lambda)$  used by Dupree and Goldberg cannot be accepted without reservation, since in computing the optical thickness in the radio spectrum, the authors simply summed the measures of emission for each temperature range, without making allowance for possible overlap. As a result, the optical thickness  $\tau$  for some  $T$  may have worked out to be too high. This point will become clearer in Chapter III, where  $T_r(\lambda)$  is actually computed.

The distribution of  $T(h)$  obtained by Dupree and Goldberg /141/ is very close to the  $T(h)$  curve in the old 1948 model of Allen and Woolley /142/, which was rejected by Allen /99/ in his computations of the short-wave line fluxes (see Chapter III). The conclusion of Dupree and Goldberg that the transitional region between the chromosphere and the corona is thin (less

\* Later, the same author /733/ obtained  $\kappa_{\text{Fe}} = 3 \cdot 10^{-6}$  and  $\kappa_{\text{Ni}} = 1 \cdot 10^{-7}$  from [Fe II] and [Ni II] lines, but the abundance ratio Fe: Ni = 30 turned to be significantly higher than for the corona (5 — 10).

than 1000 km across) is based on an arbitrary assumption of constant gas pressure in this region:  $n \cdot T = 6 \cdot 10^{14} \text{ cm}^{-3} \text{ deg}$ . Note that the temperature of the chromosphere works out to be too high:  $T = 5 \cdot 10^4 \text{ K}$  for  $h = 2000 \text{ km}$ , according to the erroneous treatment of Athay and Menzel /143/. \*

## 9. "Unusual" identifications in the short-wave spectrum

In 1964, Gell-Mann and Zweig independently predicted the possible existence of three elementary particles, "quarks" (see /145/). These hypothetical particles constitute the last element in the general theory of elementary particles, explaining mesonic and baryonic multiplets. "Quarks" have a large mass (about  $5 - 10 m_p$ ) and should possess fractional charges  $(+2/3)e$  and  $(-1/3)e$ .

Zel'dovich, Okun', and Pikel'ner /146/ considered different possibilities of quark detection. Quarks of  $(-1/3)e$  charge should be stable both in vacuum and after becoming attached to atomic nuclei. In particular, quarks can be detected spectroscopically in the spectra of the abundant elements (N, O, C, Fe) whose nuclei contain the quark  $(-1/3)e$ . As a result of the attachment of a quark, the effective charge of the ion will change, altering the energy of the spectral levels of the ion. This idea was developed by Sinanoglu, Skutnik, and Tousey /147/, who computed the wavelengths of the strongest lines of ions with quarks: C'III - C'IV, N'II - N'V, O'III - O'VI. The corresponding computations are very simple, as they are carried out by interpolation along isoelectronic series (by Edlen's method). The wavelength of a line emitted by a quark-containing ion increases approximately by 10% for an ion with  $Z = 2 - 5$ . If such a line is discovered, comparison of its intensity with the intensity of the analogous line of the "ordinary" ion provides an estimate of the partial concentration of quark-containing elements. A search for such lines in the short-wave spectrum of the Sun was undertaken in /147/. The wavelengths of 30 lines from 12 multiplets in the  $200 - 1700 \text{ Å}$  region were computed for the elements listed above. The accuracy of wavelength determination was between 0.05 and 0.2 Å. Only transitions producing sufficiently strong ("ordinary") lines in the short-wave spectrum of the Sun were naturally considered.

Comparison of the computed wavelengths for quark-containing ions with the observed spectrum of the Sun showed that 11 of the predicted lines blended with strong "ordinary" lines, whereas no emission was detected within the margin of experimental error at the wavelengths corresponding to the remaining 16 lines. The last factor provided an estimate for the upper limit of the relative concentration of quark-containing elements:  $C'/C < 10^{-4}$ ,  $N'/N < 10^{-3}$ ,  $O'/O < 3 \cdot 10^{-5}$ . These figures are substantially higher than the cosmological estimates of the quark concentration after the Big Bang:  $10^{-9} - 10^{-18}$  /146/. Weak lines are observed at the wavelengths corresponding to three lines in the main multiplets of N' II and C' IV /147/. The relevant data are summarized in Table 11.

Soon after the publication of /147/, Bennett /148/ published a list of 36 lines emitted by subordinate transitions between the levels of ordinary ions of O, N, C. Bennett remarks /148/ that these lines coincide, within the accuracy of his computations, with the emission lines of quark-containing

\* See the comments of Shklovskii and Kononovich on this work /144/.

ions from /147/. The search for quarks in the short-wave spectrum of the Sun thus seems to be a hopeless proposition, at least in the immediate future. Indeed, the wavelengths of the extremely weak emissions of quark-containing ions invariably coincide with some subordinate "ordinary" lines, which become progressively more numerous as the intensity diminishes.

TABLE 11. Identification of lines emitted by quark-containing isotopes ( $\lambda'$ ) in the short-wave spectrum of the Sun

Ion	Transition	$\lambda$ , Å	$\lambda'$ , Å /147/	$\lambda_{\text{obs}}$ , Å	Probable identification /148/
CIV	$2^2S_{1/2} - 2^2P_{3/2}^{\circ}$	1549.20	$1689.0 \pm 0.2$	Stable line	CII $4p^2P_{3/2}^{\circ} - 4f^4D_{3/2}$ 1659.11
NII	$2^3P_2 - 2^3D_3^{\circ}$	1085.70	$1207.6 \pm 0.2$	1207.77	OIII $2p^4D_2 - 4d^1P_1^{\circ}$ 1207.78
NII	$2^3P_2 - 2^3D_2^{\circ}$	1085.54	$1207.4 \pm 0.2$	1207.25	OIII $3p^3D_3^{\circ} - 3d^3P_2$ 1207.21

Table 11 lists the wavelengths of quark-containing ions which correspond to weak unidentified lines in the solar spectrum /147/. Possibly some of the "ordinary" identifications in /148/ can be questioned, but there will always be another similar identification for these emission lines, as we have noted before.

Let us analyze the subsequent conclusions of Tousey et al. /147/. The authors determined the relative content of the quark-containing nitrogen  $N'/N = 5 \cdot 10^{-4}$  by examining the 1207.8 Å line. The flux in the observed "quark" line differs by the same factor from the flux in the "ordinary" line NII 1085.54 Å, which is equal to 0.01 erg/cm<sup>2</sup>sec according to Hinteregger et al. /26/. Using our method, let us estimate the flux in the OIII 1207.78 Å line, which was proposed as a likely identification by Bennett /148/. Taking  $\sim 0.1$  for the oscillator strength and using the excitation energy of the ground state (260 Å), we find  $F = 3 \cdot 10^{-6}$  erg/cm<sup>2</sup>sec. The identification proposed in /148/ is thus quite acceptable.

To sum up: spectroscopic detection of "extraordinary" quark-containing elements in the Sun has very limited perspectives at this stage. Spectral methods will be effective only if the relative concentration of the quark-containing elements is higher than  $10^{-5} - 10^{-4}$ .

### *Chapter III*

#### *THE PHYSICS OF THE SOLAR ATMOSPHERE*

We have previously mentioned some gaps in our knowledge of the short-wave region of the solar spectrum. One of the principal gaps concerns the study of the physical conditions in the solar atmosphere. In the 1950's scientists formed a false impression that the structure of the solar atmosphere was fairly well known. Indeed, at a first glance it seemed that we knew everything or almost everything that there was to know about the Sun: this most immediately observable star regularly generates energy in its interior by fusion reactions converting hydrogen nuclei into helium, the bulk of this energy is conducted to the surface of the Sun in the form of radiation with a continuous spectrum between 3000 and 10,000 Å, and a small percentage of the total energy creates a thin convective zone on the Sun's surface, the photosphere. Material compression waves propagating from the photosphere raise the temperature of the higher layers, thus producing the chromosphere and the corona. The latter is an extended rarefied part of the solar atmosphere which is characterized by high kinetic temperatures (about  $10^6$ °K) and low density (about  $10^8 - 10^5$  atoms/cm<sup>3</sup>).

In the same period, however, new important discoveries in the physics of the Sun automatically posed new difficult problems. First and foremost in this category comes the discovery of the short-wave solar radiation, whose interpretation required a thorough revision of our concepts of the structure of the solar atmosphere. In particular, the numerous emission lines emitted by ions in so-called "intermediate" ionization stages in the short-wave spectrum pointed to the existence of a wide range of temperatures in the solar atmosphere, ranging from  $10^4$  to  $10^6$ °K. Certain phenomena, such as the fairly strong X-ray emission at  $\lambda < 10$  Å have not been adequately interpreted to this day. The physics of the solar atmosphere correspondingly attracts ever increasing attention on the part of the scientists.

#### **10. Theory of ionization of the solar corona**

The principal physical characteristics of the solar corona are the electron concentration  $n_e$  (the corona is a plasma consisting predominantly of ionized hydrogen) and the kinetic temperature  $T$ . The magnitude and the distribution of  $n_e$  may be determined from observations of the coronal brightness, and  $T$  is determined by indirect methods.

When the coronal emission lines had been identified with the emission of highly ionized atoms, it became clear that the coronal temperatures reached a million degrees. Numerous theoretical and experimental findings



subsequently confirmed this result. The coronal gas is not maintained in a state of thermodynamic equilibrium, as a result of the large difference between the temperature of the radiation field (about  $5800^\circ$ ) and the kinetic temperature (about  $10^6^\circ\text{K}$ ). If we ignore the relatively rare fast processes in the corona, the ion and the electron temperatures may be taken as virtually equal. This equality of the two temperatures is associated with the high efficiency of the particle interactions in the corona. In  $1 - 10$  sec, each particle experiences several collisions,\* the mobile electrons transmitting about  $1/1000$  of their energy to the heavier ions in each collision. Hence it follows that about 1 hour is needed to attain a complete equipartition of energy between the electrons and the ions. A Maxwellian distribution of velocities among particles of one species (among the electrons, say) is attained much faster, in  $1 - 10$  sec, since only few collisions are needed to establish this velocity distribution.

A more detailed treatment of the corona as a plasma cloud is contained in the books of Shklovskii /149, 150/, who is considered the father of the theory of ionization of the corona. A theory of ionization was also developed independently, though somewhat later, by Allen and Woolley /151/, who reached similar results. In what follows, we will use the basic elements of the theory of ionization from /149, 150, 152/, making the necessary supplementary assumptions. The final purpose of our treatment is to obtain data on the physical nature of the corona and to generalize the theory of coronal ionization to other parts of the solar atmosphere.

Shklovskii and Allen and Woolley considered an equation of ionization equilibrium

$$Z_{\text{rec}} = Z_{\text{ion}}, \quad (\text{III.1})$$

which implies that, under steady-state conditions, the number of ionization events in unit time is equal to the number of recombination events. Let ions of  $i$ -th stage of ionization be present in the corona in a concentration  $n_i$ . Most of these ions are in the ground state. Electron impact provides the most effective mechanism of ionization in the corona. Therefore,

$$Z_{\text{ion}} = n_i n_e W_{1\infty}, \quad (\text{III.2})$$

where  $W_{1\infty}$  is the coefficient of ionization from the ground level, which depends on  $T$  and on the ionization potential. Radiative recombination is the most effective among the various recombination processes. Recombination to all the levels of the ion  $i + 1$  should be considered in this case, since the probability of recombination to the excited levels is considerable and cannot be ignored:

$$Z_{\text{rec}} = n_i n_e \sum_{m=1}^{\infty} R_m, \quad (\text{III.3})$$

where  $R_m$  is the coefficient of recombination to level  $m$ , and the sum is taken over all the quantum states of the ion in the  $(i + 1)$ -th stage of ionization.

\* Particle "collisions" in the corona are determined by Coulomb interactions, which have high effective cross sections (about  $10^{-16} \text{ cm}^2$ ).

Equating (III.2) and (III.3), we obtain an expression for the concentration ratio of ions in two adjoining stages of ionization,

$$\frac{n_{i+1}}{n_i} = \frac{W_{1\infty}}{\sum_1 R_m}, \quad (\text{III.4})$$

which depends on the temperature and the atomic characteristics of the ion only. Using this expression, we can find the degree of ionization as a function of temperature for any ion:

$$\frac{n_i}{\sum_1 n_i} = \Phi(T)$$

(the sum is taken over all the ionization states).

These are the elements of the theory of ionization of the solar corona, first developed in /149—152/.

The derivation of (III.4), however, was incorrect. The processes affecting the upper levels — electron impact ionization and the reverse process of three-particle recombination (the result of the collision of two electrons with an ion) — play the leading part in the equation of ionization equilibrium  $Z_{\text{ion}} = Z_{\text{rec}}$ . According to /91/, these processes are 5—10 orders of magnitude more frequent than ionization and photorecombination, which involve the ground level. Although the computations in /91/ were carried out for hydrogen, the same observation is valid for all the elements. In this case, the equilibrium equation  $Z_{\text{ion}} = Z_{\text{rec}}$  leads to the ordinary Saha equation, which describes the ionization under conditions of local thermodynamic equilibrium. Thus the rate of ionization processes is determined by the upper levels, and the majority of ions occupying the ground level do not actively exchange electrons with the ionization continuum, forming an "inertial reservoir" of ions which determines the degree of ionization. We can now proceed with a rigorous computation of the degree of ionization.

Consider the basic elementary processes: electron impact ionization ( $W_{\text{mco}}$ ), photorecombination ( $R_m$ ), electron impact of first ( $W_{mi}$ ) and second ( $W_{im}$ ) kind, "triple" recombination ( $R_m^{(3)}$ ) and spontaneous transitions ( $A_{mi}$ ).

In the physical conditions prevailing in the corona,  $A_{mi}$  and  $R_m$  can be ignored in comparison with other processes starting with some level  $k$  (and for all higher levels). In this case, the population of all levels with  $m \geq k$  will be described by a Boltzmann distribution, which is related to the continuum by the Saha equation. In other words, a state  $m \geq k$  is characterized by local thermodynamic equilibrium, since the remaining two pairs of processes are mutually reversible.

It is readily seen that the degree of ionization is determined by ionization from the ground level  $W_{1\infty}$ , photorecombinations to all the levels  $m \leq k$  ( $R_m$ )

and spontaneous transitions from the "Boltzmann" region  $\sum_k^{m_0} (n_{im} \sum_{j=1}^k A_{mj})$ ,

where  $m_0$  is the number of levels, and  $n_{im}$  is an ion of the  $i$ -th stage of ionization in quantum state  $m$ . The equation of ionization equilibrium has the form

$$n_i n_e W_{1\infty} = n_{i+1} n_e \sum_{m=1}^k R_m + \sum_{m=k}^{m_0} n_m \sum_{j=1}^k A_{mj}. \quad (\text{III.5})$$

To fair approximation, any ion is hydrogen-like for  $m > 1$ , and we may therefore use the previous result for hydrogen /90/:

$$\sum_{m=k}^{m_0} \left( n_{im} \sum_{j=1}^k A_{mj} \right) \approx 3 \cdot 10^{-6} Z^4 m_1^{-3} T^{-3/2} e^{x_i} \times \left\{ Ei \left[ x_i \left( 1 - \left[ \frac{m_1}{m_1 + k - 1/2} \right]^2 \right) \right] - Ei(x_i) \right\} n_e n_{i+1}; \quad (\text{III.6})$$

here  $x_i = \chi_i/kT$ ,  $\chi_i$  is the ionization potential,  $m_1$  is the principal quantum number of the ground levels,  $Ei(x_i)$  is the integral exponential function,  $Z$  is the effective ionic charge.

We will use Menzel's expression for the recombination coefficient, which strictly speaking is true for hydrogen-like ions:

$$R_m = 3.2 \cdot 10^{-6} Z^4 T^{-3/2} m^{-3} e^{x_{im}} Ei(x_{im}); \quad (\text{III.7})$$

here  $Z$  may be taken numerically equal to the index of the ionization state. For CIV, for example, we may take  $Z = 4$ .

Inserting (III.6) and (III.7) in (III.5), we obtain for the concentration ratio of ions in adjacent stages of ionization

$$\frac{n_i}{n_{i+1}} = \frac{\left\{ Ei \left[ x_i \left( 1 - \left[ \frac{m_1}{m_1 + k - 1/2} \right]^2 \right) \right] \right\} / Ei(x_i)}{W_{100}} R_1 + \sum_{m=2}^k R_m. \quad (\text{III.8})$$

Here  $k$  is not particularly sensitive to the physical conditions: for the chromosphere ( $n_e = 10^{12} \text{ cm}^{-3}$ ,  $T = 10^4 \text{ }^\circ\text{K}$ )  $k = 5$  and for the corona ( $n_e = 10^8 \text{ cm}^{-3}$ ,  $T = 10^6 \text{ }^\circ\text{K}$ )  $k = 10$ .\*

Expression (III.8) is close to (III.4) and calculations of the ionization temperature from the two relations give results which differ by no more than 10%. In what follows, we will use the simple expression (III.4), which is obtained from (III.8) if the expression in braces is set equal to unity.

We can now proceed with a computation of the degree of ionization. We will first derive a convenient expression for  $n_i/n_{i+1}$ . We compute  $\sum R_m$  by replacing the sum with an integral (a computation of this kind for hydrogen was carried out in /91/:

$$\sum R_m = R_{m_1} + \int_{m_1 + \frac{1}{2}}^{\frac{m_0}{2}} R_m dm. \quad (\text{III.9})$$

The integral is taken to  $m_0/2$ , and not to  $m_0$ , so as to allow for the faster drop in  $R_m$  in the case of a finite number of levels for an ion in a real plasma /91/. Expression (III.7) can be conveniently used for  $R_m$ ; in this expression the potential of ionization from level  $m$  may be expressed as  $\chi_{im} \approx \chi_i (m_1/m)^2$ , where  $\chi_i$  is the ionization potential from the ground level. This relation is exact for hydrogen like atoms and gives adequate results for the isoelectronic series of alkali elements. For all other ions, it is highly approximate.

Inserting (III.7) in (III.9) and using the above approximation, we find after integration

\* According to /91/,  $k \approx 55 T^{1/4} n_e^{-1/2}$ .

$$\Sigma R_m = 3.2 \cdot 10^{-6} Z^4 T^{-3/2} \left\{ m_1^{-3} e^{x_i} Ei(x_i) + \frac{1}{2m_1^2 x_i} e^{\mu x_i} Ei(\mu x_i) + \frac{1}{2m_1^2 x_i} \ln[1.78 \mu x_i] \right\}, \mu = \left( \frac{m_1}{m_1 + 1/2} \right)^2. \quad (\text{III.10})$$

If  $x_i > 3$ , we may take to fair approximation

$$\Sigma R_m = \frac{3 \cdot 10^{-6} Z^4}{m_1^3 T^{3/2} x_i} \left\{ 1 + \frac{m_1}{2} \ln \left[ 1.8 \left( \frac{m_1}{m_1 + 1/2} \right)^2 x_i \right] \right\}. \quad (\text{III.11})$$

The second term in braces gives the contribution of all recombinations to all the levels, except the ground level.

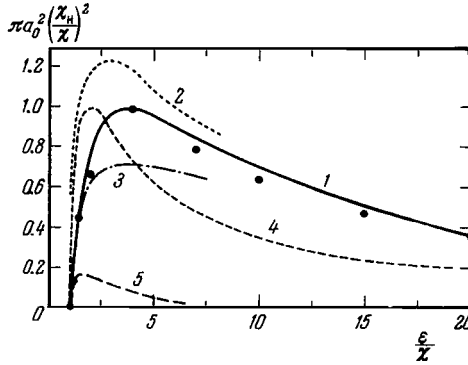


FIGURE 22. The effective cross section for the ionization of hydrogen atoms by electron impact (in units of  $\pi a_0^2$ ) vs. the relative energy of the incident electron.

Curve 1 plots the "real" cross section /93/, the dots represent the approximation based on (III.12); 2 — Malik and Trefftz (for O V) /155/; 3 — Elwert /157/; 4 — Thomson ("classical" cross section); 5 — Schwartz and Zirin (for Fe XIV) /156/.

To compute the probabilities of ionization by electron impact we use, as in /90/, the effective cross section from /93/ (the Born approximation). This cross section has its maximum for incident electron energy  $\epsilon$  equal to four times the ionization potential:  $\sigma_{\max} \approx n \pi a_0^2 (\chi_i / \chi_H)^2$ , where  $n$  is the number of outer electrons,  $\pi a_0^2$  is the area of the Bohr orbit,  $\chi_H = 1$  Ry. Allen /93/ describes this cross section as "real", as it closely corresponds to experimental data. Indeed, laboratory measurements of the effective cross sections for single and multiple ionization of He, Ar, Hg /54/ show that the cross section reaches its maximum for  $\epsilon \approx 4\chi_i$ , and its value is close to the theoretical figure.

Figure 22 plots various cross sections as a function of the relative energy of the incident electron.

The real cross section is adequately expressed by the relations /58/

$$\sigma = \frac{4}{3} \pi a_0^2 \left( \frac{\chi_H}{\chi_i} \right)^2 \left( 1 - \frac{\chi_i}{\epsilon} \right), \quad 1 \leq \frac{\epsilon}{\chi_i} \leq 4, \quad (\text{III.12})$$

$$\sigma = 8 \pi a_0^2 \left( \frac{\chi_H}{\chi_i} \right)^2 \left( \frac{\chi_i}{\epsilon} - 2 \frac{\chi_i^2}{\epsilon^2} \right), \quad \frac{\epsilon}{\chi_i} \geq 4.$$

The ionization probability obtained after integrating (III.12) over the energies has the following form for a Maxwellian distribution of electrons:

$$W_{100} = 1.8 T^{-3/2} \frac{1}{x_i} \left\{ \frac{e^{-x_i}}{x_i} - \left( 3 + \frac{1}{x_i} \right) e^{-4x_i} + 6x_i [e^{-4x_i} - 2x_i Ei(4x_i)] \right\}, \quad (\text{III.13})$$

where  $x_i = \chi_i/kT$ . If we retain only the first term in braces, the simplified expression will be applicable for  $x_i > 0.5$  with 10% accuracy:

$$W_{100} = 1.8 T^{-3/2} \frac{e^{-x_i}}{x_i^2}. \quad (\text{III.14})$$

We have thus found  $n_i/n_{i+1}$ .

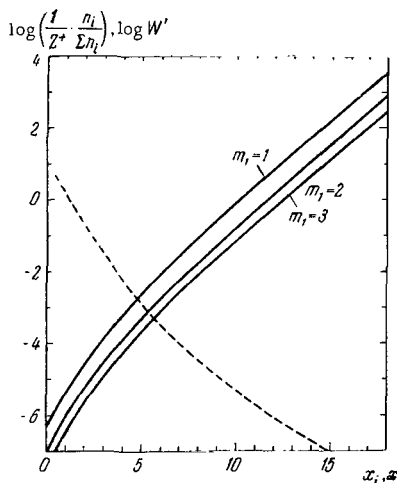


FIGURE 23. Illustrating the computation of excitation and ionization by electron impact in the transitional region and in the corona. The excitation coefficient is  $W(x) = f_{12} \cdot T^{-3/2} W'(x)$ ,  $x = \chi_{12}/kT$ ,  $n_i / \Sigma n_i$  is the degree of ionization,  $Z = i$ ,  $m_i$  is the principal quantum number of the ground level of ion  $i$ ,  $x_i = \chi_i/kT$ .

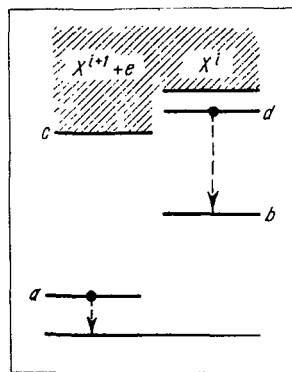


FIGURE 24. Dielectron recombination. The levels of a two-electron atom.

Figure 23 gives, as a computational aid, a plot of  $n_i/(n_{i+1} Z^4)$  vs.  $x_i$  for various  $m_i$ . The final purpose of the computations, however, is to obtain the degree of ionization  $n_i/\Sigma n_i$  as a function of temperature, in order to determine the ionization temperature  $T_i$  corresponding to the maximum degree of ionization.

The procedure for the construction of the curves  $n_i/\Sigma n_i = f(T)$  is the following. We first find the ratios  $I/II$ ,  $II/III$ , ..., for various temperatures  $T$ . From these ratios we can find  $I/i$ ,  $II/i$ , ..., and hence easily  $i/\Sigma i$  ( $n_i/\Sigma n_i$ ). Previous authors used to determine the ionization temperature from the condition  $n_i/n_{i-1} = 1$ , and only the latest publications adopt this method. For CIV and OVI, the exact values of  $T$  are  $8.7 \cdot 10^4$  and  $2.5 \cdot 10^5$ °K, respectively, whereas the approximate values are  $7.0 \cdot 10^4$  and  $2.2 \cdot 10^5$ °K.

Ionization of atoms in the corona was independently treated by Seaton /159/, who derived an expression for the coefficient of ionization by electron impact, which virtually coincided with (III.14). For the recombination coefficient Seaton used his earlier expression for hydrogen /160/, which describes the total recombinations to all levels:\*

$$\sum R = 5.2 \cdot 10^{-14} x_i^{1/2} [0.43 + 0.5 \ln x_i + 0.47 x_i^{-1/2}]. \quad (\text{III.15})$$

Seaton applied this expression in a simplified form to the corona: he took the square brackets equal to 1, and thus obtained for a hydrogen like ion

$$\sum R \approx 2 \cdot 10^{-11} Z^2 T^{-1/2}. \quad (\text{III.16})$$

Expression (III.16) contains an implied assumption that recombinations to the ground level are equal to the total recombinations to all the other levels. This follows from a comparison of (III.15) and (III.16). In certain cases however, especially for the high ionization stages, the difference between the recombinations to the ground state and all the other recombinations may be quite significant. Moreover,  $\sum R$ , according to Seaton /159/, is proportional to  $Z^2$ , whereas the recombination coefficient for hydrogen-like ions is proportional to  $Z^4$  (Menzel's formula, (III.7)). This difference apparently stems from the fact that the numerical coefficient, besides various atomic constants, also contains the ionization potential from the ground state ( $\chi_H$ ), so that the numerical coefficient will change from one ion to the next ( $Z > 1$ ), since  $\chi_i = \chi_H Z^2$ . Also note that for non-hydrogen-like atoms  $\sum R$  should contain  $m_i$ , the principal quantum number of the ground state (to allow for the non-hydrogen-like character of the ion). The problem of the dependence of  $R$  on  $Z$  is approached differently by different authors. In /93, 154, 159/,  $R \propto Z^2$ , and in /149, 150, 161/  $R \propto Z^4$ . At this point, we should note that since photorecombination is the reverse process of photoionization, a universal relation is maintained between these two processes, irrespective of the physical conditions. In thermodynamic equilibrium, the number of photoionizations by Planckian radiation from some level  $m$  is equal to the number of photorecombinations. Using Saha's equation, relating the ion and electron concentrations to the concentration of atoms in state  $m$ , we obtain an expression for which is proportional to  $Z^4$ : the probability of photoionization is the only factor dependent on  $Z$ , and it is proportional to  $Z^4$ . This procedure is equivalent to using Milne's relation from the theory of elementary processes /154/.

A detailed discussion of the expressions used for the computation of the degree of ionization in the corona is purely methodological, however. We have noted before that the ionization temperature is not oversensitive to the various parameters, so that basically the same results are obtained when using different expressions for  $n_i/n_{i+1}$ . As an illustration of this point, Table 12 lists the results obtained for  $T_i$  by Seaton /159/ and by the present authors for some coronal ions.

A new theory of coronal ionization is being developed in recent years, mainly in England. In 1961 Unsold called Seaton's attention to a possible contribution from dielectron recombination in the solar corona. It seems

\* An expression similar to (III.15) was derived for hydrogen in /91/:

$$\sum R = 5.2 \cdot 10^{-14} x_i^{1/2} [0.784 + 0.5 \ln x_i].$$

that Massey and Bates were the first to consider this elementary process. A general expression for the coefficient of dielectron recombination was derived by Bates and Dalgarno /162/. A free electron hitting an ion  $X^{i+1}$  (stage of ionization  $i + 1$ ) forms an ion  $X_{ad}^i$  with two excited electrons, one of which occupies a level  $d$  lying in the continuum of the lowest limit of ionization of the ion  $X^{i+1}$ , i.e., on autoionization levels (Figure 24). The second electron occupies an excited level  $a$  which belongs to the series with the lowest ionization potential; this explains the existence of autoionization levels. The ion  $X_{ad}^i$  in this "free-bound" state is characteristically unstable, since there is a very high probability for autoionization to occur ( $A_a \approx 10^{13} \text{ sec}^{-1}$ ), the electron from level  $d$  thus passing into the continuum. "Stabilization" is therefore essential before real recombination can occur. This "stabilization" is attained in different ways as a result of a spontaneous transition of one of the excited electrons with probability  $A_s$ . In symbols, this process may be written as



TABLE 12. Ionization temperatures of iron and calcium ions in the solar corona from the computations of Nikol'skii and Seaton ( $T_i$  in millions of degrees)

	Fe							Ca			
	X	XI	XII	XIII	XIV	XV	XVI	XII	XIII	XIV	XV
Nikol'skii (§10)	0.6	0.8	0.9	1.1	1.3	1.5	1.9	1.9	2.6	3.0	3.5
Seaton /159/ (without dielectron recombination)	0.5	0.6	0.7	0.8	1.1	1.3	1.6	1.5	1.7	2.1	2.5
Seaton /159/ (with dielectron recombination)	1.1	1.4	1.7	1.9	2.2						

The coefficient of dielectron recombination  $\alpha_d$  is obtained from the relation

$$n_{i+1}n_e\alpha_d = n_{id}A_s, \quad (\text{III.18})$$

where  $n_{i+1}$  is the concentration,  $n_{id}$  is the "instantaneous" value of the concentration of doubly excited ions  $X_{ad}^i$ , which is very close to the corresponding concentration  $\bar{n}_{id}$  for a state of local ionization equilibrium between the continuum and level  $d$ :

$$n_{id}(A_a + A_s) = \bar{n}_{id}A_a.$$

The "equilibrium" concentration is determined in /162/ from the Saha — Boltzmann equation

$$\frac{\bar{n}_{id}}{n_{i+1}n_e} = \frac{\omega_{id}}{2\omega_{i+1}} \frac{h^3}{(2\pi m_e kT)^{3/2}} e^{-\frac{\epsilon_{dc}}{kT}} \equiv f(\epsilon_{dc}, T),$$

where  $\epsilon_{dc}$  is the energy difference between the limit of series  $c$  and level  $d$ ; the other notation is standard. Taking the above remarks into consideration, we obtain from (III.18) an expression for the coefficient of dielectric recombination (with allowance for "stabilization" by a spontaneous transition):

$$\alpha_d = \frac{A_s A_a}{A_s + A_a} f(e_{dc}, T). \quad (\text{III.19})$$

Further development of the theory of dielectron recombination in application to the solar corona is due to Seaton and Burgess /163—167/. "Stabilization" is generally assumed to occur through a spontaneous transition of an inner electron from level  $a$  to the ground level /165/. Burgess computed the total coefficient of dielectron recombination for He II and Fe XV by taking a sum over all the possible levels  $d$ . Dielectron recombination at coronal temperatures turned to be much more effective than photorecombination. For He II at  $T > 10^5$ °K, the ratio is 100, and for Fe XV, it is 20. At relatively low  $T$ , dielectron recombination falls off significantly: for He at  $T < 5 \cdot 10^4$ °K the efficiency of this process is 1/1000 of the photorecombination efficiency.

The introduction of dielectron recombination led Seaton and Burgess to the conclusion that the electron temperature of the corona is on the average double the temperature predicted by "classical" theory of coronal ionization (this point will be considered in more detail in the following). The last line of Table 12 lists the values of  $T_i$  for iron ions, computed with allowance for dielectron recombination.

Numerous theoretical aspects relating to dielectron recombination remain unsolved at this stage, and the efficiency of this process under the conditions of the corona and the transitional region is not known with any certainty. Vainshtein and Syun'yaev /153/ indicated at least one elementary process which acts to lower the contribution of the dielectron recombination in the corona. This process is photoionization from high autoionization levels by photospheric radiation. After dielectron recombination and "stabilization", the  $d$ -level electron has a fairly long lifetime, until it drops spontaneously to a lower level. Photoionization may occur during this lifetime. Thus, in addition to process (III.17), the authors of /153/ also consider the process

$$X_d^i + h\nu_{\odot} \rightarrow X^{i+1} + e. \quad (\text{III.20})$$

The extent of suppression of dielectron recombination in this case is determined by the ratio of the probability of the spontaneous transition from level  $d$  (the principal quantum number  $m$ ) to all the lower levels to the probability of photoionization:

$$q = \sum_{i=m_0}^{m-1} A_{mi} \left| \int_m^{\infty} \sigma_m I_{\nu} \frac{d\nu}{h\nu} \right|.$$

Here  $\sigma_m$  is the photoionization cross section,  $I_{\nu}$  is the intensity of photospheric radiation ( $T = 6000^\circ$ ),  $m_0$  is the ground level. Assuming Planckian photospheric radiation and hydrogen-like autoionization levels, we have /153/

$$q = \int_{x_m}^{\infty} \frac{dx}{x(e^x - 1)} \cdot \frac{1}{3 \ln \left( \frac{1}{2^{1/2} m_0^{2/3}} \right)}, \quad x_m = \frac{h\nu_m}{kT_{\odot}}.$$

For an ion of charge  $Z$  and  $m_0 = 2 - 3$ , assuming a dilution factor of  $1/2$  for the corona and  $T_{\odot} = 6000^\circ\text{K}$ , we have

$$q = \frac{1}{7 \log(0.4m)} \int_{\frac{2^{1/2} Z}{m^2}}^{\infty} \frac{dx}{x(e^x - 1)}. \quad (\text{III.21})$$



The relevant computations show that for ions with  $Z = 5 - 15$  the efficiency of dielectron recombination is halved only for levels with  $m > 100$ . Auto-ionization levels have  $m > 10$ ; photoionization, affecting the uppermost levels, therefore cannot significantly alter the dielectron recombination coefficient which is determined by all the autoionization levels jointly.\*

The existence of upper levels with these high quantum numbers presents quite a problem. Even in the relatively rarefied coronal plasma, significant "broadening" of the upper levels may occur: these levels merge into a characteristic "quasi-continuum" adjoining the ionization continuum. This effect has been previously considered /127/ for chromospheric hydrogen. Using our results from /127/, we will now obtain a crude estimate of the "lowering" of the ionization continuum in coronal ions.

The energy difference between two adjoining high levels in an ion of charge  $Z$  is approximately  $2Z^2\chi_H/m^3$ . The Stark effect splits each of these levels into  $2m^2$  components, the relative energy of two adjacent Stark sublevels being

$$\Delta\epsilon \approx \chi_H Z^2 / m^5. \quad (\text{III.22})$$

Each of the Stark sublevels is subjected to continuous perturbations by electrons. The most significant perturbations are caused by impacts of first and second kind between adjacent sublevels. If each sublevel is smeared into a band of width  $\Delta\epsilon$ , the ionization continuum is "lowered" to the level  $m_*$  obtained from the Inglis — Teller relation (the relative energy of the two extreme Stark components of the level  $m_*$  is close to the energy difference of the levels  $m_*$  and  $m_* + 1$ ). In the corona and the transitional region ( $n_e \geq 10^8 \text{ cm}^{-3}$ ),  $m_* \approx 100$ .

If the frequency of the perturbations is  $W$ , the Stark sublevel is "smeared" into a band of width  $\Delta\epsilon$  when

$$\Delta\epsilon/W = h/4\pi. \quad (\text{III.23})$$

If we only consider impacts of first and second kind, we may take for the adjacent levels of a hydrogen-like ion /91/

$$W = 2 \cdot 10^{-5} T^{-1/2} Z^{-2} m_*^4 n_e. \quad (\text{III.24})$$

Inserting (III.22) and (III.24) in (III.23), we find the quantum number  $m_c$ , which identifies the new "lower limit" of the ionization continuum:

$$m_c^9 = 2 \cdot 10^{21} Z^4 T^{1/2} / n_e. \quad (\text{III.25})$$

Expression (III.25) shows that in the corona and the transitional region ( $Z \approx 10$ ,  $n_e = 10^8 - 10^{10}$ ,  $T \approx 10^6$ ) the number of upper levels is strictly limited:  $m_c \approx 100 - 200$ .

\* According to the authors of /153/, the coefficient of dielectron recombination decreases by a factor of 1.5 — 2 for various coronal ions.

## 11. The temperature of the solar corona

A number of methods are available for determining the coronal temperatures.

1)  $T$  can be found from the observed distribution of the electron concentration with altitude in the corona, assuming a hydrostatic equilibrium [168, 169]. The values of  $T$  obtained in this way fall in the range  $(1-2) \cdot 10^6$ °K depending on the particular part of the corona (polar rays, "fans") [170, 171]. The modal value is apparently  $T = 1.5 \cdot 10^6$ °K. The shortcoming of this method is the assumption of hydrostatic equilibrium, which definitely does not apply to the corona. This "barometric" method nevertheless gives the upper limit value of  $T$ , since the outward motion of the coronal gas (expanding corona) reduces the gradient of  $n_e$ . The "barometric" values of  $T$  characterize the electron temperature of an extensive part of the corona.

2) The corona contains highly ionized atoms (Fe X, Fe XIV, Ca XV, etc.) which emit conspicuous coronal lines. Using the ionization theory, we can thus determine the ionization temperature corresponding to the optimal conditions of existence of the different ions. The ionization of atoms in the corona is produced by collisions with fast electrons. The ionization temperature therefore coincides with the kinetic temperature of the electrons. The main shortcoming of this method is the paucity of data on the effective cross sections of ionization and recombination processes at high temperatures. The temperatures  $T$  obtained from the ionization theory fall between the limits  $(0.6-3.5) \cdot 10^6$ °K, depending on the particular ion treated.

Since the temperature  $T$  obtained by this method is a logarithmic function of the effective cross sections, a factor of 2 error in the cross section will result in an error not exceeding 20-20% in  $T$ .

3) The natural width of the coronal line is exceptionally small (about 0.01 Å) and the corona is optically thin ( $\tau < 0^4$ ) for radiation in the forbidden lines. The coronal line widths are therefore entirely determined by the movement of the emitting ions. Assuming purely thermal motion, we can find the ion temperature. If the particular region of the corona for which the ion temperature is to be determined may be regarded as stationary (i. e., it does not exchange matter with the surrounding coronal medium), the temperature  $T$  obtained by this method should coincide with the electron temperature. However, relatively large-scale random ("turbulent") motions, as well as thermal velocities of the ions, contributed the observed widths of the coronal lines. Quite substantial widths (about 1 Å) can be accounted for by nonthermal velocities of a few tens of km/sec. Therefore, as a rule, the ion temperature  $T$  is higher than the electron temperature. The values of  $T$  obtained by this method fall between the limits  $(1-6) \cdot 10^6$ °K.

4) Observations of the solar radio flux at centimeter and meter wavelengths may give the electron temperature. It is necessary, however, to isolate the thermal radio emission component associated with the deceleration of free electrons in ionic fields ("free-free" transitions). The main difficulty of this method is how to isolate the thermal component of the radio flux. The Sun always contains active regions which emit strong radio fluxes of nonthermal origin (plasma oscillations or synchrotron radiation in a magnetic field).

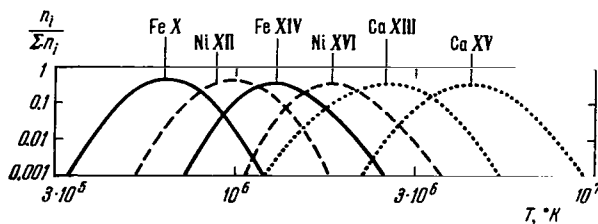


FIGURE 25. Degree of ionization of three elements in the solar corona  $n_i / \sum n_i$  vs.  $T$ .

The radio temperatures apply to an extensive part of the corona and may fall on either side of the true temperature, depending on the particular distribution of the electron concentration. The common values fall between the limits  $(0.8 - 3) \cdot 10^6$ °K for various wavelengths. At wavelengths around 1 m,  $T$  is generally close to  $10^6$ °K.

The brightest lines in the visible coronal spectrum are emitted by four elements. The curves  $n_i / \sum n_i$  were determined for various ionization stages of these elements. Some of these curves are shown in Figure 25. Examining these curves, we note that there is no one common temperature (nor even two temperatures) at which all these coronal ions can exist in sufficient quantities to make their lines observable ( $n_i / \sum n_i > 0.1 - 0.05$ ). The lines of these ions may be observable simultaneously in one part of the corona provided the line of sight intercepts coronal volumes of different temperatures. Dollfus /172/, using appropriate interference-polarization filters, managed to film the corona simultaneously in the lines 6374 Å (Fe X), 5303 Å (Fe XIV), 6702 Å (Ni XV), 5694 Å (Ca XV), 6563 Å (H I). The films show distinct differences in the fine structure of the corona in the light of various wavelengths, despite the overall similarity of the large-scale features.

The model of different-temperature regions in the corona was developed by Shklovskii /173/ in 1951. Shklovskii compared the theory of coronal ionization with observation data and came to the conclusion that there existed "hot"  $(1.2 - 1.4) \cdot 10^6$ °K and "cold"  $(0.5 - 0.6) \cdot 10^6$ °K regions. However, starting with the work of Walmeier and Petrie /174/ and up to this date, various authors try to determine the coronal temperature by comparing the intensities of lines emitted by ions with widely differing ionization potentials (mostly Fe X and Fe XIV). For example, Aly, Evans, and Orrall /175/, who studied the temperature distribution in an active coronal distribution whose excellent spectrum had been taken by Aly during the 1952 eclipse /176/, considered  $T$  as a function of the following line intensity ratios: Fe XIV (1.3)/Fe X (0.6), Ni XVI (1.8)/Ni XII (1.0), Ar XIV (2.9)/Ar X (1.2). The parenthetical figures are the ionization temperatures in millions of degrees according to their calculations. We doubt if any two ions on this list are present in sufficient quantities in one coronal region.

What then is the coronal temperature? Moreover, if different volumes have different temperatures, what is the ratio between these regions?

The "forbidden" coronal lines in the inner corona are all excited virtually by the same mechanism — electron impact. Scattering of photospheric radiation occasionally makes a certain contribution, but is noticeable only in the higher layers of the corona. The emission in coronal

lines, like that in short-wave lines, is determined by the measure of emission of a region with a sufficient concentration of appropriate ions ( $n_i$ ). The expression for this measure of emission can be derived without difficulty.

The number of ions in the principal quantum state, which also determines the total number of ions, is  $n_i \approx \kappa n_e \cdot n_i / \Sigma n_i$ . The last factor is equal to 0.5 with fair accuracy (see Figure 25).

The stationarity equation (II.1) applies to "resonance" coronal lines:

$$n_i' A = n_i n_e W. \quad (\text{III.26})$$

Impacts of first and second kind acting on excited levels may be ignored, since their probability is approximately  $1 - 10 \text{ sec}^{-1}$ , and  $A \approx 100 \text{ sec}^{-1}$ . We will now find the electron excitation coefficient of forbidden coronal lines, taking into consideration the critical comments of /177/ concerning the [O III] cross section previously used by Chubb and Menzel /178/. We will correspondingly use Blaha's figures /179/, which are one order of magnitude lower. A Hartree-Fock quantum-mechanical treatment in /179/ gave  $\sigma = 0.485/\nu^2 \text{ cm}^2$  for the transition  $3s^2 3p \rightarrow 2p_{1/2}^2$  Fe XIV (5303 Å line); here  $\nu$  is the velocity of the incident electron in cm/sec. Integration over a Maxwellian velocity distribution gives

$$W = 10^{-6} T^{-1/2} \text{ cm}^3 \text{ sec}^{-1}. \quad (\text{III.27})$$

This expression coincides with Seaton's result /180/ and, to fair approximation, it may be applied to any "forbidden" coronal line. The intensity of a coronal line is

$$I_c = \frac{h\nu}{4\pi} \int n_i' A dl, \quad (\text{III.28})$$

where  $h\nu = hc/\lambda$  is the quantum energy and the integration is over the line emission regions. Inserting (III.26), (III.27) into (III.28), we find

$$I_c = 5 \cdot 10^{-7} h\nu \kappa T_i^{-1/2} \int n_e^2 dl. \quad (\text{III.29})$$

The temperature in the region of line emission is approximately equal to the ionization temperature and may be factored out from the integrand. The intensity of coronal lines measured in eclipse observations are generally determined in angstroms of the coronal continuum produced by Thompson scattering of photospheric radiation by free electrons in the corona. The equivalent line width is thus  $A_\lambda = I_c/I_0$ , where

$$I_0 = \sigma I_\odot \int_{-\infty}^{\infty} n_e dl = \sigma I_\odot N_e. \quad (\text{III.30})$$

Here  $\sigma$  is the Thompson scattering coefficient,  $I_\odot$  is the intensity of photospheric radiation per 1 Å, incorporating a dilution factor of 1/2 for the inner corona,  $N_e$  is the total number of electrons along the line of sight per  $1 \text{ cm}^2$ . Relations (III.29) and (III.30) give an expression for the measure of emission of coronal regions of temperature  $T_i$ :

$$\frac{\int n_e^2 dl}{N_e} = C \frac{A_\lambda I_\odot \lambda}{\kappa} T_i^{1/2}, \quad C = 7 \cdot 10^{-2}. \quad (\text{III.31})$$

TABLE 13. Measure of emission of the solar corona from observations of "forbidden" lines

$\lambda, \text{\AA}$	Ion	$T_i \cdot 10^{-4}$	$A_\lambda, \text{\AA}$				$F_\odot \cdot 10^{-4}$ , erg/cm <sup>2</sup> sec	$\times$	$[M(T_i)/N_e] \cdot 10^{-4}, \text{cm}^{-3}$			
			/181/ 1929	/182/ 1936	/93/ aver.	/183/ 1952			/181/ 1929	/182/ 1936	/93/ aver.	/183/ 1952
3328.1	CaXII	2.0	0.7	—	0.6	1.5	0.60	$4 \cdot 10^{-6}$	0.33	—	0.29	0.7
3600.97	NiXVI	1.8	1.1	—	1.0	1.8	0.75	$2 \cdot 10^{-6}$	1.4	—	1.3	2.3
3801*	CoXII	1.0	—	0.7	—	0.25	1.0	?				
4086.29	CaXIII	2.6	0.3	0.2	0.15	1	1.2	$4 \cdot 10^{-6}$	0.42	0.28	0.21	1.4
4231.4	NiXII	1.0	0.8	0.7	0.6	0.45	1.3	$2 \cdot 10^{-6}$	1.5	1.34	1.1	0.86
5116.03	NiXIII	1.2	1.2	—	0.6	0.4	1.5	$2 \cdot 10^{-6}$	3.6	—	1.8	1.2
5302.86	FeXIV	1.3	27.5	18.3	20	9.3	1.5	$2 \cdot 10^{-5}$	8.8	5.8	6.4	3.0
5536	ArX	1.2	—	—	0.1	—	1.4	$3 \cdot 10^{-6}$	—	—	0.20	—
5694.42	CaXV	3.5	—	—	0.2	0.4	1.4	$4 \cdot 10^{-6}$	—	—	0.52	1.0
6374.51	FeX	0.6	2.8	9.4	4	2.15	1.3	$2 \cdot 10^{-5}$	0.64	2.1	0.91	0.49
6701.83	NiXV	1.6	2.0	1.8	1.5	1.1	1.1	$2 \cdot 10^{-6}$	6.5	5.9	4.9	3.6
7891.94	FeXI	0.8	—	—	6	—	0.90	$2 \cdot 10^{-5}$	—	—	1.2	—
10746.80	FeXIII	1.1	—	—	5.0	—	0.45	$2 \cdot 10^{-5}$	—	—	0.91	—

\* Not a resonance line.

Let us investigate the behavior of the measure of emission as a function of  $T_i$ . Table 13 lists the necessary data for computations and the results. We analyzed the observation data of Grotrian /181/ (the eclipse of 1929), Shain /182/ (the eclipse of 1936), and average data for the corona derived from the numerous observations of various authors (see Allen /93/). The coronal condensation /183/ will be considered in the following. Figure 26 plots the curve of  $\int n_e^2 d\lambda / N_e$  as a function of  $T$ . This curve reveals a fairly steady distribution with regions having temperatures around  $1.5 \cdot 10^6 \text{K}$  predominating in the corona. This figure may be adopted as the average temperature of the corona. It is remarkable that the mean temperature coincides with the "barometric" temperature (see above) which to first approximation characterizes the distribution of  $n_e$  in a "quasi-equilibrium" corona.

How many regions of different temperatures are there in the corona? Three different values of  $T$  are sufficient to cover the entire "coronal temperature range" from  $0.6 \cdot 10^6$  (FeX) to  $3.5 \cdot 10^6 \text{K}$  (CaXV), since the "half-width" of the ionization curves  $n_i / \Sigma n_i$  is approximately  $0.6 T_i$  (see below, (III.34)). The partition of the coronal temperature range into three subranges can be applied to obtain a classification of the coronal lines, which then can be compared with a purely empirical classification. Table 14 lists the limit temperatures for the three subranges, assuming that the minimum temperature is the  $T_i$  for FeX, and the mean temperature of group II is approximately  $1.5 \cdot 10^6 \text{K}$ . Ions falling "between" adjoining groups are enclosed in parentheses. This theoretical classification coincides with that of Lyot and Dollfus /184/ and with that of Shain /182/.

TABLE 14. Theoretical classification of the coronal ions

Group number	$T_1 \cdot 10^{-4},$ $^{\circ}\text{K}$	$T_2 \cdot 10^{-4},$ $^{\circ}\text{K}$	Ions
I	0.6	1.1	FeX, FeXI, NiXII, (FeXIII)
II	1.1	2.0	NiXIII, FeXIV, FeXV, NiXV, NiXVI, (FeXIII), (CaXII)
III	2.0	3.6	CaXIII, ArXIV, CaXV, (CaXII)

At a first glance, the stable form of the distribution  $M(T_i)$  may appear to rule out any line classification based on changes in relative line intensities. These changes, however, are not large: they fall within a factor of 2 and thus lead to certain difficulties in classification, whereby the same line is often assigned to different groups by different observers /184/. These changes will naturally affect the shape of the curve  $M(T_i)$ , but its general form and the position of the maximum will be preserved.

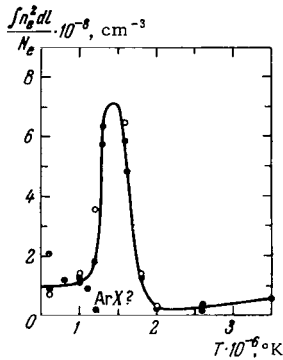


FIGURE 26. Distribution of the measure of emission  $\int n_e^2 dl$  of various regions in the solar corona as a function of temperature.

$N_e$  is the total number of electrons along the line of sight per  $1 \text{ cm}^2$ . Dark circles — average data for the equivalent widths of coronal lines /93/, light circles — the 1929 eclipse /181/, dotted circles — the 1936 eclipse /182/.

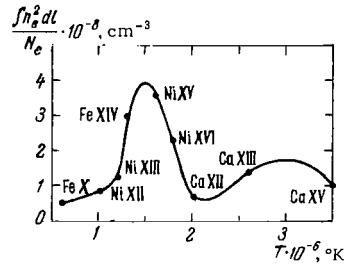


FIGURE 27. Measure of emission of regions of different temperatures in a coronal condensation for the eclipse of 1952 /183/.

To ensure a good fit of the average dependence  $M(T_i)$ , the values of for the three temperatures  $7.5 \cdot 10^5$ ,  $1.5 \cdot 10^6$ , and  $3.5 \cdot 10^6$  should be in a ratio of 0.1:1:0.1.

Considerations relating to line classification or, more precisely, to the classification of the emitting ions, naturally set only a lower limit to the number of regions with different temperatures in the corona: there clearly

should be at least three such regions. However, we can hardly expect very numerous regions with different temperatures in the corona, as these regions would then be exceedingly small, which is not likely.

Let us now consider the distribution  $M(T_i)$  for an active coronal condensation. We will use the results of the photometric analysis of the 1952 spectrogram of Lyot and Aly, carried out by Pecker /183/. The spectrogram was taken with a slit concentric to the solar limb at a distance of  $1'$ . Equivalent line widths are given in /183/ (see Table 13). The ratios  $M(T_i)/N_e$  are listed in the last column of the table. Figure 27 plots the curve  $M(T_i)$  which, in distinction from the corresponding curve for the quiet regions of the corona, has a wide "hot" maximum ( $T = 2.8 \cdot 10^6$ °K). Note that the maximum at  $T = 1.5 \cdot 10^6$ °K is also observed. Detailed photometry of the Lyot and Aly spectrogram was carried out in /175/, where a curve is given plotting the linear dimensions of the condensation at the wavelengths of various lines as a function of the ionization potential of the emitting ions. The curve has a maximum around 400 eV, which qualitatively fits the curve of  $M(T_i)$  on Figure 27. According to /175/, the condensation emits continuous radiation with intensity of  $15 \text{ erg}/(\text{cm}^2 \text{ sec sterad } \text{\AA})$ , so that the total number of electrons along the line of sight is  $N_e = 2 \cdot 10^{19} \text{ cm}^{-2}$ . Given  $N_e$ , we can readily find the  $M(T_i)$  for any ion in the condensation, e.g.,  $1 \cdot 10^{27} \text{ cm}^{-5}$  for Fe X,  $6 \cdot 10^{27} \text{ cm}^{-5}$  for Fe XIV,  $2 \cdot 10^{27} \text{ cm}^{-5}$  for Ca XV.

Since all the ions in the condensation may be provided in sufficient quantities by the three temperatures listed in Table 14, two of which correspond to the maxima, the total measure of emission  $M$  of the entire condensation is in fact a sum of three values of  $M(T_i)$ . As we have noted before, there may be more than three different temperatures, but this is of no relevance in our case, since the three values of  $T$  cover the entire coronal temperature range. From Figure 27 we have

$$M/N_e \approx 10^8 \text{ cm}^{-3}.$$

Let  $\gamma$  be the degree of inhomogeneity of gas distribution characterizing the condensation. This parameter clearly may vary from one region to the next, and we should therefore use an average value only. By definition,

$$\gamma = \bar{n}_e^2 / (\bar{n}_e)^2 \geq 1. \quad (\text{III.32})$$

It can be shown that  $M/N_e = \gamma \bar{n}_e$ . At a distance of  $1'$  (about 40,000 km) from the limb, the mean electron concentration in the corona in an epoch of maximum activity is  $n_e = 3 \cdot 10^8 \text{ cm}^{-3}$ , and we may take  $\bar{n}_e \geq n_e$  for the condensation. Thus, by (III.32),

$$1 < \gamma \leq 3.$$

The actual value of the parameter is apparently closer to the upper limit, since observations of condensations through narrow-band filters reveal their highly inhomogeneous structure.

The characteristic shape of the  $M(T_i)$  curve for the corona with the permanent maximum around  $T_i = 1.5 \cdot 10^6$ °K (the "hot" regions in condensations have an additional maximum) indicates that the number of regions with each of the three basic temperatures should be sufficiently large to ensure the fixed shape of  $M(T_i)$ . The different regions in the corona and in the

condensation should therefore be relatively small, smaller than  $(1 - 3) \cdot 10^8$  cm. Interesting results were obtained by Wlerick and Ferenback /185/ during the total solar eclipse on 15 February 1961. They obtained a high-resolution spectrogram in the red and the near infrared part of the spectrum. The lines and the continuous spectrum on this spectrogram reveal a fine structure with characteristic dimensions not exceeding  $2''$  ( $1.4 \cdot 10^8$  cm).

An alternative approach to the existence of regions of different temperatures in the corona is provided by the possible deviation of the velocity distribution of the coronal electrons from the Maxwellian distribution. This should result in a different dependence of the degree of ionization  $n_i/\Sigma n_i$  on  $T$  and, in principle, any particular ion may exist in a wider temperature interval. This is quite improbable in practice, however, since the time to establish equilibrium in the corona is short.

Let us consider one practical application of the  $M(T_i)$  curve. Shain, during the 1936 eclipse, observed a fairly strong line at  $3801 \text{ \AA}$  with equivalent width  $A_\lambda = 0.7 \text{ \AA}$  /182/. He found that the ionization potential of the corresponding ion should be relatively low.

In 1962 Rohrllich /186/ identified the  $3801 \text{ \AA}$  line with the  $^1D_2 - ^3P_1$  emission of Co XII. A similar quantum transition in the isoelectronic series of Co XII is observed in the corona for Fe XI ( $3987 \text{ \AA}$ ) and Ni XIII ( $3643 \text{ \AA}$ ). According to our computations,  $T_i = 1 \cdot 10^6 \text{ K}$  for Co XII.

The results obtained for a coronal condensation in 1952 /175/ also indicate that the  $3801 \text{ \AA}$  line is one of the "cold" lines, since the distribution of the  $3801 \text{ \AA}$  emission across the condensation is analogous to the "bimodal" curves of Fe X ( $6374 \text{ \AA}$ ) and Fe XI ( $3987 \text{ \AA}$ ), whereas the lines of Fe XIV ( $5303 \text{ \AA}$ ) and Ca XV ( $5694 \text{ \AA}$ ) have characteristic "unimodal" curves. On a previous occasion /158/ we estimated the intensity of the Co XII  $^3P_1 - ^3P_2$  resonance line, which should follow the  $3801 \text{ \AA}$  line by cascade emission. The wavelength of this line was determined approximately by interpolating the splitting of the  $^3P$  term between the known splittings for Fe XI ( $7892 \text{ \AA}$ ) and Ni XIII ( $5116 \text{ \AA}$ ). For Co XII we obtained  $\lambda \approx 6330 \text{ \AA}$ . A more accurate ( $\lambda = 6300 \text{ \AA}$ ) result can be obtained if we consider the variation of the product  $\lambda Z^3$  along the isoelectronic series. Wlerick and Ferenback /185/ discovered a previously unknown line at  $6304.60 \text{ \AA}$  on the spectrograms of the corona taken during the 1961 eclipse. The intensity of this line was approximately 1/10 of the intensity of the red line  $6374 \text{ \AA}$  (Fe X). Making allowance for the inevitable errors which arise in the interpolation of the  $^3P$  term, we should identify the  $6304.60 \text{ \AA}$  line /185/ with the emission of Co XII /187/.

The equivalent width of this line, if it is regarded as cascade emission following the  $3801 \text{ \AA}$  line, is  $A_{6304} \geq (I_{3801}^{\odot}/I_{6304}^{\odot}) \cdot (3801/6304) \cdot A_{3801} \approx 0.4 \cdot A_{3801}$ . Note that the true value of  $A_{6304}$  (assuming that the identification is correct) will be fairly close to this lower limit.

For the 1952 condensation,  $A_{3801} = 0.25 \text{ \AA}$ , whence  $A_{6304} \geq 0.1 \text{ \AA}$ . The ionization temperature of Co XII ( $1 \cdot 10^6 \text{ K}$ ) is equal to that of Ni XII, and the emission regions of the two ions therefore coincide; the corresponding measures of emission  $M(T_i)$  are also equal. Turning to expression (III.31) for the measure of emission, we can readily find a relation between the abundances of Co and Ni:  $\kappa_{Co}/\kappa_{Ni} = A_{6304} \cdot I_{6304}^{\odot} / 6304 / A_{Ni} \cdot I_{Ni}^{\odot} \cdot \lambda_{Ni}$ . The "quasi-resonance" line Ni XII  $4231 \text{ \AA}$  was observed in the spectrum of the condensation ( $A_{4231} = 0.45 \text{ \AA}$ ). Inserting the relevant numerical data in the last expression, we obtain  $\kappa_{Co}/\kappa_{Ni} > 0.3$  or  $\kappa_{Co} > 6 \cdot 10^{-7}$ . Using Shain's data, we obtain  $A_{6304} > 0.3 \text{ \AA}$  and  $\kappa_{Co} > 8 \cdot 10^{-7}$ .



Analysis of the photospheric spectrum (by the method of the curves of growth) gives  $\kappa_{\text{co}} = 6 \cdot 10^{-8} / 92$ . Our estimate is approximately a factor of 10 higher. It is therefore highly important to study the coronal line 6304.6 Å and the identification of cobalt lines in the short-wave spectrum of the Sun.

In conclusion of this section let us again consider the topic of dielectron recombination. As we have noted before, this process is of the greatest importance for correct understanding of the nature of the corona. If the dielectron recombination is indeed as efficient as it is thought to be, the coronal temperature should be double the traditional value, i.e., the mean temperature of the corona should reach  $(2.5 - 3) \cdot 10^6$ °K, rising to  $(5 - 7) \cdot 10^6$ °K in isolated regions where ions with high ionization potentials emit (Ca XV). This problem is not readily soluble if we concentrate on computations of the dielectron recombination coefficient. In other words, it is difficult to show with sufficient certainty and reliability that dielectron recombination in the corona predominates over radiative recombination or to disprove this assertion. Numerous phenomena in the corona, however, are related to its temperature, and a substantial change in this parameter by as much as a factor of two cannot fail to have a marked effect on these phenomena.

1) "Thermal" radiation of the Sun or, to use an alternative appellation, the radio emission of the "quiet" Sun at meter and decimeter wavelengths is generated by the bremsstrahlung of electrons in the field of ions in the inner corona. The radio flux characterized by the radio temperature  $T_r$  is proportional to the electron temperature  $T$  and  $T_r = \int T \cdot \exp(-\tau) d\tau$ . As we have seen, various  $T_r$  observations indicate that  $T_r \leq 1 \cdot 10^6$ °K, and it virtually never exceeds  $2 \cdot 10^6$ °K.

The attempts to derive a high electron temperature from relatively low radio temperatures /188/ do not stand up to close scrutiny /189/. The observed distribution of the radio temperature over the solar disc (meter wavelengths) led Fokker /189/ to the conclusion that there was a good fit with the results of computations based on the model of "hot" ( $T = 1.5 \cdot 10^6$ °K) and "cold" ( $T = 0.5 \cdot 10^6$ °K) coronal regions.

2) For average coronal temperatures of  $(2 - 3) \cdot 10^6$ °K, the density gradient in the corona turned out to be much less than in reality. We recall that the hydrostatic model of the corona yields  $T = 1.6 \cdot 10^6$ °K /169/. This is the upper limit value since in the real corona the density gradient is lower than the barometric value for the same  $T$ .

3) The mean temperature of the corona, which significantly affects the ejection of coronal matter, the so-called "solar wind." Comparing the computed power of the "solar wind" with observations of electron concentration in the interplanetary space, one can estimate the temperature of the inner corona  $T_0$ .

The latest determinations of the electron concentration near the Earth (5—16 Earth's radii) were conducted on Explorer-21 (IMP-2) in October 1964, in an epoch of relatively low solar activity. The results of the processing of the observation data give  $n_e = 25 - 50 \text{ cm}^{-3}$  /190/. These figures are apparently sufficiently reliable and provide the upper limit value for the concentration of interplanetary electrons due to the "solar wind."

Computations of "solar wind" parameters assuming various temperatures at the "base of the solar corona," i. e., various temperatures of the inner corona  $T_0$ , were carried out by Parker. An extensive discussion and results for the expanding corona model are given in his review /191/. Parker took  $n_e = 10^8 \text{ cm}^{-3}$  at the "base of the corona," which is too low even for the corona in an epoch of minimum activity. A better estimate, according to Van de Hulst /169/, is  $2 \cdot 10^8 \text{ cm}^{-3}$ . Table 15 lists, for different  $T_0$ , the values of  $v_0$ , the rate of "expansion" of the corona at its "base" and  $n_e$ , the electron concentration at the Earth's orbit (with allowance for the last comment) due to this expansion /191/.

TABLE 15. Temperature of the inner corona and solar wind parameters

$T_0 \cdot 10^{-4}, ^\circ\text{K}$	$v_0$ , km/sec	$n_e$ at the Earth's orbit, $\text{cm}^{-3}$	$T_0 \cdot 10^{-4}, ^\circ\text{K}$	$v_0$ , km/sec	$n_e$ at the Earth's orbit, $\text{cm}^{-3}$
1.0	0.2	1	2.5	50	300
1.5	4	40	3.0	100	400
2.0	25	120			

Comparison of the figures in Table 15 with the observed values of  $n_e$  shows that the coronal temperature should be close to  $1.5 \cdot 10^6 ^\circ\text{K}$  and it is definitely less than  $2 \cdot 10^6 ^\circ\text{K}$ . This conclusion is supported by additional arguments which indicate that the "expansion" speeds in the inner corona come out too high for  $T_0 > 1.5 \cdot 10^6 ^\circ\text{K}$ . Spectroscopic /174, 192/ and direct /193/ observations of the corona show that the directed velocities in the inner parts do not exceed 5 km/sec on the average, and velocities greater than a few tens of km/sec are very rare. The values of  $v_0$  in Table 15 characterize the mean velocity of directed motion in the corona.

The hydrodynamic theory of the corona which treats the "expansion" of the corona as a continuous medium is supplemented by the "exospheric" theory of the ejection of matter from the corona. The "exospheric" theory considers the escape or dissipation of individual atoms from the outer corona. Dissipation is the result of the presence of fast particles in the corona which form the "tail" of the Maxwellian distribution. The velocities of these particles exceed the escape velocity (the parabolic velocity) for the Sun. The theory of thermal dissipation for the solar corona was developed in 1950 by Pikel'ner /194/. We will consider qualitatively the principal aspects of this theory.

Thermal dissipation acts as a regulator of the coronal temperature, imposing definite constraints on the temperature: irrespective of the power output of the sources, the coronal temperature never exceeds the parabolic velocity, i. e., it is limited by the mass and the radius of the Sun. This restriction applies to any other star as well. A simple analogy clearly illustrates the physics of this "thermostating" mechanism. In many respects, dissipation is analogous to the boiling of water whose temperature at atmospheric pressure never exceeds  $100^\circ$ . The role of atmospheric pressure in the corona is taken by gravitational forces. The "boiling" temperature obtained for the corona in this way is around  $1.5 \cdot 10^6 ^\circ\text{K}$ . Note that temperatures  $T \approx (2 - 3) \cdot 10^6 ^\circ\text{K}$  in Pikel'ner's theory correspond to a star of  $1.5 - 2$  solar masses or with a radius of  $2/3 - 1/2$  of the Sun's radius.

Our arguments are somewhat simplified, however. We must not compute the temperature of the corona from thermostating considerations by assuming the energy of a proton escaping with a parabolic velocity to be equal to the mean thermal energy. This would result in exceedingly vigorous "boiling" of the corona, since the great majority of the protons would immediately escape from the corona. In a thermostating process, the coronal gas is maintained in a quasi-equilibrium state, i.e., the Maxwellian distribution is restored fairly fast without being distorted by the dissipating particles.

TABLE 16. "Turbulent" velocities in the solar corona from coronal line widths

Author	Observation method	$v_t$ , km/sec		
		$\lambda 6374$ Fe X	$\lambda 5303$ Fe XIV	$\lambda 5694$ Ca XV
Lyot /197/	Photographic, extra-eclipsing	25	19 — 36	—
Dollfus /199/	The same	18 — 23	—	—
Waldmeier /198/	" "	—	0 — 40	—
Pecker, Billings, Roberts /200/	" "	28 — 40	23 — 37	0 — 29
Prokof'eva /202/	" "	10 — 30	0 — 30	—
Billings /201/	" "	—	—	17
Nikol'skii, Sazanov /203/	" "	20	1 — 18	—
Jarrett, Klüber /204/	Interferometric, 1954 eclipse	—	14 — 32	—
Jarrett, Klüber /205/	Interferometric, 1959 eclipse	20 — 29	9 — 23	—
Wierick, Dumont, Perche /206/	Photoelectric, extra-eclipsing	30	21 — 31	—

TABLE 17. "Turbulent" velocities in the solar corona under two different assumptions concerning the ionization temperature (Billings' observations /207/)

$\Sigma I / \Sigma I_{\max}$	6374 Fe X			5303 Fe XIV		
	$T_\lambda \cdot 10^{-6}$ , °K	$v_t$ , km/sec		$T_\lambda \cdot 10^{-6}$ , °K	$v_t$ , km/sec	
		"classical" theory	dielectron recombination		"classical" theory	dielectron recombination
1/2	1.33	14.8	8.2	2.13	15.8	0
1	1.80	19.0	16.2	2.40	18.2	7.8
1/2	2.27	22.4	18.4	2.74	20.8	12.5

4) Let us consider some data on coronal line widths. The observed line widths  $\Delta\lambda$  are known to be almost double the line widths corresponding to the "classical" ionization temperatures. The solar atmosphere, however, is characterized by fairly large scale random motions, so-called turbulence. The velocities of the turbulent motion in the chromosphere reach  $v_t = 20$  km/sec /195, 196/. The values of  $v_t$  naturally can be found if the kinetic temperature of the emitting region is known. The coronal line widths have been measured on different occasions. Table 16 lists the turbulent velocities  $v_t$  computed assuming that the temperature of the emitting coronal region is

equal to the ionization temperature of the corresponding ions. The limits of  $v_i$  are attributed to differences in the results of line width measurements in different parts of the corona. Table 16 indicates that "turbulent" velocities in the corona may range between wide limits, while the mean velocity is  $v_i \approx 20$  km/sec for any ion.

To provide a more rigorous proof of the last conclusion, we need a statistical analysis of a large volume of observations. This analysis was carried out by Billings /207/ who determined about 1000 profiles of the red and the green line from 1957 — 1958 observations at Climax using an extra-eclipse coronagraph (2.5 Å/mm dispersion, 0.15 Å resolution). Billings plotted the distribution of the observed intensity totals ( $\Sigma I$ ) of these lines as a function of the temperatures  $T_\lambda$  corresponding to the line half widths. The resulting histograms are not unlike random error curves with maxima and half-value widths of approximately  $0.8 \cdot 10^6$ °K. The maxima naturally represent the typical values of  $T_\lambda$ . We computed the  $v_i$  for the  $T_\lambda$  corresponding to the maximum and to the half-value point. The initial data and the results are given in Table 17. Two values are listed under  $v_i$ : those corresponding to the "classical" theory of coronal ionization and those adjusted for dielectron recombination. In the former case,  $T_i$  were borrowed from Table 13 and in the latter, from /164/, where  $T_i = 1.1 \cdot 10^6$ °K and  $2.2 \cdot 10^6$ °K for Fe X and Fe XIV, respectively.

The results of these computations are most indicative. The "classical" theory of ionization presents a natural picture. The ions Fe X and Fe XIV emit in regions which have temperatures close to  $T_i$ . The "turbulent" velocities in the corona are independent of the local temperature and are on the average equal to 20 km/sec. The temperatures obtained with allowance for dielectron recombination, on the other hand, present an odd picture: the "turbulent" velocity varies between wide limits and increases in regions with lower temperature (the "red" regions).

Analysis of observations and theoretical findings thus indicates that the mean temperature of the corona is definitely lower than  $(2.5 - 3) \cdot 10^6$ °K, the most probable value being  $T = 1.5 \cdot 10^6$ °K. This supports the "classical" theory of ionization of the corona and indicates that the process of dielectron recombination does not contribute to the ionization balance of the corona /208/.

## 12. Distribution of temperature and matter in the transitional region between the corona and the chromosphere

One of the basic results of the analysis of short-wave lines in the solar spectrum is the determination of the "generalized measure of emission"  $\Delta\varphi = \int n_i^2 T^{-1/2} dh$ , which characterizes the region of existence of a given ion as a function of the temperature corresponding to this ion (see Chapter II). Indeed, the function  $\Delta\varphi(T_i)$  relates the two important physical parameters — concentration of matter and temperature, whereas  $\Delta\varphi$  itself describes the binary processes in the solar plasma.

In our computations of the radiation fluxes in the predicted short-wave lines (Chapter II, Table 7), the function  $\Delta\varphi(T_i)$  was used on a purely empirical basis. We did not concern ourselves then with such pressing topics as the validity of expression (II.5) relating  $\Delta\varphi$  to the intensity of the emission line

and the characteristics of the emission ion or the differences between the  $\Delta\varphi$  for quiet and active regions of the solar atmosphere.

In our analysis of the observed intensities of short-wave lines in Chapter II it was further assumed that the solar atmosphere is transparent to the emission in these lines. This, however, is not a valid conclusion, since self-absorption is quite significant for a number of emission lines in the chromosphere. Let us consider this topic in more detail, along the same lines as in /90/.

The optical thickness in the resonance lines is  $\tau \approx k_0 n_i \Delta h = \kappa k_0 n_e \Delta h$ , where  $k_0$  is the absorption coefficient and  $\Delta h$  is the thickness of the absorbing layer (the rest of the notation is as before). A short-wave quantum moving in a scattering medium is analogous to a diffusing particle which changes the direction of its motion after every collision (in our case, the collision events correspond to resonance scattering). By analogy, the "diffusion coefficient" of a quantum is  $D \approx c/k_0 n_i = c \Delta h/\tau$ . The time for the quantum to traverse a layer  $\Delta h$  is  $t_d \approx (\Delta h)^2/D \approx \Delta h \cdot \tau/c$ . Irrespective of the actual number of scattering events, the quantum will escape from the layer if its energy is not completely converted into heat. Total conversion into heat is possible as a result of an inelastic collision of an atom which has absorbed the quantum with some other particle. The quantum remains in the "absorbed state" during a time  $t_a = t_d Z/A$ , where  $Z \approx c k_0 n_i$  is the number of absorption events in 1 sec, and  $1/A$  is the lifetime of an excited atom. Finally,  $t_a \approx \tau^2/A$ . If an atom which has absorbed the quantum undergoes an inelastic collision during the time  $t_a$  (electron impact of 2nd kind is the most effective mechanism in this connection), the quantum will not escape from the layer. The number of impacts of 2nd kind per second per atom is  $n_e W_{21}$  ( $W_{21} \approx W_{12} \exp(x)$ ). Thus, there will be virtually no true absorption if

$$\tau^2 \ll \frac{A_{21}}{n_e W_{21}}. \quad (\text{III.33})$$

As an example, let us consider the emission of CIV in the 1550 Å line. Somewhat exaggerating, we may take  $A \approx 10^8 \text{ sec}^{-1}$ ,  $n_e \approx 10^9 \text{ cm}^{-3}$ ,  $W_{21} \approx 10^{-8} \text{ cm}^3/\text{sec}$ ,  $k_0 \approx 10^{-13} \text{ cm}^2$ ,  $\kappa \approx 10^{-4}$ ,  $n_e \Delta h \approx \Delta\varphi T^{-1/2} \approx 10^{18} \text{ cm}^{-2}$ . Hence,  $\tau_{\text{CIV}} \approx 10$ , and  $A_{21}/n_e W_{21} \approx 10^7$ , so that inequality (III.33) is satisfied.

A more careful analysis of the transfer of resonance radiation in an optically thick layer was carried out by Ivanov /37/, who considered completely incoherent scattering and derived the condition

$$\tau \ln \tau \ll \frac{1}{4 \sqrt{\pi}} \frac{A_{21}}{n_e W_{21}},$$

which is satisfied even with a more comfortable "margin."

Inequality (III.33) does not apply to subordinate lines, but the number of absorbing atoms (ions) in this case is substantially less, as most of them are in the ground state, and  $\tau$  will be close to 1 or smaller. Computations for these ions emitting short-wave lines show that there is virtually no self-absorption in any of the cases.

Our next problem is to determine  $n_e$  and  $T$  as a function of height in the solar atmosphere. This amounts to constructing a model of the solar atmosphere. Although this model will be quite crude, ignoring the inhomogeneous structure of the solar atmosphere, it will nevertheless allow for the large "inhomogeneities," such as the active regions on the Sun.

Both the temperature and the density distribution in the solar atmosphere are highly inhomogeneous. Nevertheless, the first basic step is the development of a model of the solar atmosphere as a homogeneous medium with radial gradients of  $n_e$  and  $T$ . This "extrafocal" treatment enables us to study the most general properties of the solar atmosphere. This approach has proved to be quite effective for the solar corona /149, 150/, whose principal features have been elucidated in this way.

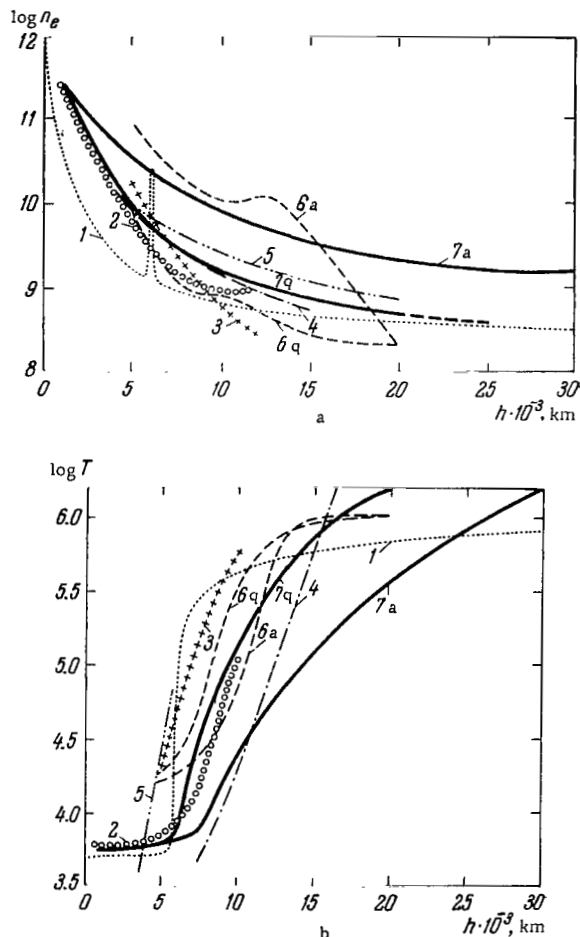


FIGURE 28. Various models of the solar atmosphere.

1 — Allen and Woolley /142/; 2 — Shklovskii and Kononovich /144/; 3 — Oster /119/; 4 — Piddington /215/; 5 — Athay and Menzel /212/; 6a, 6q — Koyama, for active and quiet regions, respectively; 7a, 7q — our model for active and quiet regions. Top (a) electron concentration distribution; bottom (b) temperature distribution.

Several models have been constructed for the intriguing transitional region between the chromosphere and the corona, but different authors came

up with widely different mean distributions of  $n_e$  and  $T$ . A quick glance at Figure 28 will show that this is indeed so. This figure plots the curves of  $n_e(h)$  and  $T(h)$  in accordance with different models which are discussed below.

Before proceeding with the construction of a model of the solar atmosphere, we have to justify the use of the generalized measure of emission  $\Delta\varphi(T_i)$  which was derived semiempirically in Chapter II. Photoionization by short-wave radiation emitted from the overlying (hot) layers may be significant in the lower part of the transition region, so that expression (II.5) relating  $\Delta\varphi(T)$  to line intensity and the parameters of the emitting ion will be invalid. The efficiency of the hard radiation of the corona as an ionizing agent for the lower layers of the solar atmosphere was first theoretically predicted by Shklovskii /113/. The decisive role of the hard radiation in the excitation of helium in the upper chromosphere was established by Nikol'skaya /209/ who compared the observation data with her theoretical estimates. Note that Shklovskii's idea had been regarded as erroneous for some 20 years following the critical comments of Athay and Menzel, which were eventually shown to be unfounded /209/.

Photoionization by short-wave radiation may be estimated quantitatively, since the energy distribution is known (Figure 20). Let us compare the number of ionization events by electrons  $Z_e$  and by hard quanta  $Z_{ph}$ . As an example, consider the Mg II ion which emits the resonance doublet 2796 Å and 2803 Å. Mg II is ionized by radiation with  $\lambda < 826$  Å. The solar radiation flux between 826 and 700 Å is approximately 0.3 erg/cm<sup>2</sup> sec (see Chapter II). In the region of Mg II emission  $n_e \approx 10^{11}$  cm<sup>-3</sup>,  $T \approx 10^4$ °K. The photoionization cross section of Mg II is  $\sigma \approx 2.4 \cdot 10^{-18}$  cm<sup>2</sup> /93/. After simple computations, we find  $Z_{ph}/Z_e \approx 10 - 100$ . Photoionization is thus quite significant in the upper chromosphere (or in the bottom part of the transitional region).

Since the kinetic temperature increases in higher layers of the solar atmosphere, the ionization potential of the ions in these layers increases and the flux of hard radiation capable of ionizing these ions correspondingly decreases. This leads to a marked drop of the ratio  $Z_{ph}/Z_e$  with increasing height. Our computations show that for ions with ionization potentials  $\chi > 25$  eV ( $\lambda < 500$  Å),  $Z_{ph}/Z_e \approx 1$ , and for regions of the solar atmosphere with  $T > 50,000$ ° ionization by electrons predominates. Thus, as a result of photoionization, ions with ionization temperatures  $T_i < 5 \cdot 10^4$ °K may exist in regions with kinetic temperature  $T < T_i$  (the chromosphere, prominences), and the values of  $\Delta\varphi(T_i)$  obtained by the method developed in Chapter II (see (II.5)) work out too high for  $T < 5 \cdot 10^4$ °K.

The limit temperatures  $T_1, T_2$  of the emission zones were determined for 25 ions with different  $T_i$  /90/. The ionization curves of  $n_i/\Sigma n_i$  vs.  $T$  were plotted, and  $T_1, T_2$  were obtained by taking  $n_i/\Sigma n_i$  equal to half the maximum value.  $T_1, T_2$  as a function of  $T_i$  are shown in Figure 29, which gives to fair approximation

$$T_1 = 0.7T_i, T_2 = 1.3T_i. \quad (\text{III.34})$$

The temperature in the solar atmosphere increases fairly rapidly with height, reaching its maximum ( $1.5 \cdot 10^6$ °K) in the inner corona and declining fairly slowly thereafter. This indicates that  $\Delta\varphi(T_i \approx 10^6)$  has two components: one belonging to the transitional region and the other to the corona. The coronal component may prove to be dominant, despite the decrease in the concentration of matter with height. Indeed, the curve  $\Delta\varphi(T_i)$  (see Figure 17)

shows a characteristic maximum corresponding to the mean coronal temperature  $T \approx 1.5 \cdot 10^6 \text{K}$ . This maximum lies in the temperature range  $(1.1 - 1.8) \cdot 10^6 \text{K}$  and occupies one "zone," i. e., the temperature interval between the limit values  $T_1$  and  $T_2$  related to the mean temperature of the corona by (III.34). The height of the maximum can be estimated independently, from the distribution of  $n_e$  in the corona. The mean electron concentration distribution  $\bar{n}_e$  in the corona in an epoch of minimum activity is given by Van de Hulst /169/. The measure of emission of an elementary column of  $1 \text{ cm}^2$  cross section at the center of the solar disk (when the line of sight coincides with the normal to the solar surface) is  $M_0 = \int_{r_c}^{\infty} n_e^2 dr$ .  $M$  is a function of the angular distance from the center of the disc. The mean value of the measure of emission is  $\bar{M} = 2M_0$ . At the edge of the disc  $M(\rho)$  (where  $\rho$  is the distance from the center of the solar disc in the plane of the sky) has a discontinuity, dropping to 1/2 of its value, since one half of the elementary coronal column is obscured by the Sun. For  $\rho < 1R_{\odot}$ ,  $M(\rho) \approx M_0(1 - \rho^2)^{1/2}$ . Similar computations were previously carried out by Shklovskii /149/, who used a different distribution of  $n_e$ .

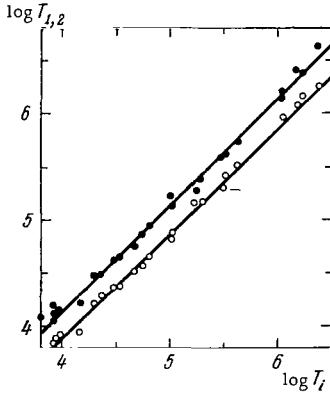


FIGURE 29. Limit temperatures  $T_1$ ,  $T_2$  of the emission zone of an ion which determine the half-width of the  $n_i/\Sigma n_i$  curve vs. the ionization temperature  $T_i$ .

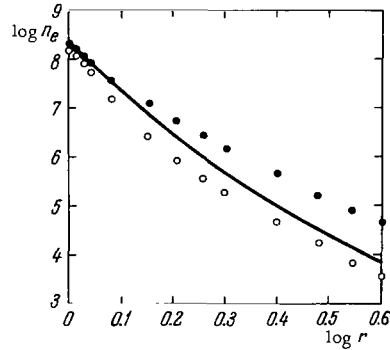


FIGURE 30. Distribution of electron concentration  $n_e$  as a function of distance  $r$  (in fractions of the solar radius) in an epoch of minimum solar activity according to Van de Hulst /169/ at the pole (light circles) and the equator (dark circles). The solid line is our approximation.

Numerous comparisons of Van de Hulst's model /169/ with observations reveal a fairly close fit. Approximating  $n_e(r)$  by a binomial power function of  $r$  (Figure 30) and integrating, we find  $\bar{M} = 4 \cdot 10^{26} \text{ cm}^{-5}$  and  $\bar{M} = 3 \times 10^{27} \text{ cm}^{-5}$  for epochs of minimum and maximum solar activity, respectively. These figures should be multiplied by  $\bar{n}_e/(\bar{n}_e)^2$ , which is equal to 3 according to the results of Sec. 11. Since the mean coronal temperature is  $T_c \approx 1.4 \times 10^6 \text{K}$ , the generalized measure of emission of the corona takes the final form

$$\Delta\varphi_c = \bar{M} T_c^{-3/2} \cdot \bar{n}_e^2 / (\bar{n}_e)^2.$$



For a "minimum" and a "maximum" corona we obtain  $\Delta\varphi_c = 7 \cdot 10^{17}$  and  $5 \cdot 10^{18}$ , respectively. The "minimum" value fits the results obtained for  $\Delta\varphi$  from observation data of coronal emission lines (see Figure 17).

Let us now proceed with the construction of a generalized measure of emission characterizing the entire thickness of the solar atmosphere above any given level  $h$ , as distinct from the generalized measure of emission  $\Delta\varphi$  for the emission zone of a single ion,

$$\varphi(T) = \sum \Delta\varphi = \int_{h(T)}^{\infty} n_e^2 T^{-3/2} dh. \quad (\text{III.35})$$

$\varphi(T)$  is readily seen to be more convenient for various computations and in particular for the construction of models.

We partition the entire temperature range into nonoverlapping sub-intervals with limit temperatures satisfying condition (III.34) and add up the values of  $\Delta\varphi$  for these subintervals. The results are presented in Table 18. Note that the values of  $\Delta\varphi$  have been read off the  $\Delta\varphi(T)$  curve after elimination of the coronal maximum (see Figure 17), since we are mainly interested in a model of the transitional region below the corona.

TABLE 18. Conversion from the generalized measure of emission of the emission zones of individual ions to the generalized measure of emission of the entire transitional region above the level  $h$

$\log T_i$	$\Delta\varphi = \int_{h(T_i)}^{h(T_{i+1})} n_e^2 T^{-3/2} dh$	$T_{i+1}$	$\bar{\varphi} = \int_{h(T)}^{\infty} n_e^2 T^{-3/2} dh$
4.70	$1 \cdot 10^{20}$	4.51	$1.1 \cdot 10^{20}$
4.97	$7 \cdot 10^{18}$	4.91	$8.3 \cdot 10^{18}$
5.24	$1.1 \cdot 10^{18}$	5.08	$1.8 \cdot 10^{18}$
5.51	$3.6 \cdot 10^{17}$	5.35	$6.7 \cdot 10^{17}$
5.77	$2 \cdot 10^{17}$	5.62	$3.1 \cdot 10^{17}$
6.05	$8 \cdot 10^{16}$	5.89	$1.1 \cdot 10^{17}$
6.32	$2.5 \cdot 10^{16}$	6.15	$3.1 \cdot 10^{16}$
6.52	$6 \cdot 10^{15}$	6.42	$6 \cdot 10^{15}$

The function  $\varphi(T)$  obtained in this way, like  $\Delta\varphi$ , is an average for the entire solar disc.  $\varphi(T)$  should be partitioned into components which correspond to active and quiet parts of the solar atmosphere. If the area of active regions relative to the area of the solar disc is  $S$ , and the surface brightness of the active regions is  $l$  times the surface brightness of the quiet regions, we have

$$\bar{\varphi} = S\varphi_a + (1 - S)\varphi_q, \quad \varphi_a/\varphi_q = l. \quad (\text{III.36})$$

This relation is applicable to optically thin emissions. The contrast  $l$  should be a function of temperature, since it is the temperature that determines the level at which a particular emission originates. For temperatures of the order of  $10^6$ °K, rocket heliograms in the X-ray

spectrum give  $l \approx 30$  (see Chapter I). The outline of the active regions in X rays and in  $L_\alpha$  light corresponds to the calcium flocculi observed from Earth. On the average, as we have noted in Chapter II,  $S = 0.02$  on the days on which the rocket data used in the construction of  $\Delta\varphi(T)$  were obtained /210/. We may approximately take  $S = 0$ , since even with a high contrast the generalized measure of emission in quiet regions does not differ from the mean value  $\bar{\varphi}(T)$ .

The computation of the generalized measure of emission in quiet regions  $\varphi_q$  for  $T < 5 \cdot 10^4$ °K from short-wave line intensities meets with considerable difficulties, as we have noted before, due to the high efficiency of photoionization, which distinctly predominates over the electron impact mechanism. Therefore, to find  $\bar{\varphi}$  in the lower part of the transitional region, we will use the measurements of the continuous radiation of the Sun in the Lyman continuum ( $\lambda \leq 912$  Å). Photoelectric /25/ and photographic /18/ estimates give a fairly reliable figure for the flux:  $F_L = 0.24$  erg/cm<sup>2</sup> sec. Thus, 1 cm<sup>2</sup> of Sun's surface emits a flux of  $\Phi_L = 10^4$  erg/cm<sup>2</sup> sec. This emission is mainly determined by the "semitransparent" layers adjoining the level of optical depth  $\tau_L \approx 1$ . The temperature  $T_L$  of the layers with  $\tau_L \geq 1$  may be approximately estimated using Planck's law, which gives the upper limit value of  $T_L$  for the quiet regions,  $T_{Lq} = 6600$ °K. The recombination emission of the "semitransparent" layers with  $\tau \leq 1$  is related to  $\varphi(T)$  by the simple equality  $\Phi_L = 2.2 \cdot 10^{-22} \bar{T} \varphi(T)$ , where  $\bar{T}$  is the average temperature in the emitting region. With fair accuracy we may take  $\bar{T} \approx 10^4$ °K, so that

$$\varphi(T_L) = 5 \cdot 10^{17} \Phi_L. \quad (\text{III. 37})$$

Thus for a quiet region  $\varphi_q(T_L) \approx 5 \cdot 10^{21}$ . The best estimate for the contrast of active and quiet regions in the Lyman continuum is  $l \approx 5$ , the contrast of  $L_\alpha$  flocculi. After all, the effective levels at which  $L_L$  and  $L_\alpha$  emissions originate virtually coincide. Indeed, for the Lyman continuum  $\tau_L \approx 1$ , and the absorption coefficient is  $k_L \approx 10^{-17}$  cm<sup>2</sup>, whereas for  $L_\alpha$  quanta  $\tau \approx 10^3 - 10^4$  (see above),  $k \approx 10^{-13}$  cm<sup>2</sup>, so that the number of hydrogen atoms in an elementary column above the effectively emitting level is almost the same in both cases,  $\tau/k = N_H \approx 10^{17}$  cm<sup>-2</sup>.

Extrapolating the curve  $\varphi_q(T)$  to the "Lyman" point  $\varphi_q(T_L)$ , we can easily find the distribution  $\varphi_q(T)$  in the entire temperature range (Figure 31). Significantly, the point  $\varphi_q(35,000^\circ)$  is offset almost by a factor of 2 in the upward direction; at temperatures below this point, the effects of photoionization apparently begin to be felt. To construct the generalized measure of emission in the active region ( $\varphi_a(T)$ ), we start with the Lyman point  $\varphi_a(7100^\circ) = 3 \cdot 10^{22}$  and with the known contrast values (see Chapter I). Radio observations of active and quiet regions give  $\varphi(T)$  quite independently.

The brightness radio temperature is expressed by

$$T_r = \int_0^\infty T e^{-\tau} d\tau. \quad (\text{III. 38})$$

where  $T$  is the electron temperature and the integral is taken over the path of the radio beam. If the emitting region lies near the center of the solar disc, the direction of propagation coincides with the normal to the Sun's surface. In this case, the "optical" thickness in the radio spectrum is

$$\tau \approx 2 \cdot 10^{-23} g \lambda^2 \varphi(T), \quad (\text{III.39})$$

where  $g = 1.3 \log(1.6 T \lambda)$  is Gaunt's factor /157/.  $T_r$  was found by numerical integration, which gives accurate results for  $T_r$ . This method had been previously applied in /90/. It calls for the construction of curves of  $T$  vs.  $\exp[-\tau(\varphi, \lambda)]$  and measuring the areas under these curves. The areas are numerically equal to  $T_r$ . The computations made use of the data from Newkirk's review /211/, which contains interferometric radio observations of quiet and active regions. The function  $\varphi_a$  and  $\varphi_q$  were plotted using different assumptions regarding  $S$  and  $l$  for  $T \geq 10^6$ °K from the data on the mean generalized measure of emission  $\bar{\varphi}$  (see Table 18 and Figure 31). Note that the contribution of the corona to  $\varphi(T)$  was taken into consideration in these calculations. This is a significant correction, since the corona contributes at all wavelengths in the radio spectrum.

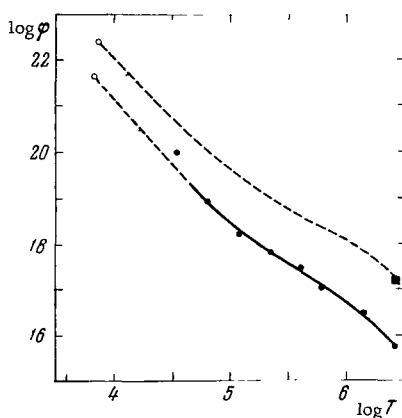


FIGURE 31. Generalized measure of emission

$$\varphi(T) = \int_{h(T)}^{\infty} n_e^2 T^{-3/2} dh \text{ characterizing the entire}$$

thickness of the solar atmosphere above a certain level  $h$  in active and quiet regions.

Dark circles and the continuous curve are based on the figures of Table 18, light circles plot  $\varphi(T)$  from the Lyman continuum data; the dark square identifies the value of  $\varphi$  for an active region in the corona; the dashed curve is extrapolation with allowance for the contrast  $l$ .

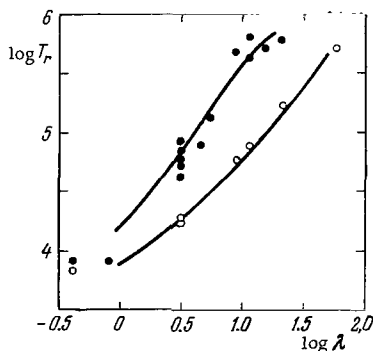


FIGURE 32. Radio temperature of the solar atmosphere vs. wavelength in active (dark circles) and quiet (light circles) regions from interferometric measurements.

The curves plot the  $T_r(\lambda)$  computed from  $\varphi(T)$ .

After a number of approximations,  $l \approx 30$  and  $S \approx 0$  were found to provide the best fit of the radio observation data for  $T \geq 10^6$ °K. The computed curves of  $T_r(\lambda)$  adequately match the observations in this case. Figure 32 plots the brightness radio temperature of the Sun vs. wavelength. It shows the  $T(\lambda)$  curves computed from our  $\varphi_a$  and  $\varphi_q$ , together with the experimental points /211/.

No accurate data on the contrast of X-ray flocculi were available at the time when the  $T_r(\lambda)$  were being computed. The requisite data were only obtained at a later stage /43/, confirming our figure  $l \approx 30$  /90/.

The final plot of the generalized measure of emission vs. temperature is given in Figure 31.

Note that regardless of the absolute values of  $\bar{\psi}$  and  $S$ , correct values of radio intensities (i. e., values which coincide with observations) may be obtained only if the magnitude and the general trend of the generalized measure of emission in active and quiet regions are roughly the same as in Figure 31.

Let us now proceed with the computation of the vertical profiles of  $n_e$  and  $T$ . So far, we have used data relating  $n_e$  to  $T$  which did not incorporate an explicit dependence on height ("short-wave" and "radio" data). We will now turn to optical observations, which establish a relation between  $n_e$ ,  $T$ , and  $h$ . Observations of the continuous radiation beyond the limit of the Balmer series ( $\lambda < 3647 \text{ \AA}$ ) at different heights give the generalized measure of emission as a function of height:

$$\psi(h) = \int_n^{\infty} n_e^2 T^{3/2} dh. \quad (\text{III.40})$$

The function  $\psi_q(h)$  for a quiet region was computed in /212, 213/ from the results of the American expedition which had observed the total solar eclipse on 25 February 1952 in Egypt. Unfortunately, the heights on the slitless spectrograms of this expedition are limited to  $h \leq 6000 \text{ km}$ . Using the same observation data, we computed the function  $\psi_a(h)$  for an active region ( $h \leq 5000 \text{ km}$ ). The generalized measures of emission  $\psi_q$  and  $\psi_a$  are exponential functions of height, and they are shown in Figure 33. Our purposes, however, require knowledge of  $\psi(h)$  up to the heights corresponding to the inner corona. The values of  $\psi$  in the inner corona are numerically equal to the values of  $\varphi(T)$  for  $T = 1.5 \cdot 10^6 \text{ }^\circ\text{K}$ , this being the mean temperature of the corona:

$$\begin{aligned} \psi_q(h_{cq}) &= \varphi_q = 3 \cdot 10^{16}, \\ \psi_a(h_{ca}) &= \varphi_a = 7 \cdot 10^{17}. \end{aligned} \quad (\text{III.41})$$

According to various observations, in particular the systematic observations of Lyot and Muller /214/, the emission maximum of the inner corona in quiet regions lies at the height  $h_{cq} = 20,000 \text{ km}$ . For active regions, this maximum height is somewhat greater,  $h_{ca} = 30,000 - 40,000 \text{ km}$ . The function  $\psi(h)$  thus may be extrapolated to these points. The resulting curves of  $\psi(h)$  are shown in Figure 33.

The distribution  $T(h)$  can be obtained from the equation

$$\varphi(T) = \psi(h);$$

then we have to find the product  $n_e^2 T^{3/2} = d\psi/dh$ , which in conjunction with  $T(h)$  enables us to determine  $n_e(h)$ . These operations were actually carried out, and the results gave the distributions  $n_e(h)$  and  $T(h)$  which are shown in Figure 34.

The model of the transitional region obtained in this way is purely empirical, since it was constructed using experimental data only, without making any significant theoretical assumptions. Joint use of the functions  $\varphi(T)$  and  $\psi(h)$  enables us to eliminate errors associated with the effect of the factor  $\bar{n}_e^2/(\bar{n}_e^2)$ ; the curves in Figure 34 are the distributions of the root-mean-square values (and not mean values).

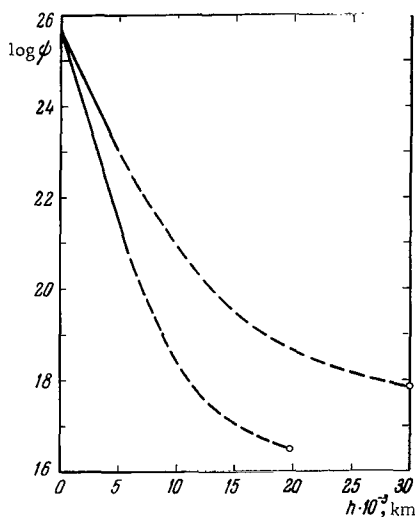


FIGURE 33. Generalized measure of emission  $\psi(h) = \int_h^\infty n_e^2 T^{-3/2} dh$  vs. height  $h$  for active and quiet regions of the solar atmosphere.

The solid curves are based on observations of the Balmer continuum [212, 213], the dots plot the measure of emission in the corona, the dashed lines are the results of interpolation.

The eclipse observations of  $\psi(h)$  used in our computations constitute the weakest link among the initial data on which the model is based. Observations of the Balmer continuum are quite adequate for the determination of  $\psi(h)$ , but they are limited to low heights, and extreme extrapolation to coronal heights is clearly uncertain. Similar criticism was voiced, in particular, by Pottasch [130]. The crucial point, however, is not the extrapolation (or more precisely the interpolation) itself, but the implied suggestion that the corona begins only at heights of  $(2 - 3) \cdot 10^4$  km.

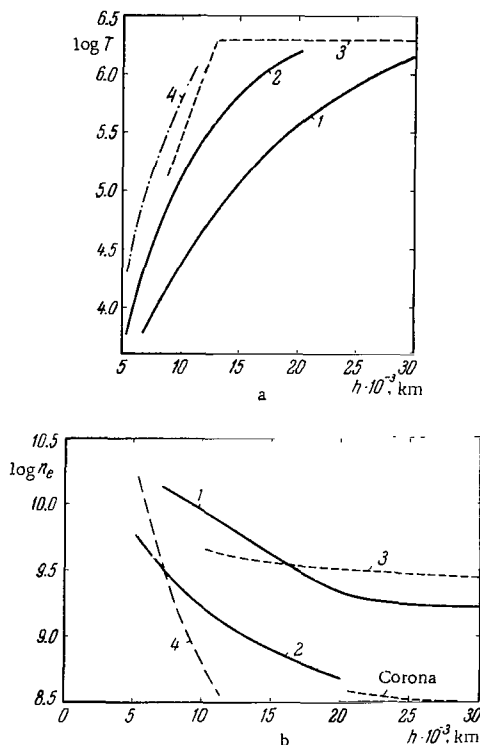


FIGURE 34. A model of the transitional region between the chromosphere and the corona in active (1) and quiet (2) regions.

Curve 3 is the model of Christiansen et al. [217]; curve 4 is Oster's model [119]. Top (a), temperature distribution; bottom (b), distribution of electron concentration.

American researchers maintain that the corona sinks to much lower heights, as low as  $(1-2) \cdot 10^3$  km. This factor will be further discussed at a later stage. Another possible source of errors affecting the temperature distribution at low heights is the interpolation of  $\varphi(T)$  to the Lyman points. A straight line has been drawn for the sake of simplicity in Figure 31 for  $T < 3 \cdot 10^4$ °K, but  $\varphi(T)$  may have a different gradient near the Lyman point (there are indications that the gradient increases at lower  $T$ ). As a result, the gradient of  $T(h)$  will change at altitudes  $h \approx 5000$  km. It will become clear from what follows, however, that the use of additional data for the determination of the trend of  $T$  in the chromosphere renders the errors in  $\varphi(T)$  relatively insignificant for  $T < 3 \cdot 10^4$ °K.

Let us compare our model of the transitional region with some other models. First, a few remarks concerning the computation of radio temperatures.  $T_r(\lambda)$  was computed by numerical integration, which markedly differs from the method proposed by Piddington /215/ and used by Shklovskii and Kononovich /144/, who worked with a functional dependence  $T_r(\lambda)$  which enabled them to conveniently solve the integral equation (III.38) between  $T_r$  and  $T$  for the electron temperature  $T$ . A detailed analysis of the solution shows that the approximation of  $T_r(\lambda)$  employed in /215/ is acceptable at low temperatures, and the models derived in /215/ and /144/ are therefore incorrect for  $T > 10^5$ °K.

As we have noted before, Allen /99/ published predictions of the intensities of 96 short-wave lines. Allen's intensities coincide, within one order of magnitude, with the values of  $F_i$  from Table I. Since our intensities were computed from observation data for bright "reference" lines (see Chapter II), whereas Allen used Oster's model /119/ (2nd version) for his prediction, we can make a comparison between the two models. Turning to Figure 34, we readily see that  $n_e$ , according to Oster, has an excessively large gradient and does not fit the distribution of  $n_e$  in the corona /169, 214/, and the gradient of  $T(h)$  according to Oster is larger than in our model. At the same time, the  $\Delta\varphi(T)$  which can be derived from Allen's initial data,\* are close to our values of  $\Delta\varphi(T)$  almost in the entire temperature range. The values of  $\Delta\varphi(T \approx 10^4$ °K) in Oster's model are 1—2 orders of magnitude less than our figures, so that the theoretical intensities of the chromospheric emission lines are lower in Allen's list /99/. The radio temperatures computed by Oster and Brooks /216/ from Oster's model with certain corrections do not fit the observations. The relation of  $n_e$  to  $T$  for the transitional region in Oster's model is thus very close to that in our model, whereas the vertical distributions of  $n_e$  and  $T$  have unacceptably large gradients. Oster's model uses a number of a priori theoretical assumptions. In particular, Oster assumes "hydrodynamic equilibrium" in the transitional region and the overall pressure  $P$  is regarded as a sum of the gas-kinetic pressure  $nkT$  and the hydrodynamic pressure associated with turbulent motions ( $\rho v_t^2/2$ ). The distribution  $v_t(h)$  used in /119/ does not fit the observations: Oster's  $v_t$  falls with the increasing height, whereas in fact  $v_t$  increases or remains constant (in the corona  $v_t \approx 20$  km/sec, in the chromosphere  $v_t \leq 20$  km/sec).

It is also interesting to compare our model with the purely empirical model of Christiansen et al. /217/ based on an analysis of interferometric radio observations at four different heights ( $\lambda = 7.5-176$  cm) (see Figure 34). Unfortunately, the calculations leading to the distributions of  $T$  and  $n_e$  are

\*In /99/ the solar atmosphere is divided into temperature zones approximately corresponding to our zones ( $T_2/T_1 \approx 2$ ). For each zone the measures of emission over the entire volume are given.

not reproduced in /217/. Using these data, we determined the generalized measure of emission  $\varphi(T)$  and then computed the radio temperature  $T_r(\lambda)$ . A slight discrepancy was detected between the initial data for  $T_r$  in /217/ and the final result. According to the observations used in Christiansen's model,  $T_\lambda(\lambda = 7.5 \text{ cm}) = 6 \cdot 10^5$ , whereas the model values of  $n_e$  and  $T$  give  $T_r = 4 \cdot 10^5$ . The model in /217/ apparently provides a relatively crude approximation, so that the identification of the various height levels is inaccurate. For example, the effective height of the layer emitting at  $\lambda = 7.5 \text{ cm}$  is estimated as  $2 \cdot 10^4 \text{ km}$  with an error of  $\pm 10^4 \text{ km}$ . Comparison of our model with the model of Christiansen et al. indicates that the heights in /217/ are too low by  $10^4 \text{ km}$ .

After the publication of our papers /90, 129/ which described the technique of construction and gave particular numerical results, Koyama applied the same technique and the same initial data in 1963 /218/ to derive a model of active and quiet regions in the solar atmosphere which differed from our model. This difference, as it later became clear, stemmed from certain computation errors in /218/. Thus Koyama assumed equal densities and temperatures for the active and the quiet corona. In computations of the generalized measure of emission he assumed electron impact ionization in the lower part of the transitional region. This assumption led to excessively high temperatures in the chromosphere. The erroneous solution in /218/ is also evident in the anomalous variation of  $n_e$ : a flat maximum is obtained for  $h \approx (10 - 15) \cdot 10^3 \text{ km}$  and the densities of the active and the quiet regions differ by as much as 1 order of magnitude.

To go one step further, we will extend the model of the transitional region to the chromosphere. This problem was tackled in /219/, and we will therefore only give the final results, briefly touching on the construction of a model of the chromosphere. The degree of ionization of hydrogen is relatively low in the lower chromosphere, and to determine the total concentration of matter we require the concentration of neutral hydrogen  $n$ . It is difficult to determine  $n_H$  from observations of hydrogen lines, since the mechanism of formation of strong lines is very complex, whereas weak lines are produced by electron — proton recombinations and their intensities are proportional to  $n_e^2$ . For these reasons,  $n_H$  is generally determined from observations of weak (i. e., optically thin) lines of some low-abundance element. Convenient lines of this type are the resonance doublet Sr II 4078 and 4215 Å ( $5^2S - 5^2P^o$  transition). The intensity distribution of these lines in the chromosphere was observed during the eclipse of 25 February 1952 by American /213/ and Soviet /220/ astrophysicists. The observations of /213/ covered both active (500 — 4800 km) and quiet (500 — 1800 km) regions. These observations give the distribution of the concentration of ionized strontium  $n_{\text{SrII}}$  between the corresponding height limits. The first ionization potential of strontium is 5.7 eV, and strontium in the chromosphere is definitely ionized at least once since the solar radiation flux at  $\lambda \leq 2200 \text{ Å}$  is sufficiently high. The second ionization potential is 11 eV, which is 2.6 eV lower than the ionization energy of hydrogen. This does not indicate, however, that the ionization of Sr II is more efficient than the ionization of H I. In either case the ionization is caused by solar radiation beyond the limit of the hydrogen Lyman series. Since the absorption coefficient of Sr II is 1/6 of the absorption coefficient of H I, both H I and Sr II are ionized almost simultaneously. We may thus take

$$n_{\text{H}}(h) = n_{\text{SrII}}(h) \cdot x_{\text{Sr}}, \quad (\text{III.42})$$

where  $x_{\text{Sr}} = 4.6 \cdot 10^{-6}$  is the abundance of Sr relative to hydrogen /92/. Above the level where Sr II lines are observed, we can find  $n_{\text{H}}$  from the previously considered distribution of  $n_e$ . The dominant ionization mechanism for  $h > 10^4$  km is electron impact, and we may therefore write  $n_{\text{H}} = n_e f(T)$ , where  $f(T)$  is a known function of temperature. At intermediate heights,  $n_{\text{H}}$  is determined fairly reliably by a simple interpolation. The distribution of neutral hydrogen obtained in this way is plotted in Figure 35.

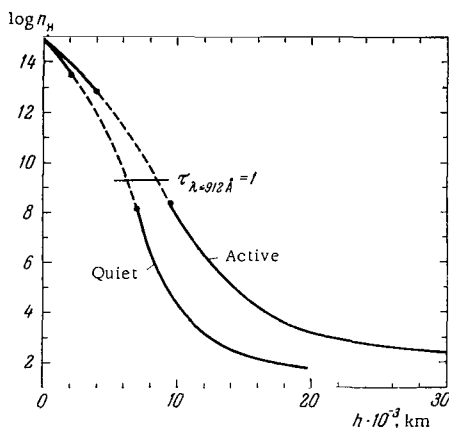


FIGURE 35. Distribution of neutral hydrogen concentration in active and quiet regions of the solar atmosphere.

At low altitudes  $n_{\text{H}}$  is determined from observations of Sr II lines and in the corona from computations using our model. The horizontal line marks the level corresponding to an optical depth of 1 in the Lyman continuum. This level is the "boundary" of the upper chromosphere (where the transitional region "begins"). The dashed curves were obtained by interpolation.

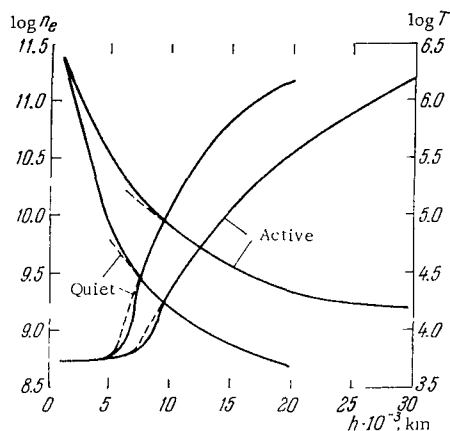


FIGURE 36. A model of active and quiet regions of the solar atmosphere from short-wave, optical, and radio observations.

The dashed curves plot  $T$  and  $n_e$  in the lower part of the transitional region (see Figure 34).

The variation of  $n_e$  and  $T$  in the chromosphere can be computed from the values of  $n_e^2 T^{3/2}$  as a function of height, which we considered before in connection with the model of the transitional region. These functions enable us to derive the distribution of the electron concentration and temperature in the chromosphere if taken in conjunction with the Saha equation

$$n_{\text{H}} = 4.13 \cdot 10^{-16} n_e^2 T^{3/2} \exp \frac{x_{\text{H}}}{kT}, \quad (\text{III.43})$$

which is applicable to an optically thin medium for radiation beyond the Lyman limit. The method used to compute  $n_{\text{H}}$ ,  $n_e$  and  $T$  in the lower chromosphere is essentially analogous to Van de Hulst's method /214/. Van de Hulst constructed a model for  $h \leq 6000$  km, using, however, somewhat unreliable initial data.



The  $n_e$  and  $T$  obtained by this method for the lower chromosphere adequately coincide with the model of the transitional region, as we see from Figure 36. The  $T(h)$  curves were matched using "Lyman" points whose height is determined by the condition  $\tau(\lambda \leq 912 \text{ \AA}) \approx 1$  and the temperature is equal to the Planckian temperature of the Lyman continuum. A contrast of 5—10 was assumed in the Lyman continuum ( $\lambda \leq 912 \text{ \AA}$ ) between active and quiet regions.

Note that the gradients of  $n_e$  and  $T$  change markedly at those heights where the solar atmosphere becomes transparent in the Lyman continuum. We can thus introduce the following definition: the boundary of the upper chromosphere (or the lower part of the transitional region) is located at the level whose optical depth in the hydrogen Lyman continuum is 1. Above this level, the ionization of hydrogen markedly increases, and this definition is therefore a reflection of the fact that the upper chromosphere is highly ionized compared with the lower chromosphere, which largely consists of neutral atoms.

### 13. Specific features of the transitional region between the chromosphere and the corona

The distribution curves  $n_e(h)$  and  $T(h)$  in Figure 36 show that the active region is a dense layer of the solar atmosphere shifted upward along the scale of heights. A characteristic feature of our model is that, virtually at any given height, the temperature in an active region is lower than in a quiet region. At a first glance, the lower temperature in the active region appears to be quite paradoxical. Note, however, that the active region can be treated independently from the quiet region. Indeed, the very existence of an active region markedly differing in its physical parameters from an adjoining quiet region is an indication of weak or nonexistent interaction between the two regions. This mutual isolation is generally thought to be a result of "adiabatic partitions" imposed by magnetic fields. Magnetic fields restraining heat conduction and diffusion are apparently a decisive factor in the solar atmosphere which contains temperature and density inhomogeneities. As a result, there is no need to assume equal gas pressures in the active and the quiet regions at the same height.

Figure 37 plots the electron concentration as a function of temperature, constructed from our model. The correlation between  $n_e(h)$  and  $T(h)$  is quite obvious: in the lower chromosphere, the rapid decrease of  $n_e$  corresponds to a relatively small change in  $T$ ; in the transitional region  $T$  falls off rapidly and  $n_e$  changes very little; in the corona, the temperature reaches a maximum and declines fairly slowly, as  $\sim r^{-1}$ , whereas the electron concentration drops much faster, as  $\sim r^{-6}$ . The most remarkable consequence of our analysis is that the same relation between  $n_e$  and  $T$  is obtained for active and quiet parts of the transitional region /129/:

$$T n_e^{2.5} = C, \quad (\text{III.44})$$

where  $C$  is a constant, which is different for active and quiet regions ( $C_a/C_q = 10$ ).

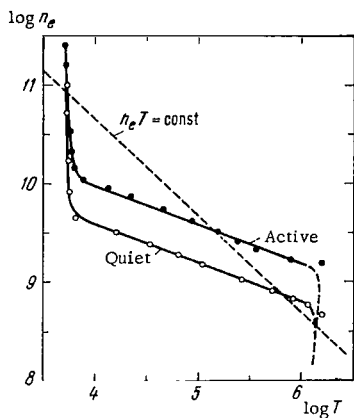


FIGURE 37. Electron concentration vs. temperature of active and quiet regions in the solar atmosphere (from our model, see Figure 36).

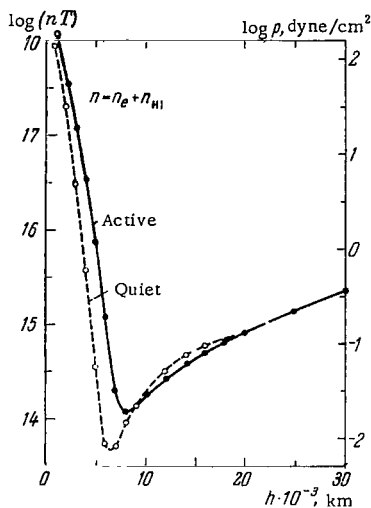


FIGURE 38. Gas pressure vs. height in active and quiet regions of the solar atmosphere, based on our model (see Figure 36).

The temperature in the active region is higher than in the quiet region, for the same electron concentration. This result is consistent with the views of Pikel'ner /221/ on the origin of active regions. According to Pikel'ner, the energy flux per unit mass in active regions is higher than in quiet regions, so that, for the same material density, the active region will heat up to higher temperatures than the quiet region. Pikel'ner's conclusion that the chromosphere in the active region "merges" into the corona at lower heights than in the quiet region /222/ is incorrect, and yet it is a necessary consequence of the theory in /221/.

Consider the vertical variation of gas pressure. Figure 38 shows the plot of  $nT \sim p$  ( $n = n_e + n_{HI}$  is the total number of atoms in  $1 \text{ cm}^3$ ). The pressure is nearly constant in active and quiet regions in the lower chromosphere. As we move higher up, the pressure falls off rapidly and "excess" pressure is formed in the active region, which reaches its maximum in the upper chromosphere (where the "excess" is about 1 order of magnitude). Approximately at the same heights, a pressure minimum is observed in regions of both types. The pressure increases with height in the transitional region, the rate of change being significantly the same in both active and quiet parts of the region. This indicates that "adiabatic barriers" are not needed in the transitional region. It is quite possible that the transitional region has no pronounced structural features, like the chromosphere or the corona. We hope that the entire question of the structure of the transitional region will be resolved in the near future by means of ground observations using the large 53-cm coronagraph /118, 128/.

The results of this chapter and Chapter II point to a considerable extent of the transitional region. This conclusion, in general, may be reached without constructing any full scale models, simply by analyzing the short-wave lines and the generalized measure of emission  $\Delta\varphi(T)$ . The transitional

region with its temperatures of  $10^4 - 10^6^\circ\text{K}$  emits a significant proportion of short-wave radiation (see Table 10) and its measure of emission is therefore high. If the transitional region is assumed to be geometrically thin, the concentration of matter in this region works out to be anomalously high.

Some authorities do not share the opinion that the transitional region is thick, reaching  $(5 - 10) \cdot 10^3$  km across. Zirin and Dietz /223/ regard the transitional region as a very thin layer (about 500 km), with the corona dropping to very low heights ( $h \approx 1.5 \cdot 10^3$  km). The latter conclusion is based on the observations of Athay and Roberts /224/ who recorded the coronal line Fe XI 7892 Å at heights  $h \geq 2 \cdot 10^3$  km. This result (which so far has remained unsupported from other sources) is probably attributed to the effect of projection of bright emission regions emitting at 7892 Å which make a certain angle with the plane of the sky. As we have noted above, systematic observations of the corona in the green and red lines reveal the existence of a 5303 Å emission maximum around  $2 \cdot 10^4$  km. Interesting data about the heights of the emitting regions were also obtained from the analysis of rocket observations. The first estimate of Blacke et al. /43/ based on X-ray heliograms of 19 April 1960 show that X-ray (coronal) emission extends up to heights of  $43 \cdot 10^3$  km. According to Tousey's estimates /225/, the OVI emission ( $T = 2.5 \cdot 10^5^\circ\text{K}$ ) attains its maximum at heights around  $5 \cdot 10^4$  km. Observations of the solar emission at 8 – 15 Å and 44 – 60 Å carried out by Friedman's group /28/ in 1963 (see Chapter I) also yield heights of the order of  $4 \cdot 10^4$  km.

Another weighty argument is provided by the spectra of the solar atmosphere obtained by British authors /9/. The description of this experiment is given in Chapter I and the spectrum is shown in Figure 6. The Sun's image was projected onto the spectrograph slit so that the line of sight intercepted different parts of the solar atmosphere above the 7000 km level. The exceptional accuracy of the guiding system ( $\pm 1000$  km) prevented the slit from being inadvertently aimed at the solar disc during the exposure. The results based on these interesting findings are shown in Figure 7 (Chapter I). We see from this figure that the lines of neutral elements, e.g., H I, C I, O I, are relatively weak: their intensity relative to the disc emission in the same lines does not exceed 0.01. We recall that the temperature of the regions emitting in these lines is  $\leq 10^4^\circ\text{K}$ . The relative intensity is a factor of 5 – 10 higher for lines emitted by ions with ionization temperatures higher than  $5 \cdot 10^4^\circ\text{K}$ . The very strong doublet 1548, 1551 Å, which reaches relative intensity of 0.11, is emitted by the ion C IV which exists at temperatures of  $10^5^\circ\text{K}$ . According to our model, the temperature in quiet parts of the solar atmosphere at heights of 7000 km is around  $10^4^\circ\text{K}$  (see Figure 36). The spectrum thus should not contain lines of ions with lower ionization temperatures. Our model, however, characterizes the mean temperature distribution and the real atmosphere, because of its inhomogeneous structure, will contain elements with other temperatures at the same heights, although their contribution should diminish as the deviation from the mean temperature increases. This is indeed the observed picture (see Figure 7). If the corona begins at heights of  $(1 - 2) \cdot 10^3$  km, there can be no strong emission of the transitional region ions at heights of  $7 \cdot 10^3$  km. The various data on hand thus tend to support the model with an extended transitional region.

Zirin and Dietz /223/ operate with a thin transitional region proceeding from the erroneous notion of an "avoidance zone" for the intermediate ionization stages among ions emitting the short-wave lines. According to /223/, the only iron ions observed are Fe I, Fe II, Fe XV, and Fe XVI. This notion is fundamentally wrong. It suffices to examine Table II which lists identifications of lines with the emission of "intermediate" ionization stages. Moreover, line intensities do not provide a single-valued indication of the concentration of the emitting ions: the atomic characteristics of the ions also play a considerable role. A good example is provided by the corona whose visible spectrum does not contain any lines of the ions Fe XII, Ni XIV, and Ca XIV, whereas lower and higher stages of ionization are all present. The curve of the generalized measure of emission  $\Delta\phi(T)$  in Figure 17 does

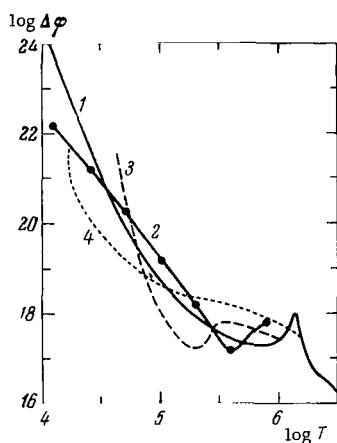


FIGURE 39. The generalized measure of emission according to various authors.

Curve 1, our data (see Figure 17); curve 2, Oster's model /119/ used by Allen /99/ to predict the intensities of short-wave lines; curve 3, Dupree and Goldberg /141/; curve 4, Pottasch /117, 130/. The deep minimum in the transitional region ( $T \approx 10^5 \text{°K}$ ) is missing.

discontinuity. The energy radiated from a given level in the transitional region is thus made up of two components: the dissipation energy of the shock waves arriving from the subphotospheric layer — the convective zone, and the energy transported from the overlying layers by thermal conduction. This energy balance, taken in conjunction with the conditions of hydrostatic equilibrium, determines the structure of the transitional region of the quiet Sun /226/.

not show any minima at temperatures between  $3 \cdot 10^4$  and  $3 \cdot 10^5 \text{°K}$ . Only the corona displays a narrow maximum attributable to its great extent.

Pottasch plotted the measure of emission  $\int n_e^2 dh$  as a function of temperature from short-wave line data /117, 130/ and obtained a curve with a minimum around  $T = 10^5 \text{°K}$ . The emission in the short-wave lines, however, depends on the generalized measure of emission which contains an additional factor  $T^{-1/2}$  missing from the ordinary measure of emission. If this dependence is taken into consideration, Pottasch's curve loses its minimum (Figure 39).

Let us now briefly consider the heating of the transitional region between the chromosphere and the corona.

The formation of the transitional region may be described as follows. The energy of the upward moving shock waves is dissipated in the upper chromosphere, which is characterized by relatively low densities (compared with the photosphere). The dissipated shock wave energy exceeds the energy losses and the temperature increases fairly rapidly to coronal values (about  $10^6 \text{°K}$ ). At high temperatures and large temperature gradients, however, the intensive downward heat conduction smooths out the temperature

The energy balance between shock waves and hydrogen  $H_2$  emission in the lower atmosphere was considered by Dubov /227/, who was the first to formulate the principle of energy balance for each level in the chromosphere.

These ideas were developed and verified by Livshits /228/ who used our model of the transitional region for active and quiet regions of the solar atmosphere. Livshits considered the energy balance in the transitional region by calculating the radiant energy at different levels (the emission  $\epsilon$ , erg/cm<sup>2</sup>sec). The dissipation energy of shock waves ( $E$ , erg/cm<sup>2</sup>sec) was computed using a somewhat modified theory of shock wave propagation /229/. The values of  $E$  and  $\epsilon$  were found to coincide within the margin of accuracy of the computations. Downward conduction of heat from the corona apparently does not make a significant contribution to the energy balance, since an improbably large flux of shock waves required to account for the existence of a corona with a mean temperature  $T \approx 1.5 \cdot 10^6$  °K if the thermal conduction is taken into consideration. The heat conduction effect, according to Livshits, is probably offset by the slow outward motion of the solar atmosphere: velocities of about 1 km/sec are quite sufficient for this purpose. This approach matches the theory of the expanding corona /191/, which gives velocities of a few km/sec at the "base of the corona" (see Table 15).

According to /226/, the transitional region is extremely thin (about 1000 km), the mean temperature of the corona is  $T_c \approx 6 \cdot 10^5$  °K, and the corresponding temperature gradient is from 1000° to 100° per 1 km. Livshits notes /228/ that these figures were obtained in /226/ from considerations of thermal conductivity. If the temperature is raised to  $1.5 \cdot 10^6$  °K, the downward energy flux in a model with a thin transitional region will grow by a factor of 10 and the outgoing energy will no longer be sufficient to maintain the high coronal temperatures. (The thermal conduction energy flux is  $\sim T^{5/2} dT/dh$ ). This is an inherent difficulty in any model with a narrow transition region. Another difficulty is that the energy influx into the lower layers of the atmosphere becomes excessively large and can no longer be balanced by radiant losses alone /230/. A possible way out of this dilemma according to /230/ is that the excess energy is spent for the excitation of dynamic instabilities in the chromosphere (so-called chromospheric spicules).

If the emissions of hydrogen and helium provide the only mechanism of radiative cooling, the vertical distribution of temperature will be dominated by two characteristic regions  $T \leq 10,000$  °K and  $T \leq 50,000$  °K, i. e., a distinct temperature discontinuity is observed. The next discontinuity is associated with ionized helium. Athay and Thomas /213/ used this model.

Another approach uses the emission of "impurity" elements, such as C, O, Si, Mg, Fe, and other elements which rank third and lower down in abundance after hydrogen and helium. The importance of these "impurities," as it emerges from the analysis of short wave radiation increases in high-temperature regions and becomes dominant in the transitional region and in the corona. This factor has led Livshits /228/ to the conclusion that our model is consistent with an extended transitional layer /129/ and with the mechanism of heating of the solar atmosphere by upward moving wave perturbations. The heat conduction effect in this case, as we have seen before, is offset by the outward motion of solar matter with velocities which do not exceed the characteristic velocities of the "solar wind" theory /191/.

In the light of the above considerations concerning an extended transitional region between the chromosphere and the corona, let us consider one of the recent publications which advocates a thin transitional layer. Athay /231/ analyzed the data for short-wave lines of 47 ions of 10 different elements. These data were used by Pottasch /117/, who derived an expression for the intensity  $F$  of short-wave lines, analogous to (II.6). After certain simplifications, Athay obtained

$$F \sim \kappa (n_e T)^2 \frac{dh}{dT} \Phi(T),$$

where  $\Phi$  is a function of temperature only. Then quite arbitrarily assuming the gas pressure to be constant ( $n_e T = \text{const} = 6 \cdot 10^{14} \text{ deg/cm}^3$ ), Athay constructed the function  $dh/dT = f(T)$  from these data. Introduction of dielectron recombination according to /231/ ( $T_i$  doubled as a result) and improved chemical composition changed the curve of  $f(T)$  very slightly and quite insignificantly. The function  $f(T)$  between  $10^5$  and  $10^6$ °K corresponds to the expression  $T^{1/2} dh/dT = \text{const}$ , i. e., the energy flux transported by heat conduction mechanisms is constant. The temperature distribution  $T = T(h - h_0)$  recovered from  $f(T)$  is characterized by very steep gradients, reaching 300 deg/km! To establish a scale of heights, Athay took  $T = 10^5$ °K for  $h \approx 2000 \text{ km}$ .

Athay's work /231/ provides an excellent illustration of the crucial importance that the assumption of constant pressure has on the final results. Using the same observation data, but without any a priori theoretical assumption, one could easily obtain a model not unlike ours, with an extended transitional layer.

The relation between density and temperature characteristic of our model ( $n_e^{2.5} T = \text{const}$ ) /129/ is naturally explained within the framework of the theory of heating of the transitional region. The volume emission of the transitional region is determined in /232/ from model data:  $\varepsilon \sim n_e^2 T^{-0.8}$ . Analysis of shock wave damping indicates that the energy dissipated per unit volume is  $E \sim T^{-(1.6-1.9)}$ . The energy balance at any level in the transitional region ( $E = \varepsilon$ ) gives

$$n_e^{(1.8-2.6)} T = \text{const}.$$

Within the margin of error of the theory, this expression coincides with relation (III.44) which is derived from our model. It has been shown in /232/ that a relation of this type is also applicable to transitional regions of stars of different spectral classes.

In concluding this chapter, let us briefly consider the future prospects of observations of the transitional region between the chromosphere and the corona. Investigation of the transitional region from its short-wave spectrum involves considerable difficulties, because the equipment has to be launched beyond the absorbing layers of the Earth's atmosphere, to altitudes  $h > 100-200 \text{ km}$ . Further studies require observation data with high spatial and spectral resolution, which is exceedingly difficult to ensure in rocket observations.

In our opinion, ground observations of the transitional layer in the "visible" spectrum should be attempted both during total solar eclipses and by extra eclipsing methods. After all, ground observations have enabled us to establish virtually all the physical properties of the solar corona. One

of the lines of the transitional region is well known and it has been repeatedly observed. This is the He II line 4686 Å corresponding to the principal transition of the Paschen series. Unfortunately, the information about this line is still fragmentary. Moreover, the 4686 Å line is generally observed only in the spectrum of active regions, i. e., condensations and flares. Astrophysicists know of a large number of other lines corresponding to the temperatures of the transitional region; these lines are observed in the spectra of stars with extended envelopes. The "allowed" lines of sufficiently abundant ions (O, N, C, Si) with low initial ionization potentials should apparently be the strongest. These lines can be found in Moore's list /96/ and in the tables of Striganov and Sventitskii /107/. The intensities of these lines may also be estimated by the method used in Chapter II for the prediction of short-wave lines or, more precisely, by matching with known intensities of short-wave lines in cases when the initial level is common for the emission of a short-wave and a "visible" line. Table 19 lists some data obtained by this method for a number of strong lines. The radiation fluxes listed in Table 19 correspond to an epoch of minimum solar activity. The values of  $F$  may be substantially higher in the active parts of the transition region.

TABLE 19. Some lines of the transitional region between the chromosphere and the corona accessible to ground observations

Ion	$T_i$ , °K	Transition	$\lambda$ , Å	$F \cdot 10^5$ , erg/cm <sup>2</sup> sec	Mitchell /233/, chromosphere		
					$\lambda$ , Å	identification	intensity (Rowland's scale)
He II	$1 \cdot 10^5$	$3d^2D-4f^2F^\circ$	4685.68	1	4685.7	He II	2
C IV	$1 \cdot 10^5$	$3s^2S-3p^2P^\circ$	5801.33	2	5798.00	Fe, Si	4
			5811.98		5804.28	Fe, Ti	2
					5811.39	Fe	1
NV	$1.8 \cdot 10^5$	$3s^2S-3p^2P^\circ$	4619.4	2	4619.50	Fe	2
			4603.2		4602.95	Fe	5
O VI	$3 \cdot 10^5$	$3s^2S-3p^2P^\circ$	3811.35	3	3811.40	Ti, Ni	2
			3834.24		3834.46	Fe	15
O III	$6 \cdot 10^4$	$3p^1P^\circ-3p^1P$	5592.37	2	5592.28	Ni	7

Energy estimates correspond to quiet regions of the solar atmosphere.

The region of emission of these lines is limited to heights of  $(5-20) \cdot 10^3$  km, so that instruments forming a sufficiently large image of the Sun on the spectrograph slit will be required. The determination of the emission heights is one of the basic problems in the detection of these lines. The large extraeclipsing coronagraphs /128/ are quite adequate at this stage for ground observations of the transitional region.

Mitchell's list of chromospheric lines based on the observations of four total solar eclipses (slitless spectrographs) /233/ contains some 3500 lines. Unfortunately, the list contains no coronal lines, and it can hardly be expected to include lines from the transitional region, especially in view of the specific properties of the slitless spectrograph which is best adapted to discovering lines characterized by a small scale of heights (narrow crescents). Table 19 also lists a number of lines from Mitchell's list /233/ whose wavelengths are close to those of the lines of the transitional lines; the

corresponding identifications and intensities on the Rowland scale are also given. To every line of the transitional region there corresponds a chromospheric line and the two lines form a blend. This naturally markedly interferes with the search for lines of the transitional region.

High-resolution spectral observations make it possible to determine whether a given line belongs to the transitional region or to the chromosphere. The line widths in the transitional region are larger than in the chromosphere (this is naturally so for weak optically thin lines only) but smaller than in the corona. The lines listed in Table 19 should have half-widths of no less than  $0.3 \text{ \AA}$ .\* The determination of the line widths for the transitional region constitutes one of the most important observational tasks. Satisfactory solution of this problem will yield the temperatures and the "turbulent" velocities in the transitional region.

\* For example, the CIV lines  $5801.3$  and  $5812.0 \text{ \AA}$  should have widths of around  $0.5 - 0.8 \text{ \AA}$  for the characteristic "turbulent" velocities of the solar atmosphere ( $10 - 12 \text{ km/sec}$ ).



## *Chapter IV*

### **BASIC OBSERVATIONAL DATA FOR THE IONOSPHERE**

The ionosphere is characterized by fairly complex behavior. The state of ionization of the gases in the ionosphere is maintained in daytime mainly by the ultraviolet and the X-ray radiation of the Sun. This short-wave ionization radiation varies with the level of solar activity. Solar activity cycles (11-years and 27-days variations) and disturbances associated with solar flares are superimposed on regular diurnal variations in the ionosphere. The ionosphere, being part of the upper atmosphere, also faithfully repeats all the changes and fluctuations of the neutral atmosphere. The properties of the neutral atmosphere, its composition, density, and temperature are, in their turn, functions of the time of day and year, latitude, and other factors, including the solar activity level.

Despite this complexity, the variations in the ionosphere mainly present a regular picture, since after all the state of the ionosphere is determined by comparatively simple physical processes. Knowledge of these processes and experimental data about the upper atmosphere and the ionizing radiation of the Sun are needed to understand the regular variations in the ionosphere and to identify the nature of some irregular disturbances. In this chapter we shall mainly discuss the results of observations relating to the regular behavior of the ionosphere, which have been obtained by different methods.

#### **14. Results of radio sounding from the ground**

Although the existence of a conducting ionized layer in the upper atmosphere was suspected back in late 19th and early 20th century, a direct proof of the existence of the ionosphere, as a permanent feature of the upper atmosphere, was only obtained in 1926, when Appleton and Barnett recorded vertical reflection of radio waves. The method of vertical sounding of the ionosphere was subsequently developed, and it remained the only experimental method of atmospheric research for a quarter of a century, until the advent of rockets. Basically, this method operates with reflections of radio signals of various frequencies from the ionosphere. By measuring the transit time of the pulse, one can estimate the effective reflection altitude; the maximum reflected frequency  $f_0$  (the critical frequency) provides a fairly reliable estimate of the electron concentration  $n_e$  in the layer maximum,

$$n_e = 1.24 \cdot 10^4 \cdot f_0^2, \quad (\text{IV.1})$$

where  $f_0$  is in MHz. The numerical relation between  $n_e$  and  $f_0$  is presented in Table 20.

TABLE 20. Relation of electron concentration to critical frequency

$n_e$ , $\text{cm}^{-3}$	$3 \cdot 10^3$	$10^4$	$10^5$	$10^6$	$5 \cdot 10^6$
$f_0$ , MHz	0.5	0.9	2.85	9	20

The wide use of the method of vertical sounding proved of the greatest importance for the development of radio communications and broadcasting. It supplied a wealth of information about diurnal, seasonal, and latitudinal variations of the electron concentration at three fixed levels in the ionosphere, the so-called  $E$ ,  $F_1$  and  $F_2$  "layers" or "regions."\*

TABLE 21. Basic parameters at the maxima of the different ionospheric regions

Region	$h_{\text{max}}$ , km	$T$ , °K	$n$ , $\text{cm}^{-3}$	$n_e$ , $\text{cm}^{-3}$		
				day		night
				solar activity		
				maximum	minimum	
$D$	(70)	220	$2 \cdot 10^{15}$	150		$\sim 10$
$E$	110	270	$2 \cdot 10^{12}$	$3 \cdot 10^5$	$1.5 \cdot 10^5$	$\sim 4 \cdot 10^3$
$F_1$	180	800—1500	$1.5 \cdot 10^{10}$	$5 \cdot 10^5$	$3 \cdot 10^5$	—
$F_2$ (winter)	220—280	1000—2000	$(2-5) \cdot 10^9$	$25 \cdot 10^5$	$6 \cdot 10^5$	$\sim 10^5$
$F_2$ (summer)	250—320		$(1-3) \cdot 10^9$	$8 \cdot 10^5$	$2 \cdot 10^5$	$(2-5) \cdot 10^5$

Table 21 summarizes some basic information about the three regions of the ionosphere. They lie at altitudes between about 50 and 300 km (Figure 40), whereas the ionized part of the atmosphere extends to much greater altitudes, up to the outer boundary of the magnetosphere with the interplanetary space (10—15 Earth radii).

The atmospheric conditions widely vary in different parts of the ionosphere. The temperature changes from around 200 to 1000—2000°K; the neutrals concentration  $n$  changes by a factor of  $10^6$ , from about  $10^{15} \text{ cm}^{-3}$  in the  $D$  region to about  $10^9 \text{ cm}^{-3}$  in the  $F$  region.

The electron concentration  $n_e$  depends on the phase of the solar cycle and the time of the day. The peak concentration of ions and electrons is attained in the topmost layer, in the  $F_2$  region at an altitude of  $h \sim 300$  km. At night, the electron concentration in this region diminishes to 1/3—1/10 of its day-time value, whereas in the  $E$  and  $F_1$  regions it drops by 1.5 and 2.5 orders of magnitude, respectively. Table 21 lists some mean values of  $n_e$ , which ignore the dependence on latitude, time of year, geomagnetic activity, etc. The seasonal variations are reflected for the  $F_2$  region only, as they are

\* We will use both terms. The term "layer" will be used when a distinct maximum of electron concentration is observed in the region.

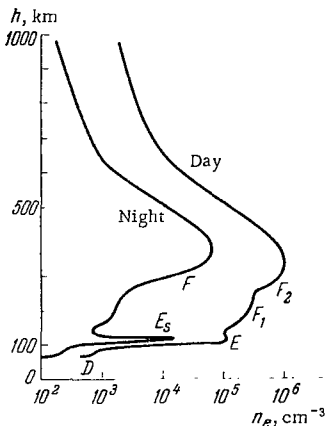


FIGURE 40. A typical vertical distribution of the electron concentration in the ionosphere for daytime and nighttime conditions. The different regions of the ionosphere are identified for each profile.

particularly large there. The  $F_1$  layer is regularly observed at daytime only, for relatively small zenith angles of the Sun,  $z_0 \leq 45^\circ$ . For these reasons it is mostly detected in summer. The  $F_1$  layer is more apparent during minimum solar activity; it is not observed altogether during the winter maximum of solar activity.

The main regular variations in the electron concentration can be classified into diurnal, latitudinal, and seasonal. The most remarkable feature is that for the  $E$  and  $F_1$  regions they are all determined on the average by the variation of the Sun's zenith distance  $z_0$ . The mean concentration  $\bar{n}_e$  is a simple function of  $z_0$ :

$$\bar{n}_e \propto (\cos z_0)^l. \quad (\text{IV.2})$$

which proves that the ionization in this region is determined by the electromagnetic radiation of the Sun. Observations during solar eclipses seem to confirm this conclusion. Indeed, as the Moon advances to eclipse the Sun,  $n_e$  di-

minishes in the  $E$  and  $F_1$  layers, only to start increasing after the maximum phase of the eclipse.

Simple theoretical considerations (the so-called theory of the simple layer) give  $l = 0.5$  in (IV.2). However, the power exponent  $l$  is not constant: it varies with location and time of year. Moreover,  $l > 0.5$  in the  $E$  region and  $l < 0.5$  in the  $F_1$  region. The deviation of  $l$  from the theoretical value of 0.5 reveals the approximate nature of the simple layer theory, whereas the seasonal and latitudinal variation of  $l$  indicates that geophysical, as well as solar radiation, factors must be taken into consideration. The same conclusion emerges from the fact that (IV.2) is valid for the mean concentrations  $\bar{n}_e$  only.

In the  $F_2$  region, not even the mean electron concentration follows the simple relation (IV.2). The diurnal maximum of  $n_e$  definitely does not fall at noon, and the magnitude of its displacement is a function of latitude, season, and also longitude. In some cases, maximum  $n_e$  is observed at night /234/. This constitutes what is known as the anomalous behavior of the  $F_2$  region. Nearly a dozen of various "anomalies" are distinguished: diurnal, seasonal, December anomaly, equatorial anomaly, etc. These factors strongly suggest that the variation of  $n_e$  in the  $F_2$  region is determined by geophysical factors, and not by the solar radiation.

Examination of the actual daily variations of  $n_e$  in the  $E$  and  $F_1$  regions (instead of the mean values) may also reveal deviations from relation (IV.2) associated with various geophysical factors. Solar radiation, however, invariably remains the decisive force. This conclusion is further corroborated by the clear dependence of the long-time averages of various ionospheric parameters on the solar activity level.

The dependence of the ionospheric parameters on the solar activity also emerges from the 27-day and 11-year periodic variations. As we have mentioned above, it is only the mean values of the ionospheric parameters

that reveal the dependence on the solar activity. The particular solar activity index selected does not markedly affect the results.\* Ratcliff and Weeks /234/ in their famous review give the following functional relations between  $n_e$  and the sunspot number  $R$ :

$$(\bar{n}_e)^2 = 1.8 \cdot 10^{10} (1 + aR) \text{ for the } E \text{ region,} \quad (\text{IV.3})$$

where  $a = (7-9.5) \cdot 10^{-3}$ ;

$$(\bar{n}_e)^2 = 5 \cdot 10^{10} (1 + 0.016R) \text{ for the } F_1 \text{ region;} \quad (\text{IV.4})$$

$$\bar{n}_e \propto (1 + 0.02R) \text{ for the } F_2 \text{ region.} \quad (\text{IV.5})$$

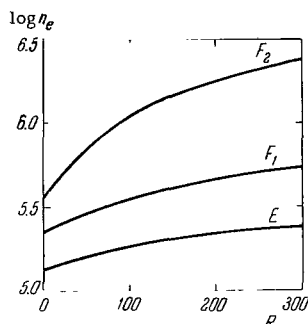


FIGURE 41. Variation of the mean values of the electron concentration  $n_e$  in  $E$ ,  $F_1$ , and  $F_2$  regions vs. the sunspot number  $R$ .

The most pronounced dependence of  $\bar{n}_e$  on the solar activity is thus characteristic of the  $F_2$  region. This is clearly seen from Figure 41, which plots the three functions.

Another clear manifestation of the dependence on the solar activity is provided by ionospheric disturbances during solar flares. These disturbances constitute a complex of various ionospheric phenomena, which mainly occur in the lower part of the ionosphere, in the  $D$  region, although  $n_e$  is occasionally observed to increase in the  $E$  and  $F$  regions also /235, 236, 807/. During chromospheric flares, the hardest component of the solar radiation is markedly intensified, and it penetrates throughout most of the ionosphere.

Ground ionospheric stations yielded a rich crop of observational data. Observations of regular phenomena are supplemented by irregular effects (sudden ionospheric disturbances SID, sporadic  $E_s$  layer,  $F$  scattering, inhomogeneities and moving disturbances, etc.) which have to be studied for practical reasons: proper understanding of these effects is important for elucidating the conditions of formation of the ionosphere and its changes. Although ionograms provide a fairly clear classification of these phenomena, they do not always shed enough light on the various processes which take place in the ionosphere.

The difficulties associated with the interpretation of the ionograms stem from one basic factor: although the value of  $n_e$  can be determined with fair certainty from (IV.1), the actual altitude to which this  $n_e$  is to be assigned is highly uncertain. Ratcliff and Weeks /234/ note that superficial examination of ionograms reveals with great clarity the penetration of radio waves through  $E$  and  $F_2$  layers. It would therefore seem that the corresponding critical frequencies are amenable to simple interpretation. However, radio wave propagation through the  $E$  layer is a highly complex effect in reality, and the penetration of radio waves through the  $F$  layer, although easily detected, is not so simple to interpret. Even the numerous regular features detected in ionograms were interpreted only after a fairly detailed picture of the

\* In Chapter I we mentioned that the decimeter radio emission of the Sun provides a better index of the intensity of the short-wave solar radiation.

physical processes in the ionosphere had become available. Some of the irregular phenomena observed in the ionograms also have been identified: they are linked with changes in the intensity of ionizing agents or with variations in the atmosphere. Most of the irregular phenomena, however, remain quite puzzling. Recent results obtained with rockets and satellites, and by means of some new ground methods of research which will be considered at a later stage, enabled to reach a better understanding of a number of basic processes in the ionosphere and to form a clearer picture of the reasons for the changes in the critical frequencies in the ionograms. One of the main tasks was to obtain the vertical profiles of  $n_e$ .

#### 15. Rocket measurements of electron and ion concentration at altitudes of 60–300 km

The early methods of ionosphere sounding from the ground only yielded the variation of  $n_e$  in the maxima of the  $E$ ,  $F_1$ , and  $F_2$  layers. The main advantage of the rocket method is that it measures  $n_e$  in a range of accurately known altitudes, thus yielding the vertical profiles of  $n_e(h)$ . Another achievement of rocket measurements is that they provide more reliable data on the altitudes of those layers which are picked up by the ground sounding stations. Over 150 rocket measurements of  $n_e(h)$  profiles have been carried out so far, both in the USSR (by K. I. Gringauz's group) and elsewhere. A new technique was recently developed for the computation of the  $n_e(h)$  profiles from the ionograms. In this section, we present the main results relating to the  $n_e(h)$  profiles in different parts of the ionosphere and describe the diurnal variation of these profiles, their dependence on latitude, on solar and geomagnetic activity, and on other factors.

#### The $D$ region

Let us consider the results of rocket (33 tests) and ground measurements of  $n_e$  at altitudes between 60 and 100 km presented in /237/. It follows from Kane's work /238/ that the electron collision frequencies used in the earlier treatment of radio wave absorption in the  $D$  region were exaggerated. The electron concentrations  $n_e$  obtained with the use of new electron collision frequencies, by ground methods of absorption, cross modulation, and partial radio wave reflection virtually coincide with the values of  $n_e$  obtained with rockets by the method of wave propagation. The rapidly developing method of rocket probe measurements for the  $D$  region still gives less reliable results than the other methods.

A characteristic feature of the  $D$  region is the permanent irregular variation of  $n_e$  which is superimposed on the regular daily, seasonal, and latitudinal variations. The mean values of  $n_e$  under characteristic conditions, based on the results of rocket and ground measurements, are given in Table 22. Analogous results for  $n_e$  under quiet conditions were recently obtained by other authors as well /239–241/.

TABLE 22. Mean electron concentrations  $n_e$ ,  $\text{cm}^{-3}/237/$ 

Altitude, km	60	65	70	75	80	85	90	95	100
Conditions									
Polar night /242/									
Night			10	20	5	10	15	20	22
Day (winter)	20	50	50	90	40	100	300	$10^3$	$3 \cdot 10^3$
Day (summer)	50	120	160	800	$2 \cdot 10^3$	$4 \cdot 10^3$	$1.5 \cdot 10^4$	$3 \cdot 10^4$	$6 \cdot 10^4$
Highly disturbed ionosphere	500	$1.5 \cdot 10^3$	$3 \cdot 10^3$	$4 \cdot 10^3$	$6 \cdot 10^3$	$1.2 \cdot 10^4$	$3 \cdot 10^4$	$8 \cdot 10^4$	$1.2 \cdot 10^5$

The regular variations of  $n_e$  can be described as follows. At night  $n_e$  is  $1/10 - 1/30$  of its daytime values. At high latitudes and during strong ionospheric disturbances (SID) entailing strong absorption of radio waves,  $n_e$  increases at all altitudes; below 90 km,  $n_e$  increases by a factor of 10. A similar increase in  $n_e$  is noted in the presence of the sporadic  $E_s$  layer, although only at altitudes around 85 km. Slight seasonal variations in  $n_e$  are also observed (in summer  $n_e$  is higher than in winter). All these factors indicate that the electron concentration in the  $D$  region undergoes definite regular variations related to the effects of solar and corpuscular radiation and to seasonal variations in the atmosphere.

The  $D$  region also shows irregular variations of the electron concentration and formation of sporadic inhomogeneities in  $n_e$ . The agent responsible for the ionization of this part of the ionosphere, both in daytime and at night, can thus be identified as variable and sporadic. The sporadic variations in  $n_e$  and the increase of  $n_e$  during geomagnetic disturbances and near the auroral latitudes reveal the significant role of the corpuscular radiation in the ionization of the  $D$  region /237, 668–672/.

In distinction from the  $n_e$  values, for which fairly complete data are available, the concentrations of positive and negative ions ( $n_i^+$  and  $n_i^-$ ) in the lower ionosphere are quite uncertain to this day. Contradictory data on the values of the ratio  $l = n_i^-/n_e$  (according to some authors  $l \ll 1$  at 75 km, while according to other sources  $l > 1$ ) have so far prevented clearcut conclusions from being formed regarding the nature of the effective recombination coefficient and the importance of the various photochemical processes in  $D$  region ionization.

The  $n_e(h)$  profiles at 100 – 300 km

The vertical distribution of the electron concentration, or the  $n_e(h)$  profile, shows diurnal and seasonal variations, and also depends on the solar activity. The changes in the  $n_e(h)$  profile caused by changes in the Sun's zenith distance  $z_0$  during a summer day for low and high solar activity conditions are clearly evident from Figures 42a, b, based on rocket data for middle latitudes /243/. Comparison of these figures with Figure 42c corresponding to winter conditions reveals the seasonal variations.

Let us consider in more detail the dependence of  $n_e$  on the altitude and on  $z_0$ , and the variation of the altitude of the  $E$  and  $F$  layers.

**Dependence on altitude.** Two distinct daytime periods are observed: the "noon" period with  $z_{\odot} = 0-45^{\circ}$  and the "sunset-sunrise" period with  $z_{\odot} = 80-90^{\circ}$ . During these two periods,  $n_e$  varies synchronously at all altitudes, and the general profile is not broken. Figure 42 shows a family of midday profiles  $n_e(h)$  (thin lines) and a family of twilight profiles  $n_e(h)$  (thick lines), which are all quite similar to one another. The profiles reveal the following changes on passing from midday values of  $z_{\odot}$  to larger zenith distances: the gradient  $d \log n_e / dh$  increases by a factor of 2-3 at altitudes of 150-200 km, a maximum of  $n_e$  is formed in the E region at 110-130 km, and a "dip" with minimum  $n_e$  is observed under the maximum.

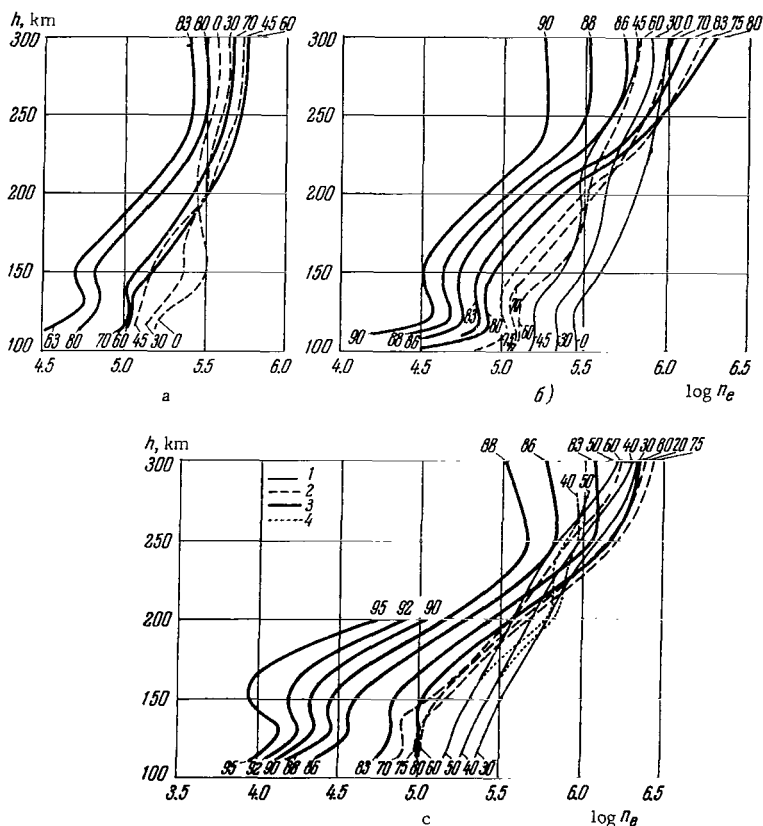


FIGURE 42. The mean profiles  $n_e(h)$  for various zenith distances of the Sun  $z_{\odot}$  (indicated against each curve) from rocket measurements /243/:

a) summer, low solar activity; b) summer, high solar activity; c) winter (above 200 km only high solar activity, except for  $z_{\odot} = 40^{\circ}$  and  $z_{\odot} = 50^{\circ}$ ); 1) midday profiles; 2) "transitional" profiles; 3) twilight profiles; 4) low solar activity.

For intermediate values of  $z_{\odot}$ , intermediate profiles  $n_e(h)$  are observed (the dashed lines in Figure 42). At altitudes over 170-190 km, the intermediate profiles show an odd phenomenon:  $n_e$  increases with the increase in

$z_0$ . We see from Figure 42a that under conditions of low solar activity in summer, no "midday" profiles are observed.

We have noted before that equation (IV.2) describes the seasonal variations of  $n_e$  due to the direct changes in solar radiation with changing  $z_0$ . The difference in the  $n_e(h)$  profiles obtained for identical  $z_0$  is associated with seasonal variations in the atmosphere. Comparison of Figures 42b and 42c and  $n_e(h)$  profiles for identical  $z_0$  shows that the seasonal variations in the ionosphere not only produce the famous winter anomaly of the  $F_2$  region (the  $n_e$  in  $F_2$  is higher in winter than in summer) but also other changes in the  $n_e(h)$  profiles. In particular, the height of the maximum of the  $F_2$  region diminishes in winter, while the gradient  $d \ln n_e / dh$  at 150–250 km increases, and the amplitude of variation of  $n_e$  for equal increments  $\Delta z_0$  at  $z_0 = 80$ – $90^\circ$  in the  $E$  region also increases. These seasonal changes in the ionosphere are associated with seasonal variations in the structure parameters of the neutral atmosphere.

Above  $h \approx 200$  km, significant seasonal variations are observed mainly for the midday profiles, whereas in the  $E$  region the seasonal effect, resulting in marked differences in the rate of change of  $n_e$ , is observed with the Sun near the horizon. The effect of the seasonal changes in the properties of the atmosphere in the morning and in the evening is, apparently, most prominent in the lower ionosphere, whereas the midday effects are particularly noticeable in the upper part of this ionospheric layer.

The effect of the variations in solar radiation during the solar cycle for large  $z_0$  is conversely most prominent in the upper part of the ionosphere. The gradients  $d \log n_e / dh$  for the sunrise-sunset profiles therefore significantly differ in different phases of the solar activity cycle.

With the Sun low above the horizon, shows a characteristic maximum at 110–130 km and a higher minimum at 140–150 km. Above the minimum,  $n_e$  increases fairly monotonically, up to the  $n_e$  region maximum. This vertical distribution of  $n_e$  appears to contradict the results of IGY rocket studies, which revealed the absence of a sharply defined  $E$  layer in the daytime ionosphere and of the  $n_e$  minimum above it [244]. This contradiction is merely apparent, however, since at altitudes of 110–130 km the layer is clearly observed only for  $z_0 \geq 60$ – $70^\circ$ , remaining very indistinct during the entire day.

Figures 42b and 42c show that as the Sun approaches the horizon, the  $n_e$  maximum shifts from  $h \approx 110$ – $120$  km to  $h \approx 120$ – $130$  km. At night, the  $n_e(h)$  profile retains a sharply defined  $E$  layer and a minimum at 140–150 km.

**Dependence on  $z_0$ .** As we shall see in the next chapter, the theory requires knowledge of the variation of  $n_e$  as a function of the overlying atmosphere, which is characterized by Chapman's function  $\text{Ch } z_0$  (see Chapter V). As an example, Figure 43 shows the variation of  $n_e$  at 110–200 km vs.  $\text{Ch } z_0$  in summer [243].

A linear relation between  $\log n_e$  and  $\log \text{Ch } z_0$  (the straight lines in Figure 43) in a certain range of  $z_0$  is observed at every altitude, and not only in the maxima of the  $E$  and  $F_1$  layers, as indicated in (IV.2). The slope of these lines, characterizing the exponent  $l$  in the relation

$$n_e \propto (\text{Ch } z_0)^{-l}, \quad (\text{IV.6})$$

and the intervals of  $z_0$  where this relation is applicable change with altitude. The value of  $l$  also depends on time of year. The curve of  $l(h)$  for the summer months is shown in Figure 44. At  $h \approx 120$  km,  $l$  has a minimum. In



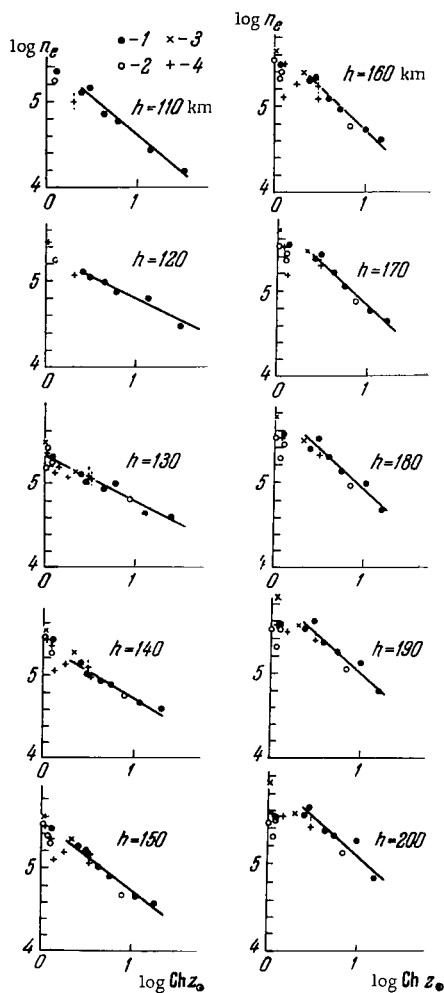


FIGURE 43.  $\log n_e$  vs.  $\log Ch z_0$  at various altitudes between 110 and 200 km in summer according to rocket measurements /243/:

circles — data obtained from radio wave propagation measurements; crosses — probe measurements. The linear segments correspond to the approximation (IV.6); 1, 3) high solar activity; 2, 4) low solar activity.

other words,  $n_e$  at these altitudes varies more slowly during the day than at nearby altitudes. This leads to the formation of an  $n_e$  maximum for large  $z_0$ .

Another feature of the  $n_e(z_0)$  curves is that at altitudes of  $h \approx 200$  km and higher, for  $\log Ch z_0 < 0.4 - 0.5$ ,  $n_e$  decreases as the Sun's altitude above the horizon increases. However, for  $z_0 \lesssim 50^\circ$  in epochs of high solar activity,  $n_e$  is again proportional to the Sun's altitude above the horizon. The inverse dependence of  $n_e$  on  $z_0$  corresponds to the intermediate  $n_e(h)$  profiles which were considered above. This phenomenon is possibly responsible for the disappearance of the  $F_1$  layer from the ionograms for some definite value of  $z_0$ .

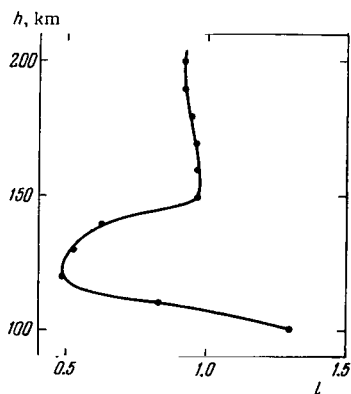


FIGURE 44. The parameter  $l$  from (IV.6) vs. altitude in summer for  $\text{Ch}z_{\odot} > 3$  according to rocket measurements /243/.

It is observed only above the  $F_1$  layer and could not be studied by ground sounding methods. The variations in the properties of the neutral atmosphere at altitudes above 200 km during the day probably produce this phenomenon.

Let us now consider the dependence of  $n_e$  on the magnetic activity. We have mentioned before that the ionization in the  $D$  region at altitudes below 80–90 km depends on the geomagnetic activity and increases at higher geomagnetic latitudes. In the  $E$  region, no such dependence is generally observed. Rocket data on the  $n_e(h)$  profile enable us to investigate the altitudes between the  $E$  and  $D$  regions /246/. As the geomagnetic index\*  $K_p$  increases to 3–5, the concentration  $n_e$  at altitudes of 100 and 110 km increases by a factor of no less than 1.5 and 2, respectively. The added ionization effect observed during geomagnetic disturbances thus in-

creases at lower altitudes, apparently reaching a maximum in the  $D$  region at altitudes  $h \approx 70$  km, where  $n_e$  increases by one order of magnitude. In the  $E$  region at  $h \approx 120$  km, the effect is smaller and less conspicuous.

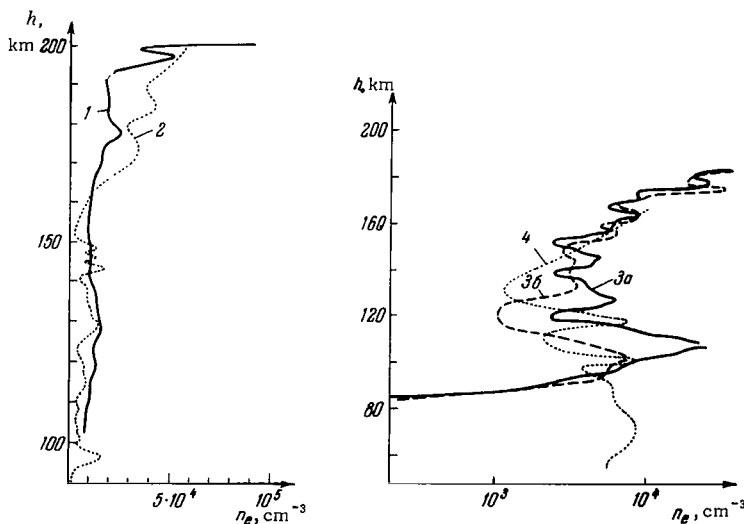


FIGURE 45. Vertical distribution of the electron concentration at nighttime from rocket measurements /245/:

curve 1 — 9 September 1957 (Gringauz); curve 2 — 4 February 1958 (Jackson and Kane); curves 3 — 26 September 1960 (Aono et al., ascent (a) and descent (b)); curve 4 — 28 April 1960 (Sagalyn and Smiddy).

\* Geomagnetic field disturbances are generally expressed in terms of the index  $K$ , varying from 0 to 8.  $K_p$  is the planetary index, representing an average over many stations.

**Nighttime ionosphere.** The  $n_e(h)$  profiles measured with rockets after sunset invariably reveal a nighttime  $E$  layer at 110–130 km and a "dip" in the electron concentration at 125–160 km /245/. Typical nighttime profile curves are shown in Figures 45 and 46. In the "dip" region, sharp irregularities in  $n_e$  are observed;  $n_e$  drops markedly (down to  $3 \cdot 10^2$ – $10^3$  cm $^{-3}$ ) between the irregular layers. The comparatively wide nighttime  $E$  layer generally shows very narrow (up to 0.5 km thick) sporadic  $E_s$  layers (see Figure 46).

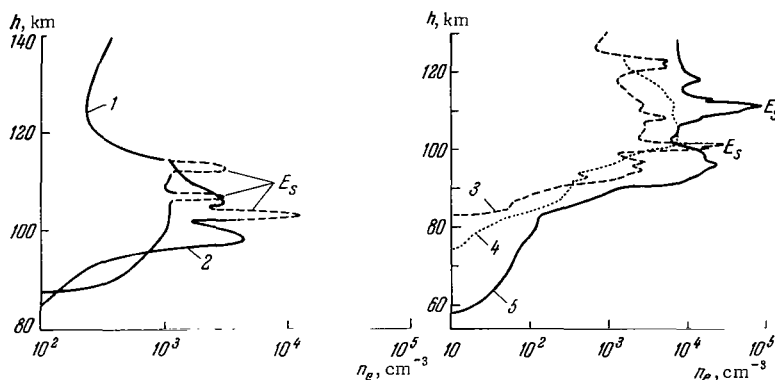


FIGURE 46. Vertical distribution of the electron concentration at nighttime from rocket measurements of Smith et al. /565, 758/:

curve 1 — 27 October 1961; curve 2 — 17 August 1961; curve 3 — 7 September 1962;  
curve 4 — 30 November 1962; curve 5 — 5 December 1962.

The  $n_E$ , the nighttime  $E$  layer, and the additional layers in the "dip" are all due to some nocturnal source of ionization. This can be proved by the following considerations.

Without a nocturnal ionization source, the electron concentration would follow a hyperbola

$$\frac{1}{n_e} = \frac{1}{n_{e0}} + \alpha' \tau, \quad (\text{IV.7})$$

where  $\tau$  is the time after sunset,  $\alpha'$  is the recombination coefficient, equal to  $(3-10) \cdot 10^{-8}$  cm $^3$ /sec. A nocturnal ionization source should result in a slower decrease of  $n_e(\tau)$ .

Let us now consider the results of observations. In /247/ it is shown that sunset corresponds to  $z_0 = 92-95^\circ$  at  $h = 120-160$  km and to  $z_0 = 90-93^\circ$  at  $h = 110$  km.

Figure 47 plots the variation of  $\log n_e$  for the  $E$  region and for the "dip" at 125–160 km as a function of  $\tau$ . The theoretical curves supplementing the experimental data give the decrease of  $n_e$  according to (IV.7) for three values of  $\alpha'$  and two assumed values of  $n_{e0}$  (solid and dashed lines). The different values of  $n_{e0}$  have an insignificant effect on the  $n_e(\tau)$  curves 1–2 hours after sunset, so that the nighttime concentration  $n_e$  without a nocturnal ionization source may be used to determine  $\alpha'$ .

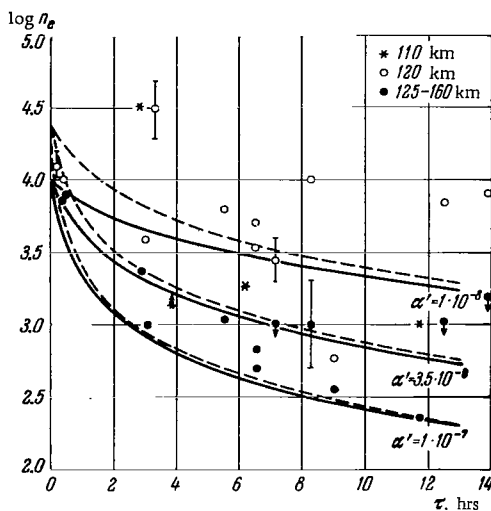


FIGURE 47. Nocturnal variation of the electron concentration at 110 km, 120 km, and 125–160 km according to rocket measurements /247/. The curves plot the theoretical decrease of  $n_e$  according to (IV.7) for different  $\alpha'$  and two values of  $n_{e0}$ , equal to  $1 \cdot 10^4 \text{ cm}^{-3}$  (solid curves) and  $2.5 \cdot 10^4 \text{ cm}^{-3}$  (dashed curves).

All the points at 125–160 km fall between the theoretical curves with  $\alpha'$  equal to  $3.5 \cdot 10^{-8}$  and  $1 \cdot 10^{-7} \text{ cm}^3/\text{sec}$ , in close fit with the photochemical value of  $\alpha'$  (see section 21). It thus follows that the effect of the nocturnal ionization source on  $n_e$  in the "dip" is insignificant. At the same time, the value of  $n_e$  in the  $E$  region is generally a factor of 10–30 higher than in the "dip". The high value of  $n_e$  in the nocturnal  $E$  layer is evidently associated with a nocturnal ionization source /247, 802/.

In the  $E$  layer, the excess concentration  $\Delta n_e$  compared with the theoretical curve is found to depend on the solar and geomagnetic activity: in epochs of high activity it is a factor of 3–4 higher than in epochs of low activity. The nocturnal ionization source in the  $E$  layer is thus at least one order of magnitude stronger in epochs of high activity.

**The altitude of the base of the  $E$  region.** In the lower part of the  $E$  region,  $n_e$  rapidly decreases with decreasing altitude. The region of the steep gradient at altitudes of 100–110 km is often sharply distinguished from the main part of the  $E$  region, where  $n_e$  increases very gradually or even remains constant. Let  $h_0 E$  be the altitude at which the  $n_e(h)$  profile develops the kink. In certain cases, this altitude can be determined to within 1–2 km /247/.

The altitude  $h_0 E$  was found to be independent of time of day and of the solar activity cycle. Yet it is correlated with the geomagnetic activity index  $K_p$  and undergoes semiannual variations. In winter and summer it drops approximately from 104 to 100 km as  $K_p$  varies from 0 to 5–6. In spring and in autumn,  $h_0 E$  is 3–5 km higher than in summer and winter.

The semiannual variations in  $h_0 E$  are apparently associated with the existence of a semiannual wave in the intensity of the mixing processes at  $h \approx 100 \text{ km}$ , which are relatively stronger in spring and in autumn. The decrease

of  $h_oE$  with increasing geomagnetic activity, like the growth of the electron concentration in the  $D$  region and at the altitude of 100–110 km discussed above, are apparently all due to corpuscular ionization.

**The altitude of the  $F$  region.** In rocket experiments, the altitude  $h^{\max}F$  is determined with high accuracy, generally to within 2–5 km. Note that the altitude  $h^{\max}F$  from ionograms is determined to within 20–50 km. Figure 48, borrowed from /247/ and supplemented with fresh data from section 15, plots the altitude  $h^{\max}F$  as a function of the local time. The altitude is seen to vary with the season and the solar activity level, as well as the time of day.

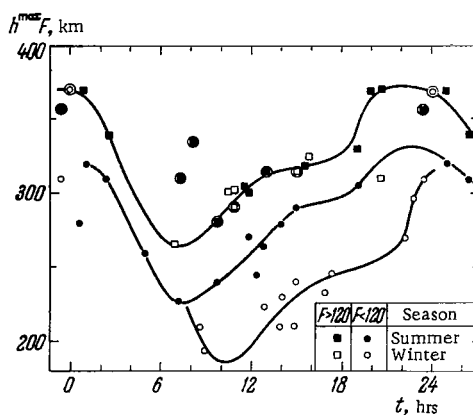


FIGURE 48. The altitude of the  $F$  region maximum during the day for various solar activity levels and various seasons (summer, March–September, and winter, October–February) from rocket measurements.

The experimental points corresponding to the same activity level are joined by winter and summer curves. Data relating to high geomagnetic activity ( $K_p \geq 4$ ) are encircled.

At night, the altitude of the  $F$  region is higher than in daytime. On passing from minimum to maximum solar activity,  $h^{\max}F$  at night increases from 310–320 km to 350–370 km. A deep minimum in  $h^{\max}F$  is observed at sunrise; in winter this minimum appears at later hours than in summer. After the morning minimum,  $h^{\max}F$  gradually increases during the day, and after sunset it rapidly grows to its nocturnal value. In mornings with strong geomagnetic disturbances, as we see from Figure 48,  $h^{\max}F$  markedly increases. A similar pattern is observed at nighttime in middle latitudes. The diurnal variations of  $h^{\max}F$  are sometimes detectable in ground soundings /234/, although the exact altitudes are not as accurate.

Distinct seasonal changes are observed in daytime. In epochs of low solar activity in summer and spring,  $h^{\max}F$  is markedly higher than in winter. The minimum altitudes  $h^{\max}F_2 \approx 200$  km are, therefore, observed on winter mornings in epochs of low solar activity; in epochs of high solar activity, the daytime  $h^{\max}F_2$  reaches 320 km. The changeover from summer to winter altitudes is very abrupt, occurring at the equinoxes. The diurnal variation of  $h^{\max}F_2$  may be interpreted in terms of a new theory, and the dependence of

$h^{\max}F$  on time of year and solar activity may be related to variations in the parameters of the neutral atmosphere (see section 28).

## Measurements of the ion composition

A qualitatively new contribution to ionospheric research was made by rocket-borne mass spectrometers. Successful mass-spectrometry from rockets provided reliable information about the ion composition, conclusively verified the basic facts relating to the photochemistry of the ionosphere, and identified the elementary processes which determine the behavior of the ionosphere.

A complete resumé of the rocket experiments which have been carried out so far with the purpose of determining the ion composition of the ionosphere, is given in Table 23 ( $h \approx 120-200$  km) and Table 24 ( $h < 100-110$  km).

TABLE 23. Rocket measurements of the ion composition at altitudes of 120–200 km

Date	Local time	$z_{\odot}$	$F_{10.7} \cdot 10^{-22}$ , W/m <sup>2</sup> Hz	Reference
20.XI.1956	23 hrs 21 min	140	210	Johnson et al. /248/
9.IX.1957	evening	96	233	Istomin /249, 250/
21.II.1958	20 hrs 02 min	114.5	170	Johnson et al. /248, 251/
23.III.1958	12 hrs 07 min	58.5	270	Johnson et al. /248/
2.VIII.1958	morning	54.5	250	Istomin /250/
13.VIII.1958	morning	~90	230	Istomin /250/
22.VII.1959	morning	~90	178	Istomin /252/
29.IV.1960	10 hrs 47 min	27.5	140	Taylor and Brinton /253/
15.VI.1960	morning	75	166	Istomin /252/
15.XI.1960	11 hrs 41 min	56.5	175	Taylor and Brinton /253/
15.XI.1961	16 hrs 00 min	70	100	Pokhunkov /254/
15.II.1963	09 hrs 36 min	57.5	70	Holms et al. /255, 341/
1.VIII.1963	01 hr 06 min	127	87	Holms et al. /255/
17.I.1964	00 hr 01 min	162	72	Hoffman /256/
26.I.1966	18 hrs 29 min	103	85	Young et al. /257/
8.VIII.1967	05 hrs 57 min	84	136	Young et al. /257/
11.VIII.1967	23 hrs 30 min	133	135	Young et al. /257/

First experiments dealing with the ion composition of the upper atmosphere were carried out in the USA by Johnson and co-workers /248/ and in the USSR by Istomin /249/. The measurements employed Bennett's rf mass spectrometer /258/ which, with some modifications, has been used since in all the determinations of the ion composition at altitudes of 100–200 km (Figure 49). The results of three series of high-latitude experiments (Churchill,  $\varphi = 59^{\circ}$  N) were published in /248, 251/; these data provide information about the ion composition of the polar atmosphere. An extensive series of experiments in middle latitudes were carried out by Istomin in 1957–1960 /249, 250, 252/. Measurements with Sputnik III at altitudes above 200 km also made a significant contribution to our knowledge of the ion composition of the ionosphere /260, 261/. The most remarkable and unexpected fact was the discovery of molecular ions in large quantities at these altitudes, including ions of nitrogen

TABLE 24. Rocket measurements of the ion composition at altitudes of  $h < 100$ —110 km

Date	Time	Altitude, km	Reference
8.VII.1955	01 hr 39 min	93—115	Johnson et al. /259/
20.XI.1956	23 hrs 21 min	$\geq 105$	Johnson et al. /248, 259/
21.II.1958	20 hrs 02 min	$\geq 90$	Johnson et al. /248, 259/
23.III.1958	12 hrs 03 min	$\geq 90$	Johnson et al. /248, 259/
3.V.1962	13 hrs 30 min	87—114	Pharo et al. /265/
31.X.1963	$z_{\odot} = 44^{\circ}$	64—112	Narcisi /268/
6.III.1965	Polar aurora	64—192	Narcisi /268/
16.XI.1965	12 hrs 22 min	70—113	Narcisi et al. /264, 268/
17.XI.1965	23 hrs 20 min	75—107	Narcisi et al. /267, 268/
5.XI.1966	$z_{\odot} = 20^{\circ}$	70—106.5	Narcisi et al. /753/
12.XI.1966	11 hrs 54 min (80% solar eclipse)	73—107	Narcisi et al. /753/
12.XI.1966	12 hrs 08 min (total eclipse)	71—95	Narcisi et al. /753/
12.IV.1967	$z_{\odot} = 88.5^{\circ}$ ; evening	75—100	Narcisi et al. /752/
12.IV.1967	$z_{\odot} = 98.6^{\circ}$ ; evening	75—100	Narcisi et al. /752/
18.IV.1967	$z_{\odot} = 102.5^{\circ}$ ; morning	75—100	Narcisi et al. /752/
18.IV.1967	$z_{\odot} = 90^{\circ}$ ; morning	75—100	Narcisi et al. /752/
4.XII.1967	16 hrs 20 min	65—147	Narcisi et al. /751/
4.XII.1967	$z_{\odot} = 99^{\circ}$	70—120	Narcisi et al. /751/
6.XII.1967	12 hrs 05 min	Up to 132	

Local time is used

oxide which occurs in negligible amounts in the neutral atmosphere. According to mass spectrometric measurements, the main ions at 100—200 km are  $\text{NO}^+$ ,  $\text{O}_2^+$ , and  $\text{O}^+$ . The relative content of atomic oxygen ions increases with altitude, whereas that of the molecular ions decreases.

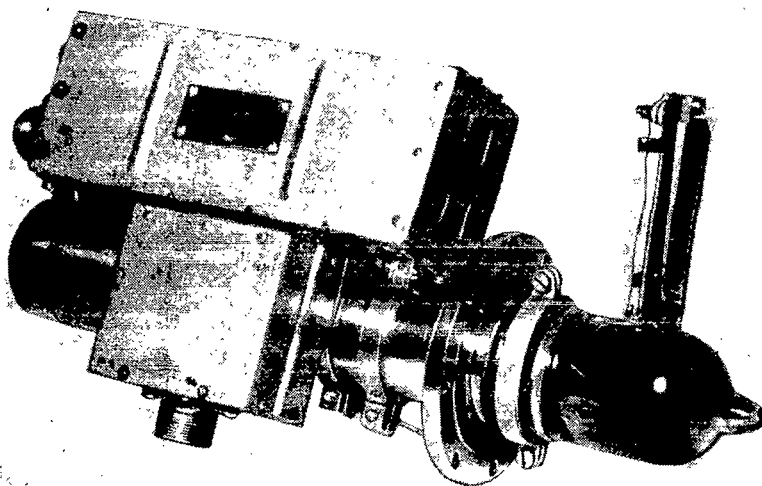


FIGURE 49. The MX-6405 mass spectrometer used on Elektron satellites /285/.

We see from Table 23 that mass spectrometric measurements of the ion composition on rockets at altitudes  $h \geq 120$  km were performed for widely varying conditions of solar activity and different zenith distances of the Sun  $z_0$ . The data thus permit drawing certain conclusions about the variations of the ion composition during the day and during a single solar activity cycle. A discussion of the ion composition variation in daytime at altitudes of 120–200 km will be given in Chapter VI, where a theoretical interpretation of the various observed effects is advanced.

Let us now consider the diurnal variations. The change in the ion composition between day and night depends on the solar activity level. For example, in epochs of maximum solar activity, the fraction of atomic ions at night, at altitudes of 160–200 km, is virtually the same as in daytime, whereas in epochs of low solar activity it markedly diminishes.

The diurnal variation of the molecular ions  $\text{NO}^+$  and  $\text{O}_2^+$  is quite characteristic. Because of their close masses, the relative concentration is determined with fairly high accuracy. In daytime above 120–140 km, the variations in  $\text{NO}^+$  and  $\text{O}_2^+$  follow parallel curves, but the concentration of the  $\text{NO}^+$  ions is a factor of 2–3 higher than the concentration of the  $\text{O}_2^+$  ions, in accordance with the photochemical theory /266/. However, at 90–120 km, the proportion of the  $\text{NO}^+$  ions in daytime decreases, whereas at still lower altitudes it again increases.

At night, in epochs of low solar activity,  $[\text{O}_2^+] > [\text{NO}^+]$  above the 180–200 km level (where the atomic ions  $\text{O}^+$  begin to predominate), contrary to daytime conditions, whereas below  $h \approx 150$  km (down to 90–95 km) the concentration of  $\text{NO}^+$  ions is more than one order of magnitude higher than the concentration of  $\text{O}_2^+$ . It is thus clear that the photochemistry of the night ionosphere is significantly different from the photochemistry of the daytime ionosphere, and the lower ionosphere at altitudes of 100–150 km is different from the upper ionosphere.

Let us consider the sporadic  $E_s$  layer. Measurements of the ion composition in the sporadic layer were first carried out by Istomin /262, 263/ on 15 June 1960 in the morning hours. The  $E_s$  layer, observed between 103 and 105 km, was unusual compared to the surrounding ionosphere in that it contained a high concentration (up to about 20%) of metal ions  $\text{Mg}^+$ ,  $\text{Ca}^+$ ,  $\text{Fe}^+$ , and of the ion  $\text{Si}^{+*}$  /263/. Later Young et al. /257/ also detected  $\text{Na}^+$  in the  $E_s$  layer, and quite recently the ion  $\text{S}^+$  was observed. The concentration of the atmospheric ions, e.g.,  $\text{NO}^+$ , in the  $E_s$  layer at 106 km altitude was vanishingly small, although the ion  $\text{NO}^+$  actually predominates in the ionosphere at distances of about 1 km above and below the  $E_s$  layer. A similar predominance of metal ions in the  $E_s$  layer at 89 km altitude on the night of 17 November 1965 was recorded by Narcisi et al. /264/, and at altitudes of 113 and 93 km in daytime on 3 May 1962 by Smith et al. /265, 266/. Daytime rocket measurements on 16 November 1965 detected in the sporadic  $E_s$  layer, at 110 km altitude, the two silicon ions  $\text{Si}^+$ ,  $\text{SiO}^+$ , and an unidentified ion of mass  $48^+$ , as well as the metal ions /267/. The photochemistry of the narrow  $E_s$  layers thus seems to differ from the photochemistry of the ordinary ionosphere.

Several mass-spectrometric measurements have been carried out in the  $D$  region. The various experiments listed in Table 24 indicate that the

\* In a previous similar case, in the presence of an  $E_s$  layer, the ion  $\text{Si}^{+*}$  of mass  $28^+$  was erroneously associated with  $\text{N}_2^+$  /259/.



"ordinary" ionospheric ions  $\text{NO}^+$  and  $\text{O}_2^+$  appear only at altitudes above 80--87 km in daytime and above 90--95 km at night. Below 79 km in daytime and below 86 km at night, complex ions of the form  $\text{H}^+(\text{H}_2\text{O})_n$  with masses  $37^+(\text{H}_5\text{O}_2^+)$ ,  $19^+(\text{H}_3\text{O}^+)$ , and  $>48^+$  predominate. At higher altitudes, these ions rapidly disappear. Thus, below  $h \approx 80$  km, there is a region with a highly specific composition of positive ions.

We have mentioned before that negative ions also play an important role in the *D* region. Their mass composition, however, was investigated only once by Johnson et al. /248, 259/ in a daytime experiment on 29 November 1955. At all altitudes between 93 and 131 km, ions with masses  $46^- (\text{NO}_2^-)$ ,  $32^- (\text{O}_2^-)$ ,  $22^- (?)$ , and  $16^- (\text{O}^-)$  were discovered. The ions of mass  $46^-$  predominated. This result, obtained in the early days of ionospheric mass spectrometry, remained uncorroborated for a long time and it is only recently, in a rocket launch on 4 December 1967, again in Churchill,\* that the ions  $16^-$  and  $46^-$  were detected at the sensitivity threshold between 70 and 120 km, whereas in the *E* region the ions  $35^-$  and  $37^-$  were detected as well. Another report\*\* of a European experiment (10 March 1966, during a polar aurora) describes the detection of the ion  $46^-$  at 88 km altitude at nighttime (high ion concentrations were observed  $n_i^- \approx n_i^+ \approx 10^5 \text{ cm}^{-3}$  and  $n_e \ll n_i^+$ ). The presence of the ions  $\text{O}_2^-$  and  $\text{O}^-$  is not surprising, but the observed predominance of ions  $46^- (\text{NO}_2^- \text{ or } \text{O}_3^-)$  necessitated the development of a new theory to account for the formation of negative ions in the lower part of the *D* region.

## 16. Investigation of the upper ionosphere

The part of the ionosphere directly above the maximum of the *F* region will be called the upper ionosphere in this context. This part of the ionosphere was inaccessible to ground sounding stations, since it lies above the main electron concentration maximum. The first measurements of  $n_e$  in this region up to 470 km were carried out by a Soviet geophysical rocket on 21 February 1958 (Gringauz /269/). Later a number of further successful rocket experiments were performed. Systematic measurements in the ionosphere above the *F* region were begun only recently, with the launching of satellites equipped with probes and ionospheric stations. A large contribution was made by observations by the method of noncoherent backscattering. We will now consider the various results obtained by these new methods which helped to solve a number of radical problems in the physics and photochemistry of the ionosphere below the *F*-layer maximum and opened an entirely new world above the *F* layer.

### Rocket measurements

The first three rocket-borne experiments undertaken by Gringauz and Rudakov /270/ showed that above the *F*-region maximum the electron concentration monotonically decreases with altitude and does not show any further maxima. The gradient  $dn_e/dh$  was found to be relatively small; the

\* USA national report at the COSPAR Symposium, Tokyo 1968.

\*\* ESRO report, same symposium.

corresponding scale height was

$$H_e = \left( -\frac{d \ln n_e}{dh} \right)^{-1} = 100 - 200 \text{ km}, \quad (\text{IV.8})$$

which is equivalent to temperatures of 800–1700°K.

Comparison of different rocket experiments /271, 272/ shows that immediately above the *F*-region maximum the gradient  $dn_e/dh$  is generally smaller in the evening than in the morning and at night (Figure 50). Detailed analysis of rocket data showed /273/ that the gradient  $d \log n_e / dh$  varies with height, i.e., the scale height is also variable. This may be due either to changes in the temperature or to changes in the composition of the ionosphere with altitude.

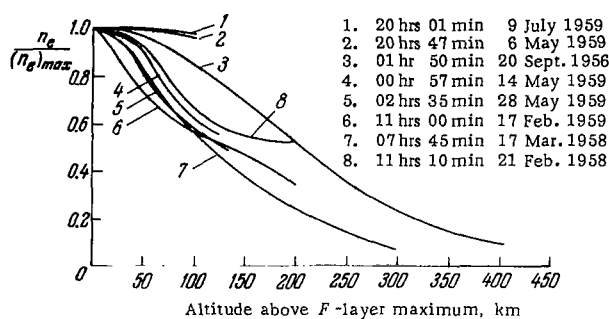


FIGURE 50. Vertical distribution of the electron concentration above the *F*-region maximum from rocket data /272/.

The gradient  $dn_e/dh$  for evening measurements (curves 1, 2) is minimal.

The first rocket experiments were carried out during the IGY in an epoch of high solar activity. Measurements in the epoch of low solar activity in 1963–1965 showed that the decrease of the electron concentration, above the *F*-region maximum, becomes more pronounced /274/ as the temperature of the ionosphere decreases.

## Satellite measurements

Satellites proved a highly convenient tool for measurements in the upper ionosphere. Several satellites were specifically designed for upper ionosphere research.

The first Soviet satellites with radio transmitters in the payload measured the variation of the total number of electrons  $N$  in the column of the ionosphere from the satellite to the ground. These measurements were carried out by a method which measured the Faraday rotation of the plane of polarization of the radio wave transmitted by the satellite. Numerous data were obtained which helped to elucidate the seasonal and the diurnal variations in the content of charged particles in the entire ionosphere.

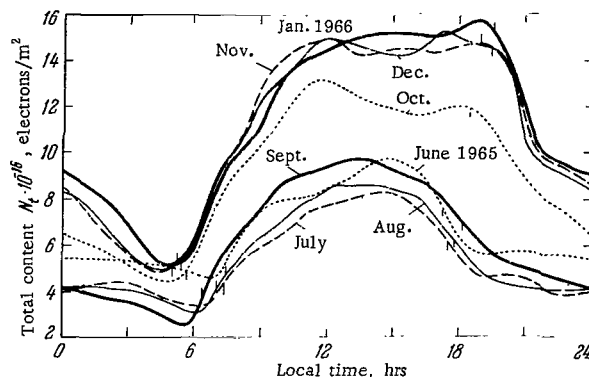


FIGURE 51. Diurnal variation of the monthly average values of the total electron content in the ionosphere at 34°S and 176°E from measurements of the Syncom 3 geostationary satellite /275/.

Vertical bars mark sunrise and sunset.

The geostationary satellite Syncom 3 (with an orbital period close to 24 hrs) made continuous observations in a fixed direction and measured variations in  $N$  with an accuracy of up to 0.1% /275/. The regular diurnal and seasonal variations which emerged from these measurements are shown in Figure 51. In summer and in winter, the diurnal variations of  $N$  follow similar curves in different months. The transition from winter to summer is fairly abrupt, taking place in 25 days following 27 September. This points to a rapid rearrangement in the structure of the upper atmosphere and to its instability during the equinoctial period. At the geomagnetic latitude of about 35°S, the average diurnal variations in  $N$  are 2.5:1 in winter and 3:1 in summer. Irregular variations of up to 10% in  $N$  are also observed, in times ranging from 1 min to a few hours. At night  $N$  both decreases and increases in the ionosphere /276/. The increase is due to the effect of the electron stream from the exosphere.

Satellites equipped with traps, probes, and mass spectrometers provided information about the global distribution of the local characteristics ( $n_e$ ,  $T_e$ ,  $T_i$  and the ion composition) in the upper atmosphere at fixed altitudes (the results of temperature measurements will be considered in the next section, together with the data of ground observations). Satellites in circular orbit, i. e., satellites with a constant flight altitude, are the most suitable for this purpose, since the measurements obtained in eccentric orbits are influenced by the combined effects of latitude, longitude, and altitude, which are difficult to separate.

The first measurements of the ion composition were carried out in 1958 by Istomin with Sputnik III at altitudes from 225 to 1000 km /260, 261/. The upper ionosphere was found to consist mainly of  $O^+$  ions. The concentration of molecular ions above  $h \approx 200$  km markedly decreases with altitude and above  $h \approx 500$  km it is less than  $10^{-3} n_e$ . The fraction of the lighter  $N^+$  ions naturally increases with altitude. It is remarkable that at altitudes  $h \approx \approx 350$  km the fraction of molecular ions increases by a certain factor at higher latitudes.

A similar phenomenon of the fraction of the heavier ions increasing toward the auroral latitudes was later observed by other satellites. For example, trap measurements at  $h \approx 350$  km on a satellite moving along the terminator (the line of separation between night and day on Earth) showed that the fraction of molecular ions  $M^+/n_e$  at auroral latitudes was quite high, reaching about 0.04 /277/. This figure was substantially higher than at middle latitudes. At the geomagnetic equator, conversely, there was a sharp dip in the concentration of molecular ions at  $h \approx 230$  km.

A number of measurements were also carried out at altitudes  $h \approx 1000$  km. The growth of  $[O^+]/n_e$  toward the poles in daytime was detected by the Ariel satellite /278/. The data of Alouette-1 /279, 280/ indicate that at latitudes of  $30-40^\circ$  the  $H^+$  ions account approximately for 50% of the total, whereas in the polar regions  $O^+$  predominate. This trend is also evident from the increase of the average molecular weight of the ions from 8 to 16 /281/. This conclusion was recently confirmed by direct mass spectrometric measurements on Explorer-31 /282/. The growth of the relative concentration of the heavy ions in auroral latitudes is apparently associated with the increase in temperature in the auroral zone. (According to the measurements of Ariel /283/ and Alouette-1 /279, 281/,  $T_e$  and  $T_i$  at high latitudes are double the corresponding values at middle latitudes.) The day-to-night temperature changes also lead to diurnal variations of the ion composition in the upper atmosphere. Let us consider these data in more detail.

The ion composition of the upper atmosphere is generally characterized by the altitude  $h^*$  at which the region with predominance of  $O^+$  ions gives way to the region with the predominance of  $H^+$  ions. In epochs of low solar activity, at middle latitudes  $h^* \approx 1200$  km in daytime and  $h^* \approx 650$  km at night. As we have mentioned before,  $h^*$  at auroral latitudes is over 1000 km, i.e., it is a few hundred kilometers higher than at middle latitudes. The altitude  $h^*$  is roughly characterized by the condition  $[O^+] = [H^+] \approx 10^4 \text{ cm}^{-3}$  /284/. The data obtained with the Elektron-2 satellite /285/ show that the diurnal variation of the relative concentrations  $[O^+]/n_e$  and  $[H^+]/n_e$  is offset relative to midday: the maximum of  $[O^+]/n_e$  and the minimum of  $[H^+]/n_e$  are observed at 14–16 hrs local time.

Satellites of the Alouette series proved the most suitable for ionospheric research. The payload includes an ionospheric station for high-altitude sounding. Most of the experimental material has been processed by now and the variations of  $n_e(h)$  have been established.

A typical curve showing the variation of  $n_e$  in the upper ionosphere during 24 hrs at two latitudes in different seasons in 1962–1963 is shown in Figure 52, which is based on the data of Alouette-1 /286/. The midday offset of the  $n_e$  curves is synchronous at all altitudes. A secondary (nocturnal) maximum is also observed, which at longitudes of  $90-120^\circ\text{E}$  appears only at middle geomagnetic latitudes in the Southern Hemisphere. At other longitudes, a secondary maximum is sometimes observed at equatorial latitudes also, where it may occur at different times of the day.

A remarkable result of the satellite research of the upper ionosphere /287–292, 293–298/ was the discovery of a fairly narrow region of low concentrations  $n_e$  (not exceeding  $10^3 \text{ cm}^{-3}$  even in the maximum of the  $F$  region), which extends along the auroral zone, where  $n_e$  is relatively high. For this region,  $L = 3.5-4$ .<sup>\*</sup> The region extends over  $3-5^\circ$  in latitude, so

<sup>\*</sup> The parameter  $L$  is equal to the distance from the Earth's center to a given line of force in the equatorial plane.  $L$  is expressed in units of the Earth's radius.

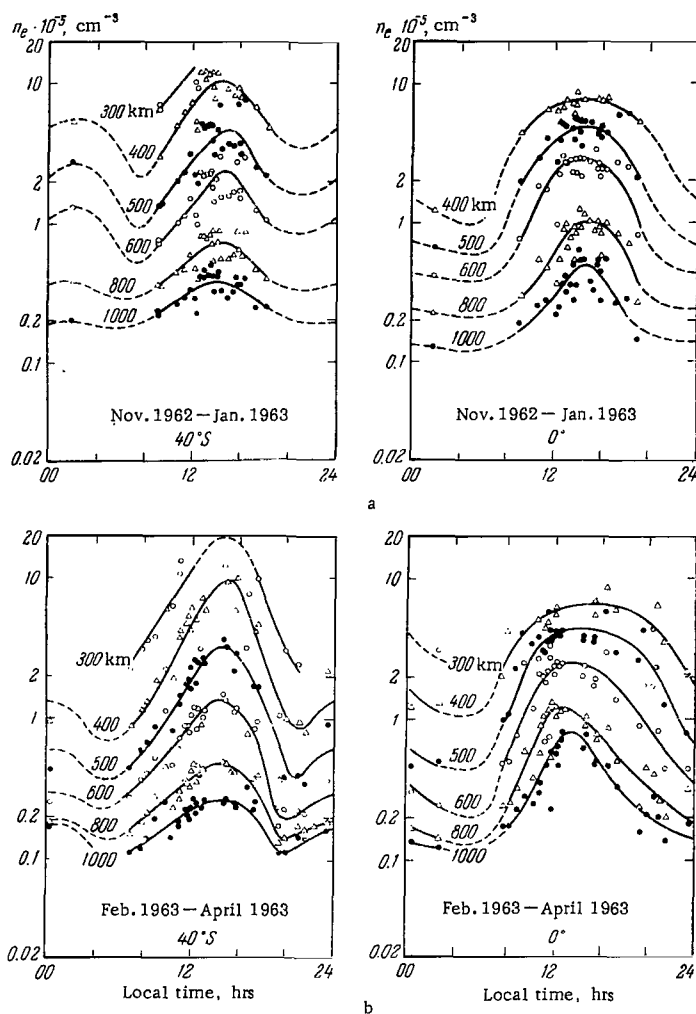


FIGURE 52. Diurnal variations of the electron concentration at fixed altitudes from the data of Alouette-1 /286/ for locations with magnetic declination of  $0^\circ$  and  $40^\circ\text{S}$ .

that high latitudinal gradients are observed,  $dn_e/dx \approx 3.7 \cdot 10^3 \text{ cm}^{-3}/\text{km}$  /296/ or 6% per km /299/. The growth of  $n_e$  in the auroral zone, which is accompanied by a marked increase in the intensity of the corpuscular streams, is naturally associated by Sharp et al. /297/ with these streams. Several hypotheses have been advanced to account for the existence of the low- $n_e$  region, but no satisfactory explanation is available.

A detailed analysis of the latitudinal variations in the upper atmosphere revealed the existence of three zones; auroral, middle-latitude, and equatorial /300, 301/. The auroral zone is distinguished from the middle-latitude zone by its higher variability and complex irregular structure. Sharp variations in  $n_e$  (by up to a factor of 2) are observed over distances of a few

kilometers. We have previously mentioned the increased values of  $n_e$ ,  $M^+/n_e$ , and  $T_e$  in this region.

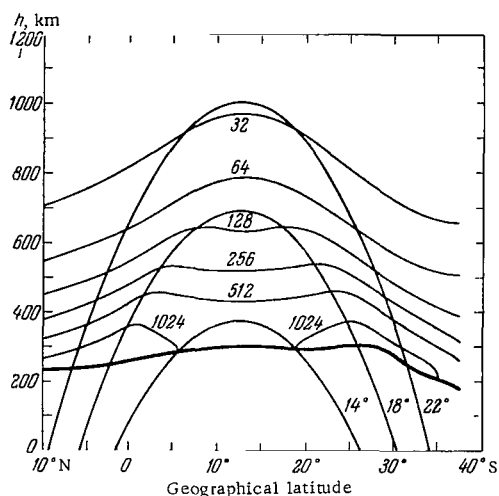


FIGURE 53. The equatorial anomaly in the latitudinal distribution of levels with different electron concentrations (indicated against the curves in units of  $10^3 \text{ cm}^{-3}$ ) / 303/.

The thick curve marks the position of the F-region maximum.  
The arched curves mark the position of the magnetic lines of force for three magnetic declinations, 14°, 18°, and 22°.

In the equatorial zone, the electron concentration of the upper ionosphere above the geomagnetic equator has a daytime maximum, whereas  $T_e$  has a minimum. The isoelectron profiles ascend toward the equator (Figure 53), but inside the magnetic line "supported" by 18° latitude,  $n_e$  remains virtually constant. At night, the electron concentration in the equatorial region shows two maxima, corresponding to geomagnetic latitude of  $\pm 15^\circ$ . At sunrise, the two maxima start moving apart to higher latitudes and rapidly disappear, while a new maximum is formed at the equator /302/. Satellite measurements established the variations in the equatorial ionosphere and linked up into a single picture the various facets of the so-called equatorial anomaly. So far, however, this interesting phenomenon remains without a proper physical explanation.

### The method of noncoherent backscattering

The method uses the radar principle. The ionosphere, like any ionized medium, scatters incident electromagnetic radiation in all directions. The intensity of the scattered radiation is proportional to the concentration of charged particles. When a short powerful radio pulse is sent to the atmosphere, a weak scattered signal comes back in the form of a pulse whose duration is a function of the distance from the scattering point. A high-speed computer analyzes the intensity of the scattered signal for each altitude, introduces corrections for distance and other distorting effects, and reconstructs the  $n_e(h)$  profile up to  $h \approx 1000 \text{ km}$  and higher. The spectrum and the

polarization of the scattered signal are generally also measured. Careful analysis of these quantities gives  $T_e$ ,  $T_i$ , and the ion composition. The accuracy of the measurements is limited by the signal-to-noise ratio. Therefore, to ensure best results, pulses of a few megawatt are used, with antennas of up to a few hundred meters. Table 25 lists some of the operating radar stations. The main results were obtained at Millstone Hill, Arecibo, and Gicamarca /304, 305, and others/ at geomagnetic latitudes of 55°N, 30°N, and 0°. The principal advantage of the new method is that it continuously yields the  $n_e(h)$  profile above a given locality during an extended period of time.

TABLE 25. Radar stations for noncoherent scattering

Station	Frequency, MHz	Peak power, MW	Antenna
Prince Albert (Canada)	435	2	Ø 25 m
Millstone Hill (Boston)	440	3	Ø 70 m
	1294	5	Ø 25 m
Arecibo (Puerto Rico)	430 and 40	2	Ø 300 m
Gicamarca (Peru, near Lima)	50	5	$8.4 \cdot 10^4 \text{ m}^2$
Nancy (France)	935	—	$40 \times 200 \text{ m}^2$
Palo Alto (California)	400	0.5	Ø 30 m
Malvern (England)	400	10	Ø 42 m

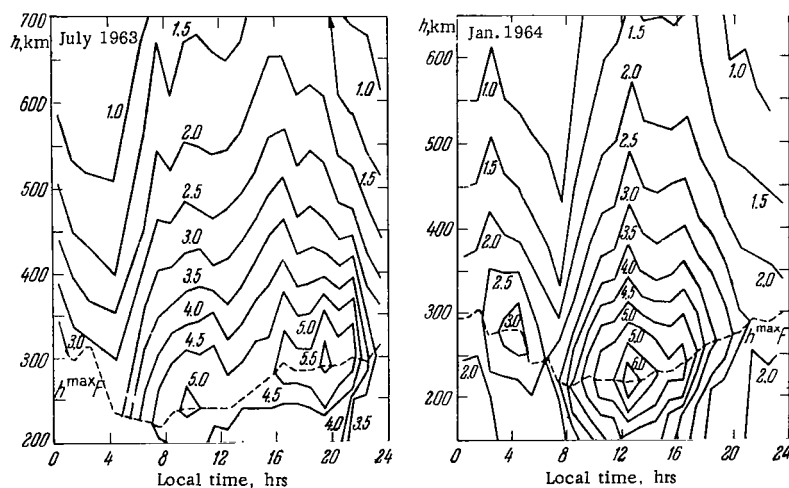


FIGURE 54. Daytime variation of the isoelectron levels from observations at Millstone Hill by the method of noncoherent back scattering /305/.

The figures against the curves are the critical frequencies in MHz. The dashed curves identify the position of the F-layer maximum.

Figures 54 and 55 show some typical curves of the variation of the electron concentration in winter and in summer. A characteristic feature of the diurnal variation of the ionosphere is the abrupt transition to a daytime

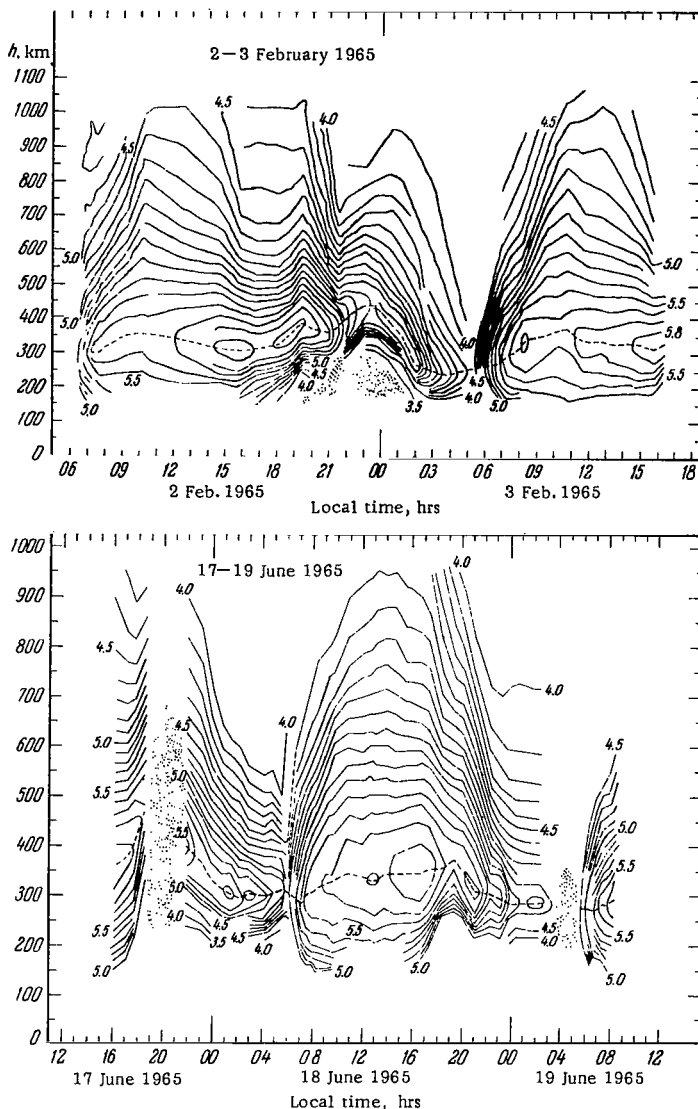


FIGURE 55. Daytime variation of the isoelectron levels from observations at Gicamarca by the method of noncoherent back scattering /305/.

The figures against the curves are  $\log n_e$ . The dashed curves identify the position of the  $F$ -layer maximum, the dots represent the scattered  $F$ -reflections.

ionosphere soon after sunrise, relatively smooth variations of  $n_e$  during the day and in the evening, and a predawn minimum in  $n_e$ . The altitude of the  $F$ -layer maximum also smoothly increases from a morning minimum to a night maximum. The seasonal effect in the equatorial atmosphere is not very pronounced. The  $n_e(h)$  profiles are sometimes seen to change abruptly



above the  $F$ -layer maximum, as on 18 June 1965 at 1700–1900 hrs or 2 February 1965 at 2000–2300 hrs (Figure 55). These changes are apparently associated with short-lived vertical motions or ion drift effects at the particular time of day. Generally, the  $n_e(h)$  profiles change very slightly above the  $F$ -layer maximum, although in the lower ionosphere large day-to-day changes may be registered.

Unlike the equatorial ionosphere, the summer ionosphere at Millstone Hill (55°N) shows a certain offset relative to midday (Figure 54, July 1963). The growth of  $n_e$  during the summer sunsets is associated with downward drift of charged particles as a result of marked changes in  $T_e$ . The offset daily curve of  $n_e$  in the upper atmosphere also clearly emerges from the data on  $N$  (Figure 51) and from satellite measurements (Figure 52). It constitutes one of the characteristic but, as we see, not permanent features of the behavior of the ionosphere. Since the offset is observed only at certain periods, it cannot be attributed to such a general property of the ionosphere as the time lag due to the finite recombination time. It is probably caused by changes in the parameters of the neutral atmosphere or by motions.

In the preceding section we indicated that the relative concentration of the heavy ions at a given altitude increases in daytime and at higher latitudes this result was obtained from satellite measurements. The method of non-coherent scattering provides detailed information about the vertical distribution of the concentration of various ions above a given locality. Detailed concentration charts of  $O^+$ ,  $H^+$ , and  $He^+$  in the upper atmosphere were obtained for various altitudes and different times of day /305–308/. The results confirm the earlier finding that in epochs of low solar activity the equality  $[O^+] = [H^+]$  is observed in daytime at altitudes of 900–1200 km and at night at  $h^* \approx 600$  km. The  $He^+$  ions at all altitudes are a small impurity. The maximum concentration of  $He^+$ , up to 20–30%, is observed at  $h \approx 1000$  km in daytime and at altitudes of 400–500 km at night, i. e., it is close to the level where  $[O^+] = [H^+]$ .

Similar results were recently obtained in direct mass-spectrometric measurements during a nocturnal rocket launch on 17 January 1964 /256/. The maximum concentration of helium ions reached 15% at an altitude of 350 km, whereas the equality  $[H^+] = [O^+]$  was observed at  $h \approx 450$  km. Differences in the vertical distribution of the concentrations of various ions are mainly determined by differences in temperature. In particular, the altitude at which the region with predominance of heavy ions gives way to the region with predominance of light ions increases with the increase in temperature /309/.

## Ion and electron temperature

Rocket and satellite research and measurements by the method of non-coherent scattering provided definite conclusions concerning the variation of  $T_e$  and  $T_i$  with altitude and latitude and their dependence on time of day and solar activity /310/. We will now briefly describe the principal results of this research.

The nighttime ion temperature  $T_i$  is approximately 700°K at 200–300 km, slightly increasing with altitude. In daytime, at 200–500 km,  $T_i$  increases to 1000°K and rapidly grows with altitude (with a gradient of about 2 deg/km),

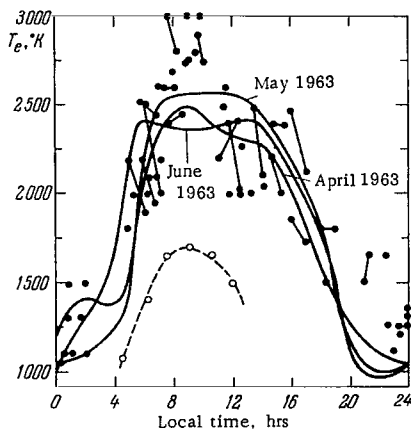


FIGURE 56. Variation of the electron temperature of the upper ionosphere from the data of Explorer-17 (solid curves) and Ariel-1 (dashed curve), and from noncoherent backscattering data (dark circles) /310/.

Evans in Millstone Hill observations /311/. In the  $F$  region, the daytime  $T_e$  is a factor of 2–3 higher than  $T_i$ . At high altitudes, in the magnetosphere,  $T_i$  approaches  $T_e$ , but at altitudes of 200–400 km the difference between  $T_e$  and  $T_i$  is maximal. The peak value of the temperature ratio  $T_e/T_i = 4–5$  is observed approximately 2 hours after sunrise. At night,  $T_e$  is approximately equal to  $T_i$ , although a small difference is, nevertheless, observed.

The diurnal variation of the electron temperature  $T_e$  in the upper ionosphere is shown in Figure 56. The growth of  $T_e$  generally begins before sunrise on the ground, for  $z_\odot = 99^\circ \pm 1^\circ$ , and reaches its maximum rate of about 30 deg/min during the equinoxes. In winter, the mean rate of growth of  $T_e$  is about 13 deg/min, and in summer about 20 deg/min. The daytime maximum of  $T_e$  at 300–400 km is observed at 16.00 local time /312/. This does not agree with the 14.00-hrs maximum obtained in some atmospheric models, but it is fully consistent with new satellite data regarding the time of the afternoon maximum of the neutral atmosphere temperature  $T_n$  (see Section 17). The afternoon maximum of  $T_i$  is also observed approximately at 16 hrs 30 min /313/. At this time, the ratio  $[O^+]/n_e$  is maximal and the ratio  $[H^+]/n_e$  is minimal, as we have noted before.

The vertical growth of the electron temperature is different at different latitudes, although in daytime, in epochs of low solar activity, the electron temperature at  $h \approx 200$  km is independent of latitude, remaining 1200°K. In Gicamarca, on the geomagnetic equator, the maximum electron temperature  $T_e = 2000–2500^\circ\text{K}$  is observed at  $h \approx 275$  km, whereas at Millstone Hill (55°N)  $T_e = 2500–3000^\circ\text{K}$  at 500–600 km. At higher altitudes,  $T_e$  diminishes in daytime. Conversely, at night, nearly constant temperatures are observed above  $h \approx 300$  km.

The observed features of the vertical and the diurnal variation in  $T_e$  and  $T_i$  were theoretically interpreted by Hanson /314/ and Dalgarno et al. /315/.

reaching some 2000°K at  $h \approx 1000$  km. Thus below  $h \approx 300$  km,  $T_i$  is approximately equal to the temperature of the neutral atmosphere both during the day and at night, whereas above this altitude the ion temperature is different. The changeover from the nocturnal  $T_i$  to the daytime temperature regime occurs within a very short time, about 2 hrs. The evening transition is more gradual. No seasonal variations were detected by any of the noncoherent scattering stations.

At nighttime, during magnetic disturbances, the ionic temperature  $T_i$  increases. The increase in  $T_i$  is approximately by 150–200°K as the geomagnetic activity index  $K_p$  increases by 1. The electron temperature increment  $\Delta T_e$  is double this figure.

The differences between the electron and the ion temperature were noted by

At altitudes above the  $F$  region, the positive difference between the electron temperature  $T_e$  and the temperature of the neutral gas  $T_n$  depends on the quantity of heat  $Q$  (eV/cm<sup>3</sup>sec) transmitted to the electron gas in unit time:

$$T_e - T_n = 2 \cdot 10^6 Q T_e^{3/2} / n_e^2. \quad (\text{IV.9})$$

The maximum difference between  $T_e$  and  $T_n$  should thus be observed in the region of maximum  $Q$  ( $h \approx 200$  km), and it should rapidly decrease at higher altitudes. When  $Q$  increases (e. g., during the day compared to nighttime conditions), the difference between  $T_e$  and  $T_n$  increases. The growth of  $T_i$  with altitude is similarly explained. Since the concentration of neutral particles decreases with altitude faster than the concentration of ions,  $T_i$  should theoretically vary from  $T_n$  at low altitudes to  $T_e$  at high altitudes. However,  $T_i \neq T_e$  even at very high altitudes. At first, this was interpreted as an indication of a local heat source or heat transfer from above /316–318/. Banks /319/ showed that ionic conductivity and the effect of  $H^+$  ions at high altitudes may account for this inequality.

Further developing Hanson's theory /314/, Dalgarno et al. /320/ found that in morning hours, when the short-wave solar radiation leads to intense ion production and heating of the electron gas (a rapid increase in  $Q$ ), while  $n_e$  is still low, the electron temperature should rapidly increase (to 8000°K) at altitudes  $h \approx 250$  km according to (IV.9). Observations at Arecibo indeed detected a winter outburst in  $T_e$ , but this phenomenon was observed before sunrise and only reached 3000°K /321/. A similar predawn increase in  $T_e$  was noted in Nancy /322/, also in winter. This effect is associated with the arrival of photoelectrons from the magnetically conjugate point /321, 323/ which is illuminated by the Sun at the time of the  $T_e$  outburst.

Arecibo observations /324/ show that the day-to-day variations of  $T_e$  and the gradient  $dT_e/dh$  are related to the variations in  $n_e$  at altitudes of 200–250 km; as  $n_e$  increases, both  $T_e$  and  $dT_e/dh$  decrease, and for very high electron concentrations  $n_e \geq 5 \cdot 10^5 \text{ cm}^{-3}$  a maximum in  $T_e$  is observed at  $h \approx 200$  km. Explorer-22 measurements /325/ also indicate that the latitudinal and diurnal variations in  $T_e$  follow an opposite trend to the variations in  $n_e$ . A negative correlation between the variations of  $T_e$  and  $n_e$  in the upper atmosphere is also observed during magnetic storms, depending on solar activity, and in other cases /326/. This naturally follows from relation (IV.9) which shows that the difference  $T_e - T_n$  is inversely proportional to  $n_e^2$ .

The temperatures  $T_e$  and  $T_i$  depend on the solar activity. At night, both temperatures increase by 3.4°K as the solar radio emission at 10.7 cm increases by  $1 \cdot 10^{-22} \text{ W/m}^2\text{Hz}$ . In daytime,  $T_i$  increases by 4.5°K /327/. The daytime variations in  $T_e$  are masked by the variations in  $n_e$ .

In summarizing our discussion of the ionospheric observations, it can be said that during the last 10–15 years the variety of data available on ionospheric parameters has consistently exceeded our understanding of the relevant physical processes in the ionosphere. This situation is the exact opposite of what had prevailed prior to the introduction of the new methods of research (rockets, satellites, noncoherent scattering). As in the early stages, when insufficient knowledge of the processes, which take place in the ionosphere, made it impossible to interpret most of the effects observed on ionograms (except the simplest effects), complete understanding of the behavior of the ionosphere requires detailed information about the spectrum of the short-wave

solar radiation and detailed treatment of the effect of such factors as atmospheric changes and the contribution of corpuscular sources of ionization. The last two topics are covered in the following two sections.

## 17. The structure of the upper atmosphere

The atmospheric layer extending below 100 km is known as the homosphere, i. e., the part of the atmosphere where the molecular weight is constant. It is made up of three main regions: the troposphere ( $\leq 10$  km), where the temperature diminishes with increasing altitude, the stratosphere and the stratopause (10–50 km), where the temperature is constant and then increases with altitude (the atmosphere is heated by those components of the UV solar radiation and the IR planetary radiation which are absorbed by ozone and carbon dioxide), and the mesosphere ( $\geq 50$  km), where the temperature again diminishes with altitude.

Above  $h \approx 105$  km, dissociation and diffusion processes alter the neutral composition of the atmosphere with altitude, so that the molecular weight decreases and the temperature increases up to 200–300 km.

The main topic in studies of the structure of the upper atmosphere is to determine the variation of the basic atmospheric parameters as a function of altitude and time. The basic physical parameters of the atmosphere are the density, the pressure, the temperature, and the composition. Decisive factors on which the variation of the atmospheric parameters depends are 1) time of observation (time of day, season, phase of the solar cycle), 2) locality (altitude, latitude), 3) ionizing and thermal agents (short-wave solar radiation, corpuscular streams), 4) physicochemical processes (heat conduction, diffusion, photoionization, dissociation, recombination, mass transport, runaway particles, etc.). Complete description of the behavior of the upper atmosphere is a formidable task, since it is shaped by the joint effect of the various factors. Numerous features in the behavior of the upper atmosphere therefore remain unclear to this day. The interaction paths transmitting the effects of atmospheric variations to the ionosphere and vice versa are far from being obvious.

Models are usually constructed in order to assemble into a single whole the multitude of scattered data about the upper atmosphere and to present one continuous picture of atmospheric variations. Moreover, clear understanding of the physical reasons for the various changes in the upper atmosphere is impossible unless these changes can be described by models. The construction of models of the upper atmosphere has therefore become one of the principal directions of rocket and satellite research.

### Elements of the theory of the vertical structure of the atmosphere

Two fundamental laws determine the vertical structure of the atmosphere in any model: the ideal gas equation

$$p = nkT \quad (\text{IV.10})$$

and the hydrostatic equilibrium equation

$$dp = -\rho g dh, \quad (\text{IV.11})$$

where  $p$ ,  $\rho = n\mu m_H$ , and  $T$  are the pressure, the density, and the temperature of the atmosphere,  $n$  and  $\mu$  are the concentration and the mean molecular weight of the atmospheric particles,  $k$  is Boltzmann's constant,  $m_H$  is the weight of a hydrogen atom,  $g$  is the gravitational acceleration. Dividing (IV.11) through by (IV.10), we obtain the barometric equation in differential form:

$$\frac{dp}{p} = -\frac{\mu m_H g}{kT} dh = -\frac{dh}{H}, \quad (\text{IV.12})$$

where  $H$  is the scale height. The integral form of the barometric equation expresses simple exponential decrease of atmospheric pressure with altitude:

$$p = p_0 \exp \left[ -\int_{h_0}^h \frac{dh}{H} \right]. \quad (\text{IV.13})$$

Atmospheric density and particle concentration are more complex functions of altitude:

$$\rho = \rho_0 \frac{T_0}{T} \exp \left[ -\int_{h_0}^h \frac{dh}{H} \right], \quad n = n_0 \frac{T_0}{T} \exp \left[ -\int_{h_0}^h \frac{dh}{H} \right]. \quad (\text{IV.14})$$

The above relations are valid for that part of the atmosphere, where turbulent and convective mixing is sufficiently strong, i. e., below 100 km.

Above 105 km, mixing is mainly determined by molecular diffusion processes\* which produce a definite redistribution of each species of particles according to its own barometric equation, with a scale height  $H_j = kT/m_j g$ . This distribution is independent of the distributions of other particle species, so that

$$p_j = p_{0j} \exp \left[ -\int_{h_0}^h \frac{dh}{H_j} \right]. \quad (\text{IV.15})$$

As we shall see in the following, however, this is true for neutral particles only. The above conclusion emerges from the simple fact that equations (IV.10) and (IV.11) at the relevant altitudes are applicable to partial, as well as total, values of pressure, concentration, and density for almost every individual component of the atmosphere. The only exception is oxygen at altitudes of 100–130 km, for which dissociation processes must be taken into account.

Temperature is clearly the basic factor which determines the vertical distribution of various atmospheric parameters. Irrespective of whether we are dealing with the homosphere or the region of diffusive mixing, knowledge

of the temperature profile  $T(h)$  enables us to compute the integral  $\int_{h_0}^h \frac{dh}{H}$  and

\* At these altitudes, laminar flow conditions are restored / 328/.

then apply (IV.13) and (IV.15) with known boundary conditions at altitude  $h_0$  to find the vertical distribution of  $p$ , and hence, using (IV.14), or directly employing (IV.10) and (IV.11), the vertical distributions of  $n$  and  $\rho$ . The temperature is thus regarded as a "backbone" of any atmospheric model.

## Temperature

It follows from the above that knowledge of the vertical distribution of the atmospheric temperature under various conditions will enable to obtain a complete picture of the structure of the atmosphere. The main effort apparently should be aimed at accurate determination of  $T(h)$  and the boundary conditions. However, the experimental methods for direct determination of the temperature in the upper atmosphere are highly inadequate.

A relatively successful method is borrowed from astrophysics and spectroscopy: temperature is determined by measuring the width of the spectral line of a certain atom. The temperature at various altitudes can be determined by releasing clouds of various elements from rockets, e. g., sodium or potassium vapors. Blamont and Lory-Chanin /329, 330/ obtained the vertical distribution of temperature in epochs of different solar activity in 1960–1964. The results are presented in Figure 57. The main region is that between 100–200 km, where the sharpest change in temperature is observed. Above  $h \approx 250$ –300 km, the temperature remains constant; here it is fairly easy to determine and more reliable methods are available for its determination (see reviews /326, 310/).

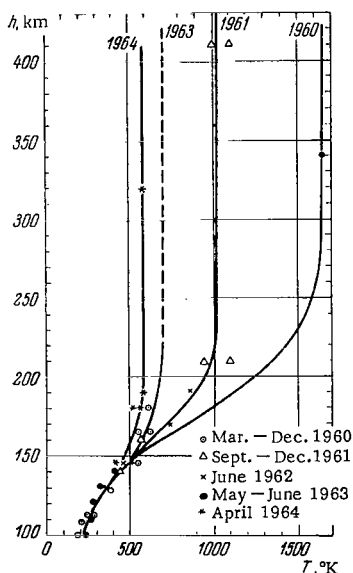


FIGURE 57. Vertical distribution of temperature obtained by observing sodium and potassium vapors released from rockets /330/ in different epochs of solar activity in 1960–1964.

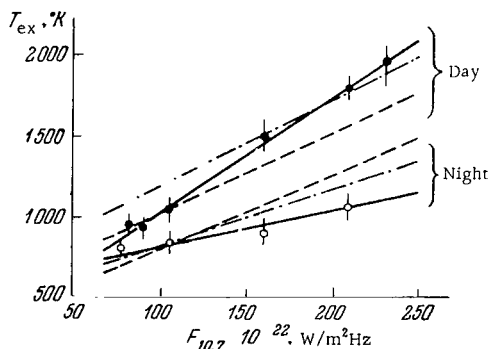


FIGURE 58. Daytime and nighttime temperature in the isothermal region of the upper atmosphere vs. the flux  $F_{10.7}$ .

Dashed lines — data of /333/; dash-dotted lines — data of /332/; solid lines and dots — data of /331/.

The constant temperature  $T_{ex}$  in the isothermal region is determined fairly reliably from satellite deceleration data, although different methods, as we see from Figure 58, give somewhat divergent results. The daily temperature maximum is observed at 1400–1600 hrs local time, and the minimum is observed at 0400–0500 hrs local time, i. e., the temperature curve is offset relative to noon. This points to a definite inertia in the temperature properties of the atmosphere. From day to night  $T_{ex}$  drops by 20–40% in epochs of low solar activity and to  $2/3$ – $1/2$  in epochs of high solar activity ( $1000 \rightarrow 800^\circ\text{K}$  and  $1800 \rightarrow 1100^\circ\text{K}$ , respectively). The short-wave radiation of the Sun thus significantly modulates the diurnal variations of  $T_{ex}$ .

The most significant changes in the upper atmosphere are related to variations in solar activity (the 27-day and 11-year cycles). These changes are caused by variations in the short-wave solar radiation, which is the main source of heat in the upper atmosphere. Each level of the solar activity, characterized by the solar radio flux  $F_{10.7}$ , corresponds to definite daytime and night values of  $T_{ex}$  (Figure 58). These relations, however, are valid only on the average, since  $T_{ex}$  also varies with latitude, time of year, and geomagnetic activity (see below).

We have considered the variations of temperature in the isothermal region above 200–250 km. An even more complex picture is observed at lower altitudes, where different vertical temperature profiles may be observed under different conditions, even though  $T_{ex}$  may remain constant. According to Mikhnevich /334/, the temperature profile  $T(h)$  between 150 and 200 km may reveal certain maxima and minima. Complete understanding of the vertical variation of temperature and its dependence on latitude and time of day is apparently impossible without knowledge of the dynamics of the atmosphere and, in particular, the possibility of horizontal motions /335, 336/.

Ejection of sodium vapors and vapors of other alkali and alkaline-earth metals from rockets provides the temperature with fairly low accuracy,  $\pm 100^\circ\text{K}$ . Higher accuracy would appear attainable by determining the relative vertical variation of temperature from an analysis of the density or pressure gradients, which can be measured with fair accuracy on rockets with pressure gages or by the method of falling spheres. However, at  $h \geq 120$  km, the accuracy of these methods for absolute temperature determination is actually limited by the inaccuracy of our data on the composition of the atmosphere (see below). In view of the difficulties in temperature determination, models of the upper atmosphere are generally based on other parameters, e. g., density and composition, although this approach introduces additional computational difficulties. Examples of construction of such atmospheric models are considered below.

## Density

The values of the atmospheric parameters are derived either from direct satellite and rocket measurements or from indirect data based on observations of meteors, sky glow, ionospheric phenomena, etc. All these data are highly fragmentary and refer to different epochs and altitudes; they are, moreover, often unreliable. The most accurate and complete data are available for the density of the atmosphere above  $h \approx 200$  km. These data are

obtained from satellite deceleration observations and they reveal certain regular variations in the upper atmosphere with time of day and solar activity.

Significant changes in  $\rho$  are observed from day to night, especially in epochs of minimum solar activity. This is clear from Table 26, borrowed from /337/. The amplitude of the diurnal variations in atmospheric density increases with altitude, and the upper atmosphere therefore shows a characteristic "bulge" on the day side of the Earth. Hence, it follows that the upper atmosphere above every point on Earth expands in daytime and shrinks at night. The resulting gas flow is large enough to cause breakdown of the fundamental equation (IV.11), in which a dynamic term should be introduced on the right /338/.

TABLE 26. Variation of atmospheric density  $\rho$ , g/cm<sup>3</sup>

Time	Altitude, km	1958—1959	1962—1964
Day	200	$4.3 \cdot 10^{-13}$	$2.7 \cdot 10^{-13}$
	300	$4 \cdot 10^{-14}$	$1.5 \cdot 10^{-14}$
Night	200	$4 \cdot 10^{-13}$	$1.8 \cdot 10^{-13}$
	300		$10^{-15}$

The daily variation of density in the upper atmosphere is offset relative to noon (like the temperature curve). This accounts for the offset of some other ionospheric phenomena considered in the following sections.

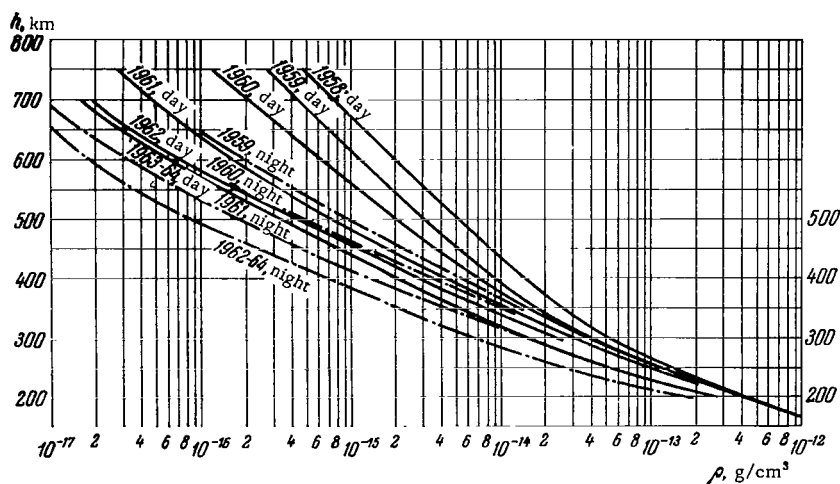


FIGURE 59. Vertical distribution of the density of the upper atmosphere for various solar activity levels in 1958—1964 from satellite deceleration observations /343/.

Solid lines — daily maxima; dash-dotted lines — nocturnal minima.



In epochs of high solar activity, the diurnal variations in  $\rho$  at 200 km are small, and below 200 km they even reverse their sign /339, 340/. For low solar activity, the isopycnic level, i. e., the level at which the diurnal density variations reverse their sign, occurs at lower altitudes, probably at  $h \approx 150$  km. The density variations at 200 km are quite large, reaching an amplitude of 1.8 according to the recent estimates of King-Hele /342/.

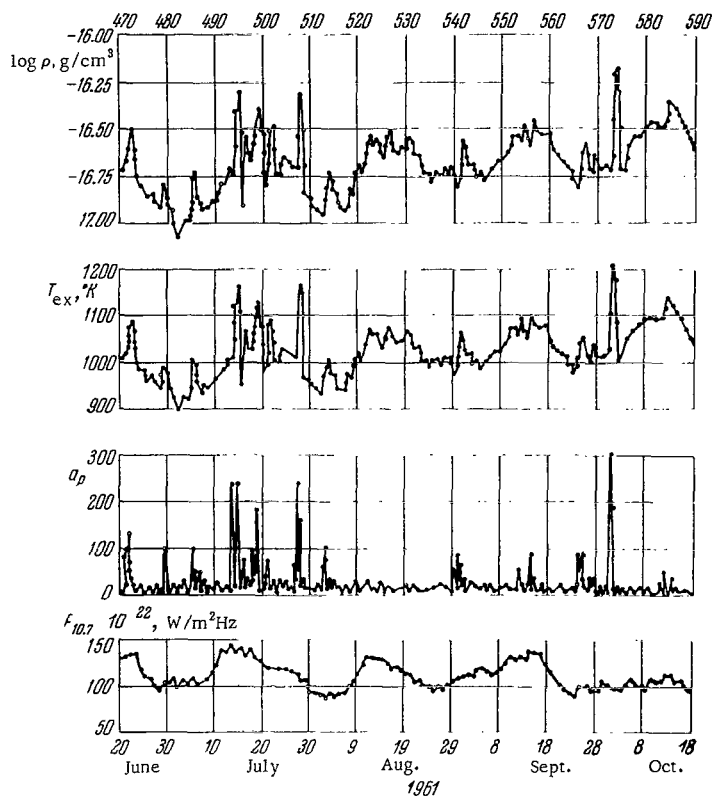


FIGURE 60. Variations of density and temperature of the upper atmosphere during June–October 1961 from deceleration observations of Explorer-9 /344/ ( $\log \rho$  is reduced to 730 km altitude).

The bottom curves give the variation of the geomagnetic index  $a_p$  and the solar radio flux  $F_{10.7}$  at 10.7 cm wavelength during the same period. The temperature and the density of the upper atmosphere significantly increase with the increase in  $a_p$  and  $F_{10.7}$ .

The density of the atmosphere markedly increases with the increase in solar activity (Figure 59). The overall density at altitudes of 200 and 300 km increases by a factor of 2 and 3–4, respectively, between minimum and maximum activity. This is the best illustration of the effect of the short-wave radiation intensity during the 11-year solar cycle. The density and the temperature of the atmosphere also reveal distinct 27-day variations, corresponding to the variations in the intensity of the short-wave solar radiation

as represented by the solar radio flux index  $F_{10.7}$ . An example of this dependence emerges from Figure 60, which is reproduced here in order to illustrate still another important phenomenon. It is readily seen that each magnetic storm (as indicated by an increase in the geomagnetic indices  $a_p$  or  $K_p$ ) corresponds to an increase in  $T_{ex}$  and  $\rho$ . Thus, 5–7 hours after a magnetic storm /344–347/,  $T_{ex}$  increases (for an increase of unity in  $K_p$ ,  $\Delta T$  is 28°K at middle latitudes and 32–35°K at high latitudes) and an atmospheric "bulge" forms, especially in the auroral zone. The mechanism of interaction between magnetic storms and the upper atmosphere is not clear at this stage; it is probably related to an enhancement of the corpuscular streams.

The density and the temperature of the upper atmosphere also depend on latitude, time of year, and other factors. King-Hele established that the atmosphere as a whole rotates relative to the Earth. The sense of this rotation coincides with the Earth's axial rotation, and the velocity of rotation at altitudes of 200–300 km relative to the ground, according to new data /348–350/, is 1.3 in units of the Earth's axial rotation; this is equivalent to a westerly wind of about 100 m/sec at middle latitudes.

We will now construct a model of the upper atmosphere from a vertical density distribution  $\rho(h)$  and the boundary conditions (composition of the atmosphere) at altitude  $h_0$ . Using  $\rho(h)$ , we readily find the total pressure  $p(h)$ . Indeed, integration of (IV.11) gives

$$p = p_0 - \int_{h_0}^h \rho g dh. \quad (\text{IV.16})$$

Writing  $z = \int_{h_0}^h \frac{g dh}{kT}$ , we rewrite (IV.15) in the form

$$p_j^{1/m_j} = p_{0j}^{1/m_j} e^{-z}. \quad (\text{IV.17})$$

Then in the region of diffusive and gravitational equilibrium, the total pressure  $p = \sum_k p_k$  may be expressed in terms of the partial pressure  $p_j$  of any component (Anderson and Francis /351, 352/) and the set of all partial pressures  $p_{0k}$  at the boundary  $h_0$ :

$$p = \sum_k p_{0k} \left( \frac{p_j}{p_{0j}} \right)^{\frac{m_k}{m_j}}. \quad (\text{IV.18})$$

Conversely, if  $p$  is known, equation (IV.18) may be used to find  $p_j$ , and then from (IV.17) we can find  $z$  and hence  $T(h)$ . This completes the construction of the model. The main difficulty in this method is the solution of equation (IV.18), which is impossible without a computer /351, 352/. Newton's difference method was applied to solve this equation in /339/.

Bhatnagar and Mitra /353/ used general relations between the gradients of density, pressure, and concentration in a nonisothermal atmosphere to construct a model of the upper atmosphere. Their relations are equivalent to the above formulas. Other methods of model construction are available,

which make use of additional assumptions that simplify the solution. Simplifying assumptions regarding the composition of the atmosphere are considered below.

## Neutral composition of the atmosphere

Let us consider the relative variations of the main components O and N<sub>2</sub> at altitudes of 100–200 km. There are very few data on the other atmospheric components at these altitudes.

TABLE 27. Rocket measurements of the neutral composition at altitudes above 130 km

Date	Local time	Components	$h^*$ , km	Reference
Absorption of short-wave solar radiation				
23.VIII.1961	10 hrs 03 min	N <sub>2</sub> , O	135	354
5.VI.1962	05 45	N <sub>2</sub> , O	~ 195	355
25.X.1962	16 30	N <sub>2</sub> , O	~ 170	355
10.VII.1963	07 30	N <sub>2</sub> , O	150	355
2.III.1965	17 13	N <sub>2</sub> , O	~ 180	357
3.III.1965	17 19	N <sub>2</sub> , O	181	357
4.III.1965	17 15	N <sub>2</sub> , O	~ 180	357
2.III.1966	12 59	N <sub>2</sub> , O	167	357
Rf mass spectrometer and "mass filter"				
23.IX.1960	00 hrs 56 min	N <sub>2</sub> , O	~ 210	358
15.XI.1961	16 00	N <sub>2</sub>	—	359
11.XII.1965	04 43	N <sub>2</sub> , O	~ 165	360
Magnetic mass spectrometer and omegatron				
6.VI.1963	07 hrs 30 min	N <sub>2</sub> , O	197	361, 362
15.IV.1965	03 15	N <sub>2</sub> , O	> 200	362, 363
20.XI.1962	16 41	N <sub>2</sub>	—	364, 365
19.IV.1963	16 04	N <sub>2</sub>	—	364, 365
20.VII.1963	16 54	N <sub>2</sub>	—	364, 365
28.I.1964	22 09	N <sub>2</sub>	—	364, 365
19.III.1965	13 09	N <sub>2</sub>	—	364, 365
20.III.1965	00 42	N <sub>2</sub>	—	364, 365
2.III.1966	13 00	N <sub>2</sub> , O	300	366
Explorer-17	Noon	N <sub>2</sub> , O	~ 275	368
	Night	N <sub>2</sub> , O	~ 325	368

We will compare the various results available for the altitude  $h^*$  at which  $[O] = [N_2]$ . Table 27 lists the rocket experiments in which the neutral composition was measured by three methods /356/. Table 28 gives the theoretical values of  $h^*$  obtained from different models.

The barometric equation suggests that the ratio  $[O]/[N_2]$  will decrease with the increase in temperature, whereas the altitude  $h^*$  should increase, if the composition is assumed to remain unchanged at the level of gravitational separation. Therefore, Norton and van Zandt /369/, for instance, indicate

that the ratio  $[O]/[N_2]$  should gradually increase during the day, due to the heating of the atmosphere. In the CIRA 1965 model /332/ (Table 28), as in many other models,  $h^*$  at night is indeed lower than during the day.

We see from Table 27 that different measurement methods give widely differing absolute values of  $h^*$  (and, hence, widely differing relative compositions). Our data on the neutral composition of the atmosphere are thus not very reliable. There is one consistent feature, however: measurements by the same method invariably give for  $h^*$  values which in the evening and in early morning are 25–50 km higher than at noon. Danilov's review /370/ shows that, according to the most reliable rocket data, the ratio  $[O]/[N_2]$  is generally less than 1 at altitudes of 180 km, but increases to values greater than 1 around noon, so that at noon  $h^* < 180$  km. This contradicts the theoretical scheme in the CIRA 1965 model /332/ and others.

TABLE 28. The altitude  $h^*$  (km) from different models of the atmosphere

Time	Solar activity			
	high		low	
Day	256	195	210	185
Night	228	183	220	195
Model	CIRA 1965 /332/		Kallmann-Bijl and Sibley /339/	Bhatnagar and Mitra /353/

Recently, Kallmann-Bijl and Sibley /339/ and later Bhatnagar and Mitra /353/ proposed original models of the atmosphere which account for the observed effect of the nocturnal density increase at altitudes below 170 km. In these models, the altitude  $h^*$  slightly increases at night (Table 28), although to a lesser extent than according to actual observations. The effect is partly reduced, owing to the assumption that the ratio  $[O]/[O_2]$  at  $h \approx 110$  km is higher at night than in daytime. This is a reasonable assumption, since according to the computations of Stein and Walker /371/, the decrease in the temperature of the exosphere is causally linked with the increase in the relative concentrations of O at  $h \approx 120$  km (this follows from the satellite data on atmospheric density). New experimental confirmation has been recently obtained indicating that the ratio  $[O]/[O_2]$  at  $h \leq 120$  km is indeed lower in daytime than at night, while a reverse picture is observed above 120–140 km /372–375, 808/.

It is significant that the decrease of the ratio  $[O]/[O_2]$  at altitudes  $h < 120$ –140 km is observed not only on the diurnal curves (in daytime) but also on the seasonal curves (in winter), and possibly in the latitudinal distribution (the equatorial zone) and in dependence on solar activity (for low activity) /375/. This phenomenon is mainly due to the change in the temperature conditions in the atmospheric region above the level of gravitational separation ( $h \approx 105$  km). Indeed, a similar picture is observed for the ratio of the  $N_2$  concentration to the concentration of the heavier Ar. At altitudes below 118 km, the ratio  $[N_2]/[Ar]$  is higher at night than in daytime, whereas above 118 km a reverse picture is observed /375/. The behavior of atomic oxygen at  $h \approx 100$  km is apparently influenced by dissociation processes, as well as the diffusive-gravitational separation, while the total content of atomic oxygen in the

atmospheric column above 80–90 km remains approximately constant from day to day, showing only a seasonal variation. As a result of these factors, the following phenomena are observed.

As the relative concentration of the components remains constant at the level of gravitational separation despite the changes in temperature, the barometric equation shows that the ratio  $[X]^{m_y}/[Y]^{m_x}$ , where  $m_x$  and  $m_y$  are the masses of components X and Y, respectively, should remain constant at all altitudes. Mirtov /376/ established from numerous data that the ratio  $[O_2]/[O]^2$  is indeed independent of altitude in the isothermal region  $h \geq 180$  km. It is surprising, however, that the value of this ratio fluctuates by a significant factor from one experiment to the next. No clear seasonal or diurnal variation was observed. Reber /377/ considered a similar invariant ratio  $[O]^{2+\frac{7}{3}\alpha}/[N_2]^{1+\frac{4}{3}\alpha} [He]$ , where the thermal diffusion factor  $\alpha$  allows for the effect of thermal diffusion of helium. According to Explorer-17 data, this ratio does not remain constant, varying by a certain factor with altitude and time of day. The simple assumption of constant lower boundary conditions is thus inapplicable to the upper atmosphere.

The experimental data point to the complex and variable conditions and processes which determine the state of the upper atmosphere (and, in particular, its composition), even at the lower levels around 100–200 km. Let us consider one further aspect of this problem.

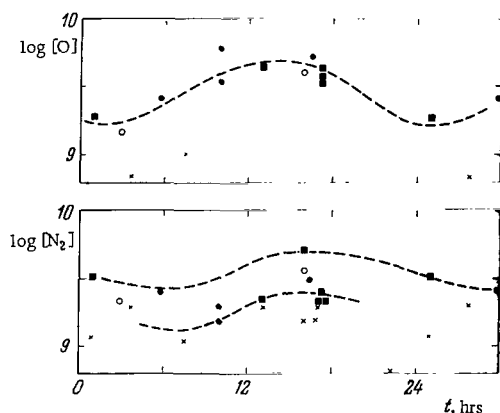


FIGURE 61. Diurnal variation of the concentrations of atomic oxygen and molecular nitrogen at 200 km altitude in an epoch of low solar activity from rocket measurements /356/.

Dark circles, squares, and crosses identify the measurements carried out by the three different methods listed in Table 27. Light circles are the concentrations obtained from an analysis of satellite density data /367/. The curve in the top figure is drawn through the circles and the squares (the first two methods in Table 27) and in the bottom figure the scatter of the experimental data is emphasized by drawing two separate curves.

Table 27 lists all the experiments in which the particle concentrations were measured. Let us consider the results of these experiments in order to detect possible variations in the composition of the upper atmosphere at altitudes  $h \approx 200$  km in epochs of low solar activity. When comparing the results of different measurements, we should remember the differences in experimental conditions and techniques.

The concentrations of atomic oxygen O and molecular nitrogen  $N_2$  as a function of the local time  $t$  at an altitude of 200 km are shown in Figure 61. The distribution of atomic oxygen reveals a distinct diurnal variation with a maximum around 1400 hrs local time, and a minimum around 0300 hrs. The maximum to minimum ratio of oxygen concentrations is approximately 2.5. Magnetic mass spectrometer and omegatron data (crosses in Figure 61) agree with the general diurnal trend of [O], but the absolute concentrations work out to be less than in other methods.

For  $[N_2]$ , the scatter of measurement data is more pronounced (partly due to seasonal variations), but measurements carried out by the same method during the same season reveal night-to-day changes by approximately a factor of 2 in the concentration of molecular nitrogen. Measurements also point to such diurnal variations below 200 km, their amplitude diminishing toward the 150 km level. According to /808/, the daytime  $[N_2]$  at  $h = 200$  km is a factor of 1.4–1.7 higher than the night concentration.

The atmosphere at  $h \approx 200$  km thus undergoes definite diurnal variations in epochs of low solar activity (the curves in Figure 61). The most reliable data give on the average  $h^* = 150$ –200 km in daytime and  $h^* \approx 225$  km at night. The Explorer-17 data for the concentrations of O and  $N_2$ , and for  $h^* / 368$  obtained with a magnetic mass spectrometer, follow the same diurnal curve, but differ in absolute values from the other data (see Table 27).

## Models of the upper atmosphere

The CIRA 1965 models are now widely used. They were developed by Harris and Prister /332/ for  $h \geq 120$  km using a variety of experimental data collected by the COSPAR work group for the creation of an international reference atmosphere. The models of Harris and Prister /332/ are convenient for practical work, since they have been constructed at sufficiently frequent intervals of time and altitude, and list data on the concentrations of the individual atmospheric components.

The CIRA 1965 models have been constructed for different solar activity levels and different times of day. It is readily seen, however, that the nocturnal atmospheres are close to the daytime models corresponding to a lower level of solar activity. To elucidate the general effects of density and temperature variations on the ionosphere, we shall henceforth use two typical models, the "maximum" and the "minimum" model. The "maximum" model (see Table 47) corresponds to high solar activity ( $F_{10.7} = 200 \cdot 10^{-22} \text{ W/m}^2\text{Hz}$ ) and the "minimum" model (see Table 48) corresponds to low activity ( $F_{10.7} = 100 \cdot 10^{-22} \text{ W/m}^2\text{Hz}$ ). Both models refer to noon hours. As we have noted above, the minimum model is close to nocturnal models for high solar activity.

The CIRA 1965 model, despite its obvious advantages, is inadequate in certain respects. The main shortcoming of the model is the assumption of constant atmospheric conditions at the 120 km level, which many now realize

to be unfounded /378—380/. This was corrected in later models /339, 353/ constructed for conditions of low solar activity. Detailed computations should be made using these improved models. No new models have been constructed so far for periods of high solar activity.

For 100—120 km, an interpolation between CIRA 1965 and the homosphere model was carried out. Major difficulties were encountered in estimating the concentration of atomic oxygen. We used the results obtained for [O] by a new method based on the luminescence of NO /372/. At altitudes of 103—107 km, a maximum concentration of O was observed in daytime, reaching  $1.5 \cdot 10^{11} \text{ cm}^{-3}$ , which is  $1/3$ — $1/4$  of the earlier estimates.

#### Variation of atmospheric parameters below 90—100 km

Large-scale rocket studies of the atmosphere below 90—100 km were begun during the IGY. The measurement results are much more comprehensive than the results of meteor and ionospheric observations. We will try to summarize the basic findings.

The density of the atmosphere at altitudes of 50—100 km undergoes seasonal, diurnal, and latitudinal variations. The amplitude of these variations is maximal at 60—80 km and minimal at 90 km. It is universally agreed that

the density of the atmosphere is higher in summer than in winter, especially at high latitudes. The estimates of the amplitude of density and pressure variations supplied by two groups of researchers, however, differ almost by an order of magnitude. Thus, at altitudes  $h \approx 70$  km, where the maximal seasonal variations are observed, some data indicate a summer increase of 10—20% at middle latitudes and 25—40% at high latitudes /381, 382/, whereas other data suggest that the density of the atmosphere in summer at high latitudes increases by a factor of 2—3 /383—385/. At  $h \approx 90$  km, the seasonal variations in  $\rho$  are minimal or nil /382, 386—389/. This is clear from Figure 62, which plots the seasonal density variations according to the latest rocket measurements in the form of the percentage deviations  $\Delta\rho/\rho$  from the USA 1962 model for two latitudes  $\varphi$  (30° and 60°).

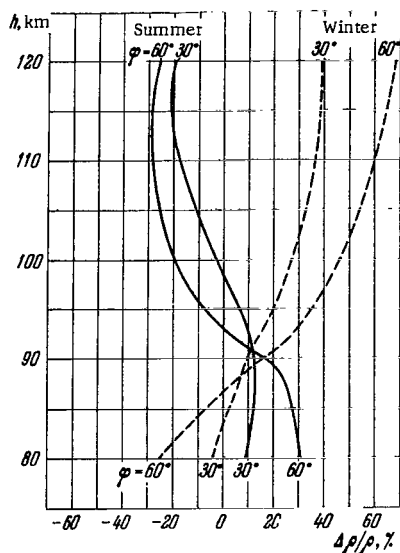


FIGURE 62. Mean density variations at altitudes of 80—120 km for different seasons and two latitudes from rocket data /389/.

The horizontal axis plots the percentage deviation of density from the 1962 USA model of the atmosphere.

The temperature at altitudes below 90 km also experiences seasonal variations, which increase at higher latitudes. In summer the temperature below 60 km increases, whereas above 60 km it decreases /387/. Around the 90-km level,

the winter and summer values are approximately the same /384, 387/. The latitudinal variations have the following pattern /382/: in winter, below 60 km, the temperature decreases toward the pole, whereas above 70 km, in high latitudes, the winter temperature is conversely higher than the summer temperature. Seasonal variations in  $T$  are not large, falling approximately within the limits of  $20^\circ$ , and their effect on the ionosphere probably can be ignored.

## 18. Observations of electron streams in the ionosphere

### Trapped and injected electrons

We have mentioned before that the discovery in the upper atmosphere of streams of energetic electrons capable of producing additional ionization is one of the leading achievements of rocket and satellite research, which is of fundamental importance in our studies of the physics of the ionosphere. Electron fluxes with energies of 10–100 keV were detected at  $h \approx 100$  km in high latitudes in rocket measurements carried out in 1953–1955 under Van Allen /390, 391/. Sputnik III was the first satellite to record these electron streams (Krasovskii et al. /663, 664/). Fast electron streams were also detected by rockets in middle latitudes /392–395/. Electron streams with energies of 1–10 keV at altitudes of 200–500 km reach fluxes of about  $0.3 \text{ erg/cm}^2 \text{ sec}$  during the day, and thus account for a significant fraction (up to 10%) of the flux of short-wave solar radiation. These electron streams penetrating the ionosphere to altitudes of 60–300 km are different from the large belts of trapped electrons and protons discovered above the ionosphere by satellites in 1958 (Van Allen, Vernov). It has now become clear that, besides the trapped particles, there are also particles with small pitch angles (the angle between the particle velocity vector and the direction of the magnetic force line) capable of penetrating deep into the atmosphere and thus causing ionization and other phenomena. These are the particles picked up in rocket measurements. We will call them injected particles.

Before proceeding with a discussion of the experimental results, we will define a number of basic quantities.

Trapped and injected particles are quantitatively characterized by their flux and intensity. Both these quantities can be expressed as a number of particles or in energy units. The flux is the number of particles or the particulate energy passing through  $1 \text{ cm}^2$  in 1 sec in all directions from a fixed hemisphere. It is designated by

$$P \text{ [particles/cm}^2 \text{sec]} \text{ or } w \text{ [erg/cm}^2 \text{sec]}.$$

The intensity  $I$  is the flux arriving from a certain direction in a solid angle of 1 sterad:

$$I \text{ [particles/cm}^2 \text{sec sterad]} \text{ or } \text{ [erg/cm}^2 \text{sec sterad]}.$$

The energy distribution of the particles is described by a differential or an integral spectrum. The differential spectrum  $p(E) dE$  is the flux (or the intensity) of the particles in unit energy interval between  $E$  and  $E + dE$ . The



integral spectrum

$$P(\geq E') = \int_{E'}^{\infty} p(E) dE \quad (\text{IV.19})$$

is the flux of all particles with energies exceeding a certain  $E'$ . The total energy flux is clearly

$$w = \int_0^{\infty} pE dE. \quad (\text{IV.20})$$

We distinguish between monoenergetic, exponential, and power fluxes, depending on the particular energy spectrum. A monoenergetic flux is made up of particles of one fixed energy. The exponential spectrum

$$p(E) \propto \exp\left[-\frac{E}{E_0}\right]$$

is characterized by the effective energy  $E_0$ , which is the same for the differential and the integral spectrum. A power differential spectrum

$$p(E) \propto E^{-\gamma}$$

is characterized by the power index  $\gamma$ , which is 1 less for the integral spectrum,  $P(\geq E) \propto E^{-\gamma+1}$ .

The streams of injected particles are a sporadic phenomenon, characterized by intensities and spectra which change markedly in short times and over small distances: in some cases quite powerful streams are detected, whereas in others there is nothing at all. Only numerous rocket measurements combined and prolonged satellite observations provide certain mean characteristics of these streams, which are highly significant for elucidating their contribution to the ionization of the upper atmosphere. Let us briefly consider the principal results of these observations in the auroral zone and in middle latitudes. A full resume of the various experiments is given in Table 29 (rockets) and Table 30 (satellites). Our main problem is to reach some conclusions regarding the intensity and the spectrum of the electron streams.

We see from Tables 29 and 30 that the most complete data have been recently obtained for the auroral zones, where the electron streams are of relatively high intensities. The electron streams at middle latitudes have been mainly measured in daytime, since at night they are much weaker. In addition to depending on latitude and the time of day, the intensity of the injected electron streams also depends on the solar activity level. We will start the analysis of the experimental data with the simpler of the two characteristics, the energy flux of the electrons.

## Energy flux

The total energy flux of the injected electrons at ionospheric altitudes was measured by a number of authors both on rockets and satellites. The main

fraction of the energy is associated with 1–10 keV electrons, which are the most difficult to detect.

The electron energy flux in the auroral zone generally reaches at night about  $0.1 \text{ erg/cm}^2\text{sec}$  in epochs of low solar activity and about 1 to  $10 \text{ erg/cm}^2\text{sec}$  for high solar activity (or in periods when the absorption of the cosmic radio waves is increased to  $A \approx 1 \text{ dB}$ ). When the electron stream intensity reaches about  $0.5 \text{ erg/cm}^2\text{sec sterad}$  (a flux of about  $3 \text{ erg/cm}^2\text{sec}$ ), polar aurorae of class I are observed /429/. The flux in bright aurorae increases by two or three orders of magnitude, reaching  $10^3 \text{ erg/cm}^2\text{sec}$ . At middle latitudes at night, the total electron flux, according to satellite /452, 429/ and rocket /422/\* measurements, simultaneously drops to  $\leq 10^{-2} \text{ erg/cm}^2\text{sec}$ .

The total electron flux at middle latitudes in daytime was measured in some rocket experiments /417, 419, 420, 421, 426/. At altitudes of 200–500 km it is about  $0.3 \text{ erg/cm}^2\text{sec}$  for conditions of medium solar activity, i. e., it is about 1.5 times stronger than at night. At altitudes below 150–200 km, the flux of injected electrons is gradually attenuated.

We see from Tables 29 and 30 that in certain cases the measured fluxes may differ by as much as one order of magnitude from these mean values. This deviation is due to the sporadic nature of the electron flux and the technical difficulties of absolute measurements.

## Spectrum

Another important characteristic of the electron stream is its spectrum. Some idea of the energy spectrum can be gained by comparing the integral intensities measured at various energies. Average data should be compared, in view of the small total number of the experiments and the possibility of large variations in intensity and energy. Satellite /436–438/ and rocket /410, 415, 447, 448/ measurements indicate that the intensity of an electron stream may change by up to 1.5 orders of magnitude in either direction in a few seconds.

Figure 63 plots the integral electron intensity vs. the energy  $E$  for the auroral zone (both without aurorae and for class I aurorae). The numbers inside the circles (satellites) and the squares (rockets) identify the corresponding lines in Tables 29 and 30. The solid curve gives a rough picture of the mean spectrum in the auroral zone at night.

The spectrum of electrons with energies up to 20 keV in polar aurorae is often approximated by an exponential function of the form  $\exp[-E/E_0]$ , where  $E_0$  varies from 3.5–5 keV to 8.5–12 keV. In some cases, the electron flux is almost monochromatic, with  $E \approx 6$  or 8–12 keV. At high energies, the intensity drops markedly following a power function  $E^{-\gamma}$ , where  $\gamma \geq 4$ . Thus, most of the energy is concentrated in electrons with  $E \leq 10 \text{ keV}$ . This fact was established by McIlwain /396/, Hegblom /411/, and Albert /416/ from rocket measurements in bright aurorae.

Figure 64 gives the spectrum for middle latitudes, according to /757, 448/ and the data from Tables 29 and 30. Although the scatter of experimental data for daytime measurements is quite considerable, especially in the 30–50 keV region, the intensity of the electron streams clearly diminishes with

\* In June 1968, Kazachevskaya /734/ used the phosphor  $\text{CaSO}_4(\text{Mn})$  to measure the 3–20 keV electron flux at altitudes of 140–165 km. Its intensity was about  $10^{-3} \text{ erg/cm}^2\text{sec sterad}$ .

TABLE 29. Rocket measurements of electron streams

No.	Author and reference	Date	Polar aurora or time of day	Altitude, km	Detector	Energy range, keV	Intensity		Flux		Remarks
							particles/cm <sup>2</sup> sec·sterad	erg/cm <sup>2</sup> sec·sterad	erg/cm <sup>2</sup> sec		
Auroral zone											
1	McIlwain /396/	22.II.1958	Diffuse aurora, cl. I	122	Scintillator, magnetic analyzer	3-250 (mainly <10)	$\sim 1.6 \cdot 10^{10}$	$\sim 20$	—	Intensity increases with altitude	
2	Meredith and Davis /397, 398/	25.I.1958	Diffuse aurora, cl. I	$\leq 178$	Scintillator	3-100 (mainly $\leq 8$ )	$(\sim 10^8)$	$\sim 1$	—		
		15.III.1958	Extinguished	$\leq 145$		0.03-1	$< 10^9$	—	—		
		22.III.1958	Extinguished	$\leq 167$		3-100	—	$< 10^{-2}$	—		
		16.XI.1958	Bright arch	—		3-100	—	$< 0.06$	—		
						8-100	—	$< 0.02$	—		
3	McIlwain /396/	25.II.1958	Bright arch	120	Scintillator	6	up to $5 \cdot 10^{10}$	100	2000		
4	Antonova /392/	6.XI.1958	Night	70-102	Luminescence detector	$\geq 20$	$\leq 5 \cdot 10^5$	$\sim 10^{-2}$	—		
5	McDiarmid /399/	28.X.1960	Dawn	$\sim 150$	Geiger counter	$> 30$	$\sim 2 \cdot 10^5$	—	—	$A = 2-3.8$ dB, spectrum exp $(-E/E_0)$ , $E_0 = 22$ keV	
6	Heikkila and Mathews /400/	7.V.1963	Day	139	Spectrometer with open-type photomultiplier	$\geq 1$	$1 \cdot 10^7$	$\approx A$	—	$A = 0.2-0.4$ dB	
		10.VI.1963	—	135		$\geq 1$	$2 \cdot 10^7$	$\approx A$	—	$A = 1-3$ dB	
		13.X.1963	—	145		$\geq 1$	$1 \cdot 10^8$	$\approx A$	—	$A = 1$ dB	

TABLE 29 (continued)

No.	Author and reference	Date	Polar aurora or time of day	Altitude, km	Detector	Energy range, keV	Intensity		Flux	Remarks
							particles/cm <sup>2</sup> sec·sterad	erg/cm <sup>2</sup> sec·sterad	erg/cm <sup>2</sup> sec	
Auroral zone										
7	McDiarmid and Budzinski /401/	6.IV.1963	CL.IV	145	Geiger counter and scintillator	≥40	(1-2) · 10 <sup>6</sup>	—	—	Isotropic angular distribution A = 0.3 dB, isotropic For 90° pitch angle, A = 1-1.5 dB
		7.V.1963	Day	139		≥41	(0.3-1) · 10 <sup>5</sup>	—	—	
		10.VI.1963	—	135		≥12	~10 <sup>7</sup>	≈ A	—	
						≥35	10 <sup>6</sup>	—	—	
		13.X.1963	—	146		≥12	(1-10) · 10 <sup>5</sup>	≈ A	—	A = 1 dB, spectrum exp(-E/E <sub>0</sub> ), E <sub>0</sub> = 12 keV
						≥35	(0.3-3) · 10 <sup>5</sup>	—	—	
14.I.1964	CL.I	147.5	≥80	(0.3-3) · 10 <sup>5</sup>	—	—	Intensity increases with altitude, isotropic angular distribution			
			≥4	—	0.03-0.07	—				
8	Ulwick /402/	8.II.1964	CL.I	228	Electrostatic analyzer and probe	1.28-160 ~10	No signal <3 · 10 <sup>8</sup>	— —	— —	
9	Evans /403/	II-III.1964 (4 rockets)	Active	—	Scintillator and multiplier	2-25	—	up to ~40	—	No 60-80 keV electrons detected
10	Riedler /404, 405/	12.III.1964	—	≤146.5	Semiconductor detector	40-104	>5 · 10 <sup>2</sup>	—	—	A = 1.5 dB
11	Cummings, La Quey, O'Brien, Walt /406/	18.III.1964	CL.II	≤140	Geiger counter	—	—	—	—	Intensity increases with altitude
		20.III.1964	CL.II	≤140		≥40	10 <sup>2</sup> -10 <sup>3</sup>	—	(~5)	
		23.III.1964	z <sub>0</sub> = 110°	≤140		≥40	up to 10 <sup>5</sup>	—	(~1)	
		April 1965	—			—	—	—	—	

TABLE 29 (continued)

No.	Author and reference	Date	Polar aurora or time of day	Altitude, km	Detector	Energy range, keV	Intensity		Flux		Remarks
							particles/cm <sup>2</sup> sec·sterad	erg/cm <sup>2</sup> sec·sterad	erg/cm <sup>2</sup> sec		
Auroral zone											
12	Mozer /407/	1.VIII.1964 7.VIII.1964	— —	415 425	Luminescence detector	} ≥150	~10 <sup>3</sup>	—	—	Injected electrons 10 <sup>2</sup> of the trapped electrons	
13	Mozer /408/	3.IX.1965	—	up to 450	Luminescence detector		65–400	—	—		—
14	McDiarmid, Budzinski, et al./409/	28.XI.1964	Polar disturbance	150	Geiger counter, scintillators (current and pulse mode) semiconductor detectors	≥40	(1–2) · 10 <sup>4</sup>	—	—	A ≈ 1.5 dB, ΔH ≈ 400γ, for ≥4 keV the flux with 80–90° pitch angle is given, power spectrum with γ = 4.7–5.7; the intensity and the distribution angle do not change during Δt = 1 min	
		25.III.1965		155		≥4	—	(6–50) · 10 <sup>-3</sup>	—		
				22.IV.1965		150	≥40	10 <sup>3</sup> –10 <sup>5</sup>	—		—
						≥4	—	0.02–0.3	—		—
15	Matthews /410/	14.X.1963	Moving band and diffuse glow	145	Spectrometer with open-type photomultiplier	0.03–0.3 1–7	~10 <sup>8</sup> 4 · 10 <sup>7</sup>	— —	— —	Spectrum and pitch angles change in t ≤ 1 sec	
16	Hegblom, Reidy, Ulwick /411, 750/	6.III.1965	C1.I	193	Scintillator with electrostatic analyzer	5–20	—	—	1	Spectrum exp(– E/E <sub>0</sub> ), E <sub>0</sub> = 3.5 keV	
		13.III.1965	C1.II	185		5–20	—	—	30	Spectrum exp(– E/E <sub>0</sub> ), E <sub>0</sub> = 8.5 keV	
		18.X.1965	Strong	101		2–20	—	0.2	—	Maximum in diffuse spectrum at 5 keV	

TABLE 29 (continued)

No.	Author and reference	Date	Polar aurora or time of day	Altitude, km	Detector	Energy range, keV	Intensity		erg/cm <sup>2</sup> sec	Remarks
							particles/cm <sup>2</sup> sec·sterad	erg/cm <sup>2</sup> sec·sterad		
Auroral zone										
16 (cont.)	Hegblom, Reidy, Ulwick /411, 750/	22.X.1965	Weak	138	Scintillator with electrostatic analyzer	1-40	—	0.2	—	Maximum in diffuse spectrum at 1.5-2 keV
		14.XII.1966	Strong	211		1-40	—	1	—	Spectrum exp(-E/E <sub>0</sub> ), E <sub>0</sub> = 5-7 keV
17	Doering /412, 413/	20.II.1966	Active, cl.II	165	Scintillator with accelerator	≥1 0.04-0.9	~3·10 <sup>8</sup> ~3·10 <sup>8</sup>	— —	— —	Spectrum exp(-E/E <sub>0</sub> ), E <sub>0</sub> = 0.125 keV
18	Chase /414/	1.IX.1966	Day	250	Magnetic spectrometer with channel multiplier and plastic scintillator	2-5	(2·10 <sup>8</sup> )	1	—	Spectrum peak: 6·10 <sup>7</sup> , 1·10 <sup>8</sup> , 1.6·10 <sup>8</sup> cm <sup>-2</sup> sec <sup>-1</sup> sterad <sup>-1</sup> keV <sup>-1</sup> . More hard electrons (80-320 keV) at night
		6.IX.1966	Day	240		2-5	(3·10 <sup>8</sup> )	~1.5	—	
			Night	240		5-20	(10 <sup>9</sup> )	4	—	
19	Lampton /415/	1966 (4 rockets)	Day	—	Scintillation counters	≥60	~10 <sup>5</sup>	—	—	Ten-fold intensity outbursts in 0.003 sec
20	Albert /416/	16.IX.1966	Bright	170 250	Scintillator, electrostatic analyzer	3-70 (mainly 8-12)	6·10 <sup>10</sup> 8·10 <sup>10</sup>	— 10 <sup>3</sup>	— —	Quasitrapped, almost monochromatic electrons

TABLE 29 (continued)

No.	Author and reference	Date	Polar aurora or time of day	Altitude, km	Detector	Energy range, keV	Intensity		Flux	Remarks
							particles/cm <sup>2</sup> sec-sterad	erg/cm <sup>2</sup> sec-sterad	erg/cm <sup>2</sup> sec	
Middle latitudes										
21	Antonova /392,393/	4.X.1958 23.XII.1958 25.XII.1958 21.VII.1959	Day	70-100	Luminescence counter	≥20 ≥20 ≥40 20-40	- - ~10 <sup>6</sup> -	<10 <sup>-2</sup> <10 <sup>-2</sup> ~5 · 10 <sup>-2</sup> ~10 <sup>-2</sup>	- - - -	
22	Kazachevskaya /394/	15.II.1961	Day	95-100	Thermoluminescence phosphor	≥10	(6.5 · 10 <sup>5</sup> )	~0.02	0.06-0.07	During a solar eclipse
23	Antonova /395,417/	18.X.1962	Day	200-500	Secondary electron multiplier	30-35 ≥1-8	2 · 10 <sup>5</sup> 5 · 10 <sup>7</sup>	0.01 0.1-0.6	- -	Intensity independent of altitude
24	Tindo /82/	X.1962 (2rockets)	Day	200-500	Geiger counter	≥50 ≥50	<400 <40	- -	- -	10-20% of cosmic background
25	Kazachevskaya /419/	18.X.1962	Day	150-500	Thermoluminescence phosphor	≥1	-	-	~1	
26	Antonova /420/	6.VI.1963	Morning, z <sub>⊙</sub> = 85°	200-500	Secondary electron multiplier	≥1	3 · 10 <sup>6</sup>	(2-4) · 10 <sup>-2</sup>	-	Intensity independent of altitude
27	Kazachevskaya /421/	6.VI.1963	Morning, z <sub>⊙</sub> = 85°	200-500	Thermoluminescence phosphor	≥2 ≥15	- -	- <2.5 · 10 <sup>-3</sup>	~0.2 -	Flux independent of altitude

TABLE 29 (continued)

No.	Author and reference	Date	Polar aurora or time of day	Altitude, km	Detector	Energy range, keV	Intensity		Flux	Remarks
							particles/cm <sup>2</sup> sec·sterad	erg/cm <sup>2</sup> sec·sterad	erg/cm <sup>2</sup> sec	
Middle latitudes										
28	O'Brien /422/	9.VII.1964	Night	100-170	Geiger counter, 3914 Å photometer	≥40 Total flux	7 —	— ≤ 2 · 10 <sup>-2</sup>	— —	
29	Nakagawa /423/	1.I.1965 18.III.1965	Day	200-1000	Geiger counter	A few hundred	—	—	—	Intensity increases with altitude
30	Shea /424/	23.VI.1965	Morning	≤156	Scintillation detector	≥0.01 ≥0.04	—	1.6 · 10 <sup>-3</sup> 1.6 · 10 <sup>-4</sup>	— —	Intensity increases with altitude
31	Tulinov /425/	1966 and 1967 (7 rockets)	— Evening	70-90 70-97	Geiger counter	≥40 ≥35-40	8-15 1-2	— —	— (~10 <sup>-6</sup> )	At altitudes of 87-97 km, the flux increases approximately five fold
32	Kazachevskaya /426/	21.XII.1966	Morning, z <sub>⊙</sub> = 85°	100-180	Thermoluminescence phosphor	≥ 1 ≥17 ≥30	— — —	~0.2 ~6 · 10 <sup>-3</sup> < 2 · 10 <sup>-3</sup>	— — —	Intensity increases with altitude

Remarks: 1) The intensities or fluxes enclosed in parentheses were computed from the data of other authors.

2) *A* is the absorption of cosmic radio waves at 20-30 MHz in decibels (dB).



TABLE 30. Satellite measurements of electron streams

No.	Author	Satellite, date	Altitude, km	Latitude	Detector	Energy range, keV	Flux		Remarks
							electrons/cm <sup>2</sup> sec	erg/cm <sup>2</sup> sec	
Auroral zone									
1	Shook /427/	XI.1965	~200	Auroral zone	—	1-70 (mainly <10)	—	$>10^{-2}-10^{-3}$ , $<10^2$	Sharp variations with pitch angle. Maximum in the region of a few keV
2	Sharp /428, 429/	19-20.V.1963 0500-0600 in the morning in Alaska	~270	$\varphi_m = 74-83^\circ$	Scintillation detector with accelerators	0.18-31 (8 thresholds) $\geq 10$	$3 \cdot 10^8 \cdot 2\pi$ (taking $E=1$ keV) $\sim 10^7 \cdot 2\pi$	For $0.5 \cdot 2\pi$ class I aurora	Pitch angle $0-43^\circ$ , i.e., only injected electrons. Structure ~1 km. For $E < 1$ keV the intensity decreases. $P(\geq 1): P(\geq 10) = 1:0.05$
3	Sharp /430, 432/	X-XI.1963 (5 days)	340	Above South Pole	—	$\geq 0.08$	—	Threshold $0.006 \cdot 2\pi$	Injected electrons mainly with $E > 1$ keV. Diurnal maximum at 1000-1200 hrs local time. Correlation with $K_i \neq K_p$
4	Pfitzer /433,434/	OGO-A 5.IX.1964-VI.1965	—	$L = 5.5$ $\chi = 40^\circ$	Magnetic spectrometer	50-120 120-290 290-690 690-1700 1700-4000	$4.7 \cdot 10^4 \cdot 2\pi$ $4.5 \cdot 10^4 \cdot 2\pi$ $3.0 \cdot 10^4 \cdot 2\pi$ $4.9 \cdot 10^3 \cdot 2\pi$ $2 \cdot 10^2 \cdot 2\pi$	— — — — —	Low-energy electron flux increases with increasing magnetic activity for $L = 4$ and decreases with altitude
5	Parthasarathy /435/	Injun-3, 1.X.1963	240-280	$L = 5.5-6.3$	—	$\geq 40$	$(300 \cdot A \text{ [dB]})^2$	—	In differential spectrum $\gamma = 4.5$ . Trapped electrons 10-100 times higher intensity than injected electrons
6	O'Brien /436-438/	Injun-1 and 3 1961-1964	—	$L = 5-7$ $L = 7-8$	—	$\geq 40$ $\geq 10$	$10^6$ $>10^6$	— —	Softer spectrum in auroral zone for $L = 7-8$

TABLE 30 (continued)

No.	Author	Satellite, date	Altitude, km	Latitude	Detector	Energy range, keV	Flux		Remarks
							electrons/cm <sup>2</sup> sec	erg/cm <sup>2</sup> sec	
Auroral zone									
7	McDiarmid /439-441/	Alouette-1 XII. 1962 - V. 1963	1000	Outer radiation belt	-	≥40	Outbursts up to 10 <sup>9</sup>	-	Variations depend on magnetic activity. Time constant 4 ± 1 days
8	Knudsen /442/	-	-	-	Ion trap	> 0.01	up to 6 · 10 <sup>10</sup>	-	Up to 10 <sup>4</sup> eV/cm <sup>2</sup> sec transmitted to the electron gas, which may account for $T_e = 3 - 4 \cdot 10^3$ °K
9	Johnson /443/	Start XI. 1965 (day)	Low	-	-	0.02 - 60	-	-	In auroral zone $E_{ef} < 10$ keV, for lower $\varphi$ , $E_{ef} \geq 25$ keV
10	Fritz /444/	Injun-3 1963 - 1964	-	Only at $\varphi_m = 58 - 76^\circ$	-	$\geq 10$ $\geq 40$	$\geq 2.5 \cdot 10^7 \cdot 2\pi$ -	- -	Only at night 1700 - 0700 hrs local time. Mostly for large $K_p$ . In power spectrum $\gamma = 1.5 - 7.4$
11	Evans /445/	1. III. 1962	≥ 270	-	-	$\geq 2$ $\geq 28$	(~10 <sup>9</sup> ) (~10 <sup>4</sup> )	~1.5 · 2π -	Bright aurora. For $E < 2$ keV, energy flux a factor of 20 - 100 higher
12	Evans /446/	Autumn 1963 (5 days)	~300	-	-	≥ 0.08 (mainly ≥ 1)	-	> 0.01	Harder spectrum in daytime. Nighttime intensity a factor of 5 higher, correlated with $K_p$
13	Blake /447/	25. II - 10. III 1965	170 - 220	$L = 4 - 7$		≥ 400	10 <sup>3</sup> - 10 <sup>5</sup>	-	Auroral zone. Five-fold variations in 0.1 sec

TABLE 30 (continued)

No.	Author	Satellite, date	Altitude, km	Latitude	Detector	Energy range, keV	Flux		Remarks
							electrons/cm <sup>2</sup> sec	erg/cm <sup>2</sup> sec	
Auroral zone									
14	Stevens /449/	Starting VIII. 1964	>2000	$L \geq 5$	Faraday cup	0.2 — 11	—	—	Energy measured in four intervals, observed only at $E = 3-8$ keV
Middle latitudes									
15	Savenko et al. /418/	Satellite spacecraft 2 VIII. 1960	~300	Middle latitudes	Scintillator	$\geq 30$	$\sim 10^5$	—	
16	Krasovskii, Gal'perin, Mulyarchik /450, 451/	Kosmos-3 and 5 1962	200—1600	—	Fluorescent screen with electron accelerator	$\approx 0.040$	$(10^7-10^8) \cdot 2\pi$	up to 0.06	Photoelectrons. $I$ growing with altitude. For $E \approx 25$ eV, intensity higher by one order of magnitude /450/
17	Giorgio /452/	Kosmos-5 V. 1962—III. 1963	200—1200	Middle latitudes	Trap	3—15	$\sim (1-3) \cdot 10^7$	up to 1.5	At night $\leq 10^7 \text{ cm}^{-2} \text{ sec}^{-1}$ ( $\leq 0.1 \text{ erg/cm}^2 \text{ sec}$ )
18	Vernov /453, 454/	Kosmos-12, 15 XII. 1962—III. 1963	200—400	—	Electrostatic spherical analyzer	0.1—10	—	—	At $E \approx 1$ keV differential spectrum, $10^7 \text{ cm}^{-2} \text{ sec}^{-1} \text{ keV}^{-1}$ . Brief outbursts observed
19	O'Brien /455/	Injun-1 and 3 1961—1964	~1000	Middle latitudes	Geiger counter	$\geq 40$	$10^2-10^3$	—	Flux increases five-fold with $K_p$ increasing by 1

TABLE 30 (continued)

No.	Author	Satellite, date	Altitude, km	Latitude	Detector	Energy range, keV	Flux		Remarks
							electrons/cm <sup>2</sup> sec	erg/cm <sup>2</sup> sec	
Middle latitudes									
20	Paulikas /456, 457/	IX. 1962 X. 1962	230—700	$L = 2$	Semiconductor or crystal detector	$\geq 900$	$3 \cdot 10^2 - 10^3$	—	On Figure 7 in /456/ the flux for $L = 2$ is $10^2 - 10^3$ electrons/cm <sup>2</sup> sec, and for $L = 4.5$ one order of magnitude higher (Figure 6 /456/)
21	Rose /458/	Alouette IX. 1962— VIII. 1965	1025	Maximum for $L = 4$ , occasionally also for $L = 2$	Geiger counter	$\geq 40$ $\geq 250$ $\geq 3900$	— — —	— — —	Top boundary shifts by $\sim 5^\circ$ in 24 hrs; diurnal variations of injected electrons with daytime and morning maximum, increasing with $L$ ; a 3-day long outburst for high $K_p$
22	Sharp /429/	0500—0600 hrs local time 19—20. V. 1963, 0330 hrs local time 19—20. V. 1963	$\sim 270$  400	South of auroral zone (North latitudes) $\Phi_m = 10 - 40^\circ S$ (Hawai)	—  —	$\geq 0.18$  $\geq 0.18$	$(10^7 \text{ for } E \approx 1 \text{ keV})$  —	$\leq 0.01$  < 0.01	Night. Top stream boundary near the instrumental sensitivity threshold
23	Paulikas, Blake /457, 459/	VIII. 1964		$L = 2.3$	Semiconductor detector	$\geq 300$ $\geq 700$	$10^2 - 10^3$ < 10	— —	Injected electrons at altitude corresponding to $B = 0.36$ gauss. Intensity decreases with distance from South-Atlantic anomaly
24	Blake /447/	25. II—10. III. 1965	170—220	Middle latitudes	Semiconductor detector	$\geq 400$	< 150	—	

Remark: In items 2, 11, and 22, the electron flux has been computed approximately from the energy flux and the spectrum.

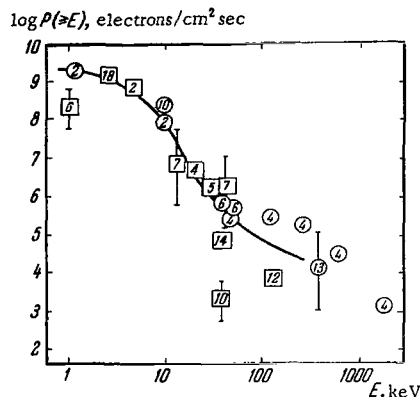


FIGURE 63. The integral electron spectrum in auroral latitudes from the data of Table 29 (rockets) and Table 30 (satellites), represented by squares and circles, respectively. The numbers identify the corresponding lines in the tables.

The solid curve is the mean spectrum drawn through points corresponding to the conditions when either  $A \approx 1$  dB or a class I aurora was observed.

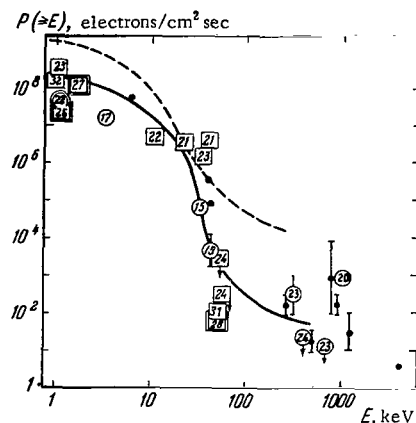


FIGURE 64. Integral electron spectrum at middle latitudes according to /757, 448/ (dark circles) and from the data of Table 29 (rockets) and Table 30 (satellites), represented by squares and circles, respectively. The numbers identify the corresponding lines in the tables.

Double squares and circles are night and morning data. The solid line is the daytime average, the dashed line is the average from Figure 63.

increasing electron energy, especially for  $E = 10-100$  keV. Figure 64 shows some mean curve which approximately (ignoring possible variations in the intensity and the spectrum of the electrons) reproduces the integral electron spectrum. This curve corresponds to the spectrum published by Antonova /417/ and, taken in conjunction with data on the total electron energy flux, it does not contradict the conclusion that the low-energy limit of the keV spectrum lies at  $E = 1-3$  keV. For  $E \leq 15-20$  keV, the electron spectrum is roughly exponential  $\exp[-E/E_0]$  with  $E_0 \approx 3-5$  keV.

The dashed curve in Figure 64 is the spectrum for the auroral zone. Its comparison with the daytime spectrum at middle latitudes shows that the flux of 100 keV electrons at middle latitudes is several orders of magnitude lower than in the auroral zone. The hard electrons ( $E = 30-1000$  keV) are thus markedly suppressed in the middle-latitude spectrum. This fact also emerged from satellite measurements of electrons with  $E \geq 40$  keV /436-438/.

Yet the intensity of 1-10 keV electrons at middle latitudes is only several times less than at auroral latitudes. The electron spectrum in the intermediate energy region  $E = 10-50$  keV is, therefore, steeper at middle latitudes than in the auroral zone. In this part of the spectrum we may take  $P(E) \propto E^{-\gamma}$  with  $\gamma \approx 4$  /417/.

Electrons with  $E = 1-10$  keV thus carry most of the energy. They constitute the most effective factor producing aurorae in the polar region and ionization in the E region at middle latitudes. In daytime at middle latitudes they are only several times weaker than the nocturnal fluxes at auroral latitudes. It has been shown /245/ that roughly the same relation is observed

for the total electron energy flux, which reaches about  $0.3 \text{ erg/cm}^2\text{sec}$  in daytime at middle latitudes and  $1-3 \text{ erg/cm}^2\text{sec}$  at night in auroral latitudes. This is quite expected, since most of the energy is accounted for by electrons with  $E=1-10 \text{ keV}$ .

This result, at a first glance, seems to contradict the results of satellite measurements, which invariably detect a marked increase in the intensity of electron streams at auroral latitudes compared to middle latitudes. There is no real contradiction, however, since satellites only measure the hard electrons or perform their measurements at night only, when the electron flux at middle latitudes is weaker by 1-2 orders of magnitude, compared with daytime conditions. Measurements of electrons with  $E=1-10 \text{ keV}$  in daytime are generally difficult, as the instruments cannot be made insensitive to daylight.

The observed differences in the electron spectrum are possibly due to certain differences in the acceleration mechanisms for the auroral and the middle-latitude electrons.

### Indirect data

The total energy flux of corpuscular streams obtained from direct measurements fits the indirect data, which can be obtained by observing the atmospheric emission in the  $\text{N}_2^+ 3914 \text{ \AA}$  band and the X-ray bremsstrahlung.

Let us first consider the  $\text{N}_2^+ 3914 \text{ \AA}$  emission, which is an outcome of ionization processes in the atmosphere. The intensity of the  $3914 \text{ \AA}$  band in class I polar aurorae is  $(0.5-1) \cdot 10^9 \text{ quanta/cm}^2\text{sec}$  (Dalgarno /460, 461/); without aurorae, in epochs of low solar activity, it is  $(2-5) \cdot 10^7 \text{ quanta/cm}^2\text{sec}$  /462, 463/. At middle latitudes, even with low solar activity, the  $3914 \text{ \AA}$  emission of the nocturnal sky generally reaches  $(5-10) \cdot 10^5 \text{ quanta/cm}^2\text{sec}$  (from ground observations /464, 465/ and from measurements with rockets /422/ and with the OVI-10 satellite /466, 467/). A corpuscular stream with energy of  $1 \text{ erg/cm}^2\text{sec}$  excites  $3914 \text{ \AA}$  emission with intensity of about  $5 \cdot 10^8 \text{ quanta/cm}^2\text{sec}$  /461, 468/. We thus find that the stream of corpuscles in a class I aurora is  $1-2 \text{ erg/cm}^2\text{sec}$ , in the auroral region in quiet conditions it is  $0.04-0.1 \text{ erg/cm}^2\text{sec}$ , and at night in middle latitudes about  $10^{-2} \text{ erg/cm}^2\text{sec}$ . These data are consistent with the results of direct rocket and satellite measurements, in periods of high solar activity.

Absorption of electrons with  $E=1-10 \text{ keV}$  in the upper atmosphere produces X-ray bremsstrahlung with  $\lambda \geq 1-10 \text{ \AA}$ . The efficiency of conversion of the electron energy into X-ray energy  $\eta$  is approximately  $10^{-5}$  /469/.

At altitudes  $h > 100 \text{ km}$ , the scattered X-ray radiation with  $\lambda = 3-10 \text{ \AA}$  is about  $10 \text{ quanta/cm}^2\text{sec sterad}$  ( $\sim 10^{-7} \text{ erg/cm}^2\text{sec}$ ) at night. Part of this scattered background is probably of galactic origin and another part is associated with the deceleration of  $1-10 \text{ keV}$  electrons in the atmosphere. These data give an upper-bound estimate for the electron energy flux at middle latitudes at night. Taking  $\eta = 10^{-5}$ , we obtain a flux of  $\sim 10^{-2} \text{ erg/cm}^2\text{sec}$ , which is close to the results of direct measurements.

The principal conclusion that emerges from the direct rocket and satellite measurements relates to the spectrum and the intensity of the electron flux at middle and auroral latitudes (see Figures 63 and 64), which fit the indirect energy flux estimates. Once the spectrum is known, we can readily find the rate of ionization and heating of the atmosphere at various altitudes.

A rigorous solution of this problem also requires knowledge of the vertical variation of the electron intensity.

### Vertical variation

The vertical profile is different for electrons of different energies. Rocket measurements /417/ indicate that the electron flux with  $E=1-10$  keV is fairly constant at altitudes  $h=180-500$  km, whereas Nakagawa's measurements /423/ show that the intensity of electrons with energies of a few hundred keV markedly increases with altitude at  $h=200-1000$  km. This increase is probably associated with the effect of trapped particles which, with energies of a few tens and hundreds of keV, may have relatively low points of reflection in the geomagnetic field. Indeed, the results of satellite measurements have established that even at altitudes of 1000 km the flux of trapped particles is significantly higher than the flux of injected particles. The intensity of trapped particles increases with altitude, but the vertical variation for injected electrons is apparently less pronounced, since electrons with energy of a few keV have much larger collision cross sections and do not have reflection points at ionospheric altitudes. It is probably for this reason that they do not show any vertical variation. At altitudes below 130-150 km, "absorption" of soft electrons begins, and the flux of these electrons should diminish. This effect is indeed observed in rocket measurements (Nos. 1, 11, 31, and 32 in Table 29).

The main difference between the fluxes of injected and trapped particles is that the former continuously lose their energy through ionization and heating of the atmosphere at altitudes of 50-300 km, where they are absorbed, whereas the latter weakly interact with the atmosphere and have long lifetimes. The lifetime of trapped particles is probably a factor of  $\sim 10^6$  higher than the lifetime of injected particles.

This situation was clearly demonstrated by the Starfish atmospheric nuclear test, which served as a source of an isotropic stream of fast particles. The injected particles produced a burst of an artificial aurora at geomagnetically conjugate points, which persisted for a few tens of seconds (weak glow excited by the decay of radioactive fragments persisted for a few hours). On the other hand, geomagnetically trapped particles with low  $L$  are still being observed, several years after their generation ( $\geq 10^8$  sec). Since the lifetimes of injected particles are a factor of  $\sim 10^6$  shorter than those of trapped particles, their source should be approximately a factor of  $10^6$  more powerful.

### Photoelectrons and secondary electrons

Besides electrons with  $E=1-10$  keV, the upper atmosphere carries electron streams with energies of up to several tens of eV. Rocket measurements led to the prediction and later detection of photoelectrons and secondary electrons in the upper atmosphere. These are electrons with energies from one to several tens of eV, which are products of ionization of atmospheric particles by short-wave solar radiation (photoelectrons) or ionizing corpuscular streams (which probably produce not only "secondary," but also "tertiary" and other electrons). The hypothesis regarding the existence of secondary electrons in the upper atmosphere was apparently first advanced by Vegard in 1938 /473, 474/.

Secondary electrons of energy  $E$  exceeding the ionization potential  $\chi_i$  of atmospheric particles take part in ionization processes, whereas electrons with energy  $E < \chi_i$  are only capable of raising the temperature of the atmosphere. The discovery of secondary electrons in the upper atmosphere constitutes a fundamentally new phenomenon. It was known, before this discovery, that ionization by energetic particles or light quanta produces comparatively fast electrons. It has become clear only now, however, that the secondary electrons do not perish immediately upon collision with neutral particles, but have sufficiently long lifetimes. As a result, the secondary electrons accumulate to a certain degree and carry energy fluxes which are comparable with the energy of the primary ionizing particles.

Experiments conducted on Kosmos-3 and Kosmos-5 satellites (see No. 16 in Table 30) in daytime at middle latitudes detected powerful fluxes of photoelectrons with  $E \geq 40$  eV. At altitudes from about 300 to about 700 km, their intensity markedly increases from  $\sim 10^7$  to  $\sim 3 \cdot 10^8$  electrons/cm<sup>2</sup>sec sterad /451/, which corresponds to energy fluxes of  $\sim 0.01$  and  $\sim 0.1$  erg/cm<sup>2</sup>sec. It is assumed /450/ that the flux of electrons with  $E \geq 25$  eV carries a total energy flux which is one order of magnitude higher. Recently, high intensities of photoelectrons with  $E \geq 10$  eV and  $E \geq 40$  eV ( $10^6$  and  $10^5$  keV/cm<sup>2</sup>sec sterad) were recorded by Shea et al. /424/ with a rocket at lower altitudes, up to 156 km, in the morning hours at middle latitudes. The intensity of secondary electrons with  $E \geq 10$  eV is about  $10^8$  electrons/cm<sup>2</sup>sec sterad (energy flux  $\sim 10^2$  erg/cm<sup>2</sup>sec). At 130 km, the flux was one order of magnitude lower. In /451/ it is reported that according to Hinteregger's measurements the intensity of electrons with  $E \geq 30$  eV is  $2 \cdot 10^7$  and  $2.5 \cdot 10^6$  electrons/cm<sup>2</sup>sec sterad at altitudes of 250 and 200 km, respectively. These measurement results indicate that the flux of photoelectrons is markedly attenuated with increasing depth of penetration in the atmosphere, approximately as shown in Table 31. These data correspond to the low level of solar activity which prevailed in 1962 and 1965. For high solar activity, the photoelectron flux may be higher, but no measurements are available.

TABLE 31. Vertical variation of the photoelectron flux

$h$ , km	700	300	150	130
Flux, erg/cm <sup>2</sup> sec	$\sim 1$	0.1	0.01	0.001

Note that although the photoelectron flux carries a high energy and should be taken into consideration at high altitudes, its ionization effects at  $h \leq \leq 200$  km are inferior to those of the electron stream with  $E = 1-10$  keV.

Having examined the main observation results, we will now proceed with an analysis of the physical processes which take place in the ionosphere and determine its state.



## Chapter V

### PHYSICAL PROCESSES IN THE IONOSPHERE

The properties of the upper atmosphere are quite unexpected in certain respects. An appropriate example is the relatively high temperature of the upper atmosphere which reaches 1000 — 2000°K and is higher than the ground temperature. The upper atmosphere is also highly ionized, and the term "ionosphere" is therefore synonymous with the upper atmosphere. At altitudes of  $h \approx 110$  km, the degree of ionization  $n_e/n$  reaches  $10^{-7}$  in daytime, whereas at  $h \approx 300$  km it is as high as  $10^{-3}$ . If the upper atmosphere were in thermodynamic equilibrium, temperatures of about 3000 and 4000°K would be needed to sustain the observed degree of ionization at altitudes of 110 and 300 km, respectively. These figures can be obtained from Saha's equation. However, Saha's equation is inapplicable to the upper atmosphere, which is in nonequilibrium conditions. The high temperature and the high degree of ionization are mainly due to the effect of the short-wave solar radiation.

In order to explain the complex behavior of the ionosphere, we first have to elucidate the mechanism of its formation, i. e., the exact nature of ionization. The balance equation for ionization in unit volume, which determines the concentration of charged particles  $n_i$  and its time dependence, has the form

$$dn_i/dt = q - r,$$

where  $q$  is the intensity or the rate of ionization,  $r$  is the number of recombinations in 1 cm<sup>3</sup> in 1 sec. The first task is thus to determine the values of  $q$  and  $r$  at various altitudes under various conditions. As the ionosphere extends from  $h \approx 50$  km to  $h \approx 500$  km, in a range of altitudes where the atmospheric density changes by ten orders of magnitude, we can naturally expect to encounter different processes in different parts of the ionosphere. We shall first consider the sources of ionization.

#### 19. Ionization by short-wave solar radiation

Theoretically, the general rate of ionization  $q$  in the ionosphere can be determined without much difficulties. In practice, however, the computation of  $q$  is not as simple as it would appear. The difficulties stem from lack of data on the cross sections of ionization and absorption processes, on the intensity and the spectrum of ionizing solar radiation, and on the density and composition of the upper atmosphere. A number of simplifying

assumptions therefore had been introduced, leading to the so-called theory of a simple layer, which was until recently the basic model for the processes of ionosphere formation. The situation has changed by now, however, and the processes of ion formation can be treated more rigorously.

## Elements of the theory of ion formation

The theory of ionization of the upper atmosphere by the short-wave solar radiation is based on two physical laws: the law of absorption of radiation and the law of ionization of gases.

Radiation of intensity  $I_\lambda$  [quanta/cm<sup>2</sup>sec] \* traversing an elementary layer of matter  $dh$  with particle concentration  $n$  [cm<sup>-3</sup>] is attenuated by the amount

$$dI_\lambda = -\sigma_\lambda I_\lambda n dh, \quad (V.1)$$

The proportionality coefficient  $\sigma_\lambda$  [cm<sup>-2</sup>] is called the effective absorption cross section. The law of elementary absorption of radiation in differential form is written for the upper atmosphere as

$$dI_\lambda = -\sigma_\lambda n I_\lambda \text{Ch } z_\odot dh, \quad (V.2)$$

where the dimensionless quantity  $\text{Ch } z_\odot$ , allows for the variation of the thickness of the atmosphere as a function of the zenith distance of the Sun  $z_\odot$ .

$\text{Ch } z_\odot$ , known as Chapman's function in geophysics, is called Bemporad's function in astronomy, after the person who first computed it in 1904 for the conditions of observation from the ground. Bemporad's computations cannot be used for different altitudes in the ionosphere, since, mainly because of the vertical variation of temperature in the atmosphere,  $\text{Ch } z_\odot$  depends on the altitude above sea level. Computations of  $\text{Ch } z_\odot$  with allowance for the vertical variation and the Earth's sphericity were carried out by Chapman in 1931 /475/. For  $z_\odot < 75^\circ$ ,  $\text{Ch } z_\odot \approx \sec z_\odot$ . For sunrise and sunset ( $z_\odot = 90^\circ$ ),  $\text{Ch } z_\odot$  on the ground is 38 whereas in the ionosphere at  $h > 150$  km it is 10 — 20, i. e., significantly lower.

The computations of  $\text{Ch } z_\odot$  for an isothermal atmosphere were extended for  $z_\odot > 90^\circ$  by Chapman in 1953 /476/ and by Wilkes in 1954 /477/. Their results are listed in Table 32. Bourne et al. /720/ and Swider /721/ allowed for the actual temperature gradient in the upper atmosphere in their computations. The corrections to  $\text{Ch } z_\odot$  for  $z_\odot \leq 105^\circ$  turned out to be insignificant, but in certain cases they must be taken into consideration. The largest corrections (10 — 13%) are observed for  $z_\odot = 85^\circ - 90^\circ$  between 120 and 180 km, where the temperature gradient is the highest.

Monochromatic ionizing radiation of wavelength  $\lambda$  and intensity  $I_\lambda$  creates  $q_\lambda$  pairs of ions in 1 cm<sup>3</sup> in 1 sec in a gas with a concentration of  $n$  particles/cm<sup>3</sup>:

$$q_\lambda = \sigma_{i\lambda} I_\lambda n. \quad (V.3)$$

The proportionality coefficient  $\sigma_{i\lambda}$  characterizes the ionizing power of the radiation of wavelength  $\lambda$  in the gas; it is called the effective ionization

\* In accordance with the established terminology, the term "intensity" is often used for the "flux" of quanta. The symbol  $F$  will be retained for the radiation flux in units of erg/cm<sup>2</sup>sec.

TABLE 32. Chapman's function  $\text{Ch } z_{\odot}$  for  $z_{\odot} \geq 70^\circ$ 

$z_{\odot} \backslash x$	50	100	150	200	250	300	350	400	450	500	600	700	800	900	1000
70°	2.615	2.744	2.797	2.825	2.843	2.856	2.865	2.872	2.877	2.882	2.889	2.893	2.897	2.900	2.902
71	2.718	2.864	2.924	2.957	2.978	2.992	3.003	3.011	3.017	3.023	3.030	3.036	3.040	3.044	3.046
72	2.830	2.996	3.064	3.102	3.126	3.143	3.155	3.165	3.172	3.178	3.188	3.194	3.199	3.203	3.206
73	2.952	3.140	3.219	3.263	3.291	3.310	3.325	3.336	3.345	3.352	3.363	3.370	3.376	3.381	3.385
74	3.084	3.298	3.390	3.441	3.474	3.497	3.514	3.527	3.538	3.546	3.559	3.568	3.575	3.581	3.586
75	3.228	3.473	3.580	3.640	3.679	3.706	3.726	3.742	3.754	3.765	3.780	3.791	3.800	3.807	3.812
76	3.386	3.667	3.792	3.863	3.909	3.942	3.966	3.985	4.000	4.012	4.031	4.045	4.055	4.064	4.070
77	3.558	3.883	4.030	4.115	4.170	4.210	4.239	4.262	4.280	4.295	4.318	4.335	4.348	4.358	4.366
78	3.748	4.125	4.298	4.400	4.468	4.516	4.552	4.580	4.603	4.621	4.650	4.671	4.687	4.700	4.710
79	3.958	4.396	4.604	4.727	4.810	4.869	4.914	4.949	4.977	5.000	5.036	5.062	5.083	5.099	5.112
80	4.189	4.704	4.953	5.104	5.205	5.279	5.336	5.380	5.416	5.445	5.491	5.525	5.551	5.572	5.590
81	4.447	5.052	5.355	5.541	5.668	5.762	5.833	5.890	5.936	5.974	6.034	6.079	6.113	6.141	6.164
82	4.734	5.452	5.822	6.054	6.216	6.335	6.428	6.502	6.562	6.613	6.692	6.752	6.799	6.836	6.867
83	5.055	5.912	6.368	6.662	6.870	7.026	7.148	7.246	7.327	7.395	7.503	7.585	7.650	7.702	7.745
84	5.416	6.445	7.015	7.391	7.663	7.870	8.034	8.167	8.278	8.372	8.523	8.639	8.732	8.807	8.870
85	5.824	7.068	7.788	8.277	8.638	8.918	9.144	9.330	9.486	9.620	9.838	10.008	10.144	10.257	10.352
86	6.287	7.804	8.722	9.368	9.857	10.246	10.563	10.830	11.058	11.255	11.580	11.839	12.051	12.228	12.378
87	6.816	8.679	9.867	10.735	11.412	11.963	12.425	12.819	13.162	13.463	13.970	14.384	14.730	15.024	15.277
88	7.421	9.731	11.290	12.477	13.437	14.242	14.933	15.538	16.075	16.556	17.388	18.087	18.686	19.209	19.670
89	8.119	11.009	13.084	14.743	16.139	17.351	18.426	19.392	20.272	21.080	22.523	23.784	24.905	25.914	26.830
90	8.928	12.580	15.388	17.758	19.846	21.735	23.472	25.090	26.609	28.046	30.719	33.177	35.466	37.615	39.648
91	9.873	14.535	18.401	21.868	25.091	28.148	31.086	33.935	36.717	39.446	44.789	50.030	55.211	60.362	65.505
92	10.982	17.001	22.421	27.628	32.771	37.929	43.150	48.468	53.906	59.485	71.132	83.522	96.753		
93	12.295	20.157	27.907	35.948	44.462	53.568	63.364	73.938	85.374	97.760	126	141	159		
94	13.858	24.257	35.575	48.371	63.032	79.920	99.422								
95	15.734	29.672	46.573	67.601	93.937	113		220							
96	18.003	36.950	62.792	98.546											
97	20.771	46.910	87.426	150			398		978						
98	24.175	60.809													
99	28.400	80.598													
100	33.692	107		714		4108		21690							

Remark.  $x = \frac{R+h}{H}$ , where  $h$  is the altitude,  $R$  the Earth's radius,  $H$  the scale height.

cross section. The rate of ionization  $q$  has the dimension  $[\text{cm}^{-3}\text{sec}^{-1}]$  and  $\sigma_{i\lambda}$  has the dimension  $[\text{cm}^2]$ .

Combining the laws of ionization (V.3) and absorption (V.2), we obtain the fundamental relation

$$q_{\lambda} = \frac{\sigma_{i\lambda}}{\sigma_{\lambda} \text{Ch } z_{\odot}} \left( \frac{\partial I_{\lambda}}{\partial h} \right), \quad (\text{V.4})$$

which shows that the rate of ionization depends on the gradient of the radiation intensity in the atmosphere.

In a mixture of gases, e.g., a mixture comprising  $\text{N}_2$ ,  $\text{O}_2$ ,  $\text{O}$ , ... with particle concentrations  $n_1$ ,  $n_2$ ,  $n_3$ , ..., the absorption of radiation is described by the modified expression

$$\frac{1}{I_{\lambda} \text{Ch } z_{\odot}} \frac{dI_{\lambda}}{dh} = - \sum_j \sigma_j n_j. \quad (\text{V.5})$$

This expression can be simplified by introducing the weighted average effective absorption cross section

$$\bar{\sigma}_{\lambda} = \sum_j \sigma_j \frac{n_j}{n}. \quad (\text{V.6})$$

A similar transformation can be applied to the rate of ionization  $q$ , replacing the cross section  $\sigma_{i\lambda}$  in (V.3) by the weighted average effective ionization cross section

$$\bar{\sigma}_{i\lambda} = \sum_j \sigma_{ij} \frac{n_j}{n}. \quad (\text{V.7})$$

TABLE 33. Ionization potentials  $\chi_i$  and the ionization limit  $\lambda_i$

Atom or molecule	$\chi_i$ , eV	$\lambda_i$ , Å	Atom or molecule	$\chi_i$ , eV	$\lambda_i$ , Å
NO	9.26	1340	N	14.55	852
O <sub>2</sub>	12.1	1026	N <sub>2</sub>	15.6	796
O	13.6	910			

If the entire spectrum of wavelengths is considered,  $q$  is more difficult to calculate. The ionizing radiation of the Sun has a wide spectrum extending from the ionization limit, which is fixed by the wavelength  $\lambda_i$  in the ultra-violet region  $\lambda \approx 1000$  Å (the wavelengths  $\lambda_i$  for various atmospheric components are listed in Table 33), to the X-ray region with wavelengths  $\lambda_r$  of a few angstroms. Thus, first, expression (V.3) is replaced by the integral

$$q(h) = n \int_{\lambda_r}^{\lambda_i} \bar{\sigma}_{i\lambda} I_{\lambda}(h) d\lambda. \quad (\text{V.8})$$

Second, at any given altitude for which  $q(h)$  is being considered, the radiation  $I_{\lambda}(h)$  is attenuated by the overlying atmospheric layers. Integration of (V.5) gives

$$I_{\lambda}(h) = I_{0\lambda} \exp \left\{ - \sum_j \sigma_j \int_h^{\infty} \text{Ch}_j(z_0, h) \cdot n_j dh \right\}, \quad (\text{V.9})$$

where  $I_{0\lambda}$  is the intensity of radiation outside the Earth's atmosphere.

Most of the short-wave solar energy is concentrated in emission lines. The integrals in (V.8) and (V.9) therefore can be replaced by sums over all the line wavelengths. The individual absorption bands should be allowed for in  $\sigma_{\lambda}$ .

#### Ionization cross section in the X-ray spectrum

The cross section  $\sigma_{i\lambda}$  in (V.3) should be considered separately for the hard region of the spectrum ( $\lambda < 150 - 250 \text{ \AA}$ ). This is particularly important for ionization in the  $E$  and  $D$  regions of the ionosphere. The effective ionization cross section is often identified with cross section for photoionization  $\sigma_{i\text{ph}}$ , which is incorrect. In ionization by relatively hard radiation with wavelengths shorter than about  $250 \text{ \AA}$ , most of the ions are not produced directly by photons but rather by the photoelectrons which these photons generate. If the radiation is sufficiently hard, the photoelectrons are capable of creating secondary electrons whose energies are high enough to cause further ionization of the atmospheric gases. This effect may be treated without going into details of subprocesses in view of the following experimental fact. In ionization by hard radiation, whatever it may be, the production of one pair of ions in a given gas requires on the average a fixed amount  $\epsilon$  of absorbed energy, which is independent of the energy  $E$  of the ionizing particle or quantum. Then

$$\sigma_i = \sigma_{i\text{ph}} E / \epsilon. \quad (\text{V.10})$$

The quantum energy  $E$  expressed in eV is related to the radiation wavelength  $\lambda$  in  $\text{\AA}$  by the equality  $E = 1.24 \cdot 10^4 \lambda^{-1}$ . Since for electromagnetic radiation with  $\lambda \lesssim 200 \text{ \AA}$ ,  $\epsilon = 32 \text{ eV}$ , we obtain

$$\sigma_i = 387 \sigma_{i\text{ph}} \lambda^{-1}. \quad (\text{V.11})$$

Nicolet and Aikin /480/ give a more complicated expression for very hard X rays with  $\lambda = 2 - 6 \text{ \AA}$ :

$$\bar{\sigma}_i / \sigma_{i\text{ph}} = (E - 500) / 35 = 355 / \lambda - 14.3. \quad (\text{V.12})$$

This further refinement, however, is not significant for most problems.

If the density and the composition of the atmosphere are known (i.e., a model of the atmosphere is given) and the spectrum of the ionizing solar radiation is available, relations (V.8) — (V.10) can be applied to compute the rates of ionization and heat release at any altitude in the upper atmosphere for different  $z_0$ . The values of  $\sigma_j$ ,  $\sigma_{ij}$ , and  $\epsilon$  needed in these computations are determined in laboratory. The complete solution of the problem requires the use of computers (the results of such computations are given in Section 25). Various approximate methods of solution for the problem of ionization in the upper atmosphere are considered below.

## Simple layer theory

The ionization of the upper atmosphere by the short-wave solar radiation was considered by Chapman in 1931 /475/. Chapman constructed the well-known simple layer theory which describes the ionosphere to first approximation. Although prior to Chapman this problem had been considered in detail by Pannekoek /481/, Kryuchkov /482/, and others, the simple layer theory is generally associated with Chapman's name.

The theory assumes an exponential distribution of the particle concentration  $n$  with altitude in the atmosphere:

$$n = n_0 e^{-h/H}, \quad (\text{V.13})$$

In this expression, the scale height does not depend on altitude ( $H = \text{const}$ ), and the atmosphere consists of a single species of particles. Moreover, the simple layer theory only considers monochromatic radiation ( $I_\lambda = I = \text{const}$ ). Under these conditions (V.3) and (V.9) give the following expression for the vertical distribution of  $q$ :

$$q(h) = \sigma_i n I_0 \exp(-\sigma H n \text{Ch } z_\odot). \quad (\text{V.14})$$

The function  $q(h)$  in the lower part of the atmosphere falls off rapidly with decreasing altitude (as a double exponential  $\exp[-\tau_0 e^{-h/H}]$ ), whereas in the upper part of the atmosphere, where the optical thickness  $\tau = \sigma H n \text{Ch } z_\odot \ll 1$ ,  $q(h)$  decreases with altitude in proportion to the atmospheric density. The last conclusion is also applicable to a more general case.

Thus, according to the simple layer theory, an ionized layer is formed in the atmosphere. The maximum of this layer is readily found to be at the altitude

$$h^{\max} = H \ln [\sigma H n_0 \text{Ch } z_\odot], \quad (\text{V.15})$$

which is determined by the condition

$$\tau = \sigma H n \text{Ch } z_\odot = 1. \quad (\text{V.16})$$

This follows from the equality  $dq/dh = 0$  by differentiating (V.14) or (V.3) and using (V.2) and (V.13). In the maximum of this layer,\* the rate of ionization, according to (V.2) and (V.4), is

$$q_{\max} = \eta_i \frac{1}{\text{Ch } z_\odot} \left( \frac{dI}{dh} \right)_{h^{\max}} = \frac{\eta_i I_0}{e H \text{Ch } z_\odot}, \quad (\text{V.17})$$

where  $\eta_i = \sigma_i / \sigma$  is the ionization efficiency. The distribution of electron concentration with altitude ( $n_e \propto \sqrt{q}$ ) in the layer maximum is roughly parabolic.

The simple layer theory provided an explanation for some simple regular features in the ionization of the upper atmosphere. Let us consider this in more detail, by analyzing (V.14) — (V.17).

\* Sometimes the term "ionization maximum" is used. We will avoid this ambiguous expression, however, and always indicate whether the maximum of  $q$  or the maximum of  $n_e$  is meant.

First, the value of  $q$  at a given altitude varies exponentially as a function of the zenith distance of the Sun  $z_0$  (which corresponds to the time of day),

$$q \propto \exp(-A \operatorname{Ch} z_0), \quad (\text{V.18})$$

where  $A$  is a constant which decreases with increasing altitude. In the layer maximum, the dependence of the rate of ionization on  $z_0$  is simpler:

$$q_{\max} \propto (\operatorname{Ch} z_0)^{-1}. \quad (\text{V.19})$$

As  $z_0$  increases, i.e., as the Sun sinks toward the horizon, the layer rises and becomes more diffuse. In this case, by (V.15),  $h^{\max}$  varies relatively slowly, as  $\ln \operatorname{Ch} z_0$ .

Second, for radiation of two wavelengths  $\lambda_1$  and  $\lambda_2$ , where  $\sigma_2 = 2\sigma_1$  and  $\sigma_{i2} = 2\sigma_{i1}$ , we have  $\tau_2 = 2\tau_1$ , therefore  $h_2^{\max}$  for the less penetrating radiation  $\lambda_2$  corresponds to a concentration  $n_2$  which is one half of the concentration  $n_1$ , i.e., it will be higher than  $h_1^{\max}$ . The profile  $q(h)$  will be shifted vertically, without changing its shape. A similar picture is observed in a more general case, when radiation components with different  $\sigma_\lambda$  are considered.

Third, if the scale heights  $H$  differ by a factor of  $k$  in two models of the atmosphere, the vertical scale of the profile  $q(h)$  will also change by a factor  $k$ , and both  $h^{\max}$  and  $q_{\max}$  will change.  $H$  has the same effect as  $\operatorname{Ch} z_0$ , i.e., as  $T$  increases,  $q_{\max}$  decreases and  $h^{\max}$  somewhat increases.

Fourth, the effect of another atmospheric parameter,  $n_0$ , is analogous to the effect of the effective cross section  $\sigma$ . It only shifts the profile  $q(h)$  vertically, without altering  $q$ .

The basic conclusions of the simple layer theory only strengthened the model of a layered ionosphere. To derive the three ionospheric layers  $E$ ,  $F_1$ , and  $F_2$ , three species of particles or different wavelength  $\lambda$  should be taken. Rocket measurements, however, do not bear out this layered structure.

Ionospheric observations of the daily variations of the electron concentration in  $E$  and  $F_1$  regions, as we saw in Chapter IV, confirm relation (V.19) indicating that  $q$  is approximately proportional to  $(\operatorname{Ch} z_0)^{-m}$ , although the power exponent  $m$  should be slightly greater than 1 for the  $E$  region and less than 1 for the  $F_1$  region. The simple layer theory is unable to account for these features, but they can be explained if we assume that the ionization of the atmosphere is produced by a wide spectral region (see Chapter VI). Measurements of the altitude of the  $E$  region indicate that it somewhat increases as the Sun approaches the horizon [483]. Qualitatively this fits the results of the simple layer theory, but more accurate measurements are needed for quantitative treatment.

Expressions (V.14) — (V.19) were derived under highly simplifying assumptions and are thus inadequate at this stage, mainly because the short-wave radiation of the Sun is definitely nonmonochromatic. Moreover, because of the variable temperature in the atmosphere and dissociation of  $O_2$ , the vertical distribution of concentration is no longer exponential and the model of a single-component atmosphere is an over-simplification. The simple layer theory thus only provides an approximate picture of the behavior of the ionosphere.

The shortcomings of the simple layer theory have now been apparent for a long time. They were discussed by Shchukin /478/, Kessenikh /479/, and others. Several attempts have been made to modify the simple layer theory by introducing the vertical variation of the temperature, the recombination coefficient, etc. These refinements, however, changed the basic results only slightly, since they retain the fundamental shortcomings of the simple layer theory.

### Radiation from a wide spectral region

One of the main limitations of the simple layer theory is the assumption of monochromatic ionizing radiation. The relation of this theory to the true picture can be compared to the reproduction of colored landscapes by black- and- white photography. The assumption of monochromatic radiation suggests that the ionization produced by radiation from a wide spectral region is equivalent to the ionization produced by monochromatic radiation of the same intensity having an appropriate effective wavelength. We will now show that this is not so. To this end, we will consider the distortion of the profile  $q(h)$  at altitudes below the maximum due to ionization by solar X rays with wavelengths of  $5.7 - 82 \text{ \AA}$ . The solution for  $q(h)$  can be obtained in analytical form in this case.

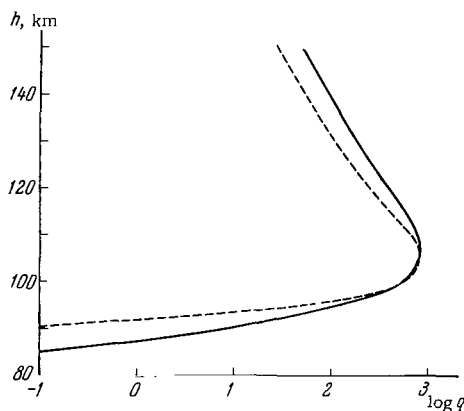


FIGURE 65. Vertical distribution of the rate of ionization. The rate of ionization has been computed for a wide range of X-ray wavelengths  $5.7 - 82 \text{ \AA}$  (the solid curve) and for monochromatic radiation with  $\lambda = 58 \text{ \AA}$  (dashed curve).

Figure 65 shows the  $q(h)$  profile for conditions of minimum solar activity and  $\text{Ch}_{\odot} = 1$ . The maximum value  $q_{\text{max}}$  is attained at an altitude of 106.5 km. The simple layer theory gives a  $q(h)$  profile with a maximum at the same altitude if we assume monochromatic radiation with  $\lambda = 58 \text{ \AA}$  and absorption cross section of  $4 \cdot 10^{-19} \text{ cm}^2$ . The  $q(h)$  profile computed from the simple layer theory has a narrower halfwidth and  $q$  is too low at high altitudes. These differences are quite clear from the figure, but it is not they that are



critical for the simple layer theory. The largest differences are observed in the bottom part of the profile, where the simple layer has a sharp "cutoff" from below. Already at altitudes of 90 km the difference in the values of  $q$  reaches 2.4 orders of magnitude, and at 85 km the simple-layer  $q$  will have decreased by another 10 orders of magnitude, whereas in reality it only drops by 2 orders of magnitude. The simple-layer theory thus gives an excessively steep gradient of  $q$  and  $n_e$  in the bottom part of the layer and is quite unusable for the description of ionization in the part of the ionosphere 1.5–2 scale heights below the layer maximum.

Although the simple layer theory predicts a double exponential decrease of  $q$  with decreasing altitude below the layer maximum, actual observations reveal a power dependence of  $q/n$  on  $N$ , specifically,  $q/n \propto N^{-\gamma}$  with  $\gamma = 5.5$ . This relation is highly significant for the theory of ionization of the bottom part of the ionosphere at  $h \leq 100$  km. It indicates that even for small variations of  $n$  with time of day, time of year, or latitude,  $q$  will change significantly, varying in counterphase with the concentration, due to the effect of the solar X-ray radiation; here  $q \propto n^{-4.5}$ .

In this example, the X-ray spectrum is characterized by a fairly steep drop of intensity  $I_\lambda$  with decreasing wavelength (and thus also as a function of the absorption cross section). At longer wavelengths, which are responsible for ionization between 100 and 200 km, the intensity is a more gradual function of  $\sigma$ . Therefore the deviation of the profiles  $q(h)$  and  $n_e(h)$  from those predicted by the simple layer theory becomes even more striking below the layer maximum and in the maximum as well (see Section 25).

### Ionization by radiation with $\lambda \geq 911 \text{ \AA}$

Two problems arising in connection with ionization by radiation at wavelengths  $\lambda \geq 911 \text{ \AA}$  require further refinement of the simple layer theory. One of these is related to the great number of narrow and strong bands in the absorption spectrum of molecular oxygen and nitrogen, whereas the other entails the effects of molecular nitrogen which absorbs these wavelengths without becoming ionized. The two problems are interrelated.

Consider a two-component atmosphere. One component (1) with concentration  $n_1$  and a scale height  $H_1$  absorbs the radiation and is ionized by it. For the second component (2) we take  $\sigma_2 \neq 0$  but  $\sigma_{i2} = 0$ . Its concentration is  $n_2$  and its scale height is  $H_2$ . For simplicity, we assume that both  $n_1$  and  $n_2$  have a barometric distribution  $n_j = n_{0j} e^{-h/H_j}$  with constant  $H_1$  and  $H_2$ . The absorption of radiation and the rate of ionization are written in this case in the form

$$I = I_0 \exp [-(\sigma_1 n_1 H_1 + \sigma_2 n_2 H_2) \text{Ch } z_0], \quad (\text{V.20})$$

$$q = \sigma_{i1} n_1 I = \frac{\sigma_{i1} n_1}{\sum_{j=1,2} \sigma_j n_j \text{Ch } z_0} \frac{\partial I}{\partial h}. \quad (\text{V.21})$$

To simplify the treatment, we consider monochromatic radiation and take  $\text{Ch } z_0 = 1$ . Let us find the maximum of  $q(h)$ . Differentiating (V.21), we get

$$\frac{\partial q}{\partial h} = q(-H_1^{-1} + \sigma_1 n_1 + \sigma_2 n_2) = 0. \quad (\text{V.22})$$

The layer thus has a maximum when

$$\tau^* = (\sigma_1 n_1 + \sigma_2 n_2) H_1 = 1, \quad (\text{V.23})$$

and this relation indicates how the altitude of the layer maximum increases when the absorbing component (2) is added to the atmosphere. Since the optical thickness of the atmosphere is determined by the absorption of both components, condition (V.23) is close to the equality  $\tau = 1$  (which is derived in the simple layer theory) only if  $H_1 \approx H_2$ . For molecular oxygen and nitrogen, the scale heights are indeed roughly equal. In general, the expression  $\tau = \sigma_1 n_1 H_1 + \sigma_2 n_2 H_2$  should be replaced by the expression  $\tau^* =$  which only contains the scale height for the ionized component.

Let us now consider the energy balance. In the simple layer theory, the total number of ions forming in an atmospheric column of  $1 \text{ cm}^2$  cross section, by (V.4), is

$$Q_0 = \int_0^\infty q \, dh = \frac{\sigma_i}{\sigma} \frac{I_0}{\text{Ch } z_\odot}. \quad (\text{V.24})$$

This expression shows that the total number of ions  $Q_0$  is determined by the number of radiation quanta hitting a horizontal surface and by the ionization efficiency  $\eta_i = \sigma_i/\sigma$ . Taking  $H_1 \approx H_2$  and integrating (V.21) over  $h$ , we find

$$Q = \frac{\sigma_{i1} \frac{I_0}{\sigma}}{\left( \sigma_1 + \frac{n_{02}}{n_{01}} \sigma_2 \right) \text{Ch } z_\odot}. \quad (\text{V.25})$$

Thus  $Q$ , unlike  $Q_0$ , is dependent on the relationship between  $\sigma_1 n_1$  and  $\sigma_2 n_2$ . For  $\sigma_2 n_2 \gg \sigma_1 n_1$ , we have  $Q \ll Q_0$ . In physical terms, this obvious conclusion indicates that when a strongly absorbing component is "mixed" into the atmosphere, the radiation is lost through absorption by this component, and is not used up in ionization.

If both components are ionized by the absorbed radiation, (V.21) and (V.23) are replaced by the more general expressions

$$q = (\bar{\sigma}_{i1} n_1 + \bar{\sigma}_{i2} n_2) I, \quad (\text{V.26})$$

$$(\sigma_1 n_1 + \sigma_2 n_2) H_1 = \frac{\bar{\sigma}_{i1} n_1 + \frac{H_1}{H_2} \bar{\sigma}_{i2} n_2}{\bar{\sigma}_{s1} n_1 + \bar{\sigma}_{s2} n_2}. \quad (\text{V.27})$$

Expression (V.27) for  $H_1 = H_2$  reduces to the standard condition (V.16)  $\tau = 1$ .

If the contribution of one of the atmospheric components to ionization is small ( $\bar{\sigma}_{i2} n_2 \ll \bar{\sigma}_{i1} n_1$ ), relation (V.27) reduces to the previous expression (V.23). The maximum  $q$  is then given by

$$q_{\max} = I_0 \bar{\sigma}_{i1} n_1 e^{-\alpha} / \text{Ch } z_\odot, \quad (\text{V.28})$$

where  $\alpha = 1 + \sigma_2 n_2 (H_2 - H_1)$ . Thus if  $H_2 \neq H_1$  and  $\sigma_2 n_2 (H_2 - H_1)$  is comparable with  $\tau^*$ ,  $q_{\max}$  is significantly less than in a one-component atmosphere.

Let us now consider in some detail the ionization of the atmosphere by radiation at wavelengths  $\lambda \geq 911 \text{ \AA}$ , which are absorbed by nitrogen molecules without ionizing them. At  $\lambda \geq 911 \text{ \AA}$ , the absorption spectrum of oxygen and nitrogen contains numerous deep absorption bands. The relationship between the effective absorption cross sections  $\sigma(\text{O}_2)$  and  $\sigma(\text{N}_2)$  inside the bands and between the bands is illustrated by Table 34. We see from the table that  $\sigma(\text{N})$  between the absorption bands is one and a half orders of magnitude less than the  $\sigma(\text{O})$  outside the bands.

TABLE 34. Mean effective absorption cross sections of  $\text{O}_2$  and  $\text{N}_2$  for  $\lambda \geq 911 \text{ \AA}$

Absorption cross sections	Between the bands	In the bands	In strong bands
$\sigma(\text{O}_2), \text{ cm}^2$	$3 \cdot 10^{-18}$	$2 \cdot 10^{-17}$	—
$\sigma(\text{N}_2), \text{ cm}^2$	$\sim 10^{-19}$	$3 \cdot 10^{-18}$	$\sim 2 \cdot 10^{-17}$

Since the concentration of  $\text{O}_2$  in the atmosphere at altitudes of 100 — 300 km is at least 0.1 of the  $\text{N}_2$  concentration, we find that the effect of nitrogen on ionization is negligible for wavelengths falling between the absorption bands, when  $\sigma(\text{N}_2)[\text{N}_2] \ll \sigma(\text{O}_2)[\text{O}_2]$ . However, wavelengths falling inside the absorption bands of nitrogen are effectively removed from the spectrum of ionizing radiation, not to mention the effect of the strong bands whose number is not less than the number of the medium intensity bands.

This effect is quite substantial, since analysis of the  $\sigma(\text{N}_2)$  cross section shows that only 35 — 40% of the spectrum between 911 and 1000  $\text{\AA}$  is free from absorption bands. Somewhat more favorable conditions are observed for radiation which corresponds to an  $\text{O}_2$  absorption band that coincides with an  $\text{N}_2$  absorption band, although such cases are rare.

For radiation in the nitrogen absorption bands we thus have  $\sigma_2 n_2 / \sigma_1 n_1 \approx 5 - 10$ . Hence it follows that only some 10% of the incident radiation is expended in the ionization of  $\text{O}_2$ . Moreover, the ionization maximum is displaced to higher altitudes, to the *E* region and higher. A large fraction of the solar radiation at  $\lambda \geq 911 \text{ \AA}$  (including the  $\text{L}_\gamma$  and  $\text{L}_\delta$  hydrogen lines) is thus mainly absorbed by molecular nitrogen and is effectively removed from the spectrum of ionizing radiation.

A similar picture is observed for radiation at 796 — 911  $\text{\AA}$ , which also falls above the ionization threshold of  $\text{N}_2$ . In this range, both molecular and atomic oxygen are ionized by the absorbed radiation, so that the fraction of radiation used up in ionization of atmospheric gases is increased. Nevertheless, some 50% of the radiation in the Lyman continuum (911—870  $\text{\AA}$ ) falls in strong absorption bands of  $\text{N}_2$  and is largely lost without causing ionization. The remaining wavelengths which are not absorbed by molecular nitrogen and are free to ionize oxygen are associated with an important effect which is considered in the next section.

#### Rate of production of various ions

Let us now consider the effect of the entire radiation spectrum on a multicomponent atmosphere. This treatment will lead to new interesting

effects which did not emerge in the simple layer theory. We will consider an idealized atmosphere consisting of only two species of molecules, which follow a common barometric distribution  $n = n_1 + n_2 = n_0 e^{-h/H}$ . Suppose that the first species of molecules ("nitrogen") is four times as abundant as the second species ("oxygen"), i. e.,  $n_1 = 4n_2$ . The entire spectrum of ionizing radiation is schematically partitioned into three parts: 0 — 82 Å (I), 82 — 911 Å (II), and 911 — 1030 Å (III).

As we have seen earlier in this section, the X-ray radiation at 5 — 82 Å, which carries some 5% of the total energy of the ionizing solar radiation, generates a layer I in the atmosphere with a maximum corresponding to fairly highly penetrating radiation with an effective cross section  $\sigma^I = 4 \cdot 10^{-19} \text{ cm}^2$ . We showed in Chapter I that most of the energy of the short-wave ionizing radiation (up to 85%) is concentrated between 82 and 911 Å. This radiation generates a thick layer at higher altitudes, since its equivalent effective cross section is  $\sigma^{II} \approx 2.5 \cdot 10^{-18} \text{ cm}^2$ . In an isothermal atmosphere, as it follows from (V.15), this radiation produces a layer at an altitude

which is higher by  $\Delta h = H \ln \frac{\sigma^{II}}{\sigma^I}$  than the altitude of layer I. Radiation III with  $\lambda \geq 911 \text{ Å}$ , which only ionizes the molecular oxygen, has the same cross section  $\sigma^{III} \approx 2.5 \cdot 10^{-18} \text{ cm}^2$  and carries about 10% of the ionizing energy. Since most of this radiation is absorbed mainly by "oxygen", whose concentration is 1/5 of the total concentration of particles in the atmosphere, the layer maximum is formed at altitudes which are  $\Delta h = H$  lower than in the previous case. According to radiation intensity data, the ratio of  $q_{\max}$  for the three layers, by (V.17), is  $q^I : q^{II} : q^{III} = 0.05 : 1 : 0.1$ . The combined profile  $q(h)$  and the three components computed approximately from the simple layer theory are shown in Figure 66a (each of the layers is actually more diffuse at the bottom, especially layer II).

Let us now find the composition of the ions generated at each altitude, remembering that radiation III only produces "oxygen" ions, whereas radiation I and II produces mainly "nitrogen" ions  $q_1 = \frac{4}{5}(q^I + q^{II})$  and only 20% as many "oxygen" ions  $q_2 = q^{III} + \frac{1}{5}(q^I + q^{II})$ . Figure 66b shows the profiles of the relative rates of production of the ions of both species,  $q_1/q$  and  $q_2/q$ . It is readily seen that at high altitudes, where the ionization is mainly produced by radiation II, the relative proportions of the "nitrogen" and "oxygen" ions correspond to the relative concentrations of the neutral components of the atmosphere. However, below a certain level, the fraction of "oxygen" ions starts increasing, and in the ionization maximum of radiation III their fraction is actually higher than the fraction of "nitrogen" ions. At these altitudes the anomalous value of the ratio  $q(\text{O}_2^+)/q(\text{N}_2^+)$  is one order of magnitude higher than the normal value (0.25). At lower altitudes, radiation I is the main ionizing agent, and the ions are formed in accordance with the relative concentrations of the atmospheric components. The ion ratio again approaches its normal value.

Introduction of the different spectral regions with different contributions to the ionization of oxygen and nitrogen thus brings out the existence of a layer with an anomalously high content of  $\text{O}_2^+$  ions. More detailed computer computations, to be considered in the next chapter, enable us to refine the numerical results and show that the anomalous  $\text{O}_2^+$  region approximately coincides with the E region or lies directly above it. This region should clearly have specific photochemical characteristics as well.

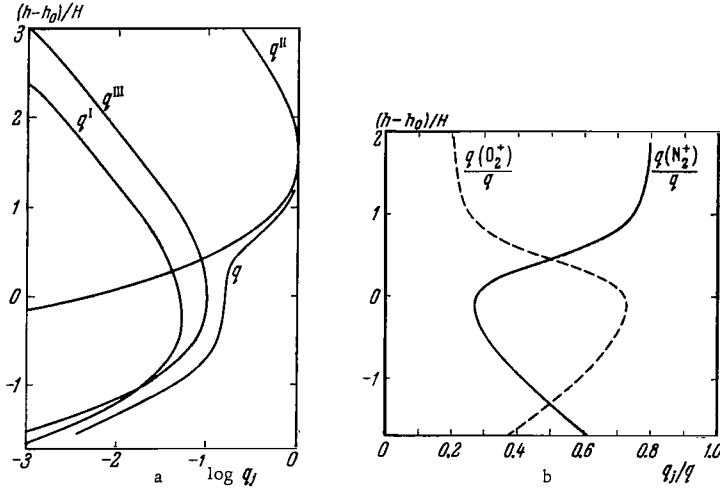


FIGURE 66. Vertical distribution of the overall rate of ionization  $q$  and the component rates  $q^I$ ,  $q^{II}$ ,  $q^{III}$  for three spectral regions:  $q^I$  for  $0 - 82 \text{ \AA}$ ,  $q^{II}$  for  $82 - 911 \text{ \AA}$ , and  $q^{III}$  for  $911 - 1030 \text{ \AA}$  (a). Vertical distribution of the relative rates of production of  $N_2^+$  (solid curve) and  $O_2^+$  (dashed curve) (b). The ratio  $q(O_2^+)/q(N_2^+)$  is anomalously high in the region  $(h - h_0)/H = 0$ .

Let us consider the diurnal behavior of this anomalous region. We have mentioned earlier that as  $z_0$  increases, the ionization layer rises and becomes more diffuse, whereas  $q_{\max}$  diminishes by a factor  $1/Chz_0$ . The anomalous region is therefore also expected to rise and to spread with increasing  $z_0$ . Therefore, at higher altitudes around noon, the ratio  $q(O_2^+)/q(N_2^+)$  should reach a minimum, whereas at lower altitudes this ratio conversely should have a midday maximum. The anomalous region thus seems to divide the ionosphere into two parts with reverse variation of the relative rate of ionization during the day. The consequences of this effect will be treated in the theory of formation of the ionosphere at altitudes of  $100 - 200 \text{ km}$  (Section 25).

### Specific rate of ionization

Let us consider some general features in the variation of  $q$  due to the changes in some of the ionization conditions. As we see from (V.8) and (V.9), the ratio  $q/n$  in general has the form

$$\frac{q}{n} = \sum_j \frac{n_j}{n} \int \sigma_{ij\lambda} I_{0\lambda} \exp \left\{ -N \sum_j \frac{N_j}{N} \sigma_{j\lambda} \cdot Chz_0 \right\} d\lambda, \quad (\text{V.29})$$

where  $N_j(h) = \int_h^\infty n_j dh \approx H_j n_j(h)$  is the number of particles of species  $j$  above the level  $h$  in an atmospheric column of  $1 \text{ cm}^2$  cross section. The ratio  $q/n$  in (V.29) is the specific rate of ionization computed per one particle.

In the simple layer theory, the expression for this quantity is

$$\frac{q}{n} = \sigma_1 I_0 \exp [-\sigma H n \text{Ch } z_0]. \quad (\text{V.30})$$

It follows from (V.30) that a change in  $I_0$  or  $\sigma_1$  by a certain factor leads to an equivalent change in  $q$ . If  $I_{0\lambda}$  and  $\bar{\sigma}_{1\lambda}$  were to change simultaneously in the entire spectrum, a similar conclusion would naturally remain valid in the general case too. However, changes in the solar activity during solar flares, the effect of solar eclipses, and even the regular variation of  $z_0$  during the day lead to different changes in  $I_\lambda(h)$  at different wavelengths. Therefore all these cases require a modified simple layer theory which, in some cases, can be accomplished fairly easily.

In the simple layer theory,  $q$  is an exponential function of  $\text{Ch } z_0$  and  $H$ . It is significant that  $q/n$  shows the same dependence on both  $\text{Ch } z_0$  and  $N$ . In other words, the vertical variation of  $q/n$  is interchangeable with its variation as a function of  $z_0$ . This interchangeability of  $N$  and  $\text{Ch } z_0$  is valid in the general case, as well as in the simple layer theory. However, the exponential dependence is replaced by a more complex functional relation if we are dealing with a wide radiation spectrum and a multicomponent atmosphere. We have previously computed the value of  $q/n$  for X-ray radiation. We have seen that for large  $N = 2 \cdot 10^{19} - 5 \cdot 10^{20} \text{ cm}^{-2}$ , the double exponential law is replaced by a slower power dependence,  $q/n \propto N^{-\gamma}$ , where  $\gamma \approx 5.5$ .

It is only in the most rigorous treatment, when the vertical variation of the composition of the atmosphere is taken into consideration, that the equivalence of  $N$  and  $\text{Ch } z_0$  breaks down. This is evident from (V.29). However, for the main part of the atmosphere extending below 110 km, the dependence of  $q/n$  on  $N$  and  $\text{Ch } z_0$  is virtually the same (within  $\pm 10\%$ ).

At sufficiently high altitudes, where the atmosphere is thin and hardly absorbs the short-wave radiation, i. e., when  $\tau = N\bar{\sigma}\text{Ch } z_0 \ll 1$ , expression (V.29) takes the much simpler form

$$\left(\frac{q}{n}\right)_\infty = \int \bar{\sigma}_{1\lambda} I_{0\lambda} d\lambda. \quad (\text{V.31})$$

Here the ratio  $q/n$  is virtually independent of altitude, which explains the subscript  $\infty$ . The vertical variation of the atmospheric composition however does have a certain effect, which can be taken into consideration if desired. The ratio  $(q/n)_\infty$  is almost uniquely related to the integral  $\int I_{0\lambda} d\lambda$ , and therefore either quantity can be used to assess the other. For low solar activity, some data give for  $(q/n)_\infty$  an average value of  $4 \cdot 10^{-7} \text{ sec}^{-1} / 484\%$ , whereas other data give  $(2.5 - 3.5) \cdot 10^{-7} \text{ sec}^{-1} / 485\%$ . In epochs of high activity, the short-wave radiation is approximately 3—4 times stronger, so that the ratio  $(q/n)_\infty$  should be a factor of 3—4 higher.

It follows from (V.31) that at high altitudes

$$q \propto n. \quad (\text{V.32})$$

This indicates that variations in atmospheric density during the day, as a result of changes in solar and geomagnetic activity (see Section 17), should produce equivalent variations in  $q$ . In particular, as the density and the temperature of the atmosphere increase daily at 1600 hrs local time

(compared with periods of low activity),  $q$  should increase while the gradient  $\partial \ln q / \partial h$  should diminish.

### The energy problem of the ionosphere

One of the first topics to be tackled in connection with the formation of the ionosphere is the question of the energy needed to sustain ionization. Let us consider the various energy estimates and the related parameter  $Q$ , which gives the total number of ions forming in an ionosphere column of  $1 \text{ cm}^2$  cross section. In the simple layer theory, for given  $z_0$ ,  $Q_0$  is only determined by the product  $\eta_i I_0$ , as we see from (V.24). In a more general case,  $q_\lambda dh$  from (V.4) has to be integrated making use of (V.6) and (V.7). Since the composition of the atmosphere remains fairly constant within the main part of the layer produced by radiation of wavelength  $\lambda$ , we may take  $N = nH$  and proceed with integration of (V.4):

$$Q_\lambda = \frac{\sum_j \sigma_{ij\lambda} n_{j/n}}{\sum_j \sigma_{j\lambda} N_{j/N}} \frac{I_{0\lambda}}{\text{Ch } z_0}. \quad (\text{V.33})$$

For different  $\lambda$ , the ionization layer forms at different altitudes, and the atmospheric composition correspondingly differs. In practice, however, these refinements can be ignored since, first,  $n_{j/n} \approx N_{j/N}$  (these quantities occupy equivalent positions in the numerator and the denominator in (V.33)) and, second, short-wave solar radiation ionizes the atmospheric gases within a relatively narrow range of altitudes. Expression (V.24) derived in the simple layer theory is therefore satisfied with an error not exceeding  $\pm 25\%$ .

In ionospheric research, for  $\text{Ch } z_0 = 1$ , we generally take

$$Q = I, \quad (\text{V.34})$$

where  $Q = \int Q_\lambda d\lambda$  and  $I = \int I_\lambda d\lambda$ . It is thus assumed that on the average  $\eta_i = 1$ . Strictly speaking, this is not so, however. In (V.33), the coefficient before  $I_{0\lambda}$  constitutes some weighted-average effective ionization coefficient. Detailed analysis of  $\sigma$  and  $\sigma_i$  and of the atmospheric composition shows that this parameter is indeed close to unity for radiation between 250 and 660 Å. It is only for  $\lambda > 750 \text{ Å}$ , as we saw in the previous section, that it may be significantly less than unity, owing to the effect of the  $\text{N}_2$  absorption bands. Moreover, in this part of the spectrum we have  $\sigma_i/\sigma < 1$ . This, however, is compensated by the higher than 1 value of this ratio in the X-ray region of the spectrum, for  $\lambda \lesssim 250 \text{ Å}$  (where  $\sigma_i/\sigma > 1$ ). Therefore, the assumptions that  $Q = I$  and that on the average the effective ionization coefficient is  $\eta_i \approx 1$  do not introduce large errors, as the radiation at  $\lambda \lesssim 250 \text{ Å}$  and  $\lambda \gtrsim 600 \text{ Å}$  on the whole accounts for as little as  $\lesssim 30\%$ .

Therefore, although the simple expression (V.34) was derived under highly simplifying assumptions, more rigorous analysis shows that it should apply to within a factor of 1.5. In the next chapter, detailed numerical results will show that (V.34) is accurate to within  $\pm 10\%$ .

We will first give some heliophysical and then ionospheric estimates of  $Q$ . All the available rocket and satellite measurements of the intensity of the short-wave solar radiation were analyzed in detail in Chapter I. For low solar activity, the total radiation flux is  $F = 2.5 \text{ erg/cm}^2 \text{ sec}$  or  $I = 5.5 \times 10^{10} \text{ quanta/cm}^2 \text{ sec}$ . For high solar activity, no such detailed and reliable measurements are available. However, data on the intensity of individual emission lines as a function of solar activity suggest (see Chapter II) that in epochs of maximum solar activity the intensity of the ionizing radiation increases by a factor of 3–4. For  $Q = I$  we thus obtain estimates of  $5.5 \cdot 10^{10} \text{ cm}^{-2} \text{ sec}^{-1}$  and  $\sim 2 \cdot 10^{11} \text{ cm}^{-2} \text{ sec}^{-1}$  in periods of low and high solar activity, respectively.

Ionospheric research requires the total number of recombinations  $R$  in a column of  $1 \text{ cm}^2$  cross section. Conditions of quasi-equilibrium give  $R = Q$ . Ionospheric data yield various estimates for  $R$ . The differences are mainly due to the large scatter of the values of the effective recombination coefficient.

TABLE 35. Number of recombinations  $R [\text{cm}^{-2} \text{ sec}^{-1}]$  for different ionospheric regions and the total  $R$

Author and reference	Year	E	Region		Total R
			$F_1$	$F_2$	
Appleton /486/ Bates and Massey /154, 487/	1937			$1 \cdot 10^9$	
	1946	$6 \cdot 10^8$	$2 \cdot 10^9$	$1.5 \cdot 10^9$	$4 \cdot 10^9$
Mitra /488/	1952	$6 \cdot 10^8$	$1.8 \cdot 10^9$	$1.5 \cdot 10^9$	$3.9 \cdot 10^9$
Al'pert /489/	1960	$3 \cdot 10^8$	$(0.5 - 1) \cdot 10^9$	$(2 - 20) \cdot 10^9$	$(3 - 20) \cdot 10^9$

Table 35 lists some of the more popular estimates of  $R$  for different ionospheric regions. Similar figures were published by other authors. Allen /490/ found that  $R$  depends on the solar activity and for minimum activity  $R \leq 4 \cdot 10^9 \text{ cm}^{-2} \text{ sec}^{-1}$ , whereas for maximum activity in 1948 Al'pert /491/ obtained a result which was higher by almost one order of magnitude,  $(1.6 - 2.5) \cdot 10^{10} \text{ cm}^{-2} \text{ sec}^{-1}$  or  $1 - 1.5 \text{ erg/cm}^2 \text{ sec}$ . These data were regarded as too high /490/, although in fact they are one order of magnitude lower than the rocket data ( $Q = I \approx 2 \cdot 10^{11} \text{ cm}^{-2} \text{ sec}^{-1}$ ).

The data of Table 35 are generally interpreted as indicating that an energy flux of  $F = 0.1 \text{ erg/cm}^2 \text{ sec}$  is required to sustain the state of ionization in the daytime ionosphere. Since an individual ionization event, according to the latest data, requires an energy of  $\varepsilon = 32 \text{ eV}$ ,  $R = 4 \cdot 10^9 \text{ cm}^{-2} \text{ sec}^{-1}$  gives more precisely  $F = 0.2 \text{ erg/cm}^2 \text{ sec}$ . The earlier ionospheric estimates of the short-wave radiation flux for both low and high solar activity were thus approximately one order of magnitude lower than the rocket and satellite findings. This effect will be considered in more detail in Section 21 in connection with the effective recombination coefficient.

Note that according to Table 35 most of the radiant energy is expended in ionizing the regions  $F_1$  and  $F_2$ , and only 10–15% is used up in region E. According to Al'pert /489/, however, most of the radiant energy is used up in ionizing the  $F_2$  region only. We have observed before in this section that most of the short-wave solar radiation is indeed expended in ionization processes at altitudes of  $h \approx 150 \text{ km}$ , i. e., between regions E and  $F_1$ .



If we find the rates of ionization and recombination in the ionosphere and determine the energy required for sustaining the state of ionization, we will have solved the fundamental problem in the theory of formation of the ionosphere which is related to a number of significant questions concerning the basic elementary processes in the ionosphere, the mechanism of nocturnal ionization, etc. We have seen that there are two different approaches to the solution of this problem. The earlier theories of the ionosphere used substantially lower fluxes of ionizing energy than the findings which emerge from recent rocket and satellite measurements. Correspondingly, there are old and new approaches to the effective recombination coefficient, to the nocturnal source of ionization, to the rate constants of the fundamental elementary processes, etc.

We have thus dealt with the general aspects of ionization in the upper atmosphere due to short-wave solar radiation. Recent advances in the research of the upper atmosphere, mainly associated with rocket and satellite measurements, made quite clear the inadequacy of the simple layer theory in its original form for the description of the ionization processes in the ionosphere. We have discussed the main limitations of the simple layer theory and advanced some generalizations which allow for the polychromaticity of the ionizing solar radiation, and the multicomponent constitution of the upper atmosphere. A more rigorous analysis of the theory of ionization enables us to approach in greater detail the processes of ionization in the ionosphere.

To complete our picture of the various sources which affect the state of ionization in the ionosphere, we will now consider ionization by corpuscular streams and cosmic rays.

## 20. Corpuscular radiation

### Computation of the ionization effect

Energetic particles, as well as short-wave solar radiation, contribute to the ionization of the upper atmosphere: corpuscular electron streams play a significant role at auroral latitudes, whereas proton streams are active in the region of the polar cap. Ionization by galactic cosmic rays and injected particle streams is significant for the *D* region of the ionosphere; during chromospheric flares, ionization by solar cosmic rays must not be ignored for this region. The rate of ionization by a corpuscular stream (like that by a stream of quanta) is defined by the relation

$$q = \sigma_i n p(E) dE, \quad (\text{V.35})$$

where  $\sigma_i$  is the effective ionization cross section,  $n$  is the concentration of atmospheric particles, and  $p(E)dE$  is the flux of particles ( $\text{cm}^{-2} \text{sec}^{-1} \text{eV}^{-1}$ ) with energy (eV) between  $E$  and  $E + dE$ . For energetic particles, however, the law of absorption  $dI = -\sigma I n dh$  does not apply, since, unlike photons, particles are not absorbed in matter but gradually lose their energy through production of numerous secondary electrons of lower energies. This process is similar to the passage of quanta of X-ray radiation of wavelengths shorter than 200 Å through matter, but it is more complex. The complexity stems

from the fact that we have to take account of the ionization produced by the particles at the end of their range. We will give some simple formulas which can be applied to assess the effect of ionization of the upper atmosphere by electrons and protons.

The range  $\rho_i$  is a common concept used in describing the interaction of particles with matter. The range is the path length that a particle of given energy traverses in a given medium; it is characterized by the quantity of matter in the layer traversed by the particle, so that  $\rho_i$  is expressed in units of g/cm<sup>2</sup>. The range depends not only on the particle species and the energy  $E$  but also, to a certain extent, on the properties of the material medium.

To compute the effect of corpuscular ionization in the atmospheric layers that lie above the level determined by the particle range, we require, as it follows from (V.35), only the differential energy spectrum  $p(E)$  and the effective ionization cross sections. Some values of  $\sigma_i$  are listed in Table 36 (based on Figure 49 in /106/, Tables 5 and 6 in /493/, and Table 20 in /154/). In corpuscular ionization processes, the effective cross section  $\sigma_i$  is often replaced by the so-called ionization coefficient

$$f(E) = \sigma_i n/\rho.$$

The function  $f(E)$  gives the number of ion pairs produced by a particle of energy  $E$  traversing 1 g of matter of density  $\rho$ .

TABLE 36. Effective cross sections for ionization by electrons (in megabarns =  $10^{-18}$  cm<sup>2</sup>)

Energy, keV	N <sub>2</sub>	O <sub>2</sub> *	Air	Energy, keV	Air
0.014	—	6	—	3	85
0.020	20	41	—	5	70
0.030	104	118	110	10	35
0.050	222	218	220	20	18
0.10	287	289	290	30	12
0.20	252	264	260	50	9
0.30	212	220	220	100	5.5
0.50	155	161	160	200	3.5
0.70	122	125	125	300	2.7
1.0	—	—	93	500	2.2
2	—	—	90	1000	1.9

\* These data are borne out by new measurements /735/.

Let us consider a flux of electrons with  $E \geq 1$  keV hitting the Earth's atmosphere from the upper hemisphere (a similar analysis is obviously applicable to protons). Only electrons of energies  $\geq E'$ , characterized by the range  $\rho_i$ , will penetrate to a level  $h$  in the atmosphere. The total rate of ionization at a given altitude  $h$  is

$$q(h) = 2\pi\rho \int_{E'(h)}^{\infty} p(E) f(E) dE. \quad (\text{V.36})$$

It is assumed that the spectrum  $p(E)$  does not change as the electron stream passes through the atmosphere. This assumption is only approximately true.

A relationship between  $E'$ ,  $\rho_l$  and the altitude  $h'$  to which the electrons penetrate into the atmosphere is given in Table 37 based on Spencer's data /494, 495/.

TABLE 37. The range  $\rho_l$  and the penetration altitude  $h'$  for electrons

$E', \text{ keV}$	$\rho_l, \text{ g/cm}^2$	$h', \text{ km}$	$\rho_H, \text{ g/cm}^2 / 538/$	$E', \text{ keV}$	$\rho_l, \text{ g/cm}^2$	$h', \text{ km}$	$\rho_H, \text{ g/cm}^2 / 538/$
0.3	$1.3 \cdot 10^{-5}$	130	$5 \cdot 10^{-7}$	30	$2.0 \cdot 10^{-2}$	88	$1.26 \cdot 10^{-3}$
1	$\sim 8 \cdot 10^{-6}$	135	$4.6 \cdot 10^{-6}$	50	$4.9 \cdot 10^{-2}$	83.5	—
2.6	$5 \cdot 10^{-5}$	$\sim 115$	$2.3 \cdot 10^{-5}$	70	$8.8 \cdot 10^{-2}$	80.5	—
3	—	—	$2.8 \cdot 10^{-5}$	100	$1.6 \cdot 10^{-1}$	77.5	—
5	$\sim 10^{-4}$	107	$6.7 \cdot 10^{-5}$	200	$5.1 \cdot 10^{-1}$	71	—
7	—	—	$1.13 \cdot 10^{-4}$	300	$9.5 \cdot 10^{-1}$	67	—
10	$2.9 \cdot 10^{-4}$	98.5	$2.05 \cdot 10^{-4}$	400	0.15	63	—
20	$\sim 10^{-3}$	92	$6.35 \cdot 10^{-4}$	1000	$\sim 0.5$	55	—

The range  $\rho_l$

Actual computations require knowledge of the range  $\rho_l$  as a function of the electron energy. Lack of experimental data for  $E \lesssim 5 \text{ keV}$  makes our  $\rho_l$  values highly unreliable, and they have been recently reviewed by a number of authors. The often quoted work of Anderson and Enemark /496/ gives the relation  $\rho_l = E/2000$  ( $E$  in keV). In 1963 Maeda /497/ used a different relation,  $\rho_l \propto E^{1.96}$ . In 1965 he revised his computations of  $\rho_l$  /498/ and for energies between 2.5 and 5 keV obtained values which were a factor of 2—4 higher than the original 1963 data. Rees /499/ in his first work used the approximation

$$\rho_l = 4.57 \cdot 10^{-6} E^{1.76} \quad (\text{V.37})$$

for the entire energy range 0.4—300 keV. And yet the original measurements referred to energies between 5 and 50 keV and this approximation is invalid for  $E < 7 \text{ keV}$ . Later Rees /500/ revised his figures for  $\rho_l$  and for  $E = 0.3 \text{ keV}$  obtained results which were almost one order of magnitude lower than those emerging from (V.37).

Makhov /501/ used new laboratory findings to derive an expression for the attenuation of an electron beam in matter. For the normal range of electrons  $\rho_n$  (this is the mass which attenuates the intensity of the electron beam to  $1/e$ ), an analytical dependence on the parameters of the material medium and the electron energy can be fitted. Makhov's results were applied by Lazarev /502/ to determine the attenuation of an electron beam in the upper atmosphere. For the normal range  $\rho_n$  he obtained

$$\rho_n = 4.6 \cdot 10^{-6} \cdot E^{1.65} \text{ (in keV)}, \quad (\text{V.38})$$

and this relation is virtually identical to (V.37) for  $E \sim 1 \text{ keV}$ . We see from Table 37 that  $\rho_n$  is approximately  $3/2 - 1/2$  of the  $\rho_l$  from /494, 495/ for  $E \geq 1 \text{ keV}$ , whereas for  $E < 1 \text{ keV}$  it is substantially higher than Rees's new data /503/.

## A power spectrum of electrons

The effect of ionization by a stream of electrons is easily computed for a power spectrum  $p(E) \propto E^{-\gamma}$ . Using (IV.19), (IV.20), and (V.36), we find immediate relations between the rate of ionization  $q$  at a given altitude  $h$ , the effective energy  $E_{ef}$ , the integral electron flux  $P(\geq E_{ef})$ , and the energy  $w$  of the electron stream:

$$q(h) = 2\pi p \int_{E'}^{\infty} p f dE = 2\pi p p(E_{ef}) f(E_{ef}) \delta E_{ef}, \quad (V.39)$$

$$P(\geq E_{ef}) = 2\pi \int_{E'}^{\infty} p dE = 2\pi (\gamma - 1)^{-1} p(E_{ef}) E_{ef} \approx \frac{q(\gamma - 1)^{-1}}{p f \delta}, \quad (V.40)$$

$$w = 2\pi \int_{E'}^{\infty} p E dE = 2\pi \beta \cdot E_{ef}^2 p(E_{ef}) = \beta (\gamma - 1) E_{ef} P(\geq E_{ef}); \quad (V.41)$$

here  $E_{ef} \approx E'$ , where  $E'$  is the energy of electrons penetrating to the altitude  $h$ ;  $\beta = (\gamma - 2)^{-1}$  and  $\delta \approx (\gamma - 1/2)^{-1}$  for  $E = 1 - 10^3$  keV, since the coefficient  $f(E)$  is inversely proportional to  $\sqrt{E}$ . These expressions were published in /504/.

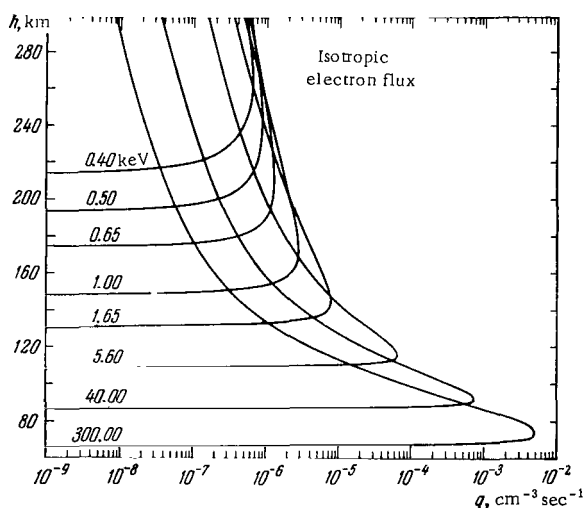


FIGURE 67. Vertical distribution of the rate of ionization per electron for monoenergetic electrons of different energies /499/.

Approximate computations often use the relation

$$w \approx E_b P(\geq E_b), \quad (V.42)$$

where  $E_b$  is the minimum energy of electrons in a power spectrum. As we see this relation gives a significant error for  $\gamma \sim 2.5$  and it is in fact inapplicable for  $\gamma \leq 2$ .

More precise computations of the profile  $q(h)$  which allow for the variation of the electron spectrum in the atmosphere were carried out by Rees /499, 500, 503/. Figure 67 shows the results of his computations, which are now often used in aeronomy. As we have seen before, the ranges used in this work require further refinement for  $E < 3$  keV.

The altitude  $h^{\max}$

Some problems do not require knowledge of the detailed features of  $q(h)$ , and some information about the maximum rate of ionization  $h^{\max}$  and the corresponding altitude  $q_{\max}$  is sufficient. Three quite different spectra are capable of producing a maximum on the  $q(h)$  profile: 1) a monoenergetic spectrum, 2) a power spectrum  $E^{-\nu}$ , and 3) an exponential spectrum  $\exp[-E/E_0]$ . These are in fact the three spectra which are mostly used in theoretical studies.

Knowledge of the range for a given electron energy enables us to estimate the altitude  $h^{\max}$  at which the profile  $q(h)$  develops a maximum. For an isotropic flux and for vertical incidence of a stream of monoenergetic electrons,  $h^{\max}$  should obviously somewhat differ. Different  $h^{\max}$  are also obtained for different electron spectra. The computations of Rees /499, 500, 503/ and others show that for  $E > 0.3$  keV,  $h^{\max}$  is always determined by the depth of penetration  $h'$ . For an exponential spectrum

$$h^{\max} \approx h'(E_0), \quad (\text{V.43})$$

for a monoenergetic beam

$$h^{\max} \approx h' + H, \quad (\text{V.44})$$

where  $H$  is the scale height. For a power spectrum with a cutoff at some energy  $E_b$ ,  $h^{\max}$  is approximately the same as for monoenergetic electrons of energy  $E_b$ .

TABLE 38.  $h^{\max}/108/$  and  $h' + H$

$E$ , keV	0.4	0.65	1.0	3.0	10	30	40	100	300	1000
$h^{\max}$ , km	270	210	163 — 170	126	106 — 108	94	90	84	71	—
$h' + H$ , km	150	—	145	~120	106	94	91	84	73	61

In Table 38, the values of  $h^{\max}$  computed by Rees /499/ for a monoenergetic electron beam (the lower values correspond to a vertical beam, and the higher to an isotropic beam) are compared with the values of  $h' + H$ , where  $h'$  is the altitude from Table 37 and  $H$  is the scale height. Clearly,  $h' + H$  and  $h^{\max}$  virtually coincide everywhere, except the energies  $E \lesssim 3$  keV. At these energies,  $h^{\max}$  and  $h' + H$  do not coincide only because Rees used approximation (V.37) whereas the values of  $h'$  in Table 37 are Spencer's.

A comparison of the different sets of data shows that more attention should be paid to the approximate selection of the dependence of  $\rho_i$  on  $E$  than on the choice of the spectrum or the accuracy of the computations.

## Estimating $q_{\max}$

Let us now determine the maximum rate of ionization  $q_{\max}$ . As indicated in Section 18, the power loss is one of the most important characteristics of the injected particles. Most of the energy of a fast particle is expended in ionization and heating of the upper atmosphere. The effective ionization is estimated in terms of the rate of ion formation  $q$ . Each ionization event requires an average energy of  $\epsilon_0$ , which is approximately equal to 32 eV for atmospheric gases. The total rate at which a particle stream loses energy through ionization, heating, and excitation of atmospheric components is thus proportional to the integral rate of ion formation in an atmospheric column of  $1 \text{ cm}^2$  cross section, i. e.,  $\int q \epsilon_0 dh$ . Identical particle fluxes may evidently show different rates of energy loss in the atmosphere, depending on the particle energy  $E$  and the distribution over the pitch angles  $\theta$ . Injected particles are completely absorbed in the atmosphere after they have lost their entire energy,

$$w = \int_0^{\infty} p(E) E dE.$$

We thus have for these particles

$$\int_{h'(E_{\max})}^{\infty} q dh = \frac{w}{\epsilon_0}, \quad (\text{V.45})$$

since the entire energy of the electrons is absorbed above the level of penetration of electrons with the maximum energy  $E_{\max}$ . Estimates often make use of the fact that most of the ions form near the ionization maximum,

i. e.,  $\int q dh = q_{\max} \Delta h$ . Rees's computations [499] for monoenergetic electrons show that the profile  $q(h)$  has a halfwidth  $\Delta h \approx 2H$ . In other cases, this is only approximate.

Using (V.45), we obtain the simple relation

$$q_{\max} \lesssim \frac{w}{\epsilon_0 2H}. \quad (\text{V.46})$$

Expressing  $H$  in km and  $w$  in  $\text{erg/cm}^2 \text{ sec}$ , we find an expression

$$q = 1.5 \cdot 10^4 \left[ \frac{7.5}{H} \right] w, \quad (\text{V.47})$$

which is highly convenient for approximate estimates.

For an exponential spectrum  $A \exp [-E/E_0]$ , exact computations are very difficult, and the above approximate relations have to be used. The value of  $w$  for an exponential spectrum  $A \exp [-E/E_0]$  is conveniently computed from the following expressions:

$$\begin{aligned} w &= \int_0^{\infty} A E \exp \left[ -\frac{E}{E_0} \right] dE = (A E_0) E_0, \\ &\int_{E_0}^{\infty} A E \exp \left[ -\frac{E}{E_0} \right] dE = \frac{2}{3} w. \end{aligned} \quad (\text{V.48})$$

These relations make use of the fact that the integrand has its maximum  $AE_0 e^{-1}$  for  $E = E_0$  and the halfwidth of the maximum is  $\Delta E = 2.5E_0$ .

## Examples

Let us consider a few examples of application of the above formulas. As we saw in Section 18, most of the energy is concentrated in electrons with  $E = 1-10$  keV. The spectrum of these electrons is roughly exponential,  $\exp[-E/E_0]$  with  $E_0 \approx 3-5$  keV. We thus obtain  $h^{\max} = 110-120$  km, which corresponds to the  $E$  region of the ionosphere. Taking for daytime conditions  $w \approx 0.3$  erg/cm<sup>2</sup>sec, we find that the electron stream gives  $q_{\max} \approx 3 \cdot 10^3$  cm<sup>-3</sup> sec<sup>-1</sup>. This figure is comparable with the rate of ionization in the  $E$  region caused by solar radiation.

At night, for  $h \leq 150$  km, the flux  $w$  is  $10^{-3}-10^{-2}$  erg/cm<sup>2</sup>sec, which gives  $q_{\max} = 10-10^2$  cm<sup>-3</sup> sec<sup>-1</sup>; the equilibrium electron concentration is  $n_e = (1-3) \cdot 10^4$  cm<sup>-3</sup>. These are typical values for a night ionosphere in the  $E$  region at middle latitudes in a period of high solar activity. For low solar activity,  $w$  will be lower by one order of magnitude for electrons with  $E \geq 3$  keV, and in the auroral zone it will be approximately two orders of magnitude higher /810/.

TABLE 39. Ionization of  $D$  region by electrons

$h$ , km	70	80	90
$E_{ef}$ , keV	$\sim 300$	$\sim 100$	$\sim 30$
$P(\geq E_{ef})$ , cm <sup>-2</sup> sec <sup>-1</sup>	10	$10^2$	$10^3$
$n$ , cm <sup>-3</sup>	$2.5 \cdot 10^{15}$	$5 \cdot 10^{14}$	$10^{14}$
$\sigma_i$ , cm <sup>2</sup>	$2.5 \cdot 10^{-18}$	$6 \cdot 10^{-18}$	$10^{-17}$
$q$ , cm <sup>-3</sup> sec <sup>-1</sup>	0.05	0.3	1

We saw in Section 18 that for  $E \geq 30$  keV the electrons have a power spectrum (with  $\gamma \geq 3$ ). The integral electron flux  $P$  for  $E \geq 30$ ,  $E \geq 100$  and  $E \geq 300$  keV in daytime at middle latitudes is apparently not less than  $10^3$ ,  $10^2$ , and  $10$  electrons/cm<sup>2</sup>sec, respectively. Range data (Table 37) indicate that electrons with  $E = 30-300$  keV reach  $h \approx 70-90$  km, i. e., the main part of the  $D$  region. The results obtained from the relation  $q \approx Pn\sigma_i$  according to (V.35) for this case of a minimum electron flux are presented in Table 39.

Let us consider ionization by cosmic rays. At altitudes  $h \geq 30$  km, where the absorption of cosmic rays is negligible, they create ionization rates  $q$  proportional to the density of the atmosphere  $\rho$ . At the geomagnetic equator, according to new data /505/, we have

$$q \approx 10^5 \rho \approx 5 \cdot 10^{-18} n, \quad (\text{V.49})$$

where  $n$  is the concentration of particles in the atmosphere. The rate  $q$  increases with latitude, and at geomagnetic latitude of  $60^\circ$  it is an order of magnitude higher than on the equator.

At  $h = 15 - 25$  km, the interaction of cosmic rays with the atmosphere is highly effective. At these altitudes Pfitzer's maximum is observed, with ion concentrations  $n_i \approx 6 \cdot 10^3 \text{ cm}^{-3}$  /506/ and corresponding ionization rates  $q \approx 50 \text{ cm}^{-3} \text{ sec}^{-1}$ . Using (V.47), we find  $w = 3 \cdot 10^{-3} \text{ erg/cm}^2 \text{ sec}$ , which corresponds to intensities of  $5 \cdot 10^{-4} \text{ erg/cm}^2 \text{ sec sterad}$ . The existence of a maximum ionization rate is thus responsible for the existence of a maximum in the concentration of ions (Figure 68). For low solar activity at high geomagnetic latitudes, the estimates for the cosmic ray intensity will be higher. The result is consistent with other data, e.g., the energy density of cosmic rays,  $0.5 - 1 \text{ eV/cm}^3$ . Indeed, multiplying this energy density by the velocity of light, dividing by  $4\pi$ , and changing over from eV to erg, we find intensities of  $(2 - 4) \cdot 10^{-3} \text{ erg/cm}^2 \text{ sec sterad}$ , which is close to the estimate obtained for high latitudes.

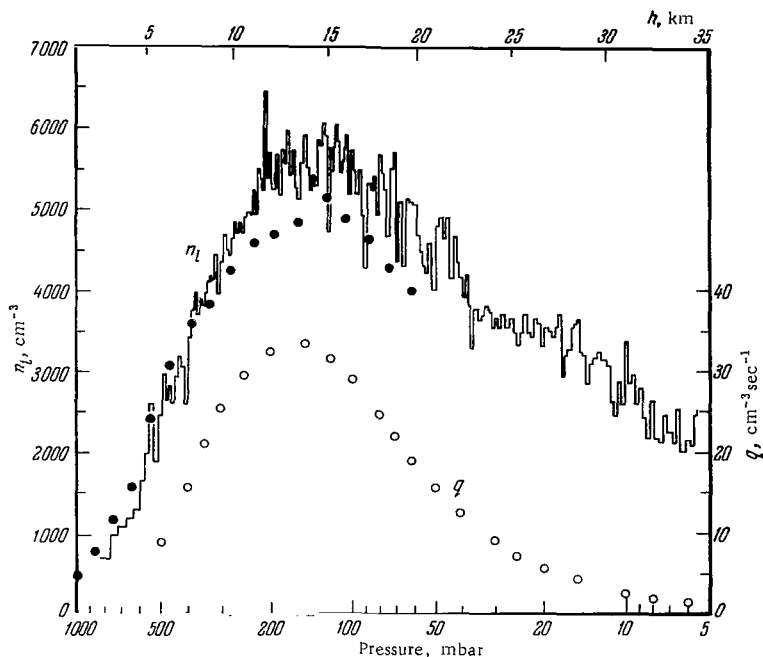


FIGURE 68. Vertical distribution of the concentration of negative ions  $n_i^-$  (left scale) from balloon measurements above Minneapolis (45°N) /506/ (solid curve) and from Explorer-2 data (black circles). Light circles give the rate of ionization (right scale) due to cosmic rays from ionization chamber measurements.

### Vertical distribution of ionization sources

In summing up the discussion of Sections 19 and 20 regarding sources of ionization in the ionosphere, we will compare the action of the various ionizing agents. The other ionization sources, apart from the solar radiation, are often disregarded, as their contribution to the total energy flux is small. In certain parts of the ionosphere, however, they may in fact be more effective than the solar radiation.



Figure 69 plots the computed curves of  $q(h)$  for various sources of ionization with a quiet Sun for maximum and minimum solar activity. The

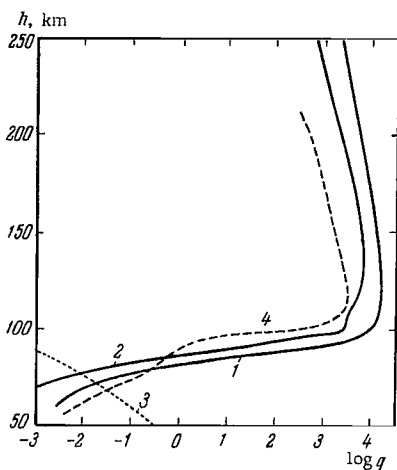


FIGURE 69. Vertical distribution of the rate of ionization due to the short-wave solar radiation in maximum (1) and minimum (2) solar activity, due to cosmic rays (3), and corpuscular streams (4).

main daytime maximum of ionization is indeed produced by the solar radiation; it lies between 125 and 160 km. Hence it follows, that most of the ionizing energy of the Sun is absorbed between the layers  $E$  and  $F_1$ .

Ionization by solar radiation dominates in the entire ionosphere above  $h \approx 80$  km. Below 65–70 km, at middle latitudes, the effect of cosmic rays is predominant even in daytime. The above estimates of  $q$  for the minimum electron flux also show that at 65–80 km in daytime (or, in any case, for large  $z_0$ ) and  $h \geq 80$  km at night, ionization by corpuscular streams injected into the lower part of the ionosphere predominates. In periods of enhanced corpuscular streams, corpuscular ionization may be particularly strong. This is indeed so during magnetic disturbances at altitudes of 100 and 110 km, even in daytime /246/.

The total flux of ionizing solar radiation varies between 2.5 and 8 erg/cm<sup>2</sup>sec (see Section 7). Cosmic rays lose about  $3 \cdot 10^{-3}$  erg/cm<sup>2</sup>sec through ionization of the atmosphere at middle latitudes, and 90% of this energy is expended in ionization of gases below 40 km. Injected particles in periods of high solar activity expend in ionization up to 1 erg/cm<sup>2</sup>sec in daytime and about  $10^{-2}$  erg/cm<sup>2</sup>sec at night. Nevertheless, in the lower part of the ionosphere, alternative sources of ionization successfully compete with solar radiation, although their total energy flux is significantly less than the flux of the short-wave solar radiation.

Having covered the various sources of ionization in the upper atmosphere, we can proceed with an analysis of the reverse processes — recombination.

## 21. Recombination processes

The equation of balance for ionization cannot be drawn up if the "lossy term," i.e., the recombination term  $r$ , is not known. Different types of recombinations generally have to be considered in systematic analysis, starting with simple recombinations for atomic ions and including the more complex processes of triple recombinations and dissociative recombinations of molecular ions. We will depart from this traditional order and start with the last named process, which is of the greatest importance in ionospheric physics.

## Dissociative recombination

The discovery of the process of dissociative recombination was a "pen-and-paper" discovery. The hypothesis concerning the possible existence of an unusual recombination process for molecular ions, involving dissociation,



where the asterisk \* indicates excitation of the product particles, was first advanced in 1937 by Massey /507/ for explanation of ionospheric processes. However, the true importance of the process of dissociative recombination for the physics of the ionosphere had remained unclear for two decades, prior to the mass spectrometric measurements of Istomin et al. using rockets and Sputnik III which established the existence of numerous positive molecular ions in the ionosphere that guarantee a high efficiency for the mechanism of charge neutralization (recombination) in the ionosphere. No other mechanism is capable of ensuring the high recombination rates observable in ionospheric regions *E* and *F*. Three species of molecular ions were discovered in the ionosphere at altitudes above 100 km:  $\text{NO}^+$ ,  $\text{O}_2^+$ , and  $\text{N}_2^+$ . The concentration of the  $\text{O}_2^+$  ions is approximately 1/2 the concentration of the  $\text{NO}^+$  ions, and that of  $\text{N}_2^+$  ions is generally less than 1%.

Figures 70 — 72 present a resume of the laboratory measurements of the coefficient of dissociative recombination  $\alpha^*$  of these ions vs. temperature /508/. The latest and most reliable measurements are encircled.\* The insufficient reliability of the earlier laboratory measurements and a certain dependence of  $\alpha^*$  on pressure, according to Biondi /515/, is partly due to the formation, at high pressures, of the composite ions  $\text{N}_3^+$ ,  $\text{N}_4^+$ , and  $\text{O}_3^+$  with high  $\alpha^*$ . The solid curves plot the function  $\alpha^*(T)$  according to the most reliable data now available. These functions are expressed in analytical form /803/ as

$$\alpha^*(\text{N}_2^+) = 3 \cdot 10^{-7} \left( \frac{T_e}{300} \right)^{-3/2} [\text{cm}^3 \text{sec}^{-1}] (200^\circ < T_e < 800^\circ), \quad (\text{V.51})$$

$$\alpha^*(\text{O}_2^+) = 2.2 \cdot 10^{-7} \left( \frac{T_e}{300} \right)^{-\gamma}, \quad (200^\circ < T_e < 3000^\circ), \quad (\text{V.52})$$

where  $\gamma = 0.5 - 1$ ,

$$\alpha^*(\text{NO}^+) = \begin{cases} 4.4 \cdot 10^{-7} \left( \frac{T_e}{300} \right)^{-1} & (200^\circ < T_e < 500^\circ), \\ 0.9 \cdot 10^{-7} \left( \frac{T_e}{1000} \right)^{-3/2} & (T_e > 1000^\circ). \end{cases} \quad (\text{V.53})$$

Quite recently /508/, the approximation of Stein et al. /510/ (the dashed curve in Figure 72) was regarded as more acceptable for the  $\text{NO}^+$  ion; new data for  $T < 500^\circ\text{K}$ , however, give preference to relation (V.53). For the  $\text{NO}^+$  ions in the region  $T_e < 1000^\circ\text{K}$ , the dependence on  $T$  is not as pronounced as in the region  $T_e > 1000^\circ\text{K}$ .

\* In addition to /508/, we also used the new data /509, 542/ for  $\text{N}_2^+$  and  $\text{O}_2^+$  (also see /742, 743/) and /511, 512, 755/ for  $\text{NO}^+$  (marked by  $\otimes$ ).

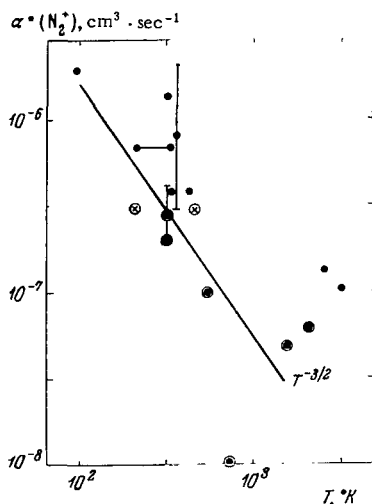


FIGURE 70. Dissociative recombination coefficient  $\alpha^*(N_2^+)$  as a function of temperature according to laboratory measurements.

Solid curve, the approximation  $T^{-3/2}$ .  
Circled crosses show new data /509, 542/.

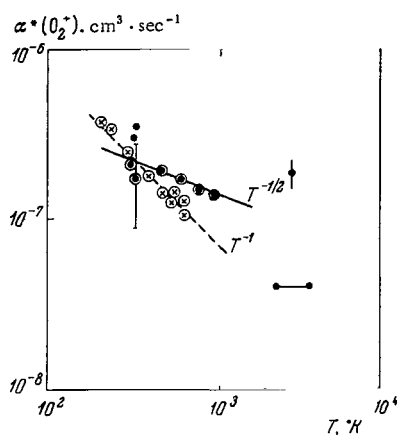


FIGURE 71. Dissociative recombination coefficient  $\alpha^*(O_2^+)$  as a function of temperature from laboratory measurements.

Dashed line — Whitten and Poppoff's approximation /574/; solid line, the approximation  $T^{-1/4}$ . Circled crosses mark new data /509, 542/.

For ionospheric conditions at  $T_e \approx (0.3 - 3) \cdot 10^3 \text{ }^\circ\text{K}$ , we clearly have  $\alpha^* \approx 3 \cdot 10^{-7} - 10^{-8} \text{ cm}^3 \text{ sec}^{-1}$ . Note that as  $T_e$  varies in the ionosphere with altitude, time of day, or level of solar activity,  $\alpha^*$  should also change. In a recent work /513/, analysis of rocket data on  $n_e$  revealed that the effective recombination coefficient at  $h \sim 200 \text{ km}$  indeed varies during the day because of this factor.

Let us compare this process with radiative recombination. Although the relative concentration of molecular ions decreases with altitude, so that the concentration of  $O^+$  and  $N^+$  predominates above 200 km, dissociative recombination is the decisive factor in charge neutralization processes up to 500—600 km. This is so because the rate constant for radiative recombination of atomic ions



emitting a quantum  $h\nu$  (which explains the name "radiative"), is very small, of the order of  $3 \cdot 10^{-12} \text{ cm}^3 / \text{sec} / 93/$ .

Radiative recombination of atomic ions may compete with dissociative recombination only for  $[O^+]/[M^+] \approx 3 \cdot 10^3$ , i. e., when the content of atomic ions is sufficiently high.

### Mutual neutralization

A binary process of mutual neutralization of positive and negative ions



is important for the lower part of the ionosphere, in the  $D$  region, where negative ions are present. Here  $X^+$  and  $Y^-$  may be atomic or molecular ions. The rate constant of this process from ionospheric data is highly uncertain,  $\alpha_i \approx 10^{-7} - 10^{-6} \text{ cm}^3/\text{sec}$ . A lower value ( $10^{-8} \text{ cm}^3/\text{sec}$ ) is sometimes used, although no reliable experimental measurements of  $\alpha_i$  have been made. A recent report /514, 744/ gives  $\alpha_i \approx (4-7) \cdot 10^{-8} \text{ cm}^3/\text{sec}$  from laboratory measurements in air—this figure is close to the results of earlier measurements. There is no certainty, however, that the ion species in these laboratory measurements corresponds to the ionosphere conditions in the  $D$  region, where composite ions are observed.

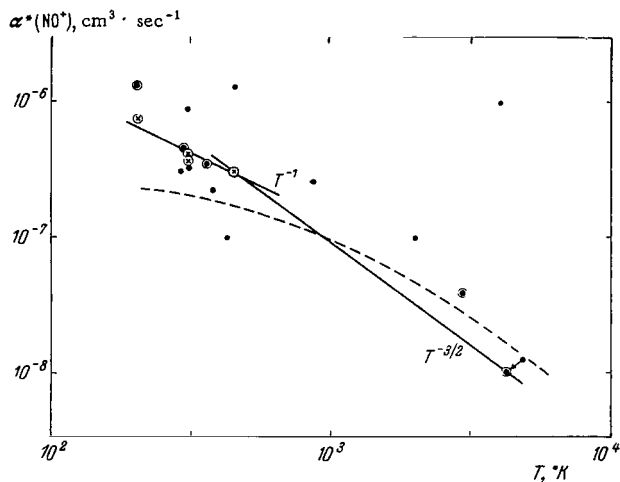


FIGURE 72. Dissociative recombination coefficient  $\alpha^*(\text{NO}^+)$  vs. temperature from laboratory measurement.

Dashed curve—the approximation of Stein et al /510/; solid curves—the approximations  $T^{-1}$  and  $T^{-3/2}$ .

Another important process observed at high atmospheric densities is recombination through triple collisions. Two types of processes /515/ are possible to ions:



For the first process, the triple recombination coefficient is  $K \lesssim 10^{-26} \text{ cm}^6 \text{ sec}^{-1}$  for  $T \approx 300^\circ\text{K}$ . It may therefore compete with dissociative recombination only for particle concentrations  $n > \alpha^*/K > 2 \cdot 10^{19} \text{ cm}^{-3}$ , which corresponds to the ground layer of the atmosphere. For process (V.57),  $K = 3 \cdot 10^{-25} \text{ cm}^6 \text{ sec}^{-1}$  for  $T \approx 300^\circ\text{K}$ . This process is comparable with the binary process of mutual neutralization for  $n \gtrsim 10^{18} \text{ cm}^{-3}$ , i. e., at altitudes  $h \lesssim 25 \text{ km}$ .

Dissociative recombination is thus the only significant process of charge neutralization in the ionosphere, while in the  $D$  region, with its high concentration of negative ions ( $[Y^-] > n_e$ ), mutual neutralization is also important. This simple system of recombination processes in the ionosphere makes it possible to tackle some important topics in the physics of the ionosphere, without going in detail into the intricacies of photochemical and other highly complex ion-molecular reactions.

The effective recombination coefficient  $\alpha'$

One of the main ionospheric parameters which characterizes the time scale of the variations in  $n_e$  is the effective recombinations coefficient  $\alpha'$ . The coefficient  $\alpha'$  can be determined in two ways: by considering recombination processes or by measuring the  $n_e$  variations in the ionosphere.

We will start with the first approach. In a sufficiently thin plasma, such as the ionosphere plasma, neutralization occurs via a binary process in which a particle interacts with an oppositely charged particle. Designating the concentrations of the two charged species by  $n^+$  and  $n^-$ , we find that the number of neutralizations or recombinations  $r$  in  $1 \text{ cm}^3$  in 1 sec in any binary process is

$$r = \alpha n^+ n^-, \quad (\text{V.58})$$

where  $\alpha$  is the recombination coefficient [ $\text{cm}^3/\text{sec}$ ]. The lifetime of the positive ion is given by  $\tau \approx (\alpha n^-)^{-1}$ . Under normal conditions, electron is the negatively charged particle. In the simplest case,  $n^+ = n_e$ ; then

$$r = \alpha n_e^2. \quad (\text{V.59})$$

As we have seen before, the rate of neutralization in the ionosphere is governed by two processes: dissociative recombination of molecular ions and mutual neutralization of positive and negative ions. The total number of recombinations  $r$  is therefore given by the sum of the rates of neutralization in each of these processes for ions of species  $j$  and  $k$ :

$$r = \sum_{j,k} (\alpha_j^+ n_j^+ n_e + \tilde{\alpha}_{jk} n_j^+ n_k^-), \quad (\text{V.60})$$

where  $\alpha^+$ ,  $\tilde{\alpha}_{jk}$  are the rate constants of the corresponding binary processes.

The effective recombination coefficient  $\alpha'$  can be introduced by writing for the total rate of recombination

$$r = \alpha' n_e^2; \quad (\text{V.61})$$

the form of this expression coincides with (V.59) for the simplest case.

We have noted that there are two different approaches to  $\alpha'$ : the photochemical theoretical approach and ionospheric experimental. In the former approach, according to (V.60),  $\alpha'$  is the weighted average of different recombination coefficients:

$$\alpha' = \sum_{j,k} \left( \alpha_j^+ \frac{n_j^+}{n_e} + \tilde{\alpha}_{jk} \frac{n_j^+}{n_e} \frac{n_k^-}{n_e} \right). \quad (\text{V.62})$$

This expression discloses the physical meaning of  $\alpha'$  in terms of elementary processes. For a single ion species, it reduces to the well-known relation

$$\alpha' = \left(1 + \frac{n_i^-}{n_e}\right) \left(\alpha^* + \alpha_i \frac{n_i^-}{n_e}\right), \quad (\text{V.63})$$

in which the concentration  $n_i^+ = n_e + n_i^-$  does not appear.

Another approach to the coefficient  $\alpha'$  is possible via experimental research of the ionosphere, when  $\alpha'$  is determined from the equation of ionization balance and (V.61):

$$\frac{dn_e}{dt} = \frac{q}{(1+l^-)} - \alpha' n_e^2, \quad (\text{V.64})$$

where  $q$  is the ionization rate,  $l^- = n_i^-/n_e$  is the relative concentration of negative ions. To measure  $\alpha'$ , we have to consider the variations in  $n_e$  in the ionosphere in a variety of conditions. The characteristic time lag of the ionospheric plasma associated with the finite value of the effective recombination coefficient (see below) is used in this method.

### Quasi-equilibrium in the ionosphere

The equation of ionization balance (V.64) with  $l^- \ll 1$  for the main part of the ionosphere above the  $D$  region, is a Riccati equation which cannot be solved in general form. An analytical solution can be obtained if  $\alpha' = \text{const}$  and the function  $q$  may be expressed in the form  $q_0 t^\kappa$ , where  $\kappa = -2$  or  $\kappa = 4k(1-2k)^{-1}$  with integral positive or negative  $k$ . The solution of equation (V.64) has an important retardation property, which should be considered in more detail for the ionosphere.

It is readily seen that for  $\alpha' = \text{const}$ , the function  $\alpha' n_e^2 = \varphi(t) = q(t - \Delta t)$  is a solution of (V.64) if

$$\Delta t = (2\alpha' n_e)^{-1}. \quad (\text{V.65})$$

Indeed, series expanding  $q(t - \Delta t)$ , we find  $q(t) - \varphi(t) = \Delta t \cdot \varphi' = (2\alpha' n_e)^{-1} 2\alpha' n_e \dot{n}_e = \dot{n}_e$ . This means that the value of  $\alpha' n_e^2$  at the time  $t$  is equal to the value of the function  $q$  at an earlier time  $t - \Delta t$ . The values of  $n_e^2$  thus repeat the variations of  $q/\alpha'$  with a certain phase shift, which increases as  $n_e$  diminishes. This retardation is an expression of the inertia of the ionospheric plasma, which is fully determined by the effective recombination coefficient  $\alpha'$  and the value of  $n_e$ .

The inertial properties of the plasma suggest the quasi-equilibrium approach to the physics of the ionosphere. In quasi-equilibrium, the stationarity condition  $q = \alpha' n_e^2$  is observed with sufficient accuracy, since  $\dot{n}_e \ll q$ ,  $\alpha' n_e^2$ . This is not a state of equilibrium, since  $n_e \neq \text{const}$  ( $q$  is time dependent, so that  $dn_e/dt \neq 0$ ). It is assumed, however, that the variation of  $q$  is relatively slow. The concept of "relative slowness" in this case indicates that the time constant for the variation of  $q$  is significantly larger than  $\Delta t$ , since otherwise the condition of quasi-equilibrium breaks down. Under normal daytime conditions, at 100–200 km,  $\Delta t \lesssim 10^2$  sec, and  $q$  varies approximately by a factor of 2 in about 1 hour time. It should be remembered, however, that the conditions are less favorable during sunrise and sunset.

Experimental work has established that the coefficient  $\alpha'$  in  $E$  and  $F_1$  regions generally does not change with rapid changes in  $n_e$ , whereas in the  $F_2$  region  $\alpha'$  is a function of  $n_e$ , such that  $\alpha' \propto n_e^{-1}$ . In this case, for  $q = 0$ , equation (V.64) takes the form

$$dn_e/dt = -\beta n_e, \quad (\text{V.66})$$

where  $\beta = \alpha' n_e = \text{const.}$  Here  $\beta$  is known as the linear recombination coefficient.

Several methods are available for experimental determination of the effective recombination coefficient  $\alpha'$  in the ionosphere, which are based on measurements of the variation of  $n_e$  under different conditions: after sunset, during solar eclipses, during the day, during various ionospheric disturbances, etc. These methods based on an analysis of (V.64) give widely varying and often contradictory results.

#### Earlier measurements of $\alpha'$

The coefficient  $\alpha'$  has often been determined from measurements of the daytime variation of  $n_e$ . A significant shortcoming of this method is that the parameters of the upper atmosphere (temperature, density, ion and neutral composition) are assumed to be constant, which implies that  $\alpha'$  is also constant during the entire day. This assumption is not borne out by rocket measurements.

A review of the methods and the results of measurements of  $\alpha'$  were published by Al'pert /489/ (p. 131) and later by Mitra /516/ in considerable detail, and we do not intend to describe the methods for measuring  $\alpha'$ . Note, however, that we must distinguish between the old and the new determinations of  $\alpha'$ . The many years of research have helped to crystallize certain ideas concerning the values of  $\alpha'$  in different ionospheric regions which are inconsistent with the rocket data. We will first consider the results of the old determinations of  $\alpha'$  in regions  $E$ ,  $F_1$ , and  $F_2$ , which have recently undergone marked revision.

Table 40 lists the values of  $\alpha'$  which are most often quoted in the literature and the corresponding references. The first measurements carried out in the pre-War period were rare and insufficiently reliable.

Numerous determinations of  $\alpha'$  were performed after World War II, when intensive ionospheric research began. It is quite obvious that the estimates of  $\alpha'$  had not undergone any significant changes prior to 1960 — 1961. Let us consider the data of Table 40 for the different regions of the ionosphere.

**The  $E$  region.** There were two distinct periods with different methods of measurement and different initial values of  $\alpha'$ : 1) the post-War period, when Bates and Massey /487, 521/ introduced the value of  $10^{-8}$  cm<sup>3</sup>/sec in place of the earlier values  $\alpha' \gtrsim 10^{-8}$  cm<sup>3</sup>/sec /486, 517 — 520/; 2) the post-1956 period, when the underestimated eclipse value  $\alpha' \approx 10^{-8}$  cm<sup>3</sup>/sec of Ratcliffe /530/ was popular. Ratcliffe reviewed all the old measurements which ignored the nonuniform distribution of radiation over the solar disc and the radiation of the solar corona beyond the Sun's limb which is not eclipsed by the Moon. If these effects are allowed for, we get  $\alpha'_E = (4 - 10) \times 10^{-8}$  cm<sup>3</sup>/sec. Ratcliffe called attention to this point in his resume presented at the symposium on solar eclipses and the ionosphere /538/ back in 1955, soon after the first rocket data had become available, confirming both the

nonuniformity of radiation from the solar disc and the existence of a corona beyond the Sun's limb. The two different values  $\alpha'_E \sim 10^{-7} \text{ cm}^3/\text{sec}$  and  $10^{-8} \text{ cm}^3/\text{sec}$  were often discussed at a number of international gatherings /539 - 541/. Recent reports again stress the fact that  $10^{-8} \text{ cm}^3/\text{sec}$  is too low /543, 587/.

TABLE 40. List of previously used values of  $\alpha'$  [ $\text{cm}^3 \text{sec}^{-1}$ ] and  $\beta$  [ $\text{sec}^{-1}$ ]

Author and reference	Year	$\alpha'$ (day)			$\alpha'$ (night)		$\beta$ (day)	$\beta$ (night)
		$E$	$F_1$	$F_2$	$E$	$F$	$F$	$F$
		$10^{-8}$	$10^{-9}$	$10^{-11}$	$10^{-9}$	$10^{-10}$	$10^{-4}$	$10^{-4}$
Appleton /486/	1937	$\approx 1$	$\approx \alpha'_E$	8.1 - 8.7	2	3		
Ratcliffe et al. /517/	1938	1.2	4		4			
Bates and Massey /518/	1939	1.2 - 2		8	4	3		
Sayers /519/	1943	1 - 2		8 - 9		1.8 - 6		
Massey and Bates /520/	1943	2	1 - 10	10	4			
Bates and Massey /487, 521/	1946-47	$\sim 1$	4 - 8.5	4 - 8	1 - 4	$\sim 3$		
Bates /522/	1949		4	1 - 8		3		
Bates /523/	1951			4 - 100				
Massey and Burhop /154/	1952	1	4	8				
Mitra /488/	1952	1	4	8		3		
Al'pert, Ginzburg, and Feinberg /524/	1953			$\sim 10$		$\sim 3$		
Al'pert and Krasovskii in /488/	1955	1		40	2	2		
Mitra and Jones /525/	1954	2 - 3						
Mohler /526/	1940		5 - 6	7 - 40		0.9	0.29	
Yonezawa /527/	1955						1	
Ratcliffe and Schmerling /528/	1956							$\frac{300 - h}{e \ 50}$
Bates /529/	1956	1	$\approx \alpha'_E$	10			$\frac{300 - h}{e \ 35}$	
Allen /490/	1956	1.1	5				$\frac{300 - h}{e \ 50}$	
Ratcliffe /530/	1956	$\sim 1$	5 - 9					
Krasovskii /531/	1957	$\sim 1$		$\sim 10$				
Al'pert /489/	1960	0.7 - 1.6	7	30 - 50				
Mitra /532/	1957	0.8			1			
Mitra /533/	1959	1.4	8	7.7				
Mitra /516/	1963	$\sim 1$	5	1		1		
Appleton /534/	1959	1.5 - 4						
MacElhinny /535/	1959	2.4 - 5						$\frac{300 - h}{e \ 50}$
Ratcliffe and Weeks /234/	1960	$\sim 1$	5					
Bates and Nicolet /536/	1960	(1.4)	10					
Bowhill /537/	1961	0.1 - 5					1	

**The nocturnal  $E$  region.** The early value of  $\alpha'$  was  $(2 - 4) \cdot 10^{-9} \text{ cm}^3/\text{sec}$ , which indicated a drop in  $\alpha'$  by a factor of 2 - 5 compared with daytime conditions ( $\alpha'_E = 10^{-8} \text{ cm}^3/\text{sec}$ ). In 1957, Mitra obtained  $\alpha' \approx 1 \cdot 10^{-9} \text{ cm}^3/\text{sec}$  for nighttime conditions. The observed nocturnal value of  $\alpha'$  is thus more than one order of magnitude smaller than the daytime value. These changes in  $\alpha'$  are difficult to account for on the basis of the existing photochemical theories. This topic is considered in more detail in Section 27.



**The  $F_1$  region.** Very few measurements of  $\alpha'$  were available for the  $F_1$  region. We see from Table 40 that all the authors cite almost the same value of  $\alpha_{F_1}$ , which falls within the limits  $(4-10) \cdot 10^{-9}$  cm<sup>3</sup>/sec. This value almost coincides with the old value of  $\alpha'_E$  or is a factor of 1.5—2 smaller.

**The  $F_2$  region.** Originally  $0.8 \cdot 10^{-10}$  cm<sup>3</sup>/sec was taken as the daytime value of  $\alpha'$  and  $3 \cdot 10^{-10}$  cm<sup>3</sup>/sec at night /486/. Lower values were also used,  $\alpha'_{F_2} \sim 1 \cdot 10^{-11}$  cm<sup>3</sup>/sec /522/, as well as higher values, up to  $10^{-9}$  cm<sup>3</sup>/sec /523/. High values were suggested by Al'pert /498, 491/,  $(3-5) \cdot 10^{-10}$  cm<sup>3</sup>/sec.

In recent years, the coefficient  $\alpha'$  for the  $F$  region has been replaced by the linear effective recombination coefficient  $\beta = n_e \alpha'$ , which is mainly estimated from the Ratcliffe—Schmerling expression\* /528/  $\beta = 10^{-4} \times \exp[(300-h)/H]$  sec<sup>-1</sup>, in which Bates /529/ has substituted a scale height of 35 km for the previous value  $H = 50$  km. This estimate, for 300 km altitude and  $n_e = 10^6$  cm<sup>-3</sup>, gives the commonly used value of  $\alpha'_F = 10^{-10}$  cm<sup>3</sup>/sec. The fact that the data of Schmerling et al. /528/ were obtained for a nocturnal atmosphere is ignored, and the results are often used for daytime atmosphere too.

#### New measurements of $\alpha'$

The flux of solar ionizing radiation according to rocket measurements was found to be approximately one order of magnitude higher than the ionospheric estimates (see end of Section 19). It became necessary to revise the ionospheric data and, in particular, the values of  $\alpha'$  which did not fit the laboratory measurements of  $\alpha^*$  /544/. It was established that, on the one hand, the commonly used values  $\alpha'_E \approx 10^{-8}$  cm<sup>3</sup>/sec had been determined mainly from daytime variations of  $n_e$  or from old eclipse data, i. e., by methods which are far from being unobjectionable. On the other hand, a rigorous analysis of eclipse data and methods allowing for short-time variations of  $n_e$ , when the atmospheric parameters remain unchanged because of inertia, yielded higher values of  $\alpha'_E$ . Let us briefly consider the results of the latest determinations of  $\alpha'$ , which are treated in more detail in /544, 545/.

The nonuniform distribution of the ionizing radiation over the Sun's disc was first correctly taken into consideration by Piddington /546/, and later by authors listed in Table 41. As a result, the same eclipse data yielded higher values  $\alpha'_E = (0.4-1) \cdot 10^{-7}$  cm<sup>3</sup>/sec. Recently, similar results were obtained for  $\alpha'$  from observations of a number of solar eclipses (Table 41). It is significant that during these measurements the distribution of the short-wave ionizing radiation over the Sun's disc and in the corona was monitored by measuring the decimeter radio waves from the Sun during the eclipse. Without this monitoring technique, Shashun'kina and Turbin /557/ and Jasinski /558/ obtained on 15 February 1961 a lower value  $\alpha'_E \sim 1.5 \times 10^{-8}$  cm<sup>3</sup>/sec.

Correct analysis of the eclipse data for the  $E$  region thus gives  $\alpha'_E = (0.4-1) \cdot 10^{-7}$  cm<sup>3</sup>/sec, where the higher value  $1 \cdot 10^{-7}$  cm<sup>3</sup>/sec is the more probable.

\* The linear recombination law in the  $F$  region was first obtained by Mohler /526/ and the figure  $\beta = 10^{-4}$  sec<sup>-1</sup> was previously used in /527/.

TABLE 41. The effective recombination coefficient  $\alpha$  [ $\text{cm}^3\text{sec}^{-1}$ ] for  $E$  and  $F_1$  regions from solar eclipse observations

Date of eclipse	$E$	$F_1$	Author and reference
1 October 1940	$\sim 10^{-7}$	$\sim 5 \cdot 10^{-8}$	Piddington /546/
30 June 1954	$\geq 1 \cdot 10^{-7}$	$\approx 3 \cdot 10^{-8}$	Bible and Delobbeau /547/
25 February 1952	$4 \cdot 10^{-8}$		Hunaerts, Nicolet /548/, Minnis /549/, Bonnet et al. /550/
Review	$10^{-7}$	$\alpha_E'/1.8$	Ratcliffe /538/
25 December 1954	$(0.4 - 1) \cdot 10^{-7}$		Mac Elhinny /535/
25 December 1954	$4 \cdot 10^{-8}$		Gladhill /551/
Review	$4 \cdot 10^{-8}$		Chubb et al. /58/
	$10^{-6} - 10^{-7}$		Odintsova and Ogir' /552/
15 February 1961	$10^{-7}$		Nestorov and Taubenkhaim /553, 554/
	$(0.6 - 2.3) \cdot 10^{-7}$		Serafimov /555/
20 December 1963 (rockets)	$\geq 10^{-7}$		Smith et al. /556/

Let us consider another method for the determination of  $\alpha'_E$ , which uses data on  $n_e$  and  $q$  and the relation

$$\alpha' = q/n_e^2, \quad (\text{V.67})$$

applicable under quasi-equilibrium conditions. If the values of  $q$  based on new rocket data are employed, high values of  $\alpha'_E$  are obtained, e.g.,  $\alpha'_E \sim 10^{-7} \text{ cm}^3/\text{sec}$  /559/ or  $3 \cdot 10^{-8} \text{ cm}^3/\text{sec}$  /560/. Incidentally, in /560/, the initial data for  $q_E$  are a factor of 3—4 too low, and the corrected value works out to be  $\alpha'_E = 1.1 \cdot 10^{-7} \text{ cm}^3/\text{sec}$  /354, 63/.

From simultaneous measurements of the brightness of polar aurorae and  $n_e$  in the  $E$  region, Omholt /561/ also obtained a high value  $\alpha' = 10^{-6} - 10^{-7} \text{ cm}^3 \text{ sec}^{-1}$ . In polar aurorae, the coefficient  $\alpha'$  is in general relatively high,  $\sim 10^{-7} \text{ cm}^3/\text{sec}$  (see Bates /562/). Nevertheless, Pudovkin, Loginov, and others in a number of works (see, e.g., /563, 564/) obtained from variations in auroral intensity and magnetic disturbances  $\beta = 5 \cdot 10^{-4} \text{ sec}^{-1}$ , which gives  $\alpha' \sim 10^{-9} \text{ cm}^3/\text{sec}$ . These results, however, are not based on direct ionospheric measurements and they are not considered here.

For the  $F_1$  region, the few data listed in Table 41 indicate that  $\alpha'_{F_1} = (3 - 5) \cdot 10^{-8} \text{ cm}^3/\text{sec}$ , i.e., almost one order of magnitude lower than previously assumed. However, in accordance with Ratcliffe's previous result /538/, we have  $\alpha'_{F_1} \approx 0.5\alpha'_E$ .

Let us now consider the new results of measurements of  $\alpha'$  for night-time conditions in the  $E$  region. Rocket measurements of the electron concentration after sunset and at dawn gave  $\alpha' = 2 \cdot 10^{-8} \text{ cm}^3/\text{sec}$  (Smith /565/). The main shortcoming of Smith's work is that the two sets of measurements were carried out on different nights. The method essentially does not differ from the old ground method of determination of  $\alpha'$  from the decrease of  $n_e$  in the  $E$  region after sunset. This method was applied by Titheridge /566/ not to a single layer, but to  $n_e(h)$  profiles for 100—200 km altitudes based on the data of ionospheric stations. After sunset, the effective recombination coefficient was found to remain constant during the night, being equal on the average to  $2 \cdot 10^{-8} \text{ cm}^3/\text{sec}$  at altitudes from 100 to 200 km. This does not correspond to the results of analysis of

nocturnal profiles computed from rocket sounding data /247/. As we saw in Section 15, there are two fundamentally different parts of the ionosphere: the 125–160 km region extending above the  $E$  region, where  $\alpha' = (3-10) \times 10^{-8} \text{ cm}^3/\text{sec}$  (in accordance with the daytime value of  $\alpha'$ ) and the  $E$  region where the observed effective recombination coefficient is different on different nights, generally reaching values of  $\alpha' \leq 10^{-8} \text{ cm}^3/\text{sec}$ . Thus ground and rocket measurements give divergent but relatively low values of  $\alpha'$  for the  $E$  region and therefore relatively high values of  $n_e$  in the  $E$  region at night. In /247/ this fact is interpreted as a result of a sporadic nocturnal source of ionization.

For the  $F_2$  region, unlike  $E$  and  $F_1$ , the effective recombination coefficient was not revised, and only more accurate values were obtained for different conditions. A detailed analysis of the measurements of  $\alpha'$  and  $\beta$  for the  $F_2$  region will be found in /544, 545/. The basic measurement results can be summarized as follows.

We see from Table 40 that high values of the coefficients are sometimes observed in the  $F_2$  region:  $\alpha' = (2-5) \cdot 10^{-10} \text{ cm}^3/\text{sec}$  and  $\beta = (2-4) \cdot 10^{-4} \text{ sec}^{-1}$ ; these high values correspond to high solar activity. In daytime, for low solar activity,  $\beta$  apparently may be one order of magnitude lower. The data in Table 40 also reveal diurnal variations in  $\alpha'_p$ .

Let us consider new data on the variations of  $\beta$  and  $\alpha'$  during a solar cycle, for different times of year and times of day. The peak values  $\beta = (3-6) \times 10^{-4} \text{ sec}^{-1}$  are observed during daytime hours in summer with high solar activity. In epochs of low solar activity, the nocturnal values of  $\beta$  according to /567/ drop to approximately 1/30 and reach minimum values of  $\sim 10^{-5} \text{ sec}^{-1}$ . The daytime variations in  $\beta$  are probably smaller.

It is significant that the seasonal and the diurnal variations of  $\alpha'$  and  $\beta$  follow opposite trends. In winter, the daytime  $\beta$  is approximately 1/2 the summer value, whereas  $\alpha'$  conversely is  $(5-8) \cdot 10^{-11} \text{ cm}^3/\text{sec}$  in summer and increases to  $(1-2) \cdot 10^{-10} \text{ cm}^3/\text{sec}$  in winter. The nocturnal values of  $\alpha'$  are a factor of 2–3 higher than the daytime values, whereas for  $\beta$  an inverse effect is apparently observed. The value of  $\beta$  diminishes during magnetic disturbances.

One of the most important results obtained in measurements of  $\beta$  during a solar eclipse is the confirmation of the exponential dependence of the linear recombination coefficient on altitude, first discovered by Ratcliffe,  $\beta \propto \exp [-h/H_0]$  (among the recent publications, see /568/). Under daytime conditions the scale height  $H_0$  is 50–100 km in periods of high solar activity.

Thus the last years have not produced radically new values of the coefficients  $\alpha'$  and  $\beta$  for the  $F$  region, but a significantly more accurate picture of the variation of  $\beta$  and  $\alpha'$  as a function of solar activity, time of year, and time of day is now available. These variations are apparently associated with temperature fluctuations in the upper atmosphere, which alter the density and the composition in the  $F$  level and lead to changes in the rate of recombination processes.

Finally, let us consider the results of measurements of the effective recombination coefficient in the  $D$  region. A detailed review of the methods for measuring  $\alpha'$  and a summary of all the observations of  $\alpha'$  for altitudes between 60 and 92 km was published by Mitra /516/. Figure 73 plots the results of these observations, supplemented by a new measurement for the 70 km level obtained by LeLevier /569/ from an analysis of the diminishing absorption of radio waves from outer space after a nuclear

explosion and later refined by Kozlov and Raizer /570/. For the *E* region at an altitude of  $\sim 110$  km, a new value was used  $\alpha' = (0.3 - 1) \cdot 10^{-7}$  cm<sup>3</sup>/sec. Although the differences between individual measurements sometimes reach one order of magnitude, the average curve (the dashed curve in Figure 73) is determined fairly reliably from all the observation data and provides a clear picture of the vertical variation of  $\alpha'$  apart from a factor of 2 - 3.

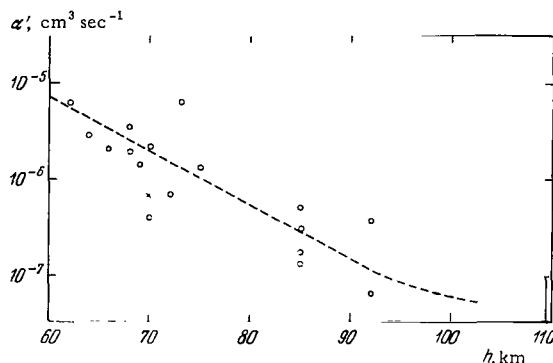


FIGURE 73. The effective recombination coefficient between 60 and 100 km.

Circles, observations from /516/ (the cross marks the point obtained in /569, 570/); dashed curve, the average.

### Summary of data on the $\alpha'(h)$ profile

We are now in a position to make a comparison between the experimental data on the values of  $\alpha'$  at different levels in order to reconstruct the full profile  $\alpha'(h)$  in the ionosphere. The reconstruction of the complete  $q(h)$  profile has previously revealed the highly important fact that most of the ionizing energy of the Sun is absorbed between regions *E* and *F*<sub>1</sub> and is therefore inaccessible to observations of the critical frequencies of the main ionospheric layers from the ground. This conclusion can be verified from the  $\alpha'(h)$  profile. It is also important to compare the theory of the effective recombination coefficient with experimental data. As we have mentioned before, there are two distinct trends in the development of the theory of the ionosphere which respectively employ low or high values of rate constants and ionization source intensities.

The dark circles in Figure 74 are the old data for  $\alpha'$ , and the light circles are the new data. Here for the *F* region,  $\alpha' = \beta n_e^{-1}$ . The solid line is the average based on new data. Let us analyze the experimental distribution  $\alpha'(h)$ .

The vertical variation of  $\alpha'$  can be divided into three regions: 1) slow decrease with altitude between 100 and 150 - 170 km, 2) a faster decrease at higher altitudes, and 3) a still faster variation for  $h < 100$  km. These three regions on the curve of  $\alpha'$  vs.  $h$ , as we shall see below, reflect certain differences in the ion composition of three different parts of the ionosphere.

Below 90 km there extends a region with negative ions, where recombination mainly proceeds through mutual neutralization. As we see from Figures 73 and 74,  $\alpha'$  steeply increases with decreasing altitude below about 90 km. Using (V.63), we see that the fraction of negative ions  $l^- = n^-/n_e$  is either  $l^- > \alpha^*/\alpha_i$  or  $l^- > 1$ . The growth of  $\alpha'$  with decreasing altitude is associated

with the growth of  $l^-$ , since for  $l^- = 0$  we should have  $\alpha' = \alpha^* \approx \text{const}$  (the dashed line in Figure 74). For altitudes  $h < 70$  km, we may take  $l^- \alpha_i \gg \alpha^*$ , so that

$$\alpha' = \alpha_i l^- (1 + l^-). \quad (\text{V.68})$$

The dependence of  $l^-$  on  $h$  will be further discussed in Section 24.

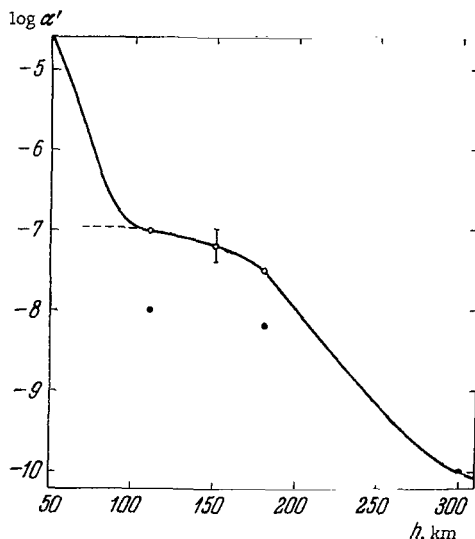


FIGURE 74. Average curve of the effective recombination coefficient between 50 and 300 km.

Light circles — new data; dark circles — old data; solid curve — average from new data; dashed line — vertical profile assuming no negative ions.

In daytime, above 90 km,  $n^- \ll n_e$ , so that

$$\alpha' = \sum_j \alpha_j^* \frac{M_j^+}{n_e}, \quad (\text{V.69})$$

where  $M_j^+$  is the concentration of molecular ions. Measurements indicate that at altitudes below  $h \sim 170$  km the fraction of molecular ions is very high in daytime, i.e.,  $\sum M_j^+ \approx n_e$ . Therefore  $\alpha'$  should remain constant. The slight decrease in  $\alpha'$  with altitude between 100 and 150–170 km may be only caused by the decrease of  $\alpha^*$  following the increase in temperature. At higher altitudes, the fraction of molecular ions  $M^+/n_e$  begins to decrease steadily with altitude. Moreover, it should be remembered that  $\alpha^*$  depends on the electron temperature which, as we saw in Section 16, increases up to 300 km.

A more detailed analysis of the vertical distribution of  $\alpha'$  requires knowledge of the actual conditions of production of molecular ions in the ionosphere and it is therefore postponed to the next chapter where the variation of  $\alpha'$  with altitude, time of day, and solar activity level is discussed.

## 22. The photochemical theory of the ionosphere

It is clear from the above discussion that detailed knowledge of the elementary processes, or the microphysics of the ionosphere is absolutely essential for complete understanding of the main features of the regular variations in the maxima of the main ionospheric layers, not to mention the fine details of the complex vertical variation of the ionosphere. One of the main objects of the photochemical theory is to determine the cycle of ion-molecular reactions triggered in the upper atmosphere by the ionizing solar radiation and by corpuscular stream and to find the vertical distribution of concentrations of the principal ionospheric ions, the diurnal variations and the dependence on the solar activity.

In this section we only present the elements of the photochemical theory which are essential for what follows. This theory is considered in detail in the book by A. D. Danilov "Chemistry of the Ionosphere" /572/ to which the reader is referred for a more thorough treatment of this topic. We do not intend to consider all the different processes whereby electrons, ions, and neutral particles interact in the ionosphere. We will only consider those topics which are relevant for our study of the variations of the ion composition and the recombination of charged particles in the part of the ionosphere between 90 and 200 km, where neither the negative ions (in daytime) nor ambipolar diffusion have much influence.

### Elementary chemical processes

The ionization of the atmospheric gases by the short-wave solar radiation mainly produces the primary ions  $O^+$ ,  $N_2^+$ , and  $O_2^+$ . To first approximation, we will ignore the primary ions  $N^+$ ,  $H^+$ ,  $He^+$  and the molecular ion  $NO^+$  which are formed in significantly lower concentrations in this region of the atmosphere. We write

$$i_1 = \frac{q(O^+)}{[O]}, \quad i_2 = \frac{q(N_2^+)}{[N_2]}, \quad i_3 = \frac{q(O_2^+)}{[O_2]} \quad (V.70)$$

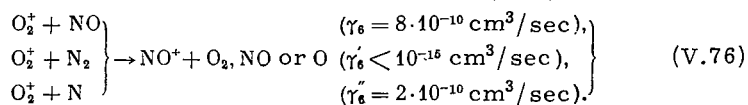
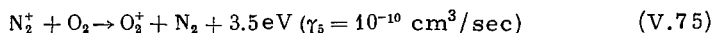
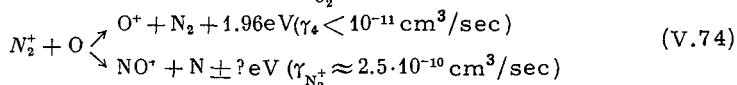
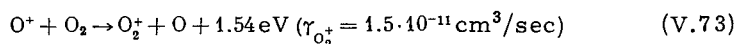
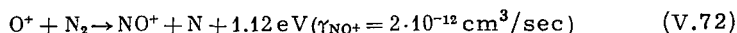
for the ionization coefficients of the corresponding particles which, according to (V.8), are defined as the integrals over  $\lambda$  of the ionization cross sections multiplied by the intensity of the ionizing radiation,  $i = \int \sigma_{i\lambda} I_\lambda d\lambda$ . We thus find that the total rate of ion formation is largely determined by the expression

$$q = [O] i_1 + [N_2] i_2 + [O_2] i_3 [\text{cm}^{-3} \text{ sec}^{-1}], \quad (V.71)$$

since the other ions form in the atmosphere in relatively small numbers. At altitudes below 110 — 120 km, however,  $O^+$  ions also form through ionization of the  $O_2$  molecules at a rate  $\omega \cdot q(O_2^+)$ , where  $\omega = 0.1 - 0.2 / 678, 745/$ .

Mass-spectrometric measurements have established that the concentration of ions in the atmosphere is not proportional to the rate of formation of the primary ions. This is an outcome of the transformation reactions between ions of different species in various ion-molecular processes. The complete cycle of reactions for all the ions have not been reconstructed as yet.

It follows from theoretical studies (see, e.g., /255, 354, 572 — 576, 638/) that the main processes which determine the interaction of the primary ions  $O^+$ ,  $N_2$  and  $O_2^+$  with neutrals in the ionosphere are apparently the following:



Next to each reaction, the most reliable value of the rate constant is given. The constant  $\gamma$  determines the rate of the reaction in  $1 \text{ cm}^3$  in 1 sec, i. e., the rate of destruction  $r$  of reactant ions or the rate of production  $q$  of product ions. Thus, for the reaction (V.72), we have

$$r(O^+) = q(NO^+) = \gamma_{NO^+} [O^+] [N_2]. \quad (V.77)$$

The ion  $NO^+$  occupies a special position in a mixture of gases: its ionization potential is lower than that of other ions, so it is an end product of numerous reactions and is unable to transform into other ions. Examining the concentrations of neutral and charged particles we see that in the ionosphere at  $h > 120 - 140 \text{ km}$ , the main reactions are (V.72) — (V.74), whereas at lower altitudes the two other reactions are also active.

The opinions differed concerning reaction (V.74): many authors /522, 572 — 574/ thought that the  $O^+$  ions were the only product of the reaction, but in /354, 578/ it was suggested that the formation of  $NO^+$  ions would be more efficient. Recently, the latter opinion was confirmed in laboratory /577, 637, 642, 746, 756/. Above the  $E$  region, the concentration of atomic oxygen is significantly higher than the concentration of molecular oxygen, and reaction (V.74) is therefore a more efficient sink for  $N_2^+$  ions than reaction (V.75), which is significant for  $h \leq 100 \text{ km}$  only.

There are numerous reactions which are often considered for the sake of general argument, but which are of no relevance for the determination of the equilibrium ion concentrations. Particular computations show that between 100 and 200 km, the loss of  $O^+$ ,  $N_2^+$ , and  $N^+$  through reactions with the molecule  $NO$  (leading to the production of the ions  $NO^+$ ) is significantly less

effective than through reactions of these ions with the more abundant particles in the atmosphere. However, in the  $E$  region and at lower altitudes, reactions (V.76) may contribute significantly to the production of  $\text{NO}^+$  and the destruction of  $\text{O}_2^+$ . The total specific rate of destruction of  $\text{O}_2^+$  ions through these reactions is

$$\frac{r(\text{O}_2^+)}{[\text{O}_2^+]} \equiv \mu_0 = \gamma_0 [\text{VO}] + \gamma_0' [\text{N}_2] + \gamma_0'' [\text{N}]. \quad (\text{V.78})$$

At altitudes of 90–120 km it is comparable with and sometimes even higher than the rate of destruction of  $\text{O}_2^+$  ions through dissociative recombination. At altitudes above 130–140 km, the contribution from reactions (V.76) is negligible in daytime, but for high  $z_0$  and at night they must be allowed for in the balance of processes which determine the concentration of  $\text{NO}^+$  and  $\text{O}_2^+$ .

As we saw in the preceding section, neutralization in the entire ionosphere below the  $F$  region (except the  $D$  region) is completely determined by dissociative recombination of molecular ions. The total number of neutralization events in  $1 \text{ cm}^3$  in 1 sec is, by (V.60),

$$r = n_e \{ \alpha_{\text{NO}^+}^* [\text{NO}^+] + \alpha_{\text{O}_2^+}^* [\text{O}_2^+] + \alpha_{\text{N}_2^+}^* [\text{N}_2^+] \}.$$

This expression is quite general. It is not affected by the transformation of molecular ions into other ions through ion-molecular reactions, nor by the lack of equilibrium between the number of ionizations and recombinations.

Under equilibrium conditions, equating the rates of production and destruction of the ions, we find the following expressions for the concentrations of the main ion species:

$$[\text{N}_2^+] = \frac{[\text{N}_2] i_2}{\gamma_{\text{N}_2^+} [\text{O}] + \gamma_0 [\text{O}_2] + \alpha_{\text{N}_2^+}^* n_e}, \quad (\text{V.79})$$

$$[\text{O}^+] = \frac{[\text{O}] \{ i_1 + \gamma_4 [\text{N}_2^+] \} + \omega q (\text{O}_2^+)}{\gamma_{\text{NO}^+} [\text{N}_2] + \gamma_{\text{O}_2^+} [\text{O}_2]}, \quad (\text{V.80})$$

$$[\text{NO}^+] = \frac{[\text{N}_2] \gamma_{\text{NO}^+} [\text{O}^+] + \mu_0 [\text{O}_2^+] + [\text{O}] \gamma_{\text{N}_2^+} [\text{N}_2^+]}{\alpha_{\text{NO}^+}^* n_e}, \quad (\text{V.81})$$

$$[\text{O}_2^+] = \frac{[\text{O}_2] \{ i_3 + \gamma_{\text{O}_2^+} [\text{O}^+] + \gamma_5 [\text{N}_2^+] \}}{\alpha_{\text{O}_2^+}^* n_e + \mu_0}. \quad (\text{V.82})$$

Since  $[\text{N}_2^+] \ll n_e$ , we may also write

$$[\text{O}^+] + [\text{O}_2^+] + [\text{NO}^+] = n_e. \quad (\text{V.83})$$

Sometimes it is advisable to use the equation of balance of ionizations and recombinations, which corresponds to the general condition of quasi-stationarity  $r = q$ , or

$$n_e \{ \alpha_{\text{NO}^+}^* [\text{NO}^+] + \alpha_{\text{O}_2^+}^* [\text{O}_2^+] + \alpha_{\text{N}_2^+}^* [\text{N}_2^+] \} = [\text{O}] i_1 + [\text{N}_2] i_2 + [\text{O}_2] i_3. \quad (\text{V.84})$$



Relations (V.79) — (V.83) constitute a system of five equations in five unknowns  $n_e$ ,  $[O^+]$ ,  $[NO^+]$ ,  $[O_2^+]$  and  $[N_2^+]$ . They may be applied to construct the theoretical distributions of the ion concentrations between 90 and 250 km, where these photochemical processes are dominant. However, the various parameters entering these equations are not available with sufficient accuracy. It often happens that the ion composition,  $n_e$ , and  $I$  are better known from rocket measurements than the neutral composition and the constants  $\gamma$ , so that equations (V.79) — (V.84) have been previously used for the computation of the rate constants  $\gamma$  and not for reconstructing the variations of the ion composition.

The photochemical theory, as presented, is limited to altitudes between 90 and 200 km. Below 80 — 90 km, complex hydrate ions  $H^+(H_2O)_n$  are observed, whose origin remains unclear.\* Moreover, negative ions are highly significant at these altitudes, and their production is not covered by this theory.

Theoretical models of the vertical distribution of the electron concentration and the concentrations of various positive ions can be constructed using the photochemical theory. The variation of the ion composition with the time of day or as a function of solar activity may also be considered. The next subsection analyzes the dependence of the ion concentration on the intensity of solar radiation at various altitudes in the atmosphere between 90 and 200 km. The first attempts to study the variations of  $n_e$  and the ion composition during the day were recently undertaken by Holms et al. /255/ and by Danilov /633/. This problem was reviewed again in /266/. The results of the last work are presented below.

### Variations of the ion composition

Let us consider the changes in the absolute and the relative concentrations of ions with the intensity of the ionizing solar radiation  $I$ , the concentration of particles in the atmosphere  $n$ , and the relative concentrations of the main atmospheric components O and  $N_2$ . A general solution of this problem is very difficult to obtain. In certain atmospheric regions, however, the ion concentrations follow relatively simple curves. Let us consider a few examples.

**Dependence on  $I$  and  $n$ .** Different levels in the atmosphere are primarily distinguished by the total concentration  $n$ , which is used as a starting parameter in all computations. The conditions of ionization during the day or during a solar activity cycle may be characterized by the total short-wave intensity  $I = \int I_\lambda d\lambda$  at a given altitude. We saw in Section 19 that the total rate of ionization  $q$  is directly proportional to the product  $In$ , provided changes in  $n$  do not lead to significant changes in the atmospheric composition and the radiation spectrum remains unaffected by variations in  $I$ . These or close conditions are in fact observed in some cases.

At altitudes  $h \lesssim 250$  km dissociative recombination of the ion  $N_2^+$  can be ignored compared with the reaction (V.74). Expression (V.79) is thus simplified:

$$[N_2^+] = -\frac{[N_2] i_2}{\gamma_{N_2^+} [O]}. \quad (V.85)$$

\* Swider /736, 737/ discusses the possible formation of the ions  $H_3O^+$  in a reaction between  $O_2^+$ ,  $NO^+$ , and water molecules. The ion  $H_5O_2^+$  is then produced by the reaction  $H_3O^+ + 2H_2O \rightarrow H_5O_2^+ + H_2O$ .

The absolute concentrations of both  $N_2^+$  and  $O^+$  (see (V.80)) are then proportional to  $I$  and independent of the neutrals concentration  $n$ .

In the narrow range of altitudes between 140 and 250 km, reaction (V.76) can be ignored whenever the Sun is not too close to the horizon. Then  $\mu_6 \ll \alpha_{O_2^+}^* n_e$  and expressions (V.81) – (V.83) can be simplified:

$$[NO^+] = \left(1 + \frac{1}{C}\right)^{-1} M^+, \quad (V.86)$$

$$[O_2^+] = (1 + C)^{-1} M^+, \quad (V.87)$$

$$n_e = An \frac{[O^+]}{n_e} \left(1 - \frac{[O^+]}{n_e}\right)^{-1}, \quad (V.88)$$

where  $M^+ = n_e - [O^+]$  is the concentration of molecular ions; the two parameters  $C = \frac{[N_2]}{[O_2]} \frac{\alpha_{O_2^+}^*}{\alpha_{NO^+}^*} \left( \frac{\gamma_{NO^+}}{\gamma_{O_2^+} + \frac{i_2}{[O^+]}} \right)$  and  $A = (1 + C)^{-1} \frac{[N_2]}{n} \frac{\gamma_{NO^+}}{\alpha_{NO^+}^*}$  hardly change during the day and with altitude, as they are defined as ratios of similar variables.

Relations (V.86) – (V.88) show that, given the relative concentration  $[O^+]/n_e$  for different times during the day at altitudes 140 – 250 km, we can find the relative concentrations of all the other ions and also the absolute concentration  $n_e$ , and hence the absolute concentrations of all the ions. We see from the above expressions that the relative concentrations of the molecular ions vary in an opposite direction to the variation of  $[O^+]$ : as  $[O^+]/n_e$  increases,  $[NO^+]/n_e$  and  $[O_2^+]/n_e$  should decrease, and vice versa.

**Two ionospheric regions.** To investigate the concentrations of  $NO^+$  and  $O_2^+$  and  $n_e$  as a function of radiation intensity and atmospheric density, we require the dependence of  $[O^+]/n_e$  on  $I$  and  $n$ . The latter dependence can be obtained as follows. The two sides of equation (V.88) are multiplied by  $[O^+]$  and in the left member  $[O^+]$  is replaced with  $BI$ , where  $B = \text{const}$  (since  $[O^+] \propto I$ ). We thus obtain a quadratic equation in  $n_e/[O^+]$ :

$$\left(\frac{n_e}{[O^+]}\right)^2 - \frac{n_e}{[O^+]} - \frac{An}{BI} = 0. \quad (V.89)$$

This equation has one positive solution

$$\frac{[O^+]}{n_e} = \left(\frac{1}{2} + \sqrt{\frac{1}{4} + \frac{An}{BI}}\right)^{-1}, \quad (V.90)$$

which gives the dependence of  $[O^+]/n_e$  on  $I$  and  $n$ .

The character of this dependence is determined by the atmospheric density at the given altitude. In the limiting case  $An/BI \ll 1/4$ , the concentration of the  $O^+$  ions, as we see from (V.90), is dominant, whereas  $[O_2^+] \ll n_e$  and  $[NO^+] \ll n_e$ . In this case  $[O^+] = n_e \propto I$  and it is independent of  $n$ , whereas the absolute concentrations  $[NO^+]$  and  $[O_2^+]$  are conversely proportional to  $n$  and are independent of  $I$ .

In the other limiting case, when  $An/BI \gg 1/4$ , we see from (V.90) that  $[O^+]/n_e = \sqrt{\frac{BI}{An}} \ll 1$ . The concentrations  $[NO^+]$ ,  $[O_2^+]$  and  $n_e$  in this case are proportional to  $\sqrt{In}$ , and the relative concentrations  $[NO^+]/n_e$  and  $[O_2^+]/n_e$  are

conversely independent of  $I$  and  $n$ , approaching their limiting values (for  $C = 2$ , they are equal to 67% and 33%, respectively). This situation is observed in daytime below 140–160 km. The first limiting case ( $[O^+] \approx n_e$ ) corresponds to altitudes above 180–200 km. More detailed calculations of the altitude separating between these two ionospheric regions and comparison with experimental findings will be given in Section 26. The dependence of the relative and absolute ion concentrations and of  $n_e$  on  $I$  and  $n$  is summarized in Table 42.

TABLE 42. Dependence of relative and absolute concentrations of ions and electrons on the total particle concentration  $n$  and the ionizing radiation intensity  $I$

Ionospheric region		Concentration		Dependence on $I$	Dependence on $n$
		relative	absolute		
At all altitudes			$[O^+]$	$\sim I$	independent
Upper part	$[O^+] \approx n_e$	$[O^+]/n_e$ $[NO^+]/n_e$ $[O_2^+]/n_e$ }		independent $\sim 1/I$	independent $\sim n$
	$[NO^+] + [O_2^+] \ll [O^+]$		$[NO^+]$ $[O_2^+]$ } $n_e$	independent $\sim I$	$\sim n$ independent
Lower part	$[O^+] \ll n_e$	$[O^+]/n_e$ $[NO^+]/n_e$ $[O_2^+]/n_e$ }		$\sim \sqrt{I}$ independent	$\sim 1/\sqrt{n}$ independent
	$[NO^+] + [O_2^+] \gg [O^+]$		$[NO^+]$ $[O_2^+]$ } $n_e$	$\sim \sqrt{I}$	$\sim \sqrt{n}$

It is remarkable that  $[O^+] \propto I$  at all altitudes. The absolute concentrations of the molecular ions and  $[O^+]/n_e$  show the same dependence on  $I$ , whereas the dependence on  $n$  is different for the two quantities.

The two limiting cases correspond to two different laws of recombination (linear and quadratic) which are observed in the ionosphere in  $E$  and  $F$  regions. The different recombination laws only reflect one side of the situation. We see from Table 42 that these regions are also characterized by different variation of all the absolute and relative concentrations of ions (except  $[O^+]$ ) as a function of  $I$  and  $n$ . It is clear from the above that an intermediate region exists at altitudes of 150–200 km in which the dependence of the ion concentrations on the radiation intensity and atmospheric density is more complex than what is shown in Table 42. More general expressions (V. 86)–(V. 88), combined with (V. 90), should be used to compute this dependence at these altitudes.

**Dependence on neutral composition of the atmosphere.** The ratio  $[O]/[N_2]$  is the principal parameter characterizing the relative composition of the atmosphere. The concentration of the  $N_2^+$  ions is a relatively simple function of the ratio  $[O]/[N_2]$ . For  $h < 250$  km, where dissociative recombination of  $N_2^+$  is negligible, the concentration  $[N_2^+]$  is inversely proportional to the ratio  $[O]/[N_2]$  and therefore decreases as this ratio increases. Conversely, the

concentration of the atomic oxygen ions is approximately directly proportional to  $[O]/[N_2]$ . Indeed, by (V.80), the dependence of  $[O^+]$  on composition at  $h > 110 - 120$  km is given by expression

$$[O^+] = \left\{ \frac{[O]}{[N_2]} i_1 + \frac{\gamma_4}{\gamma_4 + \gamma_{N_2^+}} i_2 \right\} \left\{ \gamma_{NO^+} + \gamma_{O_2^+} \frac{[O_2]}{[N_2]} \right\}^{-1} \propto \frac{[O]}{[N_2]}, \quad (V.91)$$

since the second bracket in (V.91) is nearly constant and in the first bracket only the first term is significant. Note that the ratio  $[O^+]/[N_2^+]$  should be highly sensitive to any changes in the neutral composition of the atmosphere.

We have so far mainly dealt with the altitudes  $h > 140$  km. In Section 19 we discussed the anomalous increase in the rate of formation of the  $O_2^+$  ions at lower altitudes. Since in the anomalous region  $O_2^+$  mainly formed as the primary ions, the  $NO^+$  ions are produced apparently only through reaction (V.76) in which  $O_2^+$  react with  $NO$ ,  $N_2$ , and  $N$ . In equilibrium, we have for these ions

$$\mu_6 [O_2^+] = \alpha_{NO^+}^* [NO^+] n_e, \quad (V.92)$$

which gives

$$\frac{[NO^+]}{[O_2^+]} = \frac{\mu_6}{\alpha_{NO^+}^*} \frac{1}{n_e}. \quad (V.93)$$

At a given altitude,  $z_0$  decreases as  $n_e$  increases and the solar activity decreases. This should result in an increase of the ratio  $[NO^+]/[O_2^+]$  in the morning and evening hours and in epochs of minimum solar activity /627/. Conversely, at sufficiently high altitudes ( $h > 140$  km), as we see from (V.86) and (V.87),  $[NO^+]/[O_2^+] = \text{const}$ , i.e., it is independent of  $n_e$  and the altitude, and remains virtually unchanged during the day and during the solar cycle /266/. This behavior of the molecular ions in the anomalous region affects the diurnal variation of the electron concentration and the effective recombination coefficient in the  $E$  region (see Section 26 in Chapter VI).

## 23. Ambipolar diffusion

### Definitions

Ambipolar diffusion is the diffusion of charged particles through a neutral medium. Since positive and negative charges do not separate in the ionosphere, which on the whole remains electrically neutral, positive ions and electrons diffuse as a single system. Hence the term "ambipolar". Let us now consider diffusion as a physical process.

The random movement of molecules in a gas leads to incessant mixing. As a result of this mixing, two different gases when brought in contact will interpenetrate or diffuse one into the other. This process is characterized by the mass flow  $G$ , which gives the number of particles  $N$  transported in a given direction through a unit section area in unit time  $t$ :

$$G = \frac{\Delta N_d}{\Delta s \Delta t}, \quad (V.94)$$

where  $\Delta s$  is the cross-section area of the gas flow. Observations show that the diffusive flow  $G$  is proportional to the concentration gradient of the transported particles  $dn/dx$  and is directed toward lower concentrations:

$$G = -D \, dn/dx, \quad (\text{V.95})$$

where  $D$  is the diffusion coefficient or the diffusivity [ $\text{cm}^2 \text{sec}^{-1}$ ], which depends on the particular gas and on the experimental conditions.

The molecular-kinetic theory of gases relates the diffusivity  $D$  to the parameters of the diffusing gas and the surrounding medium:

$$D = \frac{1}{3} \bar{v}_d \lambda \propto \frac{\sqrt{T_d}}{n}, \quad (\text{V.96})$$

where  $\bar{v}_d \propto \sqrt{T_d}$  is the mean thermal velocity of the diffusing particles,  $\lambda = (\sigma n)^{-1}$  is the mean free path of the particles in the gas, which depends on the particle concentration  $n$  and the effective collision cross section  $\sigma$ . At a fixed temperature  $T$ , the lighter particles will diffuse faster. Since  $D \propto n^{-1}$ , diffusion in rarefied gases is faster than in gases at high pressure. In highly rarefied gases the rate of mixing is independent of diffusion; the particle flow is generally determined by  $G = n\bar{v}$ , and this quantity thus provides the upper limit value for the diffusive flow. Relation (V.96) permits computing the diffusivity  $D$ , but the cross section  $D$  is uncertain. More reliable results for  $D$  are obtained in laboratory measurements.

In the ionosphere, the diffusion of the ions  $\text{O}^+$  through atomic oxygen is of the greatest interest. Laboratory measurements of the effective cross section have recently enabled Dalgarno /579/ to compute the coefficient  $D(\text{O}^+)$  at various temperatures. The earlier values were a factor of 3 too low. The bottom line of Table 43 gives the coefficient of ambipolar diffusion  $D_a = 2D(\text{O}^+)$ . All the figures in Table 43 are adequately fitted with the expression

$$D_a = n^{-1} \cdot 1.38 \cdot 10^{19} \sqrt{\frac{T}{1000}} [\text{cm}^2 \text{sec}^{-1}]. \quad (\text{V.97})$$

Other units are used in laboratory measurements for the diffusivity of ions in air and inert gases. According to latest data /511/, for the diffusion of  $\text{NO}^+$  in  $\text{NO}$  at  $T = 600^\circ \text{K}$  we have  $pD_a \approx 80 \text{ cm}^2 \text{sec}^{-1}$  (mm Hg). Changing over to our units, we find  $nD_a = 2.8 \cdot 10^{18} \text{ cm}^{-1} \text{sec}^{-1}$ .\*

TABLE 43. Ambipolar diffusion coefficient vs. temperature

$T, ^\circ \text{K}$	300	400	500	700	1000	2000
$D_a n \cdot 10^{-18}, \text{cm}^{-1} \text{sec}^{-1}$	6.6	7.8	9.0	11.2	13.8	19.2

Theoretical considerations indicate that the diffusion of charged particles transversally to the magnetic field is greatly hindered. Since the transport of ions in the ionosphere occurs in the vertical direction, one often uses the factor  $D_a \sin^2 J$ , where  $J$  is the inclination of the magnetic field. Clearly, vertical diffusion at the equator can be neglected.

\* At a pressure of 1 mm Hg,  $n = 3.54 \cdot 10^{16} \text{ cm}^{-3}$ .

**The diffusion equation.** We see from (V.95) that diffusive flow is generated only when there is a nonzero concentration gradient  $dn/dx$ . This is true for a free gas only, which is not affected by any external forces. The diffusive flow for the  $j$ -th component of the atmosphere in a gravitational field is given by

$$G_j = -D \left( \frac{dn_j}{dh} + \frac{m_j g}{kT} n_j \right). \quad (\text{V.98})$$

The effect of thermal diffusion is ignored and the  $j$ -th component is treated as a small impurity in the atmosphere. This equation shows, in particular, that in equilibrium, when  $G_j = 0$ , the distribution of the diffusing particles follows the barometric equation

$$\frac{dn_j}{dh} = -\frac{m_j g}{kT} n_j. \quad (\text{V.99})$$

Thus no vertical diffusive flow will be observed in a gravitational field only when the concentration gradient obeys the barometric equation (V.99). If (V.99) breaks down, diffusion of the corresponding component will begin, aimed at restoring the equilibrium gradient.

Diffusive flows in a gas are capable of altering the particle concentration if the intensity of  $G$  is not constant in space. Mathematically, this proposition is expressed by the equation of continuity.

$$dn/dt = -\text{div } G. \quad (\text{V.100})$$

For vertical flow  $\text{div } G = dG/dh$ , where  $G < 0$  corresponds to a downward flow. The equation of continuity for ions which are formed and destroyed in the ionosphere through photoionization and recombination processes only is

$$\frac{dn_e}{dt} = q - r - \frac{dG}{dh}. \quad (\text{V.101})$$

The last term in this equation is known as the "motion term." If only diffusive flow is considered, we can use (V.98) to write the "motion term" in explicit form:

$$\frac{dG}{dh} = -D_a \left( \frac{d^2 n_e}{dh^2} + \frac{3}{2H} \frac{dn_e}{dh} + \frac{n_e}{H^2} \right), \quad (\text{V.102})$$

since  $dD_a/dh = D_a/H$ , where  $H$  is the scale height for atomic oxygen. This equation was derived by Ferraro in 1945 /580/.

In a more general case,  $G$  in equation (V.101) incorporates not only the diffusive flow but also other ionic motions due to, say, streaming motion in the neutral atmosphere (winds) or magnetohydrodynamic effects (charge drift). In some cases, these effects are more significant than the diffusive flow.

We will now give a number of direct corollaries from the above equations, remembering that the diffusive factor is different at different altitudes in the ionosphere.

1) In the lower part of the ionosphere, the contribution from diffusive flow to the total balance of ionizations and recombinations in each cubic centimeter is small,  $|dG/dh| \ll q, r$ . Equation (V.101) thus reduces to the ordinary equation of photochemical equilibrium  $q = r$  and the electron concentration increases with altitude as

$$n_e = \frac{q}{\beta} \propto \exp \left[ h \left( \frac{1}{H_m} - \frac{1}{H} \right) \right], \quad (\text{V.103})$$

where  $H$  is the scale height for  $q$ , i. e., mainly for atoms, and  $H_m$  is the scale height for  $\beta$ , i. e., for molecules. Thus, from the physical point of view, the vertical growth of  $n_e$  is associated with the fact that the recombination coefficient decreases with increasing altitude faster than the rate of ionization  $q$  (since  $H > H_m$ ). Using (V.102) and remembering that, by (V.103),  $dn_e/dh \approx n_e/H$  and  $d^2n_e/dh^2 \approx n_e/H^2$ , we obtain for this range

$$4D_a n_e / H^2 \ll \beta n_e. \quad (\text{V.104})$$

2) The most difficult region for theoretical analysis is that where  $|dG/dh| \approx r$  or

$$4D_a / H^2 \approx \beta. \quad (\text{V.105})$$

The  $F$ -layer maximum forms in this region and it is here that the decisive mechanisms change from ionization-recombination to diffusion. This ionospheric region will be treated in some detail in Section 28.

3) The concentration of ions and electrons above the  $F$  region follows the barometric distribution (V.99). Since in the  $F$ -layer maximum  $n_e$  deviates from the barometric distribution, there should be a continuous downward flow of ions in this region according to (V.98). The deviation from the barometric distribution becomes more pronounced at lower altitudes, so that at first  $G$  increases with decreasing altitude, but then it diminishes as  $D \propto n^{-1}$ . It is readily seen that in the layer maximum, where  $dn_e/dh = 0$ , we have  $G = -D_a n_i m_i g / kT \approx -3 \cdot 10^9 \text{ cm}^{-2} \text{ sec}^{-1}$ . This flow is approximately equal to the number of ions produced by solar radiation in the upper part of the ionosphere above the  $F_e$  region. To establish this, let us consider the total number of different processes in the ionospheric column.

4) We integrate equation (V.101) over the altitude and consider the quasi-stationary case

$$Q - R + G = 0, \quad (\text{V.106})$$

where  $Q = \int q dh$  and  $R = \int r dh$ . At night  $Q = 0$ , so that  $R = G$ . This indicates that, at night, in the absence of ionization sources, the total downward flow of ions is needed to offset the recombination processes in an ionospheric column of  $1 \text{ cm}^2$  cross section. At fairly high altitudes, the rate of recombination is low, i. e.,  $R = 0$  and therefore  $G = 0$ . This case has been considered before: it corresponds to barometric distribution of particles with altitude. Above the  $F$ -region maximum, the contribution from recombinations is negligible in daytime too ( $r \ll q$ ). Therefore under stationary conditions,  $G \approx -Q$ , i. e., the resultant flow at the upper and the lower boundary of this ionospheric region is determined by the number of ions produced inside.

This is quite obvious since, because of the insignificant recombination, almost all the ions and electrons produced by photoionization should leak either up (into the exosphere reservoir) or down (into the recombination sink).

This concludes our treatment of the fundamental physical processes in the ionosphere. The aim of this chapter was to provide quantitative characteristics and notions of each process individually. In some cases, for purposes of comparison, competing processes were analyzed in order to determine which effect predominates in different ionospheric regions. Often, as in the end of this section, we had to consider the combined effect of different or oppositely directed processes in order to arrive at particular conclusions concerning the behavior of the ionosphere. Detailed treatment of the interaction between various ionization, recombination, ion-molecular, and diffusion processes, i. e., problems of the formation of the ionosphere, and comparison with observational data will be given in the next chapter. No general solution of this problem, allowing for all the relevant factors and processes, is feasible. Fortunately, it is not absolutely essential. There are ionospheric regions where  $n_e$  is determined by the combined effect of only two competing processes. It is these regions that are first considered. The transition regions, on the other hand, constitute the main difficulty. One of such hurdles is the  $F_2$  region, in which all the different processes are significant. The analysis of this ionospheric region is left to the end.



## Chapter VI

### THEORY OF FORMATION OF THE IONOSPHERE

#### 24. Formation of the ionosphere at altitudes $h \leq 100$ km

The  $D$  region has been less thoroughly studied than the other ionospheric regions so far. The main features of its behavior remained unclear, except the well-known abrupt increase in the degree of ionization during large chromospheric flares. Fairly recently Ratcliffe and Weeks /234/ noted that our data on the main ionization parameters of the atmosphere below the  $E$  region are highly incomplete and the existing theoretical models of the  $D$  region are unsatisfactory. In the last years, however, a number of fundamental parameters for the lower part of the ionosphere extending below the  $E$  region were refined. This refers mainly to the effective recombination coefficient and the electron concentration (see Sections 21 and 15). However, one of the main parameters — the concentration of negative ions — is still quite uncertain. The contradictory rocket data on the ratio  $r = n_i^-/n_e$  precluded a single-valued identification of the nature of the effective recombination coefficient and determination of the role of various photochemical processes in the ionization of the  $D$  region.

#### Elements of the photochemical theory

No generally accepted photochemical theory for the ionospheric regions with predominance of negative ions is available. Detailed treatment of the various processes leading to production and destruction of negative ions can be found in /571, 572, 581/. We will only consider those aspects of the theory which are important for further treatment.

The main primary negative ions which are readily formed in daytime in the  $D$  region are  $O_2^-$ . These ions are produced via attachment of an electron to an  $O_2$  molecule in triple collisions:



this reaction producing  $q(O_2^-) = 1.5 \cdot 10^{-30} [O_2]^2 n_e$   $O_2^-$  ions in  $1 \text{ cm}^3$  in 1 sec.  $O_2^-$  ions are lost, first, through photoneutralization, with visible radiation splitting off the attached electron at a rate of  $r_1 = \rho_1 [O_2^-]$  and, second, through collisions with atmospheric particles at a rate of

$$r_2(O_2^-) = k [O_2^-] n, \quad (VI.2)$$

where  $n$  is the concentration of the reactants,  $k$  is the rate constant of the bimolecular reaction. If we assume that the rate of production of the  $O_2^-$  ions is balanced by the rate of destruction, we obtain the first basic relation for the  $D$  region:

$$l^- = \frac{[O_2^-]}{n_e} = \frac{1.5 \cdot 10^{-30} [O_2]^2}{\rho_1 + kn}. \quad (VI.3)$$

Using ionospheric data, Bailey /582/ found  $k \approx (3-6) \cdot 10^{-17} \text{ cm}^3/\text{sec}$ , if  $n$  is the total concentration of particles. This conclusion is based on the observational fact that during PCA (Polar Cap Absorption) the radio wave absorption in daytime and at night differs by a factor of 4. Since radio wave absorption is proportional to  $n_e$ , we find  $\rho_1 + kn = 4kn$  (remembering that the same ionization source acts in daytime and at night, whereas  $r_1 = 0$  at night). According to rocket data, radio waves are absorbed mainly at altitudes of 65—75 km /237/. Using the effective value  $\rho_1 \approx 0.3 \text{ sec}^{-1}$  /574/ and  $n \approx 2 \cdot 10^{15} \text{ cm}^{-3}$ , we find  $k = 5 \cdot 10^{-17} \text{ cm}^3/\text{sec}$  in accordance with Bailey's results /582/.

Although collisions in the atmosphere may in principle detach the electron from  $O_2^-$ , it was not clear what particles  $O_2^-$  was colliding with: molecular nitrogen is ineffective in this reaction and for  $O_2$  laboratory measurements gave values 1/3—1/4 of the required rate constant. It was recently proposed that the  $O_2^-$  ions could interact with atomic oxygen /583/. This assumption is supported by the vertical variation of the concentration of these ions, which is the same as for atomic oxygen /584/, and by laboratory measurements of the rate constants of various reactions between negative ions and atmospheric particles /585/. The rate constant of the reaction between  $O_2^-$  and atomic oxygen was found to be  $k = 3.3 \cdot 10^{-10} \text{ cm}^3/\text{sec}$ . In this case, the concentration of atomic oxygen in the  $D$  region, approximately at the 70 km level, should be taken around  $3 \cdot 10^8 \text{ cm}^{-3}$ , which is not unreasonable. The rate constant  $k$  may be treated as some effective constant, possibly for an entire system of (as yet unknown) reactions whose resultant effect is to detach electrons from  $O_2^-$  ions by a process of collision.

It is quite probable that under equilibrium conditions in the  $D$  region, the main negative ion is not  $O_2^-$  but some other more stable ions, such as  $NO_2^-$  /574, 585/. The above line of argument does not change, however, since the rate of production of this ion is precisely equal to the rate of production of the  $O_2^-$  ion, and only the values of  $\rho_1$  and  $kn$  in (VI.3) will change.\*

When negative ions are present in relative concentrations  $l^- = n_i/n_e$ , the equation of ionization balance for the electrons has the form

$$\frac{dn_e}{dt} = \frac{q}{1+l^-} - (\alpha^* + l^-\alpha_i) n_e^2 - \frac{n_e}{1+l^-} \frac{dl^-}{dt}, \quad (VI.4)$$

which is readily derived from the standard equation for ions

$$\frac{dn_i^+}{dt} = q_i - \alpha' n_e^2, \quad (VI.5)$$

where  $n_i^+ = (1 + l^-) n_e$  and  $\alpha' = (1 + l^-) (\alpha^* + l^-\alpha_i)$  by (V.63) in Section 21. The equilibrium between the number of negative ions and electrons in the  $D$  region is

\* In accordance with /585/, LeVrier and Branscomb /719/ have recently developed a new photochemical theory of the  $D$  region and their general conclusions on the whole confirm our basic assumptions.

restored faster than the equilibrium between the rate of ionization and the rate of neutralization processes. As a result, the third term in (VI.4) can be ignored for quasi-stationary conditions:

$$\frac{dn_e}{dt} = \frac{q}{1+l} - (\alpha^* + l\alpha_i) n_e^2. \quad (\text{VI.6})$$

The effective recombination coefficient of electrons in the  $D$  region is thus

$$\alpha'_e = \alpha^* + l\alpha_i, \quad (\text{VI.7})$$

and the effective rate of production of electrons is

$$q_e = q_i (1+l)^{-1}. \quad (\text{VI.8})$$

The various theories of formation of the  $D$  region are reviewed in /581, 586/. These theories are contradictory and they use different approaches to the selection of the coefficients of production and destruction of negative ions and the recombination rates in the  $D$  region.

One of the authors /62/ tried to approach the problem of ionization in the  $D$  region from a different angle. The first step was to assemble the most reliable data on the ionizing agents. Once the fundamental ionization mechanisms at different levels in the  $D$  region have been identified, other parameters of this ionospheric region can be selected.

This approach requires detailed discussion of ionization effects produced by solar X rays and cosmic rays. We should consider the production of ions at altitudes  $h \leq 100$  km under quiet conditions and during solar flares. The computed ionization rates  $q$  based on solar radiation data will then be compared with the values of  $\alpha' n_e^2$  obtained from observational data on  $n_e$  and  $\alpha'$  in the ionosphere.

### Ionization under quiet conditions

We will first determine the ionization effect produced by solar radiation. The ionization rates at altitudes  $h \leq 100$  km are easier to compute than those at high altitudes, since the atmospheric composition is constant. In this case, the sum over the various atmospheric components in (V.8) and (V.29) is replaced by the appropriate averages according to (V.6) and (V.7), which markedly simplifies the computations of  $q$ . Moreover, below  $h \approx 90$  km, the short-wave radiation with  $\lambda \approx 1000 \text{ \AA}$  arrives greatly attenuated and ionization is produced mainly by X rays with wavelengths shorter than  $\lambda \sim 100 \text{ \AA}$ . The absorption and ionization cross sections of air for this radiation are fairly well known: they vary monotonically with wavelength and do not reveal any of the specific singularities characteristic for the radiation above  $800 \text{ \AA}$ , so that the computation of  $q$  is further simplified.

Let us consider the main results obtained for  $q$ , which are described in more detail in /62/.

The computations of /62/ for the altitudes  $h \leq 80$  km were supplemented by more recent computations from Section 25 for  $h \geq 85$  km. Figure 75 shows the computed values of  $q_{\odot}$  (the subscript  $\odot$  refers to ionization by the short-wave radiation of the Sun) for high and low levels of solar activity. The computations for  $\alpha_{\odot} = 60^\circ$  reflect typical daytime conditions at middle latitudes.

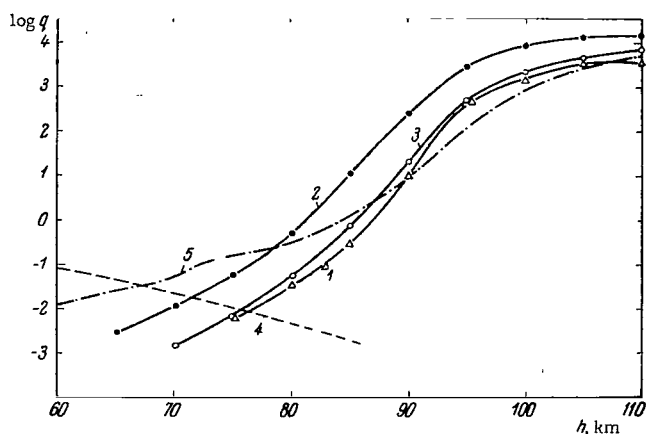


FIGURE 75. Rate of ionization for a quiet Sun;

1 — ionization by solar radiation, low solar activity,  $z_{\odot} = 0$ ; 2 and 3 — ionization by solar radiation, high solar activity,  $z_{\odot} = 0$  and  $z_{\odot} = 60^{\circ}$ ; 4 — ionization by cosmic rays; 5 —  $\alpha' n_e^2$  from ionospheric data.

Let us compare the results for  $q_{\odot}$  with the values of  $\alpha' n_e^2$  computed from the experimental data on  $n_e$  from Section 15 and the data on  $\alpha'$  from Section 21 (the dash-dotted line in Figure 75). At altitudes between 85 and 110 km, there is a good fit between  $q_{\odot}(z_{\odot} = 60^{\circ})$  and  $\alpha' n_e^2$ , if we recall that the accuracy in the numerical results is on the whole no better than by a factor of 1.5–2. Hence it follows that the short-wave solar radiation is one of the major, if not the major, sources of ionization at these altitudes. Since at  $h = 75–90$  km,  $q_{\odot}$  varies by approximately one order of magnitude during the solar cycle,  $n_e$  may vary by half an order of magnitude at these altitudes. Lack of accurate data makes it impossible to verify this conclusion.

**Cosmic rays.** Figure 75 shows that below  $h \sim 85$  km the curve of  $q_{\odot}$  departs from the  $\alpha' n_e^2$  curve. This cannot be attributed to the effect of negative ions, since for  $l = n_i/n_e \neq 0$ , we have  $q > \alpha' n_e^2$ , and not inversely. Some other source of ionization should thus be active below 85 km.

It has been firmly established that the ionization in the lower part of the *D* region is produced by cosmic rays. Figure 75 gives a curve 4 corresponding to ionization by cosmic rays according to /505/. For  $h > 75$  km in daytime, X rays with wavelengths between 10 and 100 Å and radiation with  $\lambda \approx 1000$  Å make a more significant contribution to ionization than cosmic rays.

On the other hand, comparison of  $q_{c.r.}$  and  $\alpha' n_e^2$  in Figure 75 shows that for high solar activity, in daytime, cosmic rays can account for the ionization only at altitudes below 65–70 km, and moreover only if  $l < 1$  at these altitudes. If  $l > 1$ , ionization by cosmic rays will occur at still lower altitudes. For low solar activity, the zone of ionization by cosmic rays rises to about 75 km altitudes.

**The hypothesis of  $L_{\alpha}$  radiation.** If the *D*-region ionization were only determined by cosmic rays and by solar radiation, a gentle minimum of electron concentration would be inevitably observed at altitudes of 60–75 km, especially in epochs of low solar activity. And yet no such minimum emerges from the experimental data on  $n_e$ , which systematically decreases at altitudes from 100 to 60 km. Consequently, there should exist a third source of ionization filling in the minimum at these altitudes.

According to the theory of Nicolet and Aikin /480/, the main ionization in the intermediate region, where neither the first nor the second source are very efficient, is produced in daytime by the solar  $L_\alpha$  radiation. In /480/, the rate of ionization by the  $L_\alpha$  radiation,  $q_{L_\alpha}$ , is derived assuming the existence of NO molecules in the  $D$  region with a relative concentration  $\sim 10^{-10}$ . Recently, some of the basic assumptions of the theory were reviewed. Nicolet /587/ revised the NO concentration in the upper atmosphere. For 80 km he now takes  $[\text{NO}] = 10^6 \text{ cm}^{-3}$ , which corresponds to relative concentration of  $2.5 \cdot 10^{-9}$ .

Originally the dissociative recombination coefficient for the  $\text{NO}^+$  ion was markedly underestimated,  $\alpha^* = 3 \cdot 10^{-9} \text{ cm}^3/\text{sec}$ , leading to effective recombination coefficients  $\alpha'$  which were 1 — 1.5 orders of magnitude too low /245/. In /588/, Nicolet almost doubled his original estimate  $\alpha_{\text{NO}^+}^* = 2 \cdot 10^{-7} \text{ cm}^3/\text{sec}$ , and  $\alpha'$  was correspondingly increased. The theory of Nicolet and Aikin /480/ has by now been radically revised and improved by one of its authors.

Three rocket measurements of the  $L_\alpha$  intensity and the electron concentration in the  $D$  region were recently carried out for large zenith distances of the Sun,  $z_0 = 95, 84, \text{ and } 79^\circ$ . Since the levels of constant values of  $n_e$  depend on  $z_0$  in precisely the same way as the  $L_\alpha$  intensity, it is suggested that this radiation is in fact responsible for the ionization in the  $D$  region /589/.

Two other rocket launches at sunrise, with  $z_0 = 108^\circ$  and  $95^\circ$  /590/, showed that  $dn_e/dt$  is proportional to the total energy of the  $L_\alpha$  radiation accumulated between 120 and 150 km in the period of time which elapsed between the two launches. These facts provide an indirect confirmation of the hypothesis. However, ionization by  $L_\alpha$  radiation alone cannot account in full for the actual  $n_e$  at altitudes of 65 — 80 km. One of the main objections to this stems from the exceptional stability of  $L_\alpha$ , whereas the ionization at these altitudes in the  $D$  region is subjected to incessant irregular variations and in fact increases at higher latitudes.

**The corpuscular hypothesis.** The increase of  $n_e$  in the  $D$  region during disturbances and at high latitudes may be due to the enhancement of the electron streams with  $E \gtrsim 30 \text{ keV}$ . It was thus suggested /62, 237/ that under quiet conditions electron streams may make a significant contribution to ionization at middle latitudes.

Suppose that this is indeed the missing third source of ionization. Let us estimate the expected electron flux proceeding from known cross sections for absorption and ionization. Electrons with energies of  $10^6$ ,  $3 \cdot 10^5$ , and  $10^5 \text{ eV}$ , respectively, penetrate down to altitudes of 60, 70, and 80 km (the estimates are based on the penetrating power of the electrons). To produce ionization with  $q_s = \alpha' n_e^2 = 0.01, 0.05, \text{ and } 0.3 \text{ cm}^{-3} \text{ sec}^{-1}$  at these altitudes (see Figure 75), the electron flux should be of the order of 1, 10, and  $10^2 \text{ electrons/cm}^2 \text{ sec}$ , respectively (see Section 20). Since the integral energy spectrum of electrons is of the form  $E^{-4}$  or  $E^{-3}$ , we obtain a flux of  $10^{-4} - 10^{-3} \text{ erg/cm}^2 \text{ sec}$  for electrons with  $E \gtrsim 20 - 40 \text{ keV}$ . This precisely corresponds to the flux intensity measurements of the injected electrons from rockets and satellites, described in Section 17.

It was noted in /245/ that the day-to-night and the latitudinal variations of the electron flux measured on satellites correspond to the observed variations of  $n_e$  in the  $D$  region.

On the other hand, for large  $z_0$ , the rate of ionization produced by the solar radiation only is definitely insufficient. Indeed, consider the variations during one day. As we see from Figure 75,  $q_0$  at altitudes of 80—100 km for  $z_0 = 60^\circ$  is approximately one order of magnitude smaller than for  $z_0 = 0$ . Thus, in the  $D$  region,  $q_0$  is highly sensitive to  $z_0$ ; we should therefore expect a change by 2.5—3 orders of magnitude in  $n_e$  between small  $z_0$  and  $z_0 \approx 90^\circ$ . However, the  $n_e$  at these altitudes changes only by 1—1.5 orders of magnitude between night and day. Hence it follows that a new source of ionization should become effective for large  $z_0$ .

Similarly, below 110 km,  $n_e$  retains its high value at night. Therefore, to sustain the nocturnal ionization, we require a source whose strength may only be 2—3 orders of magnitude less than the strength of the daytime source (allowing for the nighttime increase in  $\tau$ ).

Let us now consider the latitudinal variations. As we noted in Chapter IV, Gregory /242/ studied the behavior of the ionosphere at 80—100 km during a polar night at a latitude of  $79^\circ$ , where the values of  $n_e$  are low but by no means negligible (see Table 22), and came to the conclusion that cosmic rays alone were insufficient for sustaining the nocturnal polar ionosphere and that an additional flux of at least 70 electrons/cm<sup>2</sup>sec at electron energies of 10—100 keV had to be assumed. Since Gregory's values of  $n_e$  at 80—90 km in the polar ionosphere are an order of magnitude less than the values of  $n_e$  at middle latitudes, where the cosmic ray intensity is lower, the cosmic rays certainly cannot be accepted as the sole source of nocturnal ionization in the  $D$  region, anyhow not above 80 km.

In summing up, we can say that the computations of  $q_0$  and their comparison with the experimental values of  $\alpha'n_e^2$  elucidated the following basic points concerning the mechanism of ionization in the  $D$  region. In daytime, the solar X rays produce ionization above 85—90 km and cosmic rays are effective below 65—70 km. At intermediate altitudes, the solar  $L_\alpha$  radiation probably makes a certain contribution, but a more powerful source, especially during periods of high solar activity, may be provided by the sporadic flux of injected electrons with  $E = 30—1000$  keV, which possibly accounts for the ionization at high  $z_0$  and at night. These conclusions are obtained without resorting to the theory of elementary chemical processes in the  $D$  region. It is assumed, however, that the observational data for  $\alpha'$  and  $n_e$  are sufficiently reliable. Since this assumption is by no means obvious, further confirmation of this point is required. Particularly favorable conditions occur during sudden ionospheric disturbances (SID), when  $n_e$  markedly increases and the accuracy of the measurements is correspondingly improved.

## Ionization during solar flares accompanied by SID

Since rockets and satellites have measured the solar X rays during chromospheric flares, we can now try to compute the  $D$ -region ionization due to these flares during SID. Such computations have been carried out by a number of authors, but the different results are widely divergent. Figure 76 compares the values of  $q$  computed for a class 2<sup>+</sup> flare from the data of /480, 591, 592/ with the values of  $\alpha'n_e^2$  computed from the observations of  $\alpha'$  and  $n_e$  during ionospheric disturbances (Table 22). As we see, the computed values of  $q$  deviate from  $\alpha'n_e^2$  in either direction by one or more orders of magnitude. What is the reason for these pronounced deviations?

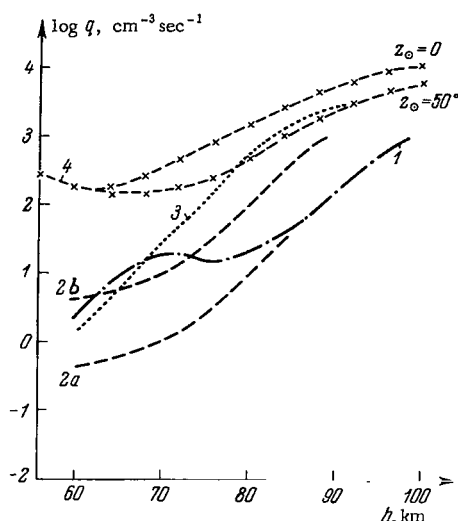


FIGURE 76. Rate of ionization during solar flares accompanied by SID:

1 —  $\alpha'n_e$  from ionospheric data; 2 — Nicolet and Aikin /480/, a — for a flare, b — for a strong flare; 3 — Whitten and Poppoff /591/; 4 — Swift /592/ for  $z_0 = 0$  and  $z_0 = 60^\circ$ .

The computations of Swift /592/ yielded exaggerated values of  $q$ , especially at low altitudes. This was due to his having used exaggerated flare radiation intensities, particularly for  $\lambda < 1 - 2 \text{ \AA}$ . The data of Whitten and Poppoff /591/ and those of Nicolet and Aikin /480/ (for a strong flare) are close to  $\alpha'n_e$  at low altitudes, but come out too high at high altitudes. These data therefore give an excessively rapid variation of  $q$  with altitude. Conversely, below 70 km, the curve of Nicolet and Aikin /480/ is too gentle. The gentle variation of  $q$  as a function of  $h$  in /480/ at these altitudes is attributed to the relatively high intensity of the hard X rays  $\lambda \leq 2 \text{ \AA}$  assumed by Nicolet and Aikin compared to the intensity of the softer X rays. The computations of Holt /593/ carried out from the data of Nicolet and Aikin show that, if the radiation with  $\lambda \leq 1.5 \text{ \AA}$  is ignored altogether, the variation of the computed radio wave absorption with the Sun's zenith angle will give a much better fit of the observations. This implies that the radiation intensity assumed for  $\lambda \leq 1.5 - 2 \text{ \AA}$  was definitely too high in /480/.

In view of the strong scatter of the computed values of  $q$  during solar flares according to different authors, we carried out the computations anew /62/. We have seen before that the profile  $q(h)$  is largely sensitive to the correct choice of the radiation spectrum. We will therefore consider in detail the data on the X-ray spectrum during class 2 and  $2^+$  flares.

**X-ray radiation of chromospheric flares.** The X-ray spectrum of a chromospheric flare of class 2 and  $2^+$  which causes a SID in the D region was assessed from experimental data. The X-ray intensity of class 2 and  $2^+$  flares has been measured with integral radiation detectors. These measurements for  $\lambda \leq 8$ ,  $\lambda \leq 20$ , and  $\lambda = 44 - 60 \text{ \AA}$ , and also for  $\lambda \leq 0.6 \text{ \AA}$  are assembled in the top part of Table 44. Since only few measurements are

available for  $\lambda \leq 2 \text{ \AA}$ , the bottom part of the table gives the current data for the shortest wavelengths of the spectrum, although in fact they refer to flares of a different class. The integrated intensity of the flares of 19 August 1960 /73/, 27 April and 3 May 1962 /81, 596/, 7 August and 28 August 1959 /599/, and also the flare described in /597/ for conditions of maximum solar activity was estimated by the present authors proceeding from the detailed spectra that had been published.

TABLE 44. Rocket measurements of the X-ray intensity  $J (\leq \lambda)$  [erg/cm<sup>2</sup> sec] during solar flares for various  $\lambda$  (Å)

Data	Flare class	$\lambda \leq 8 \text{ \AA}$	$\lambda \leq 20 \text{ \AA}$	$\lambda \leq 100 \text{ \AA}$	Other $\lambda$	References
29 VIII 1957	2	0.02	—	—	—	64, 65, 594
24 VIII 1959	2*	0.026	0.16	$\leq 2.1$	—	64, 65, 42
31 VIII 1959	2*	$>0.22$	$>0.45$	$\leq 9.2$	$4.5 \cdot 10^{-6} (\leq 0.6 \text{ \AA})$	64, 65, 42, 594
1 IX 1959	2*	$>0.088$	$>0.9$	—	—	64, 65, 42, 594
19 VIII 1960	2*	$0.045 (\leq 6 \text{ \AA})$	$0.07 (\leq 10 \text{ \AA})$	—	—	73
19 VIII 1960	2*	—	$\sim 0.01 (\leq 10 \text{ \AA})$	—	—	66, 72
20 VII 1960	2 & 2*	$0.005-0.05$	—	—	—	71, 65
6, 11 & 14 VIII 1960						
2 & 24 IX 1960	2	—	—	—	$2.5 \cdot 10^{-6} (\leq 0.6 \text{ \AA})$	595
12 X 1960	2*	—	—	—	$7 \cdot 10^{-7} (\leq 12 \text{ \AA})$	596, 81
27 IV 1962	2	0.004	—	—	$6 \cdot 10^{-7} (\leq 12 \text{ \AA})$	596, 81
3 V 1962	2	0.0025	—	—	$\sim 5 \cdot 10^{-7} (\leq 0.6 \text{ \AA})$	597
1 V 1963	2*	$\sim 1$	$\sim 4$	—	$5 \cdot 10^{-4} (\leq 2 \text{ \AA})$	598
Max. solar act.	2	—	—	—	$3 \cdot 10^{-4} (\leq 2 \text{ \AA})$	599
7 VIII 1959	1*	—	—	—	$4 \cdot 10^{-6} (\leq 1 \text{ \AA})$	599
28 VIII 1959	1*	—	—	—	$1.2 \cdot 10^{-4} (\leq 2 \text{ \AA})$	600, 594
18 IX 1957	3	—	—	—		
20 VII 1961	3*	—	0.01	—	—	75
17 III 1962	1*	—	0.4	—	—	77
13 IV 1962	1*	—	—	—	$\sim 2 \cdot 10^{-7} (\leq 0.6 \text{ \AA})$	598
19 IV 1962	1*	—	—	—	$\sim 6 \cdot 10^{-7} (\leq 0.6 \text{ \AA})$	598
21 IV 1962	1*	—	—	—	$\sim 3 \cdot 10^{-6} (\leq 0.6 \text{ \AA})$	598
					$\sim 2 \cdot 10^{-6} (\leq 0.6 \text{ \AA})$	598

All these data are assembled in Figure 77, where the numerals against the curves identify the flare class, unless it is 2 or 2\*. Figure 77 uses different signs to identify the data obtained by different groups. The scatter of the experimental data is fairly large, revealing significant variations of intensity from flare to flare. The spectrum of all flares, even the weak ones, has a maximum at  $1-2 \text{ \AA}$  /599/, whose intensity varies and whose position shifts during the evolution of the flare. At long wavelengths, the points in Figure 77 fall into two groups. Approximating curve I is passed through the high points, and curve II is passed through the low points. Curves I and II reflect the actual scatter of the currently available intensity data, and they will be used as certain characteristic limiting values for the X-ray intensity of class 2 and 2\* flares.

The X-ray emission by solar flares at  $\lambda \geq 12 \text{ \AA}$  and  $\lambda \geq 4 \text{ \AA}$  was recently measured with scintillation counters on satellites moving in orbit far from the radiation belts /601/. For nine class 2 and 2\* flares (observed in October 1963), the same radiation detector recorded widely differing radiation energies in these spectral regions. Using the calibration curves, we find that for three of these flares and one bright class 1\* flare the energy estimates are close to curve I, for four flares they coincide with



curve II, but for two flares the energy estimates are even lower than curve II. There is thus a significant scatter in the X-ray intensities of flares of the same class.

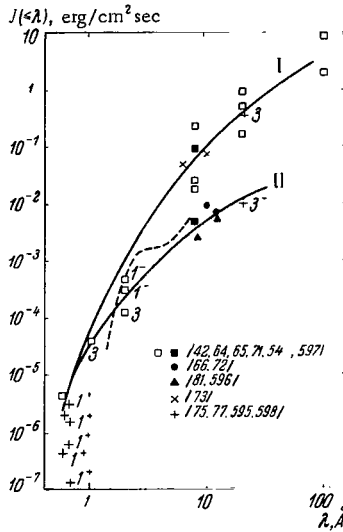


FIGURE 77. Integrated X-ray spectrum of solar flares. The solid curves are the averages for the maximum (I) and the minimum (II) values; the dashed curve is based on ionospheric data. The numbers identify the flare class, unless it is 2 or 2<sup>+</sup>.

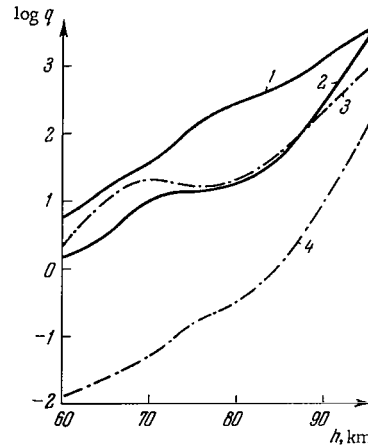


FIGURE 78. Ionization rate during solar flares for spectra I (curve 1) and II (curve 2).

Curves 3 and 4 plot  $\alpha n_e^2$  from ionospheric data during SID and for a quiet ionosphere.

The partition of flares into two categories is probably related to the effect of X rays from active regions on the Sun's disc. New satellite measurements /602, 603/ in the 44 — 60 Å region indicate that the radiation intensity is occasionally higher than the radiation intensity from flares with spectrum described by curve II (Figure 77). This probably accounts for the well-known fact that not every class 2 and 2<sup>+</sup> flare produces a SID.

Table 44 and Figure 77 give the integral intensities

$$J(\leq \lambda) = \int_0^{\lambda} I_{\lambda} d\lambda. \quad (\text{VI.9})$$

To change over to the values of  $I_{\lambda}$  used in (V.8) for the computations of  $q$ , the function  $J(\leq \lambda)$  should be differentiated.

Figure 78 plots the computed values of  $q$  based on the experimental flare spectra. Note that the values of  $q$  for  $h > 85$  km differ from the figures in /62/, since, like the computations of  $q_0$  for the undisturbed  $D$  region, they correspond to new and more comprehensive computations in the 90 — 100 km region which allow for both the X-ray radiation with  $\lambda < 20$  Å and the radiation with  $\lambda \sim 1000$  Å.

The computed values of  $q$  for spectra I and II are plotted in Figure 78 together with the experimental values of  $\alpha'n_e^2$  for disturbed and quiet  $D$  regions. Unlike the previous computations /591, 592/, here we used the average X-ray spectrum of the flare from different measurements and the average values of  $\alpha'n_e^2$  for disturbed ionospheric conditions. It would be more proper to compare the spectrum of a particular flare with the values of  $n_e^2$  for the ionosphere disturbed by that same flare, but no such data are available at this stage.

Comparison of the values of  $\alpha'n_e^2$  in Figure 78 for quiet and disturbed conditions shows that up to  $h \approx 65$  km the increment of  $\alpha'n_e^2$  during a disturbance relative to the undisturbed conditions increases with decreasing altitude. This is due to the particularly strong enhancement of the harder radiation component with  $\lambda \approx 1 - 5 \text{ \AA}$  in the flare.

On the average, curves 1 and 2 corresponding to the extreme intensity values bracket the averaged curve of  $\alpha'n_e^2$  between 60 and 90 km. Seeing that these computations refer to  $z_0 = 0$  and the observations were carried out for some higher  $z_0$ , we conclude that the top curve 1 provides a better fit for the observed intensities during SID. At altitudes of 60—70 km, where the largest increase of  $q$  during a flare is observed, curves 1, 2, and  $\alpha'n_e^2$  are on the whole close to one another, deviating by no more than a factor of 2 from the mean.

Our computations are closer to the experimental values of  $\alpha'n_e^2$  than the computations of /480, 591, 592/. New computations have recently been published /604/, whose results are close to our figures.

We thus see that a painstaking analysis of X-ray radiation from flares enables us to account for the relatively gentle variation of  $n_e$  with altitude between 60 and 80 km during ionospheric disturbances and to derive electron concentrations which are close to the experimental values of  $n_e$ . The ionospheric  $n_e$  data on the average fit the data on X-ray emission of solar flares.

Using the average ionospheric data on  $\alpha'n_e^2$  during SID and taking  $l' < 1$  at all altitudes, we computed the corresponding X-ray spectrum, which is plotted by the dashed curve in Figure 77. The flare spectrum based on SID data displays a prominent maximum at  $\lambda = 1.7 - 2.5 \text{ \AA}$ . Similar maxima were in fact observed at  $\lambda = 1 - 2 \text{ \AA}$  by Chubb et al. /599/. It is significant that, when the outburst at  $\lambda \leq 3 \text{ \AA}$  was ignored, the integrated intensity at  $\lambda \approx 6 \text{ \AA}$  dropped to 1/2. The contribution from such maxima therefore should be taken into consideration in any interpretation of photon counter data in the X-ray region of the solar spectrum.

Rocket data on the X-ray emission of the quiet Sun and during chromospheric flares are thus consistent with the experimental data for  $n_e$  and  $\alpha'$  in the  $D$  region. It should be stressed that this fact again confirms the reliability of the  $\alpha'$  values selected for this analysis. They can be thus used in the discussion of some photochemical problems and, in particular, for refining our information about negative ions. The similar trend of the  $\alpha'n_e^2$  and  $q$  curves in Figure 78 for all altitudes above  $h \approx 70$  km seems to indicate that at these altitudes we indeed have  $l' < 1$ . Let us consider this topic in more detail.

#### Estimates of $n_i$ and $l'$

The relative concentration of negative ions can be estimated by two methods using equations (VI.7) and (VI.8). Equation (VI.8) can be applied

at altitudes below 60 km, where ionization is produced by cosmic rays only, for which  $q_{c,r}$  is not difficult to compute. The value of  $q_e = \alpha_e n_e^2$  is readily estimated from data on  $n_e$  and  $\alpha_e$ . All these parameters are listed in Table 45 (borrowed from /605/). At 50 and 60 km, we find that  $l = \frac{q_{c,r}}{q_e} - 1$  is equal to 35 and 4, respectively, whereas  $n_i$  is 700 and 200  $\text{cm}^{-3}$ , respectively, to within a factor of 2–3. Comparison with various rocket measurements of  $n_i$  and  $l$  /606–611/, which differ by 2–2.5 orders of magnitude, shows that some data /608–610/ corresponding to the lowest concentrations  $n_i^+$  and  $n_i^-$  are close to our estimates. Since at 50–60 km altitudes  $\alpha^* \ll l\alpha_i$ , we have from (VI.7)  $\alpha_i = (0.7 - 2) \cdot 10^{-6} \text{ cm}^3/\text{sec}$ . This figure is higher than the laboratory data (Section 21), but it fits the earlier result  $\alpha_i = 1.4 \cdot 10^{-6} \text{ cm}^3/\text{sec}$  obtained from ionization data at low altitudes (5–30 km) /93/.

TABLE 45. Estimated concentration of negative ions in the *D* region in daytime

$h, \text{ km}$	$\alpha', \text{ cm}^3/\text{sec}$ /516/	$n_e, \text{ cm}^{-3}$ /237, 612/	$\alpha' n_e^2,$ $\text{cm}^{-3} \text{ sec}^{-1}$	$q_{c,r}, \text{ cm}^{-3}$ $\text{sec}^{-1}$ /505/	$l$	$n_i^-, \text{ cm}^{-3}$
50	$2.5 \cdot 10^{-5}$	20	0.01	0.35	35	700
60	$8 \cdot 10^{-6}$	50	0.02	0.1	4	200
70	$2.1 \cdot 10^{-6}$	160			1.1	180
80	$4.7 \cdot 10^{-7}$	800			0.1	240

Let us now move on to higher altitudes. At 70–80 km, the temperature of the atmosphere is  $T \sim 200^\circ\text{K}$ , which corresponds to  $\alpha^* = (2 - 3) \cdot 10^{-7} \text{ cm}^3 \cdot \text{sec}^{-1}$  (Section 21). Using (VI.7) and the values of  $\alpha'$  from Section 21, we obtain the values of  $l$  for 70 and 80 km altitudes which are listed in Table 45. We have advanced in the unusual direction from  $n_i$  to  $\alpha'$  and then almost all the way back from  $\alpha'$  to  $l$ , assuming that  $\sigma'$  is known with higher accuracy than the experimental concentrations of negative ions determined in rocket measurements.

Let us compare these values of  $l$  with the theoretical results obtained from (VI.3). Plotting  $1/l$  from Table 45 vs.  $n/[\text{O}_2]^2$ , we discover a linear relation between these quantities. The slope of the line and its intercept give, as usual,  $\rho_1 = (0.2 - 0.45) \text{ sec}^{-1}$  and  $k = (3 - 10) \cdot 10^{-17} \text{ cm}^3/\text{sec}$ , which confirm the earlier estimates. We thus see that  $\text{O}_2^-$  are the primary negative ions in the *D* region. In our treatment, we did not assume that the  $\text{O}_2^-$  ions were the main equilibrium ions; the only assumption was that they are destroyed via a bimolecular reaction with an effective rate constant  $k$ . At the beginning of the section we saw that this assumption is compatible with the existence of negative ions other than  $\text{O}_2^-$ , which is indeed assumed in the newer publications.

Let us now consider the parameter  $\rho$ . If  $\text{O}_2^-$  is an equilibrium ion in the *D* region, we have  $\rho_1 = 0.44 \text{ sec}^{-1}$ . If  $\rho_1$  is smaller,  $0.2 \text{ sec}^{-1}$ , say (as above), we are dealing with a different negative ion with a higher electron affinity ( $\text{NO}_2^-$ , say). Accurate determination of  $\rho_1$  would thus provide basic information concerning one of the topical problems in the photochemistry of the *D* region.

Another interesting effect associated with  $\rho_1$  should be mentioned. In daytime, as we see from (VI.3),  $\rho_1$  essentially determines the ratio  $l$ . Changes in  $\rho_1$  should thus lead to changes in  $l$  in the opposite direction. One of the possible reasons for day-to-day variation in  $l$  was recently suggested

in /613/. The authors note that the scattered radiation from the ground and from the atmosphere accounts for almost one half of the actual value of  $\rho_1$  (the other half being due to solar radiation). Variations in the Earth's albedo should thus affect the relative concentration of the negative ions in the  $D$  region and hence the absorption of the long radio waves. This, in particular, should lead to seasonal effects, since snow and winter clouds increase the Earth's albedo.

## 25. Formation of the ionosphere at altitudes of 100 — 200 km

Most of the short-wave ionizing radiation of the Sun is absorbed at altitudes of 100 — 200 km. At these altitudes, the positive effect of the solar radiation on the ionosphere is most clearly manifested. Therefore, pursuing the main purpose of this book, which is the Sun — ionosphere interaction, we will now consider in detail the formation of the ionosphere at these particular altitudes.

The 100 — 200 km region differs from that considered in the previous section (the region below 100 km) primarily in that it contains no negative ions, although the positive ions undergo complex photochemical reactions with one another and with neutrals. This region is divided into several zones with different photochemical properties. As the zenith angle of the Sun increases, the zones become wider and shift upwards.

Primary ions produced as a result of ionization by the short-wave radiation of the Sun provide the starting material for various photochemical processes. The rate of production of ions at different altitudes is therefore highly important. We will first consider in some detail the basic data on  $I_\lambda$  and  $\sigma_\lambda$ , discuss the computations of the ionization rates for various ions, and then analyze the diurnal variations of the ion composition and electron concentration at various altitudes.

### Choosing the absorption (and ionization) cross sections and solar radiation intensities

The development of the theory of ionization for the ionosphere is considerably handicapped by the lack of accurate and reliable data on the effective cross sections for absorption  $\sigma$  and ionization  $\sigma_i$ . In recent years, the rapid advances of space research encouraged detailed laboratory measurements of  $\sigma$  and  $\sigma_i$  for various atmospheric gases, which were performed by Huffman et al. /614, 615/, Cook et al. /616, 617/, Samson et al. /618, 619/, and Kosinskii and Startsev /620/.

These laboratory measurements elucidated the structure of the absorption and ionization cross sections of the molecules  $O_2$  and  $N_2$  at 600 — 1100 Å, which had been discovered earlier /621/. We see from Figures 79 and 80 (where only the results of /615/ are plotted) that the molecules  $O_2$  and  $N_2$  in this spectral region have a complex system of fairly narrow absorption bands, which could not be investigated before because of the absence of suitable continuous spectrum sources. The complexity of the system of narrow bands is not the only complicating factor: the cross section data of

various authors widely diverge. To select the most reliable cross sections in the bands and between them, all the data have to be carefully analyzed. The cross sections for  $O_2$ ,  $N_2$ , and  $O$  were selected for 150 separate spectral regions in which either the cross sections or the short-wave radiation intensities are different. The selected values of  $\sigma$  and  $\sigma_i$  are listed in Table 46, which contains the starting data for the computation of  $q$ . A few comments concerning these figures are now in order.

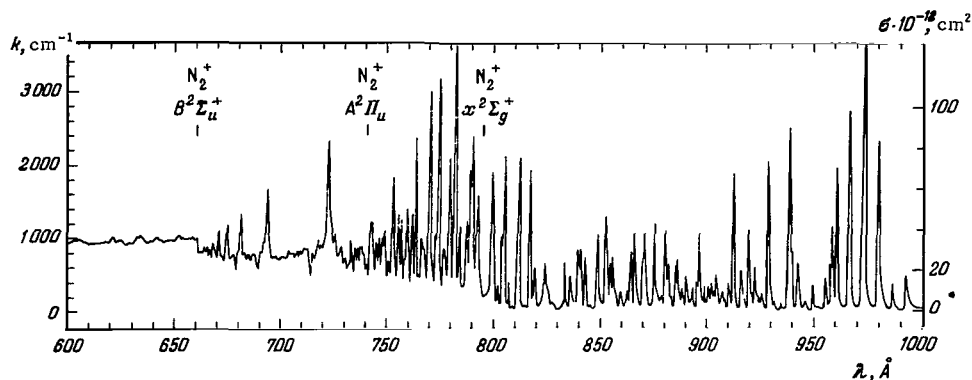


FIGURE 79. Absorption cross section  $\sigma$  (and absorption coefficient  $k$ ) of molecular nitrogen between 600 and 1000 Å /615/.

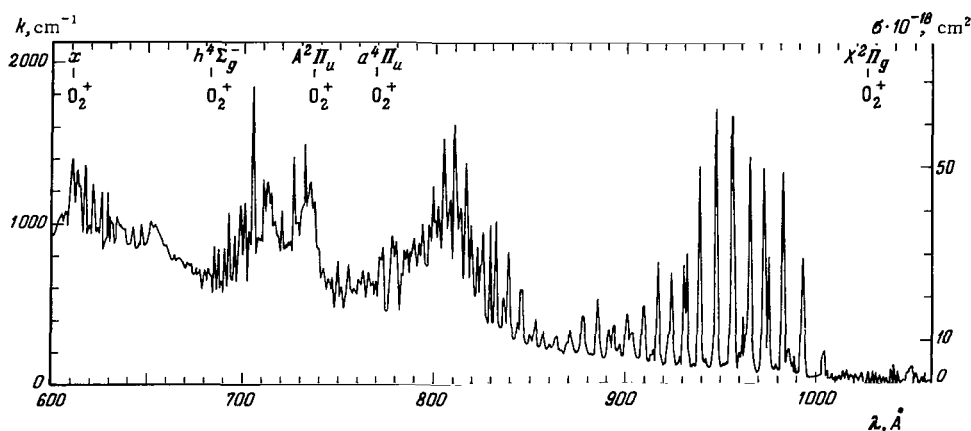


FIGURE 80. Absorption cross section  $\sigma$  (and absorption coefficient  $k$ ) of molecular oxygen between 600 and 1060 Å /615/.

The most divergent absorption cross sections  $\sigma$  are available for  $N_2$ . Nevertheless, the average values listed in Table 46 differ from the extreme values mainly by no more than a factor of 1.5. Moreover, the computations show that introduction of ionization by the entire wide spectral region reduces the resulting error in  $q$  to no more than 25%. For molecular oxygen  $O_2$  the difference in  $\sigma$  is quite large (by a factor of 2 — 3) for  $\lambda \geq 820$  Å only.

As a result, the value of  $q$  in the 95 — 110 km region, where this radiation is effectively absorbed, is obtained to within a factor of 1.5, which is worse than at other altitudes but still acceptable.

TABLE 46. Starting data for  $\sigma$ ,  $\sigma_1$ ,  $I^{\min}$  and  $I^{\max}$  used in the computation of  $q$

Wavelength $\lambda$ , Å	$\sigma \cdot 10^{18}$ , cm <sup>2</sup>			$\sigma_1 \cdot 10^{18}$ , cm <sup>2</sup>			$I_{\lambda} \cdot 10^{-7}$ , keV/cm <sup>2</sup> sec	
	O	O <sub>2</sub>	N <sub>2</sub>	O	O <sub>2</sub>	N <sub>2</sub>	$I^{\min}$	$I^{\max}$
1037.6	↑	7.8	0	↑	0.008	↑	133	266
1031.9		10.4	0		0.10		189	378
1025.7		15	0		9.7		230	320
1026—1005		11.2	0		7.0		48.2	225
1005—1003		75	0		21		4.6	23
1003—993								
991.5		18.5	0.75		12		53	155
993.0—991.4		100	40		20		0	13
991.4—986.7		37.2	1.5		4.1		8.0	48
985—984		37.2	30		4.1		0	13
986.7—985		14	1.67		9.5		25	35
989.8		185	1		90		0	15
984—982		30	350		20		0	30
982—978.3		40	0.82		24.7		340	490
978.3—976.5								
977		112	1.0		2.0		0	12
976.0—972.5		220	350		100		0	19
975.0—972.5		320	3 · 10 <sup>3</sup>		2 · 10 <sup>2</sup>		55	77
972.5		46	150		36.1		0	14
972.5—970.7		26	1.85		26		0	21
970.7—968	σ = 0	220	380	σ = 0	80	σ = 0	0	23
968—965		220	1.6		80		0	15
965—963		150	250		30		5.7	35
963—959.5		200	120		170		0	15
959.5—957.5		445	0.75		380		0	11
957.5—956		200	28		170		5.8	19
956—954.5		33.5	0.55		27		0	33
954.5—950.5		33.5	15		15		0	11
950.5—949		63	52		30		24	335
949.7								
949—948.5		185	0.75		100		0	8
947.5—947.0								
948.5—947.5		370	0.75		200		0	8
947—945.5		200	13		180		0	11
945.5—944		37.2	2.3		37		7.1	21
944—941.8		33.6	95		31		0	19
941.8—940.2		63	38		32		0	13
940.2—937.5		200	400		180		0	24
937.5		50	100		29		18.7	262
937.5—935.5		37.2	0.50		27		0	19
935.5—934.5		45.5	18.5		27		0	10
934.5—933.2		112	0.55		50		9.3	26
933.2—930.5		150	37		90		19	53.5
930.5—928.3		224	270		140		0	24
928.3—926.5		483	2.6		34		15	41
926.5—926	0	100	34	0	50		0	6.0
926—924	0	112	6.5	0	60		0	25
924—922.3	0	100	83	0	50		15	41
922.3—919.6	0	43	15	0	25		0	35
919.6—919								
922.15—921.85	0	65	4.0	0	28		0	12
919—916								
910—912	0	100	78	0	50		43	60
916—914	0	43	1.9	0	36		90	135
914—912	0	80	250	0	37		45	67.5
910—909	27	155	8.5	27	114		20	30
909—907	27	93	41	27	56		140	210
906—900								
907—906	27	63	11	27	34		77	115
890.8—887.8								
900—895.5	29	75	95	29	45		90	135
888.6—885								
885.5—884.2	28	110	8.5	28	37		20	30
884.2—883.1	28	82	48	28	70		16	24

TABLE 46 (continued)

Wavelength $\lambda$ , Å	$\sigma \cdot 10^{10}$ , cm <sup>2</sup>			$\sigma_i \cdot 10^{10}$ , cm <sup>2</sup>			$f_{\lambda} \cdot 10^{-7}$ , keV/cm <sup>2</sup> sec	
	O	O <sub>2</sub>	N <sub>2</sub>	O	O <sub>2</sub>	N <sub>2</sub>	$f_{\min}$	$f_{\max}$
893.1—892.1 } 885.0—883.3 } 870.5—868.6 }	29	82	9.3	29	55	$\sigma=0$	61	92.5
892.1—890.8 887.8—885.6 883.3—880.6 880.6—877.7 877.7—875.8 872.9—870.5 875.8—872.9 865—858.3 858.3—853.1 853.1—851 843.8—842.8 } 851—849.5 849.5—844.8 844.8—843.8 770—767.5 759—756.7 751—745.5								
842.8—840.3 840.3—838.6 838.6—837 837—835.6 835.6—834.6 834.6—827.5 827.5—824 783—781.8 760—759 756.7—755.7								
824—821.3 821.3—818.2 818.2—814.2 814.2—812.5 812.5—807.5 807.5—805.5 805.5—802.3 802.3—800.5 800.5—795.3 795.3—789 789—784.7 784.7—783 781.8—780.7 766—763.1 } 755.7—754 750.7—747 747—744.4 744.4—743 743—742 742—739 739—732 732—725 725—721 695.8—693.8 682.6—681 675.7—674.7 671.8—670.8 721—665* 665—600 584.3 600—580* 580—540 540—510 510—500 500—480								
820 82								

TABLE 46 (continued)

Wavelength $\lambda, \text{\AA}$	$\sigma \cdot 10^{18}, \text{cm}^2$			$\sigma_i \cdot 10^{18}, \text{cm}^2$			$I_{\lambda} \cdot 10^{-7},$ $\text{keV/cm}^2 \text{sec}$	
	O	O <sub>2</sub>	N <sub>2</sub>	O	O <sub>2</sub>	N <sub>2</sub>	$I_{\min}$	$I_{\max}$
480—460	121	260	160	121	230	160	70	100
460—435	105	250	160	105	230	160	49	245
435—400	125	240	150	125	240	150	99	195
400—370	111	230	150	111	230	150	56	280
368.1	103	220	113	103	220	113	58	290
370—355*	100	220	110	100	220	110	93	465
355—340	93	220	110	93	220	110	77	385
340—325	87	210	100	87	210	100	75	375
325—310	81	200	85	81	200	85	74	104
303.8	98	166	50	93	166	50	380	470
310—280*	92	187	65	92	187	65	13	220
280—260	80	160	60	80	160	60	20	76
765.1	34	230	800	34	123	660	21	29.5
256.3—257	72	144	60	109	220	91	19	26.5
260—240*	67	134	60	104	208	93	36	50.5
240—220	58	112	55	94	188	93	13.2	18.5
220—205	47	94	55	85	170	100	26.5	132
205—190	40	80	50	79	158	100	87	135
190—180	34	68	40	71	142	84	168	840
180—165	29	57	40	65	130	90	225	320
165—138	26	52	40	67	134	103	21.5	122
138—120	19.5	39	27	58	116	80.3	11.5	60
120—92	11.5	23	14	43.2	86.3	52.6	28	225
92—71	6.75	13.5	8.1	31.5	63	37.8	21	170
71—56	3.3	6.6	4.0	20.6	41.1	24.9	15	120
56—42	1.75	3.5	2.15	14	28	17.1	4.2	42
42—31	0.875	1.75	1.0	9.4	18.8	10.7	1.45	14.5
31—26	0.485	0.97	12	6.7	13.4	166	0.28	3.3
26—22.8	0.34	0.68	8.7	5.25	10.5	135	0.11	1.5
22.8—17.5	4.65	9.3	5.5	88	176	104	0.105	1.3
17.5—14.5	2.15	4.3	2.75	52	104	66.4	0.042	0.3
14.5—11.5	1.25	2.5	1.6	37.4	74.2	47.6	0.025	0.14
11.5—9	0.65	1.3	0.83	25	50	32.1	0.006	0.055
9—7	0.35	0.70	0.46	17	34	22.3	0.001	0.045
7—5.5	0.17	0.34	0.20	11	22	13	1.8 · 10 <sup>-4</sup>	0.016
5.5—4.5	0.09	0.18	0.105	7.0	14	8.1	3 · 10 <sup>-6</sup>	0.003

\* Does not include the data of the preceding lines.

Computations show that a large part of the solar radiation flux is absorbed in the absorption bands. As a result  $\eta$  decreases at altitudes  $h \leq 120$  km. There is no need to allow for the exact variation of  $\sigma$  within each narrow band falling in the solar continuum; for most narrow absorption bands, it suffices to use the average value of  $\sigma$  at the half-value point of each band, which ensures results accurate to within about 10%.

The ionization efficiency defined as  $\eta = \sigma_i/\sigma$  monotonically increases for O<sub>2</sub> to first approximation from about 25% to 85% between 850 Å and 600 Å. For N<sub>2</sub> the ionization efficiency changes from 45—60% near the ionization threshold (starting with 792 Å) to 80—100% for  $\lambda \leq 650$  Å. Therefore, between 600 and 250 Å, we have taken  $\eta = 1$  for both N<sub>2</sub> and O<sub>2</sub>. In the X-ray spectrum ( $\lambda < 250$  Å) the ionization cross section is obtained from (V.11). Measurements for atomic oxygen were only published by Cairns and Samson /622/, and the results of computations of different authors differ by as much as a factor of 2. We will take  $\sigma(\text{O}) = 0.5\sigma(\text{O}_2)$  /622/ for all wavelengths. This fits the results of laboratory measurements.

According to recent data /623/, the ionization threshold of the O<sub>2</sub> molecules is at  $\lambda = 1047$  Å. It corresponds to the lowest ionization potential of O<sub>2</sub>,  $\chi_i = 11.84$  eV. Table 33 gives a higher value  $\chi_i = 12.08$  eV from Watanabe and Marmo /624/. In accordance with the latest data on  $\chi_i$ , the



ionization effect from the two strong emission lines of O VI 1031.9 Å and 1037.6 Å was taken into consideration for the first time in the computation of  $q$ .

On the basis of the analysis of the short-wave radiation spectrum from Chapters I and II, Table 46 lists two intensity values:  $I^{\min}$  for low solar activity and  $I^{\max}$  for high solar activity. The values of  $I^{\min}$  for  $\lambda = 310 - 740$  Å were derived from the most reliable spectral observations of Hinteregger (which were carried out for low solar activity), the values in the spectral region  $\lambda < 100$  Å were obtained from counter measurements, and those for 740—1038 Å are the summary data of various authors /62/. All these data are essentially consistent with the summary data published by Hinteregger in his recent work /625/.

The spectrum  $I^{\max}$  for high solar activity was computed with allowance for the solar activity effects. The solar activity is determined by the size and the dimensions of the active regions on the Sun and its enhancing effect is different for emission lines of ions with different ionization potentials. The coefficient for conversion from the intensity at low solar activity to the intensity at high solar activity was measured in the X-ray spectrum and for a number of bright lines for  $\lambda = 170 - 400$  Å; it was found to be  $\approx 5$  on the average for lines of ions with high ionization potentials and  $\sim 1.5$  for lines of ions with low ionization potentials (as for the continuous solar radiation in the Lyman continuum 740—911 Å, at 911—1038 Å, and in other regions). The  $I^{\min}$  values are thus experimental, whereas  $I^{\max}$  are semiempirical, reflecting the current state of our knowledge concerning the effects of solar activity on the short-wave radiation.

As we have mentioned before, the spectrum was divided, for the computations of  $q$ , into 150 intervals and  $I_\lambda$ ,  $\sigma$ ,  $\sigma_i$  were assumed to remain constant within each of these intervals. The main parameter which determines the width and the position of the intervals is  $\sigma$ .

To elucidate the general effect of density and temperature variations on the computation results, we will use two typical models from /332/, the so-called "maximal" and "minimal" models. The maximal model (Table 47) corresponds to high solar activity ( $F_{10.7} = 200$ ) and the "minimal" model (Table 48) corresponds to low activity ( $F_{10.7} = 100$ ). Both models refer to noon hours. As we noted in Section 17, the minimal model is close to the nocturnal models for high solar activity.

Variations of the  $q(h)$  profile with time of day and with solar activity

We will start our analysis with conditions of low solar activity. The computed profiles  $q(h)$  for various zenith distances  $z_0$  are shown in Figure 81. The average effective cross sections for absorption and ionization were used (Table 46), together with the "minimal" model from Table 48.

Each  $q(h)$  profile in Figure 81 has a principal maximum  $q_{\max}$  and occasionally a secondary maximum  $q_E$  in the  $E$  region. The first maximum  $q_{\max}$  shifts from  $h \approx 135$  km to  $h \approx 250$  km as  $z_0$  varies from small distances to  $90^\circ$ , whereas  $q_E$  shifts from  $h \approx 115$  km to  $\sim 150$  km. A relatively small negative gradient  $d\ln q/dh$  is observed in the upper part of the ionosphere, whereas in the lower part the gradient is positive and large. To better trace

the variations of the profile during sunrise and sunset, near  $z_{\odot} = 90^{\circ}$ , the profiles were plotted at more frequent  $z_{\odot}$  intervals. Profiles for  $z_{\odot} > 90^{\circ}$  are also shown: the Sun has already set on the ground, but not in the ionosphere.

TABLE 47. The "maximal" model of the atmosphere

h, km	T, °K	n, cm <sup>-3</sup>			N, cm <sup>-2</sup>		
		N <sub>1</sub>	O <sub>2</sub>	O	N <sub>1</sub>	O <sub>2</sub>	O
90	185	4.90 13	1.32 13	9.00 11	4.62 19	1.23 19	2.90 18
95	185	1.95 13	5.25 12	8.63 11	1.777 19	4.79 18	2.12 18
100	209	7.75 12	1.96 12	6.75 11	8.71 18	1.92 18	1.46 18
110	260	1.52 12	3.20 11	2.55 11	2.18 18	4.15 17	6.80 17
120	355	4.00 11	7.50 10	1.14 11	7.52 17	1.23 17	3.73 17
130	524	1.309 11	2.213 10	3.398 10	3.61 17	5.36 16	1.643 17
140	668	6.025 10	9.445 9	1.966 10	2.425 17	2.91 16	1.21 17
150	799	3.273 10	4.825 9	1.285 10	1.38 17	1.78 16	9.48 16
160	918	1.975 10	2.764 9	9.074 9	9.56 16	1.17 16	7.70 16
170	1023	1.283 10	1.745 9	6.770 9	6.94 16	8.10 15	6.40 16
180	1115	8.783 9	1.126 9	5.256 9	5.17 16	5.74 15	5.42 16
190	1194	6.257 9	7.722 8	4.205 9	3.96 16	4.27 15	4.64 16
200	1263	4.595 9	5.470 8	3.441 9	3.065 16	3.19 15	4.00 16
220	1373	2.644 9	2.945 8	2.422 9	1.917 16	1.863 15	3.06 16
240	1453	1.617 9	1.693 8	1.785 9	1.24 16	1.134 15	2.386 16
260	1512	1.029 9	1.016 8	1.355 9	8.20 15	7.05 14	1.865 16
280	1555	6.732 8	6.284 7	1.051 9	5.72 15	4.71 14	1.52 16
300	1587	4.492 8	3.970 7	8.270 8	3.76 15	2.89 14	1.262 16

Remarks. 1)  $N = \int n dh$ .

2) In columns for  $n$  and  $N$ , 4.90 13 corresponds to  $4.90 \cdot 10^{13}$ .

TABLE 48. The "minimal" model of the atmosphere

h, km	T, °K	n, cm <sup>-3</sup>			N, cm <sup>-2</sup>		
		N <sub>1</sub>	O <sub>2</sub>	O	N <sub>1</sub>	O <sub>2</sub>	O
90	190	4.90 13	1.32 13	6.00 11	4.62 19	1.23 19	1.935 18
95	190	1.95 13	5.25 12	5.75 11	1.78 19	4.79 18	1.42 18
100	206	7.75 12	1.96 12	4.50 11	8.65 18	1.88 18	9.76 17
110	288	1.48 12	2.90 11	1.70 11	2.14 18	3.89 17	4.54 17
120	355	4.00 11	7.50 10	7.60 10	7.52 17	1.23 17	2.49 17
130	457	1.418 11	2.379 10	3.774 10	3.42 17	5.04 16	1.596 17
140	547	6.291 10	9.616 9	2.195 10	1.81 17	2.44 16	1.11 17
150	633	3.184 10	4.524 9	1.398 10	1.063 17	1.32 16	8.18 16
160	711	1.774 10	2.359 9	9.526 9	6.66 16	7.73 15	6.25 16
170	779	1.062 10	1.330 9	6.832 9	4.36 16	4.80 15	4.91 16
180	838	6.709 9	7.951 8	5.094 9	2.96 16	3.07 15	3.94 16
190	888	4.411 9	4.966 8	3.910 9	2.06 16	2.05 15	3.19 16
200	930	2.991 9	3.208 8	3.070 9	1.47 16	1.38 15	2.63 16
220	997	1.470 9	1.439 8	1.987 9	7.74 15	6.64 14	1.83 16
240	1044	7.684 8	6.906 7	1.345 9	4.24 15	3.33 14	1.30 16
260	1077	4.184 8	3.465 7	9.377 8	2.37 15	1.72 14	9.35 15
280	1101	2.343 8	1.793 7	6.671 8	1.45 15	9.21 13	6.91 15
300	1118	1.339 8	9.480 6	4.814 8	7.90 14	4.91 13	4.97 15

Remarks. 1)  $N = \int n dh$ .

2) In columns for  $n$  and  $N$ , 4.90 13 corresponds to  $4.90 \cdot 10^{13}$ .

The curves in Figure 81 primarily show that  $q_{\max}$  changes by 1.5 orders of magnitude during the day, as the Sun moves from the zenith to the horizon. The ionization maximum shifts from the  $F_1$  region or below, where it is located in daytime, to the  $F_2$  region in the evening and in the morning. The

results of computations show that the effect of the short-wave solar radiation on the atmosphere cannot be approximated with monochromatic radiation. Indeed, the total intensity of the short-wave radiation drops to  $1/e$  at an altitude of 170 km, so that apparently  $\bar{\sigma}_{ef} \approx 10^{-17} \text{ cm}^2$ . However,  $q_{\max}$  is observed at significantly lower altitudes, which correspond to  $\bar{\sigma}_{ef} \approx 2.5 \cdot 10^{-18} \text{ cm}^2$ , and the total radiation intensity at this altitude drops by more than an order of magnitude (by about a factor of 15, and not by a factor of  $e$ ).

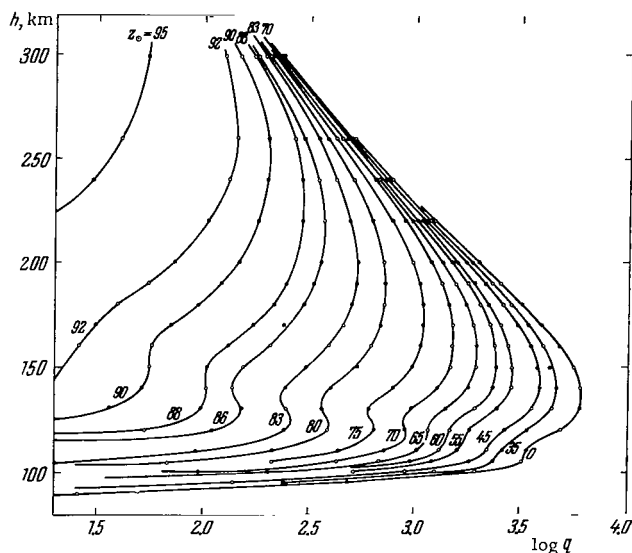


FIGURE 81. Vertical distribution of the ionization rate for various zenith distances of the Sun (low solar activity).

The daytime variation of  $q$  is different for regions  $F_1$  and  $F_2$ . In the  $F_1$  region and below (for  $h \leq 180-200 \text{ km}$ )  $q$  in daytime is 1-2 orders of magnitude higher than in the morning and in the evening (which leads to a marked dependence of the electron concentration on  $z_0$  in regions  $F_1$  and  $E$ ), whereas in the  $F_2$  region, at  $h \approx 300 \text{ km}$ ,  $q$  varies insignificantly, remaining virtually constant during most of the day, as long as  $\text{Ch } z_0$  has not exceeded 10 ( $z_0 > 85^\circ$ ).

One of the remarkable features of  $q(h)$  is the formation of a small peak  $q_E$  at  $h \approx 120 \text{ km}$  for large zenith distances of the Sun. The appearance of this peak is associated with the peculiar distribution of the solar radiation energy in the short-wave spectrum, described in Chapter II (see Figure 20): a radiation maximum is observed at  $40-85 \text{ \AA}$ , giving way to a minimum in the adjoining fairly wide region  $85-180 \text{ \AA}$ . It is remarkable that the electron concentration profile  $n_e(h)$  in daytime at altitudes of  $95-200 \text{ km}$  is also fairly smooth, whereas at altitudes of  $105-125 \text{ km}$  a small peak is observed, which shows almost on all the rocket profiles  $n_e(h)$ . This fact was first reported by Rudakov [274]. As we saw in Chapter IV in our discussion of the rocket data on  $n_e(h)$ , the  $n_e$  peak observed at  $105-125 \text{ km}$  and the "valley"

under the peak are markedly enhanced as the Sun approaches the horizon (like the  $q_E$  peak). In what follows, we will try to establish whether or not the  $n_e$  peak is related to  $q_E$ .

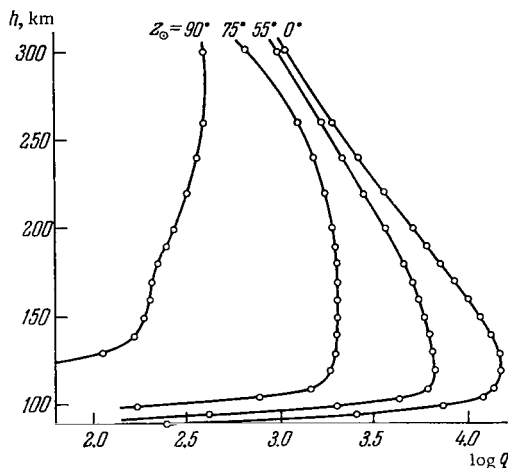


FIGURE 82. Vertical distribution of the ionization rate for various zenith distances of the Sun (high solar activity).

Figure 82 shows the computed profiles  $q(h)$  for  $I^{\max}$  (high solar activity). The general trend of the  $q(h)$  profiles during the daytime is the same as for low solar activity, although some differences are noted. These differences, in addition to the expected increase in  $q_{\max}$  by approximately a factor of 2.5, are reflected in a certain reduction of the gradient  $|d\ln q/dh|$  in the top part of the profile and the disappearance of the secondary maximum. In the next section we will show that these differences in the  $q(h)$  profiles are mainly caused by changes in the parameters of the neutral atmosphere.

The power of the short-wave solar radiation absorbed mainly in the 100–200 km layer varies during the solar cycle, thus altering the temperature conditions in the atmosphere and affecting the density and the composition of the upper atmosphere. Similar changes in the upper atmosphere occur as a result of the diurnal variations in the absorption of solar radiation. These changes in the atmosphere, in their turn, affect the  $q(h)$  profiles, whose variation will now be considered.

**The effect of variations in the parameters of the upper atmosphere.** To elucidate the effect of the changes in the density and the temperature of the upper atmosphere on the  $q(h)$  profile, we assembled in Figure 83 the profiles  $q(h)$  computed from  $I^{\min}$  for the two atmospheric models, all other conditions remaining equal.

We see from Figure 83 that as the density and the temperature of the atmosphere are increased, there exists a certain altitude  $h^*$  for each  $z_{\odot}$  with  $q$  increasing above it and decreasing below. The altitude  $h^*$  increases from  $\sim 200$  km to  $\sim 300$  km as  $z_{\odot}$  grows during the day. In the "maximal" model,  $q$  decreases at altitudes  $h < h^*$  because the softest solar radiation reaches

these altitudes greatly attenuated by absorption at higher altitudes, which is enhanced by the increase in the temperature and the density of the atmosphere. Since for high solar activity  $q_{\max}$  lies below  $h^*$ , the increase in atmospheric density reduces  $q_{\max}$  approximately to  $2/3$ . It is for this reason that the values of  $q_{\max}$  for high and low solar activity levels differ by only a factor of  $\sim 2.5$ , although the radiation fluxes differ by more than a factor of 3.

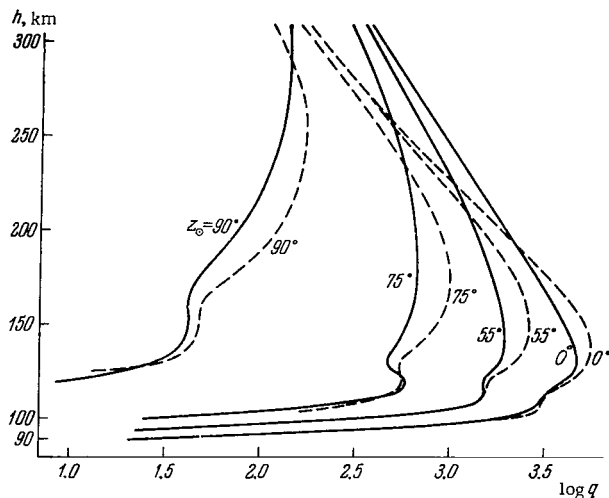


FIGURE 83. Vertical distribution of the ionization rate for different zenith distances of the Sun for the "maximal" (solid curves) and the "minimal" (dashed curves) models of the atmosphere.

Above  $h^*$ ,  $q$  increases and the gradient  $|d\ln q/dh|$  diminishes. This is so because at sufficiently high altitudes  $I_\lambda = \text{const}$  and by (V.32)  $q$  is directly proportional to  $n$ . Therefore, in epochs of high solar activity, the decrease of the gradient  $|d\ln q/dh|$  is brought about by a decrease in the gradient of the density of the atmosphere due to the higher temperatures (and the correspondingly greater scale height).

Besides the changes caused by solar activity, the density and the temperature of the upper atmosphere reveal regular daytime variations. These should lead to corresponding changes in the value of  $q$ , which have not been allowed for in the computations presented in Figure 81. Suitable corrections will have to be made when the variations of the atmosphere during the day are established.

Observations of satellite deceleration have now shown that a density and temperature maximum is observed in the atmosphere in the afternoon at  $h \gtrsim 200$  km (Section 17). Thus, in the afternoon hours,  $q$  should increase at altitudes above  $h^* = 200 - 250$  km and decrease at low altitudes (150—200 km); the gradient  $|d\ln q/dh|$  should correspondingly diminish in the  $F_2$  region /559/. The 2—4 hour delay of the  $q(t)$  maximum in the upper part of the ionosphere relative to noon should result in a certain offset of the daily curve  $n_e(t)$ . The predicted variation of  $n_e$  has indeed been observed, and many of its features are well known /234/. The offset of the daily  $n_e$  curves is often

employed, in Appelton's method /486/, to determine the effective recombination coefficient  $\alpha'$ . If the offset of the density curve is ignored, this method will give purely fictitious values of  $\alpha'$ .

Let us now consider the daytime variations of  $q$  at other altitudes.

### The rate of variation of $q$ during the day

We saw in Chapter IV that the changes in the electron concentration during the day are determined by the Chapman function  $\text{Ch } z_0$ . This function is conveniently employed as a parameter for studying the variations of  $q$ . At every given altitude in a limited range of  $z_0$  values,  $q$  may be described as a power function

$$q \propto \text{Ch}^{-m} z_0. \quad (\text{VI.10})$$

The higher  $m$ , the more pronounced is the variation of  $q$  during the day. Therefore, the index

$$m = - \frac{\partial \lg q}{\partial \lg (\text{Ch } z_0)} \quad (\text{VI.11})$$

may be adopted as a parameter characterizing the rate of relative variation of  $q$  during the day.

The computed values of  $\log q$  at some altitudes are plotted in Figure 84 vs.  $\log (\text{Ch } z_0)$ . The slope of the curves in this figure, according to (VI.10), gives the parameter  $m$ . Clearly, the index  $m$  is not constant. It varies depending on altitude and on time of day.

a) For a given  $z_0$ ,  $m$  gradually decreases with increasing altitude. In distinction from the simple layer theory, the monotonic decrease of  $m$  with altitude breaks down at altitudes of 120 — 150 km.

b) At a fixed altitude,  $m$  varies during the day. A particularly sharp change of  $m$  from small values (0.1 — 0.3) for small zenith angles of the Sun to  $m \approx 1.5$  for  $z_0 \rightarrow 90^\circ$  (a change by almost one order of magnitude) occurs at high altitudes (over 200 km). The values of  $z_0$  at which a fairly sharp change in  $m$  occurs thus systematically increase with increasing altitude. Variation of  $m$  during the day is also observed at other altitudes, but there it is more gradual.

Figure 85 shows the vertical variations of  $m$  for two different times of day,  $z_0 = 0 - 60^\circ$  and  $\text{Ch } z_0 = 10$ . The curve for  $\text{Ch } z_0 = 10$  virtually repeats the curve for  $z_0 = 0 - 60^\circ$ , but it is shifted upward and is stretched along the vertical scale. The monotonic decrease of  $m$  with increasing altitude breaks down at 110 — 120 km for  $z_0 = 0 - 60^\circ$  and at 130 — 150 km for  $\text{Ch } z_0 = 10$ . This anomaly in the gradient of  $m$  in the upper part of the ionospheric  $E$  region is associated with changes in the radiation spectrum which takes part in ionization processes in this region of the ionosphere (see below).

We have previously discussed the variation of  $q$  at various altitudes as a function of  $z_0$  and noted that, besides the principal maximum at 135 — 200 km (see Figure 81), a secondary maximum  $q_E$  appears at  $h \approx 115$  km for  $z_0 \geq 60^\circ$ , which is displaced up to  $h \approx 150$  km for  $z_0 = 90^\circ$ . The data for the secondary maximum are marked by circles in Figure 84. The data for the principal maximum lie along the outer envelope of the curves in Figure 84.

The principal maximum is associated with the formation of the  $F_1$  layer, whereas the secondary maximum corresponds to the  $E$  region in the ionosphere. At altitudes corresponding to these maxima,  $m$  is independent of  $z_0$ , being equal to 1.30 and 1.37, respectively. In the simple layer theory,  $m = 1$  for a layer maximum. These  $m$  values are higher; this is quite significant, as it resolves one of the fundamental riddles in the behavior of the  $E$  and  $F_1$  regions, which will now be considered.

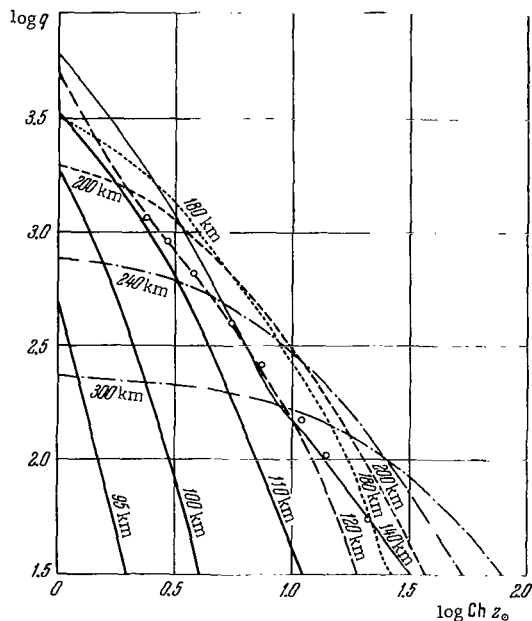


FIGURE 84. Ionization rate at different altitudes (numbers against the curves) vs. Chapman's function  $Ch z_0$ .

The circles represent data for the secondary maximum  $q_E$ .

Measurements performed on ionospheric stations have established that the critical frequency  $f_0$  in  $E$  and  $F_1$  regions is proportional to  $(\cos z_0)^v$ . Ratcliffe and Weeks [234] indicate that for the  $E$  layer in periods of minimum solar activity  $v_E = 0.3 - 0.36$ , and for the  $F_1$  layer  $v_{F_1} \leq 0.25$ , whereas the simple layer theory leads one to expect  $v = 0.25$  (for a constant effective recombination coefficient  $\alpha'$  we have  $q \propto n_e^2 \propto f_0^4$  and  $v = m/4$ ). This contradiction with the experimental data stems from the erroneous assumption of monochromatic solar radiation.

We will now use the above values of  $m$ . Since  $m = 1.37$  for the  $q_E$  maximum in the  $E$  region, we find  $v_E = 0.34$  taking  $\alpha' = \text{const}$ , and this fits the observation findings. The anomalous value of  $v_E$  thus can be accounted for by a theory which allows for the nonmonochromatic spectrum of the ionizing radiation.

Let us now consider the low value  $v_{F_1} \leq 0.25$ . We know that the  $F_1$  layer is observed at altitudes of 180–200 km mostly in summer around noon, i.e., for low  $z_0$ . We see from Figures 84 and 85 that at these altitudes, for

low  $z_0$ , we have  $m \approx 0.5$ . Thus, since  $q_{F_1} \propto n_z^\gamma$ , where  $1 < \gamma < 2$  (in the  $F_1$  region the recombination law is intermediate between linear and quadratic, whereas in the  $E$  region  $\gamma = 2$ ), we find, in accordance with observations,  $0.15 < \nu_{F_1} \leq 0.25$ .

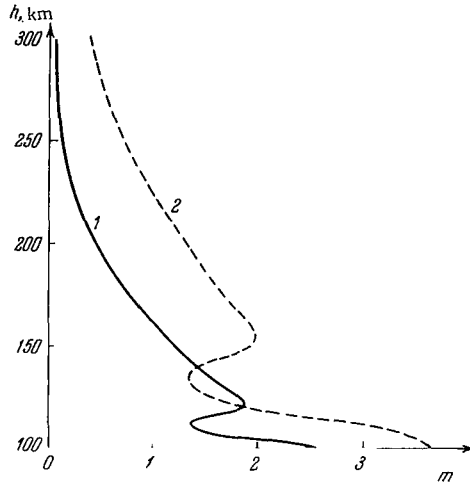


FIGURE 85. Vertical variation of the parameter  $m$  from (VI.10) for  $z_0 = 0 - 60^\circ$  (1) and  $\text{Ch } z_0 = 10$  (2).

Clearly  $\nu_{F_1}$  should increase with increasing  $z_0$  because of the increase in  $m$ . Indeed, in Washington, D. C.  $\nu_{F_1} = 0.18$  in summer and  $\nu_{F_1} = 0.25$  in winter /234/. These data are accounted for by the increase of  $z_0$  in winter.

An analysis of the rate of variation of  $q$  during the day, computed for nonmonochromatic ionizing radiation, thus accounts both for those  $\nu_E$  which are too high and for those which are too low (relative to the simple-layer theoretical value  $\nu = 0.25$ ).

The characteristic changes in the rate of variation of  $q$  during the day are also reflected in another curious feature of the  $F_1$  and  $F_2$  regions. We see from Figure 84 that in the morning and in the evening  $\log q$  varies much faster as a function of  $\log (\text{Ch } z_0)$  than in daytime. Thus above  $h \approx 230$  km, the index  $m$  increases by more than a factor of 5 for  $\text{Ch } z_0 = 10$ . This feature is reflected in observations. A significantly faster growth of the rate of ionization in the  $F_1$  and  $F_2$  layers was noted in the morning relative to noon hours, especially in periods of maximum solar activity.

### The reduced profile $q/n$

We saw in Section 19 that the dependence of the reduced profile  $q/n$  on  $N = \int n \, dh$  and on  $\text{Ch } z_0$  is interchangeable, i. e., the dependence of  $q/n$  on  $\text{Ch } z_0$  for  $h = \text{const}$  can be applied to construct the profile of  $q/n$  vs.  $h$  for the given  $\text{Ch } z_0$ , and vice versa. Thus, instead of computing a whole family of profiles  $q(h)$  as in Figure 81, it suffices to compute a single universal profile of  $q/n$



as a function of  $N \text{Ch } z_0$ , which will then be used to characterize the rate of ionization at various altitudes for various  $z_0$ .

Figure 86 shows the curve of  $\log q/n$  vs.  $\log (N \text{Ch } z_0)$  plotted from the computed  $q/n$  profiles for three different values of  $\text{Ch } z_0$  (1, 10, and 100). For  $\log (N \text{Ch } z_0) < 18.5$ , the individual points fall along a well-defined curve, which is characterized by the following properties.

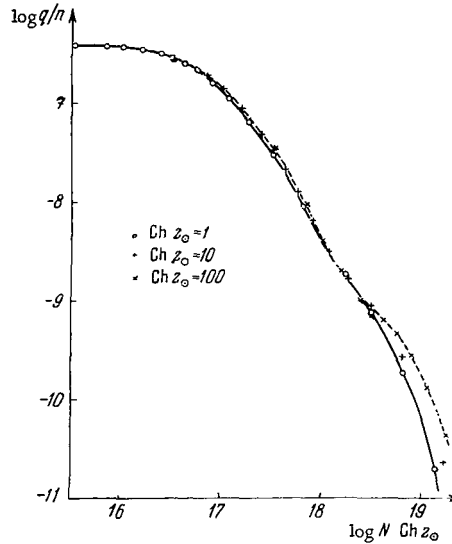


FIGURE 86. Reduced  $q/n$  profile vs.  $N \text{Ch } z_0$  for three values of  $\text{Ch } z_0$ .

1) For „ $\text{Ch } z_0 < 10^{16} \text{ cm}^{-2}$ “, the curve asymptotically approaches some constant value  $\log q/n = -6.42$ . This part of the curve corresponds to high altitudes, where the absorption of solar radiation is low. The specific ionization rate at high altitudes for low levels of solar activity is thus

$$\left(\frac{q}{n}\right)_{\infty} = 4 \cdot 10^{-7} \text{ cm}^{-6} \text{ sec}^{-1}. \quad (\text{VI.12})$$

This figure is one order of magnitude smaller for  $\log (N \text{Ch } z_0) \approx 17.3$ , which for  $z_0 = 0$  corresponds to  $h \approx 140 \text{ km}$ , i. e., the altitude near which the maximum  $q_{\text{max}}$  is attained.

2) As the parameter  $N \text{Ch } z_0$  increases, the curve in Figure 86 becomes steeper, i. e., the gradient of  $\log q$  with respect to  $\log \text{Ch } z_0$  increases as the radiation penetrates deeper into the atmosphere. The monotonic increase of the slope breaks down at  $\log (N \text{Ch } z_0) \approx 18$ , which corresponds to an altitude of 115 km for  $z_0 = 0$ . This phenomenon has been commented upon in our discussion of the daily rate of variation of  $\log q$ . Figure 84 in fact consists of two branches of the curve in Figure 86, displaced by the appropriate  $\log n$  for each  $h$ . This again stresses the universal character of the curve everywhere except the region of high values of  $N \text{Ch } z_0$ .

3) For high values  $\log (N \text{Ch } z_0) > 18.5$ ,  $q/n$  is not single-valued, being higher for higher  $\text{Ch } z_0$ . For example, for  $\log (N \text{Ch } z_0) \approx 19.3$  (which corresponds to altitudes of 92 and 135 km for  $\text{Ch } z_0$  equal to 1 and 100, respectively),  $q/n$  increases by one order of magnitude as  $\text{Ch } z_0$  goes from 1 to 100. The reason for this is to be sought in the marked differences in the radiation spectrum and primarily in the values of  $q(\text{O}_2^+)/q$  at these altitudes. Calculations show that at high altitudes the value of  $q_i/n_i$  for the  $\text{O}_2^+$  ions is only a factor of 1.5–2 higher than for  $\text{N}_2^+$  and  $\text{O}^+$ . And yet for  $\log N = 18.5 - 19.5$ , the corresponding values differ by one order of magnitude for  $\text{Ch } z_0 = 1$  and by two orders of magnitude for  $\text{Ch } z_0 = 100$ . In this case  $q \approx q(\text{O}_2^+)$  and the sharp growth of  $q/n$  with increasing  $\text{Ch } z_0$  is not surprising. The whole problem of variations in the rates of formation of various ions will be considered in more detail in the next subsection.

It is clear from the above that for  $N \text{Ch } z_0 \approx 10^{19} \text{ cm}^{-2}$  the universal character of the  $\log q/n$  vs.  $\log (N \text{Ch } z_0)$  curve breaks down if we consider high  $z_0$ . Note that for still higher values of  $N \text{Ch } z_0$  the  $q/n$  profile restores its single-valuedness.

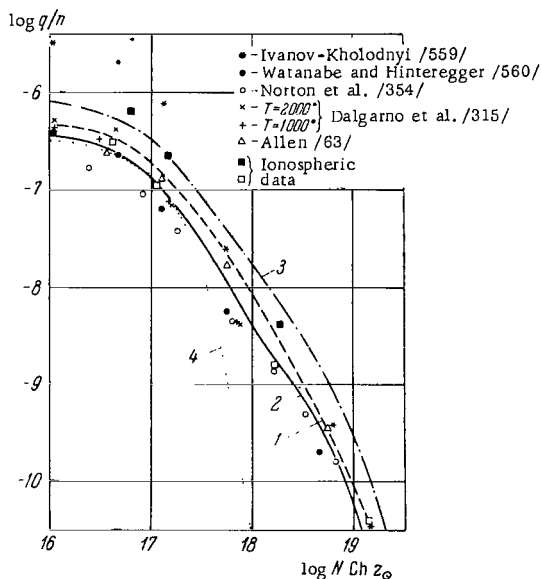


FIGURE 87. Reduced ionization rate vs.  $\log (N \text{Ch } z_0)$ ,

where  $N = \int n dh$ , from computations of various authors and according to ionospheric data.

Curve 1 — Hinteregger /31/; 2, 3 — the author's computations for  $i^{\min}$  and  $i^{\max}$ , respectively; 4 — simple layer theory (V.30) for  $\sigma = 10^{-17} \text{ cm}^2$ .

Several computations of  $q(h)$  profiles for various  $z_0$  and various atmospheric models have been conducted so far. The values of  $q/n$  obtained from these computations are shown in Figure 87. The early computations

of Watanabe and Hinteregger /560/ relating to low solar activity suffered from significant omissions: ionization by photoelectrons was ignored, the values of  $I_\lambda$  used for the X-ray spectrum were 1/4 of the true values /315/, and a model of the atmosphere corresponding to high solar activity was used. Revised computations carried out with the same  $I_\lambda$  but with a different atmospheric model were published in /354/, where photoelectron ionization was taken into consideration; higher values of  $I_\lambda$  were used in /31, 315/. The greatest improvement in the  $q/n$  value was noticeable for small  $NCh z_0$ : this was a result of higher X-ray intensities having been used. Our values of  $q$  computed from  $I_{\min}$  /484/ and Allen's computations /63/ for medium solar activity are higher than the old data but still lower than the new results /31/. All computations, however, may be treated as fairly consistent, since the differences between the individual sets of data are at most by a factor of 2.

Figure 87 also shows the old computations of  $q$  for high solar activity /559/. These computations are less reliable. Note, however, that like the computations for  $I_{\max}$ , they reveal the growth of  $q/n$  at all altitudes by approximately a factor of 3 for high solar activity.

To verify the validity of these  $q/n$  values, we compare them in Figure 87 with ionospheric data (the values of  $\alpha' n_e^2/n$  computed from Table 49). The absolute values and the relative changes in  $\alpha' n_e^2/n$  on passing from low activity (light squares) to high activity (dark squares) correspond to the changes in  $q/n$  at all altitudes. Thus, with allowance for the new values of  $\alpha'/247, 544/$ , the ionospheric data for the  $E$  and  $F_1$  regions, and also the data for the "valley" between  $E$  and  $F_1$ , are consistent with the computed values of  $q$ , especially for low solar activity.

Let us now consider the total number of ions  $Q = \int q dh$  forming in a vertical atmospheric column of  $1 \text{ cm}^2$  section. We see from Section 19 that the main problem is to determine the mean ionization efficiency (expression (V.33)). For epochs of low solar activity, for  $z_0 = 0$ , we have  $Q = 5.2 \cdot 10^{10}$  ion pairs/ $\text{cm}^2 \text{ sec}$ . Computations show that  $Q$  varies as  $\cos z_0$  almost up to  $z_0 = 70^\circ$ . For  $z_0 = 90^\circ$ ,  $Q$  decreases approximately by a factor of 10–15. The variation of  $Q$  is thus similar to the variation of the radiation intensity  $I$ . Taking for the initial intensity  $I = \int I_\lambda d\lambda = 5.7 \cdot 10^{10}$  quanta/ $\text{cm}^2 \text{ sec}$ , we find 0.9 ion pairs/quantum for the mean ionization efficiency, or

$$Q = 1.1I. \quad (\text{VI.13})$$

Thus, as indicated in Section 19,  $Q = I$  to within 10%. Seeing that the radiation flux carries  $2.5 \text{ erg/cm}^2 \text{ sec}$ , we find that on the average energy of  $\varepsilon = 28 \text{ eV}$  is required to produce one ion pair by short-wave solar radiation. This is close to the figure for the hard radiation ( $\varepsilon = 32 \text{ eV}$ ). Similar results are obtained for the period of high solar activity.

#### Relative rates of production of various ions

We saw in Chapter V that deeper understanding of the factors leading to the specific features in the  $q(h)$  profiles requires a detailed analysis of the ionization produced by different spectral regions and the relative rates of production of the individual ions.

TABLE 49. Starting data for the computation of  $\frac{\alpha' n_e^2}{n}$

Ionospheric region	Solar activity	$h$ , km	$n$ , cm <sup>-3</sup> /332/	$N$ , cm <sup>-2</sup>	$n_e$ , cm <sup>-3</sup> /237, 243/	$\alpha'$ , cm <sup>3</sup> sec <sup>-1</sup> (Section 21)
$D$	Medium	100	$1 \cdot 10^{13}$	$1.25 \cdot 10^{19} *$	$6.3 \cdot 10^4$	$\sim 10^{-7}$
$E$	High	$\sim 110$	$2.1 \cdot 10^{12}$	$1.85 \cdot 10^{18}$	$2.8 \cdot 10^5$	$\sim 10^{-7}$
	Low		$1.9 \cdot 10^{12}$	$1.7 \cdot 10^{18}$	$1.6 \cdot 10^5$	
$E - F_1$	High	$\sim 150$	$5 \cdot 10^{10}$	$1.45 \cdot 10^{17}$	$4 \cdot 10^5$	$7 \cdot 10^{-8} **$
	Low			$1.15 \cdot 10^{17}$	$2.8 \cdot 10^5$	
$F_1$	High	$\sim 180$	$1.5 \cdot 10^{10}$	$6.4 \cdot 10^{16}$	$5 \cdot 10^5$	$5 \cdot 10^{-8}$
	Low		$1.25 \cdot 10^{10}$	$4.1 \cdot 10^{16}$	$3 \cdot 10^5$	

\* For  $Ch \approx 2$ .

\*\* From /247/.

The contribution from the four main spectral regions to the overall ionization in epochs of low solar activity at various altitudes is shown in Figure 88 for  $z_{\odot} = 55^\circ$  and  $90^\circ$ . The two sets of curves are similar, but for  $z_{\odot} = 90^\circ$  the curves are naturally displaced upward and stretched along the vertical scale. At altitudes between 95 and 115 km (for  $z_{\odot} = 90^\circ$ , at 110 – 160 km), i. e., in the ionospheric  $E$  region, the 911 – 1038 Å radiation is the most effective. At higher altitudes, the 85 – 740 Å radiation is the most effective ( $L_c$  contributing some 10 – 15%), whereas at lower altitudes the X-ray radiation, mainly from the 0 – 85 Å region. According to Section 19, ionization by the 911 – 1038 Å component produces only molecular oxygen ions, and the composition of the primary ions in the corresponding ionospheric region is anomalous.

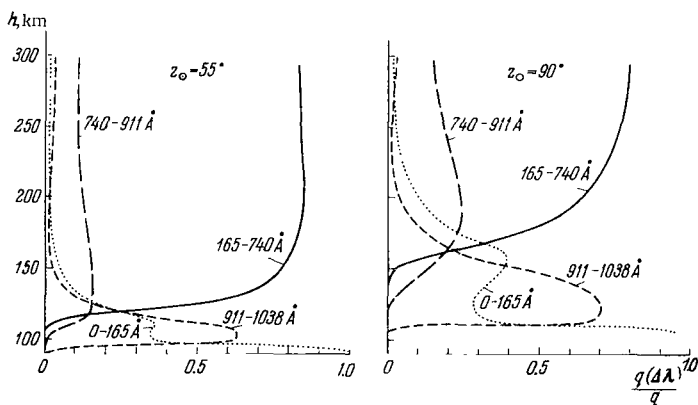


FIGURE 88. Vertical variation of the relative ionization rate  $q(\Delta\lambda)/q$  for low solar activity in four spectral regions  $\Delta\lambda$ : 0 – 165 Å, 165 – 740 Å, 740 – 911 Å ( $L_c$ ), and 911 – 1038 Å for  $z_{\odot} = 55^\circ$  and  $z_{\odot} = 90^\circ$  /627/.

Figure 89 plots the relative rates of production of various ions vs. the altitude and the zenith distance of the Sun. Above a certain level, the relative quantity of atomic oxygen ions  $q(O^+)/q$  monotonically increases with

altitude from 2 — 6% in the  $E$  region to about 70% at  $h \sim 300$  km. This closely corresponds to the variation in the fraction of neutral oxygen atoms in the atmosphere at these altitudes. However, the ratio  $q(\text{O}_2^+)/q$  monotonically increases with decreasing altitude, at first following the variation of the  $\text{O}_2$  content in the atmosphere, but below a certain level, at 140 — 180 km, it increases abruptly so that the ratio  $q(\text{O}_2^+)/q(\text{N}_2^+)$  becomes greater than unity. The relative content  $q(\text{N}_2^+)/q$  also at first increases, but below 140 — 180 km it rapidly diminishes, dropping to about 15% in the minimum. At still lower altitudes (below 100 — 110 km), the ratio  $q(\text{O}_2^+)/q(\text{N}_2^+)$  diminishes and again becomes consistent with the molecular composition of the atmosphere. The profile of the relative rate of production of  $\text{N}_2^+$  thus shows an unusual minimum, whereas for  $\text{O}_2^+$  a curious maximum is observed. For low  $z_0 \leq 60^\circ$ , the minimum and the maximum fall approximately in the  $E$  region. As  $z_0$  increases, they shift upward. Comparison of the upper and the lowermost parts of the curves  $q(\text{N}_2^+)/q$  and  $q(\text{O}_2^+)/q$  shows that this region should be considered anomalous. Traces of a similar anomaly are also noted for the ion  $\text{O}^+$ , whose profile  $q(\text{O}^+)/q$  is noticeably altered for high  $z_0$ .

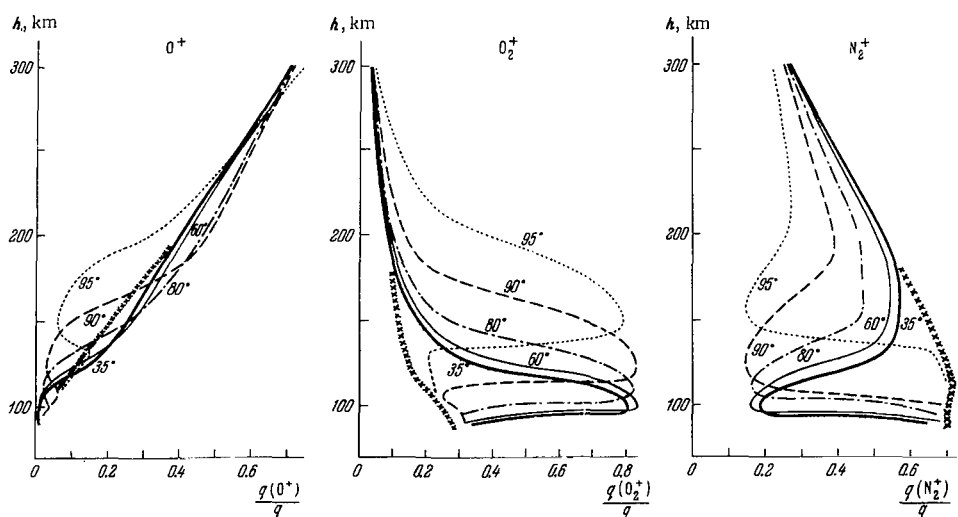


FIGURE 89. Relative ionization rates  $q(\text{O}^+)/q$ ,  $q(\text{O}_2^+)/q$  and  $q(\text{N}_2^+)/q$  for various zenith angles  $z_0$  and low solar activity /627/.

The formation of the anomalous region explains the breakdown of single-valuedness of the ratios  $q/n$  for large  $z_0$  and the anomaly of the gradient  $m$  at altitudes between 100 and 150 km.

According to Section 19, the anomaly in the relative ionization rate between 100 and 150 km is associated with the changes which occur in the spectral composition of the ionizing radiation as it penetrates deeper into the atmosphere. The main contribution in this respect comes from the 911 — 1038 Å region, which produces only  $\text{O}_2^+$  ions. At high altitudes and at  $h < 100$  km the short-wave radiation 0 — 740 Å predominates, which produces ions in correct proportion to the neutral composition of the atmosphere. This explains, in particular, the predominance of  $q(\text{O}^+)$  over  $q(\text{N}_2^+)$  and  $q(\text{O}_2^+)$  at high altitudes. As  $z_0$  increases, the ionospheric region

where ionization is mainly caused by the 911 — 1038 Å radiation shifts upward. This accounts for the vertical migration of the anomalous region with  $z_0$ .

As the conditions change from minimum to maximum solar activity, the 0 — 740 Å radiation is enhanced to a greater extent than the longer wavelengths; the anomaly is therefore expected to be less pronounced than for low solar activity. Computations bear out this assumption.

The rates of production of individual ions were previously computed by Watanabe and Hinteregger /560/ and by Hinteregger et al. /31/, but they did not consider the anomalous behavior of  $q_i/q$  in the  $E$  region.

The curves of Figure 89 for  $O_2^+$  and  $N_2^+$  for various  $z_0$  show that at each fixed altitude for  $h > 130 - 150$  km, the fraction of  $O_2^+$  in the total number of ions monotonically decreases and the fraction of  $N_2^+$  monotonically increases as  $z_0$  goes from  $90^\circ$  to  $55^\circ$  (i. e., between morning and noon). A reverse change is observed between noon and evening. Above the  $E$  region, at  $h \sim 150$  km, the changes in  $q(O_2^+)/q$  and  $q(N_2^+)/q$  may reach one order of magnitude. Below the anomalous region, the composition of the primary ions varies in the opposite direction.

To better illustrate the origin of the anomaly in the profiles  $q(N_2^+)/q$  and  $q(O_2^+)/q$ , Figure 89 also shows the results of computations for a case of no absorption (crosses). These data for  $N_2^+$  roughly fall along an envelope for the maximum values  $q(N_2^+)/q(a_{\max})$ , and for  $O_2^+$  they fall along an envelope for  $q(O_2^+)/q(a_{\min})$ . These data indicate the hypothetical variation in the composition of the primary ions at various altitudes for an unchanging spectrum of ionizing radiation. The deviation of the actual points from these monotonic curves is associated with the changes which take place in the radiation spectrum as it penetrates deeper into the atmosphere. At high altitudes, the soft radiation is readily absorbed and the 911 — 1038 Å component of the spectrum becomes particularly significant, producing only  $O_2^+$  ions. The fraction  $q(N_2^+)/q$  thus decreases. Below  $h \approx 100$  km, the curves again approach the envelope, because at these altitudes the 911 — 1038 Å radiation is absorbed and ionization is mainly caused by X rays. The various ions therefore form almost in the same proportions as by the entire spectrum before its absorption in the atmosphere.

To bring out the effects of the changes in the spectral composition of the short-wave radiation, Figure 90 gives the curves of  $q(\Delta\lambda)/q$  for maximum solar activity, using the same  $\Delta\lambda$  as in Figure 88 for minimum solar activity. The relative contribution of the short-wave radiation with  $\lambda = 165 - 740$  Å and 0 — 165 Å increases in epochs of maximum solar activity, as these wavelengths are enhanced by a factor of 2.5 and 7, respectively, whereas the longer wavelengths are only enhanced by a factor of about 1.5. The relative contribution of the longer wavelengths with  $\lambda \geq 911$  Å therefore decreases for high solar activity, and below  $q_{\max}$  a less abrupt increase in  $q(O_2^+)/q$  is observed, with only a small reduction in  $q(N_2^+)/q$ . The value of  $q(O^+)/q$  hardly changes, but for  $z_0 = 90^\circ$  the contrast in the profiles becomes less pronounced, as for  $N_2^+$  and  $O_2^+$ . The value of  $a_{\min}$  corresponding to the minimum of the  $q(O_2^+)/q$  profiles (see above) and the value of  $a_{\max}$  for the  $q(N_2^+)/q$  profiles both change significantly.  $a_{\min}$  increases from about 15% to 40% (by a factor of 2.5) and  $a_{\max}$  diminishes from 83% to 57% as the conditions change from low to high solar activity. As a result, the ratio  $a_{\min}/a_{\max}$  changes approximately by a factor of 4.

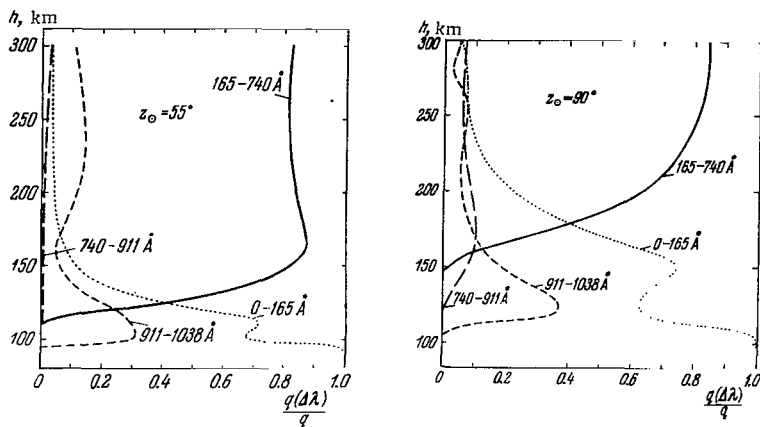


FIGURE 90. Vertical variation of the relative rate of ionization  $q(\Delta\lambda)/q$  for high solar activity in four spectral regions for  $z_0 = 55^\circ$  and  $z_0 = 90^\circ$ .

The marked increase of the ratio  $a_{\min}/a_{\max}$  thus reflects the fact that in periods of high solar activity the radiation with  $\lambda < 796 \text{ \AA}$  is enhanced to a greater extent than the radiation with  $\lambda > 911 \text{ \AA}$ . Hence the important conclusion that the variations in the ratio  $[N_2^+]/[O_2^+]$  may be applied for comparing the intensities in the corresponding spectral regions and estimating the variation of their relative values during a solar cycle.

#### Variations of the relative ion concentrations

To enable us to compare the computed values of  $q$  with the results of ionospheric observations, we have to compute the concentrations of ions and electrons. The ionization processes in this context should be considered jointly with the reverse recombination processes. When comparing the theory with experiment, we shall first consider the comparatively simple question of the behavior of the relative ion concentrations (their vertical distribution, and also the variation of the ion composition during the day and as a function of solar activity). Measurements of the relative ion composition are simpler than measurements of the absolute ion concentration, which have been made on some of the rockets only.

Figure 91 plots the results of mass-spectrometric measurements of the ion composition at altitudes of 160–200 km according to the data of Table 23 from Section 15, Chapter IV. The curves plotting the daytime variation of the ion composition for high ( $F \geq 230$ , solid curves) and low ( $F \leq 180$ , dashed curves) solar activity have been drawn through the experimental points.

The variation of the ion composition at various altitudes as a function of  $z_0$  is quite regular and systematic. The great similarity of the curves at various altitudes between 160 and 200 km only strengthens our conclusions concerning these variations of the ion composition.

Comparison of the curves for the ions  $O^+$  and  $NO^+$  shows that the curves for  $[NO^+]/n_e$  are to a certain extent mirror images of the curves  $[O^+]/n_e$  about the horizontal axis for both day and night conditions. The ions  $O_2^+$  in daytime behave like the ions  $NO^+$ . As we saw in Section 22, Chapter V, the

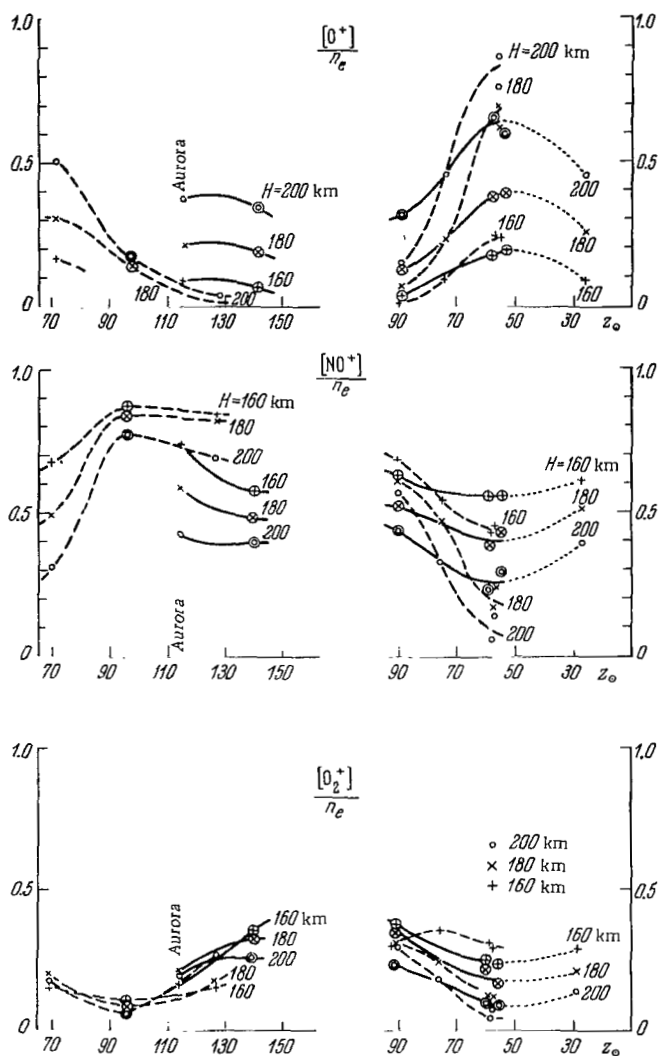


FIGURE 91. Diurnal variation of the relative ion concentrations  $\frac{[O^+]}{n_e}$ ,  $\frac{[NO^+]}{n_e}$ , and  $\frac{[O_2^+]}{n_e}$  as a function of  $z_{\odot}$  from the results of rocket measurements (Table 23) at altitudes of 200, 180, and 160 km.

Circles mark points corresponding to high solar activity. Solid curves trace the expected variation in epochs of high solar activity, dashed curves correspond to low solar activity, dotted curves are extrapolation.

relative concentration of the molecular ions  $NO^+$  and  $O_2^+$  should indeed follow similar curves, which go against the variation of the relative concentration of the  $O^+$  ions. This is a natural consequence of the constancy of the concentration ratio of the main molecular ions  $NO^+$  and  $O_2^+$ , so that when



one of the terms in the sum  $[M^+]/n_e + [O^+]/n_e = 1$  decreases the other automatically increases.

If we ignore the data for  $z_0 = 27^\circ$ , we see that in daytime the concentration  $[O^+]/n_e$  monotonically decreases with increasing  $z_0$  and  $[M^+]/n_e$  increases. Qualitatively, this can be explained by using the theory of Section 22, and in particular Table 42, if we recall that the intensity of solar radiation  $I$  diminishes with increasing  $z_0$  because of atmospheric absorption, whereas the intensity dependence of atomic ions is the reverse of that of the molecular ions. Another remarkable fact is that the concentration amplitude of the molecular ions increases with altitude, whereas that of the atomic ions conversely diminishes. It indeed follows from Table 42 (Section 22) that on passing from the bottom part of the ionosphere to the upper regions, the dependence of  $[O^+]/n_e$  on  $I$  becomes less pronounced whereas the corresponding dependence for  $[NO^+]/n_e$  and  $[O_2^+]/n_e$  is conversely intensified. These results are consistent with observations.\*

It is also essential to allow for the dependence on the solar activity. We see from Figure 91 the differences in the variation of  $[O^+]/n_e$ ,  $[NO^+]/n_e$ , and  $[O_2^+]/n_e$  for high and low solar activity. The variation of the relative concentrations of the ions  $O^+$ ,  $NO^+$ , and  $O_2^+$  with  $z_0$  increasing from  $50^\circ$  to  $90^\circ$  is less pronounced for low solar activity than for high activity. The origin of this effect is unclear at this stage. It may be associated with differences in the contribution of the radiation with  $\lambda \geq 911 \text{ \AA}$  or with differences in the diurnal variations of the atmospheric parameters at the relevant altitudes for high and low solar activities. Let us consider the vertical variation of the ion composition. It follows from the photochemical theory (Section 22) that the ratio  $[NO^+]/[O_2^+]$  should be constant at altitudes of 140–250 km. Figure 92 plots the ratio  $[NO^+]/[O_2^+] = C$  vs. altitude for daytime conditions from experimental data. We see that at altitudes of 150–250 km the ratio  $C$  is indeed fairly constant in all the experiments: on the average  $[NO^+]/[O_2^+] \approx 2$ . In individual experiments,  $C$  does deviate from the mean, but not more than by a factor of 1.5.

Some regular features can be noted in the behavior of the curves in Figure 92. At altitudes  $h > 130$  km, for high solar activity and during a magnetic disturbance, the ratio  $[NO^+]/[O_2^+]$  is generally somewhat higher than for low and medium activity. Some curves reveal a systematic increase of the ratio  $[NO^+]/[O_2^+]$  with altitude between 150 and 200 km. These regular features are relatively easily to explain.

Using (V.81) and (V.82), we obtain the simple relation

$$\frac{[NO^+] \alpha_{NO^+}^*}{[O_2^+] \gamma_{O_2^+}} = \frac{0.5q(O^+) + q(N_2^+)}{0.5q(O^+) + q(O_2^+)}, \quad (\text{VI.14})$$

since  $\gamma_{NO^+}[O^+][N_2] \approx \gamma_{O_2^+}[O^+][O_2] \approx 0.5q(O^+)$  and  $\gamma_6[N_2][O_2] \ll \gamma_{N_2^+}[N_2^+][O] \approx q(N_2)$ . In daytime, for  $z_0 \leq 60^\circ$ , particular computations show (see the first subsection of Section 25) that the ratio on the right in (VI.14) is virtually independent of altitude and solar activity between 150 and 200 km and is approximately equal to 1.65–1.9.\*\* The increase in  $T_e$  between 140 and 200 km

\* Hence it follows that in order to explain the unusual ion composition in the experiment carried out at  $z_0 = 27^\circ$  during a magnetic disturbance /253/, we have to assume certain changes in the atmospheric parameters, e.g., increase of the relative molecule concentration. This assumption for magnetic storms was previously advanced by Seaton /626/.

\*\* In an earlier work /266/, while attempting to account for the near constancy of  $[NO^+]/[O_2^+]$  at altitudes of 140–200 km, we ignored the contribution of  $q(N_2^+)$  to  $q$  and erroneously assumed  $i_3/[O^+] = \text{const}$ .

leads to a certain increase in the ratio  $\alpha_{O_2^+}/\alpha_{NO^+}$ , which rises from 0.6 to 0.75 for low solar activity and from 0.7 to 1.1 for high solar activity. Relation (VI.14) then shows that  $[NO^+]/[O_2^+] = 1 - 2$ . The slight increase of the ratio  $\alpha_{O_2^+}/\alpha_{NO^+}$  with increasing  $T_e$  accounts for the slight increase of the ratio  $[NO^+]/[O_2^+]$  with altitude and with increase in solar activity. The same effect is probably observed in the diurnal variation of the ratio  $[NO^+]/[O_2^+]$ . As we noted in Section 15,  $[NO^+]/[O_2^+] < 1$  for low solar activity at night at altitudes  $h \geq 180 - 200$  km, whereas in daytime this ratio is close to 2, i. e., several times higher. In the presence of an ionization source, a relation of the form (VI.14) is valid at night also. It shows that at night, when  $T_e$  drops down to about  $700^\circ$ , and the ratio  $\alpha_{O_2^+}/\alpha_{NO^+}$  therefore decreases to approximately  $1/3$  of the daytime value, we should expect a decrease of the ratio  $[NO^+]/[O_2^+]$ , which is indeed observed.

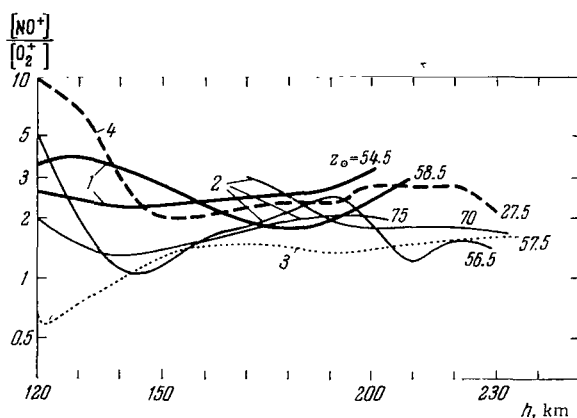


FIGURE 92. The ratio  $\frac{[NO^+]}{[O_2^+]}$  vs. altitude for various  $z_0$  (rocket measurements):

1 - high solar activity; 2 - medium solar activity; 3 - low solar activity; 4 - during a magnetic disturbance.

As we see from Figure 92, some irregular variations of the ratio  $[NO^+]/[O_2^+]$  are observed at altitudes around 200 km and higher. At high altitudes, the concentration of molecular ions diminishes and the determination of the concentrations  $[NO^+]$  and  $[O_2^+]$  becomes less accurate, so that we should not attach considerable significance to these irregularities.

Let us consider another effect which is observed at  $h \approx 200$  km at night. The ratio  $[O^+]/n_e$  in epochs of low solar activity markedly decreases at night, whereas in polar aurorae and for high solar activity, the nocturnal value of  $[O^+]/n_e$  is virtually equal to the daytime value. It follows from an analysis of (V.90) that, in the presence of ionization sources we have  $[O^+]/n_e < 0.5$  at altitudes where  $n \geq \frac{BI}{4A}$ . It is clear that as  $I$  diminishes, this range of altitudes shifts upward. Experimental data indicate (see below, p. 245) that the level at which  $[O^+]/n_e = 0.5$  shifts from 170 - 180 km during the day to  $h \approx 220$  km for  $z_0 = 90^\circ$  and at night, so that in periods of low solar activity

$[\text{O}^+]/n_e > 0.5$  at 200 km altitude in daytime and  $[\text{O}^+]/n_e < 0.5$  at night. Moreover, the intensity of the ionization sources diminishes at night to such an extent that a nonequilibrium concentration of ions and electrons prevails for a long time after sunset. In this case, the  $\text{O}^+$  ions are rapidly destroyed and their relative concentration becomes lower than the equilibrium concentration for the same  $n_e$ .

Let us now consider the *E* region, where (VI.14) does not apply. We see from Figure 92 that the ratio  $[\text{NO}^+]/[\text{O}_2^+]$  reaches a minimum at 130–150 km, and then rapidly increases with decreasing altitude. A particularly deep minimum is observed for low solar activity. The formation of this minimum is associated with the anomalously high ratio  $q(\text{O}_2^+)/q(\text{N}_2^+)$  in this region. The growth of the ratio  $[\text{NO}^+]/[\text{O}_2^+]$  at still lower altitudes, according to (V.93), is evidently related to the growth of  $\mu_e$  from (V.78) as a result of the increase in the concentration of  $\text{NO}$ ,  $\text{N}_2$ , or  $\text{N}$ .

An unusual situation is observed at night for low solar activity at  $h = 100 - 150$  km (Section 15): the concentration of  $\text{NO}^+$  ions is more than an order of magnitude higher than the concentration of  $\text{O}_2^+$  ions. We noted in Section 22 that the effect of reactions (V.76) should be taken into consideration at the relevant altitudes for high values of  $z_0$  and at night. The ratio  $[\text{NO}^+]/[\text{O}_2^+]$  is then determined by (V.93) which indicates that the ratio  $[\text{NO}^+]/[\text{O}_2^+]$  increases with decreasing  $n_e$ . Since in periods of low and medium solar activity  $n_e$  at night drops to  $1/30 - 1/100$  of its daytime value, we have an obvious explanation for the decrease of the ratio  $[\text{NO}^+]/[\text{O}_2^+]$  from 1–3 to  $< 0.1$ , as observed in rocket measurements (Section 15).

The theory of the formation of the ionosphere created in recent years thus accounts for numerous experimental features in the variation of the relative ion concentrations at altitudes of 100–200 km during the day and the solar activity cycle. Let us now proceed with an analysis of the absolute ion and electron concentrations.

## Variation of the absolute ion concentrations

In the previous section we compared the results of the photochemical theory with mass-spectrometric measurements, which only yield the relative concentrations of ions. More valuable information can be obtained if the absolute ion concentrations are known. First we shall consider the total ion concentration  $n_i^+$ , which is equal to the electron concentration  $n_e$ , since at altitudes  $h > 100$  km the concentration of negative ions is negligible.

**Total concentration of ions and electrons.** Using the profiles  $q(h, z_0)$  computed in the first subsection of Section 25, we can find the equilibrium profiles  $n_e(h, z_0)$  using the relation  $n_e = \sqrt{q/\alpha'}$  and assuming that the effective recombination coefficient  $\alpha'$  is known at various altitudes for various  $z_0$ . However,  $\alpha'$  is currently known with less accuracy than  $q$  and  $n_e$ . Therefore in the next section we will adopt the reverse course, using  $q$  and  $n_e$  to find the variations in  $\alpha'$ . In this section, however, we shall try to account for the observed features of the  $n_e(h)$  profiles to first approximation, ignoring the variations of  $\alpha'$  with time of day and solar activity (this being the usual policy).

A superficial comparison of the profiles  $q(h)$  in Figure 81 with the profiles  $n_e(h)$  of the empirical rocket model of the ionosphere (Figure 42) reveals a number of common features. Primarily this applies to the formation of a maximum in the *E* region for high  $z_0$  and a "valley" above it. On the other

hand, in the upper part of the ionosphere, above  $h \approx 200$  km, a qualitative difference is observed between the bundle of convergent  $q(h)$  profiles and the fan of the divergent  $n_e(h)$  profiles. Let us proceed with a quantitative comparison of the profiles  $q$  and  $n_e$ .

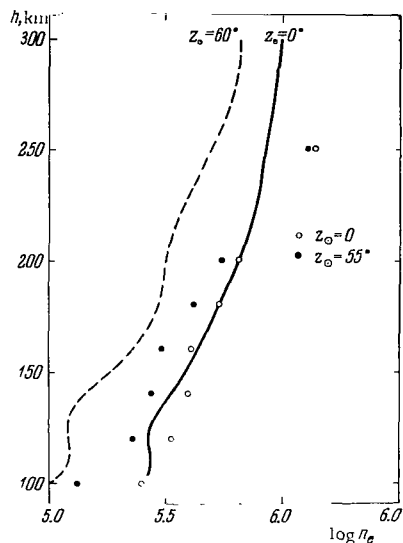


FIGURE 93. Computed values of  $n_e = \sqrt{q/\alpha'}$  (circles) for  $z_0 = 0$  and  $z_0 = 55^\circ$  compared with rocket data  $n_e^{\text{obs}}$  (from Figure 42) for  $z_0 = 0$  and  $z_0 = 60^\circ$ .

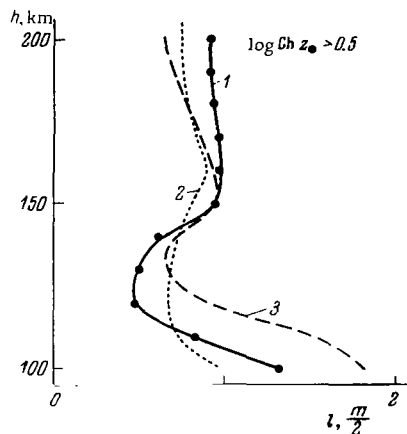


FIGURE 94. Experimental values of the parameter  $l$  from /243/ ((IV.6), curve 1) compared with the theoretical values of  $m/2$  (from (VI.10)) computed from the data of /560/ (curve 2) and in the present chapter (curve 3).

Using the average profile  $\alpha'(h)$  from Section 21 (Figure 74), we marked with circles in Figure 93 the values of  $\sqrt{q/\alpha'}$  for  $z_0 = 0$  and  $55^\circ$ . Comparison with the corresponding  $n_e(h)$  profiles in summer for maximum solar activity clearly shows the following: 1) for  $z_0 = 0$ , below 200 km, the values of  $\sqrt{q/\alpha'}$  are close to  $n_e^{\text{obs}}$ ; 2) for  $z_0 = 60^\circ$ , even below 200 km, significant differences are observed between  $n_e^{\text{obs}}$  and  $\sqrt{q/\alpha'}$ ; 3) above 200 km, the gradient of  $\sqrt{q/\alpha'}$  is much higher than the gradient of  $n_e^{\text{obs}}(h)$ . Hence it follows that the average profile  $\alpha'(h)$  for altitudes  $h \lesssim 200$  km may be quite adequate for midday conditions in epochs of high solar activity but is inapplicable to other  $z_0$  and other solar activity conditions. This points to variations in the gradient  $dx'/dh$  during the day.

Above  $\sim 200$  km, the difference between  $\sqrt{q/\alpha'}$  and  $n_e$  is particularly pronounced. However, it is due to the neglect of diffusion effects, and not to improper choice of the gradient  $da'/dh$  (see Section 28).

The effect of the variations in  $\alpha'$  during the day is best illustrated by the mismatch between the experimental values of the parameter  $l$ , which characterizes the rate of change of the electron concentration during the day ( $l$  in Figure 44 in Section 15), and the theoretical values of  $m/2$ . The mismatch is quite evident from Figure 94, which shows the experimental values of  $l$  (curve 1) for  $\log Ch z_0 > 0.5$  compared with the corresponding values of  $m/2$  from Figure 85. Both the theoretical and the experimental

curves show a minimum at 120 — 130 km. As we have seen before in this section, the minimum of  $m$  is associated with the formation of a "layer" of primary ions  $O_2^+$  produced by radiation with  $\lambda \geq 911 \text{ \AA}$ . Although the shape of the theoretical curve is not unlike that of the experimental curve, we consistently have  $m/2 > l$  below 150 km and  $m/2 < l$  above 150 km.

The variation of  $\alpha'$  thus must be taken into consideration if we are to account for the daily variations of the profile  $n_e(h)$  and the vertical variation of the parameter  $l$ .

Let us consider still another feature of the electron concentration profiles  $n_e(h)$ .

We have noted before that the formation of a  $n_e$  maximum in the  $E$  region for high  $z_0$  corresponds to a maximum on the  $q(h)$  profile, which in its turn is associated with the low value of the parameter  $m$  at 120 — 130 km and thus reflects the particular distribution of energy in the solar spectrum. The difference between the values of  $l$  and  $m/2$  at 120 — 130 km indicates that the above reasons do not completely account for the formation of the  $n_e$  maximum in the  $E$  region. Another argument disputing the original hypothesis is provided by the  $n_e$  maximum in the nocturnal  $E$  layer: this maximum forms at night before the ionosphere is exposed to solar radiation. Solar radiation may thus sustain an existing peak in the  $E$  region (for large  $z_0$ ), but its origin is apparently attributable to a nocturnal ionization source.

Various authors, starting with Havens et al. /628/, Hertzberg /629, 630/, Yonezawa /631, 690/, Bates and Nicolet /632/, Danilov /633, 634/, and in later publications /559, 573, 354, 574, 635, 636, 255, 637, 575, 576, 638/, compared the theoretical concentration profiles of electrons and various ions with the results of mass-spectrometric rocket measurements. These investigations proved of considerable importance for the development of the photochemical theory of the ionosphere. Comparison of theory with experiment permitted choosing the correct cycle of the fundamental ion-molecular reactions and determining the constants of these reactions with higher reliability than in earlier laboratory work. The detailed studies are discussed in detail in Danilov's book /572/, and we will only consider some results here. An appropriate choice of the rate constants on the whole ensures a fair fit between the computed and the observed ion concentrations at altitudes of from 130 to 200 — 250 km. The constants of various authors somewhat differ, mainly depending on the particular solar radiation intensity chosen (whether high or low), the rate constants of dissociative recombination, and the particular atmospheric model. These differences for the main reactions are in fact less than half an order of magnitude /639/. New laboratory measurements /577, 578, 637, 642/ agree with the high values of the ionization and recombination rates.

Now, that the vertical distribution of the ion concentration for  $h = 140 - 200$  km has been largely deciphered, the next problem is to account for the variation of the ion concentration at fixed altitudes during the day and as a function of the solar activity. The solution of this problem met with greater difficulties. The photochemical theory and ionization rate computations proved insufficient for disclosing all the fine features of the time curves of the ion concentrations.

**The  $N_2^+$  ion.** Up to 200 — 250 km, molecular nitrogen is the dominant component of the neutral atmosphere, and the rate of production of the  $N_2^+$  ions through photoionization is fairly high. However, the equilibrium

concentrations of  $N_2^+$ , according to mass spectrometric measurements, are very low and do not exceed 1% of the total concentration of charged particles. Since the rate constant of dissociative recombination for  $N_2^+$  ions is only several times higher than for  $NO^+$  and  $O_2^+$ , this concentration of  $N_2^+$  is unexpectedly low. Another significant feature of the  $N_2^+$  ions is that their vertical distribution has a sharp maximum which lies, according to Istomin's measurements /260, 261/, substantially lower than the  $n_e$  maximum, namely at altitudes of 250–270 km in periods of high solar activity. Later mass-spectrometric and optical measurements have shown that for low solar activity the altitude of the maximum drops to 200–250 km, and the concentration  $[N_2^+]$  in the maximum decreases from  $10^4 \text{ cm}^{-3}$  for high solar activity to  $(1-3) \cdot 10^3 \text{ cm}^{-3}$  for low activity.

If dissociative recombination were the only reaction destroying  $N_2^+$  ions, the concentration of these ions for low solar activity at  $h \approx 200 \text{ km}$  would be

$$[N_2^+] = \frac{q(N_2^+)}{\alpha_{N_2^+} n_e} \approx \frac{10^8}{10^{-7} \cdot 3 \cdot 10^5} \approx 3 \cdot 10^4 \text{ cm}^{-3}, \quad (\text{VI.15})$$

i. e., 1–1.5 orders of magnitude less than the actually observed concentration, and moreover  $[N_2^+]$  would monotonically increase with decreasing  $h$  up to the  $q(N_2^+)$  maximum at  $h \approx 150 \text{ km}$ . At first Lytle and Hunten /640/, somewhat uncertainly, and later Norton et al. /354/, Nicolet and Swider /573/, Danilov /635/, and Dalgarno /578/ came to the conclusion that the  $N_2^+$  ions are destroyed in the ionosphere not by dissociative recombination but mainly through more efficient conversion reactions



There is, however, no unanimity of opinion as to the end product of  $N_2^+$ , whether  $O^+$  or  $NO^+$ .

Estimates show that the constant  $\gamma$  for reactions of the type  $N_2^+ + X \rightarrow$ , irrespective of the exact nature of the second reactant  $X$  and the reaction product, should be fairly high. Taking  $[N_2^+] = 2 \cdot 10^3 \text{ cm}^{-3}$  for low solar activity at altitudes of 200 km and using the computations of  $q(N_2^+)$  from Section 19, we find

$$\gamma_{N_2^+} = \frac{q(N_2^+)}{[N_2^+][X]} \approx \frac{0.5}{[X]} \approx (1-2) \cdot 10^{-10} \text{ cm}^3/\text{sec}, \quad (\text{VI.17})$$

assuming that the second reactant is atomic oxygen. This estimate of the rate constant, based on purely ionospheric data, is close to the laboratory figure  $\gamma_{N_2^+} = (2-2.5) \cdot 10^{-10} \text{ cm}^3/\text{sec}$  obtained by Fite et al. /641/ and confirmed by the new measurements of Ferguson et al. /577, 637, 642/. It was given in (V.74). If  $X$  were identified with  $O_2$ , the estimate  $\gamma_X$  would be 1.5 orders of magnitude higher than in recent laboratory experiments. Bourdeau et al. /610/ assume that reaction (VI.16) should proceed at a higher rate than the reaction



at all altitudes  $h > 90 \text{ km}$ .

Using the above estimate for  $\gamma_{N_2^+}$  and  $\alpha_{N_2^+} \geq 10^{-7}$  cm<sup>3</sup>/sec (Section 21), we find  $\alpha_{N_2^+} n_e \geq \gamma_{N_2^+} [O]$  for those altitudes only where  $[O] < 10^3 \cdot n_e$ , i. e., above 250 km in daytime. Thus, below 250 km, the dissociative recombination of  $N_2^+$  can be ignored, as we actually did in Section 22.

Let us now consider the maximum of the  $[N_2^+]$  profile. Above  $h \approx 200$  km, around noon, the ionizing solar radiation is not absorbed and the rate of ionization fairly rapidly diminishes with altitude, since by (V.79), we have  $q(N_2^+) \propto [N_2]$ . Therefore, at  $h \geq 250$  km, where  $N_2^+$  ions are destroyed by dissociative recombination, the concentration  $[N_2^+]$  should diminish with increasing altitude. Below 200–250 km, the rate of destruction of the  $N_2^+$  ions increases with decreasing altitude in proportion to the concentration  $[O]$ , whereas the growth of  $q(N_2^+)$  is slowed down first because of the approach to the maximum  $q_{\max}$  and then because of the increasing fraction of  $O_2^+$  in the product ions. Therefore below 200–250 km, the concentration  $[N_2^+]$  should diminish with increasing altitude. The maximum of the  $[N_2^+]$  profile should evidently shift upward with increasing  $z_0$ , as the maximum  $q(N_2^+)$  moves upward; it should also rise with increasing solar activity, when the increase in atmospheric density displaces upward the zone with  $[O] < 10^3 \cdot n_e$ . These considerations explain the result of mass-spectrometric observations of  $N^+$ .

Since the concentration of  $N_2^+$ , according to (V.79), is directly proportional to the intensity of the ionizing agent, the latter factor can be determined from  $[N_2^+]$ . The relatively high concentration of  $N_2^+$  ( $\sim 30$  cm<sup>-3</sup>) observed in the nighttime experiment of Holms et al. /255/ (as in the experiment of Johnson et al. /251/, which was apparently conducted during a weak polar aurora and gave  $[N_2^+]/n_e \approx 3 \cdot 10^{-3}$ ) points to the existence of a significant nocturnal ionization source. Since by (VI.17)  $q \approx 15$  cm<sup>-3</sup>sec<sup>-1</sup> at night at altitude of 200 km, which is 1/100 of the daytime figure, the strength of the nocturnal source should be approximately two orders of magnitude less than the ionizing power of solar radiation.

Similarly the difference in the concentration  $[N_2^+]$  in daytime rocket experiments is associated with differences in the intensity of the ionizing solar radiation for different solar activity levels, although the variation of  $[O]$  or, more precisely, of the ratio  $[O]/[N_2]$  may also produce a certain effect. For example, Sputnik III measurements gave  $[N_2^+] = 10^4$  cm<sup>-3</sup> at altitudes of about 250 km. This is a factor of 10 higher than in Holms's daytime experiment /255/. The change in the intensity of the solar radiation could account for a change in  $[N_2]$  by about a factor of 3. The additional difference is a reflection of the increase in the ratio  $[O]/[N_2]$  by a factor of about 3 in an epoch of low solar activity (if the seasonal and the latitudinal effects are ignored).

**Atomic oxygen ions.** By (V.91), the concentration of  $O^+$  at a given altitude should increase with decreasing  $z_0$  and with increasing solar activity in proportion to  $i_1[O]/[N_2]$  at those altitudes where  $\omega q(O_2^+) \ll q(O^+)$ . The variations of the relative, and not the absolute, concentrations of atoms and molecules are of the main importance here. We will consider the experimental data on the variation of the absolute concentrations of atomic oxygen, using the mass-spectrometric results (Table 23) together with measurements of the electron concentration  $n_e$  from Section 15.

Figure 95 plots the variation of the absolute concentration  $O^+$  for  $z_0 = 50 - 100^\circ$  at three altitudes, 160, 180, and 200 km. The most striking feature of this figure is that the variation of  $[O^+]$  follows the same curve for high (encircled dots) and low solar activity. It is only at altitudes of 200 km that

a certain systematic divergence between the data for high and low solar activity is noted. Since the absolute concentration  $[O^+]$  at a given altitude

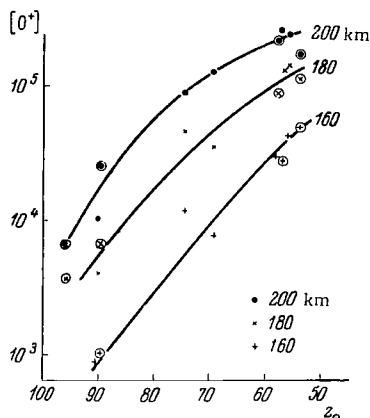


FIGURE 95. Daily variation of absolute concentration of  $O^+$  as a function of  $z_0$  for altitudes 160, 180, and 200 km, according to rocket measurements.

The encircled dots refer to the period of high solar activity. The curves represent average values of  $[O^+]$ .

between 160 and 200 km is virtually independent of solar activity, although the intensity of the short-wave solar radiation and also the composition of the atmosphere both change. Using (V.91) we see that the ratio  $[N_2]/[O]$  is proportional to the ionization coefficient  $i_1$ , which diminishes by a factor of 2 — 3 at these altitudes in periods of low solar activity. This is consistent with the previous conclusion derived from the data on  $[N_2^+]$ , namely that the ratio  $[O]/[N_2]$  increases for low solar activity. The reason for the significant variations in  $[N_2^+]/[O^+]$  and  $[N_2^+]$  during the solar cycle is thus clear.

It follows from the above considerations that the computed  $q(h)$  profiles are insufficient for explaining the variations of the absolute ion concentrations: variations of density and composition of the atmosphere during the day and during the solar activity cycle should also be taken into account. A similar problem was observed to arise in connection with the variations in  $n_e/513$ .

Comparison of the data on  $[O^+]$  with the data on the rate of ionization  $q$  enables us to derive the rate constants of the fundamental

ion-molecular reactions (V.72) and (V.73) (see /266/). We have previously mentioned estimates of other constants based on ionospheric data. The principal shortcomings of these estimates do not only stem from the fact that one often has to use radiation intensity data and atmospheric parameters corresponding to one set of conditions and ion composition or  $n_e$  data corresponding to entirely different conditions. The reaction rate constants are generally assumed independent of altitude. This is valid only if we further assume that they are independent of temperature as well. The latter assumption, however, is highly questionable. The new laboratory techniques recently made it possible to establish the dependence of the rate constants on temperature. For the reaction  $O^+ + N_2 \rightarrow NO^+ + N$  the rate constant was found to increase with temperature /643 — 647, 738/, whereas for the reaction  $O^+ + O_2 \rightarrow O_2^+ + O$  it conversely decreases with temperature /647, 739, 740/  $\gamma_{O_2^+} = 3.4 \cdot 10^{-10} T^{-0.48} \approx 2 \cdot 10^{-11} (360/T)^{1/2}$ . This does not agree with theoretical computations /648/, which indicate that the rate constants of both reactions increase with temperature, nor with ionospheric estimates /575, 638/ which reveal a reverse effect.\*

We have considered in some detail the variation of the absolute concentrations of the ions  $N_2^+$  and  $O^+$ . Using the concentration ratio  $[NO^+]/[O_2^+]$ , we can also find the absolute concentrations of the ions  $NO^+$  and  $O_2^+$ . These ions will be considered in the next section, since they affect the value of  $\alpha'$ .

\* Recently, a decrease of  $\gamma$  with temperature was observed for the reaction  $O^+ + N_2 \rightarrow NO^+ + N$  in laboratory /747/.



## 26. Variation of the effective recombination coefficient and formation of the $F_1$ region

We saw in Section 21 that neutralization in the entire ionosphere below the  $F$  region (except the  $D$  region) is completely determined by dissociative recombination of molecular ions. Thus, the theoretical expression for the coefficient  $\alpha'$  is

$$\alpha' = \alpha_{\text{NO}^+}^* \frac{[\text{NO}^+]}{n_e} + \alpha_{\text{O}_2^+}^* \frac{[\text{O}_2^+]}{n_e} + \alpha_{\text{N}_2^+}^* \frac{[\text{N}_2^+]}{n_e}. \quad (\text{VI.19})$$

Expression (VI.19) describes fully and in the most general form the variation of the coefficient  $\alpha'$  if the concentration of negative ions is low. Using this expression, we can predict some basic features in the variation of  $\alpha'$ , if  $\alpha^*$  and the relative concentrations of the molecular ions are known.

### Linear and quadratic recombination

One of the most characteristic differences between the upper and the lower ionosphere stems from the different dependence of the recombination rate  $r$  on the electron concentration: the  $E$  region is characterized by the ordinary quadratic dependence ( $r \propto n_e^2$ ) whereas the  $F$  region has a linear dependence ( $r \propto n_e$ ). These dependences were established experimentally in ionospheric observations from the ground which show that the rate of change of the electron concentration  $dn_e/dt$  (during various disturbances or after sunset) in the  $E$  region is quite high and is proportional to  $n_e^2$ , whereas in  $F$  region it is substantially smaller in magnitude and is proportional to  $n_e$ . The proportionality coefficients —  $\alpha$  for the  $E$  region and  $\beta$  for the  $F$  region — have the dimensions  $[\text{cm}^3 \text{sec}^{-1}]$  and  $[\text{sec}^{-1}]$ , respectively.

The linear recombination is of the greatest importance from the theoretical point of view. As we have noted earlier, it was first discovered by Mohler /526/, and Bates and Massey /487/ tried to interpret it using the negative ion hypothesis (the coefficient  $\beta$  is still called the "attachment" coefficient, although this nomenclature does not reflect the true physics of the situation). Later Ratcliffe et al. /528/ in nocturnal measurements determined the vertical variation of  $\beta$ , which was found to be proportional to the change in the concentration of molecules. Later the linear recombination and the exponential dependence of  $\beta$  on altitude were confirmed by other authors, in particular during solar eclipses /649, 568/.

Ratcliffe /650/ advanced an elementary theory which explains the transition from quadratic recombination in the lower part of the ionosphere to linear recombination in the upper atmosphere and the exponential decrease of  $\beta$  with altitude. Ratcliffe's theory introduced two significant new assumptions: neutralization was assumed to occur as a result of dissociative recombination of molecular ions, and the molecular ions  $M^+$  were assumed to form from atomic ions  $A^+$  in certain ion-molecular reactions:



where  $\alpha^*$  and  $\gamma$  are rate constants. In (VI.21) we indicate two types of ion-molecular reactions, although Ratcliffe only considered the first reaction. Reactions of the second type (attachment of the charged particle  $A^+$ ) are more efficient, and the overall argument should not change if we retain the symbol  $\gamma$  for the reaction rate constant.

By (VI.20), the number of recombinations is defined as

$$r = \alpha^* n_e M^+, \quad (\text{VI.22})$$

where  $M^+$  is the concentration of the molecular ions. Seeing that  $n_e = M^+ + A^+$ , we find for  $r = \alpha' n_e^2$

$$\alpha' = \alpha^* \frac{M^+}{n_e} = \frac{\alpha^*}{1 + \frac{A^+}{M^+}}. \quad (\text{VI.23})$$

The ratio  $A^+/M^+$  is obtained from the condition that the molecular ions only form from the reaction (VI.21) which proceeds at a rate

$$q(M^+) = \gamma n A^+, \quad (\text{VI.24})$$

where  $n$  is the concentration of neutral particles. Taking  $r = q(M^+)$  or  $\alpha^* n_e M^+ = \gamma n A^+$  and inserting the ratio  $A^+/M^+$  from this expression into (VI.23), we obtain Ratcliffe's basic formula

$$\alpha' = \frac{\alpha^*}{1 + \frac{\alpha^* n_e}{\gamma n}} = \frac{\alpha^* \gamma n}{\gamma n + \alpha^* n_e}. \quad (\text{VI.25})$$

Let us consider some extreme cases. In the lower part of the ionosphere, where  $M^+ \gg A^+$ , we have by (VI.23)  $\alpha'/\alpha^* \approx 1$  and  $r = \alpha' n_e^2 \approx \alpha^* n_e^2$  (quadratic recombination, since  $\alpha^* = \text{const}$ ). In the upper part of the ionosphere, where  $\gamma n \ll \alpha^* n_e$  (which is equivalent to  $M^+ \ll A^+$ ), we have by (VI.25)  $\frac{\alpha'}{\alpha^*} = \frac{\gamma n}{\alpha^* n_e} \ll 1$  and also  $r = \alpha' n_e^2 = \beta n_e$ . Here  $\alpha'$  is a function of  $n_e$ , specifically  $\alpha' \propto n_e^{-1}$ , but  $\beta = \gamma n = \text{const}$ , i. e., a case of linear recombination. Thus Ratcliffe's theory successfully explains the two main types of recombination in the ionosphere and the proportionality between  $\beta$  and  $n$ .

The transition from quadratic to linear recombination occurs at altitudes where  $M^+ \approx A^+ \approx 0.5 n_e$ . According to experimental mass-spectrometric data from Section 15, this corresponds to 170–175 km in daytime for low solar activity; for  $z_0 = 90^\circ$  the corresponding altitudes are much higher, about 230 km (for high solar activity we have 180–200 km and about 220 km, respectively). At night, the transition from molecular to atomic ions occurs at altitudes of 225–215 km.

Between the lower and the upper ionosphere there is a region in which an intermediate recombination law should be valid and where  $\alpha'$  is computed from (VI.25). In practice, however, the application of (VI.25) involves certain difficulties, since the ionosphere contains several species of molecular ions  $\text{NO}^+$ ,  $\text{O}_2^+$ , and  $\text{N}_2^+$  which are moreover characterized by different values of the dissociative recombination coefficient  $\alpha^*$ . Ratcliffe's theory ignores this fact. Another theoretical simplification stems from the fact that molecular ions are actually formed through primary ionization, as well

as through ion-molecular reactions involving atomic ions. The elementary theory thus should be rendered more precise.

Let us first consider the lower ionosphere. In this part of the ionosphere the ions  $O^+$  and  $N_2^+$  are much more abundant than the ions  $NO^+$  and  $O_2^+$ , so that  $[NO^+] + [O_2^+] \approx n_e$  and the third term in (VI.19) can be ignored. Seeing that at these altitude, according to the photochemical theory (Section 22),

$$\frac{[NO^+]}{[O_2^+]} = C \approx \text{const} \quad \text{and} \quad n_e = [NO^+] \left(1 + \frac{1}{C}\right) = [O_2^+] (1 + C),$$

we have from (VI.19)

$$\alpha' = \frac{\alpha_{NO^+}^*}{1 + \frac{1}{C}} + \frac{\alpha_{O_2^+}^*}{1 + C}. \quad (\text{VI.26})$$

As in the elementary theory, the coefficient  $\alpha'$  is independent of  $n_e$  and  $n$ , i. e., it should not depend on altitude either. This is valid to first approximation only. Using new data on the coefficients  $\alpha_i^*$ , and in particular their dependence on  $T_e$ , we can expect a certain reduction of  $\alpha'$  with altitude, in inverse proportion to  $T_e$  or  $\sqrt{T_e}$  (this was mentioned in Section 21 during our analysis of the experimental data on Figures 70—72). For the same reason we can expect a certain decrease of  $\alpha'$  on passing from night to day and from low to high solar activity, when the temperature of the upper atmosphere at  $h \gtrsim 100$  km increases.  $C$  also somewhat changes during the day and during the solar cycle (see Section 25).

Let us now consider the upper part of the ionosphere. In this region, a significant proportion of the ions  $N_2^+$  may be destroyed by mechanisms other than dissociative recombination, so that the dependence of  $[N_2^+]/n_e$  on  $I$  and  $n$  in general does not coincide with the dependence of  $[NO^+]/n_e$  and  $[O_2^+]/n_e$  on  $I$  and  $n$ . However, since  $[N_2^+] \ll n_e$ , the contribution of the ions  $N_2^+$  to expression (VI.19) for  $\alpha'$  may be ignored altogether. Moreover, for sufficiently high altitudes, where  $I = \text{const}$  and  $\alpha_{N_2^+}^* n_e > \gamma_{N_2^+} [O]$ , as it follows from (V.79) — (V.82), we have  $M^+/n_e \propto M/n_e$ , where  $M$  is the concentration of molecules in the atmosphere. Thus, by (VI.19) we find for the total number of recombinations

$$r \propto M n_e, \quad (\text{VI.27})$$

in agreement with Ratcliffe's elementary theory.

At intermediate altitudes, again ignoring the contribution of  $N_2^+$  to  $\alpha'$ , we obtain, using the sufficiently general expressions (V.86) — (V.88)

$$\alpha' = \left\{ \frac{\alpha_{NO^+}^*}{1 + \frac{1}{C}} + \frac{\alpha_{O_2^+}^*}{1 + C} \right\} \frac{M^+}{n_e}, \quad (\text{VI.28})$$

since  $1 - \frac{[O^+]}{n_e} = \frac{M^+}{n_e}$ . Thus, in general, the effective recombination coefficient depends on temperature (through  $\alpha_i^*$  and  $C$ , see above) and is proportional to the relative concentration of molecular ions. Note that the general expression (VI.28) is similar to the fairly general expression (VI.23) in

Ratcliffe's theory, where  $\alpha^*$  has been replaced by  $\left(\frac{\alpha^{*NO+}}{1+1/C} + \frac{\alpha^{*O_+}}{1+C}\right)$ , but it is significantly different from the widely used expression (VI.25).

The intensity of the ionizing solar radiation  $I$  at a given level in the atmosphere varies during the solar cycle (roughly by a factor of 3) and during the day (to an even greater extent). The variations in  $n$  are apparently also significant. Theoretically, we should therefore expect a decrease in  $\alpha'$  at intermediate altitudes and in the upper ionosphere around midday and in epochs of high solar activity owing to the increase in  $I$ . We mentioned in Section 21 that the daytime value of  $F$  in the  $\alpha'$  region is indeed less than the nocturnal value. The variation of  $\alpha'$  at altitudes  $h \geq 150$  km will somewhat slow down the growth of  $n_e$  caused by the increase in  $I$ . The theory thus predicts that  $\alpha'$  should vary during the day and during the solar cycle. We will now consider this topic quantitatively, proceeding from experimental data on the ion composition and the electron concentration (Chapter IV).

#### Variations of the effective recombination coefficient

A simple analytical expression for  $\alpha'$  at intermediate altitudes is difficult to select, and we therefore studied the dependence of  $\alpha'$  on the time of day and the solar activity level by actually computing  $\alpha'$  for a number of particular cases. There are two methods for the determination of the  $\alpha'(h)$  profile at altitudes between 100 and 200 km.

The first method uses the laboratory data on  $\alpha^*$  for  $O_2^+$  and  $NO^+$  and experimental rocket data on the ion composition of the ionosphere; employing (VI.19), one then obtains  $\alpha'$ . Because of the limited availability of rocket data, the computations in /508/ were only carried out for three points during the day, i.e., for  $z_0 \approx 55^\circ$ , for  $z_0 = 90^\circ$ , and for nocturnal conditions (Figure 96a). In these computations old laboratory data on  $\alpha^*$  were used and the difference in the temperatures of the electrons and the neutral particles was ignored. These shortcomings were rectified by Korsunova /741/. Figure 96b shows the new computation results in which  $\alpha^*$  has been taken from (V.52) and (V.53), and  $T_e$  increases linearly with altitude between 100 and 200 km from 450 to 1200°K for low solar activity and from 450 to 2000°K for high solar activity. These computations were only carried out for those cases when several mass-spectrometric measurements were available (see Table 23, Section 15). These results differ significantly from the previous data in that  $\alpha'$  is a factor of 2—5 higher at altitudes below 150 km in daytime and at all altitudes at night (mainly owing to the four-fold increase in  $\alpha^*(NO^+)$  for  $T_e < 500^\circ K$ ).

The second independent method /627/ uses the expression

$$\alpha' = q/n_e^2, \quad (VI.29)$$

which is valid for quasi-equilibrium conditions. The values of  $n_e$  were borrowed from the empirical rocket model of Section 15 (Chapter IV), and the values of  $q$  were taken from the computations of Section 25. Expression (VI.29) solved for  $\alpha'$  is as general as expression (VI.19), the only difference being that it is written for equilibrium conditions. Since at altitudes of 100—200 km in the ionosphere the time constant is  $\tau = (\alpha' n_e)^{-1} \approx 1-10$  min,

the equilibrium condition is always satisfied in daytime. Expression (VI.29) is thus successfully used in computations of  $\alpha'$  in the  $E$  and  $F_1$  regions of the ionosphere.

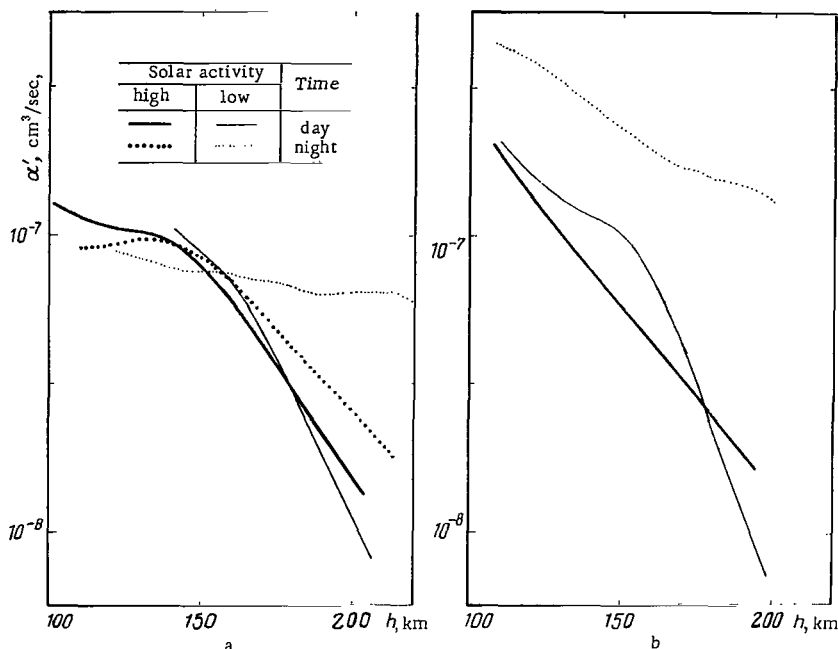


FIGURE 96. Computation of the effective recombination coefficient from (VI.19) according to /508/ (a) and from (V.52) and (V.53) (b) for high (thick lines) and low (thin lines) solar activities in daytime for  $z_0 \approx 55^\circ$  (solid lines) and at night (dashed lines).

The vertical distribution of  $q/n_e^2$  for low solar activity at  $z_0 = 55^\circ$  and  $z_0 = 80^\circ$  is presented in Figure 97 together with the  $\alpha'(h)$  profile (for  $z_0 \approx 55^\circ$ ) obtained by the first method.

In our analysis of the data in Figure 96 and 97 we shall first consider the vertical variation of  $\alpha'$ , i. e., the profile  $\alpha'(h)$ . The figures reveal the common features of these profiles: rapid growth between 200 and 150 km and a maximum or an inflexion at 130 — 150 km. Thus, two independent methods yield the same results.

The conclusion regarding the existence of a substantial gradient of  $\alpha'(h)$  between 150 and 200 km is important for quantitative interpretation of the differences between the profiles  $n_e(h)$  and  $q(h)$ . In particular, it enables us to resolve the following two contradictions: 1) we see from Figure 81 that for  $z_0 < 50^\circ$ ,  $q(200 \text{ km}) < q(150 \text{ km})$ , whereas the corresponding profiles  $n_e(h)$  (Figure 42 in Chapter IV) invariably reveal the reverse relation  $n_e(200 \text{ km}) > n_e(150 \text{ km})$ ; 2) for angles  $z_0 > 75^\circ$  the gradient  $d \ln q / dh$  is generally less than the gradient  $d \ln n_e / dh$  and is definitely less than the gradient  $d \ln (n_e)^2 / dh$ . The increase of the gradient  $d \ln (n_e)^2 / dh$  compared with the gradient  $d \ln q / dh$  at altitudes of 150 — 200 km, as well as the first effect, are naturally explained by the decrease of  $\alpha'$  with altitude, since  $n_e^2 = q / \alpha'$ .

A few comments about the reliability of the determination of  $\alpha'$ . In computations by the first method, the accuracy of  $\alpha'$  is limited by the

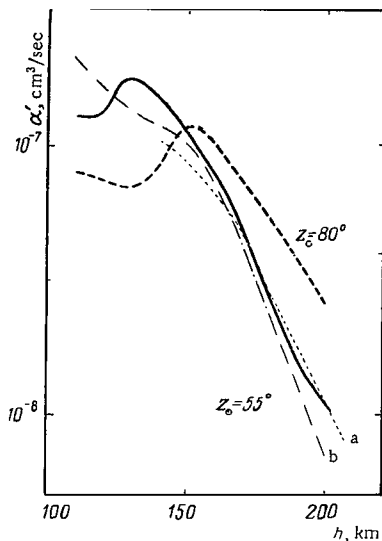


FIGURE 97. Computation of the effective recombination coefficient from (VI.29) for  $z_0 = 55^\circ$  and  $z_0 = 80^\circ$  for low solar activity.

The thin lines a and b were borrowed from Figure 96 a and 96 b for  $z_0 \approx 55^\circ$  for comparison.

accuracy of our data on  $\alpha'_i$ , which are currently measured in laboratory experiments probably to within a factor of about 2. In the second method,  $n_e$  is available with an error of up to 25%, but the values of  $q$  are uncertain to within a factor of 1.5, even for low solar activity conditions, when numerous spectrum measurements are on hand. The second method therefore also gives  $q/n_e^2 = \alpha'$  to within a factor of  $\sim 2$ . The curves of  $q/n_e^2$  and  $\alpha'$  for  $z_0 = 55^\circ$  in Figure 97 are close to each other; they diverge only at altitudes  $h < 150$  km, but then the divergence does not exceed a factor of 1.5–2.

Let us now consider the diurnal variations of  $\alpha'$  (Figure 96b). First note that  $\alpha'$  markedly increases at night. As we noted on p. 246, we probably have  $M^+/n_e \approx 1$  at altitudes 100–150 km, where the ions  $\text{NO}^+$  and  $\text{O}_2^+$  are dominant, and the variations in  $\alpha'$  are caused by the variations in  $\alpha^*$  which are associated with the changes in  $T_e$  and in the relative concentration of  $\text{NO}^+$  and  $\text{O}_2^+$ . The increase in  $\alpha'$  by approximately a factor of 2.5 at night at altitudes of 100–150 km is associated both with the decrease of  $T_e$  and with the increase of the fraction of the  $\text{NO}^+$  ions (in daytime, the 911–1038 Å radiation increases the fraction of

$\text{O}_2^+$ ). Unfortunately, no experimental data are available for verifying this conclusion, due to Korsunova /741/.

As we see from Figure 96,  $\alpha'$  at 200 km increases approximately ten-fold at night for low solar activity. These changes in  $\alpha'$  are mainly due to the changes in the fraction of the molecular ions  $M^+/n_e$ . (Danilov /651/ first came to the conclusion that  $\alpha'$  should markedly increase at night at altitudes above 200 km). As a result, the nocturnal gradient  $da'/dh$  between 100 and 200 km should decrease. A recent rocket experiment /652/ revealed a much more gradual variation of  $\alpha'(h)$  at altitudes of 115–190 km during sunset ( $z_0 \approx 90^\circ$ ) than at daytime.

Let us consider the daytime variation of  $\alpha'(h)$ . The changes in  $T_e$  and in ion composition for altitudes  $h \lesssim 150$  km reduce  $\alpha'$  as  $z_0$  increases from  $55^\circ$  to  $80^\circ$ ; above  $h \approx 150$  km a reverse situation is mainly observed. These variations are particularly pronounced for low solar activity.

Figure 97 shows that the curves for different  $z_0$  cross at  $h \approx 150$  km. This indicates that around 150 km the ionosphere is divided into two regions essentially opposed in character. In the lower region  $\alpha'$  varies in phase with  $q$  (during daytime), and in the upper region  $\alpha'$  varies in counter phase with  $q$ .

Hence it follows that the variations of the squared electron concentration  $n_e^2$  ( $=q/a'$ ) brought about by the variation of  $q$  will be enhanced in the upper region and suppressed in the lower region. For example, at  $h \approx 200$  km,  $q$  (see Figure 81, Section 25) changes by one order of magnitude during the day as  $z_0$  goes from  $60^\circ$  to  $90^\circ$ , whereas  $n_e^2$  (Figure 42, Section 15) varies by 1.5–2 orders of magnitude. This also explains the high value of  $v_E$  considered in Section 25.

The variation of  $\alpha'$  accounts both for the difference between  $\sqrt{q/a}$  and  $n_e$  (Figure 93) and for the difference between the parameters  $l$  and  $m/2$  from (IV.6) and (VI.10), respectively (Figure 94). The dependence of  $\alpha'$  on  $\text{Ch } z_0$  will be expressed by a power relation, not unlike that for  $q(z_0)$ ,

$$\alpha' = (\text{Ch } z_0)^k, \quad (\text{VI.30})$$

which is universally valid if a sufficiently narrow range of  $z_0$  values is chosen. In the upper region  $k > 0$  and in the lower region  $k < 0$ . Using the relations  $\alpha' n_e^2 = q$ ,  $n_e \propto (\text{Ch } z_0)^{-l}$ ,  $q \propto (\text{Ch } z_0)^{-m}$  and (VI.30), we find

$$k - 2l = -m, \text{ or } l = \frac{m}{2} + \frac{k}{2}, \quad (\text{VI.31})$$

where  $m$ ,  $l > 0$ . We find from (VI.31) that in the upper region, i. e., above  $h \sim 150$  km,  $l > m/2$ , whereas below  $\sim 150$  km,  $l < m/2$ . The difference between  $l$  and  $m/2$  should be slight. This is indeed the situation observed in Figure 94, which compares the experimental values of  $l$  for  $\log(\text{Ch } z_0) > 0.5$  with the computed values of  $m/2$ . The values of  $m$  given in Figure 94 were computed from the data of /560/ and show a poorer fit with the experiment. The daytime variations of the effective recombination coefficient  $\alpha'$  thus account for the slight systematic differences in the rates of change of  $n_e$  and  $q$  during the day for  $z_0 = 55^\circ - 90^\circ$ . This same factor accounts for the difference between  $\sqrt{q/a'}$  and  $n_e$  in Figure 93.

Thus, on the one hand, detailed computations of  $q$  and rocket data for  $n_e$  brought out definite variations of the effective recombination coefficient  $\alpha'$  at altitudes between 100 and 200 km, which had been previously unknown. On the other hand, detailed analysis of the behavior of  $\alpha'$  within the framework of the photochemical theory has shed light on the origin of these variations. Our analysis of the rate of ionospheric processes, as determined by the coefficient  $\alpha'$ , reveals a good fit between the rocket data for  $I_0$  used in the computations of  $q$ , the new ground observations of  $\alpha'$  in the ionosphere, and the recent laboratory measurements of  $\alpha^*$ .

### Theory of formation of the $F_1$ layer

We noted in Chapter IV that the  $F_1$  layer is observed only under certain conditions: mainly for low  $z_0$  (around noon and mostly in summer) and preferably low solar activity. The variation of  $n_e F_1$  during the day is proportional to  $(\cos z_0)^l$ , where  $l < 0.5$ , i. e., it does not correspond to the simple layer theory. In Section 25 we saw that this proportionality corresponds to the actual variation of  $\sqrt{q}$  or  $q$  during the day at the altitudes of the  $F_1$  region. No complete theory of  $F_1$  layer formation is available at this stage. The main emphasis is generally placed on the reasons for the formation of the  $F_1$  layer at low values of  $z_0$  only. Several explanations of

this effect were proposed. We will adopt the recent approach of Rishbeth /653/ and Shchepkin /654/, refining some of their arguments.

It is assumed that the conditions for the appearance of the  $F_1$  layer on ionograms — the formation of a certain "ledge" on the  $n_e(h)$  profile — arise only under a certain combination of circumstances in the transitional region between regions with quadratic and linear recombination. To identify these conditions, we will construct the  $n_e(h)$  profile of the transitional region, using the main elementary processes. All the  $O^+$  ions, which are produced at a rate of  $q(O^+)$  by the short-wave solar radiation and by reaction (V.74) from  $N_2^+$ , are converted into the molecular ions  $NO^+$  and  $O_2^+$ , i. e.,

$$q(O^+) = \beta [O^+], \quad (VI.32)$$

where  $\beta = \gamma_{NO^+}[N_2] + \gamma_{O_2^+}[O_2] = \bar{\gamma}[N_2]$ . The molecular ions  $NO^+$  and  $O_2^+$  produced by this process and also through primary ionization of molecules by solar radiation are destroyed by dissociative recombination, so that

$$q(O^+) + q(M^+) = q = \bar{\alpha} [M^+] n_e, \quad (VI.33)$$

where  $[M^+]$  is the concentration of the molecular ions,  $\bar{\alpha} = \alpha_{NO^+}^* \frac{[NO^+]}{[M^+]} + \alpha_{O_2^+}^* \frac{[O_2^+]}{[M^+]}$  (the recombination of  $N_2^+$  can be ignored because of its low concentration). Substituting  $(n_e - [O^+])$  for  $[M^+]$  in (VI.33) and taking  $[O^+]$  from (VI.32), we obtain a quadratic equation for  $n_e$  under quasi-stationary conditions:

$$n_e^2 - n_e \frac{q(O^+)}{\beta} - \frac{q}{\bar{\alpha}} = 0, \quad (VI.34)$$

which is equivalent to equation (V.89). At low altitudes, where the concentration of molecules is high and the second term of the equation is correspondingly small, a quadratic dependence is observed  $q = \bar{\alpha} n_e^2$ , whereas at high altitudes, where the last term of the equation is small, the process is linear  $q(O^+) = \beta n_e$ .

Let us find the altitude at which the second and the third term in (VI.34) are comparable. Using the numerical values

$$\bar{\alpha} \approx 10^{-7} \text{ cm}^3/\text{sec}, \quad \bar{\gamma} = \left\{ \gamma_{NO^+} + \gamma_{O_2^+} \frac{[O_2]}{[N_2]} \right\} \approx 4 \cdot 10^{-12} \text{ cm}^3/\text{sec}, \\ q(O^+)/q \approx 0.5 - 1,$$

we obtain the condition  $[N_2]/n_e \approx 2 \cdot 10^4$ . Since in daytime  $n_e \approx (3 - 10) \times 10^5 \text{ cm}^{-3}$ , this condition corresponds to altitudes  $h \lesssim 180 \text{ km}$ . For higher  $z_0$ , when  $q(O^+)/q$  and  $n_e$  are smaller, the transition from linear to quadratic dependence occurs at higher altitudes. Similar results can be obtained proceeding from the expression  $An/BI = 1/4$  in (V.90) (p. 197). They coincide with the previously considered mass-spectrometric data on the altitude at which  $A^+ = M^+$  or  $[O^+] = [O_2^+] + [NO^+]$  (see p. 245).

The solid curves in Figure 98, borrowed from /653/, give the profiles  $n_e(z)/n_e(0)$  from (VI.34), where  $n_e(0) = \sqrt{q_{\max}/\bar{\alpha}}$ ,  $z = (h - h^{\max})/H$ ,  $q = q_{\max} \exp(1 - z - e^{-z})$ ,  $h^{\max}$  is the altitude of the maximum  $q_{\max}$ . The dotted curve is the  $n_e(z)$  profile for the pure quadratic dependence ( $n_{e1} = \sqrt{q/\bar{\alpha}}$ ), and the dashed



curves correspond to the linear dependence ( $n_{e0} = q(0^+)/\beta$ ). The solution is plotted for several values of the parameter  $G_0$ , which is defined as the ratio

$$G_0 = \frac{n_1^2}{n_2^2} = \frac{\beta_0^2 q_{\max}}{q_0^2(0^+) \bar{\alpha}} \quad (\text{VI.35})$$

at the level  $h^{\max}$ , i. e., for  $z = 0$ .

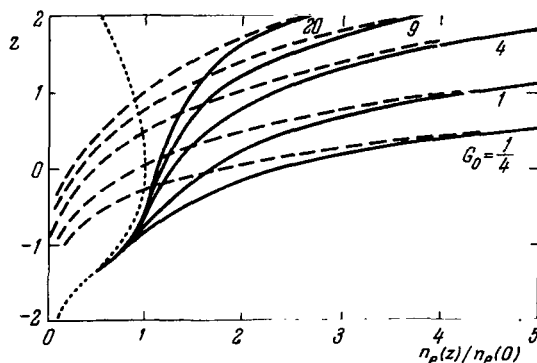


FIGURE 98. Vertical distribution of the electron concentration in the transitional region between quadratic and linear recombination coefficients for various values of the parameter  $G_0$ .

Dashed curves — computed from  $\frac{n_{e2}}{n_e(0)} = \frac{q}{\beta_0} e^{1.75z}$  for several

values of  $\beta_0$ ; dotted curve — computed from  $\frac{n_1}{n_e(0)} = \sqrt{\frac{q}{\bar{\alpha}}}$  for

$\bar{\alpha} = \text{const}$ ; solid curves — totals. The ledge on the  $n_e(z)$  profile is clearly seen for  $G_0 \geq 20$ .

The maximum  $n_e$  or a ledge on the  $n_e(h)$  profile corresponding to the formation of the  $F_1$  region is observed at altitudes near  $h^{\max}$  (or above  $h^{\max}$ , since  $\bar{\alpha} \neq \text{const}$  and diminishes with altitude). The higher the ratio  $G_0$ , the higher is the altitude of the transitional region above  $h^{\max}$ . The higher the altitude of the transition region above  $h^{\max}$ , the more pronounced is the ledge on the  $n_e(h)$  profile. We see from the figure that a ledge on the  $n_e(z)$  profile appears only for  $G_0 > 10$  and becomes prominent for  $G_0 \geq 20$ . Since the variation in  $z_0$  leads to a change in  $h^{\max}$ ,  $q_0$ , and  $n$ , we conclude according to Section 25 that the product  $N \text{Ch } z_0$  does not change in the layer maximum, and the above condition can be rewritten in the form

$$\frac{\tilde{\gamma}^2}{\bar{\alpha}} \frac{[N_2]^2}{N^2} \frac{[N \text{Ch } z_0]^2}{\text{Ch}^2 z_0} \frac{q_{\max}}{q_0^2(0^+)} \geq 20. \quad (\text{VI.36})$$

The  $q(h)$  profile in the upper part of the ionosphere was approximated with the profile from the simple layer theory according to (V.30):  $q/n = \sigma_i I_0 \times \exp\{-\text{Ch } z_0 N \sigma_{\text{ef}}\}$ . In the previous section we showed that in this case  $\sigma_{\text{ef}} \approx 10^{-17} \text{ cm}^2$ , which gives  $h^{\max} = 170 \text{ km}$  and  $q_{\max} = 3 \cdot 10^2 \text{ cm}^{-3} \text{ sec}^{-1}$ . Shchepkin /654/ showed that in this case, a necessary condition for the formation of the  $F_1$  layer (i. e., for the inequality  $dn_e/dh \leq 0$  to be observed)

is  $\bar{\gamma}^2/\bar{\alpha} \geq 1.4 \cdot 10^{-16} \text{ cm}^3/\text{sec}$ . In fact  $\bar{\gamma}^2/\bar{\alpha} = 1.6 \cdot 10^{-16} \text{ cm}^3/\text{sec}$ , i. e., the required conditions are satisfied, although quite marginally. These conditions are more than sufficient in practice, since according to the computations in Section 25  $q_{\max}$  is an order of magnitude higher than the figure used in our approximation, and  $h_{\max}$  is lower, lying around  $h \approx 140 \text{ km}$ .

Let us estimate the value of  $z_0$  for which the  $F_1$  layer may form. We will use (VI.36) for our quantitative computations. The upper-bound estimate of  $z_0$  is obtained from the simple layer approximation of the upper part of the  $q(h)$  profile. Taking  $N \text{ Ch } z_0 = 10^{17} \text{ cm}^{-2}$ ,  $[N_2]/N = 10^{-7}$  and  $q/q^*(O^+) \approx 1/30$ , we find by (VI.36)  $\text{Ch}^2 z_0 \lesssim 30$  or  $z_0 \lesssim 80^\circ$ . The lower-bound estimate for  $z_0$  is obtained by taking the true altitude  $h_{\max} \approx 140 \text{ km}$ . Using  $N \text{ Ch } z_0 = 3 \cdot 10^{17} \text{ cm}^{-2}$ ,  $[N_2]/N = 2 \cdot 10^{-7}$  and  $q/q^*(O^+) \approx 1/200$ , we find  $\text{Ch}^2 z_0 \lesssim 10$ , or  $z_0 \lesssim 70^\circ$ , i. e., almost the same result.

Thus, for low solar activity, the  $F_1$  layer appears only for  $z_0 \lesssim 70^\circ$ , i. e., around noon and in summer.

For high solar activity,  $[N_2]^2/N^2$  and  $N \text{ Ch } z_0$  hardly change, but the ratio  $q^*(O^+)/q_{\max}$  is a factor of 2 — 3 higher and therefore the range of allowed  $z_0$  radically shrinks to  $z_0 = 0$ . Such low values of  $z_0$  are clearly only attainable at noon in summer.

What is the physics of this mechanism leading to the formation of the  $F_1$  layer? We see from Figure 98 that for high  $G_0$  the region of linear recombination is shifted to high altitudes. This produces the "ledge" effect on the profile above  $q_{\max}$  at 180 — 200 km. If the contribution from the linear recombination were to decrease further, a maximum would form on the  $n_e(h)$  profile (the dotted curve in Figure 98). Therefore the main condition for the formation of the  $F_1$  layer is not that it is observed at altitudes where the transition from quadratic to linear recombination occurs but that the transitional region is located sufficiently high above the maximum of the total ionization rate. The altitude of this region has been estimated before.

This theory constitutes only a first approximation to the description of the conditions of formation of the  $F_1$  layer depending on  $z_0$  and the solar activity level. It does not account for all the various features of the behavior of the  $F_1$  region. Moreover, the theory uses certain simplifying assumptions, such as the simple layer approximation for  $q(h)$ , neglect of the dependence of  $\alpha^*$  and  $\gamma$  on  $T$  (which can be easily allowed for in (VI.36)), and neglect of ambipolar diffusion. The last process is quite significant, since it would enable us to terminate the unbounded growth of  $n_e$  with altitude in Figure 98 and bring the theoretical results in line with the experimental facts. We will come back to this problem in Section 28.

## 27. Ionization of the nocturnal ionosphere at altitudes of 60 — 200 km and the corpuscular hypothesis

The nocturnal ionosphere constitutes a special phenomenon in certain respects, and its properties are appropriately considered in a separate section. After sunset, when the source of short-wave radiation is "turned off," one would normally expect a gradual decrease of ionization in the ionosphere, since only recombination processes remain active. Knowledge of processes which determine the behavior of the daytime ionosphere enables us to compute without much difficulty the rate of decrease of  $n_e$  in the

absence of nocturnal ionization sources. Some observations, however, and particularly the results of rocket measurements, do not fit into this simple scheme. We are thus faced with the problem of identifying the mechanism or the source of nocturnal ionization in the ionosphere.

## Observation data

We will first list the principal features in the behavior of the nocturnal ionosphere that distinguish it from the daytime ionosphere and consider the vertical profile of ionization, its diurnal variation, geographical distribution, and ion composition.

**Vertical profile.** Figures 45 and 46 show the rocket profiles of  $n_e(h)$  for nocturnal conditions, which clearly reveal the following distinctive features.

1) All nighttime rocket launches (a total of more than 25) reveal the existence of the sporadic  $E_s$  layer, which constitutes a characteristic feature of the nocturnal ionosphere, although sometimes it is also observed in daytime. The vertical width of the  $E_s$  layer is often very small, not exceeding 1–3 km. Nighttime observations from the ground also generally register the existence of sporadic layers.

2) At 100–200 km, marked irregularities of the  $n_e(h)$  profile are generally observed. In daytime (and also at night at altitudes  $h > 200$  km), the  $n_e(h)$  profiles are known to be relatively smooth. The position and the number of the maxima on the  $n_e(h)$  profile differ for different experiments. Since the  $n_e$  maxima appear at different altitudes and have different intensities, it is difficult to speak of some nighttime average  $n_e$ , not to mention any regular variation of the electron concentration during the night. The maxima apparently form as a result of some disturbance, and the values of  $n_e$  between the maxima correspond to a relatively undisturbed ionosphere. The value of  $n_e$  between the maxima is  $1/3$ – $1/10$  of the maximum values, reaching  $(1-3) \cdot 10^3 \text{ cm}^{-3}$  and less. Similar values of  $n_e$  are sometimes obtained in ground observations.

3) Although the position of the maxima above 100 km has not been identified, a wide peak of increased electron concentration  $n_e \approx (3-30) \times 10^3 \text{ cm}^{-3}$  is systematically observed at 90–120 km, which is ascribed to the regular nocturnal  $E$  layer. Right above this peak, the value of  $n_e$  generally diminishes and, despite the possible presence of other maxima, it seldom exceeds the peak value. Observations with ground-based ionospheric stations with cutoff frequency  $< 0.5$  MHz also generally reveal a highly variable nocturnal  $E$  layer at middle latitudes. Marked variations in  $n_e$  are also observed below 100 km in the  $D$  region. Rocket data indicate that the base of the  $E$  region drops from 100–110 km in daytime to about 95 km at night /247/.

**Time-dependent variations.** In the absence of disturbances in the ionosphere below the  $F$  region, the nighttime electron concentration should be lower than in daytime. A particularly marked decrease of  $n_e$ , approximately by 1.5–2 orders of magnitude, is observed in the "dip" above the  $E$  layer. The low nocturnal values  $n_e = (1-3) \cdot 10^3 \text{ cm}^{-3}$  cannot be accounted for unless we assume a higher effective recombination coefficient  $\alpha' \approx (4-10) \times 10^{-8} \text{ cm}^3/\text{sec}$  /247, 590/.

In the  $E$  layer and at altitudes of 70–90 km in the  $D$  layer at middle latitudes, the nocturnal  $n_e$  decreases to a smaller extent, approximately by 1–1.5 orders of magnitude or even less. For the  $E$  layer this apparently suggests a low value of the effective recombination coefficient at night,  $\alpha'_E = 10^{-8} - 10^{-9}$  cm<sup>3</sup>/sec, which contradicts the photochemical theory of  $\alpha'$ . An essentially similar situation is observed in the  $D$  region. Introduction of a nocturnal source at the corresponding altitude, with an intensity 2–3 orders of magnitude lower than the daytime intensity, obviously eliminates this contradiction. If a sporadic nocturnal source is assumed, we can account for the variation of  $n_e$  during the night and from night to night; this effect is difficult to explain in the absence of any nocturnal ionization sources.

Significant irregular changes in  $n_e$  are observed during ionospheric disturbances. However, disturbances require a special treatment altogether.

**Geographical and spatial distribution.** The two main features in this category are the increase of  $n_e$  at auroral latitudes and spatial inhomogeneity. Both at night and in daytime, the electron concentration in the  $E$  and  $D$  regions in the auroral zone is higher than at middle latitudes. A particularly large difference (by an order of magnitude and more) is observed at altitudes below 80–85 km. This points to a significant increase in the concentration of negative ions or, alternatively, to a marked enhancement of the nocturnal ionization source.

We noted in Section 15 that at altitudes of 80–100 km, the  $n_e$  is higher at middle latitudes than in the polar ionosphere. Hence it follows that the cosmic rays are reinforced at middle latitudes by an additional ionization source.

The horizontal structure of the nocturnal ionosphere is also of considerable importance. Since the  $n_e$  values are irregular, one can try to determine the extent of the regions of enhanced electron density. Such information is available for the sporadic  $E_s$  ionization. Smith /565, 758/ discovered an  $E_s$  layer of fairly large horizontal extent, extending over more than 72 km. At the same time, ground observations indicate that the  $E_s$  layer has an inhomogeneous and patchy structure with elements measuring a few hundred meters across. No similar data are available for the nocturnal  $E$  and  $D$  layers.

**Ion composition.** Data relating to the ion composition are particularly important, since they characterize the inner physical properties of the ionosphere, and not its extrinsic morphology. Different features of the nocturnal ion composition are prominent at different altitudes.

The diurnal variations of the ion composition at  $h \approx 200$  km were discussed in Section 25. The most significant feature is that large quantities of the ions  $O^+$  and  $N_2^+$  are preserved at night, although these ions should disappear rapidly after sunset. We see from Figure 91 that the relative concentration  $O^+/n_e$  at night is no less than 1/2 of the daytime figure. These data correspond to auroral conditions and to epochs of high solar activity. During a solar activity minimum (the experiment dated 1 August 1963,  $z_\odot = 127^\circ$ ), the ratio  $O^+/n_e$  is much lower than in daytime (the dashed curve in Figure 91). We are thus inevitably led to the conclusion that in the former case there is a nocturnal ionization source at  $h \approx 200$  km. In Section 25, we used the concentration  $[N_2^+]$  to estimate that the intensity of the nocturnal ionization source is approximately 2 orders of magnitude less than the daytime intensity. Similar estimates are obtained from examination of  $O^+$ .

In the "dip" at  $h \approx 150$  km and in the  $E$  region the content of  $O^+$  and  $N_2^+$  is on the whole low, and the diurnal variation of the ratio  $[NO^+]/[O_2^+]$  is of no significance for these altitudes. In polar aurorae and during high solar activity, the ratio  $[NO^+]/[O_2^+]$  at night is seen to be higher than in epochs of low solar activity. We will see in what follows that the increase of the ratio  $[NO^+]/[O_2^+]$  also points to an existence of an ionization source in the first two cases.

The concentration of negative ions in the  $D$  region markedly increases at night, whereas the concentration of positive ions below about 75 km remains fairly constant during day and night, slightly increasing at night (Bragin /606/); some rocket data, however, lead to the opposite conclusion. Theoretical predictions of this effect will be considered at a later stage.

Thus observations of the nocturnal ionosphere at altitudes between 60 and 200 km point to the existence of a nocturnal ionization source which is approximately 2 orders of magnitude weaker than the daytime ionization source. Because of its dependence on geomagnetic latitude and magnetic activity, we are led to the conclusion that this is a corpuscular source.

#### The theory of the nocturnal ionosphere without a source

When the daytime ionization source is "turned off", the total concentration of ions and electrons begins to diminish gradually. We saw in Section 21 that for a constant effective recombination coefficient, the electron concentration  $n_e$  decreases hyperbolically  $n_e^{-1} = (n_e)_0^{-1} + \alpha' t$ . Since at 100–150 km,  $\alpha' \approx 10^{-7}$  cm<sup>3</sup>/sec,  $n_e$  will drop to 1/10 and 1/100 in 0.25 and 1.5 hrs, respectively, and during the night  $n_e$  should diminish by a factor of several hundreds. This simplified scheme, however, is applicable to a plasma consisting of a single ion species. And yet, at altitudes of 100–200 km, there are at least two species of recombining ions,  $NO^+$  and  $O_2^+$ , and below 100 km the picture is further complicated by the presence of negative ions. The effective recombination coefficient of the real ionosphere consisting of a mixture of ions was investigated by Bowhill /537/.

Denoting by  $n_r$  the concentration of the  $r$ -th species ions, we write the fundamental equations ( $q = 0$ ) in the form

$$\dot{n}_r = -\alpha_r n_r n_e, \quad (\text{VI.37})$$

$$\dot{n}_e = -n_e \sum_1^m \alpha_r n_r, \quad (\text{VI.38})$$

$$\alpha' = \sum \frac{n_r}{n_e} \alpha_r. \quad (\text{VI.39})$$

For the time rate of change of the relative concentration of the  $r$ -th species ions, we have

$$\frac{d \ln (n_r/n_e)}{dt} = (\alpha' - \alpha_r) n_e. \quad (\text{VI.40})$$

Hence it follows that the fraction of ions with low  $\alpha_r$  ( $< \alpha'$ ) will increase and the fraction of ions with large  $\alpha_r$  will conversely diminish. At the same

time, the arithmetic weighted average  $\alpha'$  will steadily decrease. For the  $E$  region and the overlying "dip", a finite solution can be obtained for the two ion species  $\text{NO}^+$  and  $\text{O}_2^+$  with  $\alpha_1 \approx 8 \cdot 10^{-8}$  and  $\alpha_2 \approx 1.6 \cdot 10^{-7} \text{ cm}^3/\text{sec}$ , respectively. Indeed, writing  $[\text{NO}^+] = n_1$  and  $[\text{O}_2^+] = n_2$  we have

$$\dot{n}_1 = -\alpha_1 n_1 n_e, \quad (\text{VI.41})$$

$$\dot{n}_2 = -\alpha_2 n_2 n_e. \quad (\text{VI.42})$$

Dividing the first equation through by the second and integrating, we find

$$n_2 = n_{02} \left( \frac{n_1}{n_{01}} \right)^{\alpha_2/\alpha_1} \text{ and } n_e = n_1 + n_{02} \left( \frac{n_1}{n_{01}} \right)^{\alpha_2/\alpha_1}, \quad (\text{VI.43})$$

where  $n_{01}, n_{02}$  are the initial concentrations. Equation (VI.41) thus reduces to an equation in one unknown

$$\dot{n}_1 = -\alpha_1 n_1 \left[ n_1 + n_{02} \left( \frac{n_1}{n_{01}} \right)^{\alpha_2/\alpha_1} \right]. \quad (\text{VI.44})$$

Taking  $\alpha_2 = 2\alpha_1$  and changing over to dimensionless variables  $x = n_1/n_{01}$  and  $\tau = \alpha_1 n_{01} t$ , we find

$$dx/d\tau = -x^2 - ax^3, \quad (\text{VI.45})$$

where  $a = (\alpha_1 n_{01})/(\alpha_2 n_{02})$ . The solution of this equation is

$$\frac{1}{x} - a \ln \frac{1+ax}{x} \Big|_0^\tau = \tau. \quad (\text{VI.46})$$

Initially, for  $z_\odot = 90^\circ$ ,  $x = 1$  and  $a = 1.24$ , which gives  $[\text{O}_2^+]/[\text{NO}^+] = 0.62$ . The change in the various parameters after 10 min, 1 hour, and 3 hrs is shown in Table 50.

TABLE 50. Variation of ion and electron concentration after sunset for  $q = 0$

$t$ , sec	$\tau$	$n_e$ , $\text{cm}^{-3}$	$[\text{NO}^+]/n_e$	$[\text{O}_2^+]/n_e$	$\alpha \cdot 10^4$ , $\text{cm}^3/\text{sec}$
0	0	$2.5 \cdot 10^4$	0.62	0.38	11
600	1.2	$6.2 \cdot 10^3$	0.83	0.17	9.4
3 600	7.2	$1.65 \cdot 10^3$	0.94	0.06	8.5
10 800	21.6	$5.8 \cdot 10^2$	0.93	0.02	8.2

Approximately an hour after sunset the concentration of the second ion  $\text{O}_2^+$  becomes negligible, and both  $[\text{NO}^+]$  and  $n_e$  decrease hyperbolically, in inverse proportion to time, with an effective recombination coefficient  $\alpha' \approx \alpha_{\text{NO}^+}$ . At the same time, the variation of  $[\text{O}_2^+]$  by (VI.43) is proportional to  $t^{-1}$ .

Since ions with a higher recombination coefficient vanish faster, the effective recombination coefficient should steadily diminish after sunset. This decrease is not large, however, since  $\alpha'$  cannot drop below  $\alpha_{\text{NO}^+}$ .

## Comparison with experiment

According to the data in Table 50, three hours after sunset we should have  $[\text{NO}^+]/[\text{O}_2^+] = 50$ . Only a single mass-spectrometric experiment (1 August 1963 /255/) at altitudes of 120–140 km detected a ratio close to 30–40 six hours after sunset (a similar result was recently obtained in an experiment carried out on 26 January 1966). Thus, in epochs of low solar activity, the nocturnal source is indeed weak. For high solar activity, however, the ratio is higher, thus pointing to the existence of a nocturnal ionization source.\*

At altitudes around 200 km, on the other hand, the effective recombination coefficient increases quite substantially for low elevations of the Sun above the horizon ( $z_0 = 90^\circ$ ) and at night (see Section 26). We will try to establish the reason for this behavior. At  $h \approx 200$  km, the above considerations are inapplicable, since besides molecular ions, there are also large quantities of  $\text{O}^+$  ions. Mass-spectrometric measurements indicate that the fraction of the  $\text{O}^+$  ions diminishes for  $z_0 = 90^\circ$  and at night. The fraction of molecular ions is correspondingly almost doubled during high solar activity and increases several-fold for low solar activity. By (VI.19) and (VI.28),  $\alpha'$  is directly proportional to the relative concentration of molecular ions. The reason for the increase in  $M^+/n_e$  was considered in Section 22; as we see from Table 42, the ratio  $M^+/n_e$  at these altitudes is inversely proportional to the intensity of the ionizing agent.

Let us now consider the *D* region. In Section 24 the coefficient of mutual neutralization of positive and negative ions  $\alpha_i$  was found to be higher than the coefficient  $\alpha^*$ . The growth of the relative concentration of negative ions expected after sunset may thus only increase the rate of neutralization. The time constant for the disappearance of free electrons  $\tau = (\alpha' n_e)^{-1}$  is equal to 200–500 sec in the undisturbed *D* region at altitudes of 90–100 km, i. e., without a nocturnal ionization source, the electron concentration should drop very rapidly. No such effect was observed. This evidently proves the existence of a nocturnal ionization source in the *D* region. Since  $q$  diminishes at night whereas  $\alpha'$  may only increase,  $n_i$  should apparently decrease in the *D* region at night.

## The corpuscular hypothesis of ionization of the nocturnal ionosphere

A number of hypotheses have been advanced to account for the source of ionization of the nocturnal ionosphere at various altitudes: meteor streams, scattered radiation in  $L_\alpha$  and  $L_\beta$  lines, ionization transfer by horizontal or vertical motions, and corpuscular streams. Some authors ignore the possibility of an additional ionization source, treating the nocturnal ionosphere as a remnant of daytime ionization (Ratcliffe and Weeks /234/, Krasovskii et al. /655/). We have repeatedly mentioned above that experiments seem to point to the existence of a nocturnal source of ionization, and the main emphasis will therefore be placed on the corpuscular hypothesis, it being the most promising in our opinion. We will consider separately the

\* The above analysis is essentially based on the assumption that  $\alpha_{\text{O}_2^+} \approx 2\alpha_{\text{NO}^+}$ . According to the new data which are reflected in (V.52) and (V.53),  $\alpha_{\text{O}_2^+} < \alpha_{\text{NO}^+}$ ; therefore the conclusion regarding the existence of a nocturnal ionization source in the *E* region is valid for low solar activity also.

ionization of the  $E$  and  $D$  regions and the formation of the  $E_s$  layer and irregular layers at 100—200 km.

**The  $E$  region.** The conflict between the expected and the observed value of  $n_e$  at night is quite evident for the  $E$  region. For  $\alpha' = (0.4 - 1) \cdot 10^{-7} \text{ cm}^3/\text{sec}$ , the electron concentration should drop by two orders of magnitude in 5—10 hours during the night, rendering the nocturnal ionosphere inaccessible to observations. However,  $n_e$  in the  $E$  region does not diminish by more than a factor of 10—30 (certainly not in epochs of high solar activity).

Assuming that the ionization is caused by corpuscular streams, Antonov and one of the authors /504/ used the minimum values of  $n_e$  for 90—120 km (from rocket observations) to compute the intensity and the spectrum of the minimum nocturnal flux of 3—30 keV electrons. The differential spectrum can be described by a power function with  $\gamma = 4.5$  or by an exponential function with  $E_0 = 1.5 \text{ keV}$  /420/, and the energy flux  $w$  for  $E \geq 2 \text{ keV}$  is  $\sim 10^{-3} \text{ erg/cm}^2 \text{ sec}$ . These conclusions fit the electron flux observations (Section 18). The computations ignored the "dip" overlying the  $E$  region on the nocturnal  $n_e(h)$  profile /245/; this "dip" points to a weaker electron flux at low energies  $E < 2 \text{ keV}$ . Indeed, no electrons with  $E = 200 - 1000 \text{ eV}$  were detected in rocket experiments /417, 421/. A quantitative treatment of the ionization of the nocturnal ionosphere at altitudes of 90—120 km by corpuscular streams thus yields electron flux and energy estimates which are consistent with the results of direct measurements and indirect estimates. The conclusions of /504/ for  $E < 1 \text{ keV}$  are erroneous, however /245/.

Some morphological features of the behavior of the nocturnal ionosphere, and in particular its dependence on latitude, high variability, and relation to geomagnetic activity, also point to the participation of corpuscular streams in the ionization of the nocturnal ionosphere. The first suggestion concerning the existence of corpuscular streams and their effect on the ionospheric  $F$  and  $E$  regions at high latitudes were made in 1938—1940 by Kazantsev /656/, Appleton and Naismith /657/, and Vegard /473, 474/. In 1940, Kryuchkov /658/ suggested that corpuscular streams were possibly affecting the ionization of the atmosphere at middle latitudes during disturbances. Papaleksi /659/ made an attempt to observe corpuscular effects during the solar eclipse of 9 July 1945.

A number of other geophysical effects (polar aurorae, and especially diffuse aurorae /660/, night glow /661, 662/ showing characteristic discrete glow regions, heating of the upper atmosphere /663—665/, etc.) are also correlated with geomagnetic data and have been ascribed to the action of solar corpuscular streams. A comprehensive review of solar corpuscular streams was published by Mustel' /666/. However, the mechanism of penetration of sufficiently powerful corpuscular radiation from the Sun deep into the Earth's atmosphere (to ionospheric altitudes) has remained unclear /667/. Therefore the interpretation of the upper atmospheric processes based on the corpuscular radiation hypothesis is still fragmentary and unconvincing.

Nevertheless, as indicated in Section 18, rockets and satellites have helped to establish the permanent existence of electron streams at ionospheric altitudes, which are capable of producing ionization. In /504, 245/, the hypothesis of corpuscular ionization of the nighttime ionosphere is linked up with these electron streams.



**The *D* region.** The effects of corpuscular ionization in the *D* region are observable in daytime, as well as at night. The first corpuscular effects in the *D* region were discovered during disturbances. Krasovskii /668/ in 1957 and Zevakina /669/ in 1959 linked up the anomalies in the *E* and *D* regions of the ionosphere during geomagnetic "bays" with the penetration of solar corpuscular streams into the lower ionosphere, whereas Gregory /670/ attributed these anomalies to enhancement of the soft X-ray fluxes. In 1961 Nestorov /671/ indicated that the effect of solar corpuscular streams in the *D* region is comparable in the morning with the effect of the short-wave solar radiation. Later Cumme, Knuth, and Wagner /672/ showed that for low solar activity the variation of  $n_e$  at 60 — 70 km is determined by the penetration of corpuscular streams of nonsolar origin, and not by solar radiation.

Corpuscular effects are currently associated with sporadic streams of injected electrons with  $E \geq 30$  keV which are capable of penetrating into the *D* region. These electron streams at altitudes of 70 — 100 km were investigated on Van Allen's rockets at auroral latitudes and by Antonova et al. at middle latitudes (see Section 18). The X-ray bremsstrahlung produced by these particles was picked up with balloons. The later studies of Krasovskii et al. on Sputnik III, Kosmos 3, and Kosmos 5 and of O'Brien on Injun 1 and Injun 3 provided detailed data on the diurnal, latitudinal, geomagnetic and other variations of the injected electrons with  $E \geq 40$  keV: at geomagnetic latitudes of 40 — 45° the flux is 2 — 3 orders of magnitude lower than at auroral latitudes, and at night it is 2 — 3 orders of magnitude lower than in daytime; the flux is highly variable and is seen to be sensitive to geomagnetic activity. These data on electron fluxes greatly simplify the verification of the corpuscular ionization hypothesis for the *D* region. Estimates show that the injected electron fluxes with  $E \geq 30$  keV should leave a significant imprint on the state of ionization of the *D* region. A number of additional observational facts, independent of the ionization theory, also point to corpuscular effects in the *D* region:

- 1) Both rocket and ground measurements of the electron concentration  $n_e$  indicate that the *D* region is characterized at all latitudes by incessant irregular variations in  $n_e$ , which are superimposed on the regular diurnal, seasonal, and latitudinal variations. The ionization of the *D* region is thus produced by sporadic, as well as regular, agents.

- 2) The enhancement of  $n_e$  during geomagnetic disturbances and in the direction of the auroral latitudes, and also in the region of the South-Atlantic anomaly reveals the significant role of corpuscular radiation in the ionization of the *D* region. At auroral latitudes and during significant ionospheric disturbances involving strong radio wave absorption, the electron concentration increases at all latitudes, growing almost by one order of magnitude below ~90 km.

- 3) An additional effect of *D*-region ionization at middle latitudes by sporadic corpuscular streams should be noticeable even under comparatively quiet conditions, especially at night and for large zenith angles of the Sun, mainly at 70 — 90 km /62/. The computations of Section 24 show that at these altitudes the ionization by cosmic rays and solar X rays is definitely insufficient. Moreover, marked irregularities and changes in  $n_e$  are observed. The ionization of the *D* region for various electron energies made it possible to find an upper bound estimate for the electron fluxes.

For example, for energies of  $3 \cdot 10^4$  keV,  $10^5$  keV, and  $3 \cdot 10^5$  keV, the flux does not exceed  $10^3 \text{ cm}^{-2} \text{ sec}^{-1}$ ,  $10^2 \text{ cm}^{-2} \text{ sec}^{-1}$ , and  $10 \text{ cm}^{-2} \text{ sec}^{-1}$  /62/. As we have noted before, this is close to the results of direct rocket and satellite measurements (see Section 18). Proceeding from diurnal variation of the electron concentration in the *D* region (Section 15), we find that the nighttime flux of these electrons should be approximately 2 orders of magnitude lower /62, 245/, whereas during sudden ionospheric disturbances and in the auroral zone it should be approximately 2 orders of magnitude higher. This is consistent with satellite measurements of electron fluxes with  $E > 40$  keV, mentioned above.

Korsunova et al. /246/ showed that a corpuscular effect dependent on geomagnetic activity is also apparent in daytime at altitudes of 100 and 110 km (as well as in the *D* region), i. e., in the lower part of the *E* region, where it accounts for a significant fraction of the overall ionization effect. Even for low geomagnetic activity ( $K_p = 2 - 3$ ) the flux of electrons with  $E > 20$  keV is estimated at around  $0.04 \text{ erg/cm}^2 \text{ sec}$ . This estimate fits the electron spectrum shown in Figure 64.

Note that a number of peculiar features in the behavior of the daytime *E* region, and in particular the presence of an annual effect dependent on geomagnetic activity, were attributed by Shimazaki /673, 674/ and Noci /675/ to corpuscular streams, but no quantitative estimates were given. A more detailed treatment of this topic could yield valuable results for the theory of the *E* region.

**Irregular layers in the 100 — 200 km region.** In the preceding subsection we described irregular layers, or  $n_s$  maxima, which are observed at night at 100 — 200 km. An additional ionization source is clearly required in order to sustain ionization in individual thin layers. A few general comments can be made regarding the properties of this source and its estimated intensity. In order to account for the observed electron densities in the layers, we have to assume local ionization sources with intensities of up to 10 ion pairs per  $\text{cm}^3 \text{ sec}$ , i. e., merely 2 — 2.5 orders of magnitude weaker than the daytime ionization source at the same altitudes. However, the nocturnal source is confined to individual layers, so that its total output in an atmospheric column of  $1 \text{ cm}^2$  cross section should be approximately reduced in the same ratio as the total thickness of the nocturnal layers to the overall thickness of the daytime ionosphere, i. e., by a further 0.5 — 1 order of magnitude.

Recalling that in periods of high solar activity the intensity of the short-wave solar radiation from ionospheric estimates is  $3 - 10 \text{ erg/cm}^2 \text{ sec}$  /544, 676/, we find that the nocturnal ionization source has intensities of about  $3 \cdot 10^{-2} - 3 \cdot 10^{-3} \text{ erg/cm}^2 \text{ sec}$ , as from the data for the *E* region (p. 259). A similar estimate ( $\sim 2 \cdot 10^{-2} \text{ erg/cm}^2 \text{ sec}$ ) was derived independently in the preceding section using the nighttime concentration of  $N_2^+$  ions around 200 km altitude. Giorgio /452/ and Sharp /429/ from satellite measurements and Kazachevskaya /734/ from rocket measurements at night in middle latitudes estimated the flux of electrons with  $E \geq 1 - 3$  keV, which was found to be  $\sim 10^{-2} - 10^{-3} \text{ erg/cm}^2 \text{ sec}$ .

## The mechanism of formation of the *E*<sub>1</sub> layer

No generally accepted theory is available for the formation of the sporadic *E*<sub>1</sub> layer, but there are indication that different types of *E*<sub>1</sub> layers are produced

by different sources. The main theories of formation of the  $E_s$  layer use meteor streams, inhomogeneities produced by winds and motion in magnetic fields, and corpuscular streams /677/.

One of the serious arguments in favor of the meteor hypothesis was the mass-spectrometric discovery, by Istomin /262, 263/, of a thin layer of nonatmospheric ions  $Mg^+$ ,  $Ca^+$ ,  $Fe^+$ , and  $Si^+$ . Rocket observations /565/ revealed the relatively small horizontal extent of the sporadic  $E_s$  layer (about 50 — 100 km), and this presents certain difficulties for the meteor hypothesis of the formation of the  $E_s$  layer. The meteor hypothesis is apparently incapable of accounting for the formation of layers lying much higher than 100 km, either. On the other hand, an excess of metal ions, having low efficiencies for neutralization and charge exchange, in the presence of generally low concentrations of atmospheric ions, may point to a recently active high-intensity ionization source.

Following the actuation of a high-intensity ionization source, atomic ions  $A^+$  of metals and other impurities are formed from the atmospheric molecular ions  $M^+$  with very high efficiency according to the reaction  $M^+ + A \rightarrow A^+ + M$  (Swider /748, 749/). The atomic ions are at the same time destroyed by the reactions  $A^+ + O \rightarrow AO^+ + h\nu$  and  $A^+ + O_2 \rightarrow AO_2^+ + h\nu$ , whose rates are much slower than the rate of dissociative recombination of the atmospheric molecular ions. An excess of metal ions is thus formed, while the concentration of the atmospheric ions diminishes; this was indeed observed with mass spectrometers in sporadic  $E_s$  layers (see Section 15).

The most popular theory currently associates the formation of the  $E_s$  layer with redistribution of electron density at those altitudes in the atmosphere where wind shear occurs in a magnetic field (i. e., the direction of the horizontal wind is being gradually reversed). An additional ionization source, however, is still required in this case /679, 680/.

Let us consider the sporadic layers detected by rockets. Sporadic layers at altitudes of 95 — 115 km were observed in more than 30 rocket experiments /681/. Two types of sporadic layers are observed: wide layers, up to 5 — 8 km thick, and thin layers, up to 1 — 3 km thick. As a rule, the electron density in wide layers is a mere 10 — 20% higher than at adjoining altitudes, whereas in thin layers it is up to one order of magnitude higher. The thin layers are more difficult to account for, since their formation requires an ionization source highly localized in the vertical direction /682/.

The increase in the frequency of occurrence of  $E_s$  at higher geomagnetic latitudes and its relation to geomagnetic activity indicate that the sporadic  $E_s$  ionization may be produced by a stream of charged particles in the ionosphere. Comparatively wide layers may form due to the effect of 10 — 30 keV injected electrons. Because of the high scattering of these electrons at the  $E_s$  layer altitudes, the orienting effect of the geomagnetic field is not pronounced. More detailed calculation /499/ indicate that even monoenergetic electrons at altitudes of 100 — 110 km form fairly wide layers,  $\Delta h \approx 2H = 10 — 20$  km. Therefore, to account for type I sporadic layers, we require monoenergetic electrons or electrons with a very steep spectrum. This mechanism does not account for the formation of very thin sporadic  $E_s$  layers with high electron density maxima.

The mechanism of formation of thin  $E_s$  layers by high-energy electrons (about  $10^5$  eV) trapped in the geomagnetic field was considered in /681/. According to this concept, a sufficiently thin layer of ionization may form near the reflection point by a charged particle tracing a helical trajectory

in the geomagnetic field, since the helix turns progressively condense as the particle approaches the reflection point.

Let us estimate the ionization rate profile  $q(h)$  formed by a continuous stream of hard electrons with a reflection point at 100 — 110 km. The concentration of the product ions at a height  $\Delta h$  above the reflection point is determined by the concentration of the incident electrons, which is inversely proportional along the magnetic tube of force to the particle velocity  $v_{\parallel}$ . For a particle trapped in a magnetic field,

$$v_{\parallel} = v \sqrt{1 - \frac{H}{H_0}}, \quad (\text{VI.47})$$

where  $v$  is the total electron velocity,  $H$  and  $H_0$  are the magnetic fields at the test point and at the reflection point. Near the reflection point  $(H_0 - H) \propto \Delta h$ . Therefore, as the particle approaches the reflection point, the ionization rate  $q$  increases as

$$q(\Delta h) \propto (\Delta h)^{-1/2}, \quad (\text{VI.48})$$

if we assume constant atmospheric density over the height  $\Delta h$ . Thus, as  $\Delta h$  diminishes from 1 km to 10 m,  $q$  increases ten-fold. By assuming a stream of electrons with close reflection points, we can thus account for the formation of narrow ionization layers with  $\Delta h < 1$  km. The electrons should be of sufficiently high energies to avoid scattering. The choice of the high electron energy,  $E \geq 30 - 100$  keV, is determined by the condition that the atmospheric mass traversed by the electron to the reflection point should be significantly less than its range. An alternative condition is that the electron should experience only few collisions along the last turn of its trajectory, since each collision somewhat alters the direction of motion even for the fast electrons and the reflection point shifts.

The electron flux needed to account for the formation of  $n_e$  up to  $10^5 \text{ cm}^{-3}$  in the sporadic layer is readily estimated. The formation of a sporadic layer at 100 km altitude requires electrons with  $E = 100$  keV in a flux of  $10^9 - 10^{10}$  electrons/cm<sup>2</sup>sec, whereas the formation of a layer at 110 km requires approximately the same flux of electrons with  $E \approx 30$  keV /681/. The electron energy flux is thus  $10^2 - 10^3$  erg/cm<sup>2</sup>sec. According to modern concepts, local sporadic streams of trapped electrons in the upper atmosphere may briefly reach high intensities. Electron streams with  $E \geq 40$  keV of similar intensity were observed from satellites /436 — 439/.

IGY and IQSY observations indicate that the sporadic  $E_s$  layer forms simultaneously at magnetically conjugate points /633, 684/. This is further evidence in favor of the proposed mechanism.

Since each electron loses 0.1 — 0.01% of its energy on crossing the equator, the total electron energy should be sufficient for  $10^3 - 10^4$  such crossings. This fits the observed lifetime of sporadic layers, which is  $10^2 - 10^3$  sec.

The assumption of trapped electrons with close pitch-angles at altitudes of 100 — 1000 km thus permits overcoming one of the fundamental difficulties associated with the existence of sporadic layers detected in rocket measurements — their small thickness and high electron density gradient. The proposed mechanism is also consistent with the concept of a patchy or cloudy structure of the  $E_s$  layer.

## 28. Formation of the $F_2$ region

### Vertical distribution of ions in the upper ionosphere

Diffusion and photochemical processes make comparable contributions in the  $F$  layer maximum, but in the upper part of the ionosphere the vertical distribution of ions is only determined by diffusion processes. We recall that for neutral particles diffusion processes predominate starting with significantly lower altitudes,  $h \approx 110$  km. The vertical distribution of ions is markedly different from that of neutrals: the concentration of various neutrals monotonically decreases with altitude, whereas the distribution of the ion concentrations shows maxima. We will consider this topic in more detail. For simplicity we first take an isothermal atmosphere with 2–3 components and ignore the spherical figure of the Earth and the variation of gravitational acceleration with altitude. Introduction of these effects does not lead to fundamental changes in the results.

For neutral particles the barometric distribution of pressure  $p_j$  with altitude  $h$ ,

$$\frac{dp_j}{p_j} = -\frac{m_j g}{kT} = -\frac{dh}{H_j}, \quad (\text{VI.49})$$

follows, as we saw in Section 17, from the ideal gas equation  $p_j = n_j kT$  and the equation of hydrostatic equilibrium

$$dp_j = -m_j n_j g dh. \quad (\text{VI.50})$$

For an isothermal atmosphere  $H = \text{const}$  and  $dp_j = kT dn_j$ , and we therefore obtain a barometric distribution with altitude for concentrations as well as pressures:

$$dn_j/n_j = -dh/H_j. \quad (\text{VI.51})$$

The exponential distribution of the concentration  $n_j$  is valid for each atmospheric component separately, irrespective of the distribution of the other components. For ions the situation is more complex.

For charged particles the equations of hydrostatic equilibrium are more complex

$$\frac{dn_i^+}{dh} = -\frac{n_i^+}{kT_i} (m_i g - eE), \quad (\text{VI.52})$$

$$\frac{dn_e}{dh} = -\frac{n_e}{kT_e} (m_e g + eE). \quad (\text{VI.53})$$

The electric field  $E$  is introduced in these equations, as it allows for the interaction between ions and electrons. The electric field is set up by a certain charge distribution. Since the ionosphere as a whole is electrically neutral  $\sum n_i^+ = n_e$ , we obtain the following relation for the electric field by equating expression (VI.53) for electrons to the sum of expressions of the form (VI.52) for ions:

$$eE = g \left[ m_+ - \frac{T_i m_e}{T_e} \right] \left( 1 + \frac{T_i}{T_e} \right)^{-1}; \quad (\text{VI.54})$$

here  $m_+ = \sum m_j n_j^+ / n_e$  is the mean ion mass. The electron mass is approximately  $10^{-4}$  of the ion mass, so that  $m_e T_i / T_e \ll m_+$ . Substituting (VI.54) into (VI.52) for the ionosphere in thermal equilibrium ( $T_i = T_e$ ), we obtain

$$\frac{dn_j^+}{dh} = n_j^+ \frac{g(m_+ - 2m_j)}{2kT_i} = -\frac{n_j^+}{H_j} \left( 1 - \frac{m_+}{2m_j} \right). \quad (\text{VI.55})$$

Equation (VI.55) shows that the distribution of the  $j$ -th ion depends through  $m_+$  on the distribution of the other ions. The situation is thus radically different from that observed in a neutral atmosphere.

This effect is observed even in the simplest case of a single-component ionosphere, when  $n^+ = n_e$  and the vertical distribution of ions

$$\frac{dn^+}{dh} = -\frac{n^+}{2H_i} = -\frac{n^+}{H^*} \quad (\text{VI.56})$$

is purely exponential. The scale height  $H^*$ , however, is equal to double the scale height for ions (more precisely  $1/H^* = 1/2H_i + 1/2H_e$ ). This is a manifestation of the effect of electrostatic coupling of ions with electrons: the barometric distribution does not apply to ions and electrons separately, each with its own scale height, but to a coupled "ion — electron" aggregate particle whose molecular weight is approximately half the molecular weight of ions.

To allow for the changes in the gravitational acceleration  $g$  with altitude, which is quite significant for high altitudes,  $h$  is generally replaced by the geopotential height  $z$ , which is defined by the relations

$$dz/dh = g/g_0 \quad \text{or} \quad z = Rh/(R + h), \quad (\text{VI.57})$$

where  $R$  is the Earth's radius. In this case  $z$  is replaced by  $h$  in the barometric distribution. To obtain the distribution of concentrations as a function of altitude, make the substitution  $h = Rz/(R - z)$ . Similarly, in order to allow for temperature variation with altitude, we use the reduced altitude

$$h' = \int_{h_0}^h \frac{T_0 dh}{T(h)}, \quad (\text{VI.58})$$

for which the barometric distribution derived for the isothermal atmosphere is valid.

Figure 99 shows the computation results of Angerami and Thomas /685/ for  $T = 1500^\circ\text{K}$  for the ions  $\text{O}^+$ ,  $\text{He}^+$ , and  $\text{H}^+$  and for their mixture, equal to the electron concentration. The vertical distribution of the ion concentrations in the upper ionosphere shows maxima. The maximum of  $[\text{He}^+]$  is observed at  $h \approx 1000$  km, the maximum of  $[\text{H}^+]$  is observed at  $h \approx 4000$  km. At altitudes  $h \leq 500$  km, where the ions  $\text{O}^+$  predominate, and at  $h \geq 7000$  km, where  $\text{H}^+$  predominate, the distribution  $n_e(h)$  is purely exponential, with a fixed scale height  $2H_j$ . For lower temperatures, the concentration maxima of  $\text{He}^+$  and  $\text{H}^+$  and the region of exponential distribution of  $n_e$  will evidently

shift down. The effect of the vertical variation of temperature and the difference between  $T_e$  and  $T_i$  have also been allowed for at this stage /686, 687/.

## The $F_2$ region (statement of the problem)

The structure of the ionosphere in the  $F_2$  region is more difficult to explain since this is a transition region between "purely photochemical" and "purely diffusional" parts of the ionosphere. The gradual transition from one type of processes to another and their combined effects greatly complicate the theory. No complete theory of the  $F_2$  region has been developed. In this section we will only consider some of the theoretical results pertaining to the mechanism of formation of the  $F_2$  region.

The application of the photochemical theory to the  $F_2$  region leads to outright clash with observations. Indeed, consider the vertical distribution of  $n_e$ . According to Section 25, at high altitudes

$$n_e \approx [O^+] = \frac{[O] i_1 + [N_2] i_2}{([N_2] \gamma_{NO^+} + [O_2] \gamma_{O_2^+})} \quad (\text{VI.59})$$

Above  $h \approx 200$  km, the rate constants  $\gamma_{NO^+}$  and  $\gamma_{O_2^+}$  and the ionization coefficients  $i_1$  and  $i_2$  hardly change with altitude (since the solar radiation is not absorbed). The leading term in the numerator in (VI.59) is proportional to the concentration of atomic oxygen, and the denominator contains the concentration of molecules which diminishes with altitude almost as the square of  $[O]$ . Therefore  $n_e$  should increase without bound as the altitude increases. The unbounded growth of  $n_e$  above the  $F_1$  region was commented upon in Section 26. And yet, above  $h^m F_2$ , a

FIGURE 99. Vertical distribution of the concentrations of  $O^+$ ,  $He^+$ ,  $H^+$  and  $n_e$  (solid curve) /685/.

Left, scale of geopotential heights  $z$  along a magnetic line of force; right, scale of geometrical heights  $h$ . Computations carried out for isothermal conditions ( $T = 1500^\circ K$ ) and  $[O^+] = 10^5 \text{ cm}^{-3}$ ,  $[He^+] = 6.3 \cdot 10^2 \text{ cm}^{-3}$  and  $[H^+] = 16 \text{ cm}^{-3}$  at  $h_0 = 500$  km. Dots mark the levels of equal concentrations:  $[O^+] = [He^+]$  (1),  $[O^+] = [H^+]$  (2), and  $[He^+] = [H^+]$  (3).

decrease of  $n_e$  is actually observed. This paradox was first noted by Yonezawa /688/, who also indicated that it may be due to the neglect of ambipolar diffusion in the original treatment. The diffusion mechanism restores the barometric distribution of the electron concentration above  $h^m F_2$ . The profiles  $n_e(h)$  in the  $F$  region were computed analytically with full allowance for diffusion using idealized atmospheric models by Yonezawa /688—690/, Dungey /691/, Martin /692/, Ratcliffe et al. /528/, Gliddon and Kendall /693—695/, Ferraro /696, 697/, Bowhill /698/, Nisbet /699/, Shmelovskii /700/, and others; numerical computations for real atmospheric models were carried out by Rishbeth et al. /701—703/ and Polyakov /704—706, 754/.

**Equation for the stationary  $F_2$  layer.** To elucidate in greater detail the main features of the  $F_2$  region, we will consider the solution for the simplified case of an isothermal atmosphere consisting of atomic and molecular oxygen. The ionization of the atmosphere is mainly determined by the ionization of the more common component — atomic oxygen — and we therefore take

$$q = q_0 e^{-\frac{h-h_0}{H}}, \quad (\text{VI.60})$$

where  $H$  is the scale height for atomic oxygen ( $n = n_0 e^{-\frac{h-h_0}{H}}$ ). The linear recombination coefficient is proportional to the concentration of molecules, and therefore

$$\beta = \beta_0 e^{-\frac{2(h-h_0)}{H}}. \quad (\text{VI.61})$$

The coefficient of ambipolar diffusion\* is inversely proportional to particle concentration, and therefore

$$D = D_0 e^{\frac{(h-h_0)}{H}}. \quad (\text{VI.62})$$

We recall that at high altitudes under equilibrium conditions the electron concentration follows the barometric distribution

$$n_e = [O^+] \propto e^{-\frac{h-h_0}{2H}}. \quad (\text{VI.63})$$

Let  $h - h_0 = z$ . We choose  $h_0$  in the  $h^m F_2$  region; it will be defined more precisely in the following. The equation of continuity for electrons has the form

$$\frac{dn_e}{dz} = q - \beta n_e - \frac{d}{dz} G. \quad (\text{VI.64})$$

We assume that the electron flow  $G$  is entirely determined by ambipolar diffusion (i. e., the motion of the plasma produced by electromagnetic forces and the motion of the neutral atmosphere are ignored); then

$$G = -D \left( n'_e + \frac{n_e}{2H} \right). \quad (\text{VI.65})$$

The prime denotes differentiation with respect to  $z$ . It follows from this definition that a positive value of  $G$  corresponds to upward flow.

Using the above relations, we obtain from (VI.64) the following equation for  $n_e$  in the stationary case ( $dn_e/dt = 0$ )

$$n_e'' + \frac{3}{2H} n_e' + \frac{1}{2H^2} n_e + \frac{q_0}{D_0} e^{-\frac{2z}{H}} - \frac{\beta_0}{D_0} n_e e^{-\frac{3z}{H}} = 0. \quad (\text{VI.66})$$

The lower boundary condition for the solution of this differential equation has the form  $n_e = q/\beta$  or, in more usual notation,  $n_e \xrightarrow{z \rightarrow \infty} 0$ . The upper boundary condition is that the flow  $G_\infty$  should be finite at infinity. Without sources and sinks of charged particles, we obtain the condition  $G_\infty \xrightarrow{z \rightarrow \infty} 0$ . It is

\* In what follows the coefficient of ambipolar diffusion  $D_a$  is simply designated  $D$ .



equivalent to the assumption that at high altitudes  $n_e \propto e^{-z/2H}$ , i. e., the electron concentration follows a barometric distribution. For  $G_\infty \neq 0$ , this distribution is modified in accordance with (VI.65). For  $G_\infty < 0$ , the  $F$  region of the ionosphere will be maintained in an ionized state even without sources (at night), owing to the influx of ions from other altitudes. For  $G_\infty > 0$ , ions are lost in daytime not only through recombination but also as a result of flow from the  $F_2$  region. A complete solution of equation (VI.66) involves considerable difficulties, and we will therefore first consider a simplified example which will help to elucidate some general topics.

#### Solution for the idealized case

To understand the role of diffusion in the formation of the  $F_2$  layer, Bowhill /698, 707/ considers an idealized case of an ionosphere without recombinations ( $\beta \equiv 0$ ). This approach significantly simplifies the mathematics, while the main features of the formation of the  $F_2$  layer are retained: a layer with maximum  $n_e$  is observed at altitudes where  $\tau \ll 1$  and  $q$  monotonically decreases with  $h$ , an upward critical flux  $G_c$  is derived, etc. We will now proceed with the solution of the equation for the idealized case

$$q - dG/dh = 0. \quad (\text{VI.67})$$

First let us consider the conditions corresponding to an ionosphere without ionization sources (at night). Since  $q \equiv 0$ , we have from (VI.67)  $dG/dh = 0$ , i. e.,  $G = \text{const.}$  Equation (VI.66) for  $z \geq 0$  takes the form

$$n_e'' + \frac{3}{2H} n_e' + \frac{n_e}{2H^2} = 0. \quad (\text{VI.68})$$

The general solution of this equation has the form

$$n_e = B e^{-\frac{z}{2H}} + C e^{-\frac{z}{H}}, \quad (\text{VI.69})$$

where  $B$  and  $C$  are integration constants. From the lower boundary condition ( $n_e = 0$  for  $z = 0$ ) we find  $B = -C$ . Inserting (VI.69) in (VI.65), we obtain

$$G = \frac{CD}{2H} e^{-\frac{z}{H}} = \frac{CD_0}{2H}, \quad (\text{VI.70})$$

i. e., the flow is indeed independent of altitude, and we have at infinity  $G_\infty = CD_0/2H$ . Constants  $B$  and  $C$  can be expressed in terms of  $G_\infty$ , and the solution takes the form

$$n_e = -\frac{2HG_\infty}{D_0} \left( e^{-\frac{z}{2H}} - e^{-\frac{z}{H}} \right) = -\frac{2HG_\infty}{D_0} v \left( \frac{z}{H} \right). \quad (\text{VI.71})$$

A positive solution is possible only if  $G_\infty$  is downward. Figure 100 shows that the distribution  $n_e(h)$  has a maximum, and at high altitudes it asymptotically approaches the barometric distribution  $e^{-z/2H}$ . Although the diffusive flow of ions is constant at all altitudes, an electron concentration maximum is formed at a certain altitude  $z^{\text{max}}$ . The altitude of this maximum is

$$z^{\max} = 2H \ln 2, \quad (\text{VI.72})$$

and is thus independent of  $G_{\infty}$ , as in the more general case treated in the next subsection.

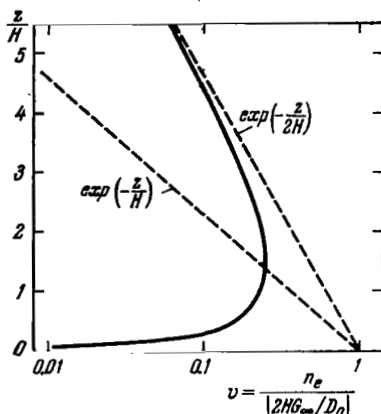


FIGURE 100. Vertical distribution of the electron concentration (expressed in units  $[2HG_{\infty}/D_0]$ ) for the idealized case of no recombination from (VI.71).

The dashed lines plot the two components of the solution (VI.71).

For daytime conditions, the stationarity equation takes the form

$$n_e'' + \frac{3}{2H} n_e' + \frac{n_e}{2H^2} + \frac{q_0}{D_0} e^{-\frac{2z}{H}} = 0. \quad (\text{VI.73})$$

Bowhill /698, 707/ gives a solution of this equation satisfying the boundary condition  $n_e = 0$  for  $z = 0$ :

$$n_e = \frac{2q_0H^2}{3D_0} u\left(\frac{z}{H}\right) - \frac{2HG_{\infty}}{D_0} v\left(\frac{z}{H}\right), \quad (\text{VI.74})$$

where

$$u\left(\frac{z}{H}\right) = e^{-\frac{z}{2H}} - e^{-\frac{2z}{H}}, \quad v\left(\frac{z}{H}\right) = e^{-\frac{z}{2H}} - e^{-\frac{z}{H}}$$

The general solution  $v(z/H)$  in this case is the solution of the homogeneous equation (VI.68). For  $z < 0$  solution (VI.74) leads to absurd negative values for  $n_e$ . Moreover, the altitude  $h_0$  remains indeterminate.

A more proper solution can be obtained if photochemical equilibrium is assumed below  $h_0$ :

$$q - \beta n_e = 0. \quad (\text{VI.75})$$

Then  $h_0$  is the level at which recombination and diffusion processes are equalized, i. e.,

$$\beta_0 n_{0e} = q_0 = \left| \frac{dG}{dh} \right|_{h_0}. \quad (\text{VI.76})$$

In this case we find for  $z \geq 0$

$$n_e = \frac{q_0}{\beta_0} u'' \left( \frac{z}{H} \right) - \frac{2HG_\infty}{D_0} v \left( \frac{z}{H} \right), \quad (\text{VI.77})$$

where  $u''(z/H) = (1 + \delta)e^{-\frac{z}{2H}} - \delta e^{-\frac{2z}{H}}$ ,  $\delta = 2\beta_0 H^2 / 3D_0$ . For  $z \leq 0$ , according to (VI.75),  $n_e = q/\beta$  and we thus avoid the difficulty with negative  $n_e$ .

Unlike the nocturnal layer (VI.71), the daytime layer (VI.74) or (VI.77) depends on  $G_\infty$ . It is significant that a certain ionized layer also forms with an upward flow at infinity  $G_\infty > 0$ . The magnitude of the positive flow at infinity, however, is restricted. Indeed, seeing that  $n_e \geq 0$  and that at high altitude by (VI.74)

$$n_e = \frac{2H}{D_0} \left( \frac{q_0 H}{3} - G_\infty \right) e^{-\frac{z}{2H}}, \quad (\text{VI.78})$$

we find that the maximum possible (critical) upward flow is  $\bar{G}_c = q_0 H / 3$ . Physically, the critical case and the case  $G_\infty > 0$  in general point to the existence of an electron sink above a certain level. We thus arrive at a model with a certain reservoir containing a source or a sink of electrons and ions above the  $F$  layer (an exosphere or a protonosphere). In distinction from nocturnal conditions, the total flux in daytime is a function of altitude,

$$G = G_\infty - q_0 H e^{-\frac{z}{H}}. \quad (\text{VI.79})$$

Even for  $G_\infty = \bar{G}_c$  the resultant flow is always directed downward near the layer maximum and below. We see from (VI.79) that the variable component of this flow at each altitude is equal to the total number of newly formed ions in the atmospheric column above a given altitude. This conclusion, however, also follows directly from the starting equation (VI.67) when it is integrated over the altitude. We will now proceed with the solution of the general equation (VI.66).

#### Exact solution

Equation (VI.66) can be simplified and reduced to Bessel's equation by the following substitution:

$$y = B e^{-\frac{3z}{2H}} \quad \text{and} \quad f = n_e e^{\frac{3z}{4H}}, \quad (\text{VI.80})$$

where  $B = \frac{2H}{3} \sqrt{\frac{\beta_0}{D_0}}$ . The equation thus takes the form

$$\frac{d^2 f}{dy^2} + \frac{1}{y} \frac{df}{dy} - \left( 1 + \frac{1}{36y^2} \right) f = \varphi y^{-\frac{7}{6}}, \quad (\text{VI.81})$$

where

$$\varphi = -4q_0H^2/9D_0.$$

The solution of this equation is expressed in terms of Bessel functions  $I_{1/6}$  and  $K_{1/6}$  of order 1/6 [689, 698, 700, 707, 715] and provides a generalization of the exponential solutions derived in the previous subsection. We will avoid the detailed mathematics, which also involve numerical computation, and proceed directly with the analysis of the results published by Geisler and Bowhill [707].

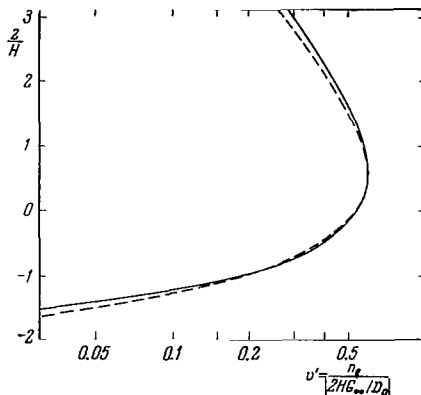


FIGURE 101. Vertical distribution of the electron concentration (expressed in units of  $|2HG_\infty/D_0|$ ) for nocturnal conditions from (VI.82).

The dashed curve plots the distribution of the electron concentration from the simple layer theory using (VI.84).

A. Night. The nocturnal solution has the form

$$n_e = -\frac{2HG_\infty}{D_0} v' \left( \frac{z}{H} \right), \quad (\text{VI.82})$$

where  $v'(z/H)$  is a function shown in graphical form on Figure 101. This function at high altitudes approaches to the barometric distribution  $e^{-z/2H}$ , like the function (VI.71), and, again like (VI.71), has a maximum which is independent of  $G_\infty$ . The position of the maximum corresponds to  $z/H \approx 0.55$  if we take  $z = 0$  at the level where photochemical and diffusive processes are equalized,

$$q_0/n_{0e} = \beta_0 = 4D_0/H^2. \quad (\text{VI.83})$$

Note that the shape of the night profile is close to the daytime profile in Chapman's simple layer theory,

$$n_e = n_{0e} \exp \left\{ \frac{1}{2} \left[ -\frac{z}{H} - \exp \left( -\frac{z}{H} \right) \right] \right\}, \quad (\text{VI.84})$$

but is not quite identical (see Figure 101).

The altitude of the maximum  $h^{\max}$  is  $0.55 H$  above the altitude  $h_0$ , and it is therefore entirely determined by atmospheric conditions. In actual computations, we will somewhat generalize the solutions, since the atmosphere is made up of nitrogen as well as oxygen. Seeing that  $\beta = [N_0]\gamma_{NO^+} + [O_2]\gamma_{O_2^+}$  and  $D = D^*[O]^{-1}\sqrt{T}$ , we obtain from (VI.83) the following condition for the altitude  $h_0$ :

$$H^2 [O] [M] T^{-1/2} = 4D^* \left\{ \frac{[N_2]}{[M]} \gamma_{NO^+} + \frac{[O_2]}{[M]} \gamma_{O_2^+} \right\}^{-1}. \quad (\text{VI.85})$$

The right member of (VI.85) is almost constant; the left member is the product of the number of oxygen atoms  $H[O]$  by the number of molecules  $H[M]$  in an atmospheric column of  $1 \text{ cm}^2$  cross section, i. e., it is proportional to atmospheric pressure, since the number of particles in the column is equal to their partial pressure.

In the neutral atmosphere model, the conditions at a certain level (120 km, say) are assumed to remain constant. Then irrespective of the actual temperature variations (e. g., during the day or a season), the relative composition of the atmosphere at the level with fixed pressure remains unchanged /708/. This follows directly from (IV.18). We thus conclude that the altitude of the nocturnal  $F$  layer corresponds to the fixed-pressure

level ( $p = (2.5 - 3) \cdot 10^{-7} \text{ mm Hg}$ ) to within  $\sqrt[4]{T}$ . Using (VI.85), we find  $H^2 [O][M] \approx 10^{30} \text{ cm}^{-4}$  which, according to /332/, corresponds to altitudes of 265 and 325 km at night for periods of low and high solar activity, respectively. Since at night  $h^{\max}$  lies  $0.55 H$  above the level  $z = 0$ , it should be 290 and 360 km for periods of minimum and maximum solar activity. According to rocket data (Section 15), the altitude  $h^{\max} F$  at night changes from about 310 km to about 370 km between periods of minimum and maximum activity. The computed and the observed altitudes thus show good agreement.

Let us now consider the parameter  $G_\infty$ . Seeing that the partial pressure of atomic oxygen is constant, we find from (VI.82) that the value of  $n_e$  in the  $F$  layer maximum is completely determined by  $G_\infty$ , since the ratio  $H/D_0$  is proportional to pressure. Using (VI.82), we find

$$G_\infty = -D_0 (n_e)_{\max} / 1.2H.$$

Hence it follows that at night, for low solar activity,  $G_\infty \approx \sim 10^9 \text{ cm}^{-2} \text{ sec}^{-1}$ . Only about 1% of this flow is used up in recombination processes at altitudes above the layer maximum, whereas most of the charged particles are transported downward and recombine below the layer maximum.

In periods of maximum solar activity at middle latitudes,  $(n_e)_{\max}$  is a factor of 3 - 4 higher than for minimum activity. If the nocturnal ionization source in the  $F$  region is ignored, this should be ascribed to a corresponding increase in  $G_\infty$ .

**B. Day.** The solution of equation (VI.66) for daytime conditions has the form

$$n_e = \frac{q_0}{\beta_0} u' \left( \frac{z}{H} \right) - \frac{2HG_\infty}{D_0} v' \left( \frac{z}{H} \right). \quad (\text{VI.86})$$

In (VI.86), the function  $v'(z/H)$  is the same as in (VI.82), and the function  $u'(z/H)$  is shown graphically in Figure 102. The function  $u'(z/H)$  describes the relative vertical distribution of  $n_e$  for  $G_\infty = 0$ . The maximum electron concentration is observed for  $\tau \ll 1$ , i. e., much higher than the maximum ionization rate  $q_{\max}$ , which occurs approximately at  $\tau \approx 1$ . At high altitudes, the function  $u'(z/H)$  coincides with the exponential barometric distribution, and at low altitudes it reduces to a curve for photochemical equilibrium  $n_e = q/\beta$ . It is significant that below the layer maximum  $n_e$  is also higher than in photochemical equilibrium. The extra increase of  $n_e$  is the result of charged particles being transported by the diffusive flow from the upper part of the layer /706/.

Solutions (VI.86) for various values of  $G_\infty$  are shown in Figure 103. The values of  $G_\infty$  are expressed in units of the critical flow

$$G_c = -2aq_0H, \quad (\text{VI.87})$$

where  $a = \frac{(1/2)!(1/\beta)!}{(1/6)! \sqrt{6}} = 0.468$ . We see that for high  $G_\infty/G_c$  the gradient  $dn_e/dh$  significantly decreases in the region directly above the layer maximum. This corresponds to evening conditions, when the rate of ionization is markedly reduced. This effect was actually observed in rocket experiments (see Figure 50, Section 15) and it was regarded as quite puzzling since it was assumed that the reduction of temperature in the evening and at night would reduce the scale height and not the gradient  $dn_e/dh$ .

All the curves in Figure 103 converge at the bottom, because for  $z \approx -1.5H$  the electron concentration is determined by photochemical processes and so, independently of  $G_\infty$ ,  $n_e = q/\beta \propto e^{z/H}$ .

Let us again consider in some detail the altitude of the layer maximum  $h^{\max}$ . As for the nocturnal layer, (VI.85) approximately determines the position of the layer maximum, but in daytime  $h^{\max}$  depends on  $G_\infty$ . When  $G_\infty$  is directed downward,  $h^{\max}$  increases; when it is directed downward, the altitude of the layer maximum diminishes. This effect is opposed to the action of the electrodynamic drift on the  $F$  layer, which displaces the altitude  $h^{\max}$  in the direction of drift (see below). The altitudes  $h^{\max}$  in units of  $z/H$  for various  $G_\infty$  (expressed in units of  $G_c$  from (VI.87)) are given in Table 51. We see that the full amplitude of the possible variations in  $h^{\max}$  is  $1.2H$ . For  $G_\infty \approx 2G_c$ , we have  $h^{\max} = h_0$ , i. e., it is precisely determined by (VI.85). For sufficiently high  $G_\infty$ , when the contribution from photoionization is negligible,  $h^{\max}$  and the profile of the upper part of the layer naturally approach the  $h^{\max}$  and the profile of the nocturnal layer. Conversely, for sufficiently high  $q_0$ , the upward outflow of ions proportionately increases ( $G_\infty \rightarrow -G_c$ ) and the altitude  $h^{\max}$  drops to its minimum. Note that directly above the maximum the vertical distribution of  $n_e$  is described by the exponential  $e^{-z/H}$ , and not by  $e^{-z/2H}$ , as for  $G_\infty \gg 0$ . It is only at very high altitudes that the barometric distribution is restored,  $n_e \propto e^{-z/2H}$ . This effect of a change in scale height may create a false impression of variation of the ion composition with altitude. As we noted on p. 117, rocket experiments reveal a decrease of  $|dn_e/dh|$  with altitude in daytime above the  $F$ -layer maximum.

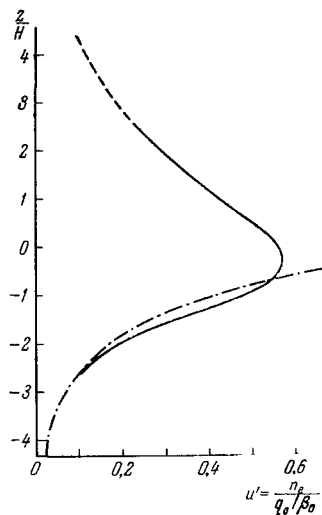


FIGURE 102. Vertical distribution of electron concentration (expressed in units of  $q_0/\beta_0$ ) for  $G_\infty = 0$  from (VI.86).

The dashed part of the curve corresponds to photochemical equilibrium.

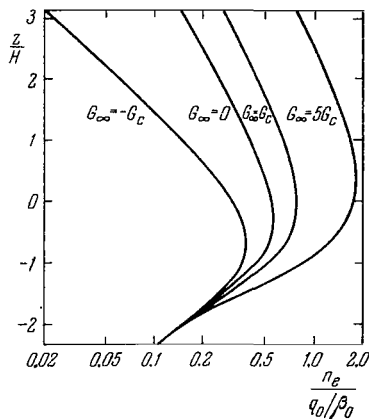


FIGURE 103. Vertical distribution of electron concentration (expressed in units of  $q_0/\beta_0$ ) for daytime conditions according to (VI.86), for various values of  $G_\infty$  marked against the curves.

TABLE 51.  $h^{\max}$  vs.  $G_\infty/G_c$

$G_\infty/G_c$	-1	0	1	2	3	5	$\infty$
$\frac{h^{\max} - h_0}{H}$	-0.66	-0.31	-0.12	$\sim 0$	0.1	0.3	0.55

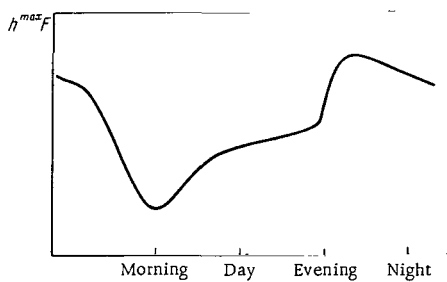


FIGURE 104. Schematic curve of the expected variation of the  $F$ -layer maximum altitude during the day under stationary conditions.

It is clear from the above that the altitude of the  $F_2$  layer reckoned from the atmospheric layer with appropriate pressure should be lower during the daytime than at night. Moreover, the altitude  $h^{\max}$  should undergo certain variations during the day as a result of changes in the parameters of the neutral atmosphere. For example, during most of the day,  $q_0$  remains constant at the altitude  $h_0$  (because of the low optical thickness  $\tau$ ), but it abruptly diminishes for sufficiently high values of  $z_0$ . In these periods we can expect the altitude  $h^{\max}$  to increase with increasing  $z_0$ . Indeed, rocket data from Figure 48 reveal an abrupt growth of  $h^{\max}$  before sunset, whereas before sunrise  $h^{\max}$  is seen to decrease markedly. A certain increase of  $h^{\max}$  during the day (approximately after 1000 hrs) is caused by the increase in the temperature of the atmosphere: because of the higher temperature, the fixed-pressure level on which the  $F_2$  layer is formed rises. Similarly, at night,  $h^{\max}$  is lower than in the evening, right after sunset, because the temperatures are lower. The expected variation of  $h^{\max}$  during the day is shown schematically in Figure 104. This figure reflects the basic features in the variation of  $h^{\max}$ , which emerge from the experimental rocket data in Figure 48. Comparison of Figures 48 and 104 shows that the times of abrupt change in the altitude of the  $F$  layer lag a few hours behind the respective times of sunrise and sunset.

The critical flow according to (VI.87) is proportional to the intensity of the ionizing solar radiation  $I_0$  and the atmospheric pressure at  $z = 0$ . Since this pressure is constant, the variations in  $G_c$  during the solar cycle are entirely dependent on the variations of  $I_0$ . Hence it follows that for high solar activity  $G_c$  should be approximately a factor of 3 higher than for low activity. In all probability,  $G_\infty = -G_c$  in daytime [710]. If there are no special sources and sinks of ions in the exosphere, it would seem (seeing that ions do not accumulate in the exosphere) that the nocturnal  $G_\infty$  is determined by the quantity of ions in the exosphere and therefore by the magnitude of the daytime flow, i. e., also by  $G_c$ . The amplitude of the variations of the nocturnal flow  $G_\infty$  during the solar cycle, which is indirectly determined by the variations of the solar radiation intensity, is thus approximately 3. This result coincides with an earlier estimate of  $G_\infty$  from the nighttime values of  $n_e F_1$ .

Let us now consider the maximum electron concentration  $(n_e)_{\max}$ . It is well known that the  $F_2$  layer displays a seasonal anomaly, i. e., at middle latitudes the daytime  $n_e F_2$  is approximately a factor of 4 higher in winter than in summer. Before we analyze this effect, we recall that the nocturnal values of  $n_e F_2$  are conversely on the average lower in winter (Figure 105). Indeed, the nocturnal values of  $n_e F$  are determined by the flow of ions from the exosphere, where the total quantity of ions apparently depends on the length of day, so that in winter these values should be lower than in summer.

The daytime values of  $n_e F_2$  according to (VI.86) and Figure 103 for  $G_\infty = -G_c$  are

$$n_e F_2 = 0.4 q_0 / \beta_0. \quad (\text{VI.88})$$

Since  $q/\beta \propto I/[O]/[M]$ ,  $n_e F_2$  in daytime, when  $I = \text{const}$ , is entirely determined by the concentration ratio of atoms and molecules at the level of the  $F_2$  layer maximum. Since for a given  $G_\infty/G_c$  this level is entirely determined by pressure, in an atmospheric model with constant conditions at the 120 km



level we should expect the value of  $n_e F_2$  to remain constant during the entire season and the solar cycle. In fact,  $n_e F_2$  varies, and this points to significant variations in the ratio  $[O]/[M]$  both at the  $F_2$ -layer altitude and at other levels during the season and the solar activity cycle (see also p. 243).

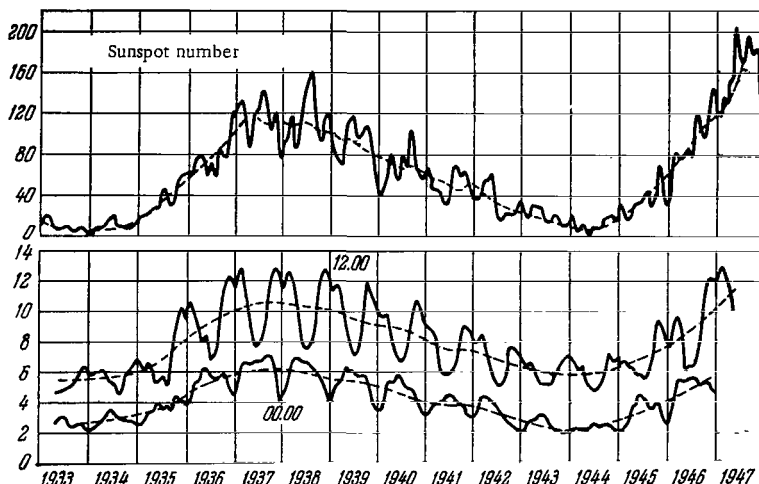


FIGURE 105. Variation of midday and midnight critical frequencies of the  $F_2$  layer during the solar cycle /488/. The top curve gives the variation of the sunspot number.

The seasonal variations of  $f^oF_2$  for 1200 hrs and 0000 hrs are in counterphase.

Seeing that  $n_e F_2$  varies approximately by a factor of 4 during one season, we conclude that the ratio  $[O]/[M]$  at the  $\sim 10^{-7}$  mm Hg level also varies approximately by a factor of 4. To obtain an exact estimate, we have to allow for the seasonal variations of the altitude  $h^{\max} F$ . It was found /709, 710/ that for low solar activity at the altitudes of the  $F$  layer  $[O]/[N_2] = 10$  in winter and  $[O]/[N_2] = 1.5$  in summer. Other values of  $[O]/[N_2]$  are generally cited for these altitudes in atmospheric models (see, e. g., the data in Tables 47 and 48).

The conclusions regarding the conditions of formation of  $h^{\max}$  and  $(n_e)_{\max}$  thus enable us to use ionospheric data in order to draw inferences about the composition of the neutral atmosphere and to verify the various models of the upper atmosphere. In particular, we have seen above that, using the ionospheric data on the variation of  $h^{\max} F$  and  $(n_e)_{\max}$  during a season and during the solar cycle, we can invalidate the condition of constant parameters at the 120 km level. Rocket data on diurnal variations of the particle concentration at  $h \approx 200$  km (Section 17) bear out the conclusion that there is indeed no fixed-composition level in the atmosphere above  $h \approx 110$  km.

The observations concerning the formation of the  $F$  layer made in this section are based on the solution of equation (VI.66) or possibly of the simpler equations (VI.68) and (VI.73). A number of simplifying assumptions were made when setting up these equations. A pure oxygen atmosphere was assumed, for example. In the presence of nitrogen  $\beta = [N_2]\gamma_{NO+} + [O_2]\gamma_{O+}$  and this coefficient is mainly determined by the concentration of  $N_2$ . Then

$\beta \propto \exp(-\frac{28z}{16H})$  and equation (VI.64) even cannot be reduced to Bessel's equation.

However, as the vertical distribution of  $n_e$  above the layer maximum is virtually independent of  $\beta$ , this simplifying assumption is not particularly restrictive. Moreover, as we indicated on p. 272, the solution is readily generalized to the case of a mixed oxygen — nitrogen atmosphere.

Below the layer maximum linear recombination is replaced by quadratic recombination. Since  $n_e$  in this region is determined by photochemical equilibrium, no difficulties need be anticipated with this factor.

It was also assumed that  $q$  is entirely determined by the ionization of atomic oxygen. In fact, the contribution of molecules is quite significant in the  $F_2$ -layer maximum. This should somewhat alter the curve of  $q$  vs.  $h$  and, as we see from the solution of equation (VI.84), also affect the value of  $G$  and its variation with altitude. We can thus predict in what direction the solution will change if the ionization effect is considered more accurately; in case of an exponential dependence of  $q$  on  $h$ , we can actually obtain a rigorous solution of the equation /705/. The vertical distribution of  $q$  is sometimes taken in the form (VI.84), which is different from the exponential distribution (VI.60). This is not particularly helpful, however, since we are not dealing with the region of maximum  $q$  but with much higher altitudes, where (VI.84) actually reduces to (VI.60).

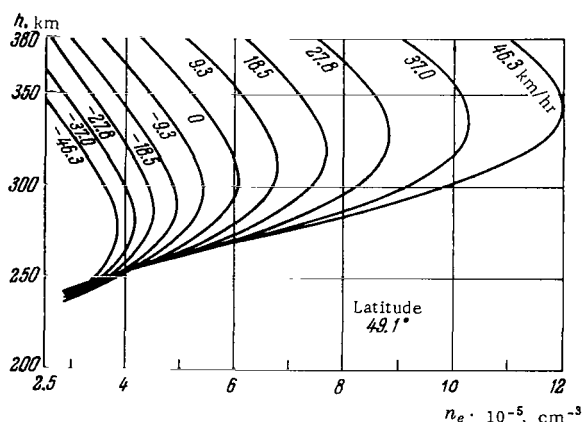


FIGURE 106. Vertical distribution of the electron concentration under stationary conditions for various vertical drift velocities from the computations of Yonezawa /688, 690/ for equinoctial noon.

Negative values correspond to downward velocities.

**Drifts.** We noted in Section 23 that  $G$  in equation (V.101) or (VI.64) may be interpreted not only as the flow of ambipolar diffusion but also as drift of charged particles produced by streaming motion in the atmosphere in conjunction with electrodynamic forces. If the combined effect of the electric and the magnetic fields in the upper atmosphere imparts a vertical motion component to the electrons and the ions, the vertical distribution of the electron concentration will change. However, if the drift velocity of the

charged particles remains constant, steady-state conditions will be established after some time. The effect of vertical drift was studied by Martin /711—713/ and others. Combined treatment of diffusion and drift is due to Yonezawa /688, 690/ (Figure 106). Upward drift lifts the  $F$  layer and increases the maximum electron concentration, whereas downward drift leads to a reverse situation. Drift effects apparently must be introduced in order to account for certain features in the variation of  $(n_e)_{\max}$  and  $h^{\max}F$  during the day and at various latitudes. Measurements of noncoherent back scattering (Section 16) reveal sudden increases of  $h^{\max}F$  in summer evenings, which are accompanied by a growth of  $(n_e)_{\max}$  (Figure 54, 1963; Figure 55, June). This effect resembles the expected effect of an upward drift.

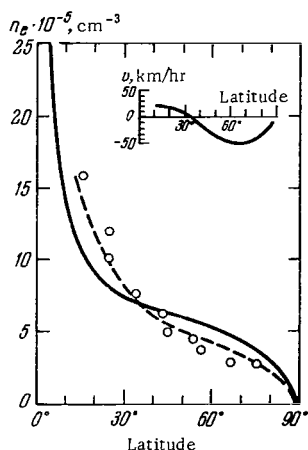


FIGURE 107. Latitudinal distribution of the electron concentration maximum in the  $F_2$  region for equinoctial noon /689/.

Dots — observations; solid curve — computed without drift effects; dashed curve — computed with drift effects. The assumed distribution of drift velocity with latitude is shown in the top right corner.

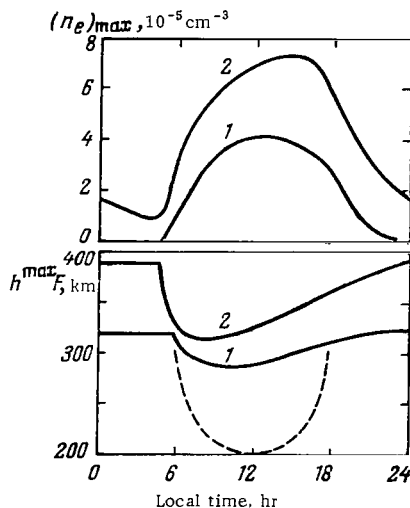


FIGURE 108. Variation of the electron concentration maximum  $(n_e)_{\max}$  and its altitude  $h^{\max}F$  vs. the local time /703/.

Curves 2 were plotted using a diffusion coefficient equal to 1/10 of that for curve 1. The values of Table 43 are thus bracketed from either side. The dashed curve gives the altitude of the ionization rate maximum.

Figure 107 (based on Yonezawa's data /689/ compares the observed values of  $(n_e)_{\max}$  (dots) at various latitudes with the theoretical expected values both without drift (solid curve) and with drift (dashed curve). The introduction of drift effects markedly improves the agreement between the theoretical and the experimental values of  $h^{\max}F$  at noon in the equatorial region, where upward drifts with velocities of about 25 km/hr should be observed /689/. At high latitudes, poor results were obtained for  $h^{\max}F$ , probably because the effect of the corpuscular source /714, 715/ and the latitudinal variation of the atmospheric composition were ignored. Drift

effects were generally introduced in order to account for the sudden changes in  $h^{\max}F$  and  $(n_e)_{\max}$  during magnetic storms. However, since at middle latitudes  $h^{\max}F_2$  increases during storms, where  $(n_e)_{\max}$  decreases, the drift mechanism is unsuitable /690/. Seaton's hypothesis /626/ of variations in the atmospheric composition is apparently closer to the truth (Section 25).

## Nonstationary solutions

So far the problem has not been solved completely for the stationary conditions. An even more complex undertaking is the solution of the equation

$$dn_e/dt = q(h, t) - r(h, t) - dG(h, t)/dh, \quad (\text{VI.89})$$

since, in addition to the time-dependent boundary conditions, we also have to consider initial conditions. The simplest solution corresponds to the case of regular diurnal variations of the electron concentration. In this case a periodic solution can be used (with a one-day period) in the quasi-stationary approximation, thereby eliminating the effect of the initial conditions.

This problem was first solved by Ferraro and Ozdoğan /696/ under significant simplifications. A constant recombination coefficient  $\beta$  was assumed, and the results were naturally far from reality. A more rigorous analytical solution was derived by Gliddon and Kendall /693, 694/. They found that the electron concentration maximum in the  $F$  layer is attained a few hours after noon (2 hours later than for  $\beta_0 = 0.75 \cdot 10^{-3} \text{ sec}^{-1}$  at the level  $h_0$ ).

Numerical solution of equation (VI.89) on analog computers for particular atmospheric models was attempted by Rishbeth /703/ and Polyakov /706, 716, 754/. The introduction of nonstationarity shows that the variation of altitude and electron concentration of the  $F$ -layer maximum is offset relative to noon, and the rate of change of these parameters in the  $F$  layer is different in the morning and in the evening (Figure 108). Polyakov showed that the daytime variation in the concentration of the molecular ions also must be taken into consideration. The lag of the concentration maximum of molecular ions proved to be somewhat less than the lag of the electron concentration maximum /706, 754/. This is so because the  $[M^+]$  maximum forms at lower altitudes than the  $n_e$  maximum, i. e., in a region of lower "inertia" of the ionosphere.

## Summary of the $F$ region theory

The basic concepts relating to the formation of the  $F_2$  region have been developed from two particular solutions of the stationarity equation. We will now try to summarize our conclusions, considering the variation of the  $F$  region during the day along the lines indicated by Rishbeth /703/.

At night the  $F$  region develops toward an equilibrium layer whose altitude depends on the intensity of the exospheric flow  $G_\infty$ . However, the electron concentration depends on  $G_\infty$ . If  $G_\infty$  ceases altogether,  $n_e$  will start decreasing, and yet the layer will retain its profile. In other words, the electron concentration will diminish simultaneously and proportionately at all levels with the same time constant  $\tau = 1/\beta_{\max}$ , where  $\beta_{\max}$  is the linear

recombination coefficient for the layer maximum. If  $G_{\infty}$  increases,  $n_e$  increases proportionately at all altitudes.

During sunrise,  $dn_e/dt$  is determined primarily by the values of  $q$  and also by the values of  $\beta$  and  $D_a$ . The altitude of the  $F$  layer diminishes and reaches its minimum. As the Sun rises above the horizon,  $n_e$  increases at all altitudes, but below the  $F$  layer its growth is faster. The layer assumes its daytime form  $F_2$  with a maximum at a lower pressures level than at night. Below the layer maximum  $n_e$  is determined by photochemical equilibrium conditions and decreases with decreasing altitude. In the upper part of the ionosphere,  $n_e$  increases mainly as a result of the upward influx of charged particles; a steady leakage of ions and electrons into the exosphere is observed. When the temperature of the upper atmosphere is raised by the short-wave solar radiation, the altitude of the constant-pressure levels increases and the  $F$  layer rises during the day.

During sunset, the photoionization source is "turned off" and the  $F$  layer assumes its nocturnal form. The altitude of the layer maximum increases fairly rapidly by  $1.2H$  above the daytime altitude. Since the rate of recombination is higher at lower altitudes, electron concentration is transported downward by diffusion in order to preserve the equilibrium form unchanged. The nocturnal downward flow  $G_{\infty}$  from the exosphere thus originates. As the temperature of the upper atmosphere decreases, the  $F_2$  layer sinks to its nocturnal altitude producing the post-sunset maximum  $h^{\max}F$ . This maximum has not been observed so far with any reliability.

Let us consider the inertia of the ionospheric plasma in the  $F$  region and its time constant. The response of the ionosphere to changes in the intensity of the ionizing radiation is characterized by the time constant  $\tau = 1/\beta$  below the layer maximum. In the layer maximum and above, the variations of  $n_e$  are independent of the local values of  $\beta$  or  $D_a$ . Diffusion closely links the variations of  $n_e$  at all altitudes in the upper part of the layer with variations in the layer maximum. The time constant at all altitudes above the  $n_e$  maximum is therefore determined by the conditions in the layer maximum,  $\tau = 1/\beta_{\max}$ .

We have only briefly touched upon the basic concepts of the theory of formation of the  $F$  layer. New problems are discussed in /759—761/. The theory of formation of the  $F$  layer has recently gained a new impetus in a long range of new studies. The numerical and analytical solutions of the equation for the nonstationary case were obtained /718, 762—765/, non-equilibrium thermal conditions  $T_e \neq T_i \neq T_n$  /764, 766—771/ and time-dependence of the neutral atmosphere /764, 772/ were allowed for, the drift effects /762, 773—775/ and the relation between the motion of ions and neutrals /762, 774—777/ were computed again, the two-dimensional problem was solved /777, 778/, the coupling between magnetic conjugate regions was considered /779/, and computations were performed for the upper part of the ionosphere /766, 768, 770, 780, 781/. The effect of corpuscular heating was considered in /782/.

New observation results for the  $F$  region and the upper ionosphere led to an improved expression of the dependence of various parameters on solar radiation and geomagnetic disturbances in different times of day and for different latitudes /783—794/, for different seasons /787, 793—795/, and during a solar eclipse /796/. This work established the existence of the diffusive flow of ions between the ionosphere and the protonosphere /760, 763, 767, 775, 783, 796—798/, and ion and electron drift in certain periods /793, 799—801/.

Table I

## PREDICTION OF SHORT-WAVE LINES IN THE SOLAR SPECTRUM

The first term of the isoelectronic series is always indicated on a separate line. The columns give the identifying number (1), the ion with the ionization potential in eV and the log ionization temperature, with rough estimates enclosed in parentheses (2), the spectral transition, with the lower level first (3), the wavelength in Å, with cases of uncertain extrapolation or interpolation enclosed in parentheses (4), the oscillator strength  $f_{12}$  for absorption, with tentative estimates derived from Allen's rule /99/ enclosed in parentheses (5), the radiation flux  $F_t$  in erg/cm<sup>2</sup>sec at a distance of 1 a.u. A supplement at the end of the table lists some lines which have not been included in Table I.

No.	Ion; $x_i$ , eV; log $T_i$	Transition	$\lambda$ , Å	$f_{12}$	$F_t$ , erg/cm <sup>2</sup> sec
H I					
1	H I	$1s^2S - 2p^2P^\circ$	1215.7	0.416	/4/ (obs.)
2	13.60	— $3p^2P^\circ$	1025.7	0.08	0.08
3	3.84	— $4p^2P^\circ$	972.5	0.03	0.03
4		— $5p^2P^\circ$	949.7	0.015	0.01
5		— $6p^2P^\circ$	937.8	0.008	0.005
6		— $7p^2P^\circ$	930.75	0.005	0.003
7	He II	$1s^2S - 2p^2P^\circ$	303.78	0.4	0.6
8	54.4	— $3p^2P^\circ$	256.31	0.08	0.004
9	4.75	— $4p^2P^\circ$	243.02	0.03	0.001
10		$2p^2P^\circ - 3d^2D$	1640.49	0.08	0.001
11	C VI	$1s^2S - 2p^2P^\circ$	33.734	0.42	0.004
12	489.8	— $3p^2P^\circ$	28.464	0.08	$5 \cdot 10^{-4}$
13	(6.3)	— $4p^2P^\circ$	27.00	0.03	$2 \cdot 10^{-4}$
14		— $5p^2P^\circ$	26.4	0.015	$6 \cdot 10^{-5}$
15		$2p^2P^\circ - 3d^2D$	182.5	0.08	$10^{-5}$

TABLE I (continued)

No.	Ion; $x_i$ , eV; $\log T_i$	Transition	$\lambda$ , Å	$f_{12}$	$F_t$ , erg/cm <sup>2</sup> sec
16	N VII 666.8 6.4	$1s^2S - 2p^2P^\circ$	24.79	0.4	$2.4 \cdot 10^{-4}$
17		$-3p^2P^\circ$	20.9	0.08	$2.4 \cdot 10^{-5}$
18		$-4p^2P^\circ$	19.8	0.03	$10^{-5}$
19	O VIII 871 6.5	$1s^2S - 2p^2P^\circ$	18.969 18.974	0.4	$1.4 \cdot 10^{-3}$
20		$-3p^2P^\circ$	16.006	0.08	$1.4 \cdot 10^{-4}$
21		$-4p^2P^\circ$	15.20	0.03	$5 \cdot 10^{-5}$
22		$-5p^2P^\circ$	14.84	0.015	$2.5 \cdot 10^{-5}$
23		$-6p^2P^\circ$	14.65	0.008	$1.2 \cdot 10^{-5}$
24		$-7p^2P^\circ$	14.54	0.004	$5 \cdot 10^{-6}$
25		$2p^2P^\circ - 3d^2D$	102.6	0.08	$1.5 \cdot 10^{-4}$
26	Ne X 1361 (6.7)	$1s^2S - 2p^2P^\circ$	12.15	0.4	$4 \cdot 10^{-6}$
He I					
27	He I 24.58 4.25	$1s^2^1S - 2p^1P^\circ$	584.4	0.36	0.07
28		$-3p^1P^\circ$	537.0	0.07	0.002
29		$-4p^1P^\circ$	522.2	0.03	0.001
30		$-5p^1P^\circ$	515.6	0.02	$3 \cdot 10^{-4}$
31		$-6p^1P^\circ$	512.0	0.01	$1 \cdot 10^{-4}$
32	C V 392.0 (5.1 — 6.0)	$1s^2^1S - 2p^1P^\circ$	40.270	0.60	0.002
33		$-2s^3S$	41.47	(0.1)	$3 \cdot 10^{-4}$
34		$-2p^3P^\circ$	40.731	(0.1)	$4 \cdot 10^{-4}$
35		$-3p^1P^\circ$	34.973	(0.1)	$1.6 \cdot 10^{-4}$
36		$-4p^1P^\circ$	33.426	(0.03)	$3 \cdot 10^{-5}$
37		$-5p^1P^\circ$	32.754	(0.02)	$4 \cdot 10^{-5}$
38		$-6p^1P^\circ$	32.400	(0.01)	$2 \cdot 10^{-5}$
39		$2p^3P^\circ - 3d^3D$	248.74 248.67	(0.5)	$3 \cdot 10^{-4}$
40	N VI 551.9 (5.28 — 6.18)	$1s^2^1S - 2p^1P^\circ$	28.787	(0.5)	0.004
41		$-2s^3S$	29.53	(0.1)	0.001
42		$-2p^3P^\circ$	29.084	(0.1)	0.001
43		$-3p^1P^\circ$	24.90	(0.1)	$3 \cdot 10^{-4}$
44		$-4p^1P^\circ$	23.77	(0.1)	$3 \cdot 10^{-4}$
45		$2p^3P^\circ - 3d^3D$	(190)	(0.5)	$3 \cdot 10^{-4}$
46		$2s^3S - 2p^3P^\circ$	1909.12 1908.76 1891.07	(0.5)	$5 \cdot 10^{-4}$

TABLE I (continued)

No.	Ion; $x_i$ , eV; $\log T_i$	Transition	$\lambda$ , Å	$f_{12}$	$F_t$ , erg/cm <sup>2</sup> sec
47	O VII 739.1 (5.58—6.36)	$1s^2 1S - 2p^1 P^\circ$	21.602	(0.4)	$2.4 \cdot 10^{-3}$
48		$- 2s^3 S$	22.10	(0.1)	$6 \cdot 10^{-4}$
49		$- 2p^3 P^\circ$	21.80	(0.1)	$6 \cdot 10^{-4}$
50		$- 3p^1 P^\circ$	18.627	(0.1)	$3 \cdot 10^{-4}$
51		$- 4p^1 P^\circ$	17.768	(0.03)	$10^{-4}$
52		$- 5p^1 P^\circ$	17.396	(0.02)	$6 \cdot 10^{-5}$
53		$- 6p^1 P^\circ$	17.200	(0.01)	$3 \cdot 10^{-5}$
54		$2p^3 P^\circ - 3d^3 D$	130.0	(0.5)	$5 \cdot 10^{-4}$
55		$2p^1 P^\circ - 3s^1 S$	138.3	(0.1)	$2 \cdot 10^{-4}$
56		$2s^3 S - 2p^3 P^\circ$	1410.64 1399.78 1411.83	(0.2)	0.001
57	Ne IX 1196 (5.92—6.66)	$1s^2 1S - 2p^1 P^\circ$	13.44	(0.5)	$10^{-5}$
58		$- 2p^3 P^\circ$	(13.6)	(0.1)	$2 \cdot 10^{-6}$
59		$- 3p^1 P^\circ$	(11.5)	(0.1)	$6 \cdot 10^{-7}$
60		$- 4p^1 P^\circ$	(11.0)	(0.1)	$5 \cdot 10^{-7}$
61	Mg XI 1761 (6.2—6.9)	$1s^2 1S - 2p^1 P^\circ$	9.168	(0.5)	$10^{-6}$
62	Si XIII 2436 (6.4—7.1)	$1s^2 1S - 2p^1 P^\circ$	6.74	(0.5)	$10^{-7}$

## Li I

63	C IV 64.48 5.00	$2s^2 S - 2p^2 P^\circ$	1548.20	0.19	0.065
			1550.77	0.09	0.035
64		$- 3p^2 P^\circ$	312.42	0.14	$4 \cdot 10^{-4}$
			312.45	0.07	$2 \cdot 10^{-4}$
65		$- 4p^2 P^\circ$	244.90	(0.1)	$6 \cdot 10^{-5}$
66		$2p^2 P^\circ - 3s^2 S$	419.52	(0.1)	$3 \cdot 10^{-4}$
			419.71		
67		$- 3d^2 D$	384.28 384.03	(0.5)	0.001
68	N V 97.86 5.25	$2s^2 S - 2p^2 P^\circ$	1238.80	0.16	0.004
			1242.78	0.08	0.002
69		$- 3p^2 P^\circ$	209.27	0.16	$8 \cdot 10^{-5}$
			209.30	0.08	$4 \cdot 10^{-5}$
70		$2p^2 P^\circ - 3s^2 S$	266.19	(0.1)	$10^{-4}$
71		$- 3d^2 D$	266.38 247.71 247.56	(0.5)	$4 \cdot 10^{-4}$



TABLE I (continued)

No.	Ion; $x_i$ , eV; $\log T_i$	Transition	$\lambda$ , Å	$f_{12}$	$F_{12}$ , erg/cm <sup>2</sup> sec
72	O VI 138.08 5.42	$2s^2S - 2p^2P^\circ$	1031.91	0.14	0.06
			1037.61	0.07	0.03
73		$-3p^2P^\circ$	150.09	0.16	0.0014
			150.12	0.08	0.0007
74		$-4p^2P^\circ$	115.82	(0.3)	$6 \cdot 10^{-4}$
75		$-5p^2P^\circ$	104.81	(0.1)	$1 \cdot 10^{-4}$
76		$2p^2P^\circ - 3s^2S$	184.12	(0.1)	$1.5 \cdot 10^{-4}$
			183.94		
77		$-3d^2D$	172.94	(0.3)	$2.5 \cdot 10^{-3}$
			173.08		
78		$-4s^2S$	132.3	(0.1)	$1.5 \cdot 10^{-4}$
79		$-4d^2D$	129.87	(0.1)	$1.3 \cdot 10^{-4}$
			129.79		
80		$-5d^2D$	116.42	(0.1)	$1.2 \cdot 10^{-4}$
81	Ne VIII 239.0 5.82	$2s^2S - 2p^2P^\circ$	770.41	0.10	0.004
			780.32	0.05	0.002
82		$-3p^2P^\circ$	88.1	0.30	$2.5 \cdot 10^{-4}$
83			67.3	0.10	$5 \cdot 10^{-5}$
84		$-5p^2P^\circ$	60.7	(0.1)	$4 \cdot 10^{-5}$
85		$2p^2P^\circ - 3d^2D$	98.1	(0.5)	$8 \cdot 10^{-4}$
			98.2		
86		$-4d^2D$	73.6	(0.1)	$3 \cdot 10^{-5}$
87		$-5d^2D$	65.9	(0.1)	$3 \cdot 10^{-5}$
88		$-6d^2D$	62.4	(0.1)	$3 \cdot 10^{-5}$
89		$-3s^2S$	103.1	(0.1)	$1.5 \cdot 10^{-4}$
			103.9		
90		$-4s^2S$	74.7	(0.1)	$3 \cdot 10^{-5}$
91	Na IX 299.8 5.97	$2s^2S - 2p^2P^\circ$	681.72	0.10	$3 \cdot 10^{-4}$
			695	0.05	$1.5 \cdot 10^{-4}$
92		$-3p^2P^\circ$	70.65	(0.5)	$8 \cdot 10^{-5}$
			71.62		
93		$2p^2P^\circ - 3s^2S$	81.35	(0.1)	$10^{-5}$
94			81.18		
		$-3d^2D$	77.91	(0.1)	$10^{-5}$
			77.76		
95	Mg X 367.4 6.08	$2s^2S - 2p^2P^\circ$	609.85	0.08	0.02
			625.28	0.04	0.01
96		$-3p^2P^\circ$	57.88	0.22	0.002
			57.92	0.10	0.001
97		$-4p^2P^\circ$	44.05	(0.1)	$3 \cdot 10^{-4}$
98		$2p^2P^\circ - 3s^2S$	65.67	(0.1)	$8 \cdot 10^{-4}$
			65.85		
99		$-3d^2D$	63.15	(0.5)	0.003
			63.29		
100		$-4d^2D$	47.31	(0.1)	$2.5 \cdot 10^{-4}$
			47.23		

TABLE I (continued)

No.	Ion: $x_i$ , eV; $\log T_4$	Transition	$\lambda$ , Å	$f_{12}$	$F_{\tau}$ , erg/cm <sup>2</sup> sec
101	Al XI 441.9 6.2	$2s^2S - 2p^2P^\circ$	550 569	0.08 0.04	0.0016 $8 \cdot 10^{-4}$
102	Si XII 523.2	$2s^2S - 2p^2P^\circ$	499.28 521.11	0.08 0.04	0.006 0.003
103	6.23	$- 3p^2P^\circ$	40.91 40.95	0.22 0.11	0.001 $5 \cdot 10^{-4}$
104		$- 4p^2P^\circ$	(30)	(0.1)	$1.5 \cdot 10^{-4}$
105		$- 5p^2P^\circ$	(24)	(0.05)	$4 \cdot 10^{-5}$
106		$2p^2P^\circ - 3d^2D$	44.02 44.16	(0.5)	0.0015
107		$- 3s^2S$	45.66	(0.1)	$5 \cdot 10^{-4}$
108	S XIV 706.4	$2s^2S - 2p^2P^\circ$	(421) (446)	(0.1)	$4 \cdot 10^{-4}$ $2 \cdot 10^{-4}$
109	6.36	$- 3p^2P^\circ$	(32)	(0.5)	$2 \cdot 10^{-4}$
Be I					
110	C III 47.86	$2s^2^1S - 2p^1P^\circ$	977.0	1.38	0.17
111	4.68	$- 2p^3P^\circ$	1908.6— 1911.5	(0.01)	0.06
112		$2p^3P^\circ - 3s^3S$	538.08 538.31 538.15	(0.1)	$2 \cdot 10^{-4}$
113		$- 4d^3D$	371.75 371.78 371.69	(0.1)	$1.6 \cdot 10^{-5}$
114		$2p^3P^\circ - 2p^3^3P$	1176.0	0.1	0.004
115		$2p^1P^\circ - 2p^2^1D$	2297.6	(0.2)	0.003
116		$- 2p^2^1S$	547.9	(0.05)	$2 \cdot 10^{-5}$
117		$- 3s^1S$	690.9	(0.1)	$1.4 \cdot 10^{-4}$
118	N IV 77.45	$2s^2^1S - 2p^1P^\circ$	765.14	1.07	0.013
119	5.05	$- 2p^3P^\circ$	1490—1488	(0.01)	$5 \cdot 10^{-4}$
120		$- 3p^1P$	247.20	(0.5)	$10^{-4}$
121		$2p^3P^\circ - 2p^2^3P$	927.27 923.67 923.21 923.04 922.51 921.93	(0.2)	0.001
122		$2p^1P^\circ - 2p^1D$	1718.5	(0.2)	0.001

TABLE I (continued)

No.	Ion; $\lambda_i$ , eV; $\log T_i$	Transition	$\lambda$ , Å	$f_{12}$	$F_{t,2}$ , erg/cm <sup>2</sup> sec
123	O V 113.9 5.26	$2s^2 1S - 2p^1 P^\circ$	629.73	0.87	0.016
124		$- 2p^3 P^\circ$	1217.7	(0.01)	0.004
			1216.9		0.002
125		$- 3p^1 P^\circ$	172.17	(0.1)	$3 \cdot 10^{-4}$
126		$2p^3 P^\circ - 2p^2 3P$	762.00		
			761.13		
			760.44		
			760.23	(0.1)	0.007
			759.44		
			758.08		
127		$- 3s^3 S$	215.03		
			215.10	(0.1)	$4 \cdot 10^{-4}$
			215.24		
128		$- 3d^3 D$	192.75		
			192.80	(0.5)	0.0018
			192.91		
129		$- 4d^3 P$	151.55	(0.1)	$6 \cdot 10^{-5}$
			151.48		
130		$2p^1 P^\circ - 3d^1 D$	220.35	(0.5)	0.001
131		$- 3p^1 P$	194.59	(0.05)	$8 \cdot 10^{-5}$
132		$- 3p^1 D$	185.75	(0.5)	$9 \cdot 10^{-4}$
133		$- 2p^2 1D$	1371.3	(0.1)	0.003
134		$- 2p^2 1S$	774.5	(0.05)	0.002
135		$2p^2 1D - 3d^1 F^\circ$	207.79	(0.5)	$4 \cdot 10^{-4}$
136		$- 3d^1 D^\circ$	216.02	(0.05)	$4 \cdot 10^{-5}$
137	Ne VII 207.3 (5.6)	$2s^2 1S - 2p^1 P^\circ$	465.21	0.63	0.008
138		$- 2p^3 P^\circ$	(892)	(0.1)	0.002
139		$- 3p^1 P^\circ$	97.5	(0.5)	$1.2 \cdot 10^{-4}$
140		$- 4p^1 P^\circ$	75.7	(0.1)	$8 \cdot 10^{-6}$
141		$2p^3 P^\circ - 3d^3 D$	106.2	(0.5)	$1 \cdot 10^{-4}$
142		$- 4d^3 D$	82.3	(0.1)	$7 \cdot 10^{-6}$
143		$2p^1 P^\circ - 3d^1 D$	116.7	(0.5)	$8 \cdot 10^{-5}$
144	Na VIII 264.1 5.86	$2s^2 1S - 2p^1 P^\circ$	411.2	0.56	$4 \cdot 10^{-4}$
145		$- 2p^3 P^\circ$	778.9 793.3	(0.01)	$2 \cdot 10^{-5}$
146	Mg IX 327.9 5.90	$2s^2 1S - 2p^1 P^\circ$	368.07	0.50	0.0015
147		$- 2p^3 P^\circ$	710.3		
			704.5	(0.1)	0.006
			692.4		
148		$- 3p^1 P^\circ$	62.75	0.56	$6 \cdot 10^{-4}$
149		$2p^3 P^\circ - 2p^2 3P$	(444)	(0.05)	$5 \cdot 10^{-4}$

TABLE I (continued)

No.	Ion; $x_i$ , eV; $\log T_i$	Transition	$\lambda$ , Å	$f_{12}$	$F_t$ , erg/cm <sup>2</sup> sec
150	Mg IX	$—3d^3D$	67.09 67.14 67.24	(0.5)	$6 \cdot 10^{-4}$
151		$—4d^3D$	61.92 61.96	(0.5)	$4 \cdot 10^{-4}$
152		$2p^2^3P — 3d^3D^o$	69.47 69.41	(0.5)	$5 \cdot 10^{-4}$
153		$—3s^3P^o$	74.32	(0.2)	$3 \cdot 10^{-4}$
154		$—4d^3D$	51.65 51.59	(0.2)	$7 \cdot 10^{-5}$
155		$2p^1P^o — 3d^1D$	65.61	(0.5)	$3 \cdot 10^{-4}$
156		$—3d^1D$	72.31	(0.5)	$4 \cdot 10^{-4}$
157		$—3s^1S$	77.74	(0.1)	$10^{-4}$
158		$2p^2^1D — 3d^1F^o$	69.95	(0.5)	$4 \cdot 10^{-5}$
159	Al X	$2s^2^1S — 2p^1P^o$	332.9	0.45	0.006
160	398.5	$—2p^3P^o$	246.14	(0.2)	0.003
161	6.1	$—3p^1P^o$	51.98	(0.5)	$5 \cdot 10^{-4}$
162		$2p^3P^o — 2p^2^3P$	401.2	(0.1)	$8 \cdot 10^{-4}$
163		$—3d^3D$	55.36 55.27	(0.5)	$2 \cdot 10^{-4}$
164		$2p^2^3P — 3d^3D^o$	56.99	(0.5)	$2 \cdot 10^{-4}$
165	Si XI	$2s^2^1S — 2p^1P^o$	303.41	0.41	0.04
166	476.0	$—2p^3P^o$	565.1	(0.01)	0.004
167	6.14	$—3p^1P^o$	591.2		0.002
168		$2p^3P^o — 2p^2^3P$	43.76	0.61	0.006
169		$—3d^3D$	365.4	(0.1)	0.018
			46.26 46.30 46.40	(0.5)	0.005
170		$2p^2^3P — 3d^3D^o$	47.90 47.61	(0.5)	0.005
171		$2p^1P^o — 3d^1D$	47.65 49.22	(0.5)	0.005
172		$—3s^1S$	49.26 52.30	(0.1)	0.001
173	P XII	$2s^2^1S — 2p^1P^o$	287.7	0.38	$6 \cdot 10^{-5}$
174	S XIII	$2s^2^1S — 2p^1P^o$	257.5	0.35	0.002
175	651.7	$—2p^3P^o$	(490)	(0.05)	$5 \cdot 10^{-4}$
176	6.33	$—3p^1P^o$	(30)	(0.5)	$1.5 \cdot 10^{-4}$
177		$2p^3P^o — 2p^2^3P$	335.6	(0.1)	$6 \cdot 10^{-4}$
178		$—3d^3D$	(32)	(0.5)	$10^{-4}$

TABLE I (continued)

No.	Ion; $x_i$ , eV; $\log T_i$	Transition	$\lambda$ , Å	$f_{12}$	$F_{12}$ , erg/cm <sup>2</sup> sec
B I					
179	C II 24.38 4.25	$2p^2P^\circ - 2p^2D$	1335.68	0.38	0.25
180		$- 2p^2S$	1334.52 1036.33 1037.02	(0.05)	0.12 0.005
181		$- 2p^2P$	903.61 904.47 903.95 904.13	(0.1)	0.006
182		$- 3s^2S$	858.6 858.1	(0.1)	$6 \cdot 10^{-4}$
183		$- 3d^2D$	687.4	(0.5)	$8 \cdot 10^{-4}$
184		$2p^2P - 2p^3S^\circ$	1010.37 1010.07 1009.85	(0.05)	$2 \cdot 10^{-4}$
185	N III 47.43 4.7	$2p^2P^\circ - 2p^2D$	989.79 991.56 991.51	0.28	0.006
186		$- 2p^2S$	764.4 763.34	(0.05)	$4 \cdot 10^{-4}$
187		$- 2p^2P$	686.34 685.82 685.51 685.00	(0.1)	$4 \cdot 10^{-4}$
188		$- 3d^2D$	374.2	(0.5)	$6 \cdot 10^{-5}$
189		$2p^2P - 2p^3P^\circ$	1183.03 1184.54	(0.1)	$10^{-4}$
190	O IV 77.39 5.05	$2p^2P^\circ - 2p^2D$	790.10 790.20 787.71	0.23	0.006
191		$- 2p^2S$	609.83 608.40	(0.1)	0.006 0.003
192		$- 2p^2P$	555.26 554.51 554.07 553.33	(0.1)	0.01
193		$- 3s^2S$	279.94 279.63	(0.1)	0.001
194		$- 3d^2D$	238.57 238.36	(0.2)	$4 \cdot 10^{-4}$

TABLE I (continued)

No.	Ion; $x_i$ , eV; $\log T_i$	Transition	$\lambda$ , Å	$f_{12}$	$F_i$ , erg/cm <sup>2</sup> sec
195	O IV	$2p^2\ ^2D - 2p^3\ ^2D^\circ$	779.8	(0.1)	0.0015
196		— $3d\ ^2F^\circ$	260.38 260.56	(0.2)	$2 \cdot 10^{-4}$
197		$2p^2\ P^\circ - 4s\ ^2S$	202.9—203.0	(0.1)	$10^{-5}$
198		$2p^2\ ^4P - 2p^3\ ^4S^\circ$	625.130 625.852 624.617	(0.1)	0.01
199	Ne VI 151.9 5.52	$2p^2\ P^\circ - 2p^2\ ^2S$	435.65	(0.1)	$6 \cdot 10^{-4}$
200		— $2p^2\ ^2D$	433.18 562.80 558.74	0.17	$3 \cdot 10^{-4}$ 0.0014 $7 \cdot 10^{-4}$
201		— $2\ p^2\ ^2P$	401,94,399,82 401,14,401,14	(0.1)	0.0012
202		— $3s\ ^2S$	138.63 138.40	(0.1)	$5 \cdot 10^{-5}$
203		$2p^2\ ^2D - 3p^2\ P^\circ$	171.21 171.11	(0.1)	$2.4 \cdot 10^{-5}$ $1.2 \cdot 10^{-5}$
204	Na VII 208.4 5.7	$2p^2\ P^\circ - 2p^2\ ^2D$	491.95 486.74	0.15	$10^{-4}$
205		— $2p^2\ ^2P$	354.95 353.29 352.28 350.65	(0.05)	$4 \cdot 10^{-5}$
206		— $2s\ ^2S$	381.3	(0.1)	$8 \cdot 10^{-5}$
207		— $3s\ ^2S$	105.35	(0.1)	$5 \cdot 10^{-6}$
208		— $3d\ ^2D$	94.47 94.29	(0.5)	$2 \cdot 10^{-6}$
209	Mg VIII 266.0 5.82	$2p^2\ P^\circ - 2p^2\ ^2S$	339.01 335.3	(0.1)	0.0016 $8 \cdot 10^{-4}$
210		— $2p^2\ ^2P$	311.78 313.73 315.02 317.01	0.08 0.14 0.22 0.055	0.0016 0.0028 0.0044 0.0012
211		— $2p^2\ ^2D$	436.72 436.68 430.47	0.13	0.003
212		— $3s\ ^2S$	82.6 82.82	(0.1)	$8 \cdot 10^{-5}$
213		— $3p^2\ P$	71.00 70.95 71.17 71.12	(0.05)	$4 \cdot 10^{-5}$

TABLE I (continued)

No.	Ion; $\lambda_i$ , eV; $\log T_i$	Transition	$\lambda$ , Å	$f_{12}$	$F_{12}$ , erg/cm <sup>2</sup> sec
214	Mg VIII	$-3p^3S$	68.45	(0.1)	$7 \cdot 10^{-5}$
215			68.41		
		$-3p^3D$	69.42	(0.5)	$3.6 \cdot 10^{-4}$
			69.47		
216		$-3d^3D$	69.58	(0.5)	$5 \cdot 10^{-4}$
			74.9		
217		$2s^1 3P$	67.24	(0.1)	$6 \cdot 10^{-5}$
			67.25		
		$2p^2 3P - 2p^3 3D^\circ$	67.3	(0.2)	$5 \cdot 10^{-4}$
218			680.3		
219		$-2p^3 3P^\circ$	490.8	(0.1)	$3 \cdot 10^{-4}$
220			442.2		
221		$2p^2 3S - 2p^3 3P^\circ$	342.2	(0.1)	$3 \cdot 10^{-4}$
222		$2p^2 3D - 2p^3 3P^\circ$	342.2	(0.05)	$2 \cdot 10^{-4}$
			352.38		
		$2p^2 4P - 2p^3 4S^\circ$	353.84	(0.05)	$8 \cdot 10^{-4}$
			356.00		
223	Al IX	$2p^2 3P^\circ - 2p^3 3S$	305.1	(0.05)	$1.8 \cdot 10^{-4}$
224			392.4—385.0	0.12	$6 \cdot 10^{-4}$
225	Si X 401.3 6.08	$2p^2 3P^\circ - 2p^3 3S$	277.27	0.012	$3 \cdot 10^{-4}$
			272.00	0.04	$9 \cdot 10^{-4}$
226		$-2p^3 3D$	356.07	0.085	0.006
			347.43	0.09	0.006
227		$-2p^3 3P$	256.58	0.12	0.007
			253.81	0.06	0.0035
			258.39	0.18	0.011
			261.27	0.04	0.003
228		$-3p^3 3P$	48.39	(0.05)	$1.5 \cdot 10^{-4}$
			48.55		
229		$-3d^3 3D$	50.52	0.55	0.0012
			50.69	0.50	0.001
			50.70	0.055	$1.2 \cdot 10^{-4}$
230			280.0	(0.05)	0.002
231		$-2p^3 3D^\circ$	349.0	(0.1)	0.003
232		$2p^2 3D - 3d^3 3F^\circ$	52.61	(0.5)	$8 \cdot 10^{-4}$
			52.49		
233		$2p^2 3P - 2p^3 3D^\circ$	555.0	(0.1)	0.002
234		$-2p^3 3P^\circ$	392.0—399.3	(0.1)	$6 \cdot 10^{-4}$
235		$-3d^3 3D^\circ$	52.07	(0.5)	0.001
236		$-3s^3 3P^\circ$	56.63	(0.1)	$3 \cdot 10^{-4}$
			56.80		
237		$2p^2 3S - 2p^3 3P^\circ$	360.8	(0.1)	0.002
238		$-3d^3 3P^\circ$	54.57	(0.1)	$2 \cdot 10^{-4}$
239		$2p^2 4P - 2p^3 4S^\circ$	287.2	(0.05)	0.004

TABLE I (continued)

No.	Ion; $x_i$ , eV; $\log T_i$	Transition	$\lambda$ , Å	$f_{12}$	$F_t$ , erg/cm <sup>2</sup> sec
240	Si X 479.4 6.2	$-3s^2^4P^\circ$	54.52	(0.1)	$6 \cdot 10^{-4}$
			54.57		$3 \cdot 10^{-4}$
			54.60	(0.5)	$10^{-4}$
241			50.33		0.0025
242	P XI 479.4 6.2	$2p^2P^\circ - 2p^2^2D$	325.2	0.10	$6 \cdot 10^{-5}$
			315.3		$3 \cdot 10^{-5}$
243		$-2p^2^2S$	254.0	(0.05)	$3 \cdot 10^{-5}$
			247.9		
244		$-2p^2^2P$	240—232	(0.05)	$3 \cdot 10^{-5}$
245		$-3s^2^2S$	46.1	(0.1)	$6 \cdot 10^{-5}$
246	S XII 564.6 6.3	$2p^2P^\circ - 2p^2^2D$	(290)	0.09	$7 \cdot 10^{-4}$
			(302)		
247		$-2p^2^2S$	231.5	(0.05)	$3 \cdot 10^{-4}$
248		$-2p^2^2P$	(212)	(0.05)	0.0035
249		$-3s^2^2S$	(38)	(0.1)	$6 \cdot 10^{-5}$
250		$-3d^2^2D$	(33)	(0.5)	$3 \cdot 10^{-4}$
251		$2p^2^4P - 2p^2^4S^\circ$	239	(0.05)	$3 \cdot 10^{-4}$

## C I

252	C I 11.26 3.85	$2p^2^3P - 3s^3P^\circ$	1656—1657	0.52	0.3
253		$-2p^3^3D^\circ$	1560.3	0.2	0.024
			1561.4		
254		$-2p^3^3P^\circ$	1328.8	(0.1)	0.001
255		$-4s^3P^\circ$	1279.7	(0.1)	$5 \cdot 10^{-4}$
256		$-3d^3D^\circ$	1277.6	(0.5)	0.002
257		$-5d^3D^\circ$	1158.1	(0.1)	$2 \cdot 10^{-5}$
258		$-5d^3P^\circ$	1156.62		
			1156.50	0.3	0.018
			1156.06		
			1156.84		
259	N II 29.61 4.40	$2p^2^3P - 2p^3^3D^\circ$	1083.99	0.38	0.017
			1085.54		
			1084.57		
			1085.70		
260		$-2p^3^3P^\circ$	915.60	(0.4)	0.0015
			916.00		
			916.70		
261		$-2p^3^3S^\circ$	645.17	(0.4)	$10^{-4}$
			644.83		
			644.62		



TABLE I (continued)

No.	Ion; $x_i$ , eV; $\log T_i$	Transition	$\lambda$ , Å	$f_{12}$	$F_t$ , erg/cm <sup>2</sup> sec
262	N II	$2p^{21}D - 2p^{31}D^\circ$	775.96	(0.1)	0.001
263		$- 3s^1P^\circ$	746.98	(0.1)	$3 \cdot 10^{-4}$
264		$2p^{21}S - 3s^1P^\circ$	858.37	(0.1)	$3 \cdot 10^{-4}$
265	O III 54.93 4.80	$2p^{23}P - 2p^{33}P^\circ$	703.9—702.3	(0.1)	0.015
266		$- 2p^{33}D^\circ$	835.29	0.28	0.10
			832.93		
			833.74		
			835.10	(0.1)	0.004
267		$- 2p^{33}S^\circ$	507.68		
			508.18		
268		$- 3d^3D^\circ$	305.879	(0.5)	$5 \cdot 10^{-4}$
			305.836		
			305.769		
			305.703		
			305.656		
			305.596		
269		$- 3s^3P^\circ$	374.3—374.0	(0.2)	0.001
270		$2p^{21}D - 2p^{31}D^\circ$	597.82	(0.1)	0.008
			599.60	(0.05)	$3 \cdot 10^{-4}$
271		$- 2p^{31}P^\circ$	525.80		
272		$2p^{33}D^\circ - 2p^{43}P$	609.70	(0.05)	$1.5 \cdot 10^{-4}$
			610.75		
			610.04		
			610.85	(0.2)	0.01
273		$2p^{21}S - 2p^{31}P^\circ$	597.82		
274		$- 3s^1P^\circ$	434.98	(0.5)	0.01
275		$- 3d^1P^\circ$	345.31		
276	Ne V 126.4 5.37	$2p^{23}P - 2p^{33}P^\circ$	483.0	(0.1)	$8 \cdot 10^{-4}$
			481.4		
			480.4		
277		$- 2p^{33}D^\circ$	572.11	0.20	0.002
			572.34		
			569.8		
			568.42	(0.05)	$2 \cdot 10^{-4}$
278		$- 2s^3S^\circ$	359.4		
			358.5		
			358.0	(0.1)	$3 \cdot 10^{-5}$
279		$- 3s^3P^\circ$	167.67		
			167.48	(0.1)	0.001
280		$2p^{21}D - 2p^{31}D^\circ$	416.20		
281		$- 2p^{31}P^\circ$	365.59	(0.05)	$2 \cdot 10^{-4}$
282		$- 3s^1P^\circ$	173.93	(0.1)	$5 \cdot 10^{-5}$
283		$- 3d^1D^\circ$	151.42	(0.5)	$1.4 \cdot 10^{-4}$

TABLE I (continued)

No.	Ion; $x_i$ , eV; $\log T_4$	Transition	$\lambda$ , Å	$f_{12}$	$F_{12}$ , erg/cm <sup>2</sup> sec
284	Na VI 172.4 5.58	$2p^3^3P - 2p^3^3P^\circ$	414.3	(0.1)	$10^{-4}$
285		$- 2p^3^3D^\circ$	494.3 491.4	0.18	$1.4 \cdot 10^{-4}$
286		$- 2p^3^3S^\circ$	313.75 312.61 311.92	(0.05)	$2 \cdot 10^{-5}$
287		$2p^3^1D - 2p^3^1D^\circ$	361.25	0.1	$4 \cdot 10^{-5}$
288		$- 2p^3^1P^\circ$	317.6	(0.05)	$2 \cdot 10^{-5}$
289	Mg VII 255.3 5.75	$2p^2^3P - 2p^2^3P^\circ$	365.24	(0.1)	$1.7 \cdot 10^{-4}$
290		$- 2p^2^3D^\circ$	435.3 434.7 429.1	0.16	0.003
291		$- 2p^2^3S^\circ$	843.03	(0.1)	0.004
292		$- 2p^2^3S^\circ$	278.40	(0.05)	$6 \cdot 10^{-4}$
293		$- 3s^3P^\circ$	95.48 95.42	(0.1)	$1.5 \cdot 10^{-4}$
294		$2p^2^1D - 2p^2^1D^\circ$	319.0	(0.1)	0.0016
295		$- 2p^2^1P^\circ$	280.7	(0.05)	$6 \cdot 10^{-4}$
296		$- 3s^1P^\circ$	98.0	(0.1)	$1.5 \cdot 10^{-4}$
297		$2p^2^1S - 3s^1P^\circ$	102.3	(0.5)	$5 \cdot 10^{-4}$
298	Al VIII 285.1 5.92	$2p^3^3P - 2p^3^3D^\circ$	388 383.7 381.1	0.14	$4 \cdot 10^{-4}$
299		$- 2p^3^3S^\circ$	749.0	(0.1)	$4 \cdot 10^{-4}$
300		$- 3s^3P^\circ$	328.2—323.5	(0.3)	$7 \cdot 10^{-4}$
301		$2p^3^1D - 3s^1P^\circ$	251.3	(0.1)	$1.7 \cdot 10^{-4}$
302		$2p^3^1S - 3s^1P^\circ$	287.0	(0.1)	$2 \cdot 10^{-4}$
303	Si IX 351.8 6.05	$2p^2^3P - 2p^2^3P^\circ$	296.19 292.83 290.63	0.09 0.09 0.09	0.007 0.007 0.007
304		$- 2p^2^3S^\circ$	666.62	(0.01)	0.001
305		$- 2p^2^3D^\circ$	342.2 345.10 349.96	0.12 0.12 0.12	0.008 0.008 0.008
306		$- 2p^2^3S^\circ$	227.01 225.03 223.72	(0.1)	0.004
307		$- 3d^3P^\circ$	55.09 55.12 55.23	(0.1)	$3 \cdot 10^{-4}$
308		$- 3p^3D^\circ$	55.27 52.81 52.84	(0.5)	0.001

TABLE I (continued)

No.	Ion: $x_i$ , eV; $\log T_i$	Transition	$\lambda$ , Å	$f_{12}$	$F_{12}$ , erg/cm <sup>2</sup> sec
309	Si IX	$— 3d^3D^\circ$	55.30	0.71	0.002
			55.36		
			55.40		
310		$— 3p^3S^\circ$	53.80	(0.1)	$2 \cdot 10^{-4}$
			53.88		
			53.99		
311		$— 3s^3P^\circ$	61.50	0.04	$1.5 \cdot 10^{-4}$
			61.55		
			61.60		
			61.65		
312		$— 4d^3D^\circ$	61.85	(0.1)	$2 \cdot 10^{-4}$
			44.22		
			44.25		
313		$2p^2^1D — 2p^3^1P^\circ$	227.3	(0.1)	0.0036
314			258.1	(0.1)	0.0045
315		$— 3d^1P^\circ$	55.38	(0.1)	$3 \cdot 10^{-4}$
316		$— 3d^1D^\circ$	57.43	(0.1)	$3 \cdot 10^{-4}$
317		$— 3d^1F^\circ$	56.03	(0.5)	0.002
318		$— 3s^1P^\circ$	62.97	(0.1)	$4 \cdot 10^{-4}$
319		$2p^2^1S — 2p^3^1P^\circ$	259.7	(0.1)	0.0036
320		$2p^3^3D — 3d^3F^\circ$	58.91	(0.5)	0.0015
			59.00		
			59.08		
321	S XI 506.4 6.25	$2p^2^3P — 2p^3^3D^\circ$	293—282	0.11	0.0015
322			239.81 247.16		
		$— 2p^3^3P^\circ$	242.83 246.90	(0.3)	0.004
			242.57		
			186.83		
323		$— 2p^3^3S^\circ$	191.26	(0.1)	0.0015
			188.67		
324		$— 3d^3D^\circ$	(39.28)	(0.5)	$3 \cdot 10^{-4}$
325	Ca XV 898.3 6.55	$2p^2^3P — 2p^3^3D^\circ$	(228)	0.8	$5 \cdot 10^{-4}$
			(227)		$5 \cdot 10^{-4}$
			(218)		$5 \cdot 10^{-4}$
			(210)		$5 \cdot 10^{-4}$
326		$— 2p^3^3P^\circ$	(185)	(0.1)	$4 \cdot 10^{-5}$
327		$— 2p^3^3S^\circ$	(144)	(0.05)	$2 \cdot 10^{-5}$
N I					
328	N I 14.54 3.91	$2p^3^4S^\circ — 2p^4^4P$	1135.00	1.0	$3 \cdot 10^{-4}$
			1134.42		
			1134.17		
329		$— 3s^4P$	1199.55 1200.71	(0.5)	0.001

TABLE I (continued)

No.	Ion; $x_i$ , eV; $\log T_i$	Transition	$\lambda$ , Å	$f_{12}$	$F_{12}$ , erg/cm <sup>2</sup> sec
330	N I	— $4s^4P$	964.0—965.1	(0.4)	$10^{-6}$
331		$2p^3^2D^\circ$ — $3d^2P$	1171.1	(0.4)	$3 \cdot 10^{-6}$
332		— $3s^2P$	1492.5	(0.1)	$3 \cdot 10^{-6}$
333		— $6d^2D$	1051.89	(0.1)	$3 \cdot 10^{-6}$
334		— $8s^2P$	1044.69	(0.4)	$3 \cdot 10^{-6}$
335		— $7d^2F$	1044.13	(0.3)	$10^{-5}$
336		— $7d^2D$	1043.58 1043.12	(0.3)	$2 \cdot 10^{-5}$
337	O II 35.15 4.50	$2p^3^4S^\circ$ — $2p^4^4P$	843.46 833.33 832.75	0.77	0.06 0.04 0.02
338		— $3s^4P$	539.8—539.1	(0.1)	0.001
339		— $3d^4P$	429.9—430.2	(0.5)	$5 \cdot 10^{-4}$
340		$2p^3^2D^\circ$ — $2p^4^2D$	718.56 718.48	(0.1)	0.006
341		$2p^3^2P^\circ$ — $2p^4^2D$	796.66	(0.2)	0.006
342	Ne IV 97.16 5.20	$2p^3^4S^\circ$ — $2p^4^4P$	543.89 542.07 541.13	0.49	0.0012 $8 \cdot 10^{-4}$ $4 \cdot 10^{-4}$
343		$2p^3^2D^\circ$ — $2p^4^2D$	469.866 469.773 469.820 469.921	(0.1)	$5 \cdot 10^{-4}$
344		$2p^3^2P^\circ$ — $2p^4^2D$	521.3	(0.2)	0.001
345	Na V 138.6 5.43	$2p^3^4S^\circ$ — $2p^4^4P$	463.26 461.05 459.90	0.42	$2 \cdot 10^{-4}$
346		$2p^3^2D^\circ$ — $2p^4^2D$	400.72	(0.1)	$4 \cdot 10^{-5}$
347		$2p^3^2P^\circ$ — $2p^4^2D$	445.05 445.19	(0.2)	$8 \cdot 10^{-5}$
348	Mg VI 186.9 5.63	$2p^3^4S^\circ$ — $2p^4^4P$	403.32 400.68 399.29	0.36	0.002 0.0015 $8 \cdot 10^{-4}$
349		$2p^3^2P^\circ$ — $2p^4^3D$	388.02 387.79	(0.2)	0.002
350		— $2p^4^2S$	314.5	(0.05)	$4 \cdot 10^{-4}$
351		$2p^3^4S^\circ$ — $3p^4^4P$	111.55 111.75 111.86	0.5	$3 \cdot 10^{-4}$
352		$2p^3^2D^\circ$ — $2p^4^2D$	349.1	(0.1)	$7 \cdot 10^{-4}$

TABLE I (continued)

No.	Ion; $x_i$ , eV; $\log T_i$	Transition	$\lambda$ , Å	$f_{12}$	$F_{12}$ , erg/cm <sup>2</sup> sec
353	Al VII 241.9 5.82	$2p^3\ ^4S^\circ - 2p^4\ ^4P$	356.9	0.32	$2 \cdot 10^{-4}$
			353.8		$1 \cdot 10^{-4}$
			352.2		$5 \cdot 10^{-5}$
354		$- 3s^4\ ^4P$	86.9—87.2	(0.5)	$4 \cdot 10^{-5}$
355		$2p^3\ ^2D^\circ - 2p^4\ ^2D$	309.0	(0.1)	$6 \cdot 10^{-5}$
356	Si VIII 303.9 5.96	$2p^3\ ^4S^\circ - 2p^4\ ^4P$	319.83	0.14	0.006
			316.20	0.10	0.004
			314.31	0.05	0.002
357		$- 3s^4\ ^4P$	69.63	(0.1)	$2 \cdot 10^{-4}$
358		$- 3p^4\ ^4P$	58.88	(0.5)	$4 \cdot 10^{-4}$
359		$- 3d^4\ ^4P$	60.99		
			61.02	1.18	$8 \cdot 10^{-4}$
			61.07		
360		$2p^3\ ^2P^\circ - 2p^4\ ^2D$	308.26	(0.2)	0.0025
361		$- 2p^4\ ^2S$	(251)	(0.05)	$5 \cdot 10^{-4}$
362		$- 2p^4\ ^2P$	233.16	(0.1)	0.001
			235.56		
363		$- 3s^2\ ^2P$	74.42	(0.1)	$1 \cdot 10^{-4}$
364		$- 3d^2\ ^2P$	62.81		
			62.85	(0.3)	$4 \cdot 10^{-4}$
365		$- 3d^2\ ^2D$	63.23		
			63.27	(0.5)	$6 \cdot 10^{-4}$
366		$2p^3\ ^2D^\circ - 2p^4\ ^2D$	277.05	(0.05)	0.001
			276.84		
367		$- 2p^4\ ^2P$	214.75	(0.05)	$5 \cdot 10^{-4}$
			216.92		
368		$- 2p^4\ ^2S$	229.8	(0.05)	$5 \cdot 10^{-4}$
			230.2		
369		$- 3s^2\ ^2P$	72.23		
			72.21	(0.1)	$2 \cdot 10^{-4}$
			72.42		
370		$- 3d^2\ ^2D$	61.80		
			61.85	(0.3)	$2.5 \cdot 10^{-4}$
			61.90		
			61.91		
371		$- 3d^2\ ^2F$	63.73	(0.5)	$4 \cdot 10^{-4}$
			63.90		
372		$- 3d'\ ^2D$	63.22	(0.1)	$10^{-4}$
373	S X 448.6 6.20	$2p^3\ ^4S^\circ - 2p^4\ ^4P$	259.56	0.08	0.003
			257.30		0.004
			264.28		0.003

TABLE I (continued)

No.	Ion; $x_i$ , eV; $\log T_i$	Transition	$\lambda$ , Å	$f_{12}$	$F_{12}$ , erg/cm <sup>2</sup> sec
374	S X	— $3s^4P$	47.65	(0.5)	0.0015
			47.79		
375		— $3d^4P$	42.51	1.74	0.003
			42.54		
			42.58		
376		$2p^3^2P^\circ - 3d^2D$	44.37	(0.5)	0.003
			44.39		
			44.42		
377	Ar XII 621.1 6.4	$2p^3^4S^\circ - 2p^4^4P$	215.49	0.24	$1 \cdot 10^{-4}$
			218.29		$1 \cdot 10^{-4}$
			224.25	0.5	$1 \cdot 10^{-4}$
			(33)		$5 \cdot 10^{-5}$
378		— $3s^4P$			
379	Ca XIV 821.2 6.48	$2p^3^4S^\circ - 2p^4^4P$	(197)	0.18	$1.5 \cdot 10^{-4}$
			(193)		
			(191)		
			(22)	0.5	$2 \cdot 10^{-5}$
380		— $3s^4P$			

## O I

381	O I 13.61 3.85	$2p^4^3P - 3s^3S^\circ$	1302.2	(0.5)	0.009
			1306.2		
			1305.0	(0.1)	0.002
			1355.7		
382		— $3s^5S^\circ$	1358.7		
383		— $4s^3S^\circ$	1040.94	(0.1)	$6 \cdot 10^{-5}$
			1039.23		
			1041.69	(0.1)	$4 \cdot 10^{-5}$
384		— $4d^3D^\circ$	1025.77		
			1027.43		
			1028.16		
385	Ne III 64.43 4.90	$2p^4^3P - 2p^5^3P^\circ$	488.87	0.46	$9 \cdot 10^{-4}$
			488.10		
			489.64		
			489.50		
			490.31		
			491.05		
		— $3s^3S^\circ$	313.0	(0.1)	$2 \cdot 10^{-5}$
386		$2p^4^1S - 2p^5^1P^\circ$	427.8	(0.2)	$2.5 \cdot 10^{-4}$
387		$2p^4^1D - 2p^5^1P^\circ$	379.3	(0.1)	$6 \cdot 10^{-5}$
388					

TABLE I (continued)

No.	Ion; $x_i$ , eV; $\log T_i$	Transition	$\lambda$ , Å	$f_{12}$	$F_{\tau}$ , erg/cm <sup>2</sup> sec
389	Na IV 98.9 5.2	$2p^4 {}^3P - 2p^5 {}^3P^\circ$	408.68 412.24 411.33 409.61 410.54 410.37	0.38	$8 \cdot 10^{-5}$
390	Mg V 141.2 5.4	$2p^4 {}^3P - 2p^5 {}^3P^\circ$	351.09 352.20 353.10 353.30 354.22 355.32	0.33	0.002
391		$-3s {}^3S^\circ$	146.62 146.08 146.46	(0.1)	$2,5 \cdot 10^{-5}$
392		$-3s {}^3D^\circ$	137.41 137.75 137.88	(0.5)	$10^{-4}$
393		$-3d {}^3D^\circ$	121.92 121.64 122.03 115.8 114.8	(0.5)	$6 \cdot 10^{-5}$
394	Al VI	$2p^4 {}^3P - 2p^5 {}^3P^\circ$	307.2—310.3	0.29	$1,5 \cdot 10^{-4}$
395	190.4	$2p^4 {}^1D - 2p^5 {}^1P^\circ$	243.8	(0.05)	$2 \cdot 10^{-5}$
396	5.66	$2p^4 {}^1S - 2p^5 {}^1P^\circ$	275.35	(0.2)	$5 \cdot 10^{-5}$
397	Si VII 246.4 5.82	$2p^4 {}^3P - 2p^5 {}^3P^\circ$	275.35 278.44 276.8 275.7 274.1 272.6	0.25	0,002 $7 \cdot 10^{-4}$ $5 \cdot 10^{-4}$ $5 \cdot 10^{-4}$ $5 \cdot 10^{-4}$ $7 \cdot 10^{-4}$ $5 \cdot 10^{-4}$
398		$-3s {}^1 {}^3D^\circ$	81.62	(0.5)	$5 \cdot 10^{-4}$
399		$-3s'' {}^3P^\circ$	79.26 79.62 79.52 79.24 79.49	(0.1)	$9 \cdot 10^{-5}$
400		$-3d {}^3D^\circ$	73.13 73.12 73.42 73.35	(0.5)	$3 \cdot 10^{-4}$
401		$-3d {}^1 {}^3D^\circ$	70.03 70.02	(0.5)	$3 \cdot 10^{-4}$

TABLE I (continued)

No.	Ion; $x_i$ , eV; $\log T_i$	Transition	$\lambda$ , Å	$f_{12}$	$F_{12}$ , erg/cm <sup>2</sup> sec
402	Si VII	— $3d^1\ ^3P^\circ$	69.60 69.66 69.78 69.80 69.86 69.87	(0.1)	$5 \cdot 10^{-5}$
403		— $3d^1\ ^3S^\circ$	69.38 69.58	(0.1)	$5 \cdot 10^{-5}$
404		$2s^4\ ^1S - 2p^5\ ^1P^\circ$	246.1	(0.2)	0.0015
405		$2p^4\ ^1D - 2p^5\ ^1P^\circ$	217.8	(0.05)	$4 \cdot 10^{-4}$
406	S IX 379.0 6.1	$2p^4\ ^3P - 2p^5\ ^3P^\circ$	223.27 (222) 224.7 225.23 (228)	0.21	0.0015 0.0015 0.0015 0.0015 0.0015
407		— $3s\ ^3D^\circ$	54.18	(0.5)	0.001
408		— $3s\ ^3S^\circ$	56.1	(0.1)	$3 \cdot 10^{-4}$
409		$2p^4\ ^1D - 2p^5\ ^1P^\circ$	(555)	(0.05)	0.0025
410		$2p^4\ ^1S - 2p^5\ ^1P^\circ$	(488)	0.2	0.008
411	Ar XI 539.5 6.3	$2p^4\ ^3P - 2p^5\ ^3P^\circ$	(188) (190) (193) (194) (195)	0.18	$3 \cdot 10^{-4}$
412		— $3s\ ^3S^\circ$	39.7	(0.1)	$2 \cdot 10^{-5}$
413	Ca XIII 728.8 6.42	$2p^4\ ^3P - 2p^5\ ^3P^\circ$	156.70 159.87  161.748 162.98 164.15 168.412	0.15	$2 \cdot 10^{-4}$
414		— $3s\ ^3S^\circ$	29.6	(0.1)	$1 \cdot 10^{-5}$
F I					
415	Mg IV 109.3	$2p^5\ ^2P^\circ - 2p^6\ ^2S$	321.00 323.31	0.22	$4 \cdot 10^{-4}$ $3 \cdot 10^{-4}$
416	5.25	— $3s\ ^2P$	180.80 180.62 180.07 181.34	(0.3)	$10^{-4}$



TABLE I (continued)

No.	Ion; $x_i$ , eV; $\log T_i$	Transition	$\lambda$ , Å	$f_{12}$	$F_t$ , erg/cm <sup>2</sup> sec
417	Al V 153.8 5.51	$2p^5\ ^2P^\circ - 2p^6\ ^2S$	278.70 281.40	0.19	$6 \cdot 10^{-5}$ $3 \cdot 10^{-5}$
418	Si VI 205.1 5.70	$2p^6\ ^2P^\circ - 2p^6\ ^2S$	246.00 249.13	0.17	$8 \cdot 10^{-4}$ $4 \cdot 10^{-4}$
419		$- 3s\ ^2P$	99.60 99.46 99.10 99.97		$1.8 \cdot 10^{-4}$
			96.02	(0.3)	
420		$- 3s^1\ ^2D$	96.49	(0.5)	$2.5 \cdot 10^{-4}$
421		$- 3s''\ ^2S$	91.37 91.80	(0.1)	$4 \cdot 10^{-5}$
422		$- 3d\ ^2P$	83.01 83.36 83.64	(0.1)	$3 \cdot 10^{-5}$
423		$- 3d\ ^2D$	83.26 83.61 83.43	(0.5)	$1.5 \cdot 10^{-4}$
424		$- 5d^1\ ^2P$	65.21	(0.1)	$1 \cdot 10^{-5}$
425	S VIII 328.8 6.00	$2p^5\ ^2P^\circ - 2p^6\ ^2S$	198.6 202.6	0.13	$5 \cdot 10^{-4}$ $2 \cdot 10^{-4}$
426		$- 3s\ ^2P$	63.30	(0.3)	$1.8 \cdot 10^{-4}$
427		$- 3s^1\ ^2D$	61.60	(0.5)	$3 \cdot 10^{-4}$
428		$- 3s''\ ^2S$	59.2	(0.1)	$6 \cdot 10^{-5}$
429		$- 3d\ ^2P$	54.3	(0.3)	$1.5 \cdot 10^{-4}$
430		$- 3d\ ^2D$	54.12	(0.5)	$2.5 \cdot 10^{-4}$
431		$- 3d^1\ ^2P$	53.0	(0.3)	$1.5 \cdot 10^{-4}$
432		$- 3d'\ ^2D$	52.9	(0.3)	$1 \cdot 10^{-4}$
433		$- 4d'\ ^2S$	44.5	(0.1)	$2 \cdot 10^{-5}$
434	Ar X 480 6.25	$2p^5\ ^2P^\circ - 2p^6\ ^2S$	(166) (171)	0.1	$2 \cdot 10^{-4}$ $1 \cdot 10^{-4}$
435		$- 3s\ ^2P$	43.8	(0.3)	$1 \cdot 10^{-4}$
436		$- 3d\ ^2P$	(50)	(0.3)	$1 \cdot 10^{-4}$
437		$- 5d\ ^2P$	(45)	(0.1)	$3 \cdot 10^{-5}$
438		$- 3s\ (^4P, ^2P)$	44.0 44.3 44.5	0.1	$3 \cdot 10^{-5}$

TABLE I (continued)

No.	Ion; $x_i$ , eV; $\log T_i$	Transition	$\lambda$ , Å	$f_{12}$	$F_{\tau}$ , erg/cm <sup>2</sup> sec
439	Ca XII 655	$2p^6\ ^2P^\circ - 2p^6\ ^2S$	141.036	0.09	$3 \cdot 10^{-4}$
440	6.28	$- 3s\ ^2P$	147.273	(0.3)	$5 \cdot 10^{-5}$
441		$- 3d\ ^2P$	(42)	(0.3)	$8 \cdot 10^{-5}$
442		$- 3s\ ^1D$	31.66		
			31.96	(0.5)	$1 \cdot 10^{-4}$
443		$- 3s\ ^2P$	32.78		
			32.60	(0.1)	$2 \cdot 10^{-5}$
444		$- 3d''\ ^2D$	27.38		
			27.41	(0.5)	$6 \cdot 10^{-5}$
			27.61		
445		$- 5d\ ^2P$	(34)	(0.1)	$2 \cdot 10^{-5}$
Ne I					
446	Si V	$2p^6\ ^1S - 3s\ ^1P^\circ$	117.9	0.19	$4 \cdot 10^{-5}$
447	166.7	$- 3s\ ^3P^\circ$	119.0	0.021	$6 \cdot 10^{-6}$
448	5.55	$- 3d\ ^1P^\circ$	96.44		
			97.14	0.84	$1.3 \cdot 10^{-5}$
449		$- 4s\ ^1P^\circ$	90.45		
			90.85	(0.3)	$5 \cdot 10^{-5}$
450	S VII	$2p^6\ ^1S - 3s\ ^1P^\circ$	72.03	0.17	$10^{-4}$
451	281	$- 3d\ ^1P^\circ$	60.80	1.42	$4 \cdot 10^{-4}$
452	5.92	$- 4s\ ^1P^\circ$	54.6	(0.1)	$2 \cdot 10^{-5}$
453		$- 3s\ ^3P^\circ$	72.66	0.036	$2.5 \cdot 10^{-5}$
454		$- 4d\ ^1P^\circ$	52.10	(0.1)	$1.5 \cdot 10^{-5}$
455	Ar IX	$2p^6\ ^1S - 3s\ ^1P^\circ$	48.73	(0.5)	$3 \cdot 10^{-4}$
456	422	$- 3s\ ^3P^\circ$	49.18		
	6.16		48.3	(0.1)	$7 \cdot 10^{-5}$
457	Ca XI	$2p^6\ ^1S - 3s\ ^1P^\circ$	35.21	0.11	$3 \cdot 10^{-5}$
458	592.5	$- 3d\ ^1P^\circ$	30.87	2.05	$3 \cdot 10^{-4}$
459	6.25	$- 3s\ ^3P^\circ$	35.58	0.066	$1.5 \cdot 10^{-5}$
460		$- 3d\ ^3P^\circ$	31.26	0.0074	$1 \cdot 10^{-6}$
461		$- 3d\ ^3D^\circ$	30.45	0.26	$5 \cdot 10^{-5}$
462		$- 3p\ ^3P^\circ$	27.08	(0.1)	$1 \cdot 10^{-5}$
463		$- 3p\ ^1P^\circ$	26.96	(0.5)	$6 \cdot 10^{-5}$
464		$- 4s\ ^3P^\circ$	26.64	(0.1)	$1 \cdot 10^{-5}$
465		$- 4s\ ^1P^\circ$	26.44	(0.3)	$3 \cdot 10^{-5}$
466		$- 4d\ ^1P^\circ$	25.52	(0.3)	$3 \cdot 10^{-5}$
467		$- 4d\ ^3D^\circ$	25.33	(0.1)	$2 \cdot 10^{-5}$

TABLE I (continued)

No.	Ion; $x_i$ , eV; $\log T_i$	Transition	$\lambda$ , Å	$f_{12}$	$F_t$ , erg/cm <sup>2</sup> sec
468	Fe XVII 1266 (6.52—6.96)	$2p^6 1S - 3s^3 P^\circ$	17.05	0.082	$8 \cdot 10^{-6}$
469		$- 3s^1 P^\circ$	16.77	0.07	$6 \cdot 10^{-6}$
470		$- 3d^1 P^\circ$	15.26	2.24	$1,3 \cdot 10^{-4}$
471		$- 3d^3 P^\circ$	15.45	0.023	$1,2 \cdot 10^{-6}$
472		$- 3d^3 D^\circ$	15.01	0.66	$4 \cdot 10^{-5}$
473		$- 3p^3 P^\circ$	13.89	(0.4)	$4 \cdot 10^{-6}$
474		$- 3p^1 P^\circ$	13.82	(0.5)	$1,6 \cdot 10^{-5}$
475		$3s^3 P - 3p^3 P^\circ$	74.45	(0.1)	$10^{-6}$
Na I					
476	Mg II 15.03 4.05	$3s^2 S - 3p^2 P^\circ$	2795.5 2802.7	0.9	[12] [6]
477		$- 4p^2 P^\circ$	1239.8 1240.4	(0.5)	0.040 0.005
478		$- 5p^2 P^\circ$	1026.0 1026.1	(0.4)	$10^{-4}$ $5 \cdot 10^{-5}$
479		$3p^2 P^\circ - 5s^2 S$	1753.6	(0.4)	$2 \cdot 10^{-4}$
480	Al III 28.44 4.40	$3s^2 S - 3p^2 P^\circ$	1854.7 1862.8	0.8	0.08
481		$- 4p^2 P^\circ$	695.82 696.21	(0.5)	$7,5 \cdot 10^{-5}$
482	Si IV 45.13 4.75	$3s^2 S - 3p^2 P^\circ$	1393.7 1402.7	0.7	0.03 0.015
483		$- 4p^2 P^\circ$	457.82 458.16	(0.5)	$2 \cdot 10^{-4}$ $1 \cdot 10^{-4}$
484		$3p^2 P^\circ - 3d^2 D$	1128.3	(0.2)	$3 \cdot 10^{-4}$
485		$- 4s^2 S$	815.05 818.03	(0.1)	$1 \cdot 10^{-4}$
486		?	1151.60	?	$\sim 0.001$
487		?	1156.58	?	$\sim 2 \cdot 10^{-4}$
488		S VI 88.03 5.18	$3s^2 S - 3p^2 P^\circ$	933.38 944.52	0.7
489	$- 4p^2 P^\circ$		249	(0.5)	$1,5 \cdot 10^{-4}$
490	$3p^2 P^\circ - 3d^2 D$		706.5 712.7	(0.2)	$10^{-4}$
491	Cl VII 96.75 5.2	$3s^2 S - 3p^2 P^\circ$	800.7 813.7	0.6	$3 \cdot 10^{-4}$ $1,5 \cdot 10^{-4}$

TABLE I (continued)

No.	Ion; $x_i$ , eV; $\log T_i$	Transition	$\lambda$ , Å	$f_{12}$	$F_t$ , erg/cm <sup>2</sup> sec
492	Ar VIII 143.5 5.45	$3s^2S - 3p^2P^\circ$	700.4 714.0	0.6	$6 \cdot 10^{-4}$ $3 \cdot 10^{-4}$
493	K IX 175.9 5.59	$3s^2S - 3p^2P^\circ$	621.4 636.3	0.6	$10^{-5}$ $5 \cdot 10^{-6}$
494	Ca X 211.3	$3s^2S - 3p^2P^\circ$	557.74 574.00	0.6	0.001 $6 \cdot 10^{-4}$
495	5.68	$-4p^2P^\circ$	110.96 111.20	(0.5)	$5 \cdot 10^{-5}$
496		$3d^2D - 5f^2F^\circ$	118.15 118.22	(0.1)	$6 \cdot 10^{-6}$
497	Ti XII 291.5 5.93	$3s^2S - 3p^2P^\circ$	460.9 480.1	0.5	$1.6 \cdot 10^{-5}$ $8 \cdot 10^{-6}$
498	Cr XIV 384.2 6.12	$3s^2S - 3p^2P^\circ$	390.1 412.5	0.5	$6 \cdot 10^{-4}$ $3 \cdot 10^{-4}$
499	Mn XV 435 6.22	$3s^2S - 3p^2P^\circ$	361.5 385.4	0.5	$1 \cdot 10^{-4}$ $5 \cdot 10^{-5}$
500	Fe XVI 48.9	$3s^2S - 3p^2P^\circ$	335.4 361.7	0.55	0.008 0.004
501	6.28	$-4p^2P^\circ$	50.35 50.56	0.24	0.001 $5 \cdot 10^{-4}$
502		$3p^2P^\circ - 3d^2D$	(250) 261.57 (264)	(0.1)	$10^{-4}$ $5 \cdot 10^{-4}$ $4 \cdot 10^{-4}$
503		$-4s^2S$	63.72 62.88	(0.1)	$8 \cdot 10^{-5}$ $1.6 \cdot 10^{-4}$
504		$-5d^2D$	40.15 39.83	(0.5)	$5 \cdot 10^{-4}$
505		$3d^2D - 4f^2F^\circ$	66.26 66.37	(0.1)	$4 \cdot 10^{-5}$ $2 \cdot 10^{-5}$
506		$-5f^2F^\circ$	46.72 46.66	(0.5)	$5 \cdot 10^{-4}$
507	Ni XVIII 607	$3s^2S - 3p^2P^\circ$	293.3 322.0	0.4	$2 \cdot 10^{-4}$ $1 \cdot 10^{-4}$
508	6.43	$3d^2D - 4f^2F^\circ$	52.72 52.62	(0.1)	$2 \cdot 10^{-5}$
509		$3p^2P^\circ - 4d^2D^\circ$	44.35 43.81	(0.5)	$4 \cdot 10^{-5}$

TABLE I (continued)

No.	Ion; $\lambda_i$ , eV; $\log T_i$	Transition	$\lambda$ , Å	$f_{12}$	$F_{12}$ , erg/cm <sup>2</sup> sec
Mg I					
510	Al II 18.82	$3s^2 1S - 3p^1 P^\circ$	1670.9	1.5	0.06
511	4.10	$- 3p^3 P^\circ$	2669.2	(0.01)	0.01
512	Si III 33.46	$3s^2 1S - 3p^1 P^\circ$	1206.5	1.1	0.07
513		$- 2p^3 P^\circ$	1895.5	(0.01)	0.003
514	4.40	$3p^3 P^\circ - 4s^3 S$	997.39 994.79 993.52	(0.1)	$2 \cdot 10^{-5}$
515	S V 72.5	$3s^2 1S - 3p^1 P^\circ$	786.5	(0.7)	0.003
516	5.00	$- 3p^3 P^\circ$	1188.7— —1203.8	(0.01)	$1.5 \cdot 10^{-4}$
517	Ar VII 124	$3s^2 1S - 3p^1 P^\circ$	585.75	(0.6)	$6 \cdot 10^{-4}$
518	5.35	$3p^3 P^\circ - 3d^3 D$	475.66 479.38	(0.5)	$2 \cdot 10^{-4}$ $1 \cdot 10^{-4}$
519		$- 4s^3 S$	249.89 250.94	(0.1)	$8 \cdot 10^{-6}$
520	Ca IX 188.2	$3s^2 1S - 3p^1 P^\circ$	466.2	(0.6)	$6 \cdot 10^{-4}$
521	5.63	$- 3p^3 P^\circ$	678.6—693.8	(0.01)	$3 \cdot 10^{-5}$
522	Fe XV 457	$3s^2 1S - 3p^1 P^\circ$	284.1	(0.5)	0.05
523		$- 3p^3 P^\circ$	414.1	(0.1)	0.01
524	6.18	$- 4p^1 P^\circ$	52.91	0.41	0.007
525		$3p^3 P^\circ - 3d^3 D$	231.50	(0.3)	0.018
526		$- 4d^3 D$	55.8 56.3 56.2	(0.5)	$6 \cdot 10^{-3}$
527		$3d^3 D - 4f^3 F^\circ$	69.95 69.99 70.05	(0.1)	0.001
528		$- 5f^3 F^\circ$	50.08 50.12 50.06	(0.2)	$8 \cdot 10^{-4}$
529		$4d^3 D - 5f^3 F^\circ$	154.4	(0.5)	$5 \cdot 10^{-4}$
530	Ni XVII 560	$3s^2 1S - 3p^1 P^\circ$	(255)	1.0	$8 \cdot 10^{-4}$
	6.4				

TABLE I (continued)

No.	Ion; $x_i$ , eV; $\log T_i$	Transition	$\lambda$ , Å	$f_{12}$	$F_t$ , erg/cm <sup>2</sup> sec
Al I					
531	Si II 16.34	$3p^2P^\circ - 3s^2S$	1523.4	(0.1)	0.008
532	4.0	$- 3p^2D$	1526.7 1817.1 1808.2	0.68	0.004 0.30 0.15
533	S IV 47.29	$3p^2P^\circ - 3p^2S$	816.0 809.7	(0.5)	0.001 $6 \cdot 10^{-4}$
534	4.67	$- 3p^2D$	1062.7 1073.3	0.6	0.006
535		$- 3p^2P$	(749) (744)	(0.05)	$10^{-4}$
536	Ar VI 91.41	$3p^2P^\circ - 3p^2S$	596.69 588.92	(0.5)	$2 \cdot 10^{-4}$ $1 \cdot 10^{-4}$
537	5.15	$- 3p^2P$	544.73 548.91 551.37 555.64	(0.2)	$1.5 \cdot 10^{-4}$
538		$- 3p^2D$	462.15 457.48 462.01	(0.5)	$2 \cdot 10^{-4}$
539	Ca VIII 148.1	$3p^2P^\circ - 3p^2S$	471.1 461.7	(0.5)	$4 \cdot 10^{-4}$ $2 \cdot 10^{-4}$
540	5.47	$- 3p^2D$	596.9 582.8	(0.5)	$6 \cdot 10^{-4}$ $3 \cdot 10^{-4}$
541	Fe XIV 390	$3p^2P^\circ - 3p^2S$	288.7 274.3	0.22 0.005	0.025 $5 \cdot 10^{-4}$
542	6.12	$- 3p^2P$	251.8 264.5 270.5	0.18 0.40 0.13	0.015 0.030 0.010
543		$- 3p^2D$	(366) (356) 344.6	0.05	0.008 0.004 0.008
544		$- 3d^2D$	211.3 219.1	0.25 0.50	0.02 0.04
545		$- 4s^2S$	71.43 72.4	(0.1)	$7 \cdot 10^{-4}$ 0.0015
546		$- 4d^2D$	58.96 59.58	0.13 0.33	0.0015 0.003

TABLE I (continued)

No.	Ion; $x_i$ , eV; $\log T_i$	Transition	$\lambda$ , Å	$f_{12}$	$F_{12}$ , erg/cm <sup>2</sup> sec
547	Ni XVI (480) 6.3	$2p^2P^\circ - 3p^2S$	250	(0.07)	$5 \cdot 10^{-5}$
			242		$1 \cdot 10^{-4}$
548		$- 3p^2P$	236	(0.4)	$4 \cdot 10^{-4}$
			233		$2 \cdot 10^{-4}$
549		$- 3p^2D$	312	(0.05)	$6 \cdot 10^{-5}$
			300		$3 \cdot 10^{-5}$
550		$- 3d^2D$	199	(0.3)	$2 \cdot 10^{-4}$
			190		$1 \cdot 10^{-4}$

## Si I

551	S III 34.7 4.48	$3p^2P - 3p^3P^\circ$ $- 3p^3D^\circ$	1012.6	(0.1)	0.001
552			1190.21		0.002
			1191.04		0.004
			1191.43		0.0015
			1200.95		0.008
		$- 3d^3P^\circ$ $- 3p^3S^\circ$ $- 3d^3D^\circ$ $3p^2S - 3p^3P^\circ$ $3p^2D - 3p^3P^\circ$	1201.70	(0.6)	0.0015
			1202.1		$1 \cdot 10^{-4}$
553			700.29		$3 \cdot 10^{-4}$
554			724.3—725.9		$2 \cdot 10^{-4}$
555			677.8—680.7		$2 \cdot 10^{-4}$
556			911.8	(0.2)	0.001
557			796.7	(0.05)	$10^{-4}$
558	Ar V 75.0 5.03	$2p^2P - 3p^3D^\circ$	822.16	(0.5)	$6 \cdot 10^{-4}$
			827.06		
			827.35		
			834.88		
			835.79		
		$- 3p^3P^\circ$	836.13	(0.1)	$1 \cdot 10^{-4}$
559			705.35		
			709.20		
			715.60		
			715.61		
560		$- 3p^3S^\circ$	527.69	(0.05)	$2 \cdot 10^{-5}$
			524.20		
			522.09		
561	Ca VII 128.0 5.39	$3p^2P - 3p^3D^\circ$	624.4	0.42	0.001
			630.6		
			639.2		
			640.5		
562		$- 3p^3P^\circ$	551.5	(0.1)	$1 \cdot 10^{-4}$
563		$- 3p^3S^\circ$	414.7	(0.05)	$8 \cdot 10^{-6}$

TABLE I (continued)

No.	Ion; $x_i$ , eV; $\log T_i$	Transition	$\lambda$ , Å	$f_{12}$	$F_{\tau}$ , erg/cm <sup>2</sup> sec
564	Fe XIII 355 6.04	$3p^2\ ^3P - 3p^3\ ^3D^\circ$	(360) (373) (386)	0.28	0.010
565		$- 3p^3\ ^3P^\circ$	(330)	(0.1)	0.004
566		$- 3p^3\ ^3S^\circ$	(250)	(0.05)	0.002
567		$- 3d^3\ ^3P^\circ$	(210)	(0.1)	0.003
568		$- 3d^3\ ^3D^\circ$	(187) (190) (193)	(0.2)	0.004
569		$- 4s\ ^3P^\circ$	75.3 75.8	(0.3)	0.001
570	Ni XV 455 6.3	$3p^2\ ^3P - 3p^3\ ^3D^\circ$	(316) (333) (346)	0.25	$4 \cdot 10^{-4}$
571		$- 3p^3\ ^3P^\circ$	(290)	(0.1)	$1.5 \cdot 10^{-4}$
572		$- 3p^3\ ^3S^\circ$	(220)	(0.05)	$6 \cdot 10^{-5}$
573		$- 3d^3\ ^3P^\circ$	(182)	(0.1)	$1 \cdot 10^{-4}$
574		$- 4s\ ^3P^\circ$	(58)	(0.3)	$1 \cdot 10^{-4}$
P I					
575	S II 23.4 4.23	$3p^3\ ^4S^\circ - 3p^4\ ^4P$	1259.5 1253.8 1250.5	1.30	0.033
576		$- 4s\ ^4P$	910.5 906.9 912.7	(0.1)	$1.6 \cdot 10^{-4}$
577	Ar IV 59.8 4.88	$3p^3\ ^4S^\circ - 3p^4\ ^4P$	840.03 843.77 850.60	1.05	0.0015
578		$3p^3\ ^2D^\circ - 3p^4\ ^2P$	683.27 688.39 689.01	(0.05)	$3 \cdot 10^{-5}$
579	Ca VI 109 5.28	$3p^3\ ^4S^\circ - 3p^4\ ^4P$	629.60 633.82 641.88	0.88	0.003
580		$3p^3\ ^2D^\circ - 3p^4\ ^2P$	510	(0.05)	$4 \cdot 10^{-5}$
581		$3p^3\ ^2P^\circ - (^2D)$	764.36	(0.1)	$2 \cdot 10^{-4}$
582		$- 3p^4\ ^2D$	674.28	(0.2)	$3 \cdot 10^{-4}$



TABLE I (continued)

No.	Ion; $x_i$ , eV; $\log T_i$	Transition	$\lambda$ , Å	$f_{12}$	$F_t$ , erg/cm <sup>2</sup> sec
583	Fe XII 325 5.95	$3p^3 4S^\circ - 3p^4 4P$	(369) (360) (356)	0.58	0.012
584		$- 4s^4 P$	79.1 79.5	(0.5)	0.001
585		$- 3d^4 D$	(238)	(0.1)	0.001
586		$- 3d^4 P$	(209)	(0.2)	0.0013
587		$3p^3 2P^\circ - 3p^4 2P$	(326)	(0.1)	$3 \cdot 10^{-4}$
588		$3p^3 2D^\circ - 3p^4 2P$	(283)	(0.05)	$3 \cdot 10^{-4}$
589		$3d^2 D^\circ - 3d^2 F$	186.87	(0.1)	$3 \cdot 10^{-4}$
590	Ni XIV 422 6.18	$3p^3 4S^\circ - 3p^4 4P$	(311) (315) (323)	0.52	0.006
591		$- 4s^4 P$	(63)	(0.5)	$8 \cdot 10^{-4}$
592		$3p^3 2D^\circ - 3d^2 F$	164.13		0.001
S I					
593	S I 10.36 3.7	$3p^4 3P - 4s^3 S^\circ$	1807.3 1820.3 1826.2	(0.1)	0.003 0.002 0.001
594		$- 3s^3 D^\circ$	1474.0 1483.0	(0.2)	$2 \cdot 10^{-5}$
595	Ar III 40.9 4.59	$3p^4 3P - 3p^5 3P^\circ$	871.10 887.40 879.62 878.73 875.53 883.18	0.77	$8 \cdot 10^{-4}$
596	Ca V 84.4 5.08	$3p^4 3P - 3p^5 3P^\circ$	637.93 643.12 646.57 647.88 651.55 656.76	0.64	$6 \cdot 10^{-4}$
597	Fe XI 290.3 5.90	$3p^4 3P - 3p^5 3P^\circ$	350 358 360		

TABLE I (continued)

No.	Ion; $x_i$ , eV; $\log T_i$	Transition	$\lambda$ , Å	$f_{12}$	$F_t$ , erg/cm <sup>2</sup> sec		
597	Fe XI	$-3d^3D^\circ$ $-4s^3D^\circ$ $-4s^3S^\circ$ $3p^4^1D - 4s^1D^\circ$ $-4s^1P^\circ$	367	0.42	0.007		
			369				
			376				
598			178.04	(0.2)	0.0015		
			180.42				
			181.13				
			182.17				
599			86.77	(0.5)	$6 \cdot 10^{-4}$		
			88.0				
			88.17				
600			89.18	(0.1)	$10^{-4}$		
			90.20				
601			89.10	(0.1)	$10^{-4}$		
602			86.51	(0.1)	$10^{-4}$		
603	Ni XIII (380) 6.1	$3p^4^3P - 3p^5^3P^\circ$ $-3d^3D^\circ$ $-4s^3S^\circ$	304	0.37	0.003		
			312				
			317				
			323				
			324				
			332				
604			157.75	(0.2)	0.001		
605			69	0.1	$8 \cdot 10^{-5}$		
Cl I							
606			Fe X 262 5.78	$3p^5^2P^\circ - 3p^6^2S$ $-3d^3P$ $-3d^2D$	(347)	0.17	$5 \cdot 10^{-4}$
	(367)	0.001					
	177.24	$3 \cdot 10^{-4}$					
607		$-3d^2D$	175.86	(0.1)	$6 \cdot 10^{-4}$		
608			175.53	(0.2)	$6 \cdot 10^{-4}$		
			175.53				
609		$-4s^4P$	97.12	(0.1)	$6 \cdot 10^{-5}$		
610		$-4s^2P$	96.12	(0.3)	$2 \cdot 10^{-4}$		
			96.78				
611		$-4s^2D$	94.01	(0.5)	$4 \cdot 10^{-4}$		
			93.97	(0.5)			
612		$-4s^1^2D$	95.37	(0.5)	$4 \cdot 10^{-4}$		
613	Ni XII 350 6.00	$3p^5^2P^\circ - 3p^6^2S$ $-3d^2D$ $-3d^2P$ $-4s^2P$	(299)	0.15	$2 \cdot 10^{-4}$		
			(322)		$4 \cdot 10^{-4}$		
614			152.14	0.5	$5 \cdot 10^{-4}$		
			152.95				
615			154.15	0.1	$1 \cdot 10^{-4}$		
616			84.8	(0.3)	$1.3 \cdot 10^{-4}$		

TABLE I (continued)

No.	Ion; $x_i$ , eV; $\log T_i$	Transition	$\lambda$ , Å	$f_{12}$	$F_{\nu}$ , erg/cm <sup>2</sup> sec
Ar I					
617	Fe IX	$3p^6 1S - 4s 1P^{\circ}$	103.58	(0.5)	$3 \cdot 10^{-4}$
618	234.6	$- 3d 1P^{\circ}$	171.075	(0.2)	$6 \cdot 10^{-4}$
619	5.73	$- 4s 3P^{\circ}$	105.24	(0.1)	$6 \cdot 10^{-5}$
620	Ni XI	$3p^6 1S - 4s 1P^{\circ}$	78.1	(0.5)	$8 \cdot 10^{-5}$
621	318 5.95	$- 3d 1P^{\circ}$	148.5	(0.2)	$1 \cdot 10^{-4}$
K I					
622	Fe VIII	$3d^2 D - 4f^2 F^{\circ}$	131.24	0.24	$1.5 \cdot 10^{-4}$
623	151 5.59	$- 3d^2 2F^{\circ}$	130.93 186.60		
624		$- 3d^2 D^{\circ}$	185.22 167.49	(0.2)	$3 \cdot 10^{-4}$
			167.67 168.01	(0.1)	$1 \cdot 10^{-4}$
625		$- 4p^3 P^{\circ}$	168.18 196.05	(0.1)	$1.6 \cdot 10^{-4}$
			195.48 194.76		
626		$4p^2 P^{\circ} - 5s^2 S$	370.43 365.87	(0.1)	$2 \cdot 10^{-5}$ $1 \cdot 10^{-5}$
627	Ni X	$3d^2 D - 3d^2 2D^{\circ}$	144.22	(0.1)	$1.6 \cdot 10^{-5}$
628	236 5.75	$- 3d^2 2F^{\circ}$	144.99 158.37 159.97		
Ca I					
629	Fe VII	$a^3 F - z^3 F^{\circ}$	233.02	(0.3)	$2.4 \cdot 10^{-4}$
630	128	$a^3 P - z^3 P^{\circ}$	235.23	(0.3)	$2.4 \cdot 10^{-4}$
631	5.38	$a^1 D - z^1 D^{\circ}$	245.93	(0.1)	$8 \cdot 10^{-5}$
632		$- y^1 P^{\circ}$	152.9	(0.1)	$1.6 \cdot 10^{-5}$
633		$a^1 G - z^1 F^{\circ}$	243.4	(0.1)	$8 \cdot 10^{-5}$
634	Ni IX	$3F_3 - 3F_4^{\circ}$	146.068	(0.1)	$6 \cdot 10^{-5}$
635	201	$3F_2 - 3D_3^{\circ}$	147.15	(0.2)	$1.2 \cdot 10^{-5}$
636	5.6	$3F_3 - 3F_2$	152.316	(0.1)	$6 \cdot 10^{-6}$
637		$1D_2 - 3F_2$			

TABLE I (continued)

No.	Ion; $x_i$ , eV; $\log T_i$	Transition	$\lambda$ , Å	$f_{12}$	$F_t$ , erg/cm <sup>2</sup> sec
Sc I					
638	Fe VI 102 5.25	$a^4F - z^4G^\circ$	295.63 295.04 295.01 294.34 293.49	(1)	0.001
639		$3a^4F - 4z^4F^\circ$	291.80 294.52 294.34 294.25 293.97 293.75 293.38	(0,1)	$10^{-4}$
640		$-4p^2F^\circ$	292.74 294.26	(0,1)	$10^{-4}$
641		$-4p^4D^\circ$	277.57 291.18	(0,5)	$4 \cdot 10^{-4}$
642		$3d^3^2H - 4p^2H^\circ$	290.27 291.23	(0,1)	$10^{-4}$
Ti I					
643	Fe V 78 5.2	$3d^4^5D - 4p^5P^\circ$	366.00 365.86 365.63 365.44 365.34 364.97 364.80 364.29	(0,1)	$10^{-4}$
644		$3d^4a^5D - 4pz^5F^\circ$	385.0 385.9 386.8	(0,5)	$2 \cdot 10^{-4}$ $3 \cdot 10^{-4}$ $1 \cdot 10^{-4}$
645			387.2 387.7 388.6 386.8	0.05	$8 \cdot 10^{-6}$ $3 \cdot 10^{-5}$ $6 \cdot 10^{-5}$ $6 \cdot 10^{-5}$
646		$a^3H - z^3G^\circ$	417.38 417.52 418.03 418.46 419.92	(0,3)	$1.6 \cdot 10^{-4}$

TABLE I (continued)

No.	Ion: $x_i$ , eV; $\log T_i$	Transition	$\lambda$ , Å	$f_{12}$	$F_{12}$ , erg/cm <sup>2</sup> sec
647	Ni VII	$3d^4 a^5 D - 4pz^5 F^\circ$	212.5—213.8	(0.5)	$6 \cdot 10^{-5}$
648	136	— $4pz^5 D^\circ$	213.9—214.4	(0.05)	$6 \cdot 10^{-6}$
649	5.45	— $4pz^5 P^\circ$	205.0— —216.0	(0.1)	$10^{-5}$

## V I

650	Fe IV 57.1 4.78	$3d^5^5 S - 4p^6 P^\circ$	525.68 526.28 526.60	(0.5)	$3 \cdot 10^{-4}$ $2 \cdot 10^{-4}$ $1 \cdot 10^{-4}$
651	Ni VI 110 5.42	$3d^5^5 S - 4p^6 P^\circ$	260.71 260.59 260.35	(0.5)	$8 \cdot 10^{-5}$

## Cr I

652	Fe III	$3d^6 a^5 D - 4pz^5 P^\circ$	(1122)	(0.1)	0.0024
653	30.63 4.5	— $4pz^5 F^\circ$	858.60 859.7 861.8	(0.2)	0.0015
654		— $4py^5 P^\circ$	811.3 844.3 847.5	(0.1)	$6 \cdot 10^{-4}$
655		$3d^6 a^3 P - 4pz^3 P^\circ$	997.08	(0.05)	0.001

## Mn I

656	Fe II 16.18 4.1	$a^6 D - z^6 D^\circ$	2598.4 2599.4 2607.1 2611.9 2613.8 2617.6 2625.7 2631.0 2631.3	(0.5)	$\sim 10$
-----	-----------------------	-----------------------	--	-------	-----------

TABLE I (continued)

No.	Ion; $x_i$ , eV; $\log T_i$	Transition	$\lambda$ , Å	$f_{12}$	$F_{\tau}$ , erg/cm <sup>2</sup> sec
657	Fe II	$a^6D - y^6F^{\circ}$	1154.40 1153.96 1153.28 1152.88 1152.44 1151.16 1150.69 1150.29 1148.30 1147.41 1146.96 1143.24 1142.33	(0.5)	0.006
Fe I					
658	Ni III 36.16 4.57	$3d^8 a^3F - 4p z^3G^{\circ}$	(867) (860) (858) (852)	(0.5)	$2.5 \cdot 10^{-4}$
659		$- 4p z^3F^{\circ}$	(853) (856) (860) (864) (870)	(0.05)	$3 \cdot 10^{-5}$
660		$- 4p z^3D^{\circ}$	(843) (846) (848) (852) (859)	(0.1)	$6 \cdot 10^{-5}$
661		$- 4p y^3G^{\circ}$	(744) (763) (748)	(0.5)	$2 \cdot 10^{-4}$
Supplement					
F I					
	Ne II 41.08 (4.6)	$2p^5 ^2P^{\circ} - 2p^6 ^2S$	462.388 460.725 447.813 446.591 446.252 445.032	(0.3)	$7 \cdot 10^{-5}$
		$- 3s ^2P$		(0.3)	$6 \cdot 10^{-5}$

TABLE I (continued)

No.	Ion; $x_i$ , eV; $\log T_i$	Transition	$\lambda$ , Å	$f_{12}$	$F_{12}$ , erg/cm <sup>2</sup> sec
Ne I					
	Na II 47.30 (4.8)	$2p^6\ ^1S - 3s1\frac{1}{2}^\circ$ $- 3s1\frac{1}{2}^\circ$	376.375 372.069	(0.3) (0.3)	$2 \cdot 10^{-5}$ $2 \cdot 10^{-5}$
	Mg III 80.43 (5.0)	$2p^6\ ^1S - 3s1\frac{1}{2}^\circ$ $- 3s1\frac{1}{2}^\circ$	234.258 231.730	(0.3) (0.3)	$3 \cdot 10^{-5}$ $3 \cdot 10^{-5}$
	Al IV 119.98 (5.3)	$2p^6\ ^1S - 3s1\frac{1}{2}^\circ$ $- 3s1\frac{1}{2}^\circ$	161.686 160.073	(0.3) (0.3)	$5 \cdot 10^{-6}$ $5 \cdot 10^{-6}$
	Ni XIX $\sim(6.6-7.0)$	$2p^6\ ^1S_0 - 4d\ ^3D_1^\circ$ $- 4d\ ^1P_1^\circ$	10.10 9.97	(0.1) (0.01)	$\sim 10^{-9}$ $\sim 10^{-10}$
Ar I					
	Ca III 51.218 (4.5)	$3p^6\ ^1S - 3d1\frac{1}{2}^\circ$	490.546	0.1	$3 \cdot 10^{-6}$
Cl I					
	Ca IV 67.196 (4.8)	$3p^5\ ^2P^\circ - 3p^6\ ^2S$	669.725 656.038	0.1	$3 \cdot 10^{-5}$ $6 \cdot 10^{-5}$
Na I					
	Fe XVI 489 6.28	$3p\ ^2P^\circ - 4d\ ^2D$	54.769 54.728 54.142	(0.5)	$10^{-4}$ 0.001 $5 \cdot 10^{-4}$
N I					
	Ca XIV 821.2 6.48	$2p^3\ ^2D^\circ - 2p^4\ ^2P$ $2p^3\ ^2P^\circ - 2p^4\ ^2P$	128.25 132.95 134.31 148.11	(0.05) (0.05)	$3 \cdot 10^{-5}$ $3 \cdot 10^{-5}$
O I					
	Ca XIII 728.8 6.42	$2p^4\ ^1D_2 - 2p^5\ ^1P_1^\circ$ $2p^4\ ^1S_0 - 2p^5\ ^1P_1^\circ$	131.23 148.84	(0.1) (0.2)	$3 \cdot 10^{-5}$ $3 \cdot 10^{-5}$

Table II

IDENTIFICATION OF LINES IN THE SHORT-WAVE SOLAR SPECTRUM ( $\lambda \leq 1216 \text{ \AA}$ )

Column 3 lists the laboratory and theoretical wavelengths, with interpolated and extrapolated values enclosed in parentheses; column 4 gives the flux  $F_t$  from Table I; columns 5 and 6 list the values of  $\lambda$  and  $F_o$  from observations /21, 26–29/ (see Section 6), the date of each observation being indicated in the appropriate subheadings (the parenthetical date is for  $\lambda$ ).

The last column gives the results of identification: + is reliable identification, +? doubtful identification, and – no identification. The results of identification can also be assessed from the summary of ionization temperatures, which shows the ions whose lines have been reliably identified (see Table 8).

No. of multiplet from Table I	Ion	$\lambda$ , A	$F_t$	$\lambda$ , A	$F_o$	Identifi- cation
				25 July 1963 /28/ (1 Oct. 1965 /29/)		
62	Si XIII	6.74	$10^{-7}$			
61	Mg XI	9.168	$10^{-8}$	(9.5)		—
	Ni XIX	9.97				
		10.10				
60	Ne IX	(11.0)	$5 \cdot 10^{-7}$	(10.9–11.9)	0.005	—
59	Ne IX	(11.5)	$6 \cdot 10^{-7}$			
26	Ne X	12.15	$10^{-7}$	13.1–13.6	$3 \cdot 10^{-5}$	+?
57	Ne IX	13.44	$10^{-5}$			
58	Ne IX	(13.6)	$3 \cdot 10^{-5}$	13.7	$3 \cdot 10^{-5}$	+
474	Fe XVII	13.82	$1,6 \cdot 10^{-5}$			
473	Fe XVII	13.89	$4 \cdot 10^{-6}$			
24	O VIII	14.54	$5 \cdot 10^{-6}$			
23	O VIII	14.65	$10^{-5}$	(14.9)	0,01	+
22	O VIII	14.84	$2 \cdot 10^{-5}$			
472	Fe XVII	15.01	$4 \cdot 10^{-5}$	15.0	$2 \cdot 10^{-4}$	
21	O VIII	15.20	$4 \cdot 10^{-5}$	(15.2)	$1 \cdot 10^{-4}$	+
470	Fe XVII	15.26	$1,3 \cdot 10^{-4}$	15.25		
471	Fe XVII	15.45	$1,2 \cdot 10^{-6}$	(16.0)	$5 \cdot 10^{-5}$	+
20	O VIII	16.006	$1,4 \cdot 10^{-4}$	16.0		
469	Fe XVII	16.77	$6 \cdot 10^{-6}$	(16.85)	$2 \cdot 10^{-4}$	+
468	Fe XVII	17.05	$7 \cdot 10^{-6}$	16.72		
				17.01	$2 \cdot 10^{-4}$	+
				(17.1)		
53	O VII	17.200	$3 \cdot 10^{-5}$	17.05	$2,4 \cdot 10^{-4}$	+
52	O VII	17.396	$6 \cdot 10^{-5}$			
51	O VII	17.768	$10^{-4}$	17.65	$3,5 \cdot 10^{-4}$	+
				17.72		
50	O VII	18.627	$3 \cdot 10^{-4}$	18.54	$3,8 \cdot 10^{-4}$	+
				18.61		
19	O VIII	18.969 } 18.974 }	0,0014	18.8 } 18.9 }		



TABLE II (continued)

No. of multiplet from Table I	Ion	$\lambda$ , Å	$F_t$	$\lambda$ , Å	$F_o$	Identifi- cation
18	N VII	19.8	$10^{-5}$	(18.9)		
17	N VII	20.9	$2.4 \cdot 10^{-5}$	20.8	?	+
47	O VII	21.602	0.0024	21.55	0.004	+
49	O VII	21.80	$6 \cdot 10^{-4}$	(21.6)		
				21.70	0.002	+
380	Ca XIV	(22)	$7 \cdot 10^{-6}$			
48	O VII	22.10	$6 \cdot 10^{-4}$			
45	N VI	23.77	$3 \cdot 10^{-4}$	23.2	$5 \cdot 10^{-4}$	—
16	N VII	24.79	$2 \cdot 10^{-4}$	(24.7)		
44	N VI	24.90	$3 \cdot 10^{-4}$	24.8	$4 \cdot 10^{-4}$	+
467	Ca XI	25.33	$2 \cdot 10^{-5}$			
466	Ca XI	25.52	$3 \cdot 10^{-5}$			
14	C VI	26.4	$6 \cdot 10^{-5}$			
465	Ca XI	26.44	$3 \cdot 10^{-5}$			
464	Ca XI	26.64	$10^{-5}$			
463	Ca XI	26.96	$6 \cdot 10^{-5}$			
13	C VI	27.00	$2 \cdot 10^{-4}$			
462	Ca XI	27.08	$10^{-5}$			
444	Ca XII	27.38				
		27.41	$6 \cdot 10^{-5}$			
		27.61				
12	C VI	28.464	$5 \cdot 10^{-4}$			
40	N VI	28.787	0.004	(28.5)		+
41	N VI	29.084	0.001	(30.0)		+
42		29.53	0.001			
414	Ca XIII	29.6	$10^{-5}$			
186	S XIII	(30)	$1.5 \cdot 10^{-4}$			
105	Si XII	(30)	$1.5 \cdot 10^{-4}$			
461	Ca XI	30.45	$5 \cdot 10^{-5}$			
458	Ca XI	30.87	$3 \cdot 10^{-4}$			
460	Ca XI	31.26	$10^{-5}$			
442	Ca XII	31.66				
		31.96	$10^{-4}$			
109	S XIV	(32.0)	$2 \cdot 10^{-4}$	(31.8)		+
443	Ca XII	32.28	$10^{-5}$			
440	Ca XII	32.31	$5 \cdot 10^{-5}$			
38	C V	32.400	$2 \cdot 10^{-5}$			
443	Ca XII	32.60	$10^{-5}$			
37	C V	32.754	$4 \cdot 10^{-5}$			
250	S XII	(33)	$3 \cdot 10^{-4}$			
378	Ar XII	(33)	$5 \cdot 10^{-5}$			
20 Sept. 1963 /21/ (1 Oct. 1965 /29/)						
36	C V	33.426	$3 \cdot 10^{-5}$	33.43	$3 \cdot 10^{-4}$	+
11	C VI	33.734	0.004	33.75	0.006	+
445	Ca XII	(34)	$2 \cdot 10^{-5}$	(33.9)		+

TABLE II (continued)

No. of multiplet from Table I	Ion	$\lambda$ , Å	$F_t$	$\lambda$ , Å	$F_o$	Identifi- cation
35	C V	34.973	$1.6 \cdot 10^{-4}$	34.97	$3 \cdot 10^{-4}$	+
457	Ca XI	35.21	$3 \cdot 10^{-5}$			
459		35.58	$1.5 \cdot 10^{-5}$			
249	S XII	(38)	$6 \cdot 10^{-5}$			
324	S XI	39.28	0.002	39.28	$7 \cdot 10^{-4}$	+
412	Ar XI	39.7	$2 \cdot 10^{-5}$			
504	Fe XVI	39.83	$5 \cdot 10^{-4}$			
		40.15				
32	C V	40.270	0.002	40.26	0.002	+
34		40.731	$4 \cdot 10^{-4}$	40.72	0.001	+
103	Si XII	40.91	0.001	40.92	0.001	+
		40.95	$5 \cdot 10^{-4}$			
33	C V	41.47	$4 \cdot 10^{-4}$	41.49	0.002	+
441	Ca XII	(42)	$8 \cdot 10^{-5}$			
375	S X	42.51				
		42.54	0.002	42.54	0.0016	+
		42.58				
167	Si XI	43.76	0.006	43.18	$5 \cdot 10^{-4}$	II n.p.?-
				43.75	0.0021	+
435	Ar X	43.8	$10^{-4}$			
509	Ni XVIII	43.81	$4 \cdot 10^{-5}$			
438	Ar X	44.0	$10^{-5}$			
106	Si XII	44.02	$8 \cdot 10^{-4}$			
97	Mg X	44.05	$3 \cdot 10^{-4}$			
106	Si XII	44.16	$8 \cdot 10^{-4}$	44.18	0.0031	+
312	Si IX	44.22	$2 \cdot 10^{-4}$			
		44.25				
438	Ar X	44.3	$10^{-5}$			
509	Ni XVIII	44.35	$4 \cdot 10^{-5}$			
376	S X	44.37				
		44.39	0.003			
		44.42				
433	S VIII	44.5	$2 \cdot 10^{-5}$			
438	Ar X	44.5	$10^{-5}$			
509	Ni XVIII	44.35	$4 \cdot 10^{-5}$			
376	S X	44.37				
		44.39	0.003			
		44.42				
433	S VIII	44.5	$2 \cdot 10^{-5}$			
438	Ar X	44.5	$3 \cdot 10^{-5}$			
437	Ar X	(45)	$3 \cdot 10^{-5}$			
107	Si XII	45.66	$5 \cdot 10^{-4}$	45.66	$4 \cdot 10^{-4}$	+
243	P XI	46.1	$6 \cdot 10^{-5}$			
169	Si XI	46.26				
		46.30	0.005	46.32	0.002	+
		46.40				
506	Fe XVI	46.66	$4 \cdot 10^{-4}$			
		46.72				

TABLE II (continued)

No. of multiplet from Table I	Ion	$\lambda$ , Å	$F_t$	$\lambda$ , Å	$F_o$	Identifi- cation
100	Mg X	47.23 } 47.31 }	$10^{-4}$			
170	Si XI	47.61 } 47.65 }	$2.5 \cdot 10^{-4}$			
374	S X	47.65 } 47.79 }	0.001	47.60	0.003	+
170	Si XI	47.90	$2.5 \cdot 10^{-4}$			
466	Ar IX	48.3	$7 \cdot 10^{-5}$			
228	Si X	48.39 } 48.55 }	$1.5 \cdot 10^{-4}$			
455	Ar IX	48.73	$3 \cdot 10^{-4}$			
180	Si XI	49.22 } 49.26 }	0.005	49.23	0.0069	+
436	Ar X	(50)	$10^{-4}$			
528	Fe XV	50.06 } 50.08 }	$8 \cdot 10^{-4}$	49.67	$8 \cdot 10^{-4}$	+
		50.12 }				
241	Si X	50.33	0.0025 } 0.001 }	50.33	$8 \cdot 10^{-4}$	+
501	Fe XVI	50.35				
229	Si X	50.52	0.002	50.52	0.007	+
501	Fe XVI	50.56	$5 \cdot 10^{-4}$			
229	Si X	50.69	0.001	50.70	0.0057	+
154	Mg IX	51.59 } 51.65 }	$7 \cdot 10^{-5}$			
161	Al X	51.93	$5 \cdot 10^{-4}$ }			
235	Si X	52.07	0.001 }	52.08	$5 \cdot 10^{-4}$	+
454	S VII	52.10	$1.5 \cdot 10^{-5}$ }			
181	Si XI	52.30	0.001	52.33	0.001	+
232	Si X	52.49 } 52.61 }	$8 \cdot 10^{-4}$	52.49	$5 \cdot 10^{-4}$	+
508	Ni XVIII	52.62 } 52.72 }	$2 \cdot 10^{-5}$			
308	Si IX	52.81 } 52.84 }	0.001 }			
432	S VIII	52.9	$10^{-4}$ }	52.83	0.0012	+
524	Fe XV	52.91	0.007 }			
431	S VIII	53.0	$1.5 \cdot 10^{-4}$			
310	Si IX	53.80 } 53.88 }	$2 \cdot 10^{-4}$			
		53.99 }				
430	S VIII	54.12	$2.5 \cdot 10^{-4}$ }			
—	Fe XVI	54.142	$5 \cdot 10^{-4}$ }	54.16	0.0019	+
407	Si VII	54.18	0.001 }			
429	S VIII	54.3	$1.5 \cdot 10^{-4}$ }			

TABLE II (continued)

No. of multiplet from Table I	Ion	$\lambda$ , Å	$F_t$	$\lambda$ , Å	$F_o$	Identifi- cation
240	Si X	54.52	$6 \cdot 10^{-4}$	54.56	0.001	+
238	Si X	54.57	$3 \cdot 10^{-4}$			
240	Si X	54.57	$2 \cdot 10^{-4}$			
—	Fe XVI	54.60	$10^{-4}$	54.75	$5 \cdot 10^{-4}$	+
		54.723	0.001			
		54.769	$10^{-4}$			
453	S VII	54.6	$2 \cdot 10^{-5}$	55.12	0.005	+
307	Si IX	55.09	$5 \cdot 10^{-4}$			
		55.12				
		55.23				
		55.27				
163	Al X	55.27	$10^{-4}$	55.34	0.01	+
309	Si IX	55.30	0.0015			
		55.36				
163	Al X	55.36	$10^{-4}$			
315	Si IX	55.38	$3 \cdot 10^{-4}$			
309	Si IX	55.40	$5 \cdot 10^{-4}$	56.03	0.001	+
526	Fe XV	55.8	0.002			
317	Si IX	56.03	0.002			
408	S IX	56.1	$3 \cdot 10^{-4}$			
526	Fe XV	56.2	0.004			
		56.3				
240	Si X	56.68	$3 \cdot 10^{-4}$	56.64	$5 \cdot 10^{-4}$	+
		56.80				
164	Al X	56.99	$2 \cdot 10^{-4}$	56.80	$5 \cdot 10^{-4}$	+
2 May 1963 /27/ (20 Sept. 1963 /21/)						
316	Si IX	57.43	$3 \cdot 10^{-4}$	57.5 (57.90)	0.003 0.002	+
96	Mg X	57.88	0.002			
		57.92	0.001			
574	Ni XV	(58)	$10^{-4}$	58.8	0.003	+
546	Fe XIV	58.82	0.0015			
358	Si VIII	58.88	$4 \cdot 10^{-4}$			
320	Si IX	58.91	0.0015	59.0 (59.03)	0.001 $5 \cdot 10^{-4}$	+
		59.00				
		59.08				
428	S VIII	59.2	$6 \cdot 10^{-5}$	59.35	0.003	+
546	Fe XIV	59.35	0.003			
84	Ne VIII	60.7	$4 \cdot 10^{-5}$			
451	S VII	60.80	$4 \cdot 10^{-4}$	60.7	0.003	+
359	Si VIII	60.99	$8 \cdot 10^{-4}$			
		61.02				
		61.07				
				61.0 (61.06)	0.004 0.0043	+

TABLE II (continued)

No. of multiplet from Table I	Ion	$\lambda$ , Å	$F_t$	$\lambda$ , Å	$F_o$	Identifi- cation
211	Si IX	61.50 } 61.55 } 61.60 }	$10^{-4}$ }	61.7 (61.51)	0.003 0.0014	+
427	S VIII	61.60	$3 \cdot 10^{-4}$ }			
311	Si IX	61.65	$3 \cdot 10^{-5}$ }			
370	Si VIII	61.80 } 61.85 }	$5 \cdot 10^{-5}$ }	61.9 (61.85)	0.003 0.0023	+
311	Si IX	61.85	$3 \cdot 10^{-5}$ }			
370	Si VIII	61.90 } 61.91 }	$10^{-4}$ }			
151	Mg IX	61.92 } 61.93 }	$4 \cdot 10^{-4}$ }			
88	Ne VIII	62.4	$3 \cdot 10^{-5}$ }	62.3	0.003	-
148	Mg IX	62.75	$6 \cdot 10^{-4}$ }			
364	Si VIII	62.81 } 62.85 }	$5 \cdot 10^{-4}$ }	62.65 (62.80)	0.003 0.0022	+
503	Fe XVI	62.88	$1,6 \cdot 10^{-4}$ }			
318	Si IX	62.97	$6 \cdot 10^{-4}$ }			
591	Ni XIV	(63)	$5 \cdot 10^{-4}$ }	63.05	0.004	+
99	Mg X	63.15	$6 \cdot 10^{-4}$ }			
372	Si VIII	63.22	$10^{-4}$ }			
365		63.23 } 63.27 }	$6 \cdot 10^{-4}$ }			
99	Mg X	63.29	$3 \cdot 10^{-4}$ }	63.2 (63.29)	0.0015 0.003	+
426	S VIII	63.30	$4 \cdot 10^{-4}$ }			
503	Fe XVI	63.72	$8 \cdot 10^{-5}$ }			
371	Si VIII	63.73 } 63.90 }	$4 \cdot 10^{-4}$ }	63.65 (63.73) 64.9 (63.90)	0.005 0.0022 0.001 0.001	+
424	Si VI	65.21	$10^{-5}$ }	64.3 65.6	0.001 0.003	-
155	Mg IX	65.61	$3 \cdot 10^{-4}$ }	(65.67)	0.001	+
93	Mg X	65.67 } 65.85 }	$3 \cdot 10^{-4}$ }	66.0 (65.85)	0.003 0.0019	+
87	Ne VIII	65.9	$3 \cdot 10^{-5}$ }			
505	Fe XVI	66.26	$4 \cdot 10^{-5}$ }	66.2 (66.26)	0.003 0.001	+
		66.37	$2 \cdot 10^{-5}$ }	66.5 (66.37)	0.001 0.002	+
150	Mg IX	67.09 } 67.14 } 67.24 }	$6 \cdot 10^{-4}$ }	66.9 67.24 (67.15)	0.003 0.004 0.0024	-
217	Mg VIII	67.24 } 67.25 }	$6 \cdot 10^{-5}$ }			+
83	Ne VIII	67.3 } 67.3 }	$5 \cdot 10^{-5}$ }	67.3	0.001	+

TABLE II (continued)

No. of multiplet from Table I	Ion	$\lambda$ , Å	$F_t$	$\lambda$ , Å	$F_o$	Identifi- cation			
214	Mg VIII	68.41	$7 \cdot 10^{-5}$	68.48	0.002	+			
		68.45							
605	Ni XIII	(69)	$8 \cdot 10^{-5}$	68.8	0.003	+			
				69.1	0.002	—			
403	Si VII	69.38	$2 \cdot 10^{-5}$	69.4	0.002	+			
152	Mg IX	69.41	$2 \cdot 10^{-4}$						
215	Mg VIII	69.42	$10^{-4}$						
152	Mg IX	69.47	$3 \cdot 10^{-4}$						
215	Mg VIII	69.47	$10^{-4}$						
403	Si VII	69.58	$3 \cdot 10^{-5}$						
215	Mg VIII	69.58	$10^{-4}$	69.5 (69.62)	0.005 0.0035	+			
402	Si VII	69.60	$10^{-5}$						
357	Si VIII	69.63	$3 \cdot 10^{-4}$						
402	Si VII	69.66	$4 \cdot 10^{-5}$	69.9 (69.99)	0.004 0.0018	+			
		69.78							
		69.80							
		69.86							
		69.87							
153	Mg IX	69.95	$4 \cdot 10^{-5}$						
527	Fe XV	69.95	0.001						
		69.99							
401	Si VII	70.02	$3 \cdot 10^{-4}$						
		70.03							
527	Fe XV	70.05	$2 \cdot 10^{-4}$						
92	Ne VIII	70.62	$8 \cdot 10^{-5}$				70.3	0.0025 0.003	— +
		70.65							
213	Mg VIII	70.95	$4 \cdot 10^{-5}$				71.1	0.0015	+
		71.00							
		71.12							
		71.17							
545	Fe XIV	71.43	$7 \cdot 10^{-4}$	71.5	0.004	+			
450	S VII	72.03	$10^{-4}$	72.1	0.003	+			
369	Si VIII	72.21	$10^{-4}$	72.2	0.004	+			
156	Mg IX	72.31	$4 \cdot 10^{-4}$						
545	Fe XIV	72.4	0.0015						
				72.4 (72.26)	0.004 0.0023	+			
369	Si VIII	72.42	$10^{-4}$	72.9	0.004	—			
453	S VII	72.66	$2 \cdot 10^{-5}$						
400	Si VII	73.12	0.001				73.3	0.003	+
		73.13							
		73.35							
		73.42							
86	Ne VIII	73.6	$3 \cdot 10^{-5}$	74.3	0.003	+			
153	Mg IX	74.32	$3 \cdot 10^{-4}$						
363	Si VIII	74.42	$10^{-4}$						
475	Fe XVII	74.45	$10^{-5}$						
90	Ne VIII	74.7	$3 \cdot 10^{-5}$						

TABLE II (continued)

No. of multiplet from Table I	Ion	$\lambda$ , Å	$F_t$	$\lambda$ , Å	$F_o$	Identifi- cation
216	Mg VIII	74.9	$5 \cdot 10^{-4}$	74.8	0.008	+
569	Fe XIII	75.3	$5 \cdot 10^{-4}$	75.28	0.003	+
140	Ne VII	75.7	$8 \cdot 10^{-6}$			
569	Fe XIII	75.8	$5 \cdot 10^{-4}$	75.8	0.003	+
157	Mg IX	77.74	$10^{-4}$	76.0	0.003	-
				(76.5)	0.003	
				77.74	0.003	+
94	Na IX	77.76	$10^{-5}$			
		77.91				
620	Ni XI	78.1	$8 \cdot 10^{-5}$	78.1	0.003	+
				78.5	0.003	-
586	Fe XII	79.1	$5 \cdot 10^{-4}$	(78.7)	0.002	-
399	Si VII	79.24	$6 \cdot 10^{-5}$	79.1	0.004	+
		79.26				
		79.49				
586	Fe XII	79.5	$5 \cdot 10^{-4}$	79.5	0.004	+
399	Si VII	79.52	$3 \cdot 10^{-5}$	79.8	0.001	-
		79.62		80.5	0.003	-
93	Na IX	81.18	$10^{-5}$	81.2	0.003	+
		81.35		81.3	0.003	+
398	Si VII	81.62	$5 \cdot 10^{-4}$	81.6	0.002	+
142	Ne VII	82.3	$7 \cdot 10^{-6}$	81.7	0.003	-
212	Mg VIII	82.6	$8 \cdot 10^{-5}$	82.57	0.005	+
		82.82	$4 \cdot 10^{-5}$	82.85	0.004	+
422	Si VI	83.01	$5 \cdot 10^{-6}$			
423		83.13	$10^{-4}$			
		83.26	$3 \cdot 10^{-5}$	83.3	0.0024	+
422		83.36	$5 \cdot 10^{-6}$			
423		83.61	$3 \cdot 10^{-5}$			
422		83.64	$2 \cdot 10^{-5}$	83.6	0.0015	+
				84.5	0.004	-
616	Ni XII	84.8	$1,3 \cdot 10^{-4}$	85.0	0.005	+
				85.8	0.001	-
602	Fe XI	86.51	$10^{-4}$			
599		86.77	$1,5 \cdot 10^{-4}$	86.8	0.003	+
354	Al VII	86.94	$4 \cdot 10^{-5}$			
		87.2		87.3	0.003	+
599	Fe XI	88.0	$1,5 \cdot 10^{-4}$	88.12	0.004	+
82	Ne VIII	88.1	$2,5 \cdot 10^{-4}$	(88.08)	0.0042	
599	Fe XI	88.17	$3 \cdot 10^{-4}$			
601		89.10	$10^{-4}$	88.8	0.004	+
600		89.18	$10^{-4}$	89.21	0.004	+
600		90.20		89.5	0.003	-
449	Si V	90.45	$5 \cdot 10^{-5}$	90.11	0.005	+
		90.85		90.8	0.003	+
421	Si VI	91.37	$4 \cdot 10^{-5}$	91.5	0.005	+
		91.80		92.7	0.004	-

TABLE II (continued)

No. of multiplet from Table I	Ion	$\lambda$ , Å	$F_t$	$\lambda$ , Å	$F_o$	Identifi- cation
611	Fe X	93.97	$4 \cdot 10^{-4}$	93.7	0.003	+
		94.01		94.0	0.005	+
208	Na VII	94.29	$10^{-5}$	94.8	0.002	—
612	Fe X	95.37	$4 \cdot 10^{-4}$	95.35	0.002	+
208	Na VII	94.47				
293	Mg VII	95.42	$1.5 \cdot 10^{-4}$	95.5	0.001	+
		95.48				
420	Si VI	96.02	$10^{-4}$	96.14	0.005	+
610	Fe X	96.12	$10^{-4}$			
448	Si V	96.44	$4 \cdot 10^{-5}$	96.64	0.004	+
420	Si VI	96.49	$1.5 \cdot 10^{-4}$			
610	Fe X	96.78	$10^{-4}$	97.1	0.005	+
609	Fe X	97.12	$6 \cdot 10^{-5}$			
448	Si V	97.14	$7 \cdot 10^{-5}$	97.6	0.001	+
139	Ne VII	97.5	$1.2 \cdot 10^{-4}$			
296	Mg VII	98.0	$1.5 \cdot 10^{-4}$	98.12	0.008	+
85	Ne VIII	98.1	$9 \cdot 10^{-4}$		98.5	<0.001
		98.2				
419	Si VI	99.10	$1.8 \cdot 10^{-4}$	99.5	<0.001	+
		99.46		100.0	0.003	+
		99.60		100.5	0.008	—
		99.57				
297	Mg VII	102.3	$5 \cdot 10^{-4}$	102.3	0.005	+
25	O VIII	102.6	$2 \cdot 10^{-5}$	102—102.7	0.004	++?
89	Ne VIII	103.1	$5 \cdot 10^{-5}$	103.1	<0.003	+
617	Fe IX	103.58	$3 \cdot 10^{-4}$	103.7	0.010	+
89	Ne VIII	103.9	$1 \cdot 10^{-4}$	103.8	<0.003	+
				104.2		—
75	O VI	104.81	$10^{-4}$	104.8	0.001	+
619	Fe IX	105.24	$6 \cdot 10^{-5}$	105.1	0.003	—
207	Na VII	105.35	$5 \cdot 10^{-6}$	105.3	0.0025	+
141	Ne VII	106.1	$10^{-4}$	106.1	0.0025	+
		106.2		107. 109	0.003	—
495	Ca X	110.96	$5 \cdot 10^{-5}$	111.0	0.005	+
		111.20				
351	Mg VI	111.55	$3 \cdot 10^{-4}$	112.0	0.005	+
		111.75				
		111.86				
393	Mg V	114.8	$2 \cdot 10^{-5}$	113.1—113.5	0.005	—
		115.0		114.8	0.004	++?
74	O VI	115.82	$6 \cdot 10^{-4}$	115.8	0.003	+
80	O VI	116.42	$1.2 \cdot 10^{-4}$	116.5	0.004	+
143	Ne VII	116.7	$8 \cdot 10^{-5}$	117.1	0.005	—



TABLE II (continued)

No. of multiplet from Table I	Ion	$\lambda$ , Å	$F_t$	$\lambda$ , Å	$F_o$	Identifi- cation
446	Si V	117.9	$4 \cdot 10^{-5}$	118.1	0.005	+?
496	Ca X	118.15 } 118.22 }	$6 \cdot 10^{-6}$	118,9—120.2	0.002	—
447	Si V	119.0	$6 \cdot 10^{-6}$			
393	Mg V	121.64 } 121.92 } 122.03 }	$4 \cdot 10^{-5}$	122.0 125.0	0.004 0.004	+? —
—	Ca XIV	128.25	$10^{-5}$			
79	O VI	129.79 } 129.87 }	$1.3 \cdot 10^{-4}$	129.5	0.003	—
54	O VII	130.0	$5 \cdot 10^{-4}$	129.9	0.003	+
622	Fe VIII	130.93 } 131.24 }	$1.5 \cdot 10^{-4}$	130.9	0.007	+
—	Ca XIII	131.23	$3 \cdot 10^{-5}$			
73	O VI	132.3	$10^{-4}$			
—	Ca XIV	132.95	$2 \cdot 10^{-6}$	133.5	0.003	—
—	Ca XIV	134.31	$2 \cdot 10^{-5}$			
392	Mg V	137.41 } 137.75 } 137.88 }	$10^{-4}$			
55	O VII	138.3	$2 \cdot 10^{-4}$	138.5	0.002	+
202	Ne VI	138.40 } 138.63 }	$5 \cdot 10^{-5}$	139.2	0.003	+?
439	Ca XII	141.04	$2 \cdot 10^{-4}$	140.0	0.003	—
—	Ca XIV	143.31	$1.5 \cdot 10^{-5}$	141.06	0.003	+
327	Ca XV	(144)	$2 \cdot 10^{-5}$	142.1	0.003	—
627	Ni X	144.22 } 144.99 }	$1.6 \cdot 10^{-6}$	144—144.8	0.005	+?
634	Ni IX	146.063	$6 \cdot 10^{-6}$	145.8	0.003	—
391	Mg V	146.03 } 146.46 } 146.62 }	$2.5 \cdot 10^{-5}$			
635	Ni IX	147.15	$1.2 \cdot 10^{-5}$			
439	Ca XII	147.27	$10^{-4}$	147.0	0.001	+
—	Ca XIV	148.11	$3 \cdot 10^{-5}$			
—	Ca XIII	148.84	$3 \cdot 10^{-5}$			
621	Ni XI	148.37 } 148.610 }	$10^{-5}$	148.3	0.017	—
73	O VI	150.09 } 150.12 }	0.002	150.0	0.005	+
293	Ne V	151.42	$1.4 \cdot 10^{-4}$	151.3	0.001	+
129	O V	151.48 } 151.55 }	$6 \cdot 10^{-5}$			
614	Ni XII	152.14	$3 \cdot 10^{-4}$	152	0.001	+
637	Ni IX	152.316	$6 \cdot 10^{-6}$	152.5	0.003	+?
632	Fe VII	152.9	$1.6 \cdot 10^{-5}$			

TABLE II (continued)

No. of multiplet from Table I	Ion	$\lambda$ , Å	$F_t$	$\lambda$ , Å	$F_o$	Identifi- cation
614	Ni XII	152.95	$2 \cdot 10^{-4}$	152.8	0.002	+
615	Ni XII	154.15	$10^{-4}$	154.0	0.004	+
529	Fe XV	154.4	$5 \cdot 10^{-4}$			
413	Ca XIII	156.70	$2 \cdot 10^{-5}$	158—159	<0.001	+
614	Ni XIII	157.75	0.001			
638	Ni X	158.37	$2.5 \cdot 10^{-5}$			
413	Ca XIII	159.87	$2 \cdot 10^{-5}$			
628	Ni X	159.97	$2.5 \cdot 10^{-5}$			
—	Al IV	160.073	$5 \cdot 10^{-6}$	160	0.002	+
413	Ca XIII	161.686	$10^{-5}$	160.3	0.0015	—
		161.748	$5 \cdot 10^{-5}$	162.6	0.001	+
		162.98	$2 \cdot 10^{-5}$			
592	Ni XIV	164.13	0.001	164.5	0.002	+
413	Ca XIII	164.15	$2 \cdot 10^{-5}$	165.6	0.002	—
434	Ar X	(166)	$2 \cdot 10^{-4}$	166.0	0.002	+
279	Ne V	167.48	$3 \cdot 10^{-5}$	167.6	0.005	+?
		167.67				
624	Fe VIII	167.49	$10^{-4}$	167.6	0.005	+?
		167.67				
		168.01				
		168.18				
413	Ca XIII	168.412	$2 \cdot 10^{-5}$	168.5	0.005	+?
434	Ar X	(171)	$3 \cdot 10^{-4}$	169.8	0.005	+
618	Fe IX	171.075	$6 \cdot 10^{-4}$	171.3	0.005	+
203	Ne VI	171.11	$1.2 \cdot 10^{-5}$			
		171.21	$2.4 \cdot 10^{-5}$	172.2	0.002	+
125	O V	172.17	$3 \cdot 10^{-4}$			
77	O VI	172.94	0.0025	172.8	0.005	+
		173.08				
292	Ne V	173.93	$5 \cdot 10^{-5}$	174.7	0.09	+?
608	Fe X	174.53	$6 \cdot 10^{-4}$			
		175.26		175	0.001	+
607	Fe X	177.24	0.003	177.3	0.08	+
598	Fe XI	178.04	$5 \cdot 10^{-4}$	178	0.004	+
598	Fe XI	180.42	$5 \cdot 10^{-4}$	180.6	0.08	+?
416	Mg IV	180.07	$10^{-4}$	181.4	0.005	+
		180.62				
		180.80				
598	Fe XI	181.13	$5 \cdot 10^{-4}$			
416	Mg IV	181.34	$2 \cdot 10^{-5}$	182.5	0.02	+?
573	Ni XV	(182)	$10^{-4}$			
598	Fe XI	182.17	$5 \cdot 10^{-4}$	183.2	0.002	—
15	C VI	182.5	$10^{-5}$	183.9	0.005	+
76	O VI	183.94	$1.5 \cdot 10^{-4}$			
		184.12				
623	Fe VIII	185.22	$2 \cdot 10^{-4}$			
326	Ca XV	(185)	$4 \cdot 10^{-5}$			

TABLE II (continued)

No. of multiplet from Table I	Ion	$\lambda$ , Å	$F_t$	$\lambda$ , Å	$F_o$	Identifi- cation
132	O V	185.75	$9 \cdot 10^{-4}$	185.5	0.006	+
623	Fe VIII	186.60	$10^{-4}$			
589	Fe XII	186.87	$3 \cdot 10^{-4}$			
323	S XI	186.83	$5 \cdot 10^{-4}$	186.9	0.03	+
568	Fe XIII	(187)	0.002			
421	Ar XI	(188)	$10^{-4}$			
		(190)				
568	Fe XIII	(190)	0.001	188.2	0.08	+
45	N VI	(190)	$3 \cdot 10^{-4}$			
560	Ni XVI	(190)	$10^{-4}$			
323	S XI	188.67	0.001	190	0.01	+
		191.26				
389	Ca XIV	(191)	$6 \cdot 10^{-5}$			
128	O V	192.75				
		192.80	0.0018	192.5	0.02	+
		192.91				
389	Ca XIV	(193)	$6 \cdot 10^{-5}$			
578	Fe XIII	(193)	0.001	193.8	0.03	+
421	Ar XI	(193)	$10^{-4}$			
		(194)				
131	O V	194.59	$8 \cdot 10^{-5}$			
635	Fe VIII	194.76	$5 \cdot 10^{-5}$			
421	Ar XI	(195)	$2 \cdot 10^{-5}$	195.3	0.04	+?
635	Fe XIII	195.48	$10^{-4}$	196.0	0.001	+
		196.05				
435	S VIII	198.6	$5 \cdot 10^{-4}$	197	0.004	+
379	Ca XIV	(197)	$6 \cdot 10^{-5}$	197.8	0.003	+?
560	Ni XVI	(199)	$2 \cdot 10^{-4}$	198.6	0.002	+
				199.6	0.002	+
				200.0	0.005	—
				201.2	0.01	—
425	S VIII	202.6	$2 \cdot 10^{-4}$	202.5	0.014	+?
197	O IV	202.9—203.0	$10^{-5}$	203.9	0.008	+?
649	Ni VII	205.0—206.0	$10^{-5}$	205.0	0.002	+?
135	O V	207.79	$4 \cdot 10^{-4}$	207.4 207.5	<0.005	+
585	Fe XII	(209)	0.0013	207.8		+
69	N V	209.27	$8 \cdot 10^{-5}$	209.3	0.007	+
		209.30	$4 \cdot 10^{-5}$	210.0	<0.001	+
567	Fe XIII	(210)	0.003	211.2	0.002	+?
325	Ca XV	(210)	$1.5 \cdot 10^{-4}$	211.8	0.005	+
544	Fe XIV	211.3	0.02	213	0.01	+
248	S XIII	(212)	0.0035		0.001	+
647	Ni VII	212.5—213.8	$6 \cdot 10^{-5}$	214.7		
648	Ni VII	213.9—214.4	$6 \cdot 10^{-6}$		<0.002	+
367	Si VIII	214.75	$2 \cdot 10^{-4}$	215		
127	O V	215.03			0.003	+
		215.10	$4 \cdot 10^{-4}$			
		215.24				

TABLE II (continued)

No. of multiplet from Table I	Ion	$\lambda$ , Å	$F_t$	$\lambda$ , Å	$F_o$	Identifi- cation
377	Ar XII	215.49	$10^{-4}$	215.5	0.001	+
136	O V	216.02	$4 \cdot 10^{-5}$	216.5	0.001	+
367	Si VIII	216.92	$3 \cdot 10^{-4}$			
405	Si VII	217.8	$4 \cdot 10^{-4}$			
325	Ca XV	(218)	$1.5 \cdot 10^{-4}$	217.2	0.007	+
377	Ar XII	218.29	$3 \cdot 10^{-4}$	219	0.002	+
544	Fe XIV	219.1	0.04	219.3	0.003	+
572	Ni XV	(220)	$6 \cdot 10^{-5}$			
130	O V	220.35	0.001	220.3	0.003	+
406	S IX	(222)	0.0015	222.3	0.003	+
306	Si IX	223.72	0.001	223.6	0.002	+
377	Ar XII	224.25	$10^{-4}$			
406	S IX	224.7	0.0015	224.9	0.007	+
306	Si IX	225.03	0.001			
406	S IX	225.23	0.0015	225.2	0.008	+
306	Si IX	227.01	0.001			
325	Ca XV	(227)	$1.5 \cdot 10^{-4}$	227	0.007	+
313	Si IX	227.3	0.0036			
325	Ca XV	(228)	$1.5 \cdot 10^{-4}$			
406	S IX	(228)	0.0015	228	0.001	+
368	Si VIII	229.8	$5 \cdot 10^{-4}$			
		230.2		230	0.001	+
535	Fe XV	231.50	0.018	231.6	0.001	+
247	S XII	231.5	$3 \cdot 10^{-4}$			
244	P XI	(232—240)	$3 \cdot 10^{-5}$			
—	Mg III	231.73	$3 \cdot 10^{-5}$			
548	Ni XVI	(233)	$2 \cdot 10^{-4}$			
629	Fe VII	233.02	$2.4 \cdot 10^{-4}$	233.2	0.001	+
362	Si VIII	233.16	$5 \cdot 10^{-4}$			
—	Mg III	234.26	$3 \cdot 10^{-5}$			
630	Fe VII	235.23	$2.4 \cdot 10^{-4}$	234.5	0.006	—
362	Si VIII	235.56	$5 \cdot 10^{-4}$	235.3	0.002	+
548	Ni XVI	(236)	$4 \cdot 10^{-4}$	236.2	0.001	+
584	Fe XII	(238)	0.001	237.0	0.003	+
				237.5		
194	O IV	238.36	$4 \cdot 10^{-4}$	238.3	0.002	+
		238.57		238.6		
251	S XII	(239)	$3 \cdot 10^{-4}$			
322	S XI	239.81	0.001	240	0.001	+
547	Ni XVI	(242)	$10^{-4}$	240.7	0.002	+
322	S XI	242.57	0.002			
		242.83		242	0.008	+
9	He II	243.02	0.001	243	0.003	+
633	Fe VII	243.4	$8 \cdot 10^{-5}$			
395	Al VI	243.8	$2 \cdot 10^{-5}$			
65	C IV	244.90	$6 \cdot 10^{-5}$	245	0.002	+
631	Fe VII	245.93	$8 \cdot 10^{-5}$			

TABLE II (continued)

No. of multiplet from Table I	Ion	$\lambda$ , Å	$F_t$	$\lambda$ , Å	$F_o$	Identifi- cation
418	Si VI	246.0	$8 \cdot 10^{-4}$	246.1	0.002	+
404	Si VII	246.1	0.0015			
160	Al X	246.14	0.003			
322	S XI	246.90	0.001			
120	N IV	247.2	$10^{-4}$	247.4	0.001	+
71	N V	247.56	$4 \cdot 10^{-4}$			
		247.71				
243	P XI	247.9—254.0	$3 \cdot 10^{-5}$			
39	C V	248.67	$3 \cdot 10^{-4}$			
		248.74				
489	S VI	(249)	$1.5 \cdot 10^{-4}$			
418	Si VI	249.13	$4 \cdot 10^{-4}$			
519	Ar VII	249.89	$8 \cdot 10^{-6}$			
		250.94				
502	Fe XVI	(250)	$10^{-4}$	2 May 1963 /27/ (23 Aug. 1961 /26/)		
547	Ni XVI	(250)	$5 \cdot 10^{-5}$	249.2	0.0015	+
566	Fe XIII	(250)	0.002			
361	Si VIII	(251)	$5 \cdot 10^{-4}$			
301	Al VIII	251.3	$1.7 \cdot 10^{-4}$			
542	Fe XIV	251.8	0.015	252	0.004	+
322	S XI	(253)	0.004	254	0.002	+
227	Si X	253.81	0.0035	255.2	0.001	+
530	Ni XVII	(255)	$8 \cdot 10^{-4}$	256.3	0.01	+
8	He II	256.31	0.005	257	0.01	+
227	Si X	256.58	0.007			
373	S X	257.16	0.004			
184	S XIII	257.5	0.002			
314	Si IX	258.1	0.0045	258.2 (255—260)	0.005 0.02 0.003	+ + +
227	Si X	258.39	0.011			
373	S X	259.52	0.003			
319	Si IX	259.7	0.004			
196	O IV	260.38	$2 \cdot 10^{-4}$	260.2	0.001	+
		260.56				
651	Ni VI	260.35	$8 \cdot 10^{-5}$	261	0.002	+
		260.59				
		260.71				
227	Si X	261.27	0.003			
502	Fe XVI	261.57	$5 \cdot 10^{-4}$			
502	Fe XVI	(264)	$4 \cdot 10^{-4}$			
373	S X	264.24	0.003			
542	Fe XIV	264.5	0.03	264.4	0.004	+
70	N V	266.19	$1 \cdot 10^{-4}$	266.4	0.001	+?
		266.38				

TABLE II (continued)

No. of multiplet from Table I	Ion	$\lambda$ , Å	$F_t$	$\lambda$ , Å	$F_o$	Identifi- cation
542	Fe XIV	270.5	0.01	270.2 (270.5)	0.002 0.005	+
225	Si X	272.0	$6 \cdot 10^{-4}$	272	0.003	+
397	Si VII	272.6	$7 \cdot 10^{-4}$			
		274.1	$5 \cdot 10^{-4}$	274.1	0.004	+
541	Fe XIV	274.3	$5 \cdot 10^{-4}$			
397	Si VII	275.35	0.002	275	0.002	+
396	Al VI	275.35	$5 \cdot 10^{-5}$	(275.5)	0.005	
397	Si VII	275.7	$5 \cdot 10^{-4}$			
397	Si VII	276.8	$5 \cdot 10^{-4}$			
366	Si VIII	276.84 } 277.05 }	0.001	277	0.003	+
255	Si X	277.27	$6 \cdot 10^{-4}$			
641	Fe VI	277.57	$2 \cdot 10^{-4}$			
292	Mg VII	278.40	$6 \cdot 10^{-4}$	278.3	0.002	+
397	Si VII	278.44	$7 \cdot 10^{-4}$	(278.5)	0.004	
417	Al V	278.7	$6 \cdot 10^{-5}$			
203	O IV	279.63 } 279.94 }	0.001	280 (280)	$6 \cdot 10^{-4}$ 0.001	+
230	Si X	280.0	0.002			
295	Mg VII	280.7	$6 \cdot 10^{-4}$	281	$6 \cdot 10^{-4}$	+?
417	Al V	281.4	$3 \cdot 10^{-5}$			
321	S XI	(282—293)	0.0015	282.3	$8 \cdot 10^{-4}$	+
588	Fe XII	(283)	$3 \cdot 10^{-4}$			
522	Fe XV	284.1	0.05	284.2	0.02	+
302	Al VIII	287.0	$2 \cdot 10^{-4}$	(283)	0.03	
239	Si X	287.2	0.004	286	0.0015	+
182	P XII	287.7	$5 \cdot 10^{-4}$			
541	Fe XIV	288.7	0.025	288.5 (288)	0.0015 0.003	+
246	S XII	(290)	$2 \cdot 10^{-4}$	289.6	$8 \cdot 10^{-4}$	+
571	Ni XV	(290)	$1.5 \cdot 10^{-4}$			
642	Fe VI	290.27	$5 \cdot 10^{-5}$			
303	Si IX	290.63	0.007	291	0.001	+
641	Fe VI	291.18	$2 \cdot 10^{-4}$	(291)	0.003	
642	Fe VI	291.23	$5 \cdot 10^{-5}$			
639	Fe VI	291.80	$10^{-5}$			
640	Fe VI	292.74	$5 \cdot 10^{-5}$			
303	Si IX	292.83	0.007	293	0.003	+
641	Fe VI	293.0	$10^{-5}$	(293)	0.001	
321	S XI	(282—293)	0.0015			
507	Ni XVIII	293.3	$2 \cdot 10^{-4}$			
639	Fe VI	293.38	$10^{-5}$			
638	Fe VI	293.49	$2 \cdot 10^{-4}$			
639	Fe VI	293.75 } 293.97 }	$2 \cdot 10^{-5}$			
639	Fe VI	294.25	$10^{-5}$			

TABLE II (continued)

No. of multiplet from Table I	Ion	$\lambda$ , Å	$F_T$	$\lambda$ , Å	$F_O$	Identifi- cation
640	Fe VI	294.26	$5 \cdot 10^{-5}$			
638	Fe VI	294.34	$2 \cdot 10^{-4}$	294	$5 \cdot 10^{-5}$	+
639	Fe VI	294.52	$10^{-5}$			
638	Fe VI	294.34	$2 \cdot 10^{-4}$			
638	Fe VI	295.0	$4 \cdot 10^{-4}$	295	0.001	+
638	Fe VI	295.63	$2 \cdot 10^{-4}$	297.3	$6 \cdot 10^{-4}$	—
				296.2	0.004	+
303	Si IX	296.19	0.007	(296)	0.005	
613	Ni XII	(299)	$2 \cdot 10^{-4}$	298.6	$8 \cdot 10^{-4}$	+
549	Ni XVI	(300)	$3 \cdot 10^{-5}$			
246	S XIII	(302)	$5 \cdot 10^{-4}$	299.6	0.001	+
				(300)	0.005	
165	Si XI	303.41	0.04	303.4	(0.025)	+
				(303.4)		
7	He II	303.78	0.6	303.8	0.25	+
				(304)		
603	Ni XIII	(304)	$5 \cdot 10^{-4}$			
223	Al IX	305.1	$1.8 \cdot 10^{-4}$	305	0.001	+
268	O III	305.8	$5 \cdot 10^{-4}$	306	0.001	+
394	Al VI	307.2—310.3	$1.5 \cdot 10^{-4}$	307.2	$4 \cdot 10^{-4}$	+
360	Si VIII	308.26	0.0025	308.5	$5 \cdot 10^{-4}$	+
355	Al VII	309.0	$6 \cdot 10^{-5}$			
394	Al VI	307.2—310.3	$1.5 \cdot 10^{-4}$			
590	Ni XIV	(311)	0.001			
210	Mg VIII	311.78	0.0016	(311)	0.001	+
286	Na VI	311.92	$7 \cdot 10^{-6}$			
603	Ni XIII	(312)	$5 \cdot 10^{-4}$			
540	Ni XVI	(312)	$6 \cdot 10^{-5}$			
64	C IV	312.42	$4 \cdot 10^{-4}$			
		312.45	$2 \cdot 10^{-4}$			
286	Na VI	312.61	$7 \cdot 10^{-6}$			
386	Ne III	313.0	$2 \cdot 10^{-5}$			
210	Mg VIII	313.73	0.003	(313)	0.005	+
286	Na VI	313.75	$7 \cdot 10^{-6}$			
356	Si VIII	314.31	0.002			
350	Mg VI	314.5	$4 \cdot 10^{-4}$			
590	Ni XIV	(315)	0.001			
210	Mg VIII	315.02	0.0044	(315)	0.006	+
242	P XI	315.3	$3 \cdot 10^{-5}$			
570	Ni XV	316	$1.3 \cdot 10^{-4}$			
356	Si VIII	316.2	0.004	(316)	0.005	+
603	Ni XIII	(317)	$5 \cdot 10^{-4}$			
210	Mg VIII	317.01	0.0012			
288	Na VI	317.6	$2 \cdot 10^{-5}$			
294	Mg VII	319.0	0.0016			
356	Si VIII	319.83	0.006	(320)	0.005	+
415	Mg IV	321.0	$4 \cdot 10^{-4}$			

TABLE II (continued)

No. of multiplet from Table I	Ion	$\lambda$ , Å	$F_t$	$\lambda$ , Å	$F_o$	Identifi- cation
507	Ni XVIII	(322)	$10^{-4}$	(321)	0.004	+
613	Ni XII	(322)	$4 \cdot 10^{-4}$			
603	Ni XIII	(323)	0.004			
590	Ni XIV	(323)	0.002			
415	Mg IV	323.31	$3 \cdot 10^{-4}$			
300	Al VIII	323.5—328.2	$7 \cdot 10^{-4}$	(325)	0.003	+
603	Ni XIII	(324)	$5 \cdot 10^{-4}$			
242	P XI	325.2	$6 \cdot 10^{-5}$			
587	Fe XII	(326)	$3 \cdot 10^{-4}$			
300	Al VIII	323.5—328.2	$7 \cdot 10^{-4}$			
565	Fe XIII	(330)	0.004	(328)	0.002	+
603	Ni XIII	(332)	$5 \cdot 10^{-4}$	(333)	0.0015	+
159	Al X	332.9	0.006			
570	Ni XV	(333)	$10^{-4}$			
209	Mg VIII	335.3	$8 \cdot 10^{-4}$			
500	Fe XVI	335.4	0.008			
183	P XII	335.6	$10^{-6}$	(335)	0.02	+
177	S XIII	335.6	$6 \cdot 10^{-4}$	(339)	0.002	+
209	Mg VIII	339.01	0.0016			
305	Si IX	342.2	0.008			
221	Mg VIII	342.2	$2 \cdot 10^{-4}$			
543	Fe XIV	344.6	0.008			
305	Si IX	345.10	0.008	(344)	0.002	+
285	O III	345.31	0.001			
570	Ni XV	(346)	$10^{-4}$			
606	Fe X	(347)	$5 \cdot 10^{-4}$			
226	Si X	347.43	0.006			
231	Si X	349.0	0.003	(347)	0.005	+
352	Mg VI	349.1	$7 \cdot 10^{-4}$			
305	Si IX	349.96	0.008			
597	Fe XI	(350)	0.001			
205	Na VII	350.65	$10^{-5}$			
390	Mg V	351.09	$3 \cdot 10^{-4}$	(353)	0.008	+
390	Mg V	352.20	$3 \cdot 10^{-4}$			
353	Al VII	352.2	$5 \cdot 10^{-5}$			
205	Na VII	352.28	$10^{-5}$			
222	Mg VIII	352.38	$3 \cdot 10^{-4}$			
390	Mg V	353.10	$3 \cdot 10^{-4}$			
205	Na VII	353.29	$10^{-5}$			
390	Mg V	353.30	$3 \cdot 10^{-4}$			
353	Al VII	353.8	$10^{-4}$			
221	Mg VIII	353.84	$2 \cdot 10^{-4}$			
390	Mg V	354.22	$3 \cdot 10^{-4}$			
205	Na VII	354.95	$10^{-5}$			
390	Mg V	355.32	$3 \cdot 10^{-4}$			



TABLE II (continued)

No. of multiplet from Table I	Ion	$\lambda$ , Å	$F_t$	$\lambda$ , Å	$F_o$	Identifi- cation			
543	Fe XIV	(356)	0.004	(36)	0.006	+			
583	Fe XII	(356)	0.004						
222	Mg VIII	356.00	$3 \cdot 10^{-4}$						
226	Si X	356.07	0.006						
353	Al VII	356.9	$2 \cdot 10^{-4}$						
597	Fe XI	(358)	0.001						
278	Ne V	358.0	$2 \cdot 10^{-4}$						
		358.5							
		359.4							
564	Fe XIII	(360)	0.003	(361)	0.015	+			
583	Fe XII	(360)	0.02						
597	Fe XI	(360)	0.001						
500	Fe XVI	360.7	0.004						
237	Si X	360.8	0.002						
287	Na VI	361.25	$4 \cdot 10^{-5}$						
499	Mn XV	361.5	$10^{-4}$						
647	Fe V	364.29	$2 \cdot 10^{-5}$	(365)	0.01	+			
		364.80							
		364.97							
168	Si XI	365.4	0.018						
281	Ne V	365.59	$2 \cdot 10^{-4}$						
647	Fe V	365.63	$10^{-5}$						
626	Fe VIII	365.87	$10^{-5}$						
647	Fe V	365.86	$2 \cdot 10^{-5}$	(368)	0.02	+			
		366.00							
543	Fe XIV	(366)	0.008				(368)	0.02	+
606	Fe X	(367)	0.001						
597	Fe XI	(367)	0.001						
146	Mg IX	368.07	0.0015						
583	Fe XII	(369)	0.004						
597	Fe XI	(369)	0.001						
626	Fe VIII	370.43	$2 \cdot 10^{-5}$						
113	C III	371.69	$1.6 \cdot 10^{-5}$	(374.5) (377)	0.002 0.002	+? +			
		371.75							
		371.78							
—	Na II	372.07	$2 \cdot 10^{-5}$				(374.5) (377)	0.002 0.002	+? +
564	Fe XIII	(373)	0.003						
198	N III	374.2	$6 \cdot 10^{-5}$						
597	Fe XI	(376)	0.001						
—	Na II	376.38	$2 \cdot 10^{-5}$						
388	Ne III	379.3	$6 \cdot 10^{-5}$						
299	Al VIII	381.1	$10^{-4}$						
206	Na VII	381.3	$8 \cdot 10^{-5}$	(384)	0.001	+			
299	Al VIII	383.7	$10^{-4}$						
67	C IV	384.03—	0.001						
		384.28							
224	Al IX	385.0—392.4	$6 \cdot 10^{-4}$						
499	Mn XV	385.4	$5 \cdot 10^{-5}$						

TABLE II (continued)

No. of multiplet from Table I	Ion	$\lambda$ , Å	$F_t$	$\lambda$ , Å	$F_o$	Identifi- cation
644	Fe V	385.0	$2 \cdot 10^{-4}$			
		385.9	$3 \cdot 10^{-4}$			
564	Fe XIII	(386)	0.003	(385)	0.001	+
644	Fe V	386.8	$10^{-4}$			
645	Fe V	386.8	$6 \cdot 10^{-5}$			
		387.2	$8 \cdot 10^{-6}$			
		387.7	$3 \cdot 10^{-5}$			
349	Mg V	387.79	0.002	(389)	0.002	+
		388.02				
299	Al VIII	(388)	$2 \cdot 10^{-4}$			
645	Fe V	388.6	$6 \cdot 10^{-5}$			
498	Cr XIV	390.1	$6 \cdot 10^{-5}$			
234	Si X	392.0—399.3	$6 \cdot 10^{-4}$			
348	Mg VI	399.29	$8 \cdot 10^{-4}$			
201	Ne VI	399.82	$10^{-4}$			
348	Mg VI	400.68	0.0015	(400—404)	0.003	+
346	Na V	400.72	$4 \cdot 10^{-5}$			
201	Ne VI	401.14	$4 \cdot 10^{-4}$			
201	Ne VI	401.94	$6 \cdot 10^{-4}$			
		403.26	$10^{-4}$			
348	Mg VI	403.32	0.002			
389	Na IV	408.68	$8 \cdot 10^{-5}$			
		409.61				
		410.37				
		410.54				
		411.33				
		412.24				
144	Na VIII	411.2	$4 \cdot 10^{-4}$	(411)	0.002	+
498	Cr XIV	412.5	$3 \cdot 10^{-4}$	(417)	0.005	+
523	Fe XV	(414)	0.01			
284	Na VI	414.3	$10^{-4}$			
563	Ca VII	414.7	$8 \cdot 10^{-6}$			
280	Ne V	416.20	0.001	(418)	0.002	+
—	Fe V	418.0	$1.6 \cdot 10^{-4}$			
66	C IV	419.2	$3 \cdot 10^{-4}$			
		419.71				
108	S XIV	(421)	$4 \cdot 10^{-4}$			
387	Ne III	427.8	$2.5 \cdot 10^{-4}$			
290	Mg VII	429.1	0.001	(430)	0.002	+
339	O II	429.9—430.2	$5 \cdot 10^{-4}$			
211	Mg VIII	430.47	0.001			
199	Ne VI	433.18	$3 \cdot 10^{-4}$			
290	Mg VII	434.7	0.001	(435)	0.004	+
284	O III	434.98	0.01			
290	Mg VII	435.3	0.001			

TABLE II (continued)

No. of multiplet from Table I	Ion	$\lambda$ , Å	$F_t$	$\lambda$ , Å	$F_o$	Identifi- cation
220	Mg VIII	442.2	$3 \cdot 10^{-4}$	(443—446)	0.002	+
149	Mg IX	(444)	$5 \cdot 10^{-4}$			
347	Na V	445.05	$8 \cdot 10^{-5}$			
		445.19	$2 \cdot 10^{-4}$			
198	S XIV	(446)		(454)	0.002	—
—	Ne II	445.03				
		446.25				
		446.53				
		447.81				
538	Ar VI	457.48	$10^{-4}$			
345	Na V	459.90	$7 \cdot 10^{-5}$			
	Ne II	460.72	$4 \cdot 10^{-5}$			
345	Na V	461.05	$7 \cdot 10^{-5}$			
539	Ca VIII	461.7	$2 \cdot 10^{-4}$			
538	Ar VI	462.01				
		462.15	$10^{-4}$			
	Ne II	462.39	$2 \cdot 10^{-5}$			
345	Na V	463.26	$7 \cdot 10^{-5}$			
137	Ne VII	465.21	0.008	(465)	0.008	+
520	Ca IX	466.2	$6 \cdot 10^{-4}$			
343	Ne IV	469.77				
		469.82				
		469.87	$5 \cdot 10^{-4}$	(469)	0.002	+
		469.92				
539	Ca VIII	471.1	$4 \cdot 10^{-4}$			
518	Ar VII	475.66	$2 \cdot 10^{-4}$			
518	Ar VII	479.38	$10^{-4}$			
497	Ti XII	480.1	$8 \cdot 10^{-6}$			
276	Ne V	480.4				
—		481.4	$8 \cdot 10^{-4}$	(481)	0.002	+
		483.0				
204	Na VII	486.74	$5 \cdot 10^{-5}$			
410	S IX	488	0.008	(488)	0.003	+
385	Ne III	488.10				
		488.87				
		489.50	$9 \cdot 10^{-4}$			
		489.64				
		490.31				
—	Ca III	490.55	$3 \cdot 10^{-6}$	(490—496)	0.001	+
219	Mg VIII	490.8	$5 \cdot 10^{-4}$			
385	Ne III	491.05	$10^{-4}$			
285	Na VI	491.4	$6 \cdot 10^{-4}$			
204	Na VII	491.95	$5 \cdot 10^{-5}$			
285	Na VI	494.3	$7 \cdot 10^{-4}$			
102	Si XII	499.28	0.006	(500)	0.012	+
267	O III	507.68				
		508.18	0.004	(508)	0.003	+

TABLE II (continued)

No. of multiplet from Table I	Ion	$\lambda$ , Å	$F_t$	$\lambda$ , Å	$F_o$	Identifi- cation
580	Ca VI	(510)	$4 \cdot 10^{-5}$			
31	He I	512.0	$10^{-4}$	(512)	0.001	+
30	He I	515.6	$3 \cdot 10^{-4}$	(515)	$5 \cdot 10^{-4}$	+
102	Si XII	521.11	0.003	(520)	0.006	+
344	Ne IV	521.3	0.001			
29	He I	522.2	0.001			
560	Ar V	522.09	$6 \cdot 10^{-6}$			
		524.20	$6 \cdot 10^{-6}$			
271	O III	525.80	$3 \cdot 10^{-4}$	(525)	0.002	+
650	Fe IV	525.68	$3 \cdot 10^{-4}$			
650	Fe IV	526.28	$2 \cdot 10^{-4}$			
		526.60	$10^{-4}$			
560	Ar V	527.69	$6 \cdot 10^{-6}$			
28	He I	537.0	0.002	(537)	0.004	+
112	C III	538.08	$2 \cdot 10^{-4}$			
		538.15				
		538.31				
338	O II	539.1—539.8	0.001			
342	Ne IV	541.13	$4 \cdot 10^{-4}$	(542)	0.001	+
		542.07	$8 \cdot 10^{-4}$			
		543.89	0.0012			
537	Ar VI	544.73	$3 \cdot 10^{-5}$			
116	C III	547.9	$2 \cdot 10^{-5}$			
537	Ar VI	548.91	$3 \cdot 10^{-5}$			
101	Al XI	550	0.0016	(550)	0.001	+
537	Ar VI	551.37	$3 \cdot 10^{-5}$			
562	Ca VII	551.5	$10^{-4}$			
192	O IV	553.33	0.01	(553)	0.01	+
		554.07				
		554.51				
		555.26				
233	Si X	555.0	0.002			
409	S IX	(555)	0.0025			
537	Ar VI	555.64	$3 \cdot 10^{-5}$			
494	Ca X	557.74	0.001	(558)	0.001	+
200	Ne VI	558.74	$7 \cdot 10^{-4}$			
200	Ne VI	562.80	0.0014	(562)	0.001	+
166	Si XI	565.1	0.004	(565)	0.001	+
277	Ne V	568.42	$5 \cdot 10^{-4}$	(568)	0.002	+
101	Al XI	569	$8 \cdot 10^{-4}$			
277	Ne V	569.81	$5 \cdot 10^{-4}$			
		572.11	0.001	(572)	0.0015	+
		572.34				
494	Ca X	574.00	$6 \cdot 10^{-4}$	(574)	0.002	+
540	Ca VIII	582.8	$3 \cdot 10^{-4}$	(581)	0.002	+
27	He I	584.4	0.03	(585)	0.03	+

TABLE II (continued)

No. of multiplet from Table I	Ion	$\lambda$ , A	$F_t$	$\lambda$ , A	$F_o$	Identifi- cation
517	Ar VII	585.75	$6 \cdot 10^{-4}$			
536	Ar VI	588.92	$10^{-4}$			
166	Si XI	591.2	0.002	(593)	0.001	+
536	Ar VI	596.69	$2 \cdot 10^{-4}$			
540	Ca VIII	596.9	$6 \cdot 10^{-4}$			
270	O III	597.82	0.004			
273	O III	597.82	0.01	(599)	0.003	+
270	O III	599.60	0.004			
191	O IV	608.40	0.003	(608)	0.01	+
191		609.83	0.006			
95	Mg X	609.85	0.02	(610)	0.014	+
272	O III	609.70				
		610.04				
		610.75	$1.5 \cdot 10^{-4}$			
		610.85				
				(617)	0.001	-
493	K IX	621.4	$10^{-5}$	(621.5)	$10^{-4}$	+
561	Ca VII	624.4	$3 \cdot 10^{-4}$			
198	O IV	624.62				
		625.13	0.01			
		625.85	0.01	(625)	0.006	+
95	Mg X	625.28				
579	Ca VI	629.60	$9 \cdot 10^{-4}$			
123	O V	629.73	0.016	(630)	0.025	+
561	Ca VII	630.6	$3 \cdot 10^{-4}$			
579	Ca VI	633.82	$9 \cdot 10^{-4}$	(634)	0.001	+
493	K IX	636.3	$5 \cdot 10^{-6}$			
596	Ca V	637.93	$10^{-4}$			
561	Ca VII	639.2				
		640.5	$6 \cdot 10^{-4}$	(639)	0.001	+
579	Ca VI	641.88	$9 \cdot 10^{-4}$			
596	Ca V	643.12	$10^{-4}$			
262	N II	644.62				
		644.8	$10^{-4}$			
		645.17				
596	Ca V	646.57	$10^{-4}$	(645)	$< 0.001$	+
		647.88	$10^{-4}$			
		651.55	$10^{-4}$	(651)	$10^{-4}$	+
—	Ca IV	656.04	$6 \cdot 10^{-5}$			
596	Ca V	656.76	$10^{-4}$			
	[Ar XIII]	658.7	?			
304	Si IX	666.62	0.001	(670)	$10^{-4}$	+
—	Ca IV	669.72	$3 \cdot 10^{-5}$			
582	Ca VI	674.28	$3 \cdot 10^{-4}$			
555	S III	677.8—680.7	$2 \cdot 10^{-4}$			
521	Ca IX	678.6—693.8	$3 \cdot 10^{-5}$			

TABLE II (continued)

No. of multiplet from Table I	Ion	$\lambda$ , Å	$F_t$	$\lambda$ , Å	$P_o$	Identifi- cation
218	Mg VIII	680.3	$5 \cdot 10^{-4}$	(680)	0.002	+
91	Na IX	681.72	$3 \cdot 10^{-4}$			
578	Ar IV	683.27	$10^{-5}$			
187	N III	685.00	$4 \cdot 10^{-4}$	(685—687)	0.004	+
		685.51				
		685.82				
		686.34				
183	C II	687.4	$8 \cdot 10^{-4}$	(690)	$< 0.001$	+
578	Ar IV	688.39	$10^{-5}$			
		689.01	$10^{-5}$			
117	C III	690.9	$10^{-4}$	(692)	$< 0.001$	+
147	Mg IX	692.4	0.002	(692)	$< 0.001$	+
91	Na IX	(695)	$1.5 \cdot 10^{-4}$	(694)	$< 0.001$	+
481	Al III	695.82	$8 \cdot 10^{-5}$	(698)	$< 0.001$	+
		696.21				
553	S III	700.29	$3 \cdot 10^{-4}$	(704)	0.007	+
492	Ar VIII	700.4	$6 \cdot 10^{-4}$			
266	O III	702.3—703.9	0.015	(710)	$< 0.001$	+
147	Mg IX	704.5	0.002			
559	Ar V	705.35	$3 \cdot 10^{-5}$	(718, 5)	0.003	+
490	S VI	706.5	$5 \cdot 10^{-5}$			
559	Ar V	709.20	$3 \cdot 10^{-5}$	(730)	0.001	—
147	Mg IX	710.3	0.002			
490	S VI	712.7	$5 \cdot 10^{-5}$	(736)	0.001	—
492	Ar VIII	714.0	$3 \cdot 10^{-4}$			
559	Ar V	715.60	$3 \cdot 10^{-5}$	(750)	$< 0.001$	+
		715.64				
340	O II	718.48	0.006	(760)	0.003	+
		718.56				
554	S III	724.3—725.9	$2 \cdot 10^{-4}$	(763)	0.001	—
535	S IV	(744)	$5 \cdot 10^{-5}$	(750)	$< 0.001$	+
661	Ni III	(744)	$7 \cdot 10^{-5}$			
264	N II	746.98	$3 \cdot 10^{-4}$	(760)	0.003	+
298	Al VII	749.0	$3 \cdot 10^{-4}$			
535	S IV	749	$5 \cdot 10^{-5}$	(763)	0.001	—
126	O V	758.68	$0.007$			
		759.44	(760)	0.003	+	
		760.23				$0.007$
		760.44	(763)	0.001	—	
		761.13				$0.007$
		762.00	(763)	0.001	—	
661	Ni III	(763)				$7 \cdot 10^{-5}$
186	N III	763.34	$4 \cdot 10^{-4}$	(763)	0.001	—
		764.4	$4 \cdot 10^{-4}$			
581	Ca VI	764.36	$2 \cdot 10^{-4}$			

TABLE II (continued)

No. of multiplet from Table I	Ion	$\lambda$ , Å	$F_t$	$\lambda$ , Å	$F_o$	Identifi- cation			
118	N IV	765.14	0.013	(765)	0.007	+			
81	Ne VIII	770.41	0.004	(771)	0.01	+			
133	O V	774.5	0.002	(774)	0.001	+			
263	N II	775.96	0.001						
661	Ni III	778	$7 \cdot 10^{-5}$						
145	Na VIII	778.9	$10^{-5}$	(780)	0.005	+			
195	O IV	779.8	0.0015						
81	Ne VIII	780.32	0.002						
515	S V	786.5	0.003	(787)	0.008	+			
190	O IV	787.7	0.002						
190	O IV	790.10	0.004	(790)	0.01	+			
		790.20							
145	Na VIII	793.3	$10^{-5}$	(796)	0.001	+			
341	O II	796.66	0.006						
557	S III	796.7	$10^{-4}$						
491	Cl VII	800.7	$3 \cdot 10^{-4}$	(799)	0.001	+			
				(802)	0.001	—			
				(806)	0.001	—			
				(809)	0.001	+			
533	S IV	809.7	$6 \cdot 10^{-4}$	(833—835)	<0.001	+			
654	Fe III	811.3	$2 \cdot 10^{-4}$						
491	Cl VII	813.7	$1.5 \cdot 10^{-4}$						
485	Si IV	815.05	$5 \cdot 10^{-5}$						
533	S IV	816.0	0.001						
485	Si IV	818.13	$5 \cdot 10^{-5}$						
558	Ar V	822.16	$10^{-4}$						
		827.06	$2 \cdot 10^{-4}$			(828)	0.001	+	
		827.35							
337	O II	832.75	0.02			>0.015	+		
267	O III	832.93	0.025						
337	O II	833.33	0.04						
267	O III	833.74	0.025						
337	O II	834.46	0.06						
558	Ar V	834.88	$10^{-4}$						
267	O III	835.10	0.05						
		835.29							
558	Ar V	835.79	$10^{-4}$		(843)			0.002	+
		836.13	$10^{-4}$						
577	Ar IV	840.03	$5 \cdot 10^{-4}$						
660	Ni III	(843)	$10^{-5}$						
291	Mg VII	843.03	0.004						
577	Ar IV	843.77	$5 \cdot 10^{-4}$						
654	Fe III	844.3	$2 \cdot 10^{-4}$						
660	Ni III	(846)	$10^{-5}$						
654	Fe III	847.5	$2 \cdot 10^{-4}$						
660	Ni III	(848)	$10^{-5}$						
577	Ar IV	850.60	$5 \cdot 10^{-4}$	(849)	0.002	+			
658	Ni III	(852)	$2 \cdot 10^{-5}$						
660	Ni III	(852)	$3 \cdot 10^{-5}$						

TABLE II (continued)

No. of multiplet from Table I	Ion	$\lambda$ , Å	$F_t$	$\lambda$ , Å	$F_o$	Identifi- cation
659	Ni III	(853)	$2 \cdot 10^{-6}$			
659	Ni III	(856)	$2 \cdot 10^{-5}$			
658	Ni III	(858)	$2 \cdot 10^{-5}$			
182	C II	858.1	$3 \cdot 10^{-4}$	(858)	0.003	+
265	N II	858.37	$3 \cdot 10^{-4}$			
653	Fe III	858.60	$5 \cdot 10^{-4}$			
182	C II	858.6	$3 \cdot 10^{-4}$			
660	Ni III	(859)	$10^{-5}$			
653	Fe III	859.7	$5 \cdot 10^{-4}$			
658	Ni III	(860)	$2 \cdot 10^{-5}$			
659	Ni III	(860)	$2 \cdot 10^{-6}$			
653	Fe IV	861.8	$5 \cdot 10^{-4}$	(863)	0.002	+
659	Ni III	(864)	$2 \cdot 10^{-6}$			
658	Ni III	(867)	$2 \cdot 10^{-4}$	(867)	0.001	+
659	Ni III	(870)	$2 \cdot 10^{-6}$	(870)	0.001	—
595	Ar III	871.10		(872)	0.001	+?
		875.53				
		878.73	$8 \cdot 10^{-4}$	(877)	0.001	+
		879.62		(879)	0.001	+?
		883.18		(883)	0.001	+?
		887.40		(885)	0.001	—
138	Ne VII	(892)	0.002	(890)	0.002	+
				(894)	0.002	—
181	C II	903.61	0.006	(900—906)	0.003	+
		903.95				
		904.13				
		904.47				
576	S II	906.9	$5 \cdot 10^{-6}$			
		910.5	$5 \cdot 10^{-6}$			
553	S III	911.8	0.001			
576	S II	912.7	$5 \cdot 10^{-6}$			
261	N II	915.60	0.0015	(916)	0.001	+
		916.00				
		916.70				
121	N IV	921.98	0.001	(923)	0.006	+
		922.51				
		923.04				
		923.21				
		923.67				
		927.27				
6	H I	930.75	0.003	(930)	0.006	+
488	S VI	933.38	0.003	(933)	<0.003	+
5	H I	937.8	0.005	(937)	0.005	+
488	S VI	944.52	0.0015	(944)	0.001	+
				(945)	0.001	—
4	H I	949.7	0.01	(950)	0.007	+
—	[Si IX]	952				



TABLE II (continued)

No. of multiplet from Table I	Ion	$\lambda$ , Å	$F_t$	$\lambda$ , Å	$F_o$	Identifi- cation
330	N I	964.0—965.1	$10^{-6}$			
3	H I	972.5	0.03	(972)	0.008	+
110	C III	977.0	0.17	(977)	0.08	+
185	N III	939.79	0.004	(989)	0.003	+
		991.51 } 991.56 }	0.002	(991)	0.01	+
514	Si II	993.52 } 994.79 }	$10^{-5}$			
655	Fe III	997.08	0.001	(999)	$<0.001$	+
514	Si III	997.39	$10^{-5}$			
184	C II	1009.85 } 1010.07 } 1010.37 }	$2 \cdot 10^{-4}$	(1007) (1010)	0.001 0.001	— +
551	S III	1012.61	0.001	(1012) (1019)	0.001 0.001	— +
2	H I	1025.7	0.08	(1025)	0.05	+
384	O I	1025.77	$9 \cdot 10^{-5}$			
478	Mg II	1026.0 } 1026.1 }	$10^{-4}$ $5 \cdot 10^{-5}$			
384	O I	1027.43 } 1028.16 }	$2 \cdot 10^{-5}$			
72	O VI	1031.91	0.06	(1032)	0.04	+
190	C II	1036.33 } 1037.02 }	0.005			
72	O VI	1037.61	0.03	(1037)	0.03	+
383	O I	1039.23 } 1040.94 } 1041.69 }	$6 \cdot 10^{-5}$			
336	N I	1043.12 } 1043.58 }	$2 \cdot 10^{-5}$	(1043)	0.005	—
335	N I	1044.13	$10^{-5}$			
334	N I	1044.69	$6 \cdot 10^{-6}$			
333	N I	1051.89	$3 \cdot 10^{-6}$	(1051)	0.005	—
534	S IV	1062.7 } 1073.3 }	0.006	(1062) (1073)	0.002 0.005	— +
260	N II	1084.00 } 1084.57 } 1085.54 } 1085.70 }	0.017	(1085)	0.016	+
—	[Si VII]	1048.9	?			
—	[Al XIII]	1058.7	?	(1103)	0.01	—
652	Fe III	1122	0.0024	(1121)	0.01	+
484	Si IV	1128.34	$3 \cdot 10^{-4}$	(1127)	0.01	+
328	N I	1134.17 } 1134.42 } 1135.00 }	$3 \cdot 10^{-4}$	(1134)	0.007	+

TABLE II (continued)

No. of multiplet from Table I	Ion	$\lambda$ , Å	$F_t$	$\lambda$ , Å	$F_o$	Identifi- cation
657	Fe II	1142—1154	0.006	(1143)	0.003	+
486	Si IV	1151.60	0.003	(1151)	0.008	+
258	C I	1156.06	0.004			
		1156.50	0.002			
487	Si IV	1156.58	$5 \cdot 10^{-4}$	(1156)	0.01	+
258	C I	1156.62	0.01			
		1156.84	0.002			
257	C I	1158.1	$2 \cdot 10^{-5}$	(1159)	0.008	—
				(1167)	0.03	—
331	N I	1171.1	$3 \cdot 10^{-5}$			
114	C III	1176.0	0.004	(1175)	0.06	+
189	N III	1183.0	$10^{-4}$	(1185)	0.01	—
		1184.5				
516	S V	1188.7—	$1.5 \cdot 10^{-4}$			
		1203.8				
552	S III	1190.21	0.002	(1189)	0.018	+
		1194.04	0.004	(1194)	0.018	+
		1194.43	0.0015			
329	N I	1199.55	0.001	(1200)	0.02	+
		1200.71				
552	S III	1200.95	0.008	(1203)	0.01	+
		1201.70	0.0015			
		1202.1	$10^{-4}$			
512	Si III	1206.510	0.07	(1206)	0.1	+
1	H I	1215.7	[4]	(1215, 7)	5	+
124	O V	1216.9	0.002			
		1217.7	0.004			

## Bibliography

1. Baum, W.A., F.S.Johnson, J.J.Oberly, C.C.Rockwood, C.V.Strain, and R.Tousey. — *Phys.Rev.*, **76**:781. 1946.
2. Rense, W.A. — *Ibid.*, **91**:229. 1953.
3. Ivanov-Kholodnyi, G.S. — *Izv. ANSSSR, Seriya Geofizika*, No.9, 1104. 1958.
4. Malitson, H.H., J.D.Purcell, R.Tousey, and G.F.Moore. — *Astrophys. J.*, **132**:746. 1960.
5. Kachalov, V.P., N.A.Pavlenko, and A.V.Yakovleva. — *Izv. ANSSSR, Seriya Geofizika*, No.9, 1099. 1958.
6. Tousey, R. — *Mem.Soc.Roy.Sci. Liège*, **4**:211. 1961.
7. Harrison, G. et al. *Practical Spectroscopy*. — New York, Prentice-Hall. 1948.
8. Stacey, D.S., B.A.Stith, R.A.Nidey, and W.A.Pietenpol. — *Electronics*, **27**:149. 1954.
9. Burton, W.M., A.Ridgeley, and R.Wilson. — *Monthly Not. R. A. S. R. A.S.*, **135**:207. 1967.
10. Weeks, L.H. — *Astrophys. J.*, **147**:1203. 1967.
11. Johnson, F.S., J.D.Purcell, and R.Tousey. — *Phys.Rev.*, **95**: 621. 1954; *Bull.Amer.Phys.Soc.*, **29**:33. 1954.
12. Johnson, F.S., H.H.Malitson, J.D.Purcell, and R.Tousey. — *Astrophys. J.*, **127**:80. 1958.
13. Jursa, A.S., F.G.LeBlanc, and Y.Tanaka. — *J.Opt.Soc.Amer.*, **45**:1085. 1955.
14. Behring, W.E., H.McAlister, and W.A.Rense. — *Astrophys. J.*, **127**:676. 1958.
15. Aboud, A., W.E.Behring, and W.A.Rense. — *Astrophys. J.*, **130**: 381. 1959.
16. Violett, T. and W.A.Rense. — *Ibid.*, **130**:954. 1959.
17. Purcell, J.D., D.M.Packer, and R.Tousey. — *Space Res.*, **1**:581. 1960.
18. Detwiller, C.R., D.L.Garrett, J.D.Purcell, and R.Tousey. — *Ann.géophys.*, **17**:263. 1961.
19. Detwiller, C.R., J.D.Purcell, and R.Tousey. — *Mem.Soc.Roy. Sci. Liège*, **4**:253. 1961.
20. Tousey, R., J.D.Purcell, W.E.Austin, D.L.Garrett, and K.G.Widing. — *Space Res.*, **4**:703. 1964.
21. Austin, W.E., J.D.Purcell, R.Tousey, and K.G.Widing. — *Astrophys. J.*, **145**:373. 1966.
22. Tousey, R., W.E.Austin, J.D.Purcell, and K.G.Widing. — *Ann. astrophys.*, **28**:755. 1965.
23. Hinteregger, H.E., K.R.Damon, L.Heroux, and L.A.Hall. — *Space Res.*, **1**:615. 1960.

24. Hinteregger, H.E. — *Astrophys. J.*, **132**:801. 1960.
25. Hinteregger, H.E. — *J. Geophys. Res.*, **66**:2367. 1961.
26. Hall, L.A., K.R. Damon, and H.E. Hinteregger. — *Space Res.*, **3**:745. 1963.
27. Hinteregger, H.E., L.A. Hall, and W. Schweizer. — *Astrophys. J.*, **140**:319. 1964.
28. Blake, R.L., T.A. Chubb, H. Friedman, and A.E. Unzicker. — *Ibid.*, **142**:1. 1965.
29. Zhitnik, I.A., V.V. Krutov, L.P. Malyavkin, S.L. Mandel'shtam, and G.S. Cheremukhin. — *Kosmich. Issled.*, **5**:276. 1967.
30. Hinteregger, H.E. — *Space Sci. Rev.*, **4**:461. 1965.
31. Hinteregger, H.E., L.A. Hall, and G. Schmidtke. — *Space Res.*, **5**:1175. 1965.
32. Nikol'skii, G.M. — *Doklady AN SSSR*, **147**:809. 1962; *Geomagn. i Aeronomiya*, **2**:1025. 1962.
33. Tousey, R. — *Astrophys. J.*, **149**:239. 1967.
34. Nikol'skii, G.M. — *Astron. Zh.*, **35**:657. 1958.
35. Purcell, J.D. and R. Tousey. — *Space Res.*, **1**:115. 1960; *J. Geophys. Res.*, **65**:370. 1960.
36. Purcell, J.D. and R. Tousey. — *Mem. Soc. Roy. Sci.*, **4**:283. 1961.
37. Ivanov, V.V. *Teoriya zvezdnykh spektrov (Theory of Stellar Spectra)*, p. 390. — "Nauka." 1966.
38. Jeffries, J.T. and R.N. Thomas. — *Astrophys. J.*, **129**:401. 1959; **131**:695. 1960.
39. Avrett, E.H. and D.G. Hummer. — *Monthly Not. R. A. S.*, **130**:295. 1965.
40. Morton, D.C. and K.G. Widing. — *Astrophys. J.*, **133**:596. 1961.
41. Obridko, V.N. — *Astron. Zh.*, **40**:466. 1963.
42. Chubb, T.A., H. Friedman, W.R. Kreplin, R.L. Blake, and A.E. Unzicker. — *Mem. Soc. Roy. Sci.*, **4**:235. 1961.
43. Blake, R.L., T.A. Chubb, H. Friedman, and A.E. Unzicker. — *Astrophys. J.*, **137**:3. 1963.
44. Mercure, R., S.C. Miller, Jr., W.A. Rense, and F. Stuart. — *J. Geophys. Res.*, **61**:573. 1956.
45. Purcell, J.D., D.M. Packer, and R. Tousey. — *Nature*, **184**:8. 1959.
46. Tousey, R. — *Quart. Bull. R. A. S.*, **5**:123. 1964.
47. Purcell, J.D., D.L. Garrett, and R. Tousey. — *Astron. J.*, **69**:147. 1964.
48. Zhitnik, I.A., V.V. Krutov, L.P. Malyavkin, and S.L. Mandel'shtam. — *Kosmich. Issled.*, **2**:920. 1964.
49. Russell, P.C. — *Nature*, **205**:684. 1965.
50. Black, W.S., D. Booker, W.M. Burton, B.B. Jones, D.B. Shenton, and R. Wilson. — *Ibid.*, **206**:654. 1965.
51. Giacconi, R., W.P. Reidy, T. Zehnpfennig, J.C. Lindsay, and W.S. Muney. — *Astrophys. J.*, **142**:1274. 1965.
52. Burton, W.M. and R. Wilson. — *Nature*, **207**:61. 1965.
53. Fredga, K. — *Astrophys. J.*, **144**:854. 1966.
54. Sloan, W.A. — *Astron. J.*, **71**:399. 1966.
55. Russell, P.C. and K.A. Pounds. — *Nature*, **209**:490. 1966.

56. Cauchois, Y., G.Senemand, C.Bonnelle, M.Montel, and C.Senemand. — C.R.Acad.Sci., 263:1082. 1966.
57. Underwood, J.H. and W.S.Muney. — Solar Phys., 1:129. 1967.
58. Chubb, T.A., H.Friedman, R.W.Kreplin, R.L.Blake, and A.E.Unzicker. — Mem.Soc.Roy.Sci. Liège, 4:228. 1961.
59. Burnight, T.R. — Phys.Rev., 76:165. 1949.
60. Purcell, J.D., R.Tousey, and K.Watanabe. — Phys.Rev., 76:165. 1949.
61. Chubb, T.A., H.Friedman, and R.W.Kreplin. — Space Res., 1:196. 1960.
62. Ivanov-Kholodnyi, G.S. — Geomagn. i Aeronomiya, 5:705. 1965.
63. Allen, C.W. — Space Sci.Rev., 4:91. 1965.
64. Kreplin, R.W. — Ann.géophys., 17:151. 1964.
65. Friedman, H. — Repts.Progr.Phys., 25:163. 1962.
66. Vasil'ev, B.N., Yu.K.Voron'ko, S.L.Mandel'shtam, I.P.Tindo, and A.I.Shurygin. — Doklady ANSSSR, 140:1058. 1961.
67. Mandel'shtam, S.L., I.P.Tindo, Yu.K.Voron'ko, A.I.Shurygin, and B.N.Vasil'ev. — Iskustv.Sputniki Zemli, No.10, 12. 1961.
68. Chubb, T.A., H.Friedman, and R.W.Kreplin. — J.Geophys. Res., 65:1831. 1960.
69. Pounds, K.A. and P.J.Bowen. — Monthly Not. R.A.S., 123:347. 1962.
70. Pounds, K.A. — Ann.astrophys., 28:132. 1965.
71. Kreplin, R.W., T.A.Chubb, and H.Friedman. — J.Geophys. Res., 67:2231. 1962.
72. Mandel'shtam, S.L., I.P.Tindo, Yu.K.Voron'ko, B.N.Vasil'ev, and A.I.Shurygin. — Iskustv.Sputniki Zemli, No.11, 3. 1961.
73. Efremov, A.I., A.L.Podmoshenskii, O.N.Efimov, and A.A.Lebedev. — Iskustv.Sputniki Zemli, No.10, 3. 1961.
74. Mandel'shtam, S.L., Yu.K.Voron'ko, I.P.Tindo, A.I.Shurygin, and B.N.Vasil'ev. — Doklady ANSSSR, 142:77. 1962.
75. Maehlum, B., L.A.Frank, and B.J.O'Brien. — J.Geophys. Res., 67:3577. 1962.
76. Van Allen, J.A., L.A.Frank, B.Maehlum, and L.W.Acton. — J.Geophys. Res., 70:1639. 1965.
77. Acton, L.W., T.A.Chubb, R.W.Kreplin, and J.F.Meekins. — Ibid., 68:3335. 1963.
78. Lindsay, J.C. — Trans.Amer.Geophys.Union, 44:722. 1963.
79. White, A. — Space Res., 4:771. 1964.
80. Lindsay, J.C. — Planet and Space Sci., 12:379. 1964.
81. Bowen, P.J., K.Norman, K.A.Pounds, P.W.Sanford, and A.P.Willmore. — Proc.Roy.Soc., A281:538. 1964.
82. Tindo, I.P. and A.I.Shurygin. — Kosmich.Issled., 3:262. 1965.
83. Manson, J.E. — Sci.Rep.Air Force Camb.Res.Lab., No.43. 1964.
84. Kreplin, R.W. — Space Res., 5:951. 1965.
85. Tindo, J.P. — In: "Issled.Kosmich.Prostranstva," p.533. — "Nauka." 1965.
86. Thomas, L., F.H.Venables, and K.M.Williams. — Planet and Space Sci., 13:807. 1965.

87. Landini, M., M. Piattelli, G. Righini, D. Russo, and G. L. Tagliaferri. — *Ann. astrophys.*, **27**:765. 1964.
88. Friedman, H. — *Agenda and Draft Reports IAU, UNESCO*, p. 985. 1967.
89. Korchak, A. A. — *Geomagn. i Aeronomiya*, **5**:601. 1965.
90. Ivanov-Kholodnyi, G. S. and G. M. Nikol'skii. — *Astron. Zh.*, **38**:45. 1961.
91. Ivanov-Kholodnyi, G. S., G. M. Nikol'skii, and R. A. Gulyaev. — *Astron. Zh.*, **37**:799. 1960.
92. Aller, L. H. *The Abundance of the Elements*. — New York, Interscience Publ. 1961.
93. Allen, C. W. *Astrophysical Quantities*. — Univ. London, Athlone Press. 1958.
94. Veselov, M. G. — *Zhurnal Eksperimental'noi i Teoreticheskoi Fiziki*, **19**:959. 1949.
95. Nikol'skii, G. M. and N. S. Shilova. — *Geomagn. i Aeronomiya*, **3**:431. 1963.
96. Moore, C. E. *Atomic Energy Levels*. — N. B. S., Washington, D. C., Vol. I. 1948; Vol. II. 1952.
97. Varsavsky, C. M. — *Astrophys. J.*, Suppl. Ser. 6, No. 53, 75. 1961.
98. Garstang, R. H. — *Ann. astrophys.*, **25**:109. 1962.
99. Allen, C. W. — *Mem. Soc. Roy. Sci. Liège*, **4**:241. 1961.
100. Gabriel, A. H. and B. C. Fawcett. — *Nature*, **206**:808. 1965.
101. Feldman, U., B. S. Fraenkel, and S. Hoory. — *Astrophys. J.*, **142**:719. 1965.
102. Gabriel, A. H., B. C. Fawcett, and C. Jordan. — *Nature*, **206**:392. 1965.
103. Cowan, R. D. and N. J. Peacock. — *Astrophys. J.*, **142**:390. 1965.
104. Stockhausen, R. — *Ibid.*, **141**:277. 1965.
105. Tilford, S. G. and L. E. Giddings, Jr. — *Ibid.*, **141**:1226. 1965.
106. Landolt-Börnstein. *Zahlenwerte und Funktionen*, Vol. I, part 1. — Berlin, Springer-Verl. 1950.
107. Striganov, A. R. and N. S. Sventitskii. *Tablitsy spektral'nykh linii neutral'nykh i ionizovannykh atomov (Tables of Spectral Lines of Neutral and Ionized Atoms)*. — Atomizdat. 1966.
108. Kastner, S. O., K. Omidvar, and J. H. Underwood. — *Astrophys. J.*, **148**:269. 1967.
109. Boiko, V. A., P. Voinov, E. Ya. Kononov, N. G. Basov, and S. L. Mandel'shtam. — *Pis'ma ZhETF*, **5**:177. 1967.
110. Alexander, E., U. Feldman, B. S. Fraenkel, and S. Hoory. — *Nature*, **206**:176. 1965.
111. Pottasch, S. R. — *Bull. Astron. Inst. Netherl.*, **18**:443. 1966.
112. Zirin, H. — *Astrophys. J.*, **140**:1332. 1964.
113. Shklovskii, I. S. — *Astron. Zh.*, **22**:249. 1945.
114. Ivanov-Kholodnyi, G. S. and G. M. Nikol'skii. — *Geomagn. i Aeronomiya*, **2**:425. 1962.
115. Ivanov-Kholodnyi, G. S. and G. M. Nikol'skii. — *Astron. Zh.*, **38**:828. 1961.
116. Nikol'skii, G. M. *Doctoral Thesis*. Moscow, 1964.
117. Pottasch, S. R. — *Space Sci. Rev.*, **3**:816. 1964.
118. Nikol'skii, G. M. and A. A. Sazanov. — *Astron. Zh.*, **43**:868. 1966.
119. Oster, L. — *Z. Astrophys.*, **40**:28. 1956.

120. Pecker, C. and F. Rohrllich. — Mem. Soc. Roy. Sci. Liège, **4**:265. 1961.
121. Zirin, H., L. A. Hall, and H. E. Hinteregger. — Space Res., **3**: 760. 1961.
122. Behring, W. E., W. M. Neupert, and J. C. Lindsay. — Ibid., **3**:814. 1963.
123. Hall, L. A., W. Schweizer, and H. E. Hinteregger. — J. Geophys. Res., **70**:2241. 1965.
124. Hall, L. A., W. Schweizer, L. Heroux, and H. E. Hinteregger. — Astrophys. J., **142**:13. 1965.
125. Behring, W. E., W. M. Neupert, and J. C. Lindsay. — Space Res., **4**:719. 1964.
126. Neupert, W. M. — Ann. astrophys., **28**:446. 1965.
127. Ivanov-Kholodnyi, G. S. and G. M. Nikol'skii. — Astron. Zh., **38**:455. 1961.
128. Gnevyshev, M. N., G. M. Nikolsky, and A. A. Sazanov. — Solar Physics, **2**:223. 1967.
129. Ivanov-Kholodnyi, G. S. and G. M. Nikol'skii. — Astron. Zh., **39**:777. 1962.
130. Pottasch, S. R. — Astrophys. J., **137**:945. 1963.
131. Pottasch, S. R. — Ann. astrophys., **28**:148. 1965.
132. Pottasch, S. R. — Bull. Astron. Inst. Netherl., **18**:237. 1966.
133. Pottasch, S. R. — Ibid., **18**:443. 1966.
134. Goldberg, L., R. A. Kopp, and A. K. Dupree. — Astrophys. J., **140**:707. 1964.
135. Withbroe, G. L. — Sci. Rep. Schock Tube Spectr. Lab., No. 17. 1967.
136. Pottasch, S. R. — Ann. astrophys., **27**:163. 1964.
137. Jordan, C. — Monthly Not. R. A. S., **132**:463. 1966.
138. Jordan, C. — Ibid., **132**:515. 1966.
139. Warner, B. — Observatory, **84**:14. 1964.
140. Goldberg, L., E. Müller, and L. H. Aller. — Astrophys. J., Suppl., Ser. 5, No. 45. 1960.
141. Dupree, A. K. and L. Goldberg. — Solar Physics, **1**:229. 1967.
142. Woolley, R., v. d. and C. W. Allen. — Monthly Not. R. A. S., **110**:358. 1950.
143. Athay, R. G. and D. H. Menzel. — Astrophys. J., **123**:285. 1956.
144. Shklovskii, I. S. and E. V. Kononovich. — Astron. Zh., **36**:37. 1958.
145. Zel'dovich, Ya. B. — Uspekhi Fizicheskikh Nauk, **86**:303. 1965.
146. Zel'dovich, Ya. B., L. B. Okun', and S. B. Nikel'ner. — Ibid., **87**:113. 1965.
147. Sinanoğlu, O., B. Skutnik, and R. Tousey. — Phys. Rev. Letters, **17**:785. 1966.
148. Bennett, Jr., W. R. — Ibid., **17**:1196. 1966.
149. Shklovskii, I. S. Solnechnaya korona (Solar Corona). — Gostekhizdat. 1951.
150. Shklovskii, I. S. Fizika solnechnoi korony (Physics of the Solar Corona), 2nd ed. — Fizmatgiz. 1962.
151. Woolley, R., v. d. and C. W. Allen. — Monthly Not. R. A. S., **108**:292. 1948; **110**:358. 1950.
152. Shklovskii, I. S. — Izvestiya ANSSSR, Seriya Fizika, **10**, Nos. 5—6. 1946.

153. Vainstein, L. A. and R. A. Suniaev. — *Astrophys. Letters*. 1958.
154. Massey, H. and E. Burhop. *Electrons and Ionic Impact Phenomena*. Oxford, Clarendon Press. 1956.
155. Malik, F. and E. Trefftz. — *Z. Naturforsch.*, **16A**:583. 1961.
156. Schwartz, S. and H. Zirin. — *Astrophys. J.*, **130**:384. 1959.
157. Elwert, G. — *Z. Naturforsch.*, **9A**:637. 1954.
158. Nikol'skii, G. M. — *Geomagn. i Aeronomiya*, **3**:417. 1963.
159. Seaton, M. J. — *Observatory*, **82**:111. 1962.
160. Seaton, M. J. — *Monthly Not. R. A. S.*, **119**:81. 1959.
161. Menzel, D. H. — *Astrophys. J.*, **85**:330. 1937.
162. Bates, D. R., and A. Dalgarno. *Atomic and Molecular Processes*, p. 244. — New York—London, Acad. Press. 1962.
163. Seaton, M. J. — *Planet and Space Sci.*, **12**:55. 1964.
164. Burgess, A. and M. J. Seaton. — *Monthly Not. R. A. S.*, **127**:355. 1964.
165. Burgess, A. — *Astrophys. J.*, **139**:776. 1964.
166. Burgess, A. — *Ibid.*, **141**:1588. 1965.
167. Burgess, A. — *Ann. astrophys.*, **28**:774. 1965.
168. Alfvén, H. *Cosmical Electrodynamics*. Oxford, Clarendon. 1950.
169. Van de Hulst, H. — *Bull. Astron. Inst. Netherl.*, **11**:135. 1950.
170. Dzyubenko, N. I. — *Astron. Zh.*, **34**:379. 1957.
171. Hepburn, N. — *Astrophys. J.*, **122**:445. 1955.
172. Dollfus, A. — *Compt. rend.*, **255**:3369. 1962.
173. Shklovskii, I. S. — *Izvestiya Krymskoi Astronomicheskoi Observatorii*, **6**:105. 1951.
174. Waldmeier, M. *Ergebnisse und Probleme der Sonnenforschung*, p. 230. — Leipzig, Akad. Verl. 1955.
175. Aly, M. K., J. W. Evans, and F. Q. Orrall. — *Astrophys. J.*, **136**:956. 1962.
176. Aly, M. K. — *Ibid.*, **122**:438. 1955.
177. Massey, H. S. — *Vistas in Astronomy*, **1**:277. 1955.
178. Hebb, M. and D. H. Menzel. — *Astrophys. J.*, **92**:408. 1940.
179. Blaha, M. — *Bull. Astron. Inst. Cz.*, **13**:81. 1962.
180. Seaton, M. — In: *The Airglow and the Aurorae*, edited by E. Armstrong and A. Dalgarno. London, Pergamon Press. 1956.
181. Grotian, W. — *Z. Astrophys.*, **7**:26. 1935.
182. Shain, G. A. — *Izvestiya Krymskoi Astronomicheskoi Observatorii*, **1**:102. 1947; **3**:64. 1948.
183. Pecker, C. — *Ann. astrophys.*, **23**:764. 1960.
184. Lyot, B. and A. Dollfus. — *Compt. rend.*, **237**:855. 1953.
185. Wlerick, G. and C. Ferenback. *The Solar Corona*. — *Proc. IAU*, Symp. No. 16, p. 199. — New York, Academic Press. 1963.
186. Röhrlich, F. *The Solar Corona*. — *Ibid.*
187. Nikol'skii, G. M. — *Astron. Zh.*, **43**:1143. 1966.
188. Oster, L. and S. Sofia. — *Astrophys. J.*, **141**:1139. 1965.
189. Fokker, A. D. — *Bull. Astron. Inst. Netherl.*, **18**:359. 1966.
190. Serbu, G. P. and E. J. R. Maier. — *J. Geophys. Res.* **71**:3755. 1966.
191. Parker, E. N. *Space Sci. Rev.*, **4**:666. 1965.
192. Waldmeier, M. — *Vierteljahrschrift*, **74**:229. 1939.
193. Vsekhsvyatskii, S. K. and E. Ya. Bugoslavskaya. — *Doklady AN SSSR*, **25**:363. 1939.



194. Pikel'ner, S.B. — *Izv. Krymskoi Astronomicheskoi Observatorii*, **5**:34. 1954.
195. Nikol'skii, G.M. and A.A. Sazanov. — *Astron. Zh.*, **43**:928. 1966.
196. Jager, C.de. *Structure and Dynamics of the Solar Atmosphere*. Berlin, Springer. 1959.
197. Lyot, B. — *Compt. rend.*, **202**:392. 1936.
198. Waldmeier, M. — *Astron. Mitt. Eid. Sternw. Zürich*, No. 143. 1947.
199. Dollfus, A. — *Compt. rend.*, **236**:996. 1953.
200. Pecker, C., D.E. Billings, and W.O. Roberts. — *Astrophys. J.*, **120**:509. 1954.
201. Billings, D.E. — *Ibid.*, **125**:817. 1957.
202. Prokof'eva, I.A. — *Izvestiya Glavnoi Astronomicheskoi Observatorii*, **22** (169):9. 1961.
203. Nikol'skii, G.M. and A.A. Sazanov. — *Solnechnye dannye*, No. 12, 57. 1964.
204. Jarrett, A.H. and H. Klüber. — *Monthly Not. R.A.S.*, **115**:343. 1955.
205. Jarrett, A.H. and H. Klüber. — *Ibid.*, **122**:223. 1961.
206. Wlerick, G., J.-P. Dumont, and J.-C. Perche. *The Solar Corona*. — *Proc. IAU, Symp. No. 16*, p. 177, New York, Acad. Press. 1963.
207. Billings, D.E. — *Astrophys. J.*, **130**:961. 1959.
208. Nikol'skii, G.M. — *Astron. Zh.*, **44**:5. 1967.
209. Nikol'skaya, K.I. — *Ibid.*, **43**:936. 1966.
210. *Solnechnye Dannye*, No. 6. 1958; No. 3. 1959; No. 1. 1960; No. 8. 1960.
211. Newkirk, G., Jr. — *Astrophys. J.*, **133**:983. 1961.
212. Athay, R.G., D.H. Menzel, J.G. Pecker, and R.N. Thomas. — *Ibid.*, *Suppl. Ser. 1*, 505. 1955.
213. Thomas, R.N. and R.G. Athay. *Physics of the Solar Chromosphere*. New York, Interscience. 1961.
214. Van de Hulst, H.C. — In: *The Solar System, Vol. I. The Sun*, edited by G.P. Kuiper. University of Chicago Press. 1953.
215. Piddington, J.H. — *Astrophys. J.*, **119**:531. 1954.
216. Brooks, C.C. and L. Oster. — *Ibid.*, **134**:940. 1961.
217. Christiansen, W., D. Mathewson, J. Pawsey, S. Smerd, A. Boischot, J. Denise, P. Simon, T. Kakinuma, H. Dodson-Prince, and J. Firor. — *Ann. astrophys.*, **23**:75. 1960.
218. Koyama, S. — *Contr. Inst. Astrophys. and Kwasan Obs., Univ. of Kyoto*, **15**:15. 1963.
219. Gulyaev, R.A., G.M. Nikol'skii, and K.I. Nikol'skaya. — *Astron. Zh.*, **40**:433. 1963.
220. Vysanitsyn, V.P. — *Izvestiya Glavnoi Astronomicheskoi Observatorii*, **20** (156):16; **21** (160):140. 1957.
221. Pikel'ner, S.B. — *Astron. Zh.*, **37**:617. 1960.
222. Pikel'ner, S.B. — *Ibid.*, **38**:551. 1961.
223. Zirin, H. and R.D. Dietz. — *Astrophys. J.*, **138**:664. 1963.
224. Athay, R.G. and W.O. Roberts. — *Ibid.*, **121**:231. 1955.
225. Tousey, R. — *Space Sci. Rev.*, **2**:3. 1963.
226. Jager, C.de. and K. Kuperus. — *Bull. Astron. Inst. Netherl.*, **16**:510. 1961.
227. Dubov, E.E. — *Izvestiya Krymskoi Astronomicheskoi Observatorii*, **22**:101. 1960.

228. Livshits, M.A. — *Astron. Zh.*, **41**:473. 1964.
229. Schatzman, E. — *Ann. astrophys.*, **12**:203. 1949.
230. Kuperus, M. and R.G. Athay. — *Solar Physics*, **1**:361. 1967.
231. Athay, R.G. — *Astrophys. J.*, **145**:784. 1966.
232. Livshits, M.A. and G.M. Nikol'skii. — *Astron. Zh.*, **41**:75. 1964.
233. Mitchell, S.A. — *Astrophys. J.*, **105**:1. 1947.
234. Ratcliffe, J.A. and K. Weekes. In: "Physics of the Upper Atmosphere," edited by J. Ratcliffe, pp. 377—470. New York. Academic Press. 1960.
235. Odintsova, I.N. — *Geomagn. i Aeronomiya*, **4**:1035. 1964.
236. Donnelly, R.F. — *Trans. Amer. Geophys. Union*, **47**:467. 1966.
237. Ivanov-Kholodnyi, G.S. — *Geomagn. i Aeronomiya*, **4**:417. 1964.
238. Kane, J.A. — *J. Atmosph. and Terr. Phys.*, **23**:338. 1961.
239. Vice, R.W. — *J. Inst. Telecommun. Engrs.*, **12**:192. 1966.
240. Gregor, J.B. and A.H. Manson. — *J. Geophys. Res.*, **72**:1073. 1967.
241. Thrane, E.V., A. Haug, B. Bjelland, M. Anastassiades, and E. Tsagaklis. — *J. Atmosph. and Terr. Phys.*, **30**:135. 1968.
242. Gregory, J.B. — *J. Geophys. Res.*, **67**:3829. 1962.
243. Kazachevskaya, T.V. and G.S. Ivanov-Kholodnyi. — *Geomagn. i Aeronomiya*, **5**:1009. 1965.
244. Newell, G. In: "Physics of the Upper Atmosphere" edited by J. Ratcliffe. New York, Academic Press. 1960.
245. Ivanov-Kholodnyi, G.S. — *Space Res.*, **5**:19. 1965.
246. Korsunova, L.P., G.S. Ivanov-Kholodnyi, T.V. Kazachevskaya, and V.M. Mishin. — *Geomagn. i Aeronomiya*, **6**:1114. 1966.
247. Kazachevskaya, T.V. and G.S. Ivanov-Kholodnyi. — *Ibid.*, **6**:27. 1966.
248. Johnson, C.Y., E.B. Meadows, and J.C. Holms. — *J. Geophys. Res.*, **63**:443. 1958.
249. Istomin, V.G. — *Iskusstv. Sputniki Zemli*, No. 2, 32. 1958.
250. Istomin, V.G. — *Ibid.*, No. 5, 64. 1960.
251. Johnson, C.Y. — *Ann. géophys.*, **17**:100. 1961.
252. Istomin, V.G. — *Iskusstv. Sputniki Zemli*, No. 11, 94. 1961.
253. Taylor, H.A., Jr. and H.C. Brinton. — *J. Geophys. Res.*, **66**:2587. 1961.
254. Pokhunkov, A.A. — *Kosmich. Issled.*, **1**:267. 1963.
255. Holms, J.C., C.Y. Johnson, and J.M. Young. — *Space Res.*, **5**:756. 1965.
256. Hoffman, J.H. — *J. Geophys. Res.*, **72**:1883. 1967.
257. Young, J.M., C.Y. Johnson, and J.C. Holms. — *J. Geophys. Res.*, **72**:1473. 1967.
258. Bennett, W.H. — *J. Appl. Phys.*, **21**:143. 1950.
259. Johnson, C.Y., J.P. Heppner, J.C. Holms, and E.B. Meadows. — *Ann. géophys.*, **14**:475. 1958.
260. Istomin, V.G. — *Doklady ANSSSR*, **129**:81. 1959.
261. Istomin, V.G. — *Iskusstv. Sputniki Zemli*, No. 4, 171. 1960.
262. Istomin, V.G. — *Doklady ANSSSR*, **136**:1066. 1961.
263. Istomin, V.G. — *Iskusstv. Sputniki Zemli*, No. 11, 98. 1961.
264. Narcisi, R.S., A.D. Bailey, and L.D. Lucca. — *Space Res.*, **7**:123. 1967.
265. Pharo, M.W., C.R. Smith, H.A. Taylor, Jr., and H.C. Brinton. — *Trans. Amer. Geophys. Union*, **47**:75. 1966; *J. Geophys. Res.*, **72**:2357. 1967.

266. Ivanov-Kholodnyi, G.S. and A.D. Danilov. — In: "Issledovanie Kosmicheskogo Prostranstva," p.216. "Nauka." 1965; Kosmich. Issled., 4:439. 1966.
267. Narcisi, R.S., A.D. Bailey, and L.D. Lucca. — Space Res., 7:446. 1967.
268. Narcisi, R.S. — Ibid., 7:186. 1967.
269. Gringauz, K.I. — Doklady ANSSSR, 120:1234. 1958.
270. Gringauz, K.I. and V.A. Rudakov. — Iskusstv. Sputniki Zemli, No.6, 48. 1961.
271. Nisbet, J.S. — J. Geophys. Res., 65:2597. 1960.
272. Nisbet, J.S. and S.A. Bowhill. — Ibid., 65:3609. 1960.
273. Chandra, S. — Ibid., 68:1937. 1963.
274. Rudakov, V.A. — Kossmich. Issled., 2:946. 1964.
275. Titheridge, J.E. — J. Atmosph. and Terr. Phys., 28:1135. 1966.
276. da Rosa, A.V. and F.L. Smith, III. — J. Geophys. Res., 72:1829. 1967.
277. Knudsen, W.C. and G.W. Sharp. — Ibid., 72:1941. 1967.
278. Boyd, R.L.F. — Roy. Inst. Gr. Brit., 40:129. 1964.
279. Barrington, R.E., J.S. Belrose, and G.L. Nelms. — In: "Electron Density Profiles in Ionosphere and Exosphere," p. 387. London, Pergamon Press. 1966.
280. Barrington, R.E. and D.J. McEwen. — Space Res., 7:624. 1967.
281. Smith, P.A. and B.A. Kaiser. — J. Atmosph. and Terr. Phys., 29:1345. 1967.
282. Hoffman, J.H. — Science, 155:322. 1967.
283. Willmore, A.P. — Proc. Roy. Soc., A286:537. 1965.
284. Brinton, H.C., R.A. Pickett, and H.A. Taylor, Jr. — Trans. Amer. Geophys. Union, 48:75. 1967.
285. Istomin, V.G. — Ann. géophys., 22:255. 1966; Space Res., 7:368. 1967.
286. Legg, A.J., J.W. King, and D.M. Preece. — J. Atmosph. and Terr. Phys., 29:1397. 1967.
287. Muldrew, D.B. — Canad. J. Phys., 41:199. 1963.
288. King, J.W. — Nature, 197:639. 1963.
289. King, J.W., P.A. Smith, D. Eccles, G.F. Fooks, and H. Helm. — Proc. Roy. Soc., A281:464. 1964.
290. King, J.W., H. Helm, G.W. Lascom, and P.A. Smith. — In: "Electron Density Profiles in Ionosphere and Exosphere." London, Pergamon Press. 1966.
291. Muldrew, D.B. — J. Geophys. Res., 70:2635. 1965.
292. Dayharsh, T.I. and W.W. Farley, IV. — J. Geophys. Res., 70:5361. 1965.
293. Sharp, G.W. and R.G. Johnson. — Trans. Amer. Geophys. Union, 45:595. 1964.
294. Sharp, G.W. and W.C. Knudsen. — Ibid., 45:606. 1964.
295. Sharp, G.W. — J. Geophys. Res., 71:1345. 1966.
296. Sharp, G.W. — Trans. Amer. Geophys. Union, 47:54. 1966.
297. Sharp, G.W., R.G. Johnson, and R.D. Sharp. — Ibid., 48:72. 1967.
298. Liszka, L. — J. Atmosph. and Terr. Phys., 29:1243. 1967.
299. Calvert, W. — J. Geophys. Res., 71:3665. 1966.
300. Chan, K.L. — Radio Sci., 1:1158. 1966.
301. Chapman, J.H. — In: "Electron Density Profiles in Ionosphere and Exosphere," p.264. London, Pergamon Press. 1966.

302. Brace, L.H., B.M.Reddy, and H.G.Mayr. — Trans. Amer. Geophys. Union, **47**:62. 1966; J. Geophys. Res., **72**:265. 1967.
303. Rishbeth, H.R., T.E.van Zandt, and R.B.Norton. — Ann. géophys., **22**:538. 1966.
304. Electron Density Profiles in Ionosphere and Exosphere. — Pergamon Press. 1966.
305. Gordon, W.E. — Rev. Geophys., **5**:191. 1967.
306. Carlson, H.C. and W.E.Gordon. — In: "Electron Density Profiles in Ionosphere and Exosphere," p.505. London, Pergamon Press. 1966.
307. Carlson, H.C. and W.E.Gordon. — J. Geophys. Res., **71**:5573. 1966.
308. Farley, D.T. — In: "Electron Density Profiles in Ionosphere and Exosphere," p.446. London, Pergamon Press. 1966.
309. Bauer, S.J. — Ibid., p.622.
310. Evans, J.V. — Uspekhi Fizicheskikh Nauk, **92**:229. 1967.
311. Evans, J.V. — Planet. and Space Sci., **13**:1031. 1965.
312. McClure, J.P., D.T.Farley, Jr., T.E.van Zandt, and D.L.Sterling. — Trans. Amer. Geophys. Union, **48**:64. 1967.
313. Carru, H., M.Petit, and P.Waldteufel. — Planet. and Space Sci., **15**:944. 1967.
314. Hanson, W.B. — Space Res., **3**:282. 1963.
315. Dalgarno, A., M.McElroy, and R.J.Moffet. — In: Elementary Processes in the Upper Atmosphere. [Russian translation. 1965.]
316. Evans, J.V. — In: "Electron Density Profiles in Ionosphere and Exosphere," p.616. London, Pergamon Press. 1966.
317. Nagy, A.F., T.B.Lee, and J.C.G.Walker. — Space Res., **7**:506. 1967; Planet. and Space Sci., **15**:95. 1967.
318. Bowhill, S.A. and J.E.Geisler. — Space Res., **6**:487. 1966.
319. Banks, P.M. — Earth a. Planet. Sci. Letters, **1**:270. 1966.
320. Dalgarno, A. and M.B.McElroy. — Planet. and Space Sci., **13**:143. 1965.
321. Carlson, H.C. — In: "Electron Density Profiles in Ionosphere and Exosphere," p.478. London, Pergamon Press. 1966.
322. Carru, H., M.Petit, and P.Waldteufel. — Compt. rend., **AB 262**:1174. 1966.
323. Evans, J.V. — Planet. and Space Sci., **15**:1557. 1967.
324. Mahajan, K.K. — J. Atmosph. and Terr. Phys., **29**:1137. 1967.
325. Brace, L.H., H.Mayr, and R.M.Reddy. Explorer XXII Measurements of Electron Temperature and Concentration in the Low-Latitude Upper F-Region. Belgrade Symposium. 1966 (Preprint).
326. Gringauz, K.I. — Uspekhi Fizicheskikh Nauk, **92**:207. 1967.
327. Mahajan, K.K. — J. Atmosph. and Terr. Phys., **29**:1153. 1967.
328. Blamont, J.E. Probl. météorol. stratosphère et mésosphère, p.151. Paris. 1966.
329. Lory-Chanin, M.L. — Ann. géophys., **21**:303. 1965.
330. Blamont, J.E. and M.L.Lory. — Nature, **201**:593. 1964.
331. Izakov, M.N. — In: "Issled. kosmich. prostranstva," p.30, "Nauka." 1965; Space Sci. Revs., **7**:579. 1967.
332. Harris, I. and W.Prister. — COSPAR Prep. Group for an International Reference Atmosphere. Compiled by H.Kallmann Bijl et al., Amsterdam, North-Holland Pub. Co. 1961.
333. Jacchia, L.G. — Spec. Rept. Smith. Astrophys. Obs., No.150. 1964.

334. Mikhnevich, V. V. — In: "Issled. kosmich. prostranstva," p. 23, "Nauka." 1965.
335. Marov, M. Ya. — Ann. géophys., 22:65. 1966.
336. Volland, H. — J. Atmosph. Sci., 23:799. 1966.
337. King-Hele, D. G. — Space Res., 5:1132. 1965.
338. Antonova, L. A. and G. S. Ivanov-Kholodnyi. — Geomagn. i Aeronomiya, 8:351. 1968.
339. Kallmann-Bijl, H. K. and W. L. Sibley. — Planet. and Space Sci., 11:1379. 1963; Space Res., 5:279. 1965.
340. King-Hele, D. G. — Nature, 203:959. 1964.
341. Johnson, C. Y. — Geophys. Res., 71:330. 1966.
342. King-Hele, D. G. — Space Res., 7:1184. 1967.
343. King-Hele, D. G. and E. Quinn. — J. Atmosph. Terr. Phys., 27:197. 1965.
344. Jacchia, L. C. — Spec. Rept. Smith. Astrophys. Obs., No. 184. 1965.
345. Jacchia, L. G. and J. Slowey. — Space Res., 4:257. 1964.
346. Jacchia, L. G., J. Slowey, and F. Verniani. — J. Geophys. Res., 72:1423. 1967.
347. Roemer, M. — Space Res., 7:1091. 1967.
348. King-Hele, D. G. and R. R. Allan. — Space Sci. Revs., 6:248. 1966.
349. King-Hele, D. G. and D. W. Scott. — Planet and Space Sci., 14:1339. 1966.
350. King-Hele, D. G. — Nature, 213:1110. 1967.
351. Anderson, A. D. and W. E. Francis. — Space Mater. Handb., p. 19. 1965.
352. Francis, W. E. — J. Atmosph. Sci., 23:431. 1966.
353. Bhatnagar, V. P. and A. P. Mitra. — J. Atmosph. Sci., 23:233. 1966.
354. Norton, R. B., T. E. van Zandt, and J. S. Denison. — Proc. Internat. Conf. Ionosphere, p. 26, London. 1963.
355. Hall, L. A., W. Schweizer, and H. E. Hinteregger. — J. Geophys. Res., 68:6413. 1963; 70:105. 1965.
356. Antonova, L. A., G. S. Ivanov-Kholodnyi, T. V. Kazachevskaya, and V. I. Lazarev. — Geomagn. i Aeronomiya, 7:913. 1967.
357. Hall, L. A., W. Schweizer, and H. E. Hinteregger. — J. Geophys. Res., 72:3425. 1967.
358. Pokhunkov, A. A. — Iskusstv. Sputniki Zemli, No. 13, 110. 1962.
359. Pokhunkov, A. A. — Kosmich. issled., 1:147. 1963.
360. Mauersberger, K., D. Muller, D. Offermann, and U. von Zahn. — Space Res., 7:1150. 1967; J. Geophys. Res., 73:1071. 1968.
361. Nier, A. O., J. H. Hoffman, C. Y. Johnson, and J. C. Holms. — J. Geophys. Res., 69:979. 1964.
362. Nier, A. O. and A. E. Hedin. — Space Res., 7:311. 1967.
363. Nier, A. O. and A. E. Hedin. — J. Geophys. Res., 71:4121. 1966.
364. Spencer, N. W., L. H. Brace, G. R. Carignan, D. R. Taesch, and H. Niemann. — J. Geophys. Res., 70:2665. 1965.
365. Spencer, N. W., D. R. Taesch, and G. R. Carignan. — Ann. géophys., 22:151. 1966.
366. Reber, C. A. and J. E. Cooley. — Trans. Amer. Geophys. Union, 48:75. 1967; J. Atmosph. and Terr. Phys., 15:15. 1968.
367. Antonova, L. A. and G. S. Ivanov-Kholodnyi. — Geomagn. i Aeronomiya, 8:348. 1968.

368. Reber, C.A. and M. Nicolet. — Planet. and Space Sci., 13:617. 1965.
369. Norton, R.B. and T.E. van Zandt. — J. Atmosph. and Terr. Phys., 26:1047. 1964.
370. Danilov, A.D. — In: "Issled. kosmich. prostranstva," p. 48, "Nauka." 1965; Kosmich. issled., 4:47. 1966.
371. Stein, J.A. and J.C.G. Walker. — J. Atmosph. Sci., 22:11. 1965.
372. Golomb, D. and R.E. Good. — J. Geophys. Res., 71:5753. 1966.
373. Schaefer, E.J. and P.A. Titus. — Trans. Amer. Geophys. Union, 48:74. 1967.
374. Offermann, D. and U. von Zahn. — Trans. Amer. Geophys. Union, 48:74. 1967.
375. Schaefer, E.J. — Space Res., 8:959. 1968.
376. Mirtov, B.A. — Geomagn. i Aeronomiya, 6:292. 1966.
377. Reber, C.A. — J. Geophys. Res., 72:295. 1967.
378. Spencer, N.W. — Space Res., 7:1148. 1967.
379. Volland, H. — Trans. Amer. Geophys. Union, 47:76. 1966; Space Res., 7:1193. 1967.
380. Reber, C.A., J.E. Cooley, and D.N. Harpold. — Trans. Amer. Geophys. Union, 48:75. 1967.
381. Kantor, A.J. and A.E. Cole. — Geofis. pura e appl., 53:171. 1962.
382. Groves, G.V. Rocket and Satell. Meteorol., p. 42. 1963; Atmospheric Structure and Its Variations in the Region from 30 to 100 km, Rept. COSPAR Working Group IV. 1963 (Preprint).
383. Nordberg, W. and W.G. Stroud. Seasonal, Latitudinal and Diurnal Variations in the Upper Atmosphere, NASA Techn. Note D-703, Goddard Space Flight Center. 1961.
384. Spencer, N.W., R.L. Boggess, and D.R. Taesch. — J. Geophys. Res., 69:1367. 1964.
385. Jespersen, M., O. Petersen, J. Rybner, B. Bjelland, O. Holt, B. Landmark, and J.A. Kane. — Planet. and Space Sci., 12:543. 1964.
386. Cole, A.E. — J. Geophys. Res., 66:2773. 1961.
387. Cole, A.E. — Space Res., 5:1242. 1965.
388. Champion, K.S.W. — Planet. and Space Sci., 13:325. 1965.
389. Champion, K.S.W. — Space Res., 7:1101. 1967.
390. Meredith, L.H., M.B. Gottlieb, and J.A. Van Allen. — Phys. Rev., 97:201. 1955.
391. Van Allen, J.A., J.A. Ellis, M.B. Gottlieb, L.H. Meredith, and F.B. McDonald. — Phys. Rev., 99:609. 1955.
392. Antonova, L.A. and G.S. Ivanov-Kholodnyi. — Izvestiya ANSSSR, Seriya Geofizika, No. 5, 756. 1960.
393. Antonova, L.A. — Ibid., No. 9, 1437. 1961.
394. Kazachevskaya, T.V. and G.S. Ivanov-Kholodnyi. — Iskusstv. Sputniki Zemli, No. 15, 81. 1963.
395. Antonova, L.A., G.S. Ivanov-Kholodnyi, N.D. Masanova, and V.S. Medvedev. — Kosmich. issled., 3:82. 1965.
396. McIlwain, C.E. — In: Exploration of the Upper Atmosphere with Rockets and Satellites. [Russian translation. 1961.]
397. Meredith, L.H., L.R. Davis, J.P. Heppner, and O.E. Berg. — Ibid. [Russian translation. 1961.]

398. Davis, L.R., O.E. Berg, and L.H. Meredith. — Space Res., 1:721. 1960.
399. McDiarmid, I.B., D.C. Rose, and E.E. Budzinski. — Canad. J. Phys., 39:1888. 1961.
400. Heikkila, W.J. and D.L. Matthews. — Nature, 202:789. 1964.
401. McDiarmid, I.B. and E.E. Budzinski. — Canad. J. Phys., 42:2048. 1964.
402. Ulwick, J.C., W. Pfister, O.C. Haycock, and K.D. Baker. — Space Res., 5:293. 1965.
403. Evans, D.S. — Trans. Amer. Geophys. Union, 46:60. 1965.
404. Riedler, W. — Proc. Sympos. High Latitude Particles and Ionosphere, p.137. 1965.
405. Riedler, W. — Arkiv för fysik, 30(32):527. 1965.
406. Cummings, W.D., R.E. LaQuey, B.J.O'Brien, and M. Walt. — J. Geophys. Res., 71:1399. 1966.
407. Mozer, F.S. — J. Geophys. Res., 70:5709. 1965.
408. Mozer, F.S. — J. Geophys. Res., 71:4451. 1966.
409. McDiarmid, I.B., E.E. Budzinski, B.A. Whalen, and N. Schopke. — Canad. J. Phys., 45:1755. 1967.
410. Matthews, D.L. — Bull. Amer. Phys. Soc., 11:707. 1966; Canad. J. Phys., 46:201. 1968.
411. Hegblom, E.R., W.P. Reidy, and J.C. Ulwick. — Trans. Amer. Geophys. Union, 48:72. 1967; Space Research, 7:656. 1967.
412. Doering, J.P. and W.G. Fastie. — Bull. Amer. Phys. Soc., 12:231. 1967.
413. Doering, J.P. and W.G. Fastie. — Canad. J. Phys., 44:2948. 1966.
414. Chase, L.M. and K.A. Anderson. — Trans. Amer. Geophys. Union, 48:61. 1967; J. Geophys. Res., 73:3469. 1968.
415. Lampton, M. — Trans. Amer. Geophys. Union, 48:180. 1967.
416. Albert, R.D. — Phys. Rev. Letters, 18:369. 1967; J. Geophys. Res., 72:5811. 1967.
417. Antonova, L.A. — Kosmich. Issled., 3:89. 1965.
418. Savenko, I.A., P.I. Shavrin, N.F. Pisarenko, V.E. Nesterov, M.V. Tel'tsov, and V.N. Erofeeva. — Geomagn. i Aeronomiya, 1:875. 1961.
419. Antonova, L.A. and T.V. Kazachevskaya. — In: "Issled. kosmich. prostranstva," p.214. "Nauka." 1965.
420. Antonova, L.A. Thesis, Moscow. 1965.
421. Kazachevskaya, T.V. — Kosmich. Issled., 5:637. 1967.
422. O'Brien, B.J., F.R. Allum, and H.C. Goldwire. — J. Geophys. Res., 70:161. 1965.
423. Nakagawa, S., M. Tsukuda, A. Sasaki, K. Nagata, and T. Doke. — Rept. Ionosph. Space Res., 19:521, Japan. 1965.
424. Shea, M.F., R.D. Sharp, and M.B. McElroy. — Trans. Amer. Geophys. Union, 47:63. 1966; J. Geophys. Res., 73:4199. 1968.
425. Tulinov, V.F. — Kosmich. Issled., 5:240. 1967; 6:892. 1968.
426. Kazachevskaya, T.V. — Ibid., 6:795. 1968.
427. Shook, G.B., R.D. Sharp, M.F. Shea, R.G. Johnson, and J.B. Reagan. — Trans. Amer. Geophys. Union, 47:64. 1966.
428. Sharp, R.D., J.E. Evans, R.G. Johnson, and J.B. Reagan. — Trans. Amer. Geophys. Union, 44:868. 1963.

429. Sharp, R.D., J.B.Reagan, S.R.Salisburg, and L.F.Smith. — J.Geophys.Res., **70**:2119. 1965.
430. Sharp, R.D., J.E.Evans, R.G.Johnson, and J.B.Reagan. — Space Res., **5**:282. 1965.
431. Sharp, R.D., J.E.Evans, and R.G.Johnson. — Trans.Amer. Geophys.Union, **46**:50. 1965.
432. Sharp, R.D., J.E.Evans, and R.G.Johnson. — Planet. and Space Sci., **14**:85. 1966.
433. Pfitzer, K.A. and J.R.Winckler. — Trans.Amer.Geophys.Union, **45**:602. 1964.
434. Pfitzer, K.A. and J.R.Winckler. — Trans.Amer.Geophys.Union, **47**:130. 1966.
435. Parthasarathy, R., F.T.Berkey, and D.Venkatesan. — Planet. and Space Sci., **14**:65. 1966.
436. O'Brien, B.J. Space Physics. [Russian translation. 1966.]
437. Dessler, A.J. and B.J.O'Brien. — In: The Space Around the Earth. Data Handbook. [Russian translation. 1966.]
438. O'Brien, B.J. — In: "Radiation Trapped in Earth's Magnetic Field," p.321, Dordrecht—N.Y. 1966.
439. McDiarmid, I.B. and J.R.Burrows. — J.Geophys.Res., **70**:3031. 1965.
440. McDiarmid, I.B. and J.R.Burrows. — Canad.J.Phys., **44**:669. 1966.
441. McDiarmid, I.B. and J.R.Burrows. — Canad.J.Phys., **44**:1361. 1966.
442. Knudsen, W.C. and G.W.Sharp. — Trans.Amer.Geophys.Union, **47**:62. 1966.
443. Johnson, R.G., R.D.Sharp, M.F.Shea, and G.B.Shook. — Trans.Amer.Geophys.Union, **47**:64. 1966.
444. Fritz, T.A. — Trans.Amer.Geophys.Union, **47**:130. 1966.
445. Evans, J.E. and A.E.Belon. — Trans.Amer.Geophys.Union, **44**:1073. 1963.
446. Evans, J.E., R.G.Johnson, J.B.Reagan, and R.D.Sharp. — Trans.Amer.Geophys.Union, **45**:595. 1964; J.Geophys.Res., **73**:969. 1968.
447. Blake, J.B., S.C.Freden, and G.A.Paulikas. — Trans.Amer. Geophys.Union, **47**:138. 1966; J.Geophys.Res., **71**:5129. 1966.
448. Zmuda, A.J. — J.Geophys.Res., **71**:1911. 1966.
449. Stevens, J.R., H.H.Hilton, and A.L.Vampola. — Trans.Amer. Geophys.Union, **45**:602. 1964.
450. Krassovsky, V.I. and N.N.Shefov. — Planet. and Space Sci., **12**:91. 1964.
451. Gal'perin, Yu.I. and T.M.Mulyarchik. — Kosmich. Issled., **4**:932. 1966.
452. Giorgio, N.V. — Geomagn.i Aeronomiya, **6**:424. 1966.
453. Vernov, S.N., V.V.Mel'nikov, I.A.Savenko, B.I.Savin, and T.I.Pervaya. — In: "Issled.kosmich.prostranstva," p.381, "Nauka." 1965.
454. Vernov, S.N., V.V.Mel'nikov, I.A.Savenko, B.I.Savin, and P.I.Shavrin. — Izvestiya ANSSSR, Seriya Fizich., **29**:1794. 1965.
455. O'Brien, B.J. Proc.Symposium High Latitude Particles and Ionosphere, p.113. 1965.



456. Paulikas, G. A. and S. C. Freden. — J. Geophys. Res., **69**:1239. 1964.
457. Paulikas, G. A., J. B. Blake, and S. C. Freden. — J. Geophys. Res., **71**:3165. 1966.
458. Rose, D. C. — In: "Radiation Trapped in Earth's Magnetic Field," p. 191, Dordrecht—N. Y. 1966.
459. Paulikas, G. A., J. B. Blake, and S. C. Freden. — Trans. Amer. Geophys. Union, **47**:130. 1966.
460. Dalgarno, A. Auroral Phenomena, p. 39. 1965.
461. Dalgarno, A., I. D. Latimer, and J. W. McConkey. — Planet. and Space Sci., **13**:1008. 1965.
462. Gal'perin, Yu. I. — Izvestiya AN SSSR, Seriya Geofiz., No. 2, 252. 1962.
463. Dalgarno, A. — In: Elementary Processes in the Upper Atmosphere. [Russian translation. 1965.]
464. Hirao, K., N. Wakai, K. Sawada, T. Nikosaka, K. Yano, and K. Maeda. — Space Res., **5**:1058. 1965.
465. Yano, K. — Planet. and Space Sci., **14**:709. 1966.
466. Becker, R. A., D. D. Elliott, and E. B. Mayfield. — Trans. Amer. Geophys. Union, **48**:149. 1967.
467. Elliott, D. D., S. R. La Valle, and R. L. Williams. — Trans. Amer. Geophys. Union, **48**:150. 1967.
468. Davidson, G. — Planet. and Space Sci., **14**:651. 1966.
469. Pfozter, G. Proc. Symposium High Latitude Particles and Ionosphere, p. 167. 1965.
470. Fisher, P. C., D. B. Clark, A. J. Meyerott, and K. L. Smith. — Nature, **204**:982. 1964.
471. Byram, E. T., T. A. Chubb, and H. Friedman. — Science, **152**:66. 1966.
472. Giacconi, R., H. Gursky, J. R. Waters, B. Rossi, et al. — In: "High Energy Astrophysics," p. 73. N. Y.—London, Academic Press. 1966.
473. Vegard, L. — Geofys. Publ., **12**:3. 1938.
474. Vegard, L. — In: "The Threshold of Space," Proc. Conf. on Chemical Aeronomy. Cambridge, Mass., June 1956. Edited by M. Zelikoff. New York, Pergamon Press. 1957.
475. Chapman, S. — Proc. Phys. Soc., **43**:26 a, 433. 1931.
476. Chapman, S. — Proc. Phys. Soc., **B66**:710. 1953.
477. Wilkes, M. V. — Proc. Phys. Soc., **B67**:304. 1954.
478. Shchukin, A. N. Fizicheskie osnovy rasprostraneniya radiovoln v ionosfere (Physical Elements of Radio Wave Propagation in the Ionosphere). — Svyaz'izdat. 1940.
479. Kessenikh, V. N. Rasprostranenie radiovoln (Radio Wave Propagation). — Gostekhizdat. 1952.
480. Nicolet, M. and A. C. Aikin. — J. Geophys. Res., **65**:1469. 1960.
481. Pannekoek, A. — Proc. Amsterd.-Acad., **29**:1165. 1926.
482. Kryuchkov, S. I. — Zh. Prikl. Fiziki, **7**(3):61. 1930.
483. Appleton, E. and A. J. Lyon. — J. Atmosph. and Terr. Phys., **10**:1. 1957; **21**:73. 1961.
484. Ivanov-Kholodnyi, G. S. — Geomagn. i Aeronomiya, **6**:382. 1966.
485. Rishbeth, H. — J. Atmosph. and Terr. Phys., **28**:911. 1967.
486. Appleton, E. V. — Proc. Roy. Soc., **A162**:451. 1937.

487. Bates, D.R. and H.S.W. Massey. — Proc. Roy. Soc., **187**:261. 1946.
488. Mitra, S.K. The Upper Atmosphere. — Calcutta, Asiatic Society. 1952.
489. Al'pert, Ya. L. Rasprostranenie radiovoln i ionosfera (Propagation of Radio Waves and the Ionosphere). — Izdatel'stvo ANSSSR. 1960.
490. Allen, C.W. — J. Atmosph. and Terr. Phys., Suppl. **6**:150. 1956.
491. Al'pert, Ya. L. — Zhurnal Eksperimental'noi i Teoreticheskoi Fiziki, **18**:995. 1948.
492. Allen, C.W. — Terr. Magn. and Atmosph. Electr., **53**:433. 1948.
493. Landolt-Börnstein. Zahlenwerte und Funktionen, Vol. I, part 5. — Berlin, Springer. 1952.
494. Chamberlain, J. Physics of the Aurora and Airglow. New York, Academic Press. 1961.
495. Brown, R.R. — Arkiv för geofysik, **4**:405. 1965.
496. Anderson, K.A. and D.C. Enemark. — J. Geophys. Res., **65**:3521. 1960.
497. Maeda, K. — J. Geophys. Res., **68**:185. 1963.
498. Maeda, K. — J. Atmosph. and Terr. Phys., **27**:259. 1965.
499. Rees, M.H. — Planet. and Space Sci., **11**:1209. 1963.
500. Rees, M.H. — Planet. and Space Sci., **12**:722. 1964.
501. Makhov, A.F. — Fizika Tverdogo Tela, **11**, pp.2161, 2172, 2176. 1960.
502. Lazarev, V.I. — Geomagn. i Aeronomiya, **7**:278. 1967.
503. Rees, M.H. — Planet. and Space Sci., **12**:1093. 1964.
504. Antonova, L.A. and G.S. Ivanov-Kholodnyi. — Geomagn. i Aeronomiya, **1**:164. 1961.
505. Velinov, P. — Proc. of Bulgar. Acad. of Sci., **19**:109. 1966.
506. Kroening, J.L. — J. Geophys. Res., **65**:145. 1960.
507. Massey, H.S.W. — Proc. Roy. Soc., **A163**:542. 1937.
508. Ivanov-Kholodnyi, G.S. — Geomagn. i Aeronomiya, **7**:83. 1967.
509. Kasner, W.H. and M.A. Biondi. — Bull. Amer. Phys. Soc., **11**:493. 1966; **12**:218. 1967; Phys. Rev., **164**:194. 1967.
510. Stein, R.P., M. Scheibe, M.W. Syverson, T.M. Shaw, and R.C. Gunton. — Physics Fluids, **7**:1641. 1964.
511. Weller, C.S. and M.A. Biondi. — Bull. Amer. Phys. Soc., **11**:495. 1966; **13**:199. 1968; Phys. Rev., **172**:198. 1968.
512. Young, R.A. and G. St. John. — Phys. Rev., **152**:25. 1966; Bull. Amer. Phys. Soc., **12**:218. 1967.
513. Kazachevskaya, T.V. and G.S. Ivanov-Kholodnyi. — Geomagn. i Aeronomiya, **7**:537. 1967.
514. Hirsh, M.N., G.M. Halpern, and N.S. Wolf. — Bull. Am. Phys. Soc., **13**:199. 1968.
515. Biondi, M.A. — Ann. géophys., **20**:34. 1964.
516. Mitra, A.P. — In: "Advances in Upper Atmosph. Research," Proc. NATO Adv. Study Institute, Corfu, 1960. Edited by B. Landmark. New York, Pergamon Press. 1963.
517. Best, J.E., F.T. Farmer, and J.A. Ratcliffe. — Proc. Roy. Soc., **A164**:96. 1938.
518. Bates, D.R., R.A. Buckingham, H.S. Massey, and J.J. Unwin. — Proc. Roy. Soc., **A170**:322. 1939.
519. Sayers, J. — Repts. Progr. Phys., **9**:52. 1943.
520. Massey, H.S.W. and D.R. Bates. — Repts. Progr. Phys., **9**:62. 1943.
521. Bates, D.R. and H.S.W. Massey. — Proc. Roy. Soc., **187**:261. 1946; **192**:1. 1947.
522. Bates, D.R. — Proc. Roy. Soc., **196**:562. 1949.

523. Bates, D.R. — Proc. Phys. Soc., **B64**:805. 1951.
524. Al'pert, Ya.L., V.L. Ginzburg, and E.L. Feinberg. Rasprostraneniye radiovoln (Propagation of Radio Waves). Gostekhizdat. 1953.
525. Mitra, A.P. and R.E. Jones. — J. Geophys. Res., **59**:391. 1954.
526. Mohler, F. — J. Res. NBS, **25**:507. 1940.
527. Yonezawa, T. — Repts. Ionosph. Res., Japan, **9**:17. 1955.
528. Ratcliffe, J.A., E.R. Schmerling, C.S.G.K. Setty, and J.O. Thomas. — Phil. Trans. Roy. Soc., **A248**:621. 1956.
529. Bates, D.R. — J. Atmosph. and Terr. Phys., Suppl. **6**:191. 1956.
530. Ratcliffe, J.A. — J. Atmosph. and Terr. Phys., Suppl. **6**:1. 1956.
531. Krasovskii, V.I. — Izvestiya ANSSSR, Seriya Geofiz., No. 4, 504. 1957.
532. Mitra, A.P. — J. Atmosph. and Terr. Phys., **10**:140. 1957.
533. Mitra, A.P. — J. Geophys. Res., **64**:733. 1959.
534. Appleton, E.V. — Proc. IRE, **47**:155. 1959.
535. McElhinny, M.W. — J. Atmosph. and Terr. Phys., **14**:273. 1959.
536. Bates, D.R. and M. Nicolet. — J. Atmosph. and Terr. Phys., **18**:65. 1960.
537. Bowhill, S.A. — J. Atmosph. and Terr. Phys., **20**:19. 1961.
538. Ratcliffe, J.A. — J. Atmosph. and Terr. Phys., Suppl. **6**:306. 1956.
539. Landmark, B., Editor. "Advances in Upper Atmosphere Research." Proc. NATO Adv. Study Institute, Corfu, 1960. New York, Pergamon Press. 1963.
540. Maehlum, B., Editor. Electron Density Profiles in the Ionosphere and Exosphere. Proc. NATO Adv. Study Institute, Skeikampen, Norway, April 1961. New York, Pergamon Press. 1962.
541. Proc. Int. Conf. Ionosphere, Inst. Physics and Phys. Soc., London, 1963.
542. Gunton, R.C. and T.M. Shaw. — Phys. Rev., **140A**:756. 1965.
543. Minnis, C.M. — Nature, **208**:476. 1965.
544. Ivanov-Kholodnyi, G.S. — Geomagn. i Aeronomiya, **2**:377. 1962.
545. Danilov, A.D. and G.S. Ivanov-Kholodnyi. — Uspekhi Fizicheskikh Nauk, **85**:259. 1965.
546. Piddington, J.H. — J. Geophys. Res., **56**:409. 1951.
547. Bibl, K. and F. Delobbeau. — Zs. Geophys., **21**:215. 1955.
548. Hunaerts, J. and M. Nicolet. — J. Geophys. Res., **60**:537. 1955.
549. Minnis, C.M. — Nature, **178**:33. 1956.
550. Bonnet, G., J. Hunaerts, and M. Nicolet. — Bull. des Séances, Académie Royale des Sciences Coloniales, **3**:964. 1957.
551. Gledhill, J.A. — J. Atmosph. and Terr. Phys., **16**:367. 1959.
552. Odintsova, I.N. and M.B. Ogir'. — Izvestiya KrAO, **29**:175. 1963.
553. Nestorov, G.N. and J. Taubenheim. — Izvestiya Geofiz. Instituta Bulgarian Academy of Sciences, **3**:259. 1962; Geomagn. i Aeronomiya, **3**:277. 1963; Doklady Bulgarian Academy of Sciences, **15**:131. 1962.
554. Nestorov, G. and J. Taubenheim. — Monatsber. Dtsch. Akad. Wiss., **4**:191, Berlin. 1962; J. Atmosph. and Terr. Phys., **24**:633. 1962.
555. Serafimov, K.B. — Pure Appl. Geophys., **57**:133. 1964.
556. Smith, L.G., C.A. Accardo, L.H. Weeks, and P.J. McKinnon. — Space Res., **5**:705. 1965; J. Atmosph. and Terr. Phys., **27**:803. 1965.
557. Shashun'kina, V.M. and R.I. Turbin. — Geomagn. i Aeronomiya, **1**:835. 1961.

558. Jasiński, S. — *Prace Inst. łączn.*, 9:23. 1962.
559. Ivanov-Kholodnyi, G.S. — *Geomagn. i Aeronomiya*, 2:674. 1962.
560. Watanabe, K. and H.E. Hinteregger. — *J. Geophys. Res.*, 67:999. 1962.
561. Omholt, A. — *J. Atmosph. and Terr. Phys.*, 7:73. 1955.
562. Bates, D.R. *Physics of the Upper Atmosphere*, p. 219. 1960.
563. Pudovkin, M.I. and A.B. Korotin. — *Geomagn. i Aeronomiya*, 1:408. 1961.
564. Loginov, G.A., M.I. Pudovkin, and R.G. Skrynnikov. — *Ibid.*, 3:59. 1963.
565. Smith, L.G. — *J. Geophys. Res.*, 67:1658. 1962.
566. Titheridge, J.E. — *J. Atmosph. and Terr. Phys.*, 17:126. 1959.
567. Nisbet, J.S. and T.P. Quinn. — *J. Geophys. Res.*, 68:1031. 1963.
568. Skinner, N.J. — *J. Atmosph. and Terr. Phys.*, 29:287. 1967.
569. LeLevier, R.E. — *J. Geophys. Res.*, 69:481. 1964.
570. Kozlov, S.I. and Yu.P. Raizer. — *Kosmich. Issled.*, 4:574. 1965.
571. Nicolet, M. *Aeronomy*. [Russian translation. 1964.]
572. Danilov, A.D. *Khimiya ionosfery (Chemistry of the Ionosphere)*. Gidrometeoizdat. 1967.
573. Nicolet, M. and W. Swider, Jr. — *Planet. and Space Sci.*, 11:1459. 1963.
574. Whitten, R.C. and I.G. Poppoff. — *J. Atmosph. Sci.*, 21:117. 1964.
575. Donahue, T.M. — *J. Geophys. Res.*, 71:2237. 1966; *Science*, 159:489. 1968; *Planet. and Space Sci.*, 14:33. 1966.
576. Horiuchi, G. — *Papers in Meteorol. and Geophys.*, Japan, 17:287. 1966.
577. Ferguson, E.E., F.C. Fehsenfeld, P.D. Goldan, A.L. Schmeltekopf, H.I. Schiff. — *Planet. and Space Sci.*, 13:823. 1965; 13:919. 1965.
578. Dalgarno, A. — *Disc. Farad. Soc.*, No. 37, 142. 1964.
579. Dalgarno, A. — *J. Atmosph. and Terr. Phys.*, 26:939. 1964.
580. Ferraro, V.C.A. — *Terr. Magn. and Atm. Electr.*, 50:215. 1945.
581. Whitten, R.C. and I.G. Poppoff. *Physics of the Lower Ionosphere*. Englewood Cliffs, N.J., Prentice-Hall. 1965.
582. Bailey, D.K. — *Proc. IRE*, 47:255. 1959.
583. Reid, G.C. — In: "Electron Density Profiles in Ionosphere and Exosphere," p. 17, London, Pergamon Press. 1966.
584. Adams, G.W. and L.R. Megill. — *Trans. Amer. Geophys. Union*, 47:459. 1966; *Planet. and Space Sci.*, 15:1111. 1967.
585. Fehsenfeld, F.C., A.L. Schmeltekopf, H.I. Schiff, and E.E. Ferguson. — *Planet. and Space Sci.*, 15:373. 1967.
586. Reid, G.C. — *Rev. of Geophys.*, 2:311. 1964.
587. Nicolet, M. — *J. Geophys. Res.*, 70:679. 1965.
588. Nicolet, M. — *J. Geophys. Res.*, 70:691. 1965.
589. Kane, J.A. and J. Troim. — *J. Geophys. Res.*, 72:1118. 1967.
590. Smith, L.G. — *J. Atmosph. and Terr. Phys.*, 28:1195. 1966.
591. Whitten, R.C. and I.G. Poppoff. — *J. Geophys. Res.*, 66:2779. 1961.
592. Swift, D.W. — *J. Atmosph. and Terr. Phys.*, 23:29. 1961.
593. Holt, O. — In: "Radio Astr. Satel. Stud. Atm.," p. 502, J. Aarons, ed. Amsterdam, North Holland Publ. Co. 1963.
594. Friedman, H. — In: *Space Astrophysics*, edited by W. Liller. New York, McGraw-Hill. 1961.

595. Vette, J.I. and F.G.Casal. — Phys. Rev. Letters, **6**:334. 1961.
596. Pounds, K.A. and A.P. Willmore. — Proc. Intern. Conf. Ionosphere, London, 1962, p. 513. London Inst. Physics and Phys. Soc. 1963.
597. Chubb, T.A. — Proc. 1st Intern. Sympos. Rocket and Satellite Meteorol., Washington, D.C., 1962, p. 210. Amsterdam, North-Holland Publ. Co. 1963.
598. Frost, K.J. — Space Res., **5**:513. 1965.
599. Chubb, T.A., H. Friedman, R.W. Kreplin. — Space Res., **5**:759. 1964.
600. Friedman, H. — In: Physics of the Upper Atmosphere, edited by J.A. Ratcliffe. New York, Academic Press. 1960.
601. Conner, J.P., W.D. Evans, M.D. Montgomery, S. Singer, and E.E. Stogsdill. — Space Res., **5**:546. 1965.
602. Venables, F.H. — Planet. and Space Sci., **15**:681. 1967.
603. Landini, M., D. Russo, and G.L. Tagliaferri. — Planet. and Space Sci., **15**:231. 1967; Space Res., **7**:1281. 1967.
604. Gregory, B.N. and R.W. Kreplin. — J. Geophys. Res., **72**:4815. 1967.
605. Ivanov-Kholodnyi, G.S. — Doklady AN SSSR, **177**:1328. 1967.
606. Bragin, Yu.A. — Kosmich. issled., **5**:478. 1967; **5**:951. 1967.
607. Smiddy, M., R.C. Sagalyn, and R. Stuart. — Space Res., **4**:371. 1964; Trans. Amer. Geophys. Union, **46**:51. 1965.
608. Pedersen, A. Tellus, **17**:2. 1965; In: "Electron Density Profiles in Ionosphere and Exosphere," p. 31. London, Pergamon Press. 1966.
609. Bragin, Yu.A. — Kosmich. Issled., **4**:453. 1966.
610. Bourdeau, R.E., A.C. Aikin, and J.L. Donley. — Trans. Amer. Geophys. Union, **46**:51. 1965; J. Geophys. Res., **71**:727. 1966.
611. Smith, L. — In: "Electron Density Profiles in the Ionosphere and Exosphere," edited by B. Maehlum. New York, Pergamon Press. 1962.
612. Kranushkin, P.E. — Geomagn. i Aeronomiya, **6**:602. 1966.
613. Keneshea, T.J., G.J. Gassman, and W. Pfister. — Trans. Amer. Geophys. Union, **48**:64. 1967.
614. Huffman, R.E., J.C. Larrabee, and Y. Tanaka. — J. Chem. Phys., **39**:910. 1963; **40**:356. 1964; Bull. Amer. Phys. Soc., **8**:299. 1963.
615. Huffman, R.E., Y. Tanaka, and J.C. Larrabee. — Disc. Farad. Soc., No. 37, 159. 1964.
616. Cook, G.R. and P.H. Metzger. — Bull. Amer. Phys. Soc., **8**:299. 1963; J. Chem. Phys., **41**:321. 1964.
617. Cook, G.R., B.K. Ching, and R.A. Becker. — Disc. Farad. Soc., No. 37, 149. 1964.
618. Samson, J.A.R. and R.B. Cairns. — J. Geophys. Res., **69**:4583. 1964.
619. Samson, J.A.R. and R.B. Cairns. — J. Opt. Soc. Amer., **55**:1035. 1965.
620. Kosinskaya, I.V. and G.P. Startsev. — Optika i Spektroskopiya, **18**:735. 1965.
621. Watanabe, K. — Adv. Geophys., **5**:153. 1958.
622. Cairns, R.B. and J.A.R. Samson. — Phys. Rev., **139**:1403. 1965.
623. Samson, J.A.R. and R.B. Cairns. — Bull. Amer. Phys. Soc., **10**:178. 1965.
624. Watanabe, K. and F.F. Marmo. — J. Chem. Phys., **25**:965. 1956.

625. Hinteregger, H. E. Effects of Solar XUV-Radiation on the Earth's Atmosphere, COSPAR Intern. Conference, VIII, London. 1967. (Preprint).
626. Seaton, M. J. — J. Atmosph. and Terr. Phys., **8**:122. 1956.
627. Ivanov-Kholodnyi, G. S. — Doklady ANSSSR, **170**:831. 1966.
628. Havens, R. J., H. Friedman, and E. O. Hulburt. — The Physics of the Ionosphere, p. 237, Phys. Soc., London. 1955.
629. Hertzberg, M. — J. Geophys. Res., **63**:856. 1958.
630. Hertzberg, M. — J. Atmosph. and Terr. Phys., **20**:177. 1961.
631. Yonezawa, T., H. Takahashi, and Y. Arima. — J. Radio Res. Labs., **6**:21. 1959.
632. Bates, D. R. and M. Nicolet. — J. Atmosph. and Terr. Phys., **18**:65. 1960.
633. Danilov, A. D. — Iskustv. Sputniki Zemli, No. 5, 60. 1960; No. 7, 56. 1961; No. 8, 72. 1961.
634. Danilov, A. D. — Doklady ANSSSR, **137**:1098. 1961.
635. Danilov, A. D. — Kosmich. issled., **2**:865. 1964.
636. Whitten, R. C. and I. G. Poppoff. — Discuss. Farad. Soc., No. 37, 185. 1964.
637. Ferguson, E. E., F. C. Fehsenfeld, P. D. Goldan, and A. L. Schmeltekopf. — J. Geophys. Res., **70**:4323. 1965.
638. Mitra, A. P. and N. R. Mitra. — J. Inst. Telecommun. Engrs., **12**:227. 1966.
639. Danilov, A. D. — Doklady ANSSSR, **169**:332. 1966.
640. Lytle, E. A. and D. M. Hunten. — Canad. J. Phys., **40**:1370. 1962.
641. Fite, W. L., J. A. Rutherford, W. R. Snow, and V. A. J. van Lint. — Discuss. Farad. Soc., No. 33, 264. 1962.
642. Ferguson, E. E., F. C. Fehsenfeld, and A. L. Schmeltekopf. — Space Res., **7**:135. 1967; Rev. Geophys., **5**:305. 1967.
643. Kaneko, Y., L. R. Megill, and J. B. Hasted. — J. Chem. Phys., **45**:3741. 1966.
644. Paulson, J. F., R. L. Mosher, and F. Dale. — Bull. Amer. Phys. Soc., **11**:733. 1966.
645. Schmeltekopf, A. L., F. C. Fehsenfeld, G. I. Gilman, and E. E. Ferguson. — Bull. Amer. Phys. Soc., **11**:505. 1966; Planet. and Space Sci., **15**:401. 1967.
646. Megill, L. R., D. K. Bohme, P. P. Ong, and J. B. Hasted. — Trans. Amer. Geophys. Union, **48**:64. 1967; Planet and Space Sci., **15**:1777. 1967.
647. Sayers, J. and D. Smith. — Discuss. Farad. Soc., No. 37, 185. 1964.
648. Stubbe, P. — In: "Electron Density Profiles in Ionosphere and Exosphere," p. 249, Pergamon Press. 1966.
649. van Zandt, T. E., R. B. Norton, and G. H. Stonehocke. — J. Geophys. Res., **65**:2003. 1960.
650. Ratcliffe, J. A. — J. Atmosph. and Terr. Phys., **8**:260. 1959.
651. Danilov, A. D. — Iskustv. Sputniki Zemli, No. 15, 38. 1963.
652. Oya, H. and T. Obayashi. — Rept. Ionosphere Space Res. Japan, **21**:9. 1967.
653. Rishbeth, H. — Proc. IEEE, **55**:16. 1967.
654. Shchepkin, L. A. — Geomagn. i Aeronomiya, **7**:532. 1967.
655. Krassovsky, V. I., Yu. L. Truttre, and N. N. Shefov. — Space Res., **5**:43. 1965.

656. Kazantsev, A.N. — *Izvestiya ANSSSR, Otd. Tekhnicheskikh Nauk*, No. 4, 3. 1938.
657. Appleton, E.V. and R. Naismith. — *Proc. Phys. Soc.*, 52:402. 1940.
658. Kryuchkov, S.I. — *Izvestiya ANSSSR, Seriya Geograf. i Geofiz.*, No. 1, 125. 1940.
659. Papaleksi, N.D. — *Ibid.*, *Seriya Fizich.*, 10:237. 1946.
660. Krassovsky, V.I. — *Planet. and Space Sci.*, 1:14. 1959.
661. Brandt, J.C. and J.W. Chamberlain. — *Astrophys. J.*, 130:670. 1959.
662. Chamberlain, J.W. and C. Sagan. — *Planet. and Space Sci.*, 2:157. 1960.
663. Krassovsky, V.I., I.S. Shklovskii, Yu.I. Gal'perin, and E.M. Svetlitskii. — *Doklady ANSSSR*, 127:78. 1959.
664. Krassovsky, V.I., I.S. Shklovskii, Yu.I. Gal'perin, and E.M. Svetlitskii. — *Ibid.*, *Seriya Geofiz.*, No. 8, 1157. 1959.
665. Pletnev, V.D. — *Ibid.*, *Seriya Geofiz.*, No. 8, 1164. 1959.
666. Mustel', E.R. — *Priroda*, No. 7, 13. 1967.
667. Krassovsky, V.I., Yu.M. Kushnir, and G.A. Bordovskii. — *Uspekhi Fizicheskikh Nauk*, 64:425. 1958.
668. Krassovsky, V.I. — *Priroda*, No. 5, 55. 1957.
669. Zevakina, R.A. — *Izvestiya ANSSSR, Seriya Geofiz.*, No. 2, 304. 1959.
670. Gregory, J.B. — *J. Geophys. Res.*, 63:273. 1958.
671. Nestorov, G. — *Proc. Bulgarian Academy of Sciences*, 14:579. 1961.
672. Cumme, G., B. Knuth, and Chr.-U. Wagner. *Schriftenreihe des Nationalkomitee für Geodäsie und Geophysik, Reihe II, Heft I*, pp. 99–138. 1966.
673. Shimazaki, T. — *J. Radio Res. Labs. Japan*, 7:95. 1960.
674. Shimazaki, T. — *Nature*, 205:889. 1965.
675. Noci, G. — *Nature*, 199:968. 1963.
676. Danilov, A.D. and G.S. Ivanov-Kholodnyi. — *Geomagn. i Aeronomiya*, 3:850. 1963.
677. Whitehead, J.D. — *Space Res.*, 7:89. 1967.
678. Swider, Jr., W. — *Trans. Amer. Geophys. Union*, 48:65. 1967.
679. Hines, C.O. — *Radio Sci.*, 1:250. 1966.
680. Cole, K.D. and R.B. Norton. — *Radio Sci.*, 1:235. 1966.
681. Ivanov-Kholodnyi, G.S. and V.I. Lazarev. — *Geomagn. i Aeronomiya*, 6:397. 1966.
682. Reid, G.C. — *Proc. Sympos. High Latitude Particles and Ionosphere*, p. 221. 1965.
683. Thomas, L. — *J. Atmosph. and Terr. Phys.*, 24:643. 1962.
684. Thomas, L. — *Proc. Intern. Conf. Ionosphere*, p. 203. 1963.
685. Angerami, J.J. and J.O. Thomas. — *J. Geophys. Res.*, 69:4537. 1964.
686. Thomas, L. — *J. Geophys. Res.*, 71:1357. 1966.
687. Banks, P.M. — *Planet. and Space Sci.*, 15:77. 1967; *J. Geophys. Res.*, 72:3365. 1967.
688. Yonezawa, T. — *J. Radio Res. Labs. Japan*, 3:1. 1956; 5:165. 1958.

689. Yonezawa, T. — *J. Atmosph. and Terr. Phys.*, **15**:89. 1959.
690. Yonezawa, T. — In: "Electron Density Profiles in the Ionosphere and Exosphere, edited by B. Maehlbium. New York, Pergamon Press. 1962.
691. Dungey, J.W. — *J. Atmosph. and Terr. Phys.*, **9**:90. 1956.
692. Martyn, D.F. — *Austral. J. Phys.*, **9**:161. 1956.
693. Gliddon, J.E.C. and P.C.Kendall. — *J. Atmosph. and Terr. Phys.*, **18**:48. 1960; **20**:183. 1961.
694. Gliddon, J.E.C. and P.C.Kendall. — *J. Atmosph. and Terr. Phys.*, **24**:1073. 1962.
695. Gliddon, J.E.C. — *Planet. and Space Sci.*, **9**:815. 1962.
696. Ferraro, V.C.A. and I. Özdoğan. — *J. Atmosph. and Terr. Phys.*, **12**:140. 1958.
697. Ferraro, V.C.A. — *Ann. géophys.*, **17**:82. 1961.
698. Bowhill, S.A. — *J. Atmosph. and Terr. Phys.*, **24**:503. 1962.
699. Nisbet, J.S. — *J. Geophys. Res.*, **68**:6099. 1963.
700. Shmelovskii, K.Kh. — *Geomagn. i Aeronomiya*, **3**:204. 1963.
701. Rishbeth, H. and D.W.Barron. — *J. Atmosph. and Terr. Phys.*, **18**:234. 1960.
702. Briggs, B.H. and H.Rishbeth. — *Proc. Phys. Soc.*, **78**:409. 1961.
703. Rishbeth, H. — *Proc. Phys. Soc.*, **81**:65. 1963; *J. Atmosph. and Terr. Phys.*, **26**:657. 1964.
704. Polyakov, V.M. — *Geomagn. i Aeronomiya*, **6**:341. 1966; **7**:183. 1967.
705. Polyakov, V.M. — In: "Rezultaty nabl. i issled. v period MGSS," No. 2, pp. 16 and 38. 1966.
706. Polyakov, V.M. — In: "Ionosfernye issledovaniya," No. 16, 6. "Nauka." 1968.
707. Geisler, J.E. and A.S.Bowhill. — *Aeronomy Report No. 5*. 1965.
708. Johnson, F.S. — In: "Electron Density Profiles in the Ionosphere and Exosphere, edited by B. Maehlbium. New York, Pergamon Press. 1962.
709. Ivanov-Kholodny, G.S. — *Space Res.*, **4**:525. 1964.
710. Kazachevskaya, T.V. — *Geomagn. i Aeronomiya*, **7**:1096. 1967.
711. Martyn, D.F. — *Philos. Trans. Roy. Soc.*, **A246**:306, London. 1953.
712. Martyn, D.F. — *Phys. Soc. Rept. Ionosphere Conf.*, pp. 254, 260. 1955.
713. Martyn, D.F. — *Proc. IRE*, **47**:147. 1959.
714. Mariani, F. — *J. Atmosph. Sci.*, **20**:479. 1963.
715. Yonezawa, T. — *J. Radio Res. Labs.*, **12**:65, Japan. 1965; *Space Sci. Rev.*, **5**:3. 1966.
716. Polyakov, V.M. and T.B.Shchukina. — In: "Rezultaty nabl. i issled. v period MGSS," No. 2, 30. 1966.
717. Baxter, R.G., P.C.Kendall, and D.W.Windle. — *J. Atmosph. and Terr. Phys.*, **27**:1263. 1965.
718. Baxter, R.G. — *Planet. and Space Sci.*, **15**:701. 1967.
719. LeLevier, R.E. and L.M.Branscomb. — *J. Geophys. Res.*, **73**:27. 1968.
720. Bourne, I.A., C.S.G.Setty, and R.A.Smith. — *J. Inst. Telecom. Engrs.*, **10**:341. 1964.
721. Swider, Jr., W. — *Planet. and Space Sci.*, **12**:761. 1964.
722. Reidy, W.P., G.S.Vaiana, T.Zehnpfennig, and R.Giacconi. — *Astrophys. J.*, **151**:333. 1968.
723. Neupert, W.M., W.Gates, M.Swartz, and R.Young. — *Astrophys. J.*, **149**, Part. 2, 79. 1967.



724. Evans, K., K. A. Pounds, and J. L. Culhane. — *Nature*, **214**:41. 1967.
725. Walker, A. B. C. and N. R. Ruge. — *Astron. J.*, **72**:835. 1967.
726. Fritz, G., R. W. Kreplin, J. E. Meekins, A. E. Unzicker, and H. Friedman. — *Astrophys. J.*, **148**, Part. 2, 133. 1967.
727. Manson, J. E. — *Space Res.*, **7/2**:1250. 1967.
728. Watts, R. N. — *Sky and Telescopes*, **35**:80. 1968.
729. Vasil'ev, B. N., I. A. Zhitnik, V. V. Korneev, V. V. Krutov, S. L. Mandel'shtam, I. P. Tindo, G. S. Cheremykhin, and A. I. Shurygin. — *Kosmich. Issled.*, **6**:420. 1968.
730. Lambert, D. L. — *Observatory*, **87**:228. 1967.
731. Beigman, I. and L. Vainstein. — *Astrophys. Lett.*, **1**:33. 1968.
732. Reidy, W. P., G. S. Vaiana, T. Zehnpfennig, R. Giacconi, S. van Broek. *Science*.
733. Warner, B. *Monthly Not. R. A. S.*, **138**:229. 1968.
734. Kazachevskaya, T. V. *Kosmich. Issled.*, **7**, No. 6. 1969.
735. Asundi, R. K., J. D. Craggs, and M. V. Kurepa. *Proc. Phys. Soc.*, **82**:967. 1963.
736. Swider, W. — *Trans. Amer. Geophys. Union*, **47**:77. 1966.
737. Swider, W. — *Proc. Conf. "Ground-Based Radio-Wave Propagation Studies of the Lower Ionosphere,"* p. 29, Canada. 1967.
738. Stebbings, R. F., B. R. Turner, and J. A. Rutherford. — *J. Geophys. Res.*, **71**:771. 1966.
739. Smith, D. and R. A. Fouracre. — *Planet and Space Sci.*, **16**:243. 1968.
740. Dalgarno, A. — *Space Res.*, **7**:849. 1967.
741. Korsunova, L. P. — *Geonagn. i Aeronomiya*, **9**:6. 1969.
742. Mehr, F. J. and M. A. Biondi. — *Bull. Amer. Phys. Soc.*, **13**:199. 1968.
743. Smith, D. and C. V. Goodall. — *Planet. and Space Sci.*, **16**:1177. 1968.
744. Coffey, D. M. and R. L. Taylor. — *Bull. Amer. Phys. Soc.*, **13**:222. 1968.
745. Frost, D. C., C. A. McDowell, and D. A. Vroom. — *Nature*, **218**:943. 1968.
746. Johnsen, R. and M. A. Biondi. — *Bull. Amer. Phys. Soc.*, **13**:613. 1968.
747. Ferguson, E. E., D. B. Dunkin, F. C. Fehsenfeld, and A. L. Schmeltekopf. — *Bull. Amer. Phys. Soc.*, **13**:212. 1968.
748. Swider, Jr., W. — *Trans. Amer. Geophys. Union*, **49**:141. 1968.
749. Swider, Jr., W. — *Nature*, **217**:438. 1968.
750. Reidy, W. P., E. R. Hegblom, and J. C. Ulwick. — *J. Geophys. Res.*, **73**:3072. 1968; *Trans. Am. Geophys. Union*, **49**:154. 1968; *Ann. Geophys.*, **24**:649. 1968.
751. Narcisi, R. S., A. D. Bailey, and L. D. Lucca. — *Trans. Amer. Geophys. Union*, **49**:149. 1968.
752. Narcisi, R. S., C. R. Philbrick, A. D. Bailey, and L. D. Lucca. "Review of Data, Sunrise and Sunset Ion Composition of the D Region." *The Third Aeronomy Conference, Urbana, Illinois, Sept. 1968 (Preprint).*

753. Narcisi, R. S., A. D. Bailey, and L. D. Lucca. "Positive Ion Composition Measurements in the Lower Ionosphere During the 12 November 1966 Solar Eclipse." The Third Aeronomy Conference, Urbana, Illinois. Sept. 1968 (Preprint).
754. Polyakov, V. M., L. A. Shchepkin, E. S. Kazimirovskii, and V. D. Kokourov. — In: "Ionosfernye protsessy." "Nauka," Sibirskoe Otdelenie, Novosibirsk. 1968.
755. Mentzoni, M. H. and J. Donohoe. — Bull. Am. Phys. Soc., **12**:218. 1967; Canad. J. Phys., **45**:1565. 1967.
756. Warneck, P. — J. Geophys. Res., **72**:1651. 1967; Planet. and Space Sci., **15**:1349. 1967.
757. Ivanov-Kholodnyi, G. S. — In: "Fizika magnitosfery i polyarnye buri" (Trudy Letnei Shkoly Kosmofizikov), p. 171, Irkutsk. 1968.
758. Smith, L. G. — In: "Aeronomy Report," No. 1, 169, Urbana, Illinois. 1963.
759. Rishbeth, H. — Rev. Geophys., **6**:33. 1968.
760. Titheridge, J. E. — J. Atmosph. and Terr. Phys., **30**:1857. 1968.
761. Willmore, A. P. — In: "Progr. Radio Sci. 1963—1966," Part 1, 957. 1967.
762. Baxter, R. G. and P. C. Kendall. — Proc. Roy. Soc., **304**:171. 1968.
763. Stubbe, P. — J. Atmosph. and Terr. Phys., **30**:243. 1968.
764. Thomas, G. R. and F. H. VENABLES. — J. Atmosph. and Terr. Phys., **29**:621. 1967; **30**:1429. 1968.
765. Tuan, T. F. — Proc. Phys. Soc., **B1**:966. 1968.
766. Banks, P. M. and T. E. Holzer. — Planet. and Space Sci., **16**:1019. 1968.
767. Bhatnagar, V. P. "Nocturnal Ion Composition in the Height Range of 200—1000 km for Solar Minimum Condition." 1968 (Preprint).
768. Colin, L. and S. W. Dufour. — J. Geophys. Res., **73**:2967. 1968.
769. Herman, J. R. and S. Chandra. — Trans. Amer. Geophys. Union, **49**:144. 1968.
770. Mayr, H. G., L. H. Brace, and G. S. Dunham. — J. Geophys. Res., **72**:4391. 1967.
771. Mayr, H. G. and H. E. Volland. — Trans. Amer. Geophys. Union, **49**:139. 1968; J. Geophys. Res., **73**:4851. 1968.
772. Bailey, G. J., R. J. Moffett, and H. Rishbeth. — J. Atmosph. and Terr. Phys., **31**:253. 1969.
773. Abur-robb, M. F. K. and D. W. Windle. — Planet. and Space Sci., **17**:97. 1969.
774. Kendall, P. C. and D. W. Windle. — Geophys. J. Roy. Astron. Soc., **15**:147. 1968.
775. Rishbeth, H. — J. Atmosph. and Terr. Phys., **29**:225. 1967; **30**:63. 1968.
776. Kohl, H., J. W. King, and D. Eccles. — J. Atmosph. and Terr. Phys., **30**:1733. 1968.
777. Sato, T. — J. Geophys. Res., **73**:127. 1968.
778. Nisbet, J. S. — J. Atmosph. and Terr. Phys., **30**:1257. 1968.
779. Cumack, C. H. — J. Atmosph. and Terr. Phys., **29**:811. 1967; **30**:125. 1968.
780. Schmelovsky, K. H. — Space Sci. Rev., **8**:74. 1968.
781. Titheridge, J. E. — J. Atmosph. and Terr. Phys., **30**:1843. 1968.

782. Cole, K.D. — Planet. and Space Sci., **16**:525. 1968.
783. Bauer, S.J. and B.V.Krishnamurthy. — Planet. and Space Sci., **16**:653. 1968.
784. Chandra, S. and B.V.Krishnamurthy. — J.Atmosph. and Terr. Phys., **30**:47. 1968.
785. Chandra, S. and B.V.Krishnamurthy. — Planet. and Space Sci., **16**:231. 1968.
786. Chapman, J.H. and E.S.Warren. — Space Sci.Rev., **8**:846. 1968.
787. Evans, J.V. — J.Geophys.Res., **73**:3489. 1968.
788. Harris, K.K., G.W.Sharp, and W.C.Knudsen. — J.Geophys.Res., **72**:5939. 1967.
789. Hoffman, J.H. — Trans.Amer.Geophys.Union, **49**:253. 1968.
790. Klobuchar, J.A., J.Aarons, and H.H.Hosseinieh. — J.Geophys. Res., **73**:7530. 1968.
791. McInnes, B.A. — J.Geophys.Res., **73**:5603. 1968.
792. Taylor, Jr.H.A., H.C.Brinton, M.W.Pharo III, and N.K.Rahman. — J.Geophys.Res., **73**:5521. 1968.
793. Shimazaki, T. and A.R.Laird. — J.Geophys.Res., **73**:7399. 1968.
794. Smith, III, F.L. — J.Geophys.Res., **73**:7385. 1968.
795. Brinton, H.C., R.A.Pickett, and H.A.Taylor, Jr. — Trans. Amer.Geophys.Union, **49**:144. 1968.
796. Anastassiades, M. and G.Moraitis. — J.Atmosph. and Terr. Phys., **30**:1471. 1968.
797. Evans, J.V. and G.P.Mantas. — J.Atmosph. and Terr. Phys., **30**:563. 1968.
798. Yoh, P. — J.Geophys.Res. **73**:253. 1968.
799. Brown, W.E., W.R.Steiger, and F.E.Roach. — Nature, **220**:568. 1968.
800. Carru, H., M.Petit, G.Vasseur, and P.Waldteufel. — Ann. géophys., **23**:455. 1967.
801. Doupnik, J.R. and J.S.Nisbet. — J.Atmosph. and Terr. Phys., **30**:931. 1968.
802. Aikin, A.C. and L.J.Blumle. — J.Geophys.Res., **73**:1617. 1968.
803. Bardsley, J.N. — Proc.Phys.Soc., **B1**:365. 1968.
804. Evans, D.S. — J.Geophys.Res., **73**:2315. 1968.
805. Ogilvie, K.W. — J.Geophys.Res., **73**:2335. 1968.
806. Evans, W.F.J., D.M.Hunten, E.J.Llewellyn, and A.Val-lance Jones. — J.Geophys.Res., **73**:2885. 1968.
807. Garriott, O.K., A.V.da Rosa, M.J.Davis, and O.G.Vil-lard, Jr. — J.Geophys.Res., **72**:6099. 1967.
808. Krankowsky, D., W.T.Kasprzak, and A.O.Nier. — J.Geophys. Res., **73**:7291. 1968.
809. Mechtly, E.A. and J.S.Shirke. — J.Geophys.Res., **73**:6243. 1968.
810. Walker, J.C.G., L.H.Brace, and M.H.Rees. — J.Geophys.Res., **73**:7285. 1968.

National Aeronautics and Space Administration

WASHINGTON, D. C. 20546

OFFICIAL BUSINESS

Penalty For Private Use, \$300.00



POSTAGE AND FEES PAID  
NATIONAL AERONAUTICS AND  
SPACE ADMINISTRATION

006 001 C3 U 13 720328 500903DS  
DEPT OF THE AIR FORCE  
AF WEAPONS LAB (AFSC)  
TECH LIBRARY/WLOL/  
ATTN: E LOU BOWMAN, CHIEF  
KIRTLAND AFB NM 87117